

**LIBRARY
Michigan State
University**

PLACE IN RETURN BOX to remove this checkout from your record.
TO AVOID FINES return on or before date due.

DATE DUE	DATE DUE	DATE DUE
_____	_____	_____
_____	_____	_____
_____	_____	_____
_____	_____	_____
_____	_____	_____
_____	_____	_____
_____	_____	_____

MSU is An Affirmative Action/Equal Opportunity Institution
c:\circ\d\date due.pn3-p.1

**MOLTEN ALKALI METAL POLYCHALCOGENIDE AND
POLYCHALCOPHOSPHATE SALT SYNTHESIS OF TERNARY
AND QUATERNARY CHALCOGENIDES**

By

Timothy J. McCarthy

A DISSERTATION

**Submitted to
Michigan State University
in partial fulfillment of the requirements
for the degree of**

DOCTOR OF PHILOSOPHY

Department of Chemistry

1994

ABSTRACT

MOLTEN ALKALI METAL POLYCHALCOGENIDE AND POLYCHALCOPHOSPHATE SALT SYNTHESIS OF TERNARY AND QUATERNARY CHALCOGENIDES

By

Timothy J. McCarthy

Using the now proven alkali metal polychalcogenide flux technique, we decided to explore the chemistry of two Group 15 main group metals, antimony and bismuth. We have isolated a number of interesting compounds with novel structural architectures such as β -CsBiS₂, γ -CsBiS₂, K₂BiSe₁₃, KBi₃S₅, Cs₂Sb₄S₈, and CsSbS₆. γ -CsBiS₂ and K₂BiSe₁₃ are potential candidates for thermoelectric cooling applications. Thermal analysis studies were conducted to probe the mechanism of compound formation and the stability of these phases. In addition, high temperature reactions with K₂S and Bi₂S₃ have resulted in the synthesis of KBi_{6.33}S₁₀ and K₂Bi₈S₁₃ with interesting semi-metallic electrical conductivity and thermoelectric power.

We utilized our experience with alkali polychalcogenide fluxes to develop a general methodology by which new

thio(seleno)phosphate (or chalcophosphate) compounds can be consistently obtained. These *polychalcophosphate* fluxes, $A_x[P_yQ_z]$, provide highly charged $[P_xQ_y]^{n-}$ anions that coordinate to the M^{n+} center. Using $[P_2S_7]^{4-}$, $[PS_4]^{3-}$, and $[P_2S_6]^{4-}$ anions as building blocks, we synthesized several quaternary compounds with bismuth and antimony metals, $ABiP_2S_7$ ($A=K,Rb$), $A_3M(PS_4)_2$ ($A=K,Rb,Cs$; $M=Sb,Bi$), $Cs_3Bi_2(PS_4)_3$, and $Na_{0.16}Bi_{1.28}P_2S_6$. Further exploration using alkali metal polyselenophosphate fluxes has allowed us to investigate the coordination chemistry of the $[P_2Se_6]^{4-}$ ligand with metals such as Sb, Bi, Mn, Fe, Cu, Ag, and Au. These reactions have resulted in the formation of a variety of new quaternary compounds including KMP_2Se_6 ($M=Sb,Bi$), $Cs_8M_4(P_2Se_6)_5$ ($M=Sb,Bi$), $A_2M'P_2Se_6$ ($A=K,Rb,Cs$; $M'=Mn,Fe$), $A_2M''P_2Se_6$ ($A=K,Rb,Cs$; $M'=Cu,Ag$), and $K_4Au_2(P_2Se_6)_2$ with novel structure types. Several of these $[P_2Se_6]^{4-}$ containing compounds possess band gaps that are potentially attractive for solar cell applications.

In this dissertation, the synthesis, characterization and properties of the above compounds will be discussed.

Dedicated to
Helen McCarthy
1906-1994

ACKNOWLEDGMENTS

None of the work described in this dissertation would have been possible without the enthusiasm, patience, guidance and support of my research advisor, Professor Mercouri G. Kanatzidis.

I would also like to thank Professor Younbong Park for assisting me in the development of my synthetic methodology, Dr. Sandeep Dhingra for his helpful suggestions and support, and Dr. Ju-Hsiou Liao for his helpful discussions concerning X-ray crystallography. All three set a superior example of what is expected of a Kanatzidis group member. I would also like to thank the rest of the Kanatzidis group for providing an enjoyable and stimulating research environment.

I also thank Professor Kannevurf and his research group at Northwestern University for charge transport measurements, Professor Stanley-Pierre Ngeyi (Madonna University) for help with calorimetric measurements, Professor Jerry Cowen for his helpful comments concerning magnetic susceptibility measurements, and Dr. Don Ward for helpful discussions on single crystal X-ray diffraction studies. I would also like to thank Troy Tanzer (REU Summer Program in Solid State Chemistry) for his help with the ion-exchange reactions and high temperature syntheses.

Most importantly I extend by deepest gratitude to my parents, Joseph and Kathleen McCarthy, for their love and support over the years. Their sacrifices for my benefit have been limitless. The only way I can repay them is by completion of this dissertation.

Financial support given by the Herbert T. Graham Fellowship (1989-1992) at the Department of Chemistry at Michigan State University, the National Science Foundation, and the Center for Fundamental Materials Research is greatly appreciated.

TABLE OF CONTENTS

List of Tables.....	xiv
List of Figures.....	xxi
 I . Introduction.....	 1
1. A Review of Antimony and Bismuth Chalcogenides.....	2
2. A Review of Metal Thio(seleno)phosphates.....	25
3. Alkali Metal Polychalcogenide Fluxes.....	48
 II . Molten Salt Synthesis and Properties of Three New Solid State Ternary Bismuth Chalcogenides, β -CsBiS ₂ , γ -CsBiS ₂ and K ₂ Bi ₈ Se ₁₃ (Part 1).....	 67
1. Introduction.....	67
2. Experimental Section.....	69
2.1. Reagents.....	69
2.2. Synthesis.....	69
Cs ₂ S.....	69
K ₂ Se.....	70
β -CsBiS ₂ (I).....	70
γ -CsBiS ₂ (I I).....	71
K ₂ Bi ₈ Se ₁₃ (I I I).....	72
2.3. Physical Measurements.....	73
2.4. X-ray Crystallography.....	76
3. Results and Discussion.....	83
3.1. Synthesis and Spectroscopy.....	83

3.2. Description of Structures.....	85
Structure of β -CsBiS ₂ (I).....	85
Structure of K ₂ Bi ₈ Se ₁₃ (I I I).....	87
3.3. Thermal Analysis.....	97
3.4. Electrical Conductivity and Thermoelectric Power Measurements.....	103
3.5. UV-Visible-Near IR Spectroscopy.....	109
3.6. Conclusion.....	112
Synthesis, Structural Characterization, Ion-Exchange Properties and Reactivity of KBi ₃ S ₅ : A New Three-dimensional Sulfide With Large Tunnels (Part 2).....	
1. Introduction.....	116
2. Experimental Section.....	118
2.1. Reagents.....	118
2.2. Synthesis.....	119
K ₂ S.....	119
KBi ₃ S ₅	119
(H ₂ O)Bi ₃ S _{4.5} ·(S ₈) _{0.06}	119
β -RbBi ₃ S ₅	120
2.3. Physical Measurements.....	121
2.4. X-ray Crystallography.....	122
3. Results and Discussion.....	129
3.1. Synthesis and Spectroscopy.....	129
3.2. Description of Structure.....	132
Structure of KBi ₃ S ₅	132
3.3. Thermal Analysis.....	138

3.4. Ion-exchange Studies.....	140
3.5. Solid State Ion-exchange Reactions with Halide Salts.....	143
3.6. Conclusion.....	150
High Temperature Synthesis and Properties of KBi _{6.33} S ₁₀ and K ₂ Bi ₈ S ₁₃ (Part 3).....	153
1. Introduction.....	153
2. Experimental Section.....	155
2.1. Reagents.....	155
2.2. Synthesis.....	156
Bi ₂ S ₃	156
KBi _{6.33} S ₁₀ (I).....	156
K ₂ Bi ₈ S ₁₃ (I I).....	157
2.3. Physical Measurements.....	157
2.4. X-ray Crystallography.....	158
3. Results and Discussion.....	169
3.1. Synthesis and Spectroscopy.....	169
3.2. Description of Structures.....	173
Structure of KBi _{6.33} S ₁₀ (I).....	173
Structure of K ₂ Bi ₈ S ₁₃ (I I).....	175
3.3. Electrical Conductivity and Thermoelectric Power Measurements.....	185
3.4. Conclusion.....	189
III. Polysulfide Ligands in Solid State Antimony Compounds. Isolation and Structural Characterization of Cs ₂ S ₄ S ₈ and CsSbS ₆	192
1. Introduction.....	192

2. Experimental Section.....	193
2.1. Reagents.....	193
2.2. Synthesis.....	193
Cs ₂ Sb ₄ S ₈ (I).....	194
CsSbS ₆ (I I).....	194
2.3. Physical Measurements.....	195
2.4. X-ray Crystallography.....	195
3. Results and Discussion.....	201
3.1. Synthesis and Spectroscopy.....	201
3.2. Description of Structures.....	204
Structure of Cs ₂ Sb ₄ S ₈ (I).....	204
Structure of CsSbS ₆ (I I).....	205
3.3. Thermal Analysis.....	212
3.4. Conclusion.....	218
IV. New Quaternary Bismuth and Antimony Thiophosphates	
ABiP ₂ S ₇ (A=K,Rb), A ₃ M(PS ₄) ₂ , (A=K,Rb,Cs; M=Sb,Bi),	
Cs ₃ Bi ₂ (PS ₄) ₃ , and Na _{0.16} Bi _{1.28} P ₂ S ₆ in Molten Alkali	
Polythiophosphate Fluxes.....	221
1. Introduction.....	221
2. Experimental Section.....	224
2.1. Reagents.....	224
2.2. Synthesis.....	224
Na ₂ S.....	225
KBiP ₂ S ₇ (I).....	225
RbBiP ₂ S ₇ (I I).....	225
K ₃ Sb(PS ₄) ₂ (I I I).....	226
Rb ₃ Sb(PS ₄) ₂ (I V).....	226

$\text{Cs}_3\text{Sb}(\text{PS}_4)_2$ (V).....	227
$\text{K}_3\text{Bi}(\text{PS}_4)_2$ (V I).....	227
$\text{Rb}_3\text{Bi}(\text{PS}_4)_2$ (V II).....	227
$\text{Cs}_3\text{Bi}(\text{PS}_4)_2$ (V III).....	228
$\text{Cs}_3\text{Bi}_2(\text{PS}_4)_3$ (IX).....	228
$\text{Na}_{0.16}\text{Bi}_{1.28}\text{P}_2\text{S}_6$ (X).....	229
2.3. Physical Measurements.....	229
2.4. X-ray Crystallography.....	229
3. Results and Discussion.....	242
3.1. Synthesis, Spectroscopy, and Thermal Analysis.....	242
3.2. Description of Structures.....	252
Structure of KBiP_2S_7 (I).....	252
Structure of $\text{K}_3\text{Bi}(\text{PS}_4)_2$ (V I).....	254
Structure of $\text{Cs}_3\text{Bi}_2(\text{PS}_4)_3$ (IX).....	255
Structure of $\text{Na}_{0.16}\text{Bi}_{1.28}\text{P}_2\text{S}_6$ (X).....	257
3.3. Conclusions.....	274
V. Coordination Chemistry of $[\text{P}_2\text{Se}_6]^{4-}$ in Molten Alkali Metal Polyselenophosphate Fluxes. Isolation of KMP_2Se_6 and $\text{Cs}_8\text{M}_4(\text{P}_2\text{Se}_6)_5$ (M=Sb,Bi).....	278
1. Introduction.....	278
2. Experimental Section.....	280
2.1. Reagents.....	280
2.2. Synthesis.....	280
Cs_2Se	280
P_2Se_5	281
KBiP_2Se_6 (I).....	281
KSbP_2Se_6 (I I).....	281

$\text{Cs}_8\text{Sb}_4(\text{P}_2\text{Se}_6)_5$ (I I I).....	282
$\text{Cs}_8\text{Bi}_4(\text{P}_2\text{Se}_6)_5$ (I V).....	282
2.3. Physical Measurements.....	283
2.4. X-ray Crystallography.....	283
3. Results and Discussion.....	294
3.1. Synthesis, Spectroscopy, and Thermal Analysis.....	294
3.2. Description of Structures.....	298
Structure of KMP_2Se_6	298
Structure of $\text{Cs}_8\text{Sb}_4(\text{P}_2\text{Se}_6)_5$	299
3.3. Electrical Conductivity Measurements.....	317
3.4. Conclusions.....	319
VI. Synthesis in Molten Alkali Metal Polyselenophosphate Fluxes. A New Family of Transition Metal Selenophosphate Compounds. $\text{A}_2\text{MP}_2\text{Se}_6$ (A=K,Rb,Cs; M=Mn,Fe), $\text{A}_2\text{M}'_2\text{P}_2\text{Se}_6$ (A=K,Cs; M'=Cu,Ag) and $\text{K}_4\text{Au}_2(\text{P}_2\text{Se}_6)_2$	322
1. Introduction.....	322
2. Experimental Section.....	324
2.1. Reagents.....	324
2.2. Synthesis.....	325
Cs_2Se	325
Rb_2Se	325
P_2Se_5	325
$\text{K}_2\text{MnP}_2\text{Se}_6$ (I).....	325
$\text{Rb}_2\text{MnP}_2\text{Se}_6$ (I I).....	326
$\text{Cs}_2\text{MnP}_2\text{Se}_6$ (I I I).....	326
$\text{K}_2\text{FeP}_2\text{Se}_6$ (I V).....	327
$\text{Cs}_2\text{FeP}_2\text{Se}_6$ (V).....	327

$\text{Cs}_2\text{Cu}_2\text{P}_2\text{Se}_6$ (V I).....	328
$\text{K}_2\text{Ag}_2\text{P}_2\text{Se}_6$ (V II).....	328
$\text{Cs}_2\text{Ag}_2\text{P}_2\text{Se}_6$ (V III).....	328
$\text{K}_4\text{Au}_2(\text{P}_2\text{Se}_6)_2$ (I X).....	329
$\text{K}_2\text{Mn}_{0.5}\text{Fe}_{0.5}\text{P}_2\text{Se}_6$ (X).....	329
2.3. Physical Measurements.....	331
2.4. X-ray Crystallography.....	332
3. Results and Discussion.....	347
3.1. Synthesis, Spectroscopy, and Thermal Analysis.....	347
3.2. Description of Structures.....	359
Structure of $\text{A}_2\text{MP}_2\text{Se}_6$	359
Structure of $\text{Cs}_2\text{Cu}_2\text{P}_2\text{Se}_6$	365
Structure of $\text{Cs}_2\text{Ag}_2\text{P}_2\text{Se}_6$	366
Structure of $\text{K}_2\text{Ag}_2\text{P}_2\text{Se}_6$	368
Structure of $\text{K}_4\text{Au}_2(\text{P}_2\text{Se}_6)_2$	370
3.3. Magnetic Susceptibility Measurements.....	381
3.4. Conclusions.....	384

LIST OF TABLES

1-1.	Properties of Binary Group 15 Chalcogenides.....	4
1-2.	Properties of ASbTe ₂ Compounds.....	19
1-3.	Ternary Antimony Chalcogenide Compounds.....	24
1-4.	Magnetic Data for M ₂ P ₂ Q ₆ Compounds.....	33
1-5.	Optical Properties of Sn ₂ P ₂ Q ₆ and Pb ₂ P ₂ Q ₆	37
1-6.	Types of Thiophosphate Ligands.....	42
1-7.	Melting Points (°C) of Some Known Alkali Metal Polychalcogenides.....	49
2-1.	Calculated and Observed X-ray Powder Diffraction Patterns for β-CsBiS ₂	79
2-2.	Calculated and Observed X-ray Powder Diffraction Patterns for K ₂ Bi ₈ Se ₁₃	80
2-3.	Summary of Crystallographic Data and Structure Analysis for β-CsBiS ₂ and K ₂ Bi ₈ Se ₁₃	81
2-4.	Fractional Atomic Coordinates and B _{eq} Values for β-CsBiS ₂ with Estimated Standard Deviations in Parentheses.....	82
2-5.	Fractional Atomic Coordinates and B _{eq} Values for K ₂ Bi ₈ Se ₁₃ with Estimated Standard Deviations in Parentheses.....	82
2-6.	Selected Distances (Å) and Angles (deg) for β-CsBiS ₂ with Standard Deviations in Parentheses.....	95
2-7.	Comparison of Bond Distances (Å) and Angles (deg) in Selected Group 15 Sulfides (M=As,Sb,Bi).....	95
2-8.	Selected Distances (Å) and Angles (deg) in the	

	[Bi ₈ Se ₁₃] ²⁻ Framework with Standard Deviations in Parentheses.....	96
2-9.	Solid State Reactions of KBi ₃ S ₅ with Alkali Metal Halides.....	125
2-10.	Calculated and Observed X-ray Powder Diffraction Patterns for KBi ₃ S ₅	126
2-11.	Summary of Crystallographic Data and Structure Analysis for KBi ₃ S ₅	127
2-12.	Fractional Atomic Coordinates and Beq Values for KBi ₃ S ₅ with Estimated Standard Deviations in Parentheses.....	128
2-13.	Selected Distances (Å) and Angles (deg) for KBi ₃ S ₅ with Standard Deviations in Parentheses.....	137
2-14.	Calculated and Observed X-ray Powder Diffraction Patterns for KBi _{6.33} S ₁₀	162
2-15.	Calculated and Observed X-ray Powder Diffraction Patterns for K ₂ Bi ₈ S ₁₃	164
2-16.	Summary of Crystallographic Data and Structure Analysis for KBi _{6.33} S ₁₀ and K ₂ Bi ₈ S ₁₃	166
2-17.	Fractional Atomic Coordinates and Beq Values for KBi _{6.33} S ₁₀ with Estimated Standard Deviations in Parentheses.....	167
2-18.	Fractional Atomic Coordinates and Beq Values for K ₂ Bi ₈ S ₁₃ with Estimated Standard Deviations in Parentheses.....	168
2-19.	High Temperature K ₂ S/Bi ₂ S ₃ Reactions.....	171
2-20.	Selected Distances (Å) in KBi _{6.33} S ₁₀ with	

	Standard Deviations in Parentheses.....	181
2-21.	Selected Angles (deg) in $\text{KBi}_{6.33}\text{S}_{10}$ with Standard Deviations in Parentheses.....	182
2-22.	Selected Distances (Å) in $\text{K}_2\text{Bi}_8\text{S}_{13}$ with Standard Deviations in Parentheses.....	183
2-23.	Selected Angles (deg) in $\text{K}_2\text{Bi}_8\text{S}_{13}$ with Standard Deviations in Parentheses.....	184
3-1.	Calculated and Observed X-ray Powder Diffraction Patterns for $\text{Cs}_2\text{Sb}_4\text{S}_8$	197
3-2.	Calculated and Observed X-ray Powder Diffraction Patterns for CsSbS_6	198
3-3.	Summary of Crystallographic Data and Structure Analysis for $\text{Cs}_2\text{Sb}_4\text{S}_8$ and CsSbS_6	199
3-4.	Fractional Atomic Coordinates and B_{eq} Values for $\text{Cs}_2\text{Sb}_4\text{S}_8$ with Estimated Standard Deviations in Parentheses.....	200
3-5.	Fractional Atomic Coordinates and B_{eq} Values for CsSbS_6 with Estimated Standard Deviations in Parentheses.....	200
3-6.	Selected Distances (Å) and Angles (deg) for $\text{Cs}_2\text{Sb}_4\text{S}_8$ with Standard Deviations in Parentheses.....	210
3-7.	Selected Distances (Å) and Angles (deg) for CsSbS_6 with Standard Deviations in Parentheses.....	211
4-1.	Calculated and Observed X-ray Powder Diffraction Patterns for KBiP_2S_7	232
4-2.	Calculated and Observed X-ray Powder Diffraction Patterns for $\text{K}_3\text{Bi}(\text{PS}_4)_2$	234

4-3.	Calculated and Observed X-ray Powder Diffraction Patterns for $\text{Na}_{0.16}\text{Bi}_{1.28}\text{P}_2\text{S}_6$	235
4-4.	Crystallographic Data for I, VI, IX, and X.....	237
4-5.	Fractional Atomic Coordinates and B_{eq} Values for KBiP_2S_7 with Estimated Standard Deviations in Parentheses.....	239
4-6.	Fractional Atomic Coordinates and B_{eq} Values for $\text{K}_3\text{Bi}(\text{PS}_4)_2$ with Estimated Standard Deviations in Parentheses.....	239
4-7.	Fractional Atomic Coordinates and B_{eq} Values for $\text{Cs}_3\text{Bi}_2(\text{PS}_4)_3$ with Estimated Standard Deviations in Parentheses.....	240
4-8.	Fractional Atomic Coordinates and B_{eq} Values for $\text{Na}_{0.16}\text{Bi}_{1.28}\text{P}_2\text{S}_6$ with Estimated Standard Deviations in Parentheses.....	240
4-9.	Far-IR Spectra for (I-X).....	245
4-10.	Optical Band Gaps and Melting Point Data for (I-X).....	246
4-11.	Selected Distances (Å) and Angles (deg) for KBiP_2S_7 with Standard Deviations in Parentheses.....	269
4-12.	Selected Distances (Å) and Angles (deg) for $\text{K}_3\text{Bi}(\text{PS}_4)_2$ with Standard Deviations in Parentheses.....	270
4-13.	Selected Distances (Å) for $\text{Cs}_3\text{Bi}_2(\text{PS}_4)_3$ with Standard Deviations in Parentheses.....	271
4-14.	Selected Angles (deg) for $\text{K}_3\text{Bi}(\text{PS}_4)_2$ with Standard Deviations in Parentheses.....	272
4-15.	Selected Distances (Å) and Angles (deg) for $\text{Na}_{0.16}\text{Bi}_{1.28}\text{P}_2\text{S}_6$ with Standard Deviations in Parentheses.....	273

5-1.	Far-IR Data for KMP_2Se_6 and $\text{Cs}_8\text{M}_4(\text{P}_2\text{Se}_6)_5$	285
5-2.	Calculated and Observed X-ray Powder Diffraction Patterns for KBiP_2Se_6	286
5-3.	Calculated and Observed X-ray Powder Diffraction Patterns for $\text{Cs}_8\text{Sb}_4(\text{P}_2\text{Se}_6)_5$	288
5-4.	Calculated and Observed X-ray Powder Diffraction Patterns for $\text{Cs}_8\text{Bi}_4(\text{P}_2\text{Se}_6)_5$	289
5-5.	Crystallographic Data for KBiP_2Se_6 , $\text{Cs}_8\text{Sb}_4(\text{P}_2\text{Se}_6)_5$ and $\text{Cs}_8\text{Bi}_4(\text{P}_2\text{Se}_6)_5$	290
5-6.	Fractional Atomic Coordinates and B_{eq} Values for KBiP_2Se_6 with Estimated Standard Deviations in Parentheses.....	291
5-7.	Fractional Atomic Coordinates and B_{eq} Values for $\text{Cs}_8\text{Sb}_4(\text{P}_2\text{Se}_6)_5$ with Estimated Standard Deviations in Parentheses.....	292
5-8.	Fractional Atomic Coordinates and B_{eq} Values for $\text{Cs}_8\text{Bi}_4(\text{P}_2\text{Se}_6)_5$ with Estimated Standard Deviations in Parentheses.....	293
5-9.	Selected Distances (\AA) and Angles (deg) for KBiP_2Se_6 with Standard Deviations in Parentheses.....	312
5-10.	Selected Distances (\AA) for $\text{Cs}_8\text{M}_4(\text{P}_2\text{Se}_6)_5$ with Standard Deviations in Parentheses.....	313
5-11.	Selected Angles (deg) for $\text{Cs}_8\text{M}_4(\text{P}_2\text{Se}_6)_5$ with Standard Deviations in Parentheses.....	316
6-1.	Calculated and Observed X-ray Powder Diffraction Patterns for $\text{K}_2\text{MnP}_2\text{Se}_6$	334
6-2.	Calculated and Observed X-ray Powder Diffraction	

	Patterns for $\text{Cs}_2\text{MnP}_2\text{Se}_6$	335
6-3.	Calculated and Observed X-ray Powder Diffraction Patterns for $\text{K}_2\text{Ag}_2\text{P}_2\text{Se}_6$	336
6-4.	Calculated and Observed X-ray Powder Diffraction Patterns for $\text{Cs}_2\text{Ag}_2\text{P}_2\text{Se}_6$	338
6-5.	Calculated and Observed X-ray Powder Diffraction Patterns for $\text{Cs}_2\text{Cu}_2\text{P}_2\text{Se}_6$	339
6-6.	Calculated and Observed X-ray Powder Diffraction Patterns for $\text{K}_4\text{Au}_2(\text{P}_2\text{Se}_6)_2$	340
6-7.	Crystallographic Data for (I), (III), (IV), (VI), (VII), (VIII), and (IX).....	341
6-8.	Fractional Atomic Coordinates and B_{eq} Values for $\text{K}_2\text{MnP}_2\text{Se}_6$ with Estimated Standard Deviations in Parentheses.....	343
6-9.	Fractional Atomic Coordinates and B_{eq} Values for $\text{Cs}_2\text{MnP}_2\text{Se}_6$ with Estimated Standard Deviations in Parentheses.....	343
6-10.	Fractional Atomic Coordinates and B_{eq} Values for $\text{K}_2\text{FeP}_2\text{Se}_6$ with Estimated Standard Deviations in Parentheses.....	343
6-11.	Fractional Atomic Coordinates and B_{eq} Values for $\text{Cs}_2\text{Cu}_2\text{P}_2\text{Se}_6$ with Estimated Standard Deviations in Parentheses.....	344
6-12.	Fractional Atomic Coordinates and B_{eq} Values for $\text{K}_2\text{Ag}_2\text{P}_2\text{Se}_6$ with Estimated Standard Deviations in Parentheses.....	345
6-13.	Fractional Atomic Coordinates and B_{eq} Values for	

	Cs ₂ Ag ₂ P ₂ Se ₆ with Estimated Standard Deviations in Parentheses.....	346
6-14.	Fractional Atomic Coordinates and B _{eq} Values for K ₄ Au ₂ (P ₂ Se ₆) ₂ with Estimated Standard Deviations in Parentheses.....	346
6-15.	Far-IR Data (cm ⁻¹) for A ₂ MP ₂ Se ₆ , A ₂ M' ₂ P ₂ Se ₆ , and K ₄ Au ₂ (P ₂ Se ₆) ₂ Compounds.....	351
6-16.	Optical Band Gaps and Melting Point Data for A ₂ MP ₂ Se ₆ , A ₂ M' ₂ P ₂ Se ₆ , and K ₄ Au ₂ (P ₂ Se ₆) ₂	353
6-17.	Selected Distances (Å) and Angles (deg) for (I), (III), and (IV) with Standard Deviations in Parentheses.....	364
6-18.	Selected Distances (Å) and Angles (deg) for Cs ₂ Cu ₂ P ₂ Se ₆ with Standard Deviations in Parentheses.....	377
6-19.	Selected Distances (Å) and Angles (deg) for Cs ₂ Ag ₂ P ₂ Se ₆ with Standard Deviations in Parentheses.....	378
6-20.	Selected Distances (Å) and Angles (deg) for K ₂ Ag ₂ P ₂ Se ₆ with Standard Deviations in Parentheses.....	379
6-21.	Selected Distances (Å) and Angles (deg) for K ₄ Au ₂ (P ₂ Se ₆) ₂ with Standard Deviations in Parentheses.....	380
6-22.	Magnetic parameters for (I-IV).....	382

LIST OF FIGURES

1-1:	Projection of Bi_2Te_3 looking down the a-axis, with labeling.....	5
1-2:	(A) ORTEP representation of Sb_2S_3 viewed down the b-axis with labeling scheme. The long $\text{Sb}\cdots\text{S}$ contacts are highlighted by dashed lines. (B) A single infinite ribbon of Sb_2S_3	8
1-3:	Packing diagrams of (A) CsBi_3S_5 and (B) $\text{Cs}_3\text{Bi}_7\text{Se}_{12}$ looking down the b-axis. Shaded spheres represent S(Se) atoms and small open spheres designate Bi atoms.....	12
1-4:	Packing diagram of $\text{Sr}_4\text{Bi}_6\text{Se}_{13}$ and labeling scheme with a view down the b-axis.....	13
1-5:	(A) Packing diagram of SrBiSe_3 viewed down the c-axis. Dark spheres indicate Bi atoms and large open spheres are Se atoms. (B) Interacting $(\text{Se}_3)^{2-}$ anions with dashed lines representing close $\text{Se}\cdots\text{Se}$ contacts.....	14
1-6:	Packing diagram of BaBiSe_3 viewed down the c-axis. Dark spheres indicate Bi atoms and large open spheres are Se atoms. The square planar Se atoms are highlighted with the arrow.....	15
1-7:	Equilibrium phase diagram of the Bi_2S_3 - K_2S system.....	17
1-8:	Projection of $\text{Cs}_2\text{Sb}_8\text{S}_{13}$ viewed down the c-axis with labeling.....	22

1-9:	(A) Packing diagram of $\text{Pd}_3(\text{PS}_4)_2$ viewed down the a-axis with labeling. (B) ORTEP representation of a single $\text{Pd}_3(\text{PS}_4)_2$ layer.....	29
1-10:	(A) Schematic representation of $\text{Ni}_2\text{P}_2\text{S}_6$ viewed down the a-axis. (B) ORTEP representation of a single $\text{Ni}_2\text{P}_2\text{S}_6$ layer. The hexagonal Ni array is outlined with dashed lines.....	32
1-11:	(A) Packing diagram of RbVP_2S_7 viewed down the a-axis. (B) ORTEP representation of the $[\text{VP}_2\text{S}_7]_n^{n-}$ anionic layer with labeling.....	41
1-12:	A schematic representation of a single $\text{V}_2\text{P}_4\text{S}_{13}$ layer. The open spheres are S atoms and dark lines highlight the bonding in the $[\text{P}_4\text{S}_{13}]^{6-}$ ligand.....	45
1-13:	(A) One-dimensional structure of $[\text{AuSe}_5]_n^{n-}$. Au...Au contacts are indicated by dashed lines. (B) Structure of the $[\text{AuSe}_{13}]_n^{3n-}$ chain.....	53
1-14:	(A) A single anionic layer in NaAuSe_2 . (B) The one-dimensional chains in KAuSe_2	54
1-15:	ORTEP representation and labeling scheme of the layered structure of $[\text{Sn}_2\text{S}_8]_n^{2n-}$. The dashed lines indicate the shortest nonbonding Sn...S contacts (2.934(5) Å).....	55
1-16:	ORTEP representation and labeling scheme of $\text{K}_2\text{Au}_2\text{Sn}_2\text{S}_6$. View down the b-axis. Au...Au contacts are shown by dashed lines.....	56

2-1:	ORTEP representation of a single $(\text{BiS}_2)_n^{n-}$ chain with labeling scheme.....	90
2-2:	ORTEP packing diagrams of the $(\text{BiS}_2)_n^{n-}$ chains along the a-axis, (A) and b-axis, (B). Dashed lines in (A) indicate $\text{Bi}\cdots\text{S}$ contacts. The shaded ellipsoids are Bi atoms, and the Cs atoms are represented by open circles.....	91
2-3:	ORTEP representation of the packing diagram of $\text{K}_2\text{Bi}_8\text{Se}_{13}$ down the c-axis. The shaded ellipsoids are the Bi atoms, and the open ellipsoids are the K atoms.....	92
2-4:	Projections of the structures of (A) Bi_2Se_3 (Bi_2Te_3 -type) (B) Bi_2Se_3 (Sb_2S_3 -type) (C) CdI_2 -type and (D) $[\text{Bi}_8\text{Se}_{13}]^{2-}$ framework. The three structure types found in this framework are designated with dashed lines.....	93
2-5:	ORTEP representation of the Bi(4) coordination in $\text{K}_2\text{Bi}_8\text{Se}_{13}$. Dashed lines designate long contacts.....	94
2-6:	(A) DSC thermogram of the Bi/ Cs_2S_3 mixture. The cooling and reheating curves are shown above the heating thermogram for clarity (Peaks F and G). Peak temperatures ($^\circ\text{C}$): A (97), B (113), C (170), D (270), E (274), F (176) and G (180). (B) DSC thermogram of the $\text{Cs}_2\text{S}/\text{S}$ mixture. Peak temperatures ($^\circ\text{C}$): A (92), B (112), C (170) and H (178).....	101

2-7:	(A) DSC thermogram of the Bi/K ₂ Se ₉ mixture. Peak temperatures (°C): I (160), II (169), III (269) and IV (152). (B) DSC thermogram of the K ₂ Se/Se mixture. Peak temperatures (°C): I (161), II (170) and V (123).....	102
2-8:	Variable temperature electrical conductivity data for a single crystal of γ -CsBiS ₂	106
2-9:	Variable temperature electrical conductivity data for a pressed pellet of K ₂ Bi ₈ Se ₁₃	107
2-10:	Thermoelectric power of a polycrystalline aggregate of K ₂ Bi ₈ Se ₁₃ as a function of temperature.....	108
2-11:	(A) Optical absorption spectrum of β -CsBiS ₂ . (B) Optical absorption spectrum of γ -CsBiS ₂	110
2-12:	Optical absorption spectrum of K ₂ Bi ₈ Se ₁₃ . The absorption maximum occurs at 1.2 eV.....	111
2-13:	Optical absorption spectrum of KBi ₃ S ₅ . Inset shows the $(\alpha/S)^2$ vs. Energy plot.....	131
2-14:	The three-dimensional structure of KBi ₃ S ₅ viewed down the b-axis. The shaped ellipsoids are Bi atoms and the open circle represent K atoms.....	135
2-15:	(a) Polyhedral representation of the [Bi ₃ S ₅] _n ⁿ⁻ framework projected in the b-direction. The octahedra that line the tunnel are shaded. (b) Adapted polyhedral representation of the hollandite anion framework projected in the c-direction showing the 2x2 tunnel structure. ^{30c}	136
2-16:	DTA thermogram of KBi ₃ S ₅	139

2-17:	Comparison of the X-ray powder diffraction patterns of: (a) KBi_3S_5 with selected h0l peaks labeled. (b) $(\text{H}_2\text{O})\text{Bi}_3\text{S}_{4.5}(\text{S}_8)_{0.06}$ and (c) Bi_2S_3	145
2-18:	SEM photographs of: (a) KBi_3S_5 before and (b) after reaction with aqueous HCl (66 hours). The white bar at the bottom of the micrographs represents a $10\mu\text{m}$ scale. The magnification is x1600.....	146
2-19:	(a) Thermogravimetric analysis plot of $(\text{H}_2\text{O})\text{Bi}_3\text{S}_{4.5}(\text{S}_8)_{0.06}$ with weight % plotted against temperature ($^{\circ}\text{C}$). Performed under flowing N_2 . Step I (3.82% weight loss starting at 140°C .) Step II (3.84% weight loss starting at 176°C). (b) DSC thermogram of $(\text{H}_2\text{O})\text{Bi}_3\text{S}_{4.5}(\text{S}_8)_{0.06}$	148
2-20:	Powder XRD pattern of $(\text{H}_2\text{O})\text{Bi}_3\text{S}_{4.5}(\text{S}_8)_{0.06}$ measured as a function of temperature. The transformation to Bi_2S_3 is complete at 124°C	149
2-21:	Mid-IR diffuse reflectance spectra of (a) $\text{KBi}_{6.33}\text{S}_{10}$ and (b) $\text{K}_2\text{Bi}_8\text{S}_{13}$	172
2-22:	ORTEP representation of the packing diagram of $\text{KBi}_{6.33}\text{S}_{10}$ down the b-axis with labeling.....	178
2-23:	Projections of the structures of (A) Bi_2Te_3 (B) CdI_2 and (C) $[\text{Bi}_{6.33}\text{S}_{10}]^-$ framework. Both structure types found in this framework are designated with dashed lines.....	179
2-24:	ORTEP representation of the packing diagram	

	of $\text{K}_2\text{Bi}_8\text{S}_{13}$ down the b-axis with labeling.....	180
2-25:	Variable temperature electrical conductivity data for polycrystalline chunks of: (a) $\text{KBi}_{6.33}\text{S}_{10}$ and (b) $\text{K}_2\text{Bi}_8\text{S}_{13}$	187
2-26:	Thermoelectric power as a function of temperature for polycrystalline chunks of: (a) $\text{KBi}_{6.33}\text{S}_{10}$ and (b) $\text{K}_2\text{Bi}_8\text{S}_{13}$	188
3-1:	(A) Optical absorption spectrum of $\text{Cs}_2\text{Sb}_4\text{S}_8$. (B) Optical absorption spectrum of CsSbS_6	203
3-2:	Two-dimensional structure of the $[\text{Sb}_4\text{S}_8]_n^{n-}$ anionic framework with labeling as drawn by ORTEP. The dashed lines represent Sb-S long interactions in the range of 3.022(2) to 3.277(2) Å. The shaded area outlines the 14-membered Sb/S rings in the structure.....	207
3-3:	(A) Stereoview of $\text{Cs}_2\text{Sb}_4\text{S}_8$ viewed down the [001] direction. (B) Packing diagram of $\text{Cs}_2\text{Sb}_4\text{S}_8$ showing a projection in the [100] direction. The dashed lines represent long Sb-S interactions underscoring the pseudo-3D character of the structure. The shaded ellipsoids are Sb atoms and the open ellipsoids are Cs atoms.....	208
3-4:	(A) Structure of a single $(\text{SbS}_6)_n^{n-}$ chain with labeling. (B) Packing diagram of CsSbS_6 looking down the a-axis (chain axis). The shaded ellipsoids are Sb atoms and the open ellipsoids are Cs atoms.....	209
3-5:	(A) Differential thermal analysis (DTA) data for	

	Cs ₂ Sb ₄ S ₈ showing the first heating and cooling cycle.	
	Heat is absorbed at 365 °C as the material melts	
	but is not released upon cooling. (B) Data for	
	reheating showing the crystallization of Cs ₂ Sb ₄ S ₇	
	at 291 °C, followed by melting of the excess glass at	
	364 and 375 °C.....	214
3-6:	X-ray diffraction patterns of: (A) Cs ₂ Sb ₄ S ₈ single	
	crystals. (B) material heated to 400 °C then	
	cooled (glassy state). (C) material after reheating to	
	310 °C (crystallization of Cs ₂ Sb ₄ S ₇).....	216
3-7:	DTA of CsSbS ₆ shows the endothermic peak at	
	232 °C corresponding to the decomposition of	
	CsSbS ₆ to Cs ₂ Sb ₄ S ₈	217
4-1:	Powder X-ray diffracton patterns of:	
	(A) A ₃ Sb(PS ₄) ₂ and (B) A ₃ Bi(PS ₄) ₂	241
4-2:	Optical absorption spectrum of: (A) KBiP ₂ S ₇	
	and (B) RbBiP ₂ S ₇	247
4-3:	Optical absorption spectra of: (A) K ₃ Sb(PS ₄) ₂	
	(B) Rb ₃ Sb(PS ₄) ₂ (C) Cs ₃ Sb(PS ₄) ₂	248
4-4:	Optical absorption spectra of: (A) K ₃ Bi(PS ₄) ₂	
	(B) Rb ₃ Bi(PS ₄) ₂ (C) Cs ₃ Bi(PS ₄) ₂	249
4-5:	Optical absorption spectrum of Na _{0.16} BiP ₂ S ₆	250
4-6:	Thermograms of: (A) RbBiP ₂ S ₇ and (B) Rb ₃ Bi(PS ₄) ₂	251
4-7:	ORTEP packing diagram of KBiP ₂ S ₇ looking down	
	the c-axis with labeling.....	259
4-8:	ORTEP representation and labeling of the KBiP ₂ S ₇ layer	
	looking down the a-axis.....	260

4-9:	ORTEP representation and labeling of the Bi-S coordination site. The polyhedron is outlined with dotted lines for clarity.....	261
4-10:	ORTEP representation and labeling of the BiS ₇ polyhedron viewed from the top of the capped trigonal prism. The probable location of the Bi ³⁺ lone pair is shown.....	262
4-11:	A single [Bi(PS ₄) ₂] ³⁻ anionic chain.....	263
4-12:	ORTEP packing diagram of K ₃ Bi(PS ₄) ₂ looking down the b-axis with labeling.....	264
4-13:	ORTEP packing diagram of Cs ₃ Bi ₂ (PS ₄) ₃ looking down the b-axis with labeling.....	265
4-14:	(A) The Bi ₂ (PS ₄) ₂ dimeric unit. The Bi(2)-Bi(2') distance is 4.519(3) Å. (B) A single [Bi ₂ (PS ₄) ₃] _n ³ⁿ⁻ layer.....	266
4-15:	ORTEP packing diagram of Na _{0.16} BiP ₂ S ₆ looking down the a-axis with labeling. The Bi-S bonds are omitted for clarity.....	267
4-16:	ORTEP representation and labeling of the Bi-S coordination site. The polyhedron is outlined with dotted lines for clarity.....	268
5-1:	Solid state optical absorption spectra of (A) KBiP ₂ Se ₆ and (B) KSbP ₂ Se ₆	296
5-2:	(A) Optical absorption spectrum of Cs ₈ Sb ₄ (P ₂ Se ₆) ₅ . (B) Optical absorption spectrum of Cs ₈ Bi ₄ (P ₂ Se ₆) ₅	297
5-3:	The extended structure of KBiP ₂ Se ₆ looking down the b-axis with labeling.....	305
5-4:	(A) Structure and labeling of a [BiP ₂ Se ₆] ⁻ chain.	

	The bridging Se atoms connecting the chains into layers are highlighted. (B) The Bi-Se coordination site with labeling.....	306
5-5:	Packing diagram of $\text{Cs}_8\text{Bi}_4(\text{P}_2\text{Se}_6)_5$ viewed down the [010] direction. The open circles represent Cs atoms. Dark solid lines highlight the layered nature of the staircase framework.....	307
5-6:	Structure of the $[\text{M}_2(\text{P}_2\text{Se}_6)_4]$ dimeric unit showing the M...M interaction.....	308
5-7:	(A) Association of two $[\text{M}_2(\text{P}_2\text{Se}_6)_4]$ "dimers" by a $[\text{P}_2\text{Se}_6]^{4-}$ unit. (B) Further sharing of $[\text{P}_2\text{Se}_6]^{4-}$ units among "dimers" results in a one-dimensional chain-like structure.....	309
5-8:	Two-dimensional structure of the $[\text{M}_4(\text{P}_2\text{Se}_6)_5]_n^{8n-}$ anionic framework with labeling as drawn by ORTEP.....	310
5-9:	The Cs^+ coordination environments. The open circles represent Cs atoms. The open square in the Cs(1) coordination site represents the vacant corner of the square prism.....	311
5-10:	Variable temperature electrical conductivity data for single crystals of $\text{Cs}_8\text{Bi}_4(\text{P}_2\text{Se}_6)_5$	318
6-1:	Far-IR spectra of: (A) $\text{K}_2\text{MnP}_2\text{Se}_6$ (B) $\text{Cs}_2\text{Cu}_2\text{P}_2\text{Se}_6$ and (C) $\text{K}_2\text{Ag}_2\text{P}_2\text{Se}_6$	352
6-2:	Optical absorption spectra of (I), (I I), and (I I I).....	354
6-3:	Optical absorption spectra of (I V) and (V).....	355
6-4:	Optical absorption spectra of (V I), (V I I), and (V I I I).....	356
6-5:	Optical absorption spectrum of (I X).....	357

6-6:	Thermogram of $\text{Rb}_2\text{MnP}_2\text{Se}_6$. Melting is observed at 781 °C, followed by recrystallization at 751 °C.....	358
6-7:	(A) ORTEP representation of a single $[\text{MnP}_2\text{Se}_6]_n^{2n-}$ chain. (B) Packing diagram of $\text{K}_2\text{MnP}_2\text{Se}_6$ viewed down the [100] direction with labeling.....	362
6-8:	(A) A single layer of the $\text{Mn}_2\text{P}_2\text{Q}_6$ framework. The dashed lines indicate the hexagonal arrangement of Mn^{2+} ions. (B) Removal of one-half of the Mn^{2+} ions results in a single layer of the hypothetical $[\text{MnP}_2\text{Q}_6]_n^{2n-}$ anion. Dashed lines highlight the possibility of chain formation.....	363
6-9:	(A) A single $[\text{Cu}_2\text{P}_2\text{Se}_6]_n^{2n-}$ chain. (B) A single $[\text{Ag}_2\text{P}_2\text{Se}_6]_n^{2n-}$ chain.....	372
6-10:	Energy levels of the d block of Cu_2^{2+} at a separation of 2.58 Å. Mixing of filled d orbitals with empty s and p orbitals results in a lowering of the antibonding (σ^*) and bonding (σ) energy levels which gives rise to a net bonding interaction. Adapted from reference 26.....	373
6-11:	Packing diagram of the three-dimensional structure of $\text{K}_2\text{Ag}_2\text{P}_2\text{Se}_6$ viewed down the [100] direction with labeling.....	374
6-12:	ORTEP representation of a fragment of the $[\text{Ag}_2\text{P}_2\text{Se}_6]_n^{2n-}$ anion showing the local AgSe_4 coordination environment with labeling.....	375
6-13:	A single $[\text{Au}_2(\text{P}_2\text{Se}_6)_2]_n^{2n-}$ chain.....	376
6-14:	Plots of $1/\chi_M$ vs. T taken at 2000 G of applied field over 2-300 K for: (A) $\text{Cs}_2\text{Mn}_2\text{P}_2\text{Se}_6$ and	

(B) $\text{K}_2\text{FeP}_2\text{Se}_6$. The inset graphs show	
expanded views of the region 2-30 K.....	383

CHAPTER 1

Introduction

The development of useful technologies often relies on the availability of solid-state materials with appropriate physicochemical properties. The exploratory synthesis of these new materials is often accomplished by traditional usually high-temperature fusion reactions to form thermodynamically stable products. This empirical method has led to several discoveries with great potential impact on our society ranging from the high-temperature superconductors and advanced ceramics to next-generation nonlinear optical solids. However, new synthetic methodology is needed to advance solid-state chemistry and insure its continued growth.

The study of new metal chalcogenides is particularly attractive given the staggering structural diversity and broad range of interesting electrical, optical, and catalytic properties that are characteristic of these compounds. In the past decade, metal chalcogenide chemistry has experienced rapid growth due to an expanding arsenal of synthetic methodology available to the

inorganic chemist. In this dissertation, we have employed and developed the now proven molten alkali polychalcogenide salt method at intermediate temperatures (150-500 °C) for the synthesis of new ternary antimony and bismuth chalcogenides. In addition, a significant variation of this technique has led to the discovery of alkali *polychalcophosphate* fluxes for synthesis of new quaternary metal thio(seleno)phosphate compounds.

1. A Review of Antimony and Bismuth Chalcogenides

The first antimony and bismuth sulfides were formed in the earth's crust by nature through the reaction of metal sulfides with Group 15/16 sulfides at elevated temperatures or through hydrothermal reaction in superheated water. These compounds belong to a large class of Group 15/16 compounds, known as sulfosalt minerals. Bismuth compounds constitute about 20% of these compounds.¹ These minerals have the general formula $M_xE_yS_z$ ($M=Ag, Cu, Pb, Hg$; $E=As, Sb, Bi$) where the trivalent E atom is coordinated by three S atoms to form a trigonal ES_3^{3-} pyramid.² Examples of these formulas include $Cu_{12}Sb_4S_{13}$ (tetrahedrite),³ $HgSb_4S_8$ (livingstonite),⁴ $PbCuBiS_3$ (aikinite),⁵ and $PbBi_2S_4$ (galenobismutite).⁶

Another class of Group 15/16 compounds are the binary chalcogenides, E_2Q_3 ($E=As, Sb, Bi$; $Q=S, Se, Te$) which have received considerable attention, due to their potential application as thermoelectric cooling materials. During the past 30 years, there have been hundreds of papers describing various solid solutions of

E_2Q_3 (M=As, Sb, Bi; Q=S, Se, Te) compounds.⁷ The best thermoelectric cooling materials near room temperature are Bi_2Te_3 ^{8a} and related compounds such as $Bi_2Te_{2.85}Se_{0.15}$.⁹ Candidates for thermoelectric cooling materials must have a high figure of merit (Z) which is defined by the following equation:

$$Z = \frac{\alpha^2 \cdot \sigma}{\kappa} \quad \text{eq. (1)}$$

where α =thermoelectric power (Seebeck coefficient), σ =electrical conductivity and κ =thermal conductivity. A useful thermoelectric material must possess high electrical conductivity and thermoelectric power while maintaining low thermal conductivity. The bismuth telluride compounds have large Z values ($2.5\text{--}3.3 \times 10^{-3} \text{ K}^{-1}$) near room temperature.^{8a}

Bi_2Te_3 possesses a unique layered structure and belongs to the space group R-3m (see Figure 1-1). The layered nature of Bi_2Te_3 has a strong influence on the properties resulting in highly anisotropic transport phenomena such as resistivity, Hall coefficient, magnetoresistivity, and thermal conductivity.⁹ The framework can be viewed as a defect NaCl structure by removing every third layer of Na atoms, which leads to the A_2B_3 stoichiometry. Each Bi atom is surrounded by six Te atoms to form an octahedral coordination geometry with Bi-Te bond distances of 3.071 and 3.247 Å. These long distances could be a result of electronic repulsions between the localized spherical and stereochemically inactive $6s^2$ orbitals and the Te atoms. As a result, the $6s^2$ electrons are thought to be delocalized throughout the solid. Interestingly, weak interlayer Te...Te

interactions are also present (3.647 Å). Bi_2Te_3 transforms to the α - In_2Se_3 structure type at high temperature and pressure,¹⁰ while Bi_2Se_3 undergoes an irreversible phase transition to the Sb_2S_3 (stibnite) structure type at high pressure.¹¹ Sb_2Te_3 ¹² and Bi_2Se_3 ¹³ are isomorphous with Bi_2Te_3 and possess E-Q bond distances of 2.974 and 3.168 Å for Sb_2Te_3 and 2.851 and 3.075 Å for Bi_2Se_3 .

Bismuth telluride is a narrow band gap semiconductor or semi-metal with an E_g of 0.17 eV and a room-temperature conductivity ranging from 10^2 to 10^3 S/cm. Typical bandgap and conductivity values for E_2Q_3 compounds are given in Table 1-1.

Table 1-1. Properties of Binary Group 15 Chalcogenides.

Compound	E_g (eV), r.t.	Ref.	σ (S/cm), r.t.	Ref.
Sb_2S_3	1.63	25	1.7×10^{-8}	25
	1.7	27		
Sb_2Se_3	1.19	25	1×10^{-5}	25
	1.2	27		
Sb_2Te_3	0.21	25	3×10^3	25
	0.3	27	1×10^4	8d
Bi_2S_3	1.3	26	3×10^{-8}	26
	1.3	27		
Bi_2Se_3	0.55	26	7×10^{-2}	26
	0.35	27	2.0	29
Bi_2Te_3	0.17	26	2.2×10^3	28
	0.15	27	6.3×10^2	8d

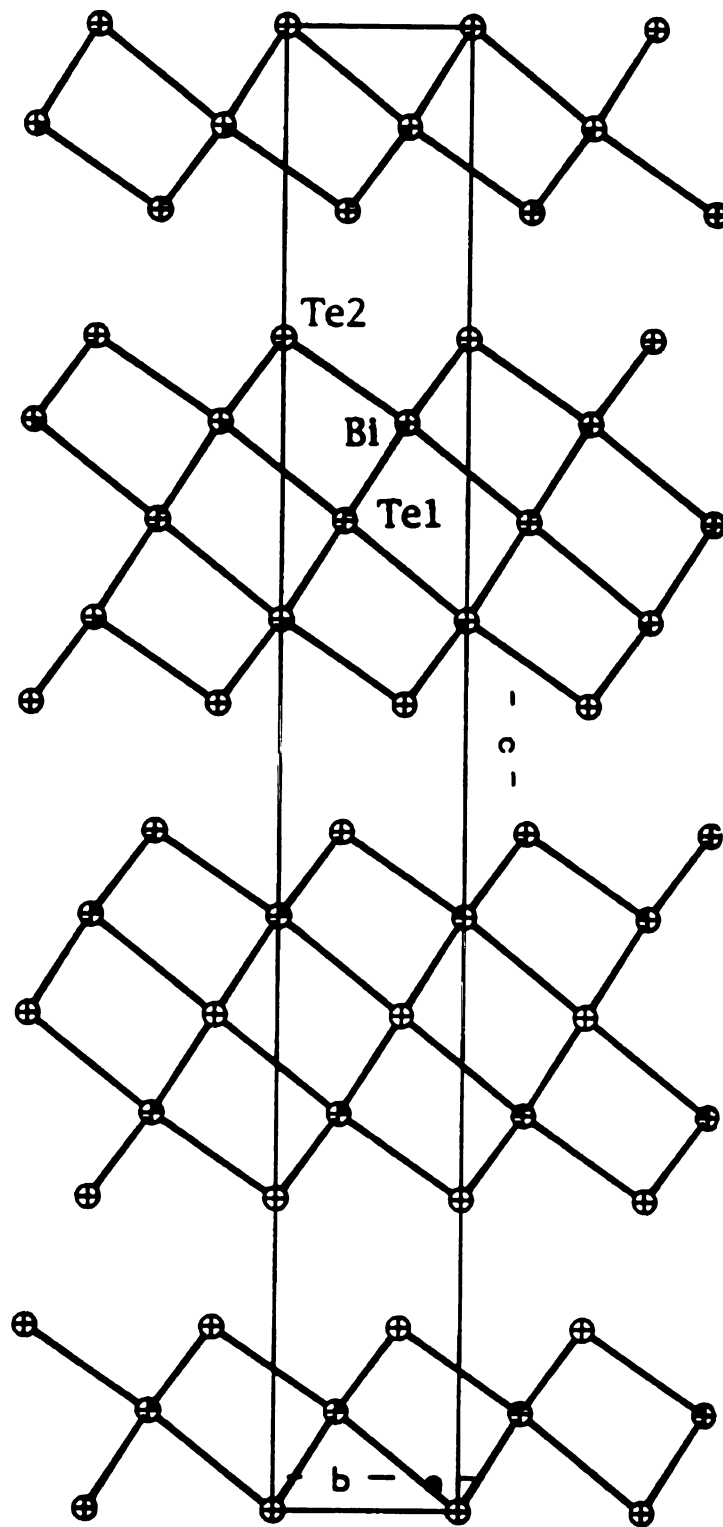


Figure 1-1: Projection of Bi_2Te_3 looking down the a -axis, with labeling.

The crystals of Bi_2Te_3 are plate-like with a shiny, metallic luster and can be made in either the n- or p-type forms. This latter feature is important for the fabrication of thermoelectric cooling devices. Large ingots of the material can be made from the elements by the Bridgman method at 800 °C. Crack-free slices along the cleavage planes of these ingots are suitable for detailed charge transport studies.^{8d}

Although this peculiar compound has attracted considerable attention, only a few theoretical calculations of the electronic band structure have been performed.¹⁴ Recently, the first density of states (DOS) calculations have been accomplished using the empirical tight binding method.¹⁵ This study was undertaken to explain recent photoemission results and provide some insight into the bonding of Bi_2Te_3 . The photoemission results and the calculations indicate that s-p hybridisation is weak and imply that p orbital bonding, like in elemental Bi, dominates. The 90° Te-Bi-Te angles allow for maximum overlap of all three p orbitals. In addition, the DOS plots illustrate that the s-orbitals of Bi are low lying and reside in the conduction band. Information on the charge transfer of this highly covalent network was obtained as follows: Te(1) -0.33, Te(2) -0.19, and Bi +0.36.

The second structure type that is prevalent in binary Group 15 chalcogenides is the Sb_2S_3 (stibnite) structure type¹⁶ which is isomorphous with Sb_2Se_3 ¹⁷ and Bi_2S_3 (bismuthite).¹⁸ Sb_2S_3 and Bi_2S_3 are frequently found naturally as sulfosalt minerals. The crystal structure of Sb_2S_3 contains two infinite ribbons $(\text{Sb}_4\text{S}_6)_n$ along the b-

axis, which are weakly bonded in the a (3.335 Å) and c (3.148-3.196 Å) directions as shown in Figure 1-2a. A single ribbon is shown in Figure 1-2b. Sb(1) is surrounded by three sulfur atoms to form the familiar SbS_3^{3-} trigonal pyramidal unit. The bonds for Sb(1) are presumably of p character with Sb-S distances of 2.58 and 2.57 Å while the mean S-Sb-S bond angle is 91.43° . Sb(2) is found in a square pyramidal geometry with five bonds to sulfur and the lone pair occupying the sixth sp^3d^2 orbital at the base of the pyramid. The distances from Sb(2) to two basal sulfur atoms are 2.68 Å while the other two basal atoms are found at 2.82 Å. The apical sulfur is shorter at 2.49 Å and the mean bond angle is 89.19° .

Binary bismuth and antimony sulfides and selenides have been studied for possible applications in many areas. Sb_2S_3 and Bi_2S_3 are known photoconductors with band gaps in the range of 1.3 to 1.5 eV (see Table 1-1) which make them good candidates for certain photovoltaic applications.¹⁹ Amorphous chalcogenide glasses such as $\text{As}_2\text{Se}_3/\text{Sb}_2\text{Se}_3$ have been investigated for possible memory switching devices because of their ability to oscillate between crystalline and amorphous states.²⁰ $\text{As}_2\text{Q}_3/\text{Sb}_2\text{S}_3$ glass fibers have been used to increase resolution in X-ray camera tubes.²¹ E_2Q_3 (E=Sb,Bi; Q=S, Se) compounds prevent deterioration of aluminosilicate cracking catalysts due to Ni and Fe deposits.²² Antimony thioantimonate (Sb_2S_4) has been shown to be a more effective antiwear additive for lubricating greases than MoS_2 ,²³ while Sb_2Se_3 is a promising material in CdSe-based thin-film solar cells.²⁴

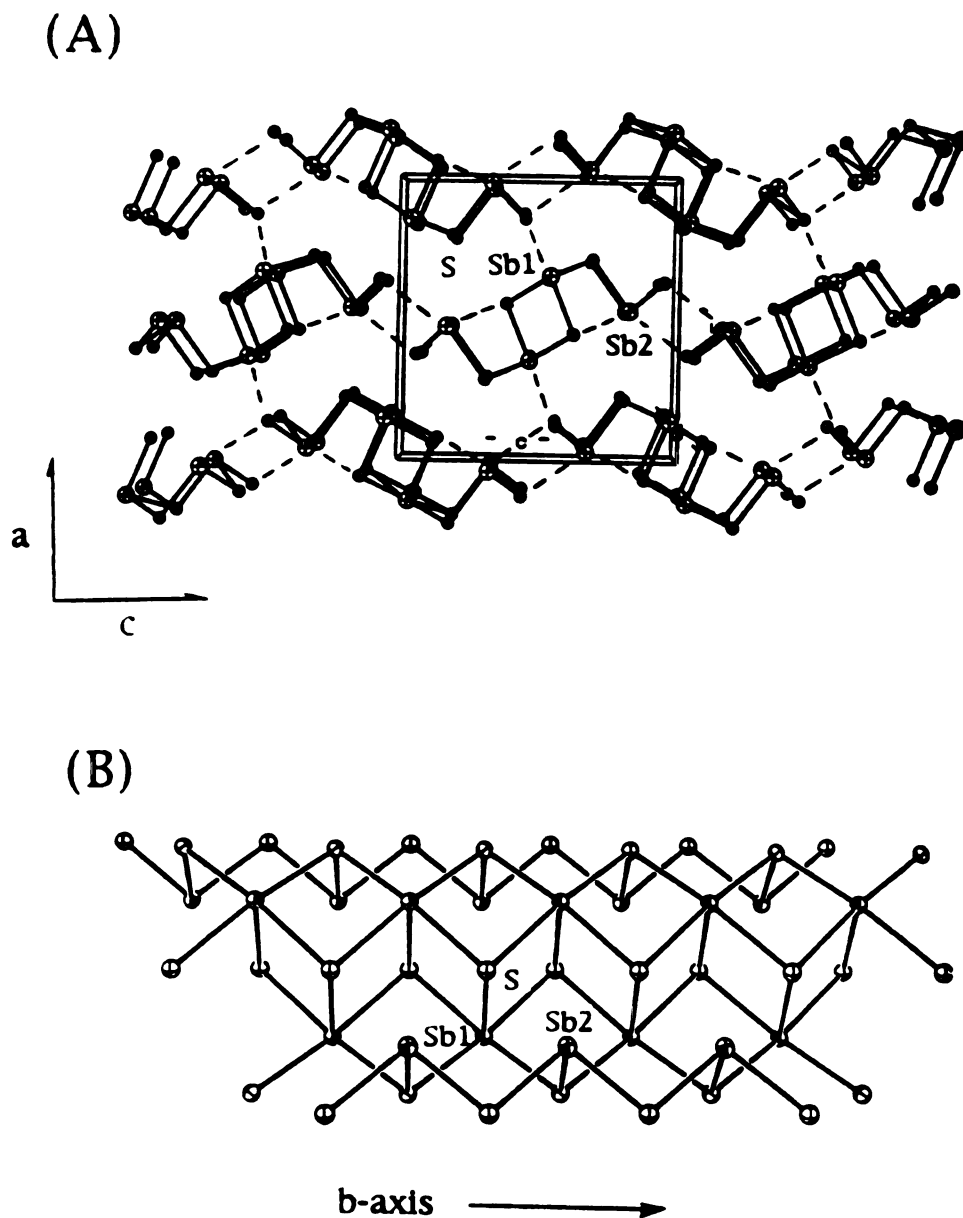


Figure 1-2: (A) ORTEP representation of Sb_2S_3 viewed down the b -axis with labeling scheme. The long $\text{Sb}\cdots\text{S}$ contacts are highlighted by dashed lines. (B) A single infinite ribbon of Sb_2S_3 .

In addition to the naturally occurring mineral sulfosalts and the binary Group 15 chalcogenides, the ternary $A_xE_yQ_z$ (A=alkali metal, alkaline earth metal, Cu, Tl; E=Sb, Bi; Q=S,Se,Te) compounds display remarkable structural diversity and potentially interesting charge transport properties.

The earliest members of this family are the $ABiS_2$ (A=Li,Na,K; Q=S,Se) compounds which were uncovered in the 1940's and 1950's.³⁰ Later, the isomorphous $ABiTe_2$ (A=Li,Na) compounds were also discovered.³¹ The units cells were determined by powder diffracton data and revealed simple NaCl-type cubic structures (Fm3m space group) where the Bi and A atoms are disordered. Further investigation with rubidium cations resulted in the formation of $RbBiQ_2$ (Q=S,Se) with a Bi-S distance of 2.953 Å.³² The larger alkali cation leads to a NaCl-type superstructure (NaCrS₂-type) with an ordered cation arrangement. Conductivity studies on polycrystalline samples of $ABiQ_2$ compounds confirm their semiconductor nature. The conductivities of $ABiSe_2$ compounds near room temperature range from 1.9×10^{-1} (KBiSe₂) to 1.6×10^{-2} S/cm (CsBiSe₂) while those of $ABiS_2$ are lower and vary between 4.55×10^{-3} (LiBiS₂) and 8.33×10^{-8} S/cm (CsBiS₂).³³

Other synthetic investigations with alkali metal counterions uncovered two new compounds with unique tunnel structures, $RbBi_3S_5$ ³⁴ and $CsBi_3S_5$.³⁵ They are reminiscent of the well-known MnO_2 hollandite frameworks.³⁶ $CsBi_3S_5$ was synthesized by direct combination of Bi_2S_3 , K_2CO_3 and S at 500 °C. The structure is shown in Figure 1-3a and consists of $[Bi_3S_5]^-$ block-like chains that share

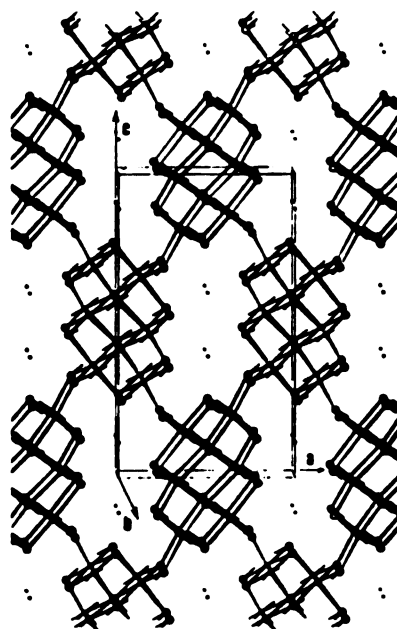
corners to form Cs-filled channels parallel to the crystallographic b-axis. Substitution of S by Se cannot stabilize the isostructural compound. The reaction of cesium acetate, bismuth and selenium in a 1:1:4 ratio at 500 °C gives rise to a new structure type, $\text{Cs}_3\text{Bi}_7\text{Se}_{12}$.³⁷ The layers (Figure 1-3b) are assembled from the same block-like chains as discussed above. These chains are bridged by BiSe_6 octahedra in an edge-sharing manner to form sheets that are separated by Cs^+ ions.

Upon changing from alkali metals to the main group Tl^+ ion, $\text{Tl}_4\text{Bi}_2\text{S}_5$ was isolated.³⁸ This compound is intriguing because the octahedrally coordinated Bi^{3+} and the four- and five-coordinate Tl^+ ions each possess stereochemically active $6s^2$ electron pairs that manifest themselves structurally. The BiS_6 octahedra are distorted with an axial Bi-S distance of 2.64(2) Å that is *trans* to a long distance of 3.05(2) Å while the two different Tl^+ ions have trigonal pyramidal (including the lone pair) and square pyramidal coordination.

In solid state chemistry, the size and charge of the counter cation can have a dramatic effect on the structure of the compound. Schäfer and coworkers have utilized alkaline earth cations such as Sr^{2+} and Ba^{2+} to stabilize an intriguing set of three unusual layered $[\text{Bi}_x\text{Se}_y]_n^{n-}$ anionic frameworks. $\text{Sr}_4\text{Bi}_6\text{Se}_{13}$ ³⁹ contains two-dimensional sheets made up of edge-sharing CdI_2 - and Bi_2Te_3 -type bismuth selenide fragments. The BiSe_6 octahedra share edges to create one-dimensional sixfold chains that extend along the b-direction and separate these layers. Sr^{2+} ions are inserted between the chains that separate the layers in this highly charged

$[\text{Bi}_6\text{Se}_{13}]_n^{8n-}$ framework (see Figure 1-4). The structure of SrBiSe_3 ⁴⁰ is shown in Figure 1-5a. It is composed of $[\text{Bi}_8\text{Se}_{18}]_n^{12n-}$ chains that interact with $(\text{Se}_3)^{2-}$ fragments to construct pseudo two-dimensional layers, between which Sr^{2+} ions are located. The $(\text{Se}_3)^{2-}$ units form long contacts with the $[\text{Bi}_8\text{Se}_{18}]_n^{12n-}$ chains as shown in Figure 1-5b. The formula can be represented as $\text{Sr}_8\text{Bi}_8\text{Se}_{18}(\text{Se}_3)_2$. In BaBiSe_3 ,⁴¹ BiSe_6 octahedra are connected by common edges to form fourfold one-dimensional chains that are bridged by unprecedented $(\text{Se}_x)^{x-}$ polymeric units. These units contain unusual square planar Se atoms. Both types of anionic chains extend along the c direction and are bonded in the b direction to give rise to sheets, between which Ba^{2+} ions reside (see Figure 1-6). A more useful formulation is $\text{Ba}_4\text{Bi}_4\text{Se}_8(\text{Se}_4)$, where the Se atoms in the $[\text{Se}_4]^{4-}$ unit each have a formal charge of 1-. The shiny appearance of the compound coupled with its electron deficiency strongly suggest that the compound is a metal but electrical conductivity studies have not been reported. The metallic character and the presence of polyselenide units in $\text{Ba}_4\text{Bi}_4\text{Se}_8(\text{Se}_4)$ are very unusual in bismuth chalcogenide chemistry. The isomorphous BaSbTe_3 compound has also been synthesized.⁴¹ Combination of Bi_2S_3 and BaS at high temperatures yielded two forms of BaBi_2S_4 .⁴² α - BaBi_2S_4 contains a slight excess of Bi_2S_3 and β - BaBi_2S_4 a slight excess of BaS in relation to the stoichiometric formula. SrBi_2S_4 was also prepared and found to be isotypic to β - BaBi_2S_4 . Both structures consist of edge- and corner-sharing BiSe_6 distorted octahedra that form narrow Ba^{2+} -filled tunnels that run along the c-axis.

(A)



(B)

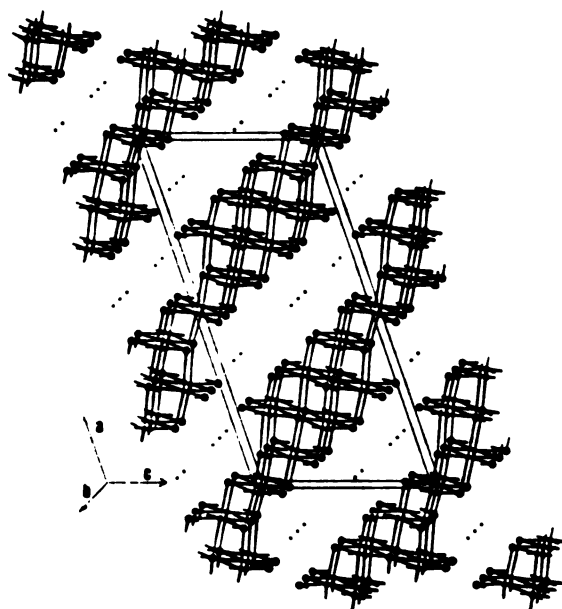


Figure 1-3: Packing diagrams of (A) CsBi_3S_5 and (B) $\text{Cs}_3\text{Bi}_7\text{Se}_{12}$ looking down the b-axis. Shaded spheres represent S(Se) atoms and small open spheres designate Bi atoms.

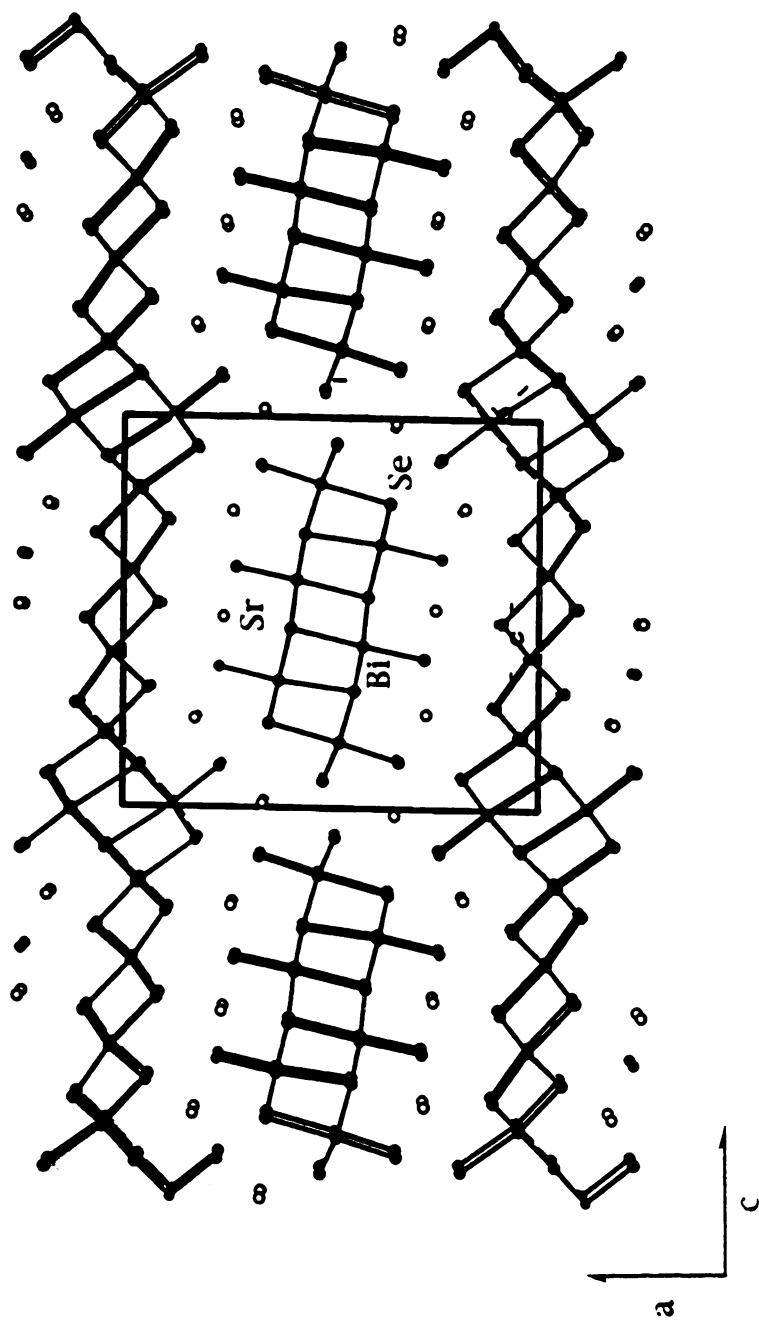
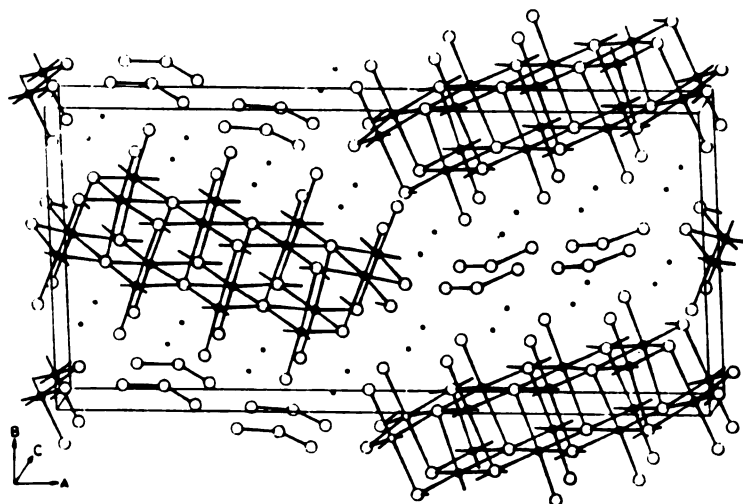


Figure 1-4: Packing diagram of $\text{Sr}_4\text{Bi}_6\text{Se}_{13}$ and labeling scheme with a view down the b -axis.

(A)



(B)

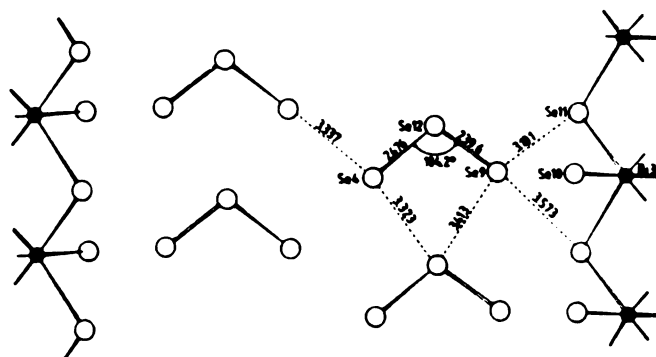


Figure 1-5:

(A) Packing diagram of SrBiSe₃ viewed down the c-axis. Dark spheres indicate Bi atoms and large open spheres are Se atoms. (B) Interacting (Se₃)²⁻ anions with dashed lines representing close Se...Se contacts.

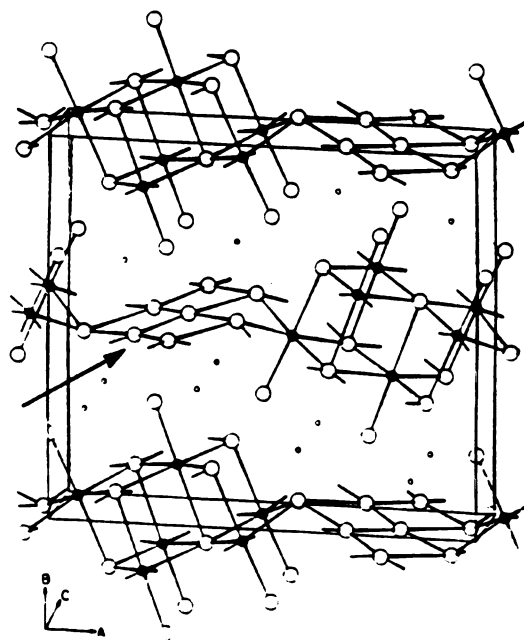


Figure 1-6: Packing diagram of BaBiSe₃ viewed down the c-axis. Dark spheres indicate Bi atoms and large open spheres are Se atoms. The square planar Se atoms are highlighted with the arrow.

The incorporation of transition metals into bismuth chalcogenide compounds has also been investigated. Many examples exist in the Cu/Bi/Q (Q=S,Se) family that are either naturally occurring or synthetic including $\text{Cu}_{1+3x}\text{Bi}_{5-x}\text{Q}_8$ (Q=S,Se),⁴³ CuBiS_2 ,⁴⁴ and Cu_3BiS_3 .⁴⁵ Other transition metal systems include $\text{Mn}_{1-x}\text{Bi}_{2+y}\text{Q}_4$ (Q=S,Se)⁴⁶ and HgBi_2S_4 .⁴⁷ The $\text{Cu}_{1+3x}\text{Bi}_{5-x}\text{Q}_8$ alloy was prepared by high temperature fusion of Cu/Bi/Q with a ratio of 1:3:5 and possesses extensive non-stoichiometry on two of the Cu sites and Cu/Bi disorder on the third site. The structure is very similar to that of the stoichiometric compound, CuBi_5S_8 , where the Bi atoms are found in three different coordination geometries: perfect octahedral, distorted octahedral and square pyramidal.⁴⁸ The Cu atoms are found in a distorted tetrahedral site with an unusually short $\text{Cu}^{+}\cdots\text{Cu}^{+}$ distance of 2.56 Å. The authors suggest that Cu-Cu pairs may exist in the structure. The polyhedra of the three independent Bi atoms are linked together to form $[\text{Bi}_5\text{S}_8]_n^{n-}$ sheets. These sheets are crosslinked by CuS_4 tetrahedra to assemble the three-dimensional framework. $\text{Mn}_{1-x}\text{Bi}_{2+y}\text{Q}_4$ are isostructural to HgBi_2S_4 ⁴⁷ and synthesized by direct combination of the elements in the 600-1000 °C temperature range. Vapor transport techniques for crystal growth formed Bi_2Q_3 which implies that the ternary phases decomposed under these conditions. Interestingly, single crystals were grown with a low temperature flux consisting of a eutectic mixture of 45% LiCl and 55% RbCl (m.p. 312 °C). It should be pointed out that the use of alkali metal halide fluxes to grow chalcogenides is somewhat uncommon. Such solvents are generally reserved for oxide crystal growth^{49a} and for hard cation phases such as LaS_2 .^{49b}

In addition to the previously mentioned synthetic work, there have been several investigations of the high temperature A_2Q/Bi_2Q_3 ($A = Li, Na, K, Rb, Cs$; $Q = S, Se, Te$) phase diagrams.⁵⁰ However, the structural information only consists of unindexed powder X-ray diffraction patterns. An example of the K_2S/Bi_2S_3 phase diagram is shown in Figure 1-7. It becomes apparent that further work in the high temperature synthesis and structural characterization of new $A_xBi_yQ_z$ compounds is warranted.

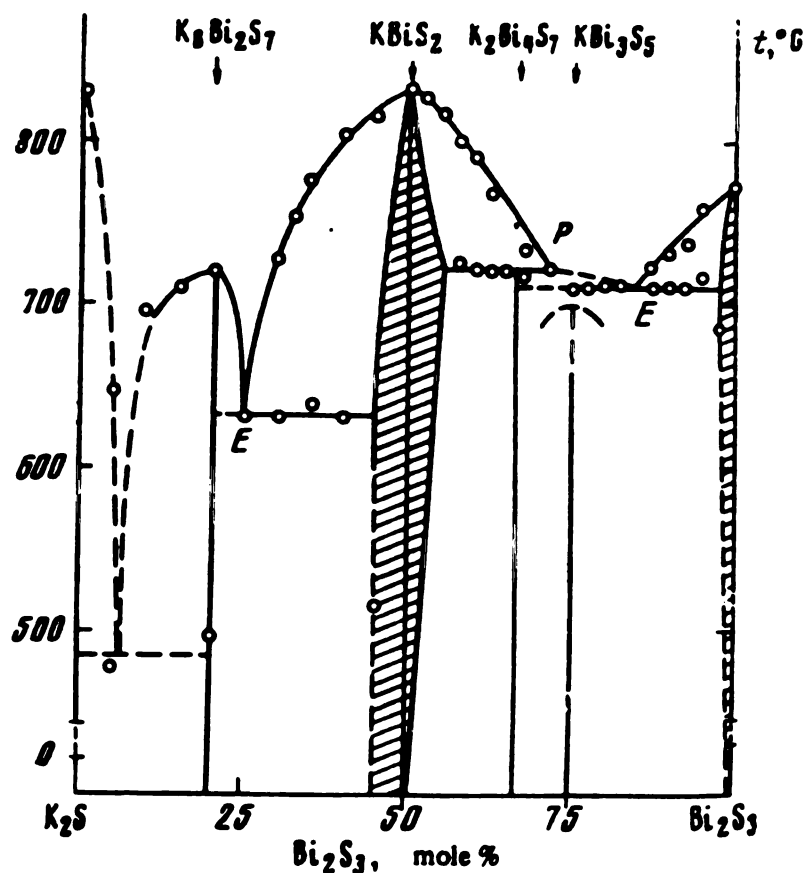


Figure 1-7: Equilibrium phase diagram of the Bi_2S_3 - K_2S system.

The synthetic solid state chemistry of ternary $A_xSb_yQ_z$ compounds is much more extensive than that of the bismuth chemistry due to the successful implementation of hydro(methanol)thermal reactions in addition to the traditional solid state methods. In general, the structural chemistry of the antimony compounds is different from that of bismuth presumably because of the preference of the Sb^{3+} ion for lower coordination numbers such as trigonal pyramidal (CN=3) and trigonal bipyramidal (including the lone pair) (CN=4). These trigonal pyramids and bipyramids can share edges and/or corners to generate a large array of chain-like and layered structures. In comparison, the Bi^{3+} ion shows a greater tendency to expand its coordination sphere to include square pyramidal (CN=5) and perfect or distorted octahedral (CN=6) geometries which share edges to form layered and three-dimensional tunnel frameworks. In addition, $A_xSb_yQ_z$ systems have the tendency to form amorphous glasses under certain high temperature conditions⁵¹ while bismuth compounds will crystallize under these conditions. Another difference between antimony and bismuth results from the reluctance of Bi to assume the 5+ oxidation state. Tetrahedral SbQ_4^{3-} (Q=S,Se) anions, with Sb in the 5+ oxidation state, have been crystallized with a variety of counter cations whereas the bismuth analog is unknown.⁵² This phenomenon is sometimes called the "inert pair effect" and refers to the resistance of the inert pair of s electrons to participate in covalent bond formation. Thus, the trivalent state becomes progressively more stable as the group is descended.^{53a} Recent theoretical work shows that

relativistic effects make an important contribution to the inert pair effect.^{53b,c}

As in the case of bismuth, the isomorphous ASbQ₂ (A=Li,Na,K; Q=S,Se,Te)⁵⁴ family of layered compounds were synthesized along with the lower symmetry RbSbQ₂ and CsSbQ₂ members. Electrical conductivity and thermopower measurements on ASbTe₂ compounds confirm the p-type semiconducting nature with room temperature conductivities that decrease upon moving from Li (4×10^{-2} S/cm) to Cs (2.5×10^{-3} S/cm), while the Seebeck coefficients (α) are positive and increase from 465 (Li) to 1440 μ V/K (Cs) (see Table 1-2).⁵⁵ The observed trend in electronic properties is dependent on the increase in alkali cation radii. The layers are separated by a larger distance in CsSbTe₂ so there is less interlayer orbital overlap which gives rise to a larger anisotropy and larger band gap.

Table 1-2. Properties of ASbTe₂ Compounds.⁵⁶

Compound	σ (S/cm), r.t.	α (μ V/K), r.t.	m. p. ($^{\circ}$ C)
LiSbTe ₂	4.0×10^{-2}	465	941
NaSbTe ₂	1.4×10^{-2}	660	910
KSbTe ₂	4.0×10^{-3}	840	728
CsSbTe ₂	2.5×10^{-3}	1440	725

One-dimensional ASbQ₂ (A=Na,K,Rb,Cs; Q=S,Se) isomers exist where the electron lone pair of Sb³⁺ is stereochemically active.⁵⁶ It has been reported that α -NaSbS₂ (one dimensional) undergoes a reversible structural transformation to β -NaBiS₂ (two-dimensional) at 580 $^{\circ}$ C.^{56a} The $\alpha \rightarrow \beta$ conversion is directly related to the loss of

the lone pair stereochemical activity of Sb^{3+} . $\alpha\text{-NaSbS}_2$ is made by direct combination of Na_2S and Sb_2S_3 at low temperature followed by slow cooling. It consists of trigonal bipyramidal SbS_4 units that share opposite edges to form a chain-like polymeric structure. The Sb-S bond distances are 2.431(2) Å (equatorial) and 2.773(2) Å (axial). $\beta\text{-NaSbS}_2$ is made by high temperature reaction of Na_2S and Sb_2S_3 followed by quenching in water. A longer Sb-S bond distance of 2.888 Å is observed due to the perfect octahedral coordination geometry. The K^+ , Rb^+ and NH_4^+ analogs possess the same structural motif as $\alpha\text{-NaSbS}_2$ but crystallize in different space groups.⁵⁷ Increasing the counterion size (Cs^+) results in a different structure consisting of SbS_3 trigonal pyramids that share opposite corners to form one-dimensional $[\text{SbS}_2]_n^{n-}$ chains.^{56d}

Schäfer and coworkers have prepared a host of ternary alkali metal antimony chalcogenides using hydrothermal techniques with a variety of starting materials. The dimensionality of these structurally fascinating compounds extends from molecular to three-dimensional. Two examples, $\text{K}_3\text{SbS}_3\cdot 3\text{Sb}_2\text{O}_3$ ⁵⁸ and $\text{Cs}_2\text{Sb}_8\text{S}_{13}$,⁵⁹ demonstrate this incredible structural diversity. $\text{K}_3\text{SbS}_3\cdot 3\text{Sb}_2\text{O}_3$ is prepared hydrothermally at 180 °C and possesses a novel macromolecular structure that is composed of Sb_2O_3 tubes that encapsulate K^+ ions. These tubes are held together by molecular SbS_3^{3-} trigonal pyramids that act as bridges by coordinating to K^+ ions from three different tubes. $\text{Cs}_2\text{Sb}_8\text{S}_{13}$ forms under hydrothermal conditions at 160 °C. SbS_3 trigonal pyramids link via corners to construct large fragments consisting of six-, eight- and fourteen-membered rings. These fragments are bridged by Sb_2S_6

units to build two-dimensional sheets. The Sb_2S_6 units are composed of two edge-sharing SbS_4 trigonal bipyramids (see Figure 1-8). This framework is representative of the types of Sb-S coordination environments that commonly prevail in this chemistry. As another illustration of the broad structural flexibility possible in this system, the isoelectronic compounds $\text{K}_2\text{Sb}_4\text{S}_7$,⁶⁰ $\text{K}_2\text{Sb}_4\text{S}_7\cdot\text{H}_2\text{O}$,⁶¹ $\alpha,\beta\text{-Rb}_2\text{Sb}_4\text{S}_7$,⁶² $(\text{NH}_4)_2\text{Sb}_4\text{S}_7$,⁶³ and $\text{Cs}_2\text{Sb}_4\text{S}_7$,⁶⁴ all have different structures. Other examples of ternary antimony chalcogenides include $\text{Cs}_6\text{Sb}_{10}\text{S}_{18}\cdot 1.2\text{H}_2\text{O}$,⁶⁵ TiSb_3S_5 ,⁶⁶ and $\alpha\text{-(}\beta\text{)-TiSbSe}_2$.⁶⁷

Upon increasing the charge on the counterion with the use of alkaline earth metal cations (Ca^{2+} , Sr^{2+} , Ba^{2+}), Schäfer and coworkers have synthesized molecular,⁶⁸ one-dimensional,⁶⁹ and two-dimensional⁷⁰ compounds with the use of hydrothermal and high temperature solid state reactions. $\text{Ca}_2\text{Sb}_2\text{S}_5$ consists of isolated $[\text{SbS}_3]^{3-}$ units and $\text{trans-}[\text{Sb}_2\text{S}_4]^{2-}$ dimers that are made up of two edge sharing SbS_3 trigonal pyramids.^{68a} Upon changing the counter cation to Ba^{2+} , $\text{Ba}_4\text{Sb}_4\text{Se}_{11}$ is formed.^{68b} It is composed of four different molecular species: Se_2^{2-} , SbSe_3^{3-} , cis- and $\text{trans-}[\text{Sb}_2\text{Se}_4]^{2-}$ dimers. $\text{Ba}_8\text{Sb}_6\text{S}_{17}$ contains SbS_3^{3-} units and the only example of an isolated $\text{Sb}_3\text{S}_8^{7-}$ anion. This anion is assembled from a central SbS_4 trigonal bipyramid that bridges two SbS_3 groups by sharing opposite corners.^{68c} Two different one-dimensional chains are observed in $\text{Sr}_3\text{Sb}_4\text{S}_9$.^{69a} Two $(\text{SbS}_2)_n^{n-}$ chains made up of corner-sharing SbS_3 trigonal pyramids and a double chain, $(\text{Sb}_2\text{S}_5)_n^{4n-}$, consisting of edge sharing SbS_5 square pyramids, make up the formula unit. The chains are oriented in a sheet-like manner and the Sb lone pairs are

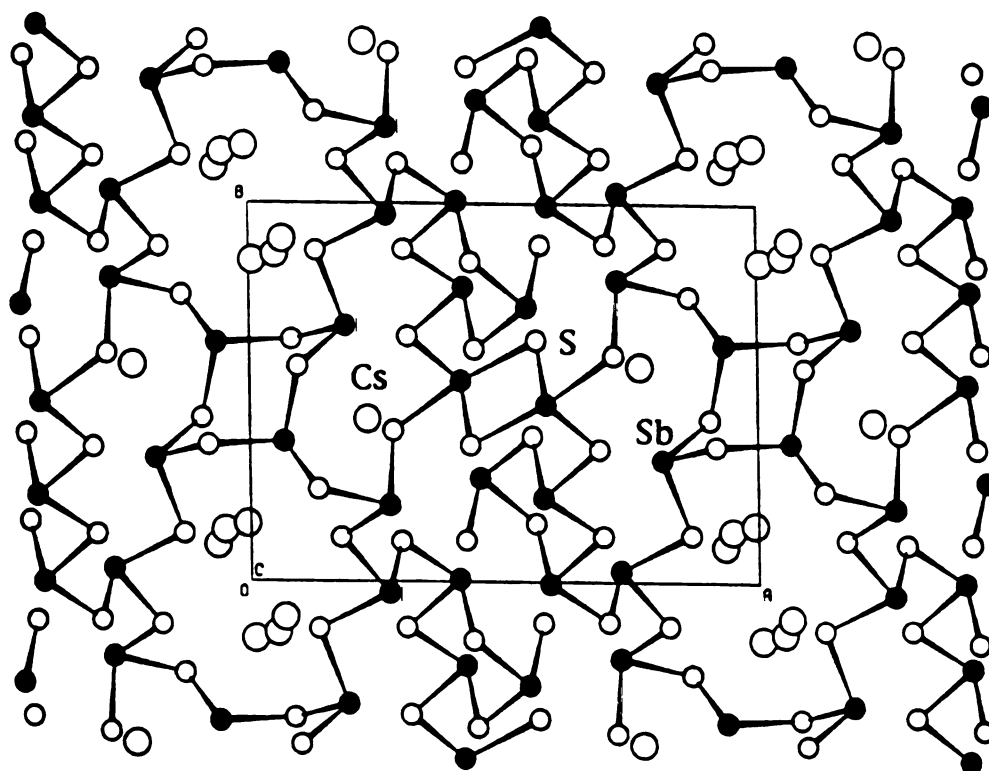


Figure 1-8: Projection of $\text{Cs}_2\text{Sb}_8\text{S}_{13}$ viewed down the c-axis with labeling.

directed into a nonpolar domain that is segregated from the polar domain of the Sr^+ cations. Edge- and corner-sharing of SbQ_3 and SbQ_4 units are also found in the layered structures of $\text{SrSb}_4\text{S}_7 \cdot 6\text{H}_2\text{O}$ and BaSb_2Se_4 .⁷⁰

Sheldrick and coworkers have shown that a number of ternary phases can be easily prepared by the simple reaction of an alkali metal carbonate with the binary antimony chalcogenide under hydro(methanol)thermal conditions. Examples include the layered RbSb_3Se_5 ,⁷¹ and the three-dimensional $\text{Cs}_3\text{Sb}_5\text{Q}_9$ ⁷² compounds. Also, $\text{Cs}_2\text{Sb}_4\text{Se}_6(\text{Se}_2)$ ⁷³ is the only known example of a covalently bonded antimony polyselenide.

The replacement of alkali metal cations with large organic counter cations leads to the formation of more open frameworks such as $[\text{N}(\text{CH}_3)_4]\text{Sb}_3\text{S}_5$, $[\text{N}(\text{C}_3\text{H}_7)_4]\text{Sb}_3\text{S}_5$ and $(\text{N}_2\text{C}_4\text{H}_8)\text{Sb}_4\text{S}_7$.⁷⁴ $[\text{N}(\text{C}_3\text{H}_7)_4]\text{Sb}_3\text{S}_5$ and $(\text{N}_2\text{C}_4\text{H}_8)\text{Sb}_4\text{S}_7$ are layered compounds that crystallize in a noncentrosymmetric space group ($\text{Ama}2$), however, the weak second harmonic generation (SHG) signal is only four times that of quartz. In the case of $[\text{Sb}_3\text{S}_5]_n^{n-}$, a counterion size effect is observed. Substitution of $[\text{N}(\text{C}_3\text{H}_7)_4]^+$ by $[\text{N}(\text{CH}_3)_4]^+$ would bring the $[\text{Sb}_3\text{S}_5]_n^{n-}$ layers close enough that considerable coulombic repulsions might develop, thus destabilizing the structure. These repulsions are overcome by combining the layers into a three-dimensional framework with intersecting channels. These compounds may serve as forerunners to a new class of microporous solids. Table 1-3 lists many of the known ternary antimony chalcogenides.

Table 1-3. Ternary Antimony Chalcogenide Compounds.

Formula	Synthesis	Structure	Ref.
ASbQ ₂ *	direct combination	2D	54
α -NaSbS ₂	direct combination	1D	56a
β -KSbS ₂	hydrothermal	1D	56b
β -ASbS ₂ (A=Rb,Cs)	direct combination	1D	56c,d
(NH ₄)SbS ₂	hydrothermal	1D	57
α -KSbSe ₂	direct combination	1D	56e
β -KSbSe ₂	direct combination	1D	56f
K ₃ SbS ₃ ·3Sb ₂ O ₃	hydrothermal	psuedo 3D	58
Cs ₂ Sb ₈ S ₁₃	hydrothermal	2D	59
K ₂ Sb ₄ S ₇	hydrothermal	3D	60
K ₂ Sb ₄ S ₇ ·H ₂ O	hydrothermal	3D	61
α -Rb ₂ Sb ₄ S ₇	hydrothermal	2D	62a
β -Rb ₂ Sb ₄ S ₇	methanolothermal	2D	62b
(NH ₄) ₂ Sb ₄ S ₇	hydrothermal	1D	63
Cs ₂ Sb ₄ S ₇	hydrothermal	2D	64
Cs ₆ Sb ₁₀ S ₁₈ ·1.2H ₂ O	hydrothermal	2D	65
TlSb ₃ S ₅	hydrothermal	2D	66
α - (β -)TlSbSe ₂	direct combination	2D	67
RbSb ₃ Se ₅	methanolothermal	2D	71
Cs ₃ Sb ₅ Q ₉ (Q=S,Se)	methanolothermal	2D	72
Cs ₂ Sb ₄ Se ₆ (Se ₂)	hydrothermal	2D	73
[N(C ₃ H ₇) ₄]Sb ₃ S ₅	hydrothermal	2D	74a
[N ₂ C ₄ H ₈]Sb ₄ S ₇	hydrothermal	2D	74a
[N(CH ₃) ₄]Sb ₃ S ₅	hydrothermal	3D	74b
CaSb ₂ S ₅	hydrothermal	molecular	68a
BaSb ₄ Se ₁₁	direct combination	molecular	68b
Ba ₈ Sb ₆ S ₁₇	direct combination	molecular	68c
Sr ₃ Sb ₄ S ₉	direct combination	1D	69a
Ba(en) ₄ (SbSe ₂) ₂	room temp. soln.	1D	69b
SrSb ₄ S ₇ ·6H ₂ O	hydrothermal	2D	70a
BaSb ₂ Se ₄	hydrothermal	2D	70b
K ₃ SbTe ₃	direct combination	molecular	70c
BaSbTe ₃	hydrothermal	2D	40

* A=alkali metal; Q=S, Se, Te

2. Review of Metal Thio(seleno)phosphates

The chemistry of metal thio(seleno)phosphate compounds features broad structural diversity and interesting physical properties. These compounds can be grouped into four main classes:

A. Orthothio(seleno)phosphate compounds with tetrahedral $[\text{PQ}_4]^{3-}$ ($\text{Q}=\text{S}, \text{Se}$) ligands. Examples include BPS_4 , AlPS_4 , GaPS_4 , InPS_4 , $\text{Pb}_3(\text{PS}_4)_2$, Cu_3PQ_4 , $\text{Pd}_3(\text{PS}_4)_2$, and LnPS_4 ($\text{Ln}=\text{La}, \text{Ce}, \text{Pr}$ etc.).^{75,76} The structures of these dense phases can be described as substituted metal chalcogenides with P occupying tetrahedral sites and M residing in tetrahedral, square planar (Pd^{2+}), and square anti-prismatic (Ln^{3+}) sites.

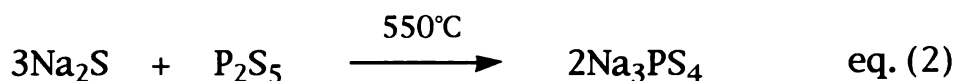
B. Thio(seleno)hypodiphosphates with $[\text{P}_2\text{Q}_6]^{4-}$ ($\text{Q}=\text{S}, \text{Se}$) ligands. These compounds fall into three subclasses depending on the metal coordination geometry. The largest and most important subclass is the $\text{M}_2\text{P}_2\text{Q}_6$ ($\text{M}=\text{Zn}, \text{Cd}, \text{Fe}, \text{Mn}, \text{Co}, \text{Ni}, \text{V}, \text{Mg}$; $\text{Q}=\text{S}, \text{Se}$) family with M^{2+} in an octahedral coordination environment.⁷⁷ They possess layered structures related to CdI_2 or CdCl_2 in which P-P pairs and M^{2+} cations reside in the octahedral sites of the framework. The second involves divalent main group metals (Sn ,⁷⁸ Pb ⁷⁹) with trigonal prismatic coordination to form dense three-dimensional $\text{M}_2\text{P}_2\text{Q}_6$ lattices. The third consists of metals in tetrahedral environments to give compounds such as $\alpha\text{-Ag}_4\text{P}_2\text{S}_6$, $\beta\text{-Ag}_4\text{P}_2\text{S}_6$, $\text{Ag}_4\text{P}_2\text{Se}_6$, and $\alpha\text{-AgGaP}_2\text{Se}_6$.⁸⁰

C. Compounds with pyrothiophosphate $[\text{P}_2\text{S}_7]^{4-}$ ligands. This ligand is not very common and only occurs in the molecular

$\text{As}_2\text{P}_2\text{S}_7$,⁸¹ and solid state compounds such as $\text{Ag}_4\text{P}_2\text{S}_7$, $\text{Ag}_7(\text{PS}_4)(\text{P}_2\text{S}_7)$, $\text{Hg}_2\text{P}_2\text{S}_7$, and RbVP_2S_7 .⁸²

D. Thiophosphates with Group 5 transition metals (V,⁸³ Nb,⁸⁴ Ta⁸⁵). These compounds generally consist of a series of face-sharing trigonal prismatic dimers (M_2S_8), linked by various $[\text{P}_x\text{S}_y]^{n-}$ anions ranging from $[\text{PS}_3]^{3-}$ to $[\text{P}_4\text{S}_{13}]^{6-}$.

The isolated $[\text{PS}_4]^{3-}$ anion has been crystallized with Li^+ and K^+ cations.⁸⁶ Recently, $\alpha\text{-Na}_3\text{PS}_4$ has been isolated in pure form by the reaction shown below:



AC-conductivity measurements show $\alpha\text{-Na}_3\text{PS}_4$ to be a good ionic conductor with values between 4.17×10^{-6} (50 °C) and 8.51×10^{-2} S/cm (500 °C).⁸⁷ This compound also undergoes an $\alpha \rightarrow \beta$ phase transition at 261 °C. Above 490 °C, there is evidence for a second high-temperature disordered phase, causing a steep increase in the conductivity.

Several main group metal thiophosphates have many interesting physical properties. InPS_4 ^{75d} crystallizes in a noncentrosymmetric tetragonal space group (I-4) which gives rise to a high non-linear susceptibility and piezo-coefficients.⁸⁸ The structure can be viewed as a defect zinc-blende (ZnS) derivative, in which P and In atoms occupy half of the tetrahedral sites. $\text{Pb}_3(\text{PS}_4)_2$ also crystallizes in a noncentrosymmetric space group P2_13 (cubic).^{75e} Second harmonic generation (SHG) measurements

revealed a weak signal about three times stronger than that of quartz. $\text{Pb}_3(\text{PS}_4)_2$ was synthesized by direct combination of the elements at 600 °C. The Pb^{2+} is coordinated by eight S atoms in a truncated tricapped trigonal prismatic geometry with Pb-S distances between 2.88(1) and 3.47(1) Å. In addition, crystals of GaPS_4 ^{75c} exhibit a considerable birefringence.⁸⁹ Another main group thiophosphate, BiPS_4 , features Bi^{3+} (stereochemically active lone pair) in two coordination environments.⁹⁰ $\text{Bi}(1)$ is coordinated by six S atoms and occupies the center of a nearly square planar assembly of four S atoms with a dovetail-like arrangement of two further S atoms extending downward. The $\text{Bi}(1)$ -S distances vary between 2.78(1) and 3.11(1) Å. $\text{Bi}(2)$ is coordinated to eight S atoms and is surrounded by four S atoms in a nearly planar rectangular geometry. In addition, two further pairs of S atoms, also in a dovetail-like configuration, are located above and below this plane. The $\text{Bi}(2)$ -S distances vary between 2.68(1) and 3.30(1) Å.²⁰ Other main group compounds include BPS_4 ,^{75a} AlPS_4 ,^{75b} and Tl_3PQ_4 .⁹¹

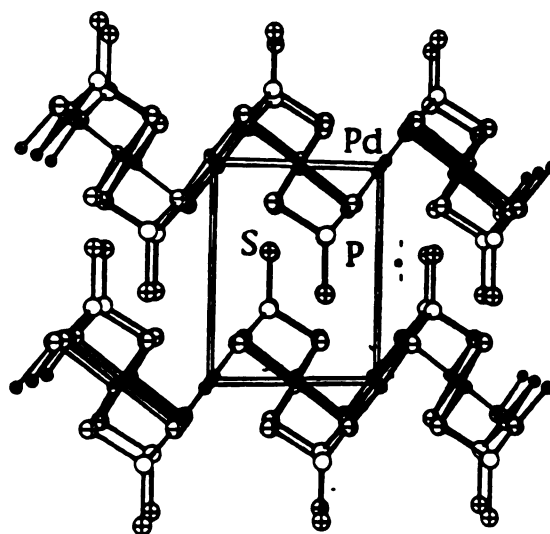
Several examples with transition metals have also been synthesized in this family of compounds. CrPS_4 is the only example of an MPS_4 compound with the metal in an octahedral coordination environment.⁹² It was synthesized from the elements in an evacuated quartz ampoule at 700 °C with a small amount of iodine added as a transport agent. Chains of edge-sharing CrS_6 octahedra run along the b direction and are connected in the a direction by PS_4 tetrahedra via corner- and edge-sharing to form the layered structure. High-temperature synthesis with Cu metal uncovered the isotypic Cu_3PQ_4 compounds, which have the wurtzite-related enargite

structure type.^{75f} Electrical measurements on single crystals of Cu_3PS_4 and $\text{Cu}_3\text{PS}_3\text{Se}$ show room temperature conductivities of 0.2 to 1.0 S/cm and carrier concentrations on the order of 10^{17} cm^{-3} . Both materials are active as cathodes for the photoelectrolysis of water. In addition, optical spectroscopic measurements demonstrate that substitution of Se for S lowers the optical band gap from 2.38(5) to 2.06(4) eV.⁹³

The use of a metal cation that prefers a different coordination geometry, such as Pd^{2+} (square pyramidal), can result in a new structure type. Purple-red crystals of $\text{Pd}_3(\text{PS}_4)_2$ were obtained by reaction of the elements at 600 °C.^{75g} Each $[\text{PS}_4]^{3-}$ uses three S atoms to triply bridge three square planar Pd^{2+} centers. The fourth S atom is nonbonding and protrudes into the van der Waals gap (see Figure 1-9b). The $\text{Pd}_3(\text{PS}_4)_2$ layers are not flat and form interdigitated sheets that stack in phase in the c direction as shown in Figure 1-9a.

Photoelectrochemical characterization of this compound was performed to measure such properties as band gap, quantum yield for electron flow, and stability in a photoelectrochemical cell. This study was undertaken to discover possible semiconductor electrodes with built-in catalytic properties.⁹⁴ The photoconductivity data suggest an indirect band gap of $E_g=2.54 \text{ eV}$ and possibly a direct gap of 2.89 eV. This compares to 2.15 eV determined by optical spectroscopy. A low quantum yield of about 1% at 3.1 eV was also measured. The small quantum yield and the large difference between the onset of optical absorption and the photoelectrochemically measured indirect transition can be ascribed to the low mobility of carriers in the material.⁹⁴

(A)



(B)

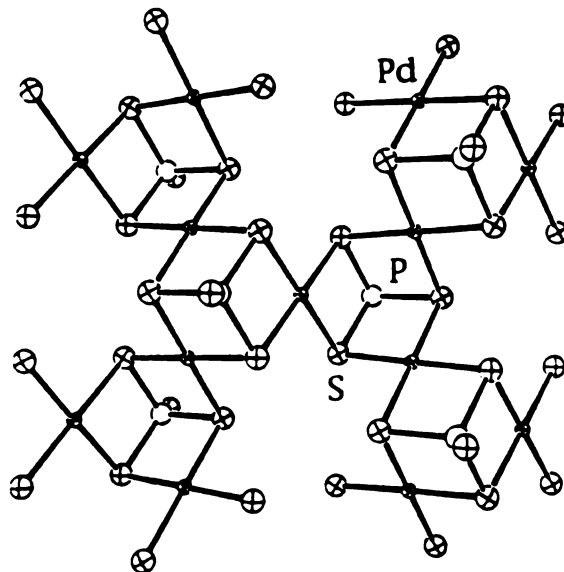


Figure 1-9: (A) Packing diagram of $\text{Pd}_3(\text{PS}_4)_2$ viewed down the a -axis with labeling. (B) ORTEP representation of a single $\text{Pd}_3(\text{PS}_4)_2$ layer.

Interestingly, extension to Au results in the formation of AuPS₄, whose structure remains elusive. Considering the tendency of Au³⁺ to form square planar species, a polymeric chain structure consisting of alternating edge-sharing PS₄ and AuS₄ units has been proposed, based on vibrational spectroscopy.⁹⁵ Quaternary mixed metal phases such as ZnAgPS₄ and TlSnPS₄ have also been investigated and structurally characterized.⁹⁶

The reaction of f-block metals with phosphorous and sulfur at high temperature yields a large number of isostructural compounds (tetragonal, space group I41/acd, Z=16) with interesting luminescence properties (Nd, Tb).⁷⁶ The compounds are air-sensitive because of the oxophilic Ln³⁺ metal center. The Ln³⁺ metal center resides in an eight-coordinate anti-square prismatic coordination site and probably prefers the [PS₄]³⁻ anion because of the charge balance with its stable trivalent oxidation state. An exception to this trend occurs with Eu. The Eu³⁺ analog could not be synthesized but instead formed Eu₂P₂S₆ (Eu²⁺, trigonal prismatic environment), which is isostructural to Pb₂P₂Q₆.⁷⁹

A large number of compounds of the formula M₃(PS₄)₂ (M²⁺ = Fe, Ni, Zn, Cd, Cu) were reported but their XRD patterns are consistent with M₂P₂Q₆.⁹⁷ Thus they probably do not exist.

The largest class of compounds are the thio(seleno)hypodiphosphates which feature the versatile [P₂Q₆]⁴⁻ ligand. The six Q atoms provide many potential bonding modes to metals. The structure of the [P₂Q₆]⁴⁻ ligand resembles that of a staggered ethane molecule and contains a P-P bond in which the

formal oxidation state of P is 4+. Alkali metal salts of the $[\text{P}_2\text{S}_6]^{4-}$ anion have been synthesized for infrared and Raman spectroscopic studies.⁹⁸

The divalent transition metals form a large subclass of compounds with the formula $\text{M}_2\text{P}_2\text{Q}_6$. The first members of this family of compounds were prepared and characterized in 1965 by Hahn and coworkers.^{77a} These compounds are structurally related to the CdI_2 or CdCl_2 structure types in which the M^{2+} cation and P-P pairs reside in the octahedral sites of the framework. It has been observed that the P-P bond lengthens to accommodate larger M^{2+} cations, thus providing a flexible lattice. The stacking of these layers most commonly gives rise to a monoclinic unit cell with space group C2/m , though hexagonal forms are also known. The lamellar structure of $\text{Ni}_2\text{P}_2\text{S}_6$ is shown in Figure 1-10a. Figure 1-10b displays a single $\text{Ni}_2\text{P}_2\text{S}_6$ layer with the hexagonal arrangement of the Ni^{2+} centers.

Optical transmission measurements on $\text{M}_2\text{P}_2\text{S}_6$ ($\text{M}=\text{Mn}, \text{Zn}, \text{Cd}$) reveal that they are transparent, slightly colored insulators with band gaps of 3.0, 3.4, and 3.5 eV, respectively, whereas $\text{M}_2\text{P}_2\text{S}_6$ with $\text{M}=\text{Fe}, \text{Ni}$ are dark semiconductors with gaps of 1.5 and 1.6 eV. The $\text{M}_2\text{P}_2\text{Se}_6$ analogs with $\text{M}=\text{Mn}, \text{Fe}$ have band gaps of 2.5 and 1.3 eV, respectively.⁹⁹

The magnetic behavior of $\text{M}_2\text{P}_2\text{Q}_6$ compounds containing magnetic ions such as Mn^{2+} (d^5), Fe^{2+} (d^6), and Ni^{2+} (d^8) have been thoroughly investigated.^{99,100,105a} In the case of $\text{Mn}_2\text{P}_2\text{S}_6$, it is best described as a two dimensional Heisenberg antiferromagnet, with a Neel temperature (T_N) of 78 K. The d^5 electrons are in the high-spin

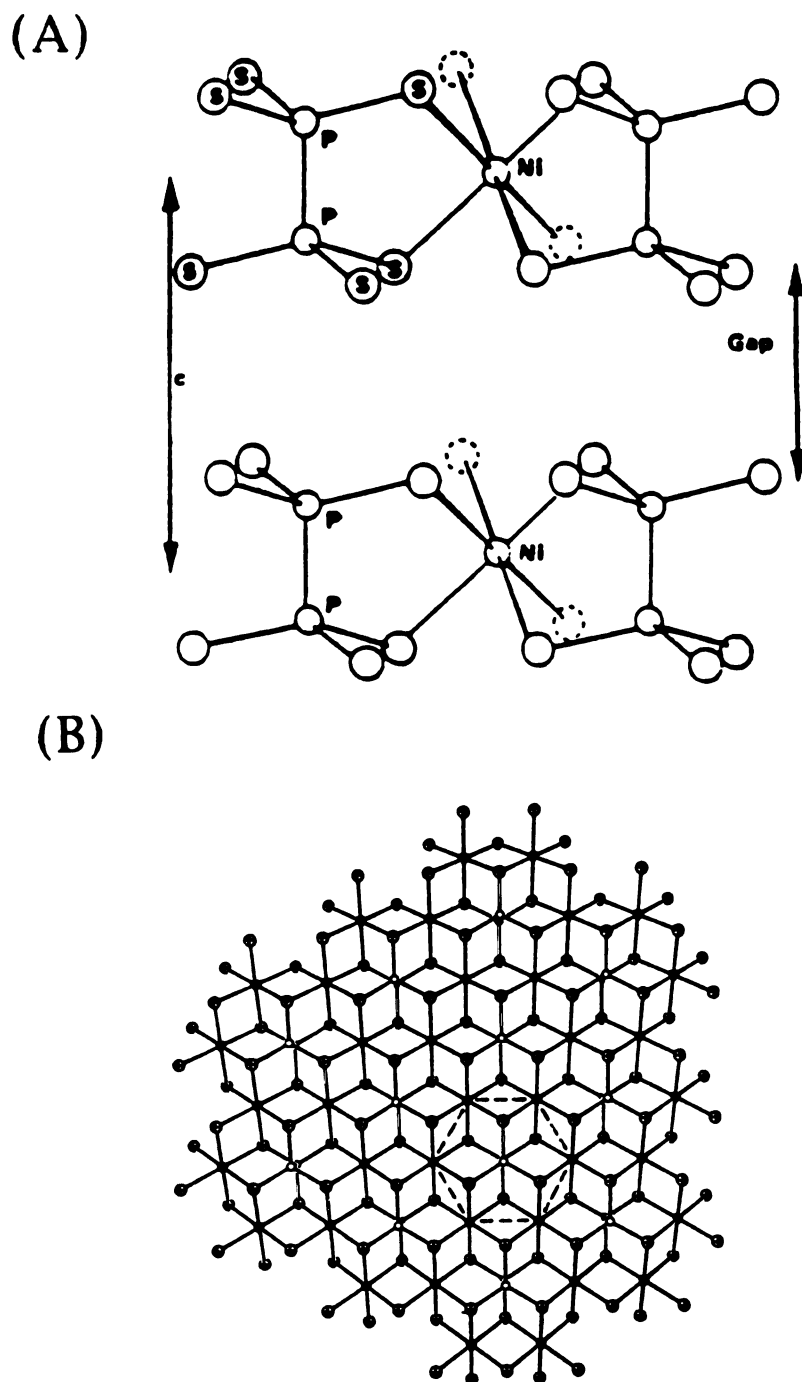


Figure 1-10: (A) Schematic representation of $\text{Ni}_2\text{P}_2\text{S}_6$ viewed down the a -axis. (B) ORTEP representation of a single $\text{Ni}_2\text{P}_2\text{S}_6$ layer. The hexagonal Ni array is outlined with dashed lines.

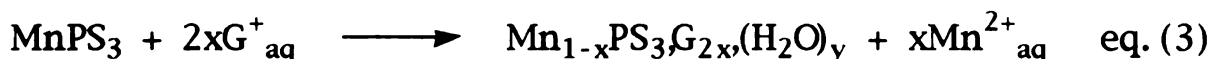
state. Neutron diffraction studies have determined the magnetic structure, which consists of a two dimensional honeycomb lattice in which each Mn^{2+} ion is antiferromagnetically coupled to its three nearest in-plane neighbors, and in which all the spins are perpendicular to the layer plane.¹⁰¹ The antiferromagnetic interactions are due to super-exchange through Mn-S-Mn bridges. Table 1-4 shows magnetic data for $\text{Mn}_2\text{P}_2\text{Q}_6$, $\text{Fe}_2\text{P}_2\text{Q}_6$ and $\text{Ni}_2\text{P}_2\text{S}_6$.

Table 1-4. Magnetic Data for $\text{M}_2\text{P}_2\text{Q}_6$ Compounds.

Compound	μ_{eff} (BM)	θ (K)	T_N (K)	M-M (\AA)	Ref.
$\text{Mn}_2\text{P}_2\text{S}_6$	5.97	-160	78	3.50	105a
$\text{Mn}_2\text{P}_2\text{Se}_6$	6.1	-201	85	3.69	99
$\text{Fe}_2\text{P}_2\text{S}_6$	5.44	+15	126	3.42	100c
	5.0	+65	133		99
$\text{Fe}_2\text{P}_2\text{Se}_6$	5.09	+37	123	3.62	100b
	5.0	-4	118		99
$\text{Ni}_2\text{P}_2\text{S}_6$	3.68	-559	254	3.36	100c
	3.9	-712	300		99

This class of compounds exhibits rich intercalation chemistry. $\text{Ni}_2\text{P}_2\text{S}_6$ and $\text{Fe}_2\text{P}_2\text{Q}_6$ have been shown to intercalate lithium either chemically,⁹⁹ upon reduction with butyl-lithium, or electrochemically.¹⁰² These compounds are of potential importance as low-dimensional cathode materials for secondary lithium batteries.¹⁰³ In 1980, Clement and coworkers discovered one of the

most unusual reactions found in intercalation chemistry.¹⁰⁴ They observed that treatment of $\text{Mn}_2\text{P}_2\text{S}_6$ with aqueous solutions of a number of ionic salts resulted in a removal of Mn^{2+} from inside the layers, and concomitant insertion of the guest cations in the inter-layer galleries. A wide variety of organometallic (cobalticenium), ammonium, and alkali metal cations intercalate into the host lattice. It has also been shown that pyridine and various polyethers can also be intercalated.¹⁰⁵ Recently, Clement and coworkers have reported that ion-exchange intercalation of $\text{M}_2\text{P}_2\text{S}_6$ ($\text{M}=\text{Cd}, \text{Mn}$) with a cationic organic dye induces a large second-order optical nonlinearity and permanent magnetization (Mn^{2+}).¹⁰⁶ These reactions are very general and can be written as in equation (3) ($\text{G}^+=\text{guest monocation}$).



This process occurs by a different mechanism than is commonly found in traditional ion exchangers, where ions already in the interlayer gallery region are exchanged with guest ions. This behavior is observed for other labile M^{2+} cations such as Zn^{2+} and Cd^{2+} , but more rigorous conditions are required for Fe^{2+} and Ni^{2+} which induce a crystal field stabilization. Interestingly, the ease of this chemistry has been related to the thermal parameters of the transition metal ion as determined by their crystal structure.¹⁰⁷ The labile Mn^{2+} ion has a high temperature factor so that it appears to rattle in the loose cage of S atoms. In addition, it has also been shown that intercalation transforms the antiferromagnetic host into a ferro or ferrimagnetic compound.¹⁰⁸

The remarkable structural flexibility of the host lattice has been demonstrated by the existence of compounds such as $V_{1.56}P_2S_6$ ¹⁰⁹ and $In_{1.33}P_2Q_6$ ^{75d,110} which contain metal deficient layers. $V_{1.56}P_2S_6$ is a mixed valence (V^{2+}/V^{3+}) compound as shown by the formula, $V^{2+}_{0.68}V^{3+}_{0.88}\square_{0.44}P_2S_6$ (\square =vacancy). $In_{1.33}P_2S_6$ ^{75d} is a metal-deficient threefold superstructure of the $Fe_2P_2S_6$ type formed by the ordering of metal vacancies. It is an electrical insulator with an optical absorption edge at 3.1(1) eV. The selenium analog crystallizes in two forms. In α - $In_{1.33}P_2Se_6$,¹¹⁰ the metal vacancies are disordered while those of the β -phase are ordered and form a sixfold superstructure of the $Fe_2P_2Se_6$ structure type.^{75d} Single crystals of α - $In_{1.33}P_2Se_6$ are highly resistive ($>10^8 \Omega\cdot cm$) with an optical band gap of 1.9 eV.^{75d} It is noteworthy that α - $In_{1.33}P_2Se_6$ may be suitable for photovoltaic devices.¹¹¹

Substitution of the M^{2+} cations, via direct combination of the elements at high temperature, has been demonstrated for $M_2P_2S_6$ to form $M^I M^{III} P_2S_6$ ¹¹² and $M^I_{2x} M^{II}_{1-2x} P_2S_6$ ¹¹³ ($M^I=Ag, Cu$; $M^{II}=Mn, Cd, Zn$; $M^{III}=V, Cr, In, Sc$), which retain the stable CdI_2 ($CdCl_2$) structure-type and subsequently enlarge this family of compounds. Recent investigations have focused on the possible existence of $Cu^{+}\cdots Cu^{+}$ or $Ag^{+}\cdots Ag^{+}$ dimers located in octahedral sites in $CuCrP_2S_6$,¹¹⁴ $CuVP_2S_6$,¹¹⁵ $Cu_{0.52}Mn_{1.74}P_2S_6$ ^{113b} and $Ag_2MnP_2S_6$.¹¹⁶ The crystal structure of $CuCrP_2S_6$ reveals a Cu electron density cloud with three extrema. One of them is in the middle on a pseudo-octahedral site and the other two are near the trigonal sulfur planes which suggests that CuS_6 octahedral sites, $Cu\cdots Cu$ pairs and vacancies all exist at room temperature in the disorder model. Complimentary EXAFS^{113b}

studies have confirmed this disorder model but recent low-temperature neutron powder diffraction studies have disputed the existence of bimetallic entities.¹¹⁷ The structure of CuVP_2S_6 features the same Cu positions as found in CuCrP_2S_6 plus a third tetrahedral site located in the van der Waals gap. The location of copper atoms in $\text{Cu}_{0.52}\text{Mn}_{1.74}\text{P}_2\text{S}_6$ remains uncertain due to some inconsistencies between X-ray diffraction and EXAFS data. It appears that the occurrence of copper pairs in these copper substitution phases is still an open question. The structure determination of $\text{Ag}_2\text{MnP}_2\text{S}_6$ confirmed the presence of $\text{Ag}^+\cdots\text{Ag}^+$ pairs with the Ag atoms found in trigonal planar coordination.

Kniep and coworkers have extended this substitution chemistry to include the $\text{M}_2\text{P}_2\text{Se}_6$ analogs and form layered quaternary selenodiphosphates for possible solar-cell applications.^{80d} Large single crystals were prepared from the elements at 750 °C followed by quenching or by cooling from the melt (Bridgman technique). The crystal structures of $\text{CuInP}_2\text{Se}_6$, $\text{AgInP}_2\text{Se}_6$, and $\beta\text{-AgGaP}_2\text{Se}_6$ are related to the CdI_2 structure type whereas the $\text{CuCrP}_2\text{Se}_6$, $\text{AgCrP}_2\text{Se}_6$, and $\text{AgAlP}_2\text{Se}_6$ are related to the CdCl_2 structure type. The most promising material in this group of compounds was found to be $\text{AgInP}_2\text{Se}_6$. The congruent melting behavior and perfect layer structure make it possible to grow thin films with crystallographic orientation directly from the melt. The crystals are dark red with a metallic luster and display a sharp band gap at $E_g=1.79$ eV.

The second subclass involving $[\text{P}_2\text{S}_6]^{4-}$ ligands are the $\text{M}_2\text{P}_2\text{Q}_6$ ($\text{Q}=\text{S},\text{Se}$) compounds with Sn^{2+} and Pb^{2+} . Sn^{2+} and Pb^{2+} are found in distorted trigonal prisms of $\text{S}(\text{Se})$. Three additional Q atoms are

located above the centers of the vertical prism faces to form a tricapped trigonal prism so the effective metal coordination is nine. The P-P pairs reside in the octahedral sites to form the dense three-dimensional network. The first representative of this group was $\text{Sn}_2\text{P}_2\text{S}_6$, prepared in single-crystalline form by iodine transport.^{78a} Several research groups synthesized and characterized $\text{Pb}_2\text{P}_2\text{S}_6$, $\text{Sn}_2\text{P}_2\text{Se}_6$, and $\text{Pb}_2\text{P}_2\text{Se}_6$ independently.^{77c,78,79} A detailed structural analysis showed $\text{Sn}_2\text{P}_2\text{S}_6$ to crystallize in the acentric space group Pc whereas the other members belong to the centric space group $\text{P2}_1/\text{c}$. It has been shown that $\text{Sn}_2\text{P}_2\text{S}_6$ undergoes a second order, exothermic phase transition from ferroelectric (Pc) to paraelectric ($\text{P2}_1/\text{c}$) at 60 °C.¹¹⁸ A crystal structure at 110 °C confirmed that the transition results from the movement of Sn atoms within the rigid $[\text{P}_2\text{S}_6]^{4-}$ lattice such that they become related by a center of symmetry. It is possible that the stereochemically active Sn^{2+} lone pair of electrons causes a distortion of the Sn-S coordination sphere during this transformation. This compound has been shown to be a promising ferroelectric material for use in memory devices.¹¹⁹ The optical band gaps and melting points of these compounds are shown in Table 1-5.

Table 1-5. Optical Properties of $\text{Sn}_2\text{P}_2\text{Q}_6$ and $\text{Pb}_2\text{P}_2\text{Q}_6$.^{78a}

Compound	E_g (eV), 295 K	E_g (eV), 77 K	m. p. (°C)
$\text{Sn}_2\text{P}_2\text{S}_6$	2.34	2.49	775
$\text{Sn}_2\text{P}_2\text{Se}_6$	1.79	2.12	670
$\text{Pb}_2\text{P}_2\text{S}_6$	2.56	2.77	914
$\text{Pb}_2\text{P}_2\text{Se}_6$	2.10	2.23	775

The third subclass of $[\text{P}_2\text{Q}_6]^{4-}$ compounds consist of metals in tetrahedral coordination. In $\alpha\text{-Ag}_4\text{P}_2\text{S}_6$,^{80a} the $[\text{P}_2\text{S}_6]^{4-}$ groups form almost planar layers that are connected with AgS_4 tetrahedra via common edges and corners to form the three-dimensional structure. $\beta\text{-Ag}_4\text{P}_2\text{S}_6$ ^{80b} is isostructural with $\text{Ag}_4\text{P}_2\text{Se}_6$ ^{80c} (space group $\text{P2}_1\text{2}_1\text{2}_1$) and possesses a higher symmetry version of the α -phase. The crystal structure of the mixed metal compound, $\alpha\text{-AgGaP}_2\text{Se}_6$, contains P_2Se_6 octahedra which share common edges with GaSe_4 tetrahedra, to give polyhedral chains running parallel to the $[100]$ direction.^{80d} In the $[010]$ direction, the chains are interconnected by sharing common edges and corners with AgSe_4 tetrahedra. The resulting layer structure is related to the three-dimensional structure of $\text{Ag}_4\text{P}_2\text{Se}_6$ by similar principles of polyhedral condensation.

Extension of this chemistry to Zn, results in the formation of $\text{Zn}_4(\text{P}_2\text{S}_6)_3$,^{120a} which contains one $[\text{P}_2\text{S}_6]^{4-}$ and two $[\text{P}_2\text{S}_6]^{2-}$ ligands. In $[\text{P}_2\text{S}_6]^{2-}$, the two P atoms are linked by two bridging S atoms (two PS_4 tetrahedra sharing an edge) so P is in the 5+ oxidation state. A second example of a compound with $[\text{P}_2\text{S}_6]^{2-}$ ligands is $\text{Ag}_2\text{P}_2\text{S}_6$.^{120b}

It should be noted that reaction with Ti metal does not result in the formation of an $\text{M}_2\text{P}_2\text{Q}_6$ compound but instead forms TiP_2S_6 , a new three-dimensional structure type.¹²¹ Although Ti prefers an octahedral environment, the stable 4+ oxidation state prevents crystallization of an $\text{M}_2\text{P}_2\text{S}_6$ derivative. In TiP_2S_6 , the Ti atoms attain a distorted octahedral coordination with Ti-S distances ranging from 2.433(3) to 2.454(5) Å.

Metal pyrothiophosphates feature a $[\text{P}_2\text{S}_7]^{4-}$ ligand formed by the corner-sharing of two PS_4 tetrahedra. The strong IR active S-P-S stretching vibration (466 cm^{-1}) is a useful diagnostic for identification of this ligand in a compound.¹²² The Se analog is unknown. The $[\text{P}_2\text{S}_7]^{4-}$ ligand is not very common and only occurs in a few compounds. It has been noted that complicated Lewis acid-base equilibria exist among $[\text{P}_2\text{S}_6]^{4-}$, $[\text{P}_2\text{S}_6]^{2-}$, $[\text{P}_2\text{S}_7]^{4-}$, and $[\text{PS}_4]^{3-}$ ligands in melts at high temperatures.¹²³ The relative scarcity of compounds with the $[\text{P}_2\text{S}_7]^{4-}$ ligand as compared to those of $[\text{PS}_4]^{3-}$ and $[\text{P}_2\text{S}_6]^{4-}$, seems to suggest that the complex equilibria favors the formation of the latter two species.

The $\text{As}_2\text{P}_2\text{S}_7$ molecule is formed at $350\text{ }^\circ\text{C}$ and is isotypic to P_4S_7 (C_{2v} symmetry).⁸¹ An As^{2+} - As^{2+} dimer is chelated by four terminal S atoms of the $[\text{P}_2\text{S}_7]^{4-}$ ligand to form two six-membered rings that are joined by the As-As bond and the bridging S-P-S unit. The terminal P-S bond distances are shorter due to their partial double bond character.¹²⁴ Reaction of P and S with Ag metal at $600\text{ }^\circ\text{C}$ resulted in $\text{Ag}_4\text{P}_2\text{S}_7$, a compound with a three-dimensional structure consisting of edge- and corner-sharing of AgS_4 tetrahedra and P_2S_7 polyhedra.^{82a} A second Ag containing phase, $\text{Ag}_7(\text{PS}_4)(\text{P}_2\text{S}_7)$, was isolated and features $[\text{P}_2\text{S}_7]^{4-}$ and $[\text{PS}_4]^{3-}$ ligands. The Ag^+ ions are disordered among the interstices of the anionic network which suggests that $\text{Ag}_7(\text{PS}_4)(\text{P}_2\text{S}_7)$ could exhibit ionic conductivity.^{82b} Reaction of P and S with HgS at $240\text{ }^\circ\text{C}$, results in the formation of $\text{Hg}_2\text{P}_2\text{S}_7$.^{82c} The Hg^{2+} ions reside in distorted tetrahedra that connect layers of P_2S_7 groups to form a three-

dimensional structure. Extension to quaternary systems involving alkali metals has recently been accomplished with the preparation of RbVP_2S_7 .^{82d} This phase was formed as a result of a failed attempt to synthesize a new substituted $\text{M}_2\text{P}_2\text{S}_6$ compound. The acentric structure is shown in Figure 1-11. Each VS_6 octahedron of RbVP_2S_7 shares two edges with the PS_4 tetrahedra of two $[\text{P}_2\text{S}_7]^{4-}$ ligands and two corners with the PS_4 tetrahedra of a third $[\text{P}_2\text{S}_7]^{4-}$ ligand to form flat sheets. The Rb^+ cations reside in between the layers.

Since the early 1980's, a new and exciting family of transition metal thiophosphates has emerged involving the Group 5 transition metals (V, Nb, Ta). Thiophosphate and disulfide ligands provide either octahedral or bicapped prismatic coordination to the metal. These compounds are found in a variety of structures which vary from low dimensional linear chains and layers to three-dimensional helical tunnel frameworks. The crystal structures of these compounds deviate sharply from those found for late transition metals and feature new $[\text{P}_x\text{S}_y]^n-$ ligands that have not been previously reported. These compounds are synthesized by direct combination of the elements in the 400-700 °C range. This class of compounds has recently been reviewed by Brec and coworkers.¹²⁵ In addition, the lithium intercalation chemistry of these compounds has been explored for possible battery cathode applications. Band structure calculations show that low-lying d-block acceptor orbitals are conducive for lithium intercalation.¹²⁵ Table 1-6 lists these new ligands along with examples of previously known thiophosphate

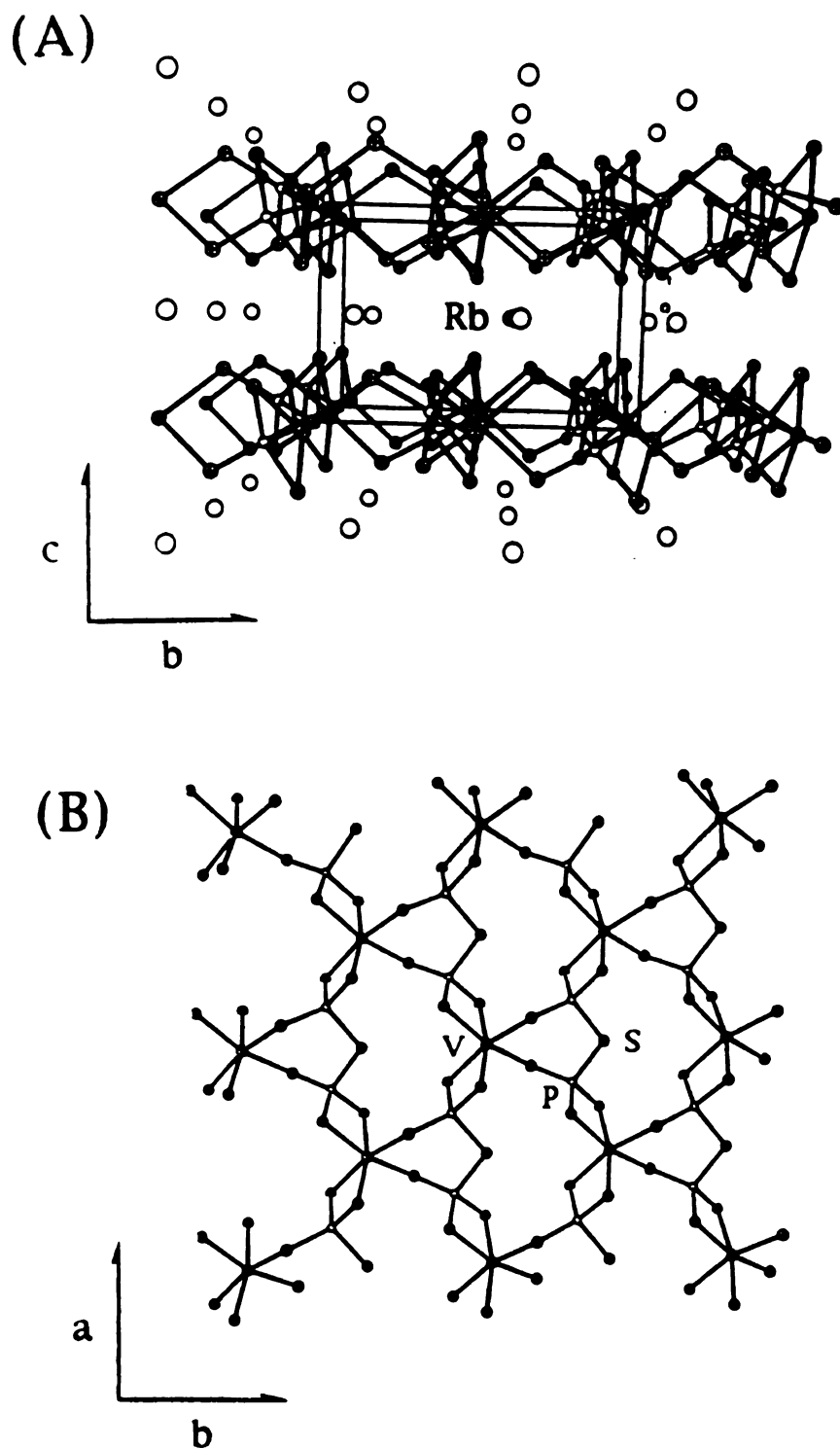


Figure 1-11: (A) Packing diagram of RbVP_2S_7 viewed down the a -axis. (B) ORTEP representation of the $[\text{VP}_2\text{S}_7]_n^-$ anionic layer with labeling.

Table 1-6. Types of Thiophosphate Ligands

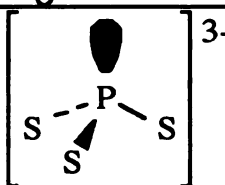
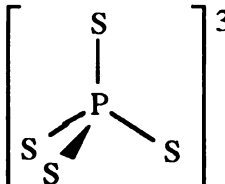
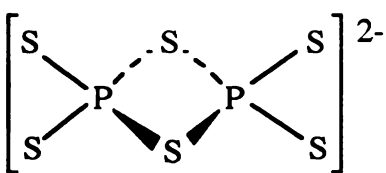
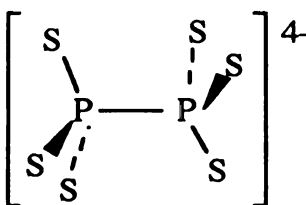
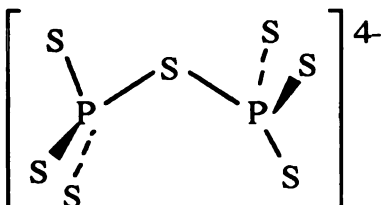
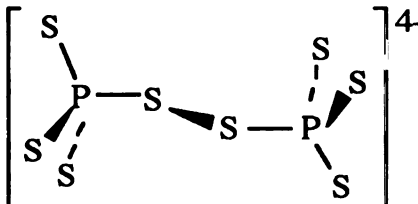
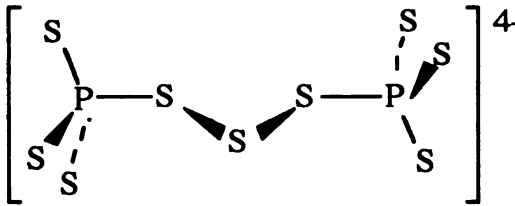
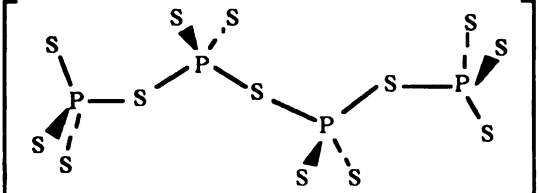
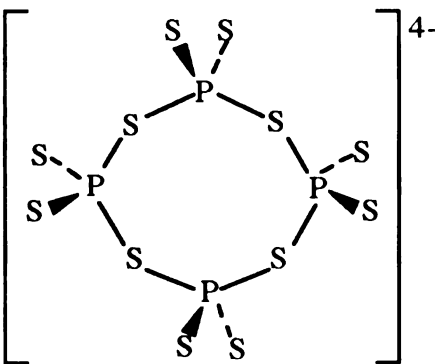
Ligand	Examples	Ref.
	$\text{P}_{0.2}\text{VS}_2$ (2D)	83a
	TaPS_6 (3D)	85a
	NbP_2S_8 (2D)	84a
	$\text{Mn}_2\text{P}_2\text{S}_6$ (2D)	107a
	$\text{Hg}_2\text{P}_2\text{S}_7$ (3D)	82c
	V_2PS_{10} (1D)	83c
	$\text{Nb}_4\text{P}_2\text{S}_{21}$ (2D)	84b

Table 1-6. (contd.)

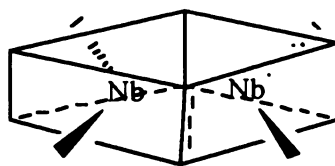
Ligand	Example	Reference
	V ₂ P ₄ S ₁₃ (2D)	83b
	NbP ₂ S ₈ (3D)	84d

units. [P₂S₆]⁴⁻ and [P₂S₇]⁴⁻ are the only two thiophosphate anions that are not found in this Group 5 chemistry.

The thiophosphate chemistry of vanadium is characterized by octahedral or bicapped trigonal prismatic coordination and an oxidation state of 3⁺ or 4⁺ to form one- or two-dimensional compounds. The structure of P_{0.2}VS₂ is closely related to the layer compound CdI₂^{83a} and possesses mixed V^{3+/4+} valency. In each layer, approximately every fifth VS₆ octahedra is capped by a P atom extending into the van der Waals gap. It represents the only example of a [PS₃]³⁻ ligand (P³⁺). The report of this ligand in this

non-stoichiometric compound seems dubious. Only polycrystalline samples of $P_{0.2}VS_2$ could be prepared so the structure was analyzed using powder X-ray and neutron diffraction techniques. The calculated P-P' bond distance is 2.70 Å which is much longer than a single P-P bond (2.20 Å). This distance raises the question of whether weakly bonded P...P pairs exist in the compound or the distance is only an artifact of the partial P occupancy. Another interesting compound is $V_2P_4S_{13}$ which possesses the unprecedented $[P_4S_{13}]^{6-}$ polymeric ligand.^{83b} The V^{3+} octahedra share edges to form dimers. Each ligand connects to four different dimers to construct the $V_2P_4S_{13}$ sheets (Figure 1-12). The one-dimensional V_2PS_{10} is also known.^{83c}

Further studies with niobium revealed several ternary metal thiophosphate compounds with layered or three-dimensional structures. The preferred coordination geometry of Nb in this thiophosphate chemistry is bicapped trigonal prismatic. This coordination is very common in the binary MQ_3 ($M=Ti, Zr, Hf, V, Nb, Ta$; $Q=S, Se$) layered chalcogenides. In MQ_3 , the bicapped trigonal prisms share triangular faces to form chains whereas the prisms in Nb/P/S compounds share rectangular faces through two S-S bonds to form $[Nb_2S_{12}]$ dimeric building blocks as shown in scheme (A).



Scheme (A)

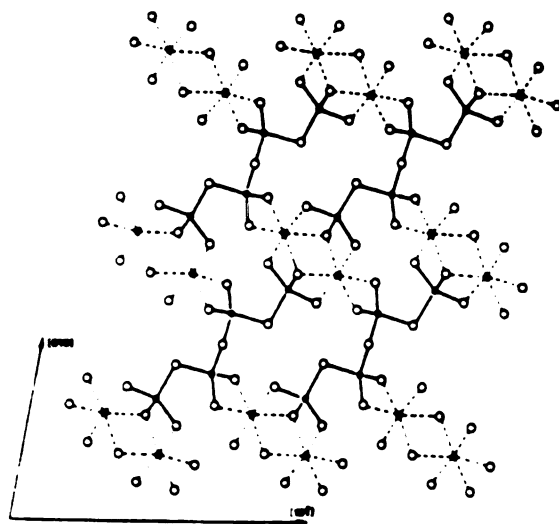


Figure 1-12: A schematic representation of a single V₂P₄S₁₃ layer. The open spheres are S atoms and dark lines highlight the bonding in the [P₄S₁₃]⁶⁻ ligand.

These building blocks feature Nb^{IV}-Nb^{IV} bonding through the rectangular face with a typical distance of 2.869(1) Å. The layered NbP₂S₈^{84a} phase is assembled through linking of [Nb₂S₁₂] units by [P₂S₆]²⁻ ligands. Two other layered compounds are obtained by end to end edge-sharing of [Nb₂S₁₂] units to form [Nb₂S₉] chains. These chains can be connected by [P₂S₉]⁴⁻ ligands (Nb₄P₂S₂₁)^{84b} or [PS₄]³⁻ units (Nb₂PS₁₀).^{84c} A three-dimensional tunnel framework, NbP₂S₈, is obtained by bridging of four [Nb₂S₁₂] units with an unusual cyclic [P₄S₁₂]⁴⁻ ligand. The formula can be represented as Nb₂(P₄S₁₂)(S₂)₂.^{84d}

Similar investigations with the more electropositive Ta results in three-dimensional tunnel networks with Ta in the 5⁺ oxidation state. Closed-tube phase iodine transport of TaS₆ (Ta(PS₄)(S₂)) yielded gray single crystals.^{85a} The compound crystallizes in a tetragonal unit cell with an acentric space group (I4₁/acd). The familiar [Ta₂S₁₂] units are connected by [PS₄]³⁻ units to form small channels along the c-direction. A structurally related phase was synthesized at 500 °C. The black needle-like crystals of Ta₄P₄S₂₉ also have a tetragonal unit cell but crystallize in a different acentric space group (P4₃2₁2).^{85b} The compositional difference between the two compounds results from right-handed, helical, polymeric S₁₀ chains inserted in the tunnels of Ta₄P₄S₂₉ which are stabilized by van der Waals forces. High temperature chalcogen substitution reactions with Se yields a mixed Se₈S₂ chain in the tunnels.^{85c} A minor phase was also characterized in these reactions and found to be Ta₂P₂S₁₁, a tunnel structure with two different size channels.^{85d}

It has been noted that niobium is a frontier element separating more covalent 1D and 2D vanadium derivatives from the more ionic 3D tantalum phases.

There is a scarcity of quaternary compounds with alkali metals. Such compounds could exist and would be very interesting as pseudo-ternary $A^+/M^{n+}/[P_xQ_y]^{z-}$ compounds. The alkali metal not only donates electrons but also would act as a structure-directing counterion to generate new anionic frameworks.

3. Alkali Metal Polychalcogenide Fluxes

About two decades ago, Scheel recognized the potential of alkali metal polysulfides as reaction media while concentrating on the recrystallization of known materials at high temperatures. Materials such as ZnS, CdS, MnS, PbS, NaCrS₂, KCrS₂, NaInS₂, KFeS₂, FeS₂, NiS₂, CoS₂, MoS₂, NbS₂, and HgS were grown successfully from sodium polysulfide fluxes at high temperatures (>700 °C) by Scheel and others.¹²⁶ Sodium polysulfides were used because of the relative inertness of Na⁺ ions toward formation of ternary compounds. Ironically, while Scheel tried to avoid alkali metal incorporation, research in the Kanatzidis group over the last six years has focussed on trying to promote it with the use of various low temperature (150-500 °C) molten alkali metal polychalcogenide fluxes. This methodology has led to the discovery of nearly one hundred novel ternary and quaternary compounds with exotic structures and desirable physical properties.

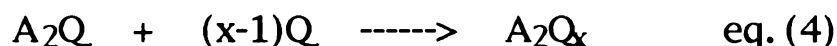
Alkali metal polychalcogenide fluxes are attractive for the synthesis of new ternary chalcogenide compounds for a variety of reasons. First, these fluxes have a wide range of melting points so that intermediate temperatures can be explored (see Table 1-7). It is necessary to remain in this temperature regime (150-500 °C) so that known thermodynamically stable compounds may be avoided. Second, the fluxes not only act as a solvent but also as sources of the elemental components of the products. Third, the polychalcogenide fluxes solidify upon cooling to a glassy solid. This glassy matrix can

be removed by dissolution in water or polar organic solvents so that pure products may be obtained. Finally, the flux is a highly oxidizing medium as well as a basic (nucleophilic) one. The basicity of the

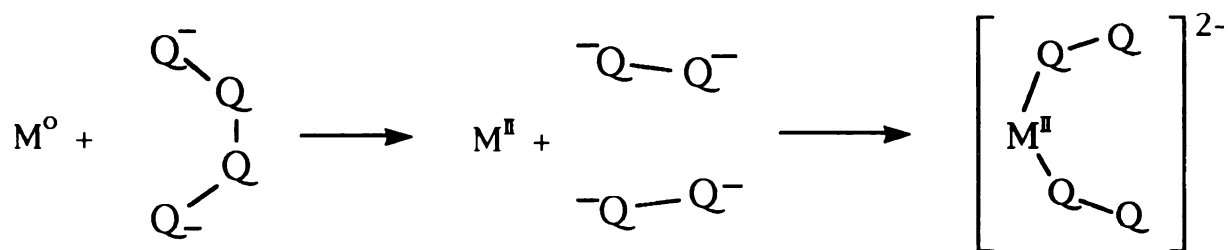
Table 1-7. Melting Points (°C) of Some Known Alkali Metal Polychalcogenides.

Li ₂ S 900-975	Li ₂ S ₂ 370				
Na ₂ S 1180	Na ₂ S ₂ 490	Na ₂ S ₃ 229	Na ₂ S ₄ 275	Na ₂ S ₅ 252	
Na ₂ Se >875	Na ₂ Se ₂ 495	Na ₂ Se ₃ 313	Na ₂ Se ₄ 290		Na ₂ Se ₆ 258
Na ₂ Te 953	Na ₂ Te ₂ 348				Na ₂ Te ₆ 436
K ₂ S 840	K ₂ S ₂ 470	K ₂ S ₃ 252	K ₂ S ₄ 145	K ₂ S ₅ 206	K ₂ S ₆ 189
K ₂ Se	K ₂ Se ₂ 460	K ₂ Se ₃ 380	K ₂ Se ₄ 205	K ₂ Se ₅ 190	
Rb ₂ S 530	Rb ₂ S ₂ 420	Rb ₂ S ₃ 213	Rb ₂ S ₄ 160	Rb ₂ S ₅ 225	Rb ₂ S ₆ 201
Cs ₂ S	Cs ₂ S ₂ 460	Cs ₂ S ₃ 217	Cs ₂ S ₄ 160	Cs ₂ S ₅ 210	Cs ₂ S ₆ 186

medium can be controlled by varying the A_2Q/Q ratio as shown below.



A short chain has strong Lewis basicity while a long Q_x^{2-} chain is less basic because the 2^- charge is dispersed over more Q atoms which reduces the negative charge on the terminal atoms. All of the Q atoms, especially the negatively charged terminal atoms, provide effective binding sites to the metal. The metal is oxidized and then attacked by the negatively charged species as shown in scheme (B).



Scheme (B)

The resulting M^{n+} cations, alkali metal cations and polychalcogenides associate to form various structures, depending on the coordination preference of the metal, the size of the alkali metal cation, the concentrations of the various ligands in the flux, and the reaction temperature.

In 1987, Ibers and coworkers reported the first examples of the use of alkali metal polychalcogenides to synthesize new ternary metal chalcogenide compounds. $K_4Ti_3S_{14}$ ¹²⁸ and $Na_2Ti_2Se_8$ ¹²⁹ were

isolated from K_2S_x and Na_2Se_x fluxes, respectively, in the 375-470 °C temperature range. The structures of these new compounds consist of one-dimensional polymeric chains of $[Ti_3(S_2)_6(S)_2]_n^{4n-}$ and $[Ti_2(Se_2)_3(Se)_2]_n^{2n-}$ and contain octahedrally coordinated Ti^{4+} centers bonded to Q_2^{2-} and Q^{2-} ligands. The full potential of this synthetic method was not realized because of the relatively high temperatures used in these reactions.

In our laboratory, Y. Park has thoroughly explored the chemistry of late transition metals (Cu, Au, Hg) in the lower temperature regime (215-450°C). He has isolated a number of new metal (poly)chalcogenides with long Q_x^{2-} ($x=2,3,4,5$) ligands.¹³⁰

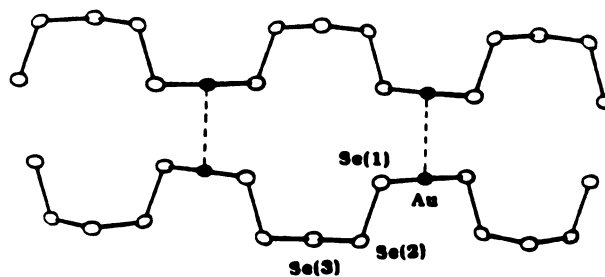
The A/Au/Se (A=Na,K,Cs) system is particularly interesting because of its structural diversity associated with various polychalcogenides from Se_3^{2-} to Se_5^{2-} and the novel $Au^{1+/3+}$ redox chemistry. $KAuSe_5$ was prepared from the reactant ratio Au/ K_2Se /Se of 1/2/8 at 250 °C. This is a Au^+ compound, composed of noncentrosymmetric one-dimensional $[Au(Se_5)]_n^{n-}$ chains running parallel to the c-axis as shown in Figure 1-13a. The $[Au(Se_5)]_n^{n-}$ chains are composed of Se_5^{2-} ligands bridging two Au atoms via terminal Se atoms. These chains interact with each other to form dimers through close $Au \cdots Au$ $d^{10}-d^{10}$ contacts (2.950(3) Å). A slight reduction in the K_2Se ratio from 2 to 1.8 yielded the novel K_3AuSe_{13} compound, the most Se rich compound known to date. The $[Au(Se_3)(Se_5)_2]_n^{3n-}$ chains can be described as a one dimensional assembly of square plane Au^{3+} centers that have two arm-like trans Se_5^{2-} ligands and are bridged by Se_3^{2-} ligands, counterbalanced by K^+ ions. (see Figure 1-13b). It is remarkable that a slight change in the

Lewis basicity from K_2Se_5 to $\text{K}_2\text{Se}_{5.4}$ can result in the formation of two completely different compounds with unusual structures. By doubling the amount of Au metal and increasing the reaction temperature to 290 °C, KAuSe_2 was isolated. The structure consists of $\text{Au}^{\text{I}}\text{Se}_4$ square planes that share opposite edges to form one-dimensional chains. By reducing the size of the alkali counter cation from K^+ to Na^+ and increasing the basicity of the flux, the one-dimensional chains are condensed into $[\text{AuSe}_2]^-$ layers, separated by the Na^+ cations. AuSe_4 square planes share edges and corners to form the anionic sheets. The structures of the two anions are shown in Figure 1-14. The layered versus one-dimensional structure is a clear manifestation of a couterion size effect.

J.-H. Liao expanded the scope of these reactions by exploring the polysulfide chemistry of the main group tin metal. Several ternary tin polysulfides such as $\text{K}_2\text{Sn}_2\text{S}_8$, $\alpha\text{-Rb}_2\text{Sn}_2\text{S}_8$, $\beta\text{-Rb}_2\text{Sn}_2\text{S}_8$, $\text{K}_2\text{Sn}_2\text{S}_5$, $\text{Cs}_2\text{Sn}_2\text{S}_6$, and $\text{Cs}_2\text{SnS}_{14}$ were synthesized.^{131a} He extended this chemistry to mixed metal systems using $[\text{SnQ}_4]^{4-}$ and $[\text{Sn}_2\text{Q}_6]^{4-}$ building blocks. Mixed metal phases such as $\text{K}_2\text{Au}_2\text{SnS}_4$, $\text{K}_2\text{Au}_2\text{Sn}_2\text{S}_6$, and $\text{Rb}_2\text{Cu}_2\text{SnS}_4$ all possess novel structures.^{131b}

In the reaction of Sn with alkali metal polysulfides, it was observed that basic fluxes favor formation of molecular compounds. The reaction of Sn with less basic fluxes such as K_2S_5 at 275 °C yielded $\text{K}_2\text{Sn}_2\text{S}_8$. The unique anionic structure contains tetrahedral and octahedral Sn^{4+} centers and is shown in Figure 1-15. These Sn centers are linked via S^{2-} and $(\text{S}_4)^{2-}$ so the layered anionic

(A)



(B)

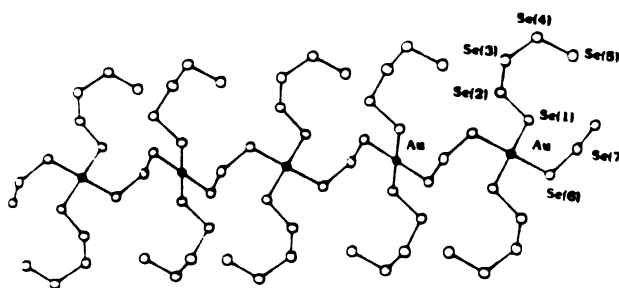
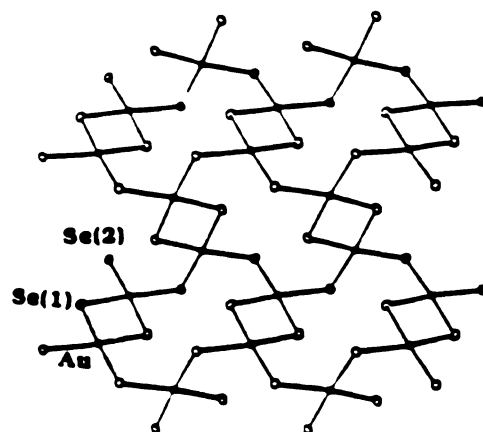


Figure 1-13: (A) One-dimensional structure of $[\text{AuSe}_5]_n^-$. $\text{Au}\cdots\text{Au}$ contacts are indicated by dashed lines. (B) Structure of the $[\text{AuSe}_{13}]_n^{3-}$ chain.

(A)



(B)

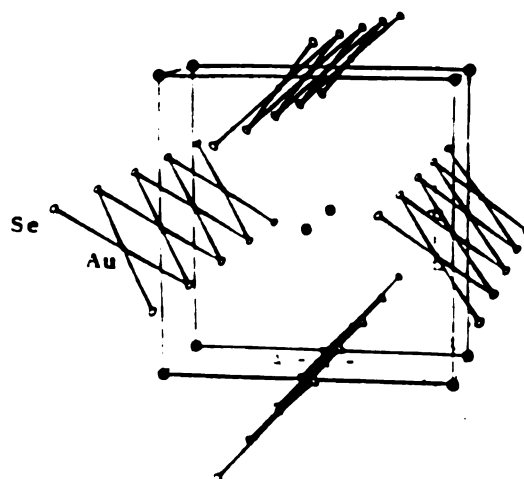


Figure 1-14: (A) A single anionic layer in NaAuSe_2 . (B) The one-dimensional chains in KAuSe_2 .

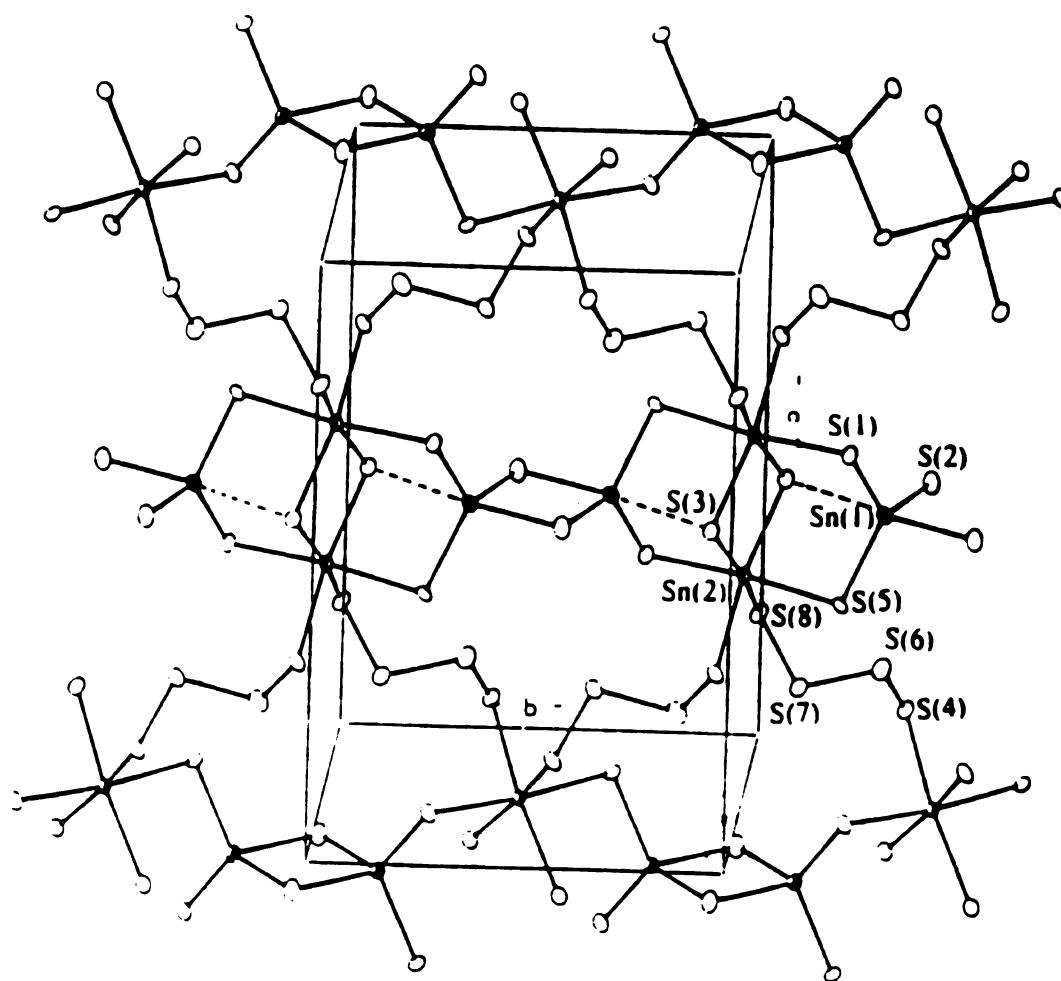


Figure 1-15: ORTEP representation and labeling scheme of the layered structure of $[\text{Sn}_2\text{S}_8]_n^{2n-}$. The dashed lines indicate the shortest nonbonding $\text{Sn}\cdots\text{S}$ contacts (2.934(5) Å).

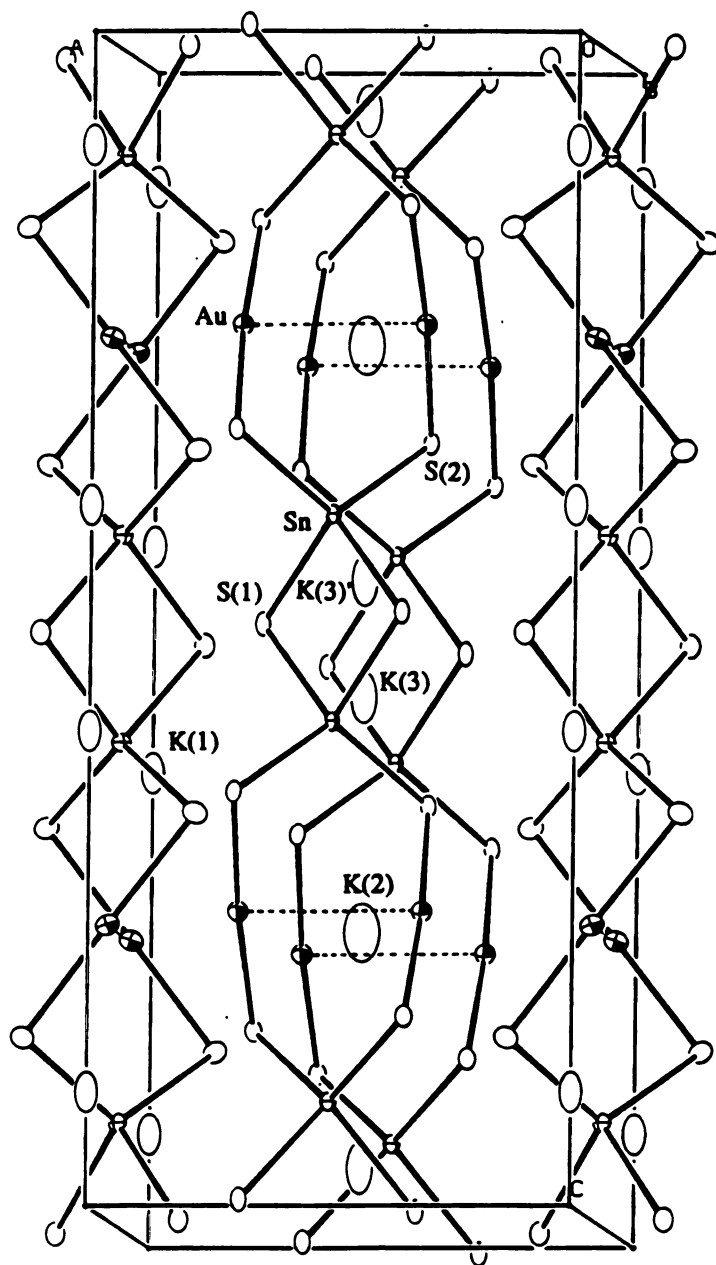


Figure 1-16: ORTEP representation and labeling scheme of $K_2Au_2Sn_2S_6$. View down the b-axis. Au...Au contacts are shown by dashed lines.

framework can be expressed as $[\text{Sn}_2\text{S}_4(\text{S}_4)]^{2-}$. This is one of the few examples of a tin polysulfide. The addition of Au in $\text{Sn}/\text{K}_2\text{S}_x$ mixtures at 350 °C can provide structural flexibility due to the preference of Au^+ for linear coordination. The $\text{K}_2\text{Au}_2\text{Sn}_2\text{S}_6$ structure is one-dimensional, featuring edge-sharing bitetrahedral $[\text{Sn}_2\text{S}_6]$ units connected by linear Au^+ atoms to form infinite chains. The $[\text{Au}_2\text{Sn}_2\text{S}_6]^{2-}$ chains lie parallel to the crystallographic c-axis and are separated by potassium cations as shown in Figure 1-16. There is also a $\text{Au}\cdots\text{Au}$ short contact at 3.010(2) Å. The $\text{Au}\cdots\text{Au}$ contact occurs inside the $\text{Sn}(\text{SAuS})_2\text{Sn}$ eight-membered ring.

Inspired by the enormous success of Park and Liao, we decided to explore the chemistry of two Group 15 main group metals, antimony and bismuth. We have isolated a number of interesting compounds with novel structural architectures. In addition, high temperature reactions with K_2S and Bi_2S_3 have resulted in compounds with interesting semi-metallic electrical conductivity and thermoelectric power. The results will be described in Chapters 2 and 3. During our studies with polychalcogenides, we noticed that the chalcophosphates $[\text{P}_x\text{Q}_y]^{n-}$ were also rather uncommon in their occurrence in solid state compounds. We utilized our experience with alkali polychalcogenide fluxes to develop a general methodology by which new thio(seleno)phosphate (or chalcophosphate) compounds can be consistently obtained. These *polychalcophosphate* fluxes, $\text{A}_x[\text{P}_y\text{Q}_z]$, provide highly charged $[\text{P}_x\text{Q}_y]^{n-}$ anions that coordinate to the M^{n+} center. We have synthesized several bismuth

and antimony thiophosphates with $[\text{P}_2\text{S}_7]^{4-}$, $[\text{PS}_4]^{3-}$, and $[\text{P}_2\text{S}_6]^{4-}$ ligands (Chapter 4). Further exploration using alkali metal polyselenophosphate fluxes with metals such as Sb, Bi, Mn, Fe, Cu, Ag, and Au resulted in the formation of a variety of new quaternary compounds with novel structure types and interesting physical properties which are also the subject of this thesis. The quaternary selenophosphate compounds will be discussed in Chapters 5 and 6.

List of References

1. Takeuchi, Y.; Sadanaga, R. *Z. Kristallogr.*, 1969, 130, 346-368.
2. Berry, L. G.; Mason, B. *Mineralogy*, W. H. Freeman and Co.: San Francisco, 1959.
3. Wuensch, B. J. *Z. Kristallogr.*, 1964, 125, 459-488.
4. Niizeki, N.; Buerger, M. J., *Z. Kristallogr.* 1957, 109, 129-157.
5. Kohatsu, I.; Wuensch, B. J. *Acta Cryst.* 1971, B27, 1245-1252.
6. Iitaka, Y.; Nowacki, W. *Acta Cryst.* 1962, 15, 691-698.
7. (a) Smith, M. J.; Knight, R. J.; Spencer, C. W. *J. Appl. Phys.* 1962, 33(7), 2186-2190. (b) Testardi, L. R.; Bierly, J. N. Jr.; Donahoe, F. J. *J. Phys. Chem. Solids*, 1962, 23, 1209. (c) Champness, C. H.; Chiang, P. T.; Parekh, P. *Can. J. Phys.* 1965, 43, 653-569. (d) Yim, W. M.; Fitzke, E. V. *J. Electrochem. Soc.* 1968, 115, 556-560.
8. (a) Rowe, D. M.; Bhandari, C. M. *Modern Thermoelectrics*, Holt, Rinehart and Winston: London, 1983; p. 103. (b) Borkowski, K.; Przyluski, J. *J. Mat. Res. Bull.* 1987, 22, 381-387. (c) Ibuki, S; Yoschimatsu, S. *J. Phys. Soc. Japan*, 1955, 10, 549-554. (d) Jeon, H-W.; Ha, H-P.; Hyun, D-B.; Shim, J-D. *J. Phys. Chem. Solids* 1991, 4, 579-585.
9. Kaibe, H.; Tanaka, Y.; Sakata, M.; Nishida, I. *J. Phys. Chem. Solids* 1989, 50, 945-950.
10. Atabaeva, E. Ya; Itskevich, E. S.; Mashkov, S. A.; Popova, S. V.; Vereshchagin, L. F. *Sov. Phys.-Solid State*, 1968, 10, 43-46.
11. Atabaeva, E. Ya; Mashkov, S. A.; Popova, S. V.; *Sov. Phys.-Crystallography*, 1973, 18, 104-105.
12. Anderson, T. L.; Krause, H. B. *Acta Cryst.* 1974, 30B, 1307-1310.
13. Nakajima, S. *J. Phys. Chem. Solids*, 1963, 24, 479-485.
14. Katsuki, S. I. *J. Phys. Soc. Japan*, 1969, 26, 53.
15. Pecher P.; Toussaint, G. *Phys. Lett. A*, 1989, 135, 223-226.
16. (a) Hofmann, W. *Z. Kristallogr.* 1933, 86, 225. (b) Scavnicar, S. Z. *Kristallogr.* 1960, 114, 85-97.
17. Tideswell, N. W.; Kruse, F. H.; McCullough, J. D. *Acta Cryst.* 1957, 10, 99-102.
18. Kanishcheva, A. S.; Mikhailov, Yu. N.; Trippel, A. F. *Inorg. Mater.* 1981, 17, 1466-1468.
19. Ibuki, S; Yoschimatsu, S. *J. Phys. Soc. Japan*, 1955, 10, 549-554.
20. Platakis, N. S. *J. Non-Crystalline Solids*, 1978, 27, 331-346.

21. Chikawa, J.; Sato, S.; Kawamura, T.; Goto, N. *Proc. Plan Meet. X-ray Instrum. Photon Fact.*, 1979, 87-88.
22. McKay, D. L. Belg. 866,332, U.S. Appl. 819,027, 1977.
23. King, J. P.; Asmerom, Y. *ASLE Trans.* 1981, 24, 497-504.
24. Bonnet, D. *Photovoltaic Sol. Energy Conf.*, 1979, 387-395.
25. Ibanez, A.; Olivier-Fourcade, J.; Jumas, J. C.; Phillippot, E.; Maurin, M. Z. *Anorg. Allg. Chem.* 1985, 540, 106-116 and references therein.
26. Ismail, F. M.; Hanafi, Z. M. Z. *Phys. Chem., Leipzig*, 1986, 267, 667-672.
27. Bube, R. H. *Photoconductivity of Solids*, John Wiley and Sons, Inc.: New York, 1960; p. 234.
28. Smith, M. J.; Knight, R. J.; Spencer, S. W. *J. Appl. Phys.*, 1962, 33, 2186-2130.
29. Gobrecht, H.; Boeters, K.-E.; Pantzer, G. *Z. Phys.*, 1964, 177, 68-83.
30. (a) Boon, J. W. *Rec. Trav. Chim. Pays-Bas*, 1944, 63, 32. (b) Glemser, O.; Filcek, M. *Z. Anorg. Allg. Chem.*, 1955, 279, 321-323 (c) Gattow, G.; Zemmann, J. *Z. Anorg. Allg. Chem.*, 1955, 279, 324-327.
31. Trippel, A. F.; Lazarev, Berul, S. I. *Russ. J. Inorg. Chem.*, 1978, 23, 390-391.
32. Voroshilov, Y. V.; Peresh, E. Y.; Golovei, M. I. *Inorg. Mater.*, 1972, 8, 777-778.
33. (a) Peresh, E. Yu.; Golovei, M. I.; Berul, S. I. *Inorg. Mater.* 1971, 7, 27-30. (b) Golovei, M. I.; Berul, S. I.; Luzhnaya, N. P.; Peresh, E. Yu. *Inorg. Mater.* 1970, 6, 961-963.
34. Schmitz, D.; Bronger, W. *Z. Naturforsch.*, 1974, 29b, 438-439.
35. Kanishcheva, A. S.; Mikhailov, J. N.; Lazarev, V. B.; Trippel, A. F. *Dokl. Akad. Nauk, SSSR (Kryst.)*, 1980, 252, 96-99.
36. R. G. Burns, M. B. Burns *Manganese Dioxide Symposium*, Tokyo, 1981; Vol. 2, Ch 6.
37. G. Cordier, H. Schäfer, C. Schwidetzky, *Rev. Chim. Miner.*, 1985, 22, 676-683.
38. Julien-Pouzol, M.; Jaulmes, S.; Laruelle, P. *Acta. Cryst.* 1979, B35, 1313-1315.
39. G. Cordier, H. Schäfer, C. Schwidetzky, *Rev. Chim. Miner.*, 1985, 22, 631-638.

40. Cook, R.; Schäfer, H. *Rev. Chim. Miner.* 1982, 19, 19-27.
41. K. Volk, G. Cordier, R. Cook, Schäfer, H. *Z. Naturforsch.*, 1990, 35b, 136-140.
42. B. Aurivillius, *Acta Chem. Scand.* 1983, A37 399-407.
43. Liautard, B.; Garcia, J. C.; Brun, G.; Tedenac, J. C.; Maurin, M. *Eur. J. Solid State Inorg. Chem.* 1990, 27, 819-830.
44. (a) Hofmann, W. *Z. Kristallogr.*, 1933, 84, 177-203. (b) Kupcik, V. *Diskussionstagung der Sektion für Kristallkunde (D.M.G.) Marburg*, 1965, 16-17.
45. Matzat, E. *Min. Petr. Mitt.*, 1972, 18, 312-316.
46. Lee, S.; Fischer, E.; Czerniak, J.; Nagasundaram, N. *J. Alloys and Compounds* 1993, 197, 1-5.
47. Mumme, W. G.; Watts, J. A. *Acta Cryst.* 1980, 36B, 1300-1304.
48. Ohmasa, M.; Nowacki, W. *Z. Kristallogr.*, 1973, 137, 422-432.
49. (a) Elwell, D.; Scheel, H. J., *Crystal Growth from High temperature Solutions*, Academic Press, London, 1975, Chapter 10. (b) Dugue', J.; Carre', D.; Guittard, M. *Acta Cryst.*, 1978, 34B, 403.
50. (a) Lazarev, V. B.; Trippel', A. F.; Berul', S. I. *Russ. J. Inorg. Chem.*, 1977, 22, 1218-1220. (b) Trippel', A. F.; Berul', S. I.; Lazarev, V. B. *Russ. J. Inorg. Chem.*, 1980, 25, 1545-1547. (c) Berul', S. I.; Lazarev, V. B.; Trippel', A. F.; Buchikhina, O. P. 1977, 22, 1390-1393. (d) Lazarev, V. B.; Trippel', A. F.; Berul', S. I. *Russ. J. Inorg. Chem.*, 1980, 25, 1694-1697.
51. Bazakutsa, V. A.; Lazarev, V. B.; Gnidash, N. I.; Salov, A. V.; Kulchitskaya, A. K. *Russ. J. Inorg. Chem.* 1988, 33, 1204-1207.
52. (a) Grund, A.; Preisinger, A. *Acta Cryst.* 1950, 3, 363-366. (b) Mereiter, K.; Preisinger, A.; Guth, H. *Acta Cryst.* 1979, B35, 19-25. (c) Eisenmann, B.; Zagler, R. *Z. Naturforsch.*, 1989, 44b, 249-256. (d) Graf, H. A.; Schafer, H. *Z. Anorg. Allg. Chem.* 1976, 425, 67-80.
53. (a) Cotton, F. A.; Wilinon, G. *Advanced Inorganic Chemistry* (5th Edition), John Wiley and Sons: New York, 1988; pp 208-209. (b) Pitzer, K. *S. Acc. Chem. Res.*, 1979, 12, 272-276. (c) Pyykkö, P.; Desclaux, J.-P. *Acc. Chem. Res.*, 1979, 12, 276-281.
54. (a) Bazakutsa, V. A.; Gnidash, N. I.; Lazarev, V. B.; Rogacheva, E. I.; Salov, A. V.; Sukhorukova, L. N.; Vasileva, M. P.; Berul, S. I. *Russ. J. Inorg. Chem.* 1973, 18, 1722-1725. (b) Kovba, L. M.; Lazarev, V. B.; Moshchalkova, N. A.; Salov, A. V. *Russ. J. Inorg. Chem.* 1978, 23, 279-280. (c) Kovba, L. M.; Lazarev, V. B.; Moshchalkova, N. A.; Salov, A. V. *Russ. J. Inorg. Chem.* 1976, 21, 857-858. (d) Kovba, L. M.; Lazarev, V. B.; Moshchalkova, N. A.; Salov, A. V. *Russ. J. Inorg. Chem.* 1978, 23, 426-430. (e) Berul, Lazarev, V. B.; Salov, A. V. *S. I. Russ. J. Inorg. Chem.* 1971, 16, 1779-1781.

55. Bazakutsa, V. A.; Lazarev, V. B.; Gnidash, N. I.; Salov, A. V.; Podyachaya, E. N.; Zozuya; Moshchalkova, N. A. *Russ. J. Inorg. Chem.* 1979, 24, 1601-1603.
56. (a) Olivier-Fourcade, E.; Phillippot, J.; M. Maurin *Z. Anorg. Allg. Chem.*, 1978, 446, 159-168. (b) Graf, H. A.; Schäfer, H. *Z. Anorg. Allg. Chem.*, 1975, 414, 211-219. (c) Kanishcheva, A. S.; Kuznetsov, V. G.; Lazarev, V. B.; Tarasova, T. G. *Zh. Strukt. Khim.*, 1977, 18, 1069. (d) Kanishcheva, A. S.; Mikhailov, Y. N.; Kuznetsov, V. G.; Batog, V. N. *Dokl. Akad. Nauk SSSR*, 1980, 251, 603-605. (e) Kanishcheva, A. S.; Palkina, K. K.; Kuznetsov, V. G.; Lazarev, V. B.; Tarasova, T. G. *Inorg. Mater.* 1976, 12, 465-466. (f) Dittmar, V. G.; Schafer, H. *Z. Naturforsch.* 1977, 32b, 1346-1348.
57. Volk, K.; Bickert, P.; Kolmer, R.; Schäfer, H. *Z. Naturforsch.* 1979, 34b, 380-382.
58. Graf, H. A.; Schäfer, H. *Z. Anorg. Allg. Chem.* 1975, 414, 220-230.
59. Volk, K.; Schäfer, H. *Z. Naturforsch.* 1979, 34b, 1637-1640.
60. Eisenmann, B.; Schäfer, H. *Z. Naturforsch.*, 1979, 34b, 383-385.
61. Graf, H. A.; Schäfer, H. *Z. Naturforsch.* 1972, 27b, 735-739.
62. Dittmar, V. G.; Schvfer, H. *Z. Anorg. Allg. Chem.* 1978, 441, 93-97. (b) Sheldrick, W. S.; Hausler, H.-J. *Z. Anorg. Allg. Chem.* 1988, 557, 105-111.
63. Dittmar, G.; Schäfer, H. *Z. Anorg. Allg. Chem.* 1977, 437, 183-187.
64. Dittmar, G.; Schäfer, H. *Z. Anorg. Allg. Chem.* 1978, 441, 98-102.
65. Parise, J. B. *J. Chem. Soc., Chem. Commun.*, 1990, 22, 1553-1554.
66. Gostojic, M.; Nowacki, W.; Engle, P. *Z. Kristallogr.* 1982, 159, 217-224.
67. Wacker, K.; Salk, M.; Decker-Schultheiss, G.; Keller, E. *Z. Anorg. Allg. Chem.* 1991, 606, 51-58.
68. (a) Cordier, G.; Schäfer, H. *Revue de Chemie Minerale*, 1981, 18, 218-223. (b) Cordier, G.; Cook, R.; Schäfer, H. *Revue de Chemie Minerale*, 1980, 17, 1-6. (c) Dörrscheidt, W.; Schäfer, H. *Z. Naturforsch.*, 1981, 36b, 410-414.
69. (a) Cordier, G.; Schwidetzky, C.; Schäfer, H. *Revue de Chemie Minerale*, 1982, 19, 179-186. (b) König, T.; Eisenmann, B.; Schäfer, H. *Z. Anorg. Allg. Chem.* 1982, 488, 126-132.
70. (a) Cordier, G.; Schäfer, H.; Schwidetzky, C. *Z. Naturforsch.*, 1984, 39b, 131-134. (b) Cordier, G.; Schäfer, H.; *Z. Naturforsch.*, 1979, 34b, 1053-1056. (c) Jung, J.-S.; Wu, B.; Stevens, E. D.; O'Connor, C. J. *J. Solid State Chem.* 1991, 94, 362-367.
71. Sheldrick, W. S.; Hausler, H.-J. *Z. Anorg. Allg. Chem.* 1988, 557, 98-104.

72. Sheldrick, W. S.; Hausler, H.-J. *Z. Anorg. Allg. Chem.* 1988, *561*, 149-156.
73. Sheldrick, W. S.; Kaub, J. *Z. Anorg. Allg. Chem.* 1986, *536*, 114-118.
74. (a) Parise, J. B.; Ko, Y. *Chem. Mater.* 1992, *4*, 1446-1450. (b) Parise, J. B. *Science*, 1991, *251*, 293-294.
75. (a) Weiss, A; Schäfer, H. *Z. Naturforsch.* 1963, *18b*, 81-82. (b) Weiss, A; Schäfer, H. *Naturwissen.* 1960, *47*, 495. (c) Buck, P.; Carpentier, C.-D. *Acta Cryst.*, 1973, *B29*, 1864-1868. (d) Diehl, R.; Carpentier, C.-D. *Acta Cryst.*, 1978, *B34*, 1097-1105. (e) Post, E.; Krämer, V. *Mat. Res. Bull.*, 1984, *19*, 1607-1612. (f) Garin, J.; Parthe, E. *Acta Cryst.*, 1972, *B28*, 3672-3674. (g) Simon, A.; Peters, K.; Peters, E.-M.; Hahn, H. *Z. Naturforsch.* 1983, *38b*, 426-427.
76. Le Rolland, B.; McMillan, P.; Moline, P.; Colombet, P. *Eur. J. Solid State Inorg. Chem.* 1990, *27*, 715-724 and references therein.
77. (a) Hahn, H.; Klingen, W. *Naturwiss.* 1965, *52*, 494. (b) Klingen, W.; Eulenberger, G.; Hahn, H. *Z. Anorg. Allg. Chem.*, 1973, *401*, 97-112. (c) Toffoli, P.; Khodadad, P.; Rodier, N. *Acta Cryst., Sect. B*, 1978, *34*, 1779-1781. (d) Klingen, W.; Ott, R.; Hahn, H. *Z. Anorg. Allg. Chem.*, 1973, *396*, 271-278. (e) Jandali, M. Z.; Eulenberger, G.; Hahn, H. *Z. Anorg. Allg. Chem.*, 1978, *447*, 105-118.
78. (a) Carpentier, C. D.; Nitsche, R. *Mater. Res. Bull.* 1974, *9*, 401-410. (b) Carpentier, C. D.; Nitsche, R. *Mater. Res. Bull.* 1974, *9*, 1097-1100.
79. (a) Becker, R.; Brockner, W.; Schäfer, H. *Z. Naturforsch.* 1983, *38a*, 874-879. (b) Becker, R.; Brockner, W.; Schäfer, H. *Z. Naturforsch.* 1984, *39a*, 357-361. (c) Yun, H.; Ibers, J. A. *Acta Cryst.* 1987, *C43*, 2002-2004.
80. (a) Toffoli, P.; Michelet, A.; Khodadad, P.; Rodier, N. *Acta Cryst.* 1982, *B38*, 706-710. (b) Toffoli, P.; Khodadad, P.; Rodier, N. *Acta Cryst.* 1983, *C39*, 1485-1488. (c) Toffoli, P.; Khodadad, P.; Rodier, N. *Acta Cryst.* 1978, *B34*, 1779-1781. (d) Pfeiff, R.; Kniep, R. *J. Alloys and Compounds*, 1992, *186*, 111-133.
81. Hönle, W. *Z. Naturforsch.* 1984, *39b*, 1088-1091.
82. (a) Toffoli, P.; Khodadad, P.; Rodier, N. *Acta Cryst.* 1977, *B33*, 1492-1494. (b) Toffoli, P.; Khodadad, P.; Rodier, N. *Acta Cryst.* 1977, *B38*, 2374-2378. (c) Jandali, M. Z.; Eulenberger, G.; Hahn, H. *Z. Anorg. Allg. Chem.*, 1978, *445*, 184-192. (d) Durand, E.; Evain, M.; Brec, R. *J. Solid State Chem.*, 1993, *102*, 146-155.
83. (a) Brec, R.; Ouvrard, G.; R. Freour, R.; Soubeyroux, J. L.; Rouxel, J. *Mater. Res. Bull.* 1983, *18*, 689-696. (b) Evain, M.; Brec, R.; Ouvrard, G.; Rouxel, J. *J. Solid State Chem.* 1985, *56*, 12-20. (c) Brec, R.; Ouvrard, G.; Evain, M.; Grenouilleau, P.; Rouxel, J. *J. Solid State Chem.*, 1983, *7*, 174-184.

84. (a) Grenouilleau, P.; Brec, R.; Evain, M.; Rouxel, J. *Rev. Chim. Miner.*, 1983, 20, 628-635. (b) Brec, R.; Evain, M.; Grenouilleau, P.; Rouxel, J. *Rev. Chim. Miner.* 1983, 20, 283-294. (c) Brec, R.; Grenouilleau, P.; Evain, M.; Rouxel, J. *Rev. Chim. Miner.*, 1983, 20, 295-304. (d) Evain, M.; Brec, R.; Ouvard, G.; Rouxel, J. *Mater. Res. Bull.*, 1984, 18, 41-48.
85. (a) Fiechter, S.; Kuhs, W. F.; Nitsche, R. *Acta Cryst.*, 1989, B36, 2217-2220. (b) Evain, M.; Queignec, M.; Brec, R.; Rouxel, J. *J. Solid State Chem.*, 1985, 56, 148-157. (c) Evain, M.; Queignec, M.; Brec, R.; Sourisseau, C. *J. Solid State Chem.*, 1988, 75, 413-431. (d) Evain, M.; Lee, S.; Queignec, M.; Brec, R. *J. Solid State Chem.* 1987, 71, 139-153.
86. (a) Mercier, R.; Malugani, J.-P.; Fahys, B.; Robert, G. *Acta Cryst.* 1982, B38, 1887-1890. (b) Schäfer, H.; Schäfer, G.; Weiss, A. *Z. Naturforsch.* 1965, 20b, 811.
87. Jansen, M.; Henseler, U. *J. Solid State Chem.* 1992, 99, 110-119.
88. Bridenbaugh, P. M. *Mat. Res. Bull.*, 1973, 8, 1055-1060.
89. Buck, P.; Nitsche, R. A. *Z. Naturforsch.*, 1971, 26b, 731.
90. Zimmermann, H.; Carpentier, C.-D.; Nitsche, R. *Acta Cryst.* 1975, B31, 2003-2006.
91. (a) Toffoli, P.; Khodadad, P.; Rodier, N. *Bull. Soc. Chim. Fr.* 1981, 11, 429-432. (b) I. J. Fritz, T. J. Isaacs, M. Gottlieb and B. Morosin, *Solid State Commun.*, 1978, 27, 535.
92. Diehl, R.; Carpentier, C.-D. *Acta Cryst.* 1977, B33, 1399-1404.
93. Marzik, J. V.; Hsieh, A. K.; Dwight, K.; Wold, A. *J. Solid State Chem.* 1983, 49, 43-50.
94. Folmer, J. C.; Turner, J. A.; Parkinson, B. A. *J. Solid State Chem.* 1987, 68, 28-37.
95. Pätzmann, U.; Brockner, W.; Cyvin, B. N.; Cyvin, S. J. *J. Raman Spectroscopy*, 1986, 17, 257-261.
96. (a) Toffoli, P.; Rouland, J. C.; Khodadad, P.; Rodier, N. *Acta Cryst.* 1985, C41, 645-647. (b) Becker, R.; Brockner, W.; Eisenmann, B. *Z. Naturforsch.*, 1987, 42a, 1309-1312.
97. Soklakov, A. I.; Nechaeva, V. V. *Inorg. Mater.*, 1970, 6, 873-874.
98. Cyvin, S. J.; Cyvin, B. N.; Wibbelmann, C.; Becker, R.; Brockner, W.; Parensen, M. *Z. Naturforsch.*, 1985, 40a, 709-713.
99. Brec, R.; Schleich, D. M.; Ouvrard, G.; Louisy, A.; Rouxel, J. *Inorg. Chem.*, 1979, 18, 1814-1818.
100. (a) Odile, J.-P.; Steger, J. J.; Wold, A. *Inorg. Chem.* 1975, 14, 2400-2402. (b) Taylor, B. E.; Steger, J. J.; Wold, A.; Kostiner, E. *Inorg. Chem.* 1974, 13,

- 2719-2421. (c) Taylor, B. E.; Steger, J. J.; Wold, A. J. *Solid State Chem.* 1973, 7, 461-467.
101. Kurosawa, K.; Saito, S.; Yamaguchi, Y. *J. Phys. Soc. Japan*, 1983, 11, 3919-3926.
 102. (a) Le Mehouste, A.; Ouvrard, G.; Brec, R.; Rouxel, J. *Mater. Res. Bull.*, 1977, 12, 1191. (b) Thompson, A. H.; Whittingham, M. S. *Mater. Res. Bull.*, 1977, 12, 741.
 103. Thompson, A. H.; Whittingham, M. S. *U. S. Patent 4,049,879* 1977. (b) Brec, R.; Le Mehaute', A. *Fr. Patents 7,704,519* 1977.
 104. Clement, R. *J. Chem. Soc., Chem. Commun.*, 1980, 647-648.
 105. (a) Joy, P.; Vasudevan, S. *J. Am. Chem. Soc.* 1992, 114, 7792-7801. (b) Lagadic, I.; Leaustic, A.; Clement, R. *J. Chem. Soc., Chem. Commun.*, 1992, 1396-1397.
 106. Lacroix, P. G.; Clement, R.; Nakatani, K.; Zyss, J.; Ledoux, I. *Science*, 1994, 263, 658-660.
 107. (a) Ouvrard, G.; Brec, R.; Rouxel, J. *Mater. Res. Bull.*, 1985, 20, 1181-1189. (b) Prouzet, E.; Ouvrard, G.; Brec, R. *Mater. Res. Bull.*, 1986, 21, 195-200.
 108. Clement, R.; Audiere, J.-P.; Renard, J.-P. *Rev. Chim. Miner.* 1982, 19, 560-571.
 109. Ouvrard, G.; Brec, R.; Rouxel, J. *Comptes Rendus Acad. Sci. Paris*, 1982, 294, 971.
 110. Katty, A.; Soled, S.; Wold, A. *Mater. Res. Bull.*, 1977, 12, 663-666.
 111. Etman, M.; Katty, A.; Levy-Clement, C.; Lemasson, P. *Mater. Res. Bull.*, 1982, 17, 579-584.
 112. (a) Ouvrard, G.; Brec, R.; Rouxel, J. *Mater. Res. Bull.*, 1985, 20, 1181-1189. (b) Lee, S.; Colombet, P.; Ouvrard, G.; Brec, R. *Inorg. Chem.*, 1988, 27, 1291-1294. (c) Lee, S.; Colombet, P.; Ouvrard, G.; Brec, R. *Mater. Res. Bull.*, 1986, 21, 917-928. (d) Lee, S. *J. Am. Chem. Soc.* 1988, 110, 8000-8006 and references therein. (e) Ouili, Z.; LeBlanc, A.; Colombet, P. *J. Solid State Chem.*, 1987, 66, 86-94.
 113. (a) Lee, S.; Colombet, P.; Ouvrard, G.; Brec, R. *Inorg. Chem.* 1988, 27, 1291-1294. (b) Mathey, Y.; Michalowicz, A.; Toffoli, P.; Vlaic, G. *Inorg. Chem.* 1984, 23, 897-902.
 114. Colombet, P.; Leblanc, A.; Danot, M.; Rouxel, J. *J. Solid State Chem.* 1982, 41, 174-184.
 115. Durand, E.; Ouvrard, G.; Evain, M.; Brec, R. *Inorg. Chem.*, 1990, 29, 4916-4920.
 116. Leblanc, A.; Ouili, Z.; Colombet, P. *Mat. Res. Bull.*, 1985, 20, 947-954.

117. Mathey, Y.; Mercier, H.; Michalowicz, A.; Leblanc, A. *J. Phys. Chem. Solids*, 1985, **46**, 1025-1029.
118. Scott, B.; Pressprich, M.; Willet, R. D.; Clearly, D. A. *J. Solid State Chem.* 1992, **96**, 294-300.
119. Arnautova, E; Sviridov, E; Rogach, E. Savchenko, E; Grekov; A. *Integrated Ferroelectrics*, 1992, **1**, 147-150.
120. (a) Bouchetiere, M.; Toffoli, P.; Khodadad, P.; Rodier, N. *Acta Cryst.* 1978, **B34**, 384-387. (b) Toffoli, P.; Khodadad, P.; Rodier, N. *Acta Cryst.* 1978, **B34**, 3561-3564.
121. Jandali, M. Z.; Eulenberger, G.; Hahn, H. Z. *Anorg. Allg. Chem.*, 1980, **470**, 39-44.
122. (a) Queignec, M.; Evain, M.; Brec, R.; Sourisseau, C. *J. Solid State Chem.* 1986, **63**, 89-109 (b) Andrae, H.; Blachnik, R. *J. Alloys and Compounds* 1992, **189**, 209-215.
123. Menzel, F.; Ohse, L.; Brockner, W. *Heteroatom Chem.* 1990, **1**, 357-362.
124. Vos, A. ; Wiebenga, E. H. *Acta Cryst.* 1955, **8**, 217-223.
125. Evain, M.; Brec, R.; Whangbo, M.-H. *J. Solid State Chem.*, 1987, **71**, 244-262.
126. (a) Scheel, H. J. *J. Cryst. Growth* 1974, **24/25**, 669-673. (b) Sanjines, R.; Berger, H.; Levy, F. *Mater. Res. Bull.* 1988, **23**, 549-553. (c) Garner, R. W.; White, W. B. *J. Cryst. Growth* 1970, **7**, 343-347.
127. Sunshine, S. A.; Kang, D.; Ibers, J. A. *J. Am. Chem. Soc.* , 1987, **109**, 6202-6204.
128. Kang, D.; Ibers, J. A. *Inorg. Chem.*, 1989, **27**, 549-551.
129. (a) *Gmelin's Handbuch der Anorganischen Chemie*; Verlag Chemie: Weinheim/Brgstr., FRG, 1966; Sodium, Suppl. Part 3, pp. 1202-1205 and references therein. (b) Pearson, T. G.; Robinson, P. L. *J. Chem. Soc.* 1931, **53**, 1304-1314. (c) The Sodium-Sulfur Battery; Sudworth, J. L.; Tilly, A. R., Eds.; Chapman & Hall: London; New York, 1985. (d) Fischer, W. *Mat. Res. Soc. Symp. Proc.* 1989, **135**, 541-551. (e) Powers, R. W.; Karas, B. R. *J. Electrochem. Soc.* 1989, **136**, 2787-2793. (f) Mathewson, G. H. *J. Am. Chem. Soc.* 1907, **29**, 867-880. (g) Klemm, W.; Sodomann, H.; Langmesser, P. Z. *Z Anorg. Allg. Chem.*, 1939, **241**, 281-304.
130. (a) Kanatzidis, M. G. *Chem. Mater.*, 1990, **2**, 353-363. (b) Kanatzidis, M. G.; Park, Y. *J. Am. Chem. Soc.*, 1989, **111**, 3767-3769. (c) Kanatzidis, M. G.; Park, Y. *Chem. Mater.*, 1990, **2**, 99-101. (d) Park, Y.; Kanatzidis, M. G. *Angew. Chem. Int. Ed. Engl.*, 1990, **29**, 914-915. (e) Park, Y. Ph.D. dissertation, 1992, Michigan State University.
131. (a) Liao, J.-H.; Varotsis, C.; Kanatzidis, M. G. *Inorg. Chem.*, 1993, **32**, 2453-2462. (b) Liao, J.-H.; Kanatzidis, M. G., *Chem. Mater.*, 1993, **5**, 1561-1569.

CHAPTER 2 (Part 1)

Molten Salt Synthesis and Properties of Three New Solid State Ternary Bismuth Chalcogenides, β -CsBiS₂, γ -CsBiS₂ and K₂Bi₈Se₁₃

1. Introduction

To date, there are only a few structurally characterized ternary alkali metal bismuth chalcogenides, outside of the well-known NaCl-type ABiQ₂ (A=Li, Na, K; Q=S, Se, Te) compounds.^{1,2} To the best of our knowledge, the only other structurally characterized phases are CsBi₃S₅,³ RbBi₃S₅,⁴ Cs₃Bi₇Se₁₂,⁵ and Sr₄Bi₆Se₁₃.⁶ This relative scarcity of ternary compounds provides a further impetus for exploratory research in this area. In particular, Bi is very attractive for study because of its inert 6s² lone pair of electrons which may or may not be manifested structurally in a given compound. Whether the lone pair is stereochemically active or not affects both the lattice structure and the properties of the resulting compounds and thus exploration of the solid state chemistry of Bi is warranted. This issue is related to the larger question of stereochemical activity of a lone pair in compounds with elements in a s² configuration.

Group 15 chalcogenide compounds have received considerable attention, due to their potential application as non-linear optical materials,⁷ photoelectrics,⁸ and thermoelectrics.⁹ The most common application that is unique to Group 15 chalcogenides is in the area of thermoelectric cooling materials. To date, the most investigated systems are various solid solutions of M_2Q_3 ($M=As, Sb, Bi$; $Q=S, Se, Te$) compounds.¹⁰ These materials possess high electrical conductivity and thermoelectric power and low thermal conductivity and are excellent materials for thermoelectric applications near room temperature.¹¹ With these properties in mind, we pursued the synthesis of new ternary alkali metal bismuth chalcogenide compounds using the now proven polychalcogenide flux method.^{12,13} The latter involves the reaction of Bi in molten salts of A_2Q_x ($A=alkali\ metal$) of varying chemical composition.

We employed thermal analysis techniques to study the metal/alkali polychalcogenide flux reaction. Namely, differential scanning Calorimetry (DSC) was used to monitor the various thermal events that occur during reaction and determine formation and crystallization of the products.

This paper describes the synthesis, structural characterization, optical and infrared spectroscopic, and charge transport properties of three new compounds, β -CsBiS₂, γ -CsBiS₂ and K₂Bi₈Se₁₃. The thermochemical characterization of the Bi/Cs₂S_x and Bi/K₂Se_x systems is also reported. The former is a new polymorph of CsBiS₂ while the latter represents a new structure type.

2. Experimental Section

2.1. Reagents

Chemicals in this work were used as obtained: (i) bismuth powder, 99.999+% purity, -100 mesh; selenium powder, 99.5+% purity, -100 mesh, Aldrich Chemical Co., Inc., Milwaukee, WI. (ii) sulfur powder, sublimed, J. T. Baker Chemical Co., Phillipsburg, NJ. (iii) potassium metal, analytical reagent, Mallinckrodt Inc., Paris, KY; cesium metal, analytical reagent, Johnson Matthey/AESAR Group, Seabrook, NH (iv) methanol, anhydrous, Mallinckrodt Inc., Paris, KY; DMF, analytical reagent, diethyl ether, ACS anhydrous, EM Science, Inc., Gibbstown, NJ.

2.2. Synthesis

Synthesis: All manipulations were carried out under a dry nitrogen atmosphere in a Vacuum Atmospheres Dri-Lab glovebox. For the preparation of Cs_2S and K_2Se we used a modified literature procedure.¹⁴

Cesium Sulfide, Cs_2S . 4.80 g (0.036 mol) of slightly heated ($\sim 30^\circ\text{C}$) cesium metal was pipetted into a 250 ml round-bottom flask. A 150-ml volume of liquid ammonia was condensed into the flask at -78°C (dry ice/acetone bath) under nitrogen to give a dark blue solution. 0.579 g (0.018 mol) of sulfur and a Teflon coated stirbar were added and the mixture was stirred for one hour to give

a light blue solution. The NH_3 was removed by evaporation under a flow of nitrogen as the bath slowly warmed to room temperature. The pale yellow solid (97% yield) was dried in vacuum overnight, flame-dried, and ground to a fine powder with a mortar and pestle in the glovebox. Caution: Cesium metal will react with Teflon and sulfur vigorously upon contact in the solid state.

Potassium Selenide, K_2Se . A 10.098 g (0.128 mol) sample of selenium was combined with 10.00 g (0.256 mol) of freshly sliced potassium metal and the reaction was carried out as above. The orange product (99% yield) was dried in vacuum overnight, flame-dried, and ground to a fine powder with a mortar and pestle in the glovebox.

β -Cesium Disulfido-bismuthate(III), $\beta\text{-CsBiS}_2$ (I). An amount of 0.052 g (0.25 mmol) Bi, 0.335 g (1.125 mmol) Cs_2S and 0.064 g (2.00 mmol) of S were mixed together with a spatula in a glass vial. The mixture was transferred to a 6 ml pyrex tube and was subsequently flame-sealed in vacuum ($\sim 10^{-3}$ torr). The reaction was heated to 290 °C over a 12 hour period in a computer controlled furnace, then isothermed at 290 °C for 96 hours, followed by cooling to 100 °C at a rate of 2 °C/hr, then to 50 °C in one hour. This gave a red-orange glassy flux. The tube was opened with a glass cutter and the excess Cs_2S_x was dissolved in 150 ml of degassed methanol to give a clear, yellow solution. The insoluble product was washed with methanol repeatedly until the washings were colorless and then with ether. 0.085 g (83% yield) of transparent, dark, red needle-like crystals were obtained along with a small amount of pale yellow

impurity material. The red crystals and the amorphous yellow powder were insoluble in ethylenediamine, CH_3CN , DMF, ethanol, and CS_2 . The mixture was quickly washed with 5 ml of water on a filter frit which removed the yellow impurity, followed by 20 ml of methanol. This final step was done quickly as the red crystals are slightly moisture sensitive. Prolonged exposure to water (several hours) resulted in the formation of a dark purple film on the surface of the crystals. Quantitative microprobe analysis on the red single crystals gave $\text{Cs}_{1.0}\text{Bi}_{1.0}\text{S}_{1.8}$ (average of four data acquisitions). It is important that the Cs_2S be made fresh using the method described here. Use of commercially available Cs_2S (e.g. Cerac Inc.) more often than not did not yield $\beta\text{-CsBiS}_2$ but resulted in Bi_2S_3 . The difference in the two starting materials was examined using SEM. The particle size of the Cs_2S (Cerac) was considerably larger than that of Cs_2S (section 2.2), which could account for the difference in reactivities.

Reactions using increased amounts of starting materials yielded larger crystals. A mixture containing 0.105 g (0.500 mmol) of Bi, 0.670 g (2.25 mmol) of Cs_2S , and 0.128 g (4 mmol) of S under the same conditions afforded 3 mm sized crystals suitable for single crystal charge transport studies.

γ -Cesium Disulfido-bismuthate(III), $\gamma\text{-CsBiS}_2$. An amount of 0.042 g (0.20 mmol) Bi, 0.238 g (0.80 mmol) Cs_2S and 0.051 g (1.60 mmol) S were thoroughly mixed and the reaction was carried out as above. The mixture was heated to 350 °C over a 12 hour period, then isothermed for 6 days, followed by cooling to 80 °C at 2 °C/hr, then to 50 °C in one hour. The excess Cs_2S_x was removed by

dissolving in degassed methanol. The product was then washed with ethyl ether (20 ml). 0.060 g (74% yield) of black hexagonal-shaped crystals were obtained. Quantitative microprobe analysis gave $\text{Cs}_{1.0}\text{Bi}_{1.0}\text{S}_{2.2}$ (average of three acquisitions). Powder XRD peaks (d-spacings, Å) 16.780 (vs), 12.468 (s), 8.268 (w), 6.267 (vw), 5.484 (w), 4.104 (vs), 3.592 (m), 3.410 (m), 3.314 (m), 3.231 (m), 3.025 (m), 2.927 (s), 2.868 (m), 2.730(vw), 2.302 (vw), 2.266 (vw), 2.181 (vw), 2.150 (vw), 2.071 (m), 2.039 (m), 1.970 (vw), 1.909 (vw), 1.862 (vw), 1.813 (w), 1.761 (vw), 1.716 (vw), 1.634 (vw), 1.632 (vw).

Dipotassium Tridecaselenido-octabismuthate(III), $\text{K}_2\text{Bi}_8\text{Se}_{13}$ (II). An amount of 0.209 g (1.00 mmol) Bi, 0.079 g (0.500 mmol) K_2Se and 0.316 g (4.00 mmol) Se were thoroughly mixed and the reaction was carried out as above. The mixture was heated to 330 °C over a 12 hour period, then isothermed for 10 days, followed by cooling to 70 °C at 2 °C/hr, then to 50 °C in one hour. The excess K_2Se_x was removed by dissolving in degassed DMF. The product was washed with ether (20 ml) and ethylenediamine (20 ml) to remove any trace amounts of Se. 0.306 g (88% yield) of thin black needles with black microcrystalline powder were obtained. Quantitative microprobe analysis gave $\text{K}_{2.0}\text{Bi}_{8.0}\text{Se}_{12.8}$ (average of four acquisitions).

The homogeneity of $\beta\text{-CsBiS}_2$ and $\text{K}_2\text{Bi}_8\text{Se}_{13}$ was confirmed by comparing the observed and calculated X-ray powder diffraction patterns. The d_{hkl} spacings observed for the bulk materials were compared, and found to be in good agreement with the d_{hkl} spacings

calculated from the single crystal data using the program POWD10.¹⁵ The results are summarized in Tables 2-1 and 2-2.

2.3. Physical Measurements.

FT-IR spectra of the β -CsBiS₂ compound were recorded as a solid in a CsI matrix. The sample was ground with dry CsI into a fine powder, and a pressure of about seven metric tons was applied to the mixture to make a translucent pellet. The spectra were recorded in the far-IR region (600-100 cm⁻¹, 4 cm⁻¹ resolution) with the use of a Nicolet 740 FT-IR spectrometer equipped with a TGS/PE detector and silicon beam splitter.

Quantitative microprobe analysis of the compounds was performed with a JEOL JSM-35CF scanning electron microscope (SEM) equipped with a Tracor Northern Energy Dispersive Spectroscopy (EDS) detector. Single crystals of each sample were mounted on an aluminum stub which was coated with conducting graphite paint to avoid charge accumulation on the sample surface under bombardment of the electron beam during measurements. A 1.8 correction factor was applied to the Se atomic percent in this system as a result of examination of several other Se containing crystals. Energy Dispersive Spectra (EDS) were obtained by using the following experimental set-up:

X-ray detector position: 55 mm

Working distance: 39 mm

Accelerating voltage: 20 kV

Take-off angle: 27 deg

Beam current: 200 picoamps

Accumulation time: 60 seconds

Window: Be

Optical diffuse reflectance measurements were made at room temperature with a Shimadzu UV-3101PC double beam, double-monochromator spectrophotometer. The instrument was equipped with an integrating sphere and controlled by a personal computer. The measurement of diffuse reflectivity can be used to obtain values for the band gap which agree rather well with values obtained by absorption measurements from single crystals of the same material. The digitized spectra were processed using the Kaleidagraph™ software program. BaSO₄ powder was used as reference (100% reflectance). Absorption data were calculated from the reflectance data using the Kubelka-Munk function:¹⁶

$$\alpha/S = \frac{(1-R)^2}{2R}$$

R is the reflectance at a given wavelength, α is the absorption coefficient and S is the scattering coefficient. The scattering coefficient has been shown to be practically wavelength independent for particles larger than 5 μm which is smaller than the particle size of the samples used here.^{16a,b}

Differential Scanning Calorimetry was performed with a computer-controlled Shimadzu DSC-50 thermal analyzer under a nitrogen atmosphere at a flow rate of 35 ml/min. The appropriate reactant mixtures (~18.0 mg total mass), as mentioned above, were crimped in an aluminum pan inside a nitrogen-filled glove box. The pan was placed on the sample side of the DSC-50 detector and an empty aluminum pan of equal mass was crimped and placed on the reference side. The samples were heated to the desired temperature at 3 °C/min, then isothermed for 800 min. followed by cooling at -0.5 °C/min. to 75 °C. The reported DSC temperatures are peak temperatures with a standard deviation of 0.2 degrees. The adopted convention in displaying data is: exothermic peaks occur at positive heat flow while endothermic peaks occur at negative heat flow.

Dc electrical conductivity and thermopower measurements were made on single crystals and polycrystalline compactions of the compounds. Conductivity measurements were performed in the usual four-probe geometry with 60- and 25- μ m gold wires used for the current voltage electrodes, respectively. Measurements of the pellet cross-sectional area and voltage probe separation were made with a calibrated binocular microscope. Conductivity data were obtained with the computer-automated system described elsewhere.¹⁷ Thermoelectric power measurements were made by using a slow ac technique¹⁸ with 60-mm gold wires serving to support and conduct heat to the sample, as well as to measure the voltage across the sample resulting from the applied temperature gradient. In both measurements, the gold electrodes were held in place on the sample with a conductive gold paste.

Conductivity specimens were mounted on interchangeable sample holders, and thermopower specimens were mounted on a fixed sample holder/differential heater. Mounted samples were placed under vacuum (10^{-3} Torr) and heated to 320 K for 2-4 h to cure the gold contacts. For a variable-temperature run, data (conductivity or thermopower) were acquired during both sample cooling and warming to check reversibility. The temperature drift rate during an experiment was kept below 1 K/min. Typically, three to four separate variable-temperature runs were carried out for each sample to ensure reproducibility and stability. At a given temperature, reproducibility was within $\pm 5\%$.

Thermoelectric power results collected by the slow-ac technique require the production of a slowly varying periodic temperature gradient across the samples and measuring the resulting sample voltage. Samples were suspended between the quartz block heaters by 60-mm gold wires thermally grounded to the blocks with GE 7031 varnish. The magnitude of the applied temperature gradient was generally 1.0 K. Smaller temperature gradients gave essentially the same results but with somewhat lower sensitivity.

2.4. X-ray Crystallography

The compounds were examined by X-ray powder diffraction for the purpose of phase purity and identification. Accurate d_{hkl} spacings (\AA) were obtained from the powder patterns recorded on a

calibrated (with FeOCl as internal standard) Phillips XRG-3000 computer-controlled powder diffractometer with Ni filtered Cu K α radiation operating at 35 kV and 35 mA. The data were collected at a rate of 0.12°/min.

Structure solution of β -CsBiS₂. A crystal with dimensions 0.50 x 0.20 x 0.10 mm was sealed in a glass capillary. Intensity data were collected using the ω -2 θ scan mode on a Rigaku AFC6S four-circle automated diffractometer equipped with a graphite-crystal monochromator. The stability of the crystal was monitored by measuring three standard reflections periodically (every 150 reflections) during the course of data collection. No crystal decay was detected. An empirical absorption correction based on ψ scans was applied to the data, followed by a DIFABS correction to the isotropically refined data.¹⁹ The structure was solved by direct methods using SHELXS86^{20a} and refined by full-matrix least-squares techniques of the TEXSAN package of crystallographic programs.^{20b} All calculations were performed on a VAXstation 3100/76 computer.

Structure Solution of K₂Bi₈Se₁₃. A crystal with dimensions 0.10 x 0.20 x 0.50mm was mounted on a glass fiber. Intensity data for the crystal were collected using the ω /2 θ scan mode on a Rigaku AFC6S four-circle automated diffractometer. The stability of the crystal was monitored by measuring three standard reflections periodically (every 150 reflections) during the course of data collection. No crystal decay was detected. Absorption corrections were applied as above. The structure was solved by direct methods using SHELXS86^{20a} and refined by full-matrix least-squares

techniques of the TEXSAN package of crystallographic programs.^{20b} A careful inspection of the final structure revealed the presence of pseudo mirror symmetry perpendicular to the c-axis. Since the α and β angles of the unit cell are very close to 90° we attempted to refine the model at the higher symmetry monoclinic space group C 2/m (#12) where $a'=2a$, $b'=c$, $c'=-b$, $\beta=87.96^\circ$. The results were characterized by divergent refinement and an unstable structure. Thus, we chose the lower symmetry triclinic space group. All calculations were performed on a VAXstation 3100 Model 76 computer.

The complete data collection parameters, details of the structure solution and refinement for both compounds are given in Table 2-3. The coordinates and average temperature factors (B_{eq}) of all atoms and their estimated standard deviations for both compounds are given in Tables 2-4 and 2-5.

Table 2-1. Calculated and Observed X-ray Powder Diffraction Patterns for β -CsBiS₂.

h k l	d _{calcd.} , Å	d _{obs.} , Å	I/I _{max} (obs)
1 0 0	7.62	7.7	70
1 1 0	5.97	6.01	20
0 1 1	5.74	5.77	8
-1 1 1	5.01	5.03	4
1 1 1	4.25	4.25	20
1 2 0	4.06	4.07	18
0 2 1	3.99	3.99	36
-1 0 2, 2 1 0	3.542, 3.541	3.549	86
-2 1 1	3.45	3.46	46
1 2 1, 0 1 2	2.38, 2.36	3.36	21
-1 1 2	3.32	3.30	61
1 0 2	3.01	3.01	22
2 1 1, 1 3 0	2.95, 2.94	2.96	51
0 2 2, 1 1 2	2.872, 2.870	2.869	61
-1 3 1, -2 1 2	2.812, 2.808	2.811	34
2 2 1	2.607	2.605	9
1 2 2	2.549	2.542	26
3 1 0, 2 3 0	2.455, 2.452	2.455	29
2 0 2	2.372	2.367	13
-3 0 2	2.315	2.331	14
-1 4 1	2.224	2.222	4
1 3 2	2.192	2.189	10
-1 2 3	2.168	2.167	18
1 4 1	2.143	2.147	17
2 2 2	2.127	2.127	19
1 1 3	2.101	2.100	23
-3 2 2, 3 2 1	2.085, 2.037	2.038	17
-3 3 1	2.005	1.993	7
4 0 0, 2 4 1	1.905, 1.900	1.908	100
4 1 0, 1 5 0	1.868, 1.864	1.874	28
-1 0 4	1.832	1.830	20
-4 2 1	1.803	1.806	17
1 3 3	1.787	1.785	9
-3 4 1	1.755	1.757	8
0 5 2, -1 5 2	1.694, 1.689	1.692	15
1 1 4, -2 4 3	1.643, 1.641	1.641	13
-3 1 4, 2 3 3	1.612, 1.605	1.606	6
-1 6 0, 0 3 4	1.578, 1.567	1.570	5

Table 2-2. Calculated and Observed X-ray Powder Diffraction Patterns for $K_2Bi_8Se_{13}$.

h k l	d _{calcd} , Å	d _{obsd} , Å	I/I _{max} (obsd)
1 0 0	13.58		
0 1 0	12.08	12.4	11
1 1 0	9.20	9.33	8
-1 1 0	8.87		
-2 1 0	5.83	5.72	16
1 2 0	5.60		
3 0 0	4.53	4.56	13
1 3 0	3.90	3.99	11
1-1 1, -2 1 1	3.595, 3.593	3.616	36
-3 2 0	3.56	3.58	33
-2 3 0	3.41	3.45	8
4 0 0, -1 2 1	3.40, 3.39	3.42	9
2 0 1, 4 1 0	3.31, 3.30	3.32	10
2 1 1, -3-1 1	3.21, 3.20	3.23	45
0 4 0	3.02	3.08	5
-3 3 0	2.96	2.98	80
2 2 1	2.93	2.953	95
-3-2 1	2.92	2.952	67
-4 2 0	2.89	2.85	5
2 4 0	2.80	2.80	10
3-1 1	2.75	2.76	10
-5 1 0	2.63	2.63	4
2-3 1	2.53	2.55	6
-3 4 0	2.472	2.490	11
-1 4 1, 0-4 1	2.429, 2.428	2.451	35
4-1 1	2.383	2.380	13
2 5 0	2.303	2.312	16
-2 5 0	2.251	2.278	8
2-4 1	2.206	2.218	8
5 0 1, -6 0 1	2.125, 2.123	2.127	42
-1 0 2	2.081	2.083	100
5 4 0, 3-4 1	2.057, 2.042	2.053	20
5-2 1	1.985	1.986	16
2 6 0	1.950	1.948	18
-7 1 0	1.905	1.907	11
0 3 2	1.837	1.847	11
-2-3 2	1.835	1.834	14
-1 6 1	1.805	1.798	15
-4 2 2	1.797	1.782	13
-5-1 2	1.760	1.763	8
-4 6 0	1.705	1.728	11
2-3 2	1.702	1.707	33
8 1 0	1.690	1.693	28
8 2 0	1.650	1.658	6
-7 4 0	1.607	1.629	9
0 7 1	1.595	1.607	8
2-4 2	1.592	1.596	6
1 5 2	1.545	1.550	13

Table 2-3. Summary of Crystallographic Data and Structure Analysis for β -CsBiS₂ and K₂Bi₈Se₁₃

Formula	β -CsBiS ₂	K ₂ Bi ₈ Se ₁₃
FW	406.01	2776.52
a, Å	7.794(5)	13.768(2)
b, Å	9.610(6)	12.096(3)
c, Å	7.329(4)	4.1656(6)
α , deg	90.000	89.98(1)
β , deg	102.16(5)	98.64(1)
γ , deg	90.000	87.96(1)
Z; V, Å ³	4; 537	1; 685
λ	0.71073 (Mo K α)	0.71073 (Mo K α)
space group	P2 ₁ /c (No. 14)	P- 1 (No. 2)
D _{calc.} , g/cm ³	5.03	6.73
μ , cm ⁻¹	400 (Mo K α)	684.2 (Mo K α)
2 θ _{max} , deg	50 (Mo K α)	50 (Mo K α)
Temp., °C	-36	23
Final R/R _w , %	7.4/10	8.2/8.9
Total Data Measured	1652	2443
Total Unique Data	1551	2406
Data with $F_o^2 > 3\sigma(F_o^2)$	1053	1171
No. of Variables	38	107

Table 2-4. Fractional Atomic Coordinates and B_{eq} Values for β -CsBiS₂ with Estimated Standard Deviations in Parentheses.

atom	x	y	z	$B_{eq},^a \text{ \AA}^2$
Cs	-0.1383(4)	-0.4314(3)	-0.7879(4)	2.16(5)
Bi	0.4115(2)	-0.1657(2)	-0.1440(2)	1.48(2)
S(1)	0.186(1)	-0.256(1)	-0.461(1)	1.8(2)
S(2)	0.319(2)	0.084(1)	-0.199(2)	3.4(3)

Table 2-5. Fractional Atomic Coordinates and B_{eq} Values for K₂Bi₈Se₁₃ with Estimated Standard Deviations in Parentheses.

atom	x	y	z	$B_{eq},^a \text{ \AA}^2$
K	0.831(1)	0.051(2)	0.415(4)	2.6(8)
Bi(1)	0.8809(2)	0.3803(3)	0.4408(6)	1.6(1)
Bi(2)	0.3787(2)	0.5464(3)	1.1887(7)	1.6(1)
Bi(3)	1.1510(2)	0.2940(3)	0.0758(6)	1.6(1)
Bi(4)	0.5628(2)	0.8671(3)	0.2822(7)	1.8(1)
Se(1)	0.2625(5)	0.4267(7)	0.632(2)	1.6(3)
Se(2)	1.0370(5)	0.1977(7)	0.516(2)	1.7(3)
Se(3)	0.7788(5)	0.2707(7)	0.887(2)	1.7(3)
Se(4)	0.5094(5)	0.3536(7)	1.254(2)	1.6(3)
Se(5)	1.2811(5)	0.1169(7)	0.140(2)	1.5(3)
Se(6)	0.5837(5)	1.0886(7)	0.293(2)	1.4(3)
Se(7)	1.0000	0.5000	0.0000	1.2(4)

$^a)B_{eq} = (4/3)[a^2B(1,1) + b^2B(2,2) + c^2B(3,3) + ab(\cos\gamma)B(1,2) + ac(\cos\beta)B(1,3) + bc(\cos\alpha)B(2,3)]$.

3. Results and Discussion

3.1. Synthesis and Spectroscopy

The synthesis of β -CsBiS₂ can be accomplished by dissolving Bi in a Cs₂S_x (x=2.5-3.0) flux at 250-300 °C followed by isolation in degassed methanol. A direct combination reaction between Bi₂S₃ and Cs₂S (1:1) at 500 °C was performed to determine if the same compound could be isolated using this approach. The major product was found, by powder X-ray diffraction, to be β -CsBiS₂ but its morphology was microcrystalline. The advantage of the molten salt technique is the lower synthesis temperature and the larger size of obtained crystals suitable for comprehensive structural studies and property measurements. A number of microcrystalline A/Bi/S (A=alkali metal) phases have been synthesized, including α -CsBiS₂, via direct combination reactions of Bi₂S₃ and A₂S (A=alkali metal) at high temperatures (>500 °C), but no structural characterization is available.²¹ To the best of our knowledge only the unit cell parameters of α -CsBiS₂ have been reported but no structural details have been found.²²

Another new ternary phase, γ -CsBiS₂, was obtained by dissolving Bi in a Cs₂S_x (x=3.0-3.7) flux at 350 °C. Stacks of black hexagonal plates were obtained from these reactions. SEM photographs showed a very thin plate-like morphology for these

crystals which made data collection difficult. A rhombohedral unit cell with $a=4.166(4)\text{\AA}$ and $c=48.77(5)\text{\AA}$, was found but the structure could not be refined to give a reasonable model. The unit cell of this compound is closely related to that of RbBiS_2 ²³ in which CdCl_2 -type $(\text{BiS}_2)^-$ layers (perpendicular to the c -axis) alternate with Rb^+ ions. The length of the c -axis suggests six $(\text{BiS}_2)^-$ layers in the unit cell. The coordination sphere of Bi is perfect octahedral.

Similar investigations of Bi reactions in Li_2S_x and Na_2S_x ($x=2.2-5$) fluxes in the temperature range of 290°C to 345°C gave LiBiS_2 (68% yield) and NaBiS_2 (72% yield), which possess NaCl-type structures.^{1a}

Far-IR spectroscopy of $\beta\text{-CsBiS}_2$ shows two absorptions at 286 cm^{-1} (s) and 226 cm^{-1} (m) which are similar to those of Bi_2S_3 at 290 cm^{-1} (w) and 220 cm^{-1} (s).²⁴ The two absorbancies are due to Bi-S stretching vibrations, but at this stage we cannot assign which modes since systematic IR spectroscopic data in this area are lacking. A solid state far-IR of $\text{K}_2\text{Bi}_8\text{Se}_{13}$ shows no peaks, the only feature being a broad absorbance beginning at 200 cm^{-1} . The presence of this sort of feature is common in electrically conducting materials.

The synthesis of $\text{K}_2\text{Bi}_8\text{Se}_{13}$ can be accomplished by dissolving Bi in K_2Se_9 flux over a wide range of molar ratios at $330\text{-}370^\circ\text{C}$ followed by isolation in DMF. Similar investigations using Na_2Se_9 flux at 320°C gave only NaBiSe_2 ^{1c} along with a small amount of elemental Se, as confirmed by powder X-ray diffraction.

β -CsBiS₂ and K₂Bi₈Se₁₃ belong to the (A₂Q)_n(Bi₂Q₃)_m (A=alkali metal; Q=S, Se) general family of compounds with n=1 and m=1, 4 respectively. Other members of this family include CsBi₃S₅ (n=1, m=3),³ Cs₃Bi₇Se₁₂ (n=3, m=7),⁵ and K₂Bi₄S₇ (n=1, m=2).¹⁶ The latter phase has an unknown structure. The synthesis of new ternary bismuth chalcogenides with various n and m values may be possible e.g. ABi₅Q₈ (n=1, m=5). Recently, another ternary bismuth sulfide KBi_{6.33}S₁₀ has also been synthesized which could belong to this family of compounds.²⁵

3.2 Description of Structures

Structure of β -CsBiS₂ (I). This compound possesses the CsSbS₂ structure type.²⁶ The Bi lone pair is stereochemically active in this compound. The anion has a one-dimensional, polymeric structure with charge balancing Cs⁺ cations found between the chains. Selected bond distances and angles for (I) are given in Table 2-6. The structure can be described as BiS₃ trigonal pyramids connected at two vertices to form fully extended (BiS₂)_nⁿ⁻ chains along the a-axis. The two chains per unit cell are related by a center of symmetry. Figure 2-1 shows a view of an individual (BiS₂)_nⁿ⁻ chain. Along the chain backbone we can observe an alternation of long and short Bi-S(1) bonds. Figure 2-2 shows two views of the unit cell along the a and b axes, respectively. The chains of β -CsBiS₂ are oriented in a sheet-like manner and the Bi lone pairs are directed into a nonpolar domain that is segregated from the polar domain of the Cs atoms. The [BiS₂]⁻ framework can be thought of as a

derivative of the well-known Bi_2S_3 compound and generated by successively dismantling the Bi_2S_3 framework by incorporation of Cs_2S . The S/Bi ratio increases from 1.50 to 2.00 upon going from Bi_2S_3 to $[\text{BiS}_2]^-$ as the structure is broken up into chains.

Since the shortest distance between chains is $3.00(1) \text{ \AA}$, the structure can be alternatively viewed as layers of $(\text{BiS}_2)_n^{n-}$ chains separated with layers of Cs^+ ions. The terminal sulfur atoms in the chain are pointed toward the Cs^+ ions. The Bi-S bond distances in $\beta\text{-CsBiS}_2$ are comparable to those found in many bismuth sulfosalts, such as PbCuBiS_3 .²⁷ Many of these sulfosalts have a fourth and fifth sulfur atom at greater distances from the Bi to form a square pyramidal coordination. In KBiS_2 , the lone inert pair is not stereochemically active so the bismuth atom is found in a perfect octahedral environment with much longer Bi-S bonds at $3.02(1) \text{ \AA}$.^{1a} The same situation is thought to be present in $\gamma\text{-CsBiS}_2$. These longer bonds are due to the electrostatic repulsion between the lone pair around the Bi nucleus and the negatively charged S atoms.

The influence of the lone pair on Bi coordination is demonstrated through the inspection of the S-Bi-S angles, shown in Table 2-7. This effect is consistent with predictions based on V.S.E.P.R. theory.²⁸ The angles of $\beta\text{-CsBiS}_2$, in Table 2-6, are compared to the S-M-S angles found in the Group 15 chain-like structures, CsSbS_2 ²⁶ and NaAsS_2 ²⁹ (Table 2-7). The angles decrease going from As to Bi, as the lone pair orbital becomes larger and more diffuse. The long and short bond alternation along the chain ($2.54(1)$

and 2.733(8) Å) and the short terminal bond of 2.531(1) Å are features that also appear in CsSbS₂ and NaAsS₂.

Structure of K₂Bi₈Se₁₃ (II). This compound has a complicated three-dimensional structure made up of BiSe₆ octahedra and BiSe₅ square pyramids, which form tunnels filled with K⁺ cations. Selected bond distances and angles for (I I) are given in Table 2-8.

The BiSe₆ octahedra form NaCl-type layers that are linked by BiSe₅ distorted square pyramids. Figure 2-3 shows the packing diagram of the extended structure down the c-axis. The [Bi₈Se₁₃]²⁻ framework can also be thought of as a hybrid of three different layered structure types interconnected to form a 3-D network. Structural features from the Bi₂Te₃,³⁰ Sb₂S₃,³¹ and CdI₂³² lattices are represented in this framework. Figure 2-4 shows the structures of the three layered materials (a-c). The features of the three structure types found in the [Bi₈Se₁₃]²⁻ framework are highlighted in Figure 2-4d. The Bi₂Te₃-type fragments are linked by CdI₂-type octahedra to form sheets that are connected in the b-direction by BiSe₅ square pyramids (Sb₂S₃-type) to form the framework. Alternatively, the [Bi₈Se₁₃]²⁻ framework can also be viewed as a derivative of the well-known Bi₂Se₃ compound generated by breaking down the Bi₂Se₃ framework by incorporation of K₂Se in the molar ratio of 4:1 (i.e. [K₂Se][Bi₂Se₃]₄). The Se/Bi ratio increases from 1.50 in Bi₂Se₃ to 1.63 for the [Bi₈Se₁₃]²⁻ anion.

K₂Bi₈Se₁₃ is structurally related to Cs₃Bi₇Se₁₂⁵ and Sr₄Bi₆Se₁₃.⁶ In Cs₃Bi₇Se₁₂, the [Bi₇Se₁₂]³⁻ anion is layered. It contains the CdI₂ and Bi₂Te₃-type fragments that were mentioned above but no Sb₂S₃

characteristics. The CdI_2 -type octahedra link the Bi_2Te_3 -type (or NaCl -type) blocks in an edge-sharing manner to form a lamellar structure. The highly charged $[\text{Bi}_6\text{Se}_{13}]^{8-}$ anion has a very interesting structure. It contains two-dimensional sheets made up of edge-sharing CdI_2 - and Bi_2Te_3 -type fragments. One-dimensional chains, comprised of Bi_2Te_3 -type blocks, extend along the *b*-direction and separate these layers.

Atoms Bi(1) and Bi(2) possess slightly distorted octahedral coordination as evidenced by the average bond distances and bond lengths in Table 2-8. The corresponding Bi-Se bond distances range from 2.847(9) Å to 3.038(3) Å for Bi(1) and 2.869(9) Å to 3.021(9) Å for Bi(2). These distances are similar to those reported for, $\text{Cs}_3\text{Bi}_7\text{Se}_{12}$.⁵ The Bi(3) coordination environment is distorted with a Bi(3)-Se(5) bond distance of 2.730(8) Å which is *trans* to a long Bi(3)-Se(7) distance of 3.172(3) Å. This same distorted coordination is found in $\text{Cs}_3\text{Bi}_7\text{Se}_{12}$.⁵ This distorted octahedral coordination has been seen in several other bismuth compounds, including $\text{Sr}_4\text{Bi}_6\text{Se}_{13}$ ⁶ and in several bismuth sulfosalts, including PbBi_2S_4 (galenobismuthite)³³ and $\text{PbCu}_4\text{Bi}_5\text{S}_{11}$.³⁴ Bi(4) is the only atom in which the inert lone pair of electrons is stereochemically active as revealed by the distorted square pyramidal coordination shown in Figures 2-3 and 2-5. This coordination site consists of four equatorial bonds of 2.95(3) Å (ave.) and a short axial distance of 2.704(9) Å. This short bond is *trans* to two Bi(4)-Se(4) interactions at 3.552(1) (ave.) which are shorter than the approximate sum of the van der Waals radii (4.4 Å).³⁵ The Se(4,4')-Bi(4)-Se(6) angles are much less than 180° at 141.8(2)° and 141.9(2)° and the Se(6)-Bi(4)-Se(6', 6'', 5, 5') angles are less than 90°

at $83(2)^\circ$ (ave.). This type of arrangement is found in the mixed metal compound, $\text{Cu}_{1.6}\text{Bi}_{4.8}\text{Se}_8$, where the Bi(3) has a short axial bond of $2.71(1)\text{\AA}$ that is trans to a Bi-Se distance of $3.54(1)\text{\AA}$ with an angle of $139.4(4)^\circ$.³⁶

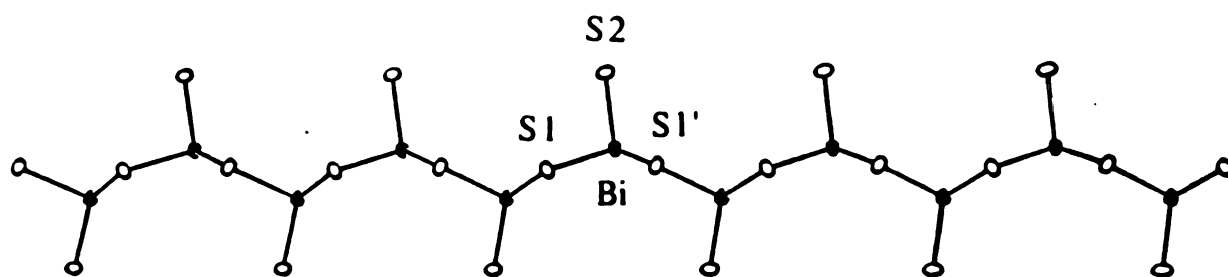


Figure 2-1. ORTEP representation of a single $(\text{BiS}_2)_n^{n-}$ chain with labeling scheme.

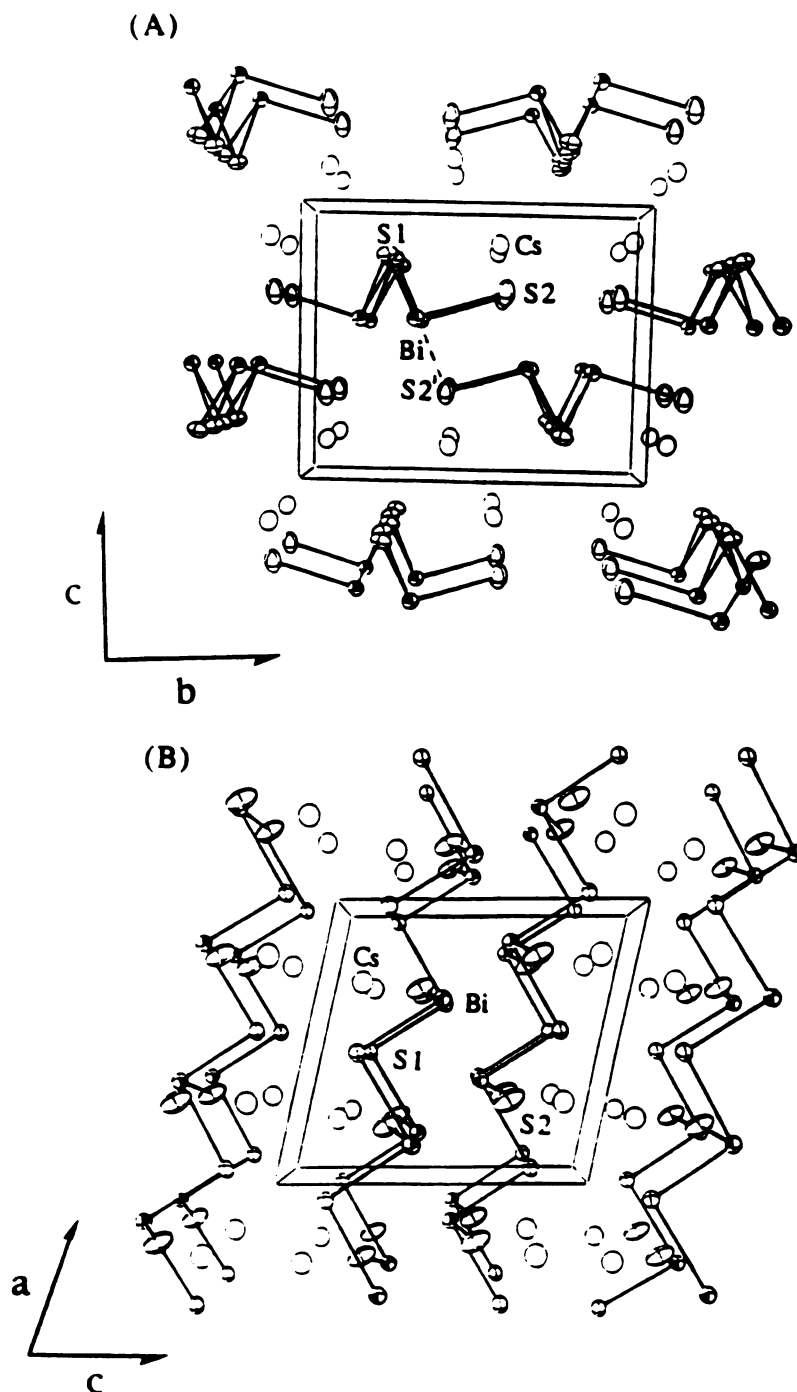


Figure 2-2. ORTEP packing diagrams of the $(\text{BiS}_2)_n^{\text{n-}}$ chains along the a-axis, (A) and b-axis, (B). Dashed lines in (A) indicate Bi...S contacts. The shaded ellipsoids are Bi atoms, and the Cs atoms are represented by open circles.

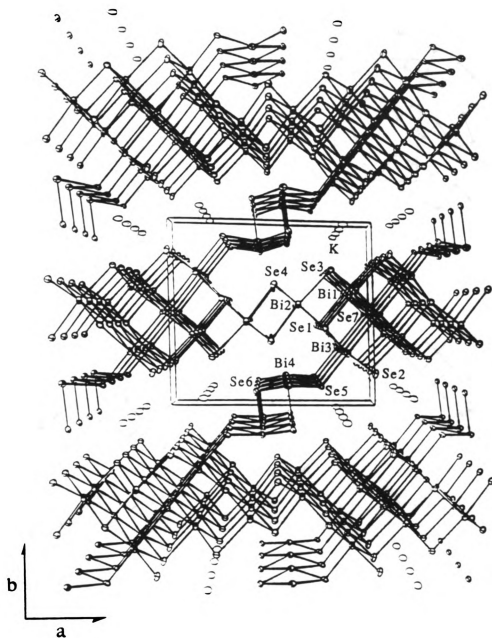


Figure 2-3. ORTEP representation of the packing diagram of $K_2Bi_8Se_{13}$ down the c -axis. The shaded ellipsoids are the Bi atoms, and the open ellipsoids are the K atoms.

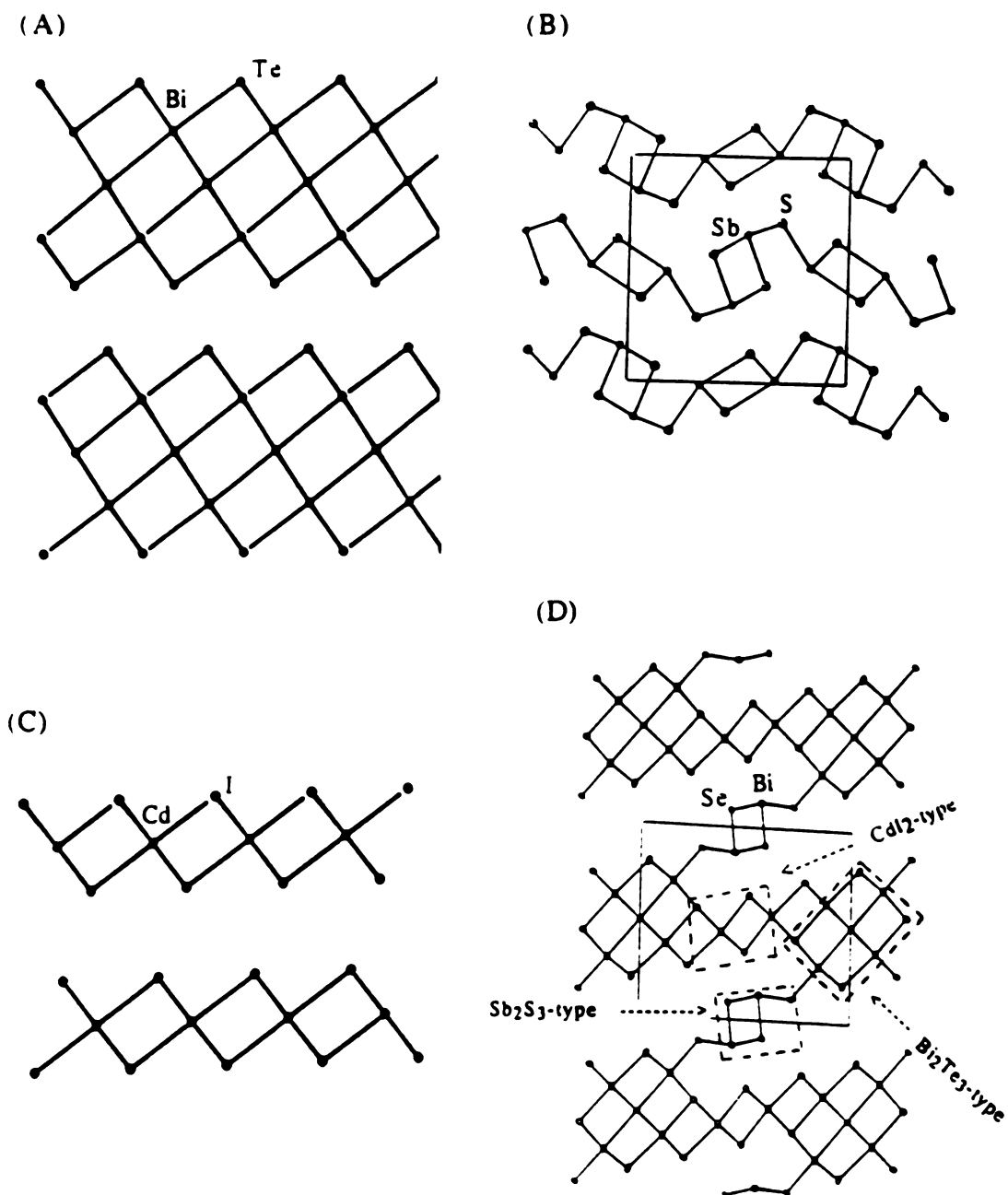


Figure 2-4. Projections of the structures of (A) Bi_2Se_3 (Bi_2Te_3 -type) (B) Bi_2Se_3 (Sb_2S_3 -type) (C) CdI_2 -type and (D) $[\text{Bi}_8\text{Se}_{13}]^{2-}$ framework. The three structure types found in this framework are designated with dashed lines.

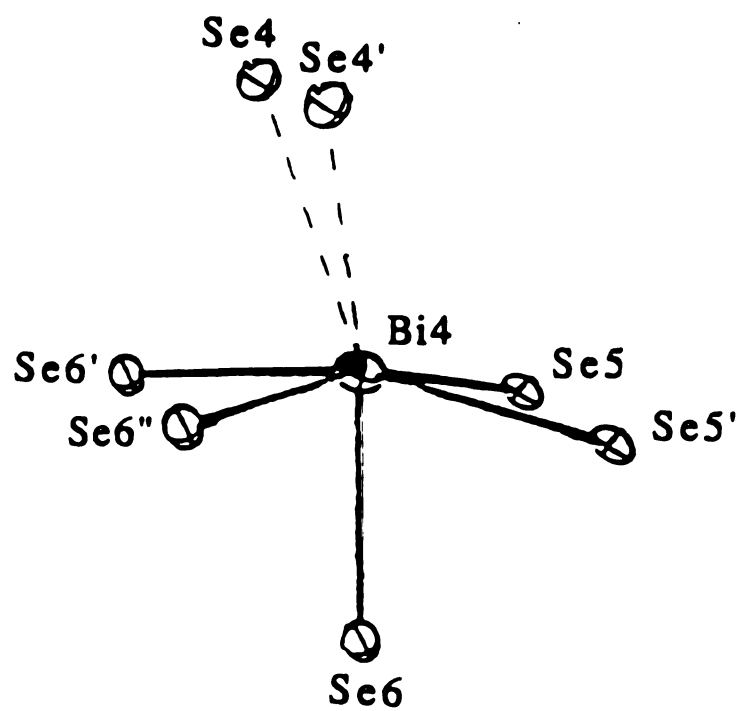


Figure 2-5. ORTEP representation of the Bi(4) coordination in $K_2Bi_8Se_{13}$. Dashed lines designate long contacts.

Table 2-6. Selected Distances (Å) and Angles (deg) in the β -CsBiS₂ with Standard Deviations in Parentheses.^a

Bi-S(1)	2.531(9)	S(1)-Bi-S(1')	88.1(3)
Bi-S(1')	2.733(8)	S(1)-Bi-S(2)	100.3(4)
Bi-S(2)	2.505(9)	S(1')-Bi-S(2)	93.5(3)
Bi-S(2')	3.00(1)	S(2)-Bi-S(2')	90.0(3)
		S(1')-Bi-S(2')	93.8(3)
		Bi-S(1)-Bi	99.0(3)
Cs-S(1)	3.533(9)	Bi-Bi'	3.909(3)
Cs-S(2')	3.589(9)	Bi-Bi''	4.004(4)
Cs-S(1'')	3.54(1)		
Cs-S(1''')	3.598(9)		
Cs-S(2'')	3.64(1)		
Cs-S(2'')	4.13(1)		
Cs-S(2''')	3.81(1)		
Cs-S (mean)	3.7(2)		

^a)The estimated standard deviations in the mean bond lengths and the mean bond angles are calculated by the equations $\sigma l = \{\Sigma_n (l_n - l)^2 / n(n-1)\}^{1/2}$, where l_n is the length (or angle) of the nth bond, l the mean length (or angle), and n the number of bonds.

Table 2-7. Comparison of Bond Distances (Å) and Angles (deg) in Selected Group 15 Sulfides (M=As,Sb,Bi).

Formula	S1-M-S1'	S1-M-S2	S1'-M-S2	M-S1	M-S2	M-S1'
NaAsS ₂	95.5(1)	103.6(1)	102.0(1)	2.31(1)	2.17(1)	2.33(1)
CsSbS ₂	89.06(5)	100.73(6)	95.28(6)	2.450(2)	2.366(2)	2.583(3)
β -CsBiS ₂	88.1(3)	100.3(4)	93.5(3)	2.531(9)	2.505(9)	2.733(8)

Table 2-8. Selected Distances (Å) and Angles (deg) in the $[\text{Bi}_8\text{Se}_{13}]^{2-}$ Framework with Standard Deviations in Parentheses.^a

Bi(1)-Se(1'')	2.988(9)	Se(1'')-Bi(1)-Se(2)	175.9(3)
Bi(1)-Se(2)	3.009(8)	Se(3)-Bi(1)-Se(7)	176.4(2)
Bi(1)-Se(3)	2.847(9)	Se(3')-Bi(1)-Se(7')	176.1(2)
Bi(1)-Se(3')	2.867(7)	Se(1'')-Bi(1)-Se(3)	92.88(2)
Bi(1)-Se(7)	3.038(3)	Se(1'')-Bi(1)-Se(3')	92.6(2)
Bi(1)-Se(7')	3.037(3)	Se(1'')-Bi(1)-Se(7)	88.3(2)
Bi(1)-Se (mean)	2.97(9)	Se(1'')-Bi(1)-Se(7')	88.5(2)
		Se(2)-Bi(1)-Se(3)	90.3(2)
Bi(2)-Se(1)	3.012(7)	Se(2)-Bi(1)-Se(3')	89.9(2)
Bi(2)-Se(1')	3.021(9)	Se(2)-Bi(1)-Se(7)	88.4(2)
Bi(2)-Se(3')	3.024(8)	Se(2)-Bi(1)-Se(7')	88.7(1)
Bi(2)-Se(4)	2.881(8)	Se-Bi(1)-Se (mean)	90(2), 176.1(2)
Bi(2)-Se(4')	2.869(9)		
Bi(2)-Se(4'')	2.878(7)		
Bi(2)-Se (mean)	2.95(7)		
Bi(3)-Se(1)	3.062(9)	Se-Bi(2)-Se (mean)	90(3), 175(1)
Bi(3)-Se(1')	3.067(7)		
Bi(3)-Se(2)	2.860(9)	Se(1)-Bi(3)-Se(2)	172.4(3)
Bi(3)-Se(2')	2.878(7)	Se(1')-Bi(3)-Se(2')	172.3(3)
Bi(3)-Se(5)	2.730(8)	Se(5)-Bi(3)-Se(7)	179.9(2)
Bi(3)-Se(7)	3.172(3)	Se-Bi(3)-Se (mean)	90(4), 175(4)
Bi(3)-Se (mean)	3.0(2)		
		Se(4)-Bi(4)-Se(4')	71.8(2)
Bi(4)-Se(4)	3.552(8)	Se(4)-Bi(4)-Se(6)	141.9(2)
Bi(4)-Se(4')	3.551(9)	Se(4')-Bi(4)-Se(6)	141.8(2)
Bi(4)-Se(5) _{eq}	2.988(8)		
Bi(4)-Se(5') _{eq}	2.987(7)	Se(5)-Bi(4)-Se(6)	80.5(2)
Bi(4)-Se(6)	2.704(9)	Se(5')-Bi(4)-Se(6)	80.5(2)
Bi(4)-Se(6') _{eq}	2.926(6)	Se(6')-Bi(4)-Se(6)	85.1(2)
Bi(4)-Se(6'') _{eq}	2.913(7)	Se(6'')-Bi(4)-Se(6)	85.0(3)
Bi(4)Se _{eq} (mean)	2.95(3)	Se-Bi(4)-Se (mean)	83(2)

^a)The estimated standard deviations in the mean bond lengths and the mean bond angles are calculated by the equations $\sigma l = \{\sum_n (l_n - l)^2 / n(n-1)\}^{1/2}$, where l_n is the length (or angle) of the n th bond, l the mean length (or angle), and n the number of bonds.

3.3. Thermal Analysis

Thermal analysis has been used previously to investigate the synthesis of solid state compounds,³⁷ the mechanism of crystallization in chalcogenide glasses³⁸ and the high temperature phase diagrams of many A_2Q/M_2Q_3 (A= alkali metal; Q= S, Se, Te; M= As, Sb, Bi) systems.³⁹ In order to study the reactions of Bi in the Cs_2S_x and K_2Se_x fluxes we employed differential scanning calorimetry. The goal was to gain further insight into the thermal events that lead to the new compounds and the temperature at which they occur. The thermogram of a Bi/ Cs_2S /nS mixture that leads to the synthesis of β -CsBiS₂ is given in Figure 2-6A and shows four exothermic peaks. To ascertain the origin of each peak, various control experiments were performed using Cs_2S /nS flux, Bi/ Cs_2S and Bi/S mixtures under identical conditions. Analysis of the Cs_2S /S reaction thermogram shown in Figure 2-6B revealed two exothermic peaks (A,B) that are a result of atomic diffusion and reaction of Cs_2S with S to form a polysulfide flux. The flux reacts further with excess S to form a new polysulfide flux thereby producing exotherm C. Upon cooling, the excess flux solidifies at 178 °C (peak H). The same exothermic peaks are observed in the Bi/ Cs_2S /nS mixture (Figure 6A) and thus are assigned to the same processes. The Cs_2S_x flux then reacts with Bi at 274 °C to produce β -CsBiS₂ giving rise to peak E in Figure 2-6. Endotherm D, at 270 °C, is assigned to the melting of Bi metal just prior to reaction with Cs_2S_x . All of the melted Bi immediately reacts at 274 °C (peak E), which is supported by the

absence of a Bi recrystallization exotherm peak upon cooling. Peak E is assigned to the reaction of Bi and initial crystal nucleation. At 176 °C, exotherm F is observed on cooling which can be attributed to crystallization of the excess Cs_2S_x flux. A melting endotherm at 180 °C (peak G) was observed as the mixture was heated to 310 °C a second time. This result verified that peak F was due to excess flux crystallization and not due to product crystallization. To verify that peak F is not due to the crystallization of $\beta\text{-CsBiS}_2$, a bulk synthesis was carried out under the same heating and isotherm conditions in a sealed pyrex tube in a computer-controlled furnace. The reaction was quenched from 275 °C (after exotherm E) to room temperature. The product was isolated and powder XRD confirmed that the red crystals were single phase $\beta\text{-CsBiS}_2$.

It should be noted that Cs_2S purchased commercially yielded only Bi_2S_3 , instead of $\beta\text{-CsBiS}_2$, under the conditions described here. This was confirmed with a bulk synthesis reaction in the furnace. Furthermore, DSC thermograms obtained from the $\text{Cs}_2\text{S}/\text{nS}$ mixtures using this Cs_2S were completely different from that shown in Figure 2-6B. The small particle-size Cs_2S synthesized from the liquid ammonia method is very reactive and provides the best starting material for the synthesis of $\beta\text{-CsBiS}_2$. Care was taken to prevent any premature reaction at room temperature during the DSC experiments.

The thermogram for the synthesis of $\text{K}_2\text{Bi}_8\text{Se}_{13}$ is shown in Figure 2-7A. As in the $\beta\text{-CsBiS}_2$ synthesis described above, thermograms from K_2Se_x , Bi/ K_2Se and Bi/Se reactions were obtained

for reference purposes. Clearly the exothermic peaks (I, II) are due to the reaction between K_2Se and Se to form a polyselenide flux as suggested by the control-reaction of K_2Se/Se whose DSC thermogram is given in Figure 2-7B. The redox reaction of Bi with the formed K_2Se_x flux occurs at 268 °C shown by the sharp exotherm III. However, the broad rise of the specific heat preceding peak III could also be attributed to product formation and reactant diffusion. DSC of the Bi + 8Se system produced a sharp endotherm at 226 °C corresponding to the melting of Se followed by a very sharp exotherm at 268 °C due to the formation of Bi_2Se_3 . The formation of Bi_2Se_3 and $K_2Bi_8Se_{13}$ occurs at the approximate melting point of Bi metal which is masked in these systems. Exotherm IV in Figure 2-7A upon cooling, can be attributed to the crystallization of the excess K_2Se_x . Exotherm IV is at a different temperature than exotherm V (Figure 2-7B) because the excess K_2Se_x flux is of different chemical composition following the reaction with Bi metal. Bulk synthesis in the furnace at 330 °C, under DSC conditions, gave black needles of $K_2Bi_8Se_{13}$ upon quenching from 275 °C to room temperature, supporting our assignment of exotherm IV.

As in $\beta\text{-CsBiS}_2$, crystal growth of $K_2Bi_8Se_{13}$ is not instantaneous, rather it is a gradual process which begins with nucleation at the reaction exotherm followed by growth at the heating and isotherm stages and briefly thereafter upon cooling. By studying these reactions with the DSC technique, we have identified the important reaction steps preceding the reaction of the metal with the flux and determined the exact reaction temperatures. Based on these results

we were able to reduce the total time of synthesis of these compounds from the original 10 days to only 24 hours.

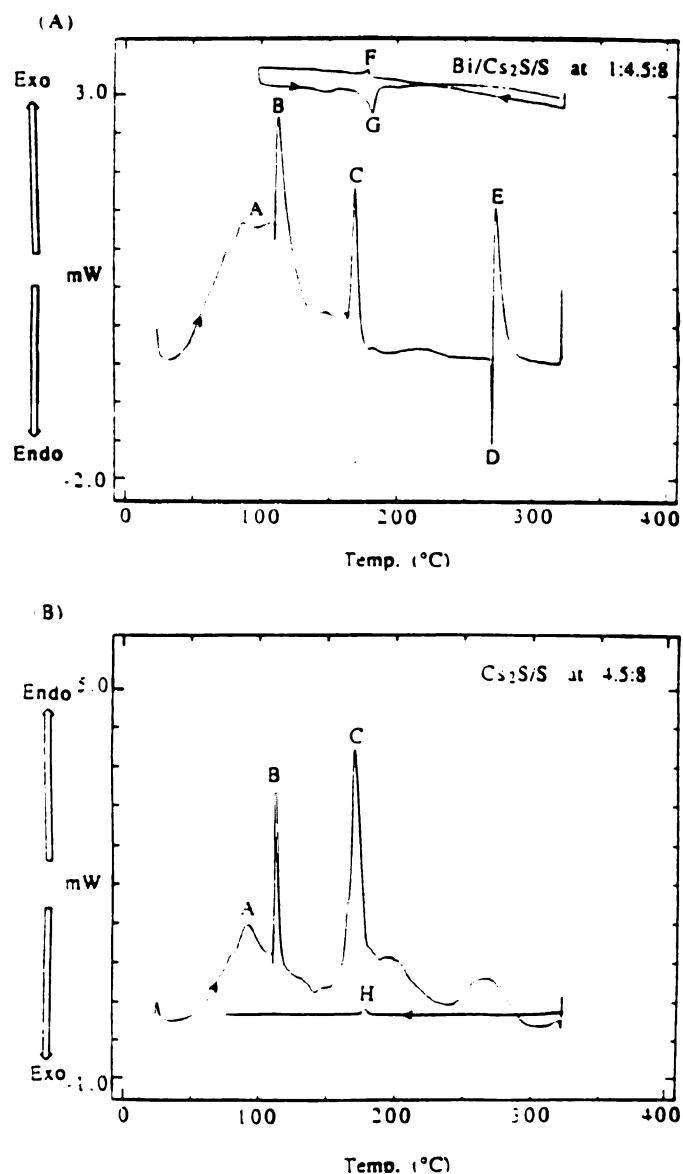


Figure 2-6. (A) DSC thermogram of the Bi/Cs₂S₃ mixture. The cooling and reheating curves are shown above the heating thermogram for clarity (Peaks F and G). Peak temperatures (°C): A (97), B (113), C (170), D (270), E (274), F (176) and G (180). (B) DSC thermogram of the Cs₂S/S mixture. Peak temperatures (°C): A (92), B (112), C (170) and H (178).

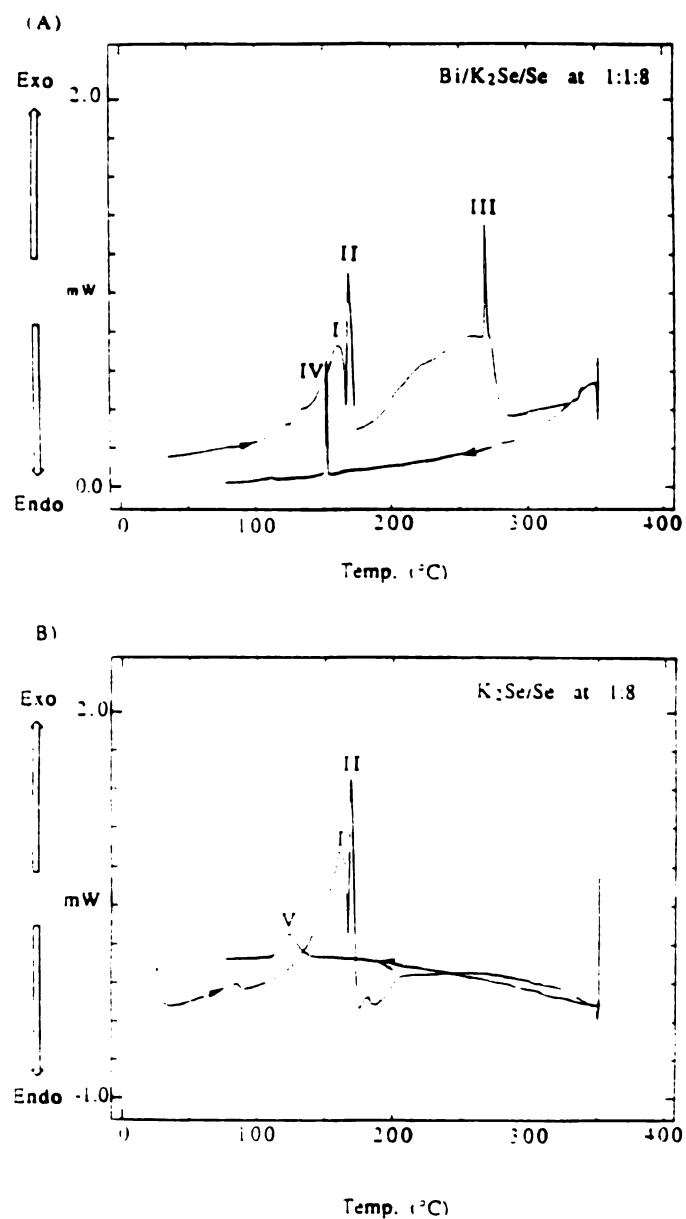


Figure 2-7. (A) DSC thermogram of the Bi/K₂Se₉ mixture. Peak temperatures (°C): I (160), II (169), III (269) and IV (152). (B) DSC thermogram of the K₂Se/Se mixture. Peak temperatures (°C): I (161), II (170) and V (123).

3.4. Electrical Conductivity and Thermoelectric Power Measurements.

Four-probe electrical conductivity measurements on single crystals of β -CsBiS₂ showed that the material is a semiconductor with room temperature conductivity $\sigma \sim 10^{-5}$ S/cm which drops quickly to 10^{-12} S/cm at 200 K. K₂Bi₈Se₁₃ is also a semiconductor but with significantly more facile charge transport as evidenced by both conductivity and thermoelectric power measurements as a function of temperature. In contrast, the room-temperature conductivity of single crystals of the layered γ -CsBiS₂ is $\sim 10^{-2}$ S/cm and exhibits a thermally activated temperature dependence, which is shown in Figure 2-8. Thermoelectric power data for γ -CsBiS₂ show a very large negative Seebeck coefficient (-580 mV/K at 120 K and -450 mV/K at 300 K) suggesting a n-type semiconductor. Figure 2-9 shows the log conductivity as a function of temperature for a pressed polycrystalline pellet of K₂Bi₈Se₁₃. This study was performed on several bulk samples of the compound with similar results. The magnitude and temperature dependence of the conductivity suggest that the compound is a semiconductor. The conductivity of $\sim 10^{-2}$ S/cm at room temperature is compared to the values $1.6\text{--}2.0 \times 10^3$ S/cm for Bi₂Se₃ (Bi₂Te₃-type),⁴⁰ and 0.6–0.8 S/cm for Bi₂Se₃ (Bi₂S₃-type) obtained from single crystals of these materials.⁴¹ The lower conductivity of K₂Bi₈Se₁₃ and the deviation from linearity particularly at low temperatures in the $\log \sigma$ vs. $1/T$ plot (see Figure 2-9) may be due to the effects of grain boundaries in the pressed

pellet. It should be noted that typically for three-dimensional materials the conductivities of polycrystalline compactions are two to three orders of magnitude lower than the corresponding values from single crystals. Efforts are continuing, to obtain larger single crystals that are suitable for conductivity measurements.

The conductivity measurements alone can not unequivocally characterize the electrical behavior of $\text{K}_2\text{Bi}_8\text{Se}_{13}$. A complementary probe to address this issue is thermoelectric power (TP) measurements as a function of temperature. TP measurements are typically far less susceptible to artifacts arising from the resistive domain boundaries in the material because they are essentially zero-current measurements. This is because temperature drops across such boundaries are much less significant than voltage drops. Figure 2-10 shows typical TP data of a polycrystalline aggregate of $\text{K}_2\text{Bi}_8\text{Se}_{13}$ as a function of temperature. The TP is negative throughout the temperature range studied ($80 < T < 300$ K) with values of -210 to -260 $\mu\text{V/K}$ at room temperature. This indicates electronic (as opposed to hole) charge transport. The TP becomes less negative as the temperature is decreased from 300 K to 80 K reminiscent of a metal-like behavior, but the very large TP values suggest a semiconductor material. The semiconducting character of this material is also supported by the fact that an optical gap exists in this material in the near-IR region (vide infra). The room temperature value of TP is comparable to that found in $\text{Bi}_2\text{Te}_{2.85}\text{Se}_{0.15}$,^{9a} which is one of the best n-type thermoelectric materials available near room temperature. The high thermoelectric power at room temperature, coupled with the conductivity data

suggest that γ -CsBiS₂ and K₂Bi₈Se₁₃ could be of interest as n-type thermoelectric cooling materials.

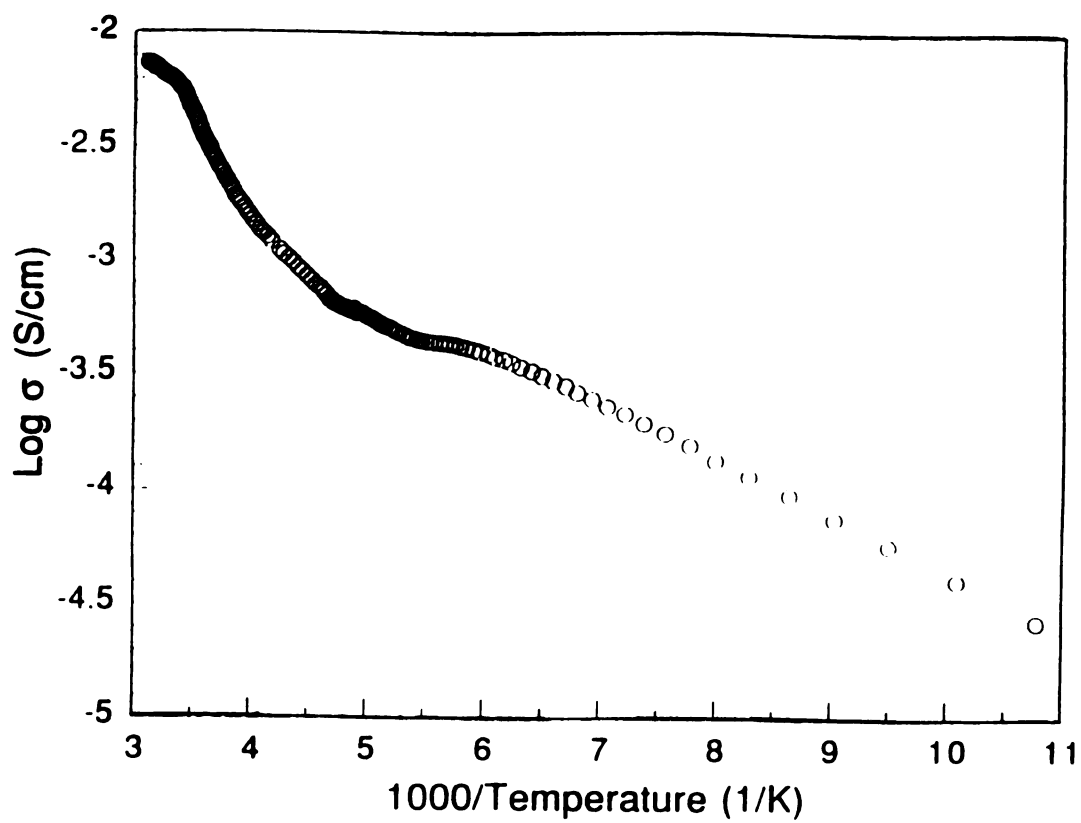


Figure 2-8. Variable temperature electrical conductivity data for a single crystal of $\gamma\text{-CsBiS}_2$.

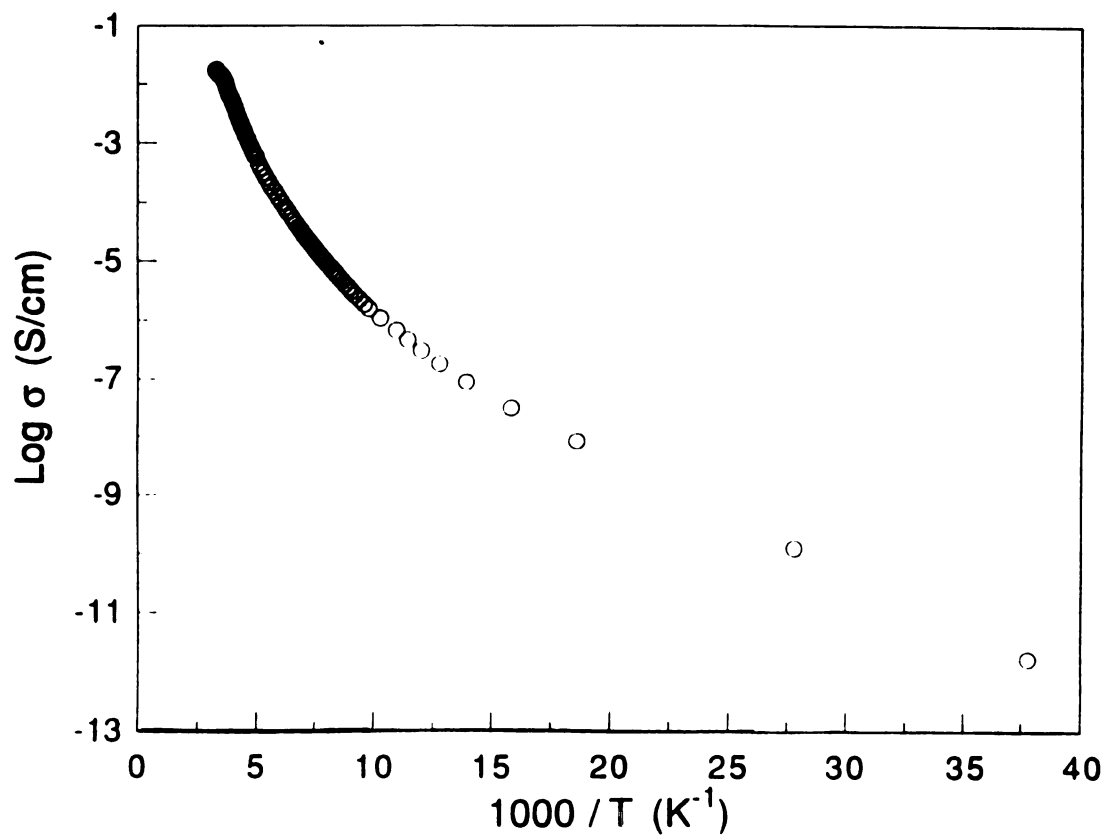


Figure 2-9. Variable temperature electrical conductivity data for a pressed pellet of $\text{K}_2\text{Bi}_8\text{Se}_{13}$.

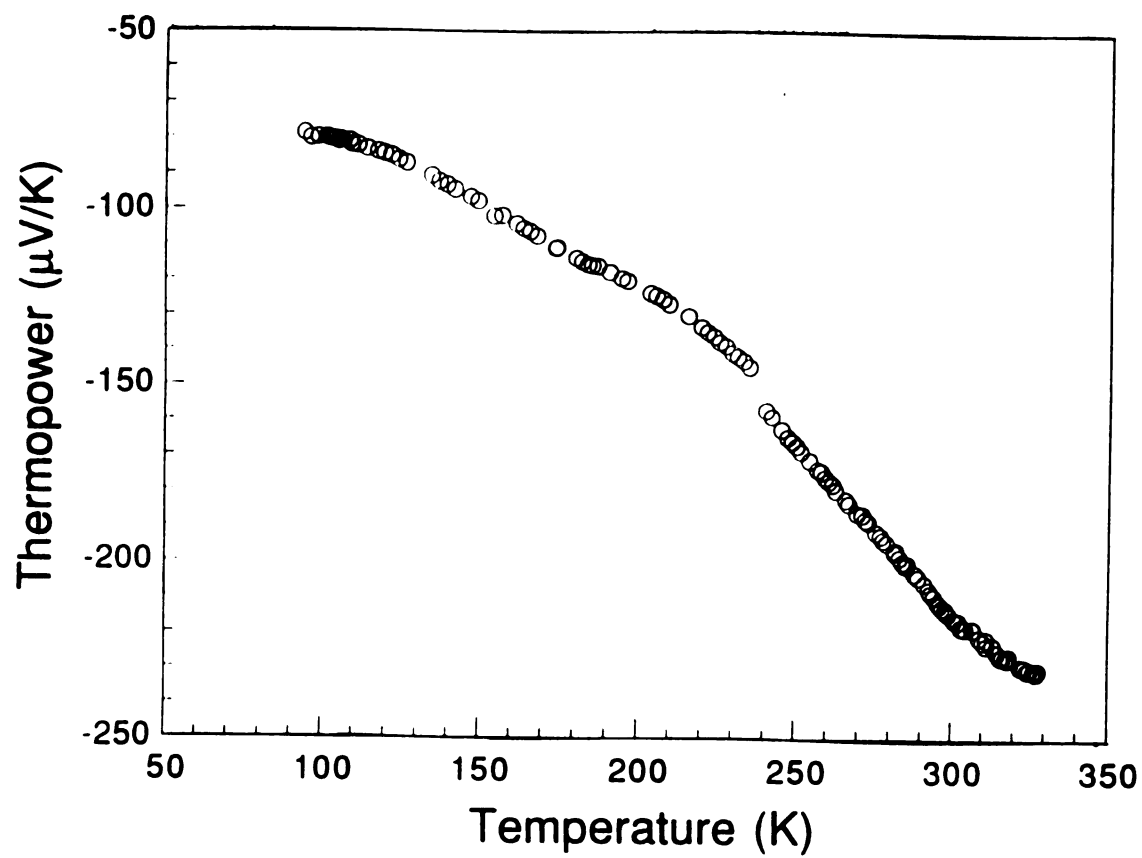


Figure 2-10. Thermoelectric power of a polycrystalline aggregate of $K_2Bi_8Se_{13}$ as a function of temperature.

3.5. UV-Visible-Near IR Spectroscopy

The optical properties of β -CsBiS₂, γ -CsBiS₂ and K₂Bi₈Se₁₃ were assessed by studying the UV-visible-near IR reflectance spectra of the materials. Such data for ternary bismuth chalcogenide compounds are reported here for the first time and thus comparisons with other materials are not possible. The spectra confirm the semiconductor nature of the materials by revealing the presence of optical gaps as shown in Figures 2-11 and 2-12. All compounds exhibit steep absorption edges from which the band-gap, E_g , can be assessed at 1.43, 1.11 and 0.76 eV respectively. The difference in band-gaps between the β - and γ - forms of CsBiS₂ is a direct consequence of the stereochemical expression of the s² lone pair of Bi which, in the two-dimensional γ -form, it is not stereochemically active. The smaller band-gaps of black K₂Bi₈Se₁₃ and γ -CsBiS₂ compared to the red β -CsBiS₂ are consistent with their respective colors. It is also consistent with the higher electrical conductivity of the selenide. A linear relationship is found in all compounds if the square of the absorption coefficient, $(\alpha/S)^2$ is plotted vs. $(E-E_g)$ suggesting that the band gaps are direct in nature.⁴² However, independent confirmation is needed to verify this conclusion. By comparison, the corresponding band-gaps of Bi₂Se₃ and Bi₂S₃ are 0.35 eV and 1.3 eV respectively.

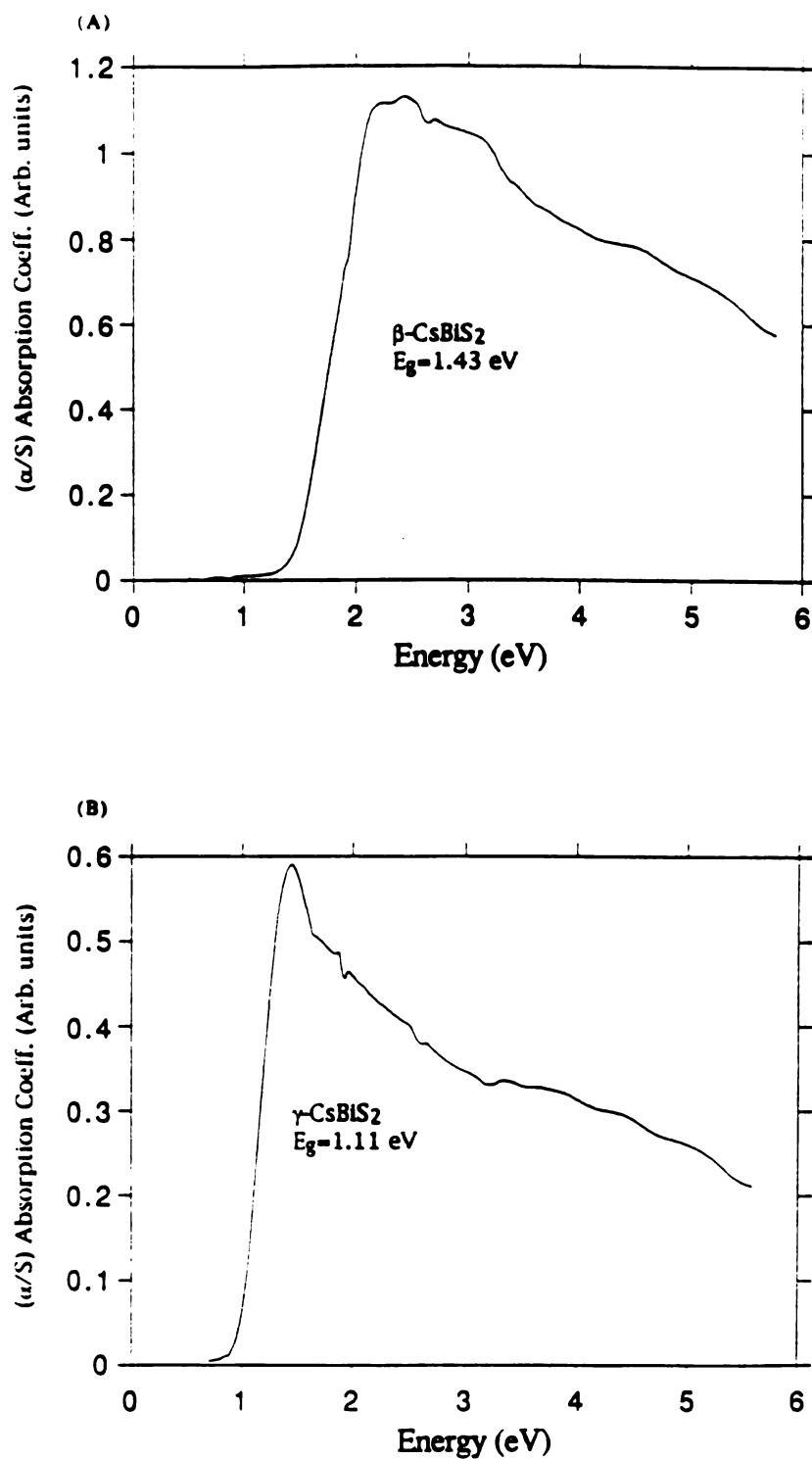


Figure 2-11. (A) Optical absorption spectrum of β -CsBiS₂. (B) Optical absorption spectrum of γ -CsBiS₂.

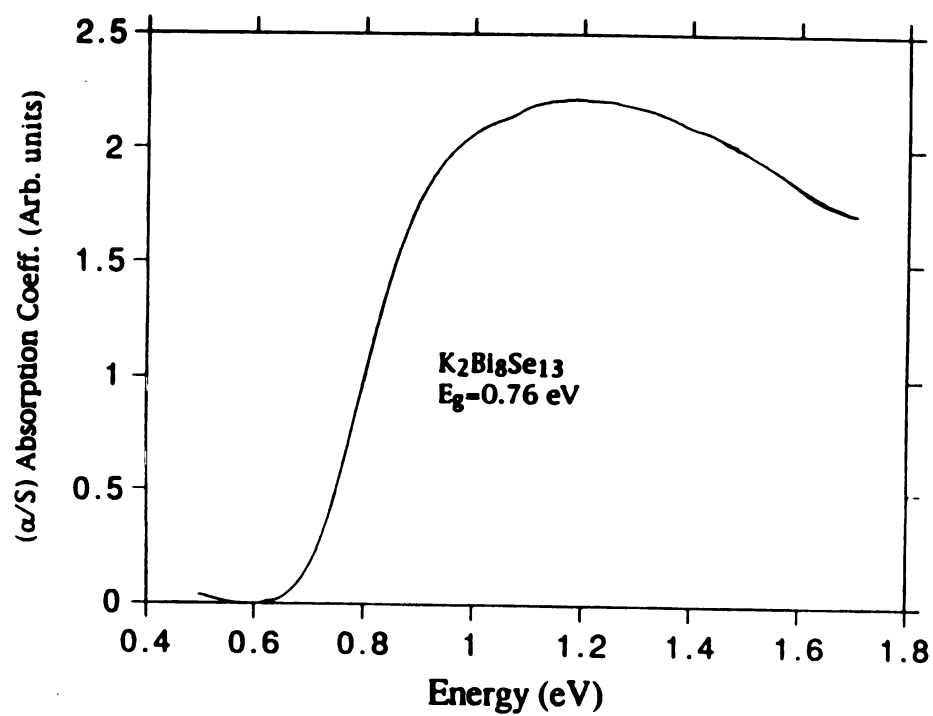


Figure 2-12. Optical absorption spectrum of $K_2Bi_8Se_{13}$. The absorption maximum occurs at 1.2 eV.

3.6. Conclusions

The reaction of Bi with molten Cs_2S_x and K_2Se_x polychalcogenide fluxes has revealed three new bismuth phases, $\beta\text{-CsBiS}_2$, $\gamma\text{-CsBiS}_2$ and $\text{K}_2\text{Bi}_8\text{Se}_{13}$ respectively. $\beta\text{-CsBiS}_2$ and $\gamma\text{-CsBiS}_2$ are semiconductors with an optical band gaps of 1.43 eV and 1.11 eV respectively. $\text{K}_2\text{Bi}_8\text{Se}_{13}$ possesses a new structure type related to that of Bi_2Se_3 . This compound is an n-type semiconductor with a large thermoelectric power and high conductivity at room temperature and a band gap of 0.76 eV.

Differential scanning calorimetry is a powerful technique in providing information on reactions of metals with polychalcogenide fluxes. We have been able to establish the region of product formation which helps to considerably shorten the reaction times. We hope to be able to use DSC to optimize the conditions of other molten salt reactions and reduce the time spent during the trial and error stage of exploratory synthesis.

List of References

1. (a) Boon, J. W. *Rec. Trav. Chim. Pays-Bas*, 1944, 63, 32. (b) Glemser, O.; Filcek, M. Z. *Anorg. Allg. Chem.*, 1955, 279, 321-323 (c) Gattow, G.; Zemmann, J. Z. *Anorg. Allg. Chem.*, 1955, 279, 324-327.
2. (a) Berul, S. I.; Lazarev, V. B.; Trippel, A. F.; Buchikhima, O. P. *Russ. J. Inorg. Chem.*, 1980, 25(11), 1695-1697. (b) Trippel, A. F.; Lazarev, V. B.; Berul, S. I. *Russ. J. Inorg. Chem.* 1978, 23(3), 390-391.
3. Kanishcheva, A. S.; Mikhailov, J. N.; Lazarev, V. B.; Trippel, A. F. *Dokl. Akad. Nauk, SSSR (Kryst.)*, 1980, 252, 96-99.
4. Schmitz, D.; Bronger, W. Z. *Naturforsch.*, 1974, 29b, 438-439.
5. Cordier, G.; Schafer, H.; Schwidetzky, C. *Rev. Chim. Miner.*, 1985, 22, 676-683.
6. Cordier, G.; Schafer, H.; Schwidetzky, C. *Rev. Chim. Miner.*, 1985, 22, 631-638.
7. (a) Feichtner, J. D.; Roland, G. W. *Appl. Opt.*, 1972, 11, 993-998 (b) Ballman, A. A.; Byer, R. L.; Eimerl, D.; Feigelson, R. S.; Feldman, B. J.; Goldberg, L. S.; Menyuk, N.; Tang, C. L. *Appl. Opt.*, 1987, 26, 224-227.
8. Ibuki, S; Yoschimatsu, S. *J. Phys. Soc. Japan*, 1955, 10, 549-554.
9. (a) Kaibe, H.; Tanaka, Y.; Sakata, M.; Nishida, I. *J. Phys. Chem. Solids* 1989, 50, 945-950. (b) Jeon, H-W.; Ha, H-P.; Hyun, D-B.; Shim, J-D. *J. Phys. Chem. Solids* 1991, 4, 579-585.
10. (a) Smith, M. J.; Knight, R. J.; Spencer, C. W. *J. Appl. Phys.* 1962, 33(7), 2186-2190. (b) Testardi, L. R.; Bierly, J. N. Jr.; Donahoe, F. J. *J. Phys. Chem. Solids*, 1962, 23, 1209. (c) Champness, C. H.; Chiang, P. T.; Parekh, P. *Can. J. Phys.* 1965, 43, 653-569. (d) Yim, W. M.; Fitzke, E. V. *J. Electrochem. Soc.* 1968, 115, 556-560.
11. (a) Rowe, D. M.; Bhandari, C. M. *Modern Thermoelectrics*, Holt, Rinehart and Winston: London, 1983; p. 103. (b) Borkowski, K.; Przyluski, J. *J. Mat. Res. Bull.* 1987, 22, 381-387.
12. (a) Kanatzidis, M. G. *Chem. Mater.*, 1990, 2, 353-363. (b) Kanatzidis, M. G.; Park, Y. *J. Am. Chem. Soc.*, 1989, 111, 3767-3769. (c) Kanatzidis, M. G.; Park, Y. *Chem. Mater.*, 1990, 2, 99-101. (d) Park, Y.; Kanatzidis, M. G. *Angew. Chem. Int. Ed. Engl.*, 1990, 29, 914-915.
13. (a) Sunshine, S. A.; Kang, D.; Ibers, J. A. *J. Am. Chem. Soc.* , 1987, 109, 6202-6204. (b) Kang, D.; Ibers, J. A. *Inorg. Chem.*, 1989, 27, 549-551.

14. Feher, F. *Handbuch der Präparativen Anorganischen Chemie*: Brauer, G., Ed.; Ferdinand Enke: Stuttgart, Germany, 1954; pp. 280-281.
15. D. K. Smith, M. C. Nichols, M. J.E. Zolensky, POWD10: "A Fortran IV Program for Calculating X-ray Powder Diffraction Patterns" version 10. Pennsylvania State University, 1983.
16. (a) Wendlandt, W. W.; Hecht, H. G. "Reflectance Spectroscopy", Interscience Publishers, 1966 (b) Kotüm, G. "Reflectance Spectroscopy", Springer Verlag, New York, 1969 (c) Tandon, S. P.; Gupta, J. P. *Phys. Stat. Sol.* 1970, 38, 363-367
17. Lyding, J.W.; Marcy, H. O.; Marks, T. J.; Kannewurf, C. R. *IEEE Trans. Instrum. Meas.* 1988, 37, 76-80.
18. Chaikin, P. I.; Kwak, J. F. *Rev. Sci. Instrum.* 1975, 46, 218-220.
19. Walker, N.; Stuart, D. *Acta Cryst.*, 1983, A39, 158-166.
20. (a) G. M. Sheldrick, In *Crystallographic Computing 3*; Sheldrick, G. M., Kruger, C., Doddard, R., Eds.; Oxford University Press: Oxford, England, 1985; pp 175-189. (b) Gilmore, G. J. *Appl. Cryst.*, 1984, 17, 42-46.
21. Lazarev, V. B.; Trippel, A. F.; Berul, S. I. *Russ. J. Inorg. Chem.*, 1980, 25 (11), 1694-1697.
22. Hoppe, R. *Bull. Soc. Chem. France*, 1965, 1115-1121.
23. Vorisholov, Y. V.; Peresh, E. Y.; Golovei, M. I. *Inorg. Mater.*, 1972, 8(4), 677-678.
24. R. O. Kagel; R. A. Nyquist, *Infrared Spectra of Inorganic Compounds*, Academic Press: New York, NY, 1971.
25. McCarthy, T. J.; Tanzer, T. A.; Chen, L.-H.; Hogan, T.; Kannewurf, C. R.; Kanatzidis, M. G. manuscript in preparation.
26. Kanishcheva, A. S.; Mikhailov, Yu. N.; Kuznetsov, V. G.; Batog, V. N. *Dokl. Akad. Nauk SSSR*, 1980, 251(3), 603-605.
27. Kohatsu, I.; Wuensch, B. J. *Acta Cryst.*, 1970, B27, 1245-1252.
28. (a) Gillespie, R. J. *Molecular Geometry*; Van Nostrand Reinhold: London, 1972, p.6. (b) Sawyer, J. F.; Gillespie, R. J. *Prog. Inorg. Chem.* 1987, 34, 65-113.
29. Palazzi, M.; Jaulmes, S. *Acta Cryst.* 1977, B33, 908-910.
30. Villars, P.; Calvert, L. D. *Pearson's Handbook of Crystallographic Data for Intermetallic Phases*; American Society for Metals: Metals Park, OH, 1985, p.1494.
31. Scavnicar S. Z. *Kristallogr.* 1960, 114, 85-97.

32. Mitchell, R. S. *Z. Kristallogr.*, 1956, *108*, 296-315.
33. Iitaka, Y.; Nowacki, W. *Acta Cryst.*, 1962, *15*, 691-698.
34. Kupcik, V.; Makovicky, E. N. *Jb. Miner. Mh.*, 1968, *7*, 236-237.
35. L. Pauling *The Nature of the Chemical Bond*, 3rd Edition, New York: Cornell University Press, 1966, p. 260.
36. Liautard, B.; Garcia, J. C.; Brun, G.; Tedenac, J. C.; Maurin, M. *Eur. J. Solid State Inorg. Chem.*, 1990, *27*, 819-830.
37. Wunderlich, B. *Thermal Analysis*, Academic Press.: 1990; pp 167-172.
38. Hfiz, M. M.; Osman, M. A.; Abd El-Halim, A. S.; Abd El-Fadl, A. *Solid State Commun.*, 1991, *80*(3) 209-211.
39. Berul, S. I.; Lazarev, V. B.; Trippel, A. F.; Buchikhina, O. P. *Russ. J. Inorg. Chem.* 1977, *22*(9), 1390-1393.
40. Black, J.; Conwell, E. M.; Seigle, L.; Spencer, C. W. *J. Phys. Chem. Solids*, 1957, *2*, 240.
41. Vereshchagin, L. F.; Itskevick, E. S.; Atabaeva, E. Y.; Popova, S. V. *Sov. Phys.-Solid State*, 1965, *6*(7), 1763.
42. Pankove, J. I. in "Optical Processes in Semiconductors" Dover Publications, New York, 1975.

CHAPTER 2 (Part 2)

Synthesis, Structural Characterization, Ion-Exchange Properties and Reactivity of KBi_3S_5 : A New Three-dimensional Bismuth Sulfide With Large Tunnels

1. Introduction

Although binary bismuth chalcogenide phases have received considerable attention for being excellent thermoelectric materials near room temperature,¹ there has been very little exploratory synthesis of new ternary bismuth chalcogenide phases. Outside of the well-known NaCl-type ABiQ_2 ($\text{A}=\text{Li}, \text{Na}, \text{K}$; $\text{Q}=\text{S}, \text{Se}$)² compounds, the only other phases that have been fully characterized structurally are CsBi_3S_5 ,³ RbBi_3S_5 ,⁴ $\text{Tl}_4\text{Bi}_2\text{S}_5$,⁵ α -(β -) BaBi_2S_4 ,⁶ $\text{Cs}_3\text{Bi}_7\text{Se}_{12}$,⁷ $\text{Sr}_4\text{Bi}_6\text{Se}_{13}$ ⁸ and BaBiSe_3 .⁹ These compounds have been prepared at high ($>450^\circ\text{C}$) temperature by direct combination of the elements or alkali carbonates with Bi and S. In addition, mixed Bi/transition metal/Q ($\text{Q}=\text{S}, \text{Se}$) solid solution systems have been investigated including $\text{Cu}_{1+3x}\text{Bi}_{5-x}\text{Q}_8$ ¹⁰ and $\text{Mn}_{1-x}\text{Bi}_{2+y}\text{Q}_4$.¹¹ Several naturally occurring bismuth sulfosalts, including PbBi_2S_4 (galenobismuthite)¹² and $\text{PbCu}_4\text{Bi}_5\text{S}_{11}$,¹³ have also been observed. When we consider the structural diversity that can result from the manifestation of the

inert lone pair of electrons on Bi^{3+} and from the variable coordination preference of this ion, it becomes apparent that further work in this area is warranted. Recently, we have synthesized three ternary bismuth chalcogenides using A_2Q_x ($\text{A}=\text{K}, \text{Cs}$; $\text{Q}=\text{S}, \text{Se}$) fluxes below 400°C that display a wide range of structural diversity.¹⁴ $\beta\text{-CsBiS}_2$ possesses a linear chain structure with corner sharing BiS_3 trigonal pyramids while $\gamma\text{-CsBiS}_2$ forms a layered superstructure of RbBiS_2 . In $\text{K}_2\text{Bi}_8\text{Se}_{13}$, layers of BiSe_6 octahedra are connected by BiSe_5 square pyramidal units to form a three-dimensional network with K^+ ions located in the channels. Both $\gamma\text{-CsBiS}_2$ and $\text{K}_2\text{Bi}_8\text{Se}_{13}$ exhibit high thermopower and reasonably high n-type electrical conductivity. In an effort to expand this very interesting chemistry, we investigated the reactivity of Bi in K_2S_x fluxes. The alkali metal polychalcogenide flux method has proven to be an extremely useful low temperature route to access new, often metastable compounds with novel structures.^{15,16}

The possibility of open metal chalcogenide framework structures that combine the utility of microporous oxides with the useful electronic properties of metal chalcogenides to form a new class of microporous chalcogenides is intriguing. Bedard and coworkers reported the hydrothermal synthesis of several tin sulfides that display microporous activity after partial removal of the occluded template.¹⁷ Another open chalcogenide framework was reported in the antimony sulfide system using the hydrothermal method.¹⁸ Recently, a novel molten salt approach using $(\text{Ph}_4\text{P})_2\text{Se}_x$ fluxes at 200°C was shown to give $(\text{Ph}_4\text{P})[\text{M}(\text{Se}_6)_2]$ ($\text{M}=\text{Ga}, \text{In}, \text{Tl}$).¹⁹ The open polymeric framework in this compound consists of

tetrahedral M^{3+} centers and bridging Se_6^{2-} ligands that form an extended structure in two dimensions with Ph_4P^+ cations residing within the layers.

In this paper, we report on KBi_3S_5 , a novel metastable compound with a three-dimensional structure with surprisingly large tunnels for a chalcogenide compound, and with topotactic ion-exchange properties.

2. Experimental Section

2.1. Reagents

Chemicals in this work were used as obtained: (i) bismuth powder, 99.999+% purity, -100 mesh, Aldrich Chemical Co., Inc., Milwaukee, WI. (ii) sulfur powder, sublimed, J. T. Baker Chemical Co., Phillipsburg, NJ. (iii) potassium metal, analytical reagent, Mallinckrodt Inc., Paris, KY. (iv) methanol, anhydrous, Mallinckrodt Inc., Paris, KY; diethyl ether, ACS anhydrous, EM Science, Inc., Gibbstown, NJ. (v) hydrochloric acid, 36.5-38% volume solution, EM Science, Gibbstown, NJ. (vi) sodium acetate, Fischer Scientific Co., Fairlawn, NJ. (vii) cesium acetate, technical grade, Penn Rare Metals Division Kawecki Chemical Co., Revere, PA. (viii) sodium chloride, EM Science, Gibbstown, NJ. (ix) rubidium chloride, cesium chloride, 99.9% pure, Cerac, Inc., Milwaukee, WI.

2.2. Synthesis

All manipulations were carried out under a dry nitrogen atmosphere in a Vacuum Atmospheres Dri-Lab glovebox. For the preparation of K_2S we used a modified literature procedure.²⁰

Potassium Sulfide, K_2S . An amount of 2.460 g (0.077 mol) sulfur and 6.00 g (0.153 mol) freshly sliced potassium metal were added to a 250 ml round-bottom flask. A 150 ml volume of liquid ammonia was condensed into the flask at $-78\text{ }^{\circ}\text{C}$ (dry ice/acetone) under nitrogen to give a light blue solution. The NH_3 was removed by evaporation under a flow of nitrogen as the bath slowly warmed to room temperature. The pale yellow solid (99% yield) was dried under vacuum overnight, flame-dried, and ground to a fine powder with a mortar and pestle.

Potassium Pentasulfido-tribismuthate(III), KBi_3S_5 . The reaction of 0.052 g (0.25 mmol) Bi, 0.072 g (0.65 mmol) K_2S and 0.096 g (3.0 mmol) S in an evacuated pyrex tube at $300\text{ }^{\circ}\text{C}$ for 5 days, followed by cooling at $4\text{ }^{\circ}\text{C/hr}$ to $120\text{ }^{\circ}\text{C}$ then to room temperature in one hour, afforded small dark gray needles (94% yield, based on Bi metal). The product, stable with respect to water and air, was isolated by dissolving the excess K_2S_x with methanol under inert atmosphere. Semi-quantitative microprobe analysis on single crystals gave $K_{1.4}Bi_{2.8}S_{5.2}$ (average of three data acquisitions). Far-IR (CsI matrix) gave a broad absorbance from 260 to 158 cm^{-1} . Raman spectroscopy gave a strong, broad shift at 267 cm^{-1} .

$(H_2O)Bi_3S_{4.5} \cdot (S_8)_{0.06}$. The stirring of 0.200 g (0.242 mmol) of finely ground KBi_3S_5 in a solution of 0.5M HCl (30 ml), at room

temperature in air, afforded a microcrystalline product with the same dark gray color as the starting material. The product was filtered and washed with distilled water, ethanol and ether. Varying the reaction time (0.5 - 66 hours) and lowering the temperature to 0 °C did not influence the final result. Extensive semi-quantitative (EDS) microprobe analyses were performed on the crystallites from several reaction products, giving a K/Bi ratio of 0.01 to 0.03,²¹ suggesting that virtually all K⁺ was removed.

β-Rubidium Pentasulfido-tribismuthate(III), β-RbBi₃S₅. An amount of 0.042 g (0.051 mmol) KBi₃S₅ was heated with excess RbCl in a 1:100 ratio in an evacuated pyrex tube at 350-380 °C for 2 days. After cooling to room temperature over 6 hours, the product was washed with distilled water, MeOH and ether. Semi-quantitative (EDS) microprobe analysis on single crystals gave Rb_{1.0}Bi_{3.5}S_{6.0} (average of three data acquisitions) suggesting that virtually all K⁺ was removed.

Solid State Reactions with Alkali Metal Chlorides. 0.042 g (0.051 mmol) KBi₃S₅ was heated with excess ACl (A=Na, Rb, Cs) in a 1:100 ratio in an evacuated pyrex tube at 200-400 °C for 2 days. After cooling to room temperature over 6 hours, the product was washed with distilled water, MeOH and ether. Details of the reaction conditions are given in Table 2-9.

The homogeneity of KBi₃S₅ was confirmed by comparing the observed and calculated X-ray powder diffraction patterns. The d_{hkl} spacings observed for the bulk materials were compared, and found to be in agreement with the d_{hkl} spacings calculated from the single

crystal data using the program POWD10.²² The results are shown in Table 2-10.

2.3. Physical Measurements

The FT-IR spectrum of KBi_3S_5 was recorded as a solid in a CsI matrix. The sample was ground with dry CsI into a fine powder, and a pressure of about seven metric tons was applied to the mixture to make a translucent pellet. The spectra were recorded in the far-IR region ($600\text{-}100\text{ cm}^{-1}$) with the use of a Nicolet 740 FT-IR spectrometer. The Mid-IR spectra ($4000\text{-}350\text{ cm}^{-1}$) were recorded as a solid in a KBr matrix. Raman spectra were recorded at room temperature with a Nicolet FT-Raman 950 spectrometer.

The instruments and experimental setups for optical diffuse reflectance measurements²³ and quantitative microprobe analysis on SEM/EDS are the same as those in Section 2.3 in Chapter 2 (Part 1).

Thermogravimetric analysis (TGA) was performed with a computer-controlled Shimadzu TGA-50. The samples were heated in a quartz cup from room temperature to $330\text{ }^{\circ}\text{C}$ at a heating rate of $3\text{ }^{\circ}\text{C}/\text{min}$. under a nitrogen flow rate of $57\text{ ml}/\text{min}$.

Differential Scanning Calorimetry (DSC) was performed with a computer-controlled Shimadzu DSC-50 thermal analyzer under a nitrogen atmosphere at a flow rate of $35\text{ ml}/\text{min}$. The samples were crimped in an aluminum pan inside a nitrogen-filled glove box. The pan was placed on the sample side of the DSC-50 detector and an empty aluminum pan of equal mass was crimped and placed on the

reference side. The samples were heated to the desired temperature at 5 °C/min. The reported DSC temperatures are peak temperatures with a standard deviation of 0.2 degrees. The adopted convention in displaying data is: exothermic peaks occur at positive heat flow while endothermic peaks occur at negative heat flow.

Differential Thermal Analysis (DTA) was performed with a computer-controlled Shimadzu DTA-50 thermal analyzer. The ground single crystals (~10.0 mg total mass) were sealed in quartz ampules under vacuum. An empty quartz ampule of equal mass was sealed and placed on the reference side of the detector. The samples were heated to the desired temperature at 20 °C/min, then isothermed for 10 min followed by cooling at 10 °C/min to 200 °C and finally by rapid cooling to room temperature. Indium (reported m.p. 156.6 °C) and antimony (reported m.p. 630.9 °C) served as calibration standards. The reported DTA temperatures are peak temperatures. The DTA samples were examined by powder X-ray diffraction after the experiments.

Mass Spectrometry (MS) was performed with a VG Instruments Trio-1000 Mass Spectrometer. The solid samples were heated at 5 °C/min. to 300 °C with a solid probe.

2.4. X-ray Crystallography

KBi₃S₅ was examined by X-ray powder diffraction for the purpose of phase purity and identification. Accurate d_{hkl} spacings (Å) were obtained from the powder patterns recorded on a Rigaku

Rotaflex Powder X-ray Diffractometer with Ni filtered Cu K α radiation operating at 45 kV and 100 mA. The data were collected at a rate of 1.0 deg/min.

The variable temperature powder XRD experiment was performed with the instrument described above. The instrument was equipped with a temperature controller and the experiment was carried out under nitrogen flow with an enclosed sample compartment. The data were collected at a rate of 2.4 deg/min. The sample was heated to 65 °C and was allowed to equilibrate for 30 minutes before the XRD was taken. The sample was then heated in 20 °C increments with 30 minute equilibration times at each step. The final XRD was taken at 145°C.

Structure solution of KBi₃S₅. A crystal with dimensions 0.50 x 0.10 x 0.10 mm was mounted on a tip of a glass capillary. Intensity data were collected using the ω -2 θ scan mode on a Rigaku AFC6S four-circle automated diffractometer equipped with a graphite-crystal monochromator. The stability of the crystal was monitored by measuring three standard reflections periodically (every 150 reflections) during the course of data collection. No crystal decay was detected. An empirical absorption correction based on ψ scans was applied to the data.

The space group was determined to be Pnma (#62), and a solution was found using the automated direct methods function in the SHELXS86 program²⁴ and refined by full-matrix, least-squares techniques of the TEXSAN package of crystallographic programs.²⁵ Three bismuth atoms, five sulfur atoms and a potassium atom were

located. Each of the nine atoms reside on a mirror plane. Inspection of the difference Fourier map revealed a significant electron density peak at a distance from S reasonable for K atoms. This peak was assigned to a second K atom which also resided on a mirror plane. Assuming Bi^{3+} and S^{2-} , electroneutrality dictates that only one K^+ atom should be found. After least squares refinement, the isotropic temperature factor for K(2) was rather high at 14.0 \AA^2 . The occupancy and the temperature factor of this atom were refined to give values of 0.23 and 8.4 \AA^2 respectively. At this stage, a disorder model $\text{K}(1)_{1-x} \text{K}(2)_x \text{Bi}_3\text{S}_5$ seemed to be reasonable. The occupancies of K(1,2) were constrained to 0.5 then refined. Least squares refinement of this model resulted in a occupancy value of 0.39 and a temperature factor of 1.67 for K(1) which decreased from 2.48. K(2) gave a occupancy of 0.11 and a temp. factor of 1.62 which decreased from 8.4. A DIFABS correction was applied to the isotropically refined data.²⁶ K(2) was refined isotropically because of its small occupancy while the rest of the atoms were refined anisotropically to give a final $R/R_w = 5.1/6.7$. All calculations were performed on a VAXstation 3100/76 computer.

The complete data collection parameters, details of the structure solution and refinement for KBi_3S_5 are given in Table 2-11. The atomic coordinates, average temperature factors and their estimated standard deviations for KBi_3S_5 are given in Table 2-12.

Table 2-9. Solid State Reactions of KBi_3S_5 with Alkali Metal Halides.

Temp. (°C)	NaCl	RbCl	CsCl
197	no reaction	no reaction	no reaction
297	$\text{NaBiS}_2 + \text{Bi}_2\text{S}_3$	$\text{Rb}_x\text{K}_{1-x}\text{Bi}_3\text{S}_5^{\text{a}}$	$\gamma\text{-CsBiS}_2$
347	$\text{NaBiS}_2 + \text{Bi}_2\text{S}_3$	$\beta\text{-RbBi}_3\text{S}_5^{\text{b}}$	$\gamma\text{-CsBiS}_2$
384		$\beta\text{-RbBi}_3\text{S}_5^{\text{b}}$	$\gamma\text{-CsBiS}_2 + \text{phase}^{\text{c}}$
400		$\alpha\text{-RbBi}_3\text{S}_5$	$\gamma\text{-CsBiS}_2 + \text{phase}$

^a EDS analysis gave $\text{Rb}_{0.54}\text{K}_{0.46}\text{Bi}_{3.1}\text{S}_{5.6}$.

^b Topotactic ion-exchange

^c EDS analysis gave $\text{Cs}_{1.0}\text{Bi}_{3.3}\text{S}_{5.1}$ (needles) and $\text{Cs}_{1.0}\text{Bi}_{2.5}\text{S}_{3.5}$ (hexagonal plates).

Table 2-10. Calculated and Observed X-ray Powder Diffraction Patterns for KBi_3S_5 .

h k l	d(calc.), Å	d(obs.), Å	I/I _{max} (obs.)
1 0 1	12.15	12.13	78
0 0 2	8.68	8.70	4
2 0 0	8.51	8.50	10
2 0 2	6.08	6.07	51
1 0 3	5.48	5.48	5
3 0 1	5.39	5.38	13
3 0 3	4.13	4.13	4
3 0 3	4.05	4.04	8
4 0 2	3.82	3.81	14
1 1 2, 2 1 1	3.61, 3.60	3.60	11
3 0 4	3.45	3.45	42
1 0 5	3.40	3.40	37
0 1 3	3.33	3.34	14
1 1 3	3.27	3.28	6
3 1 1	3.25	3.25	12
2 0 5	3.22	3.22	25
5 0 2	3.17	3.16	11
3 1 2	3.09	3.09	5
4 0 4	3.04	3.04	6
4 1 0	2.94	2.94	13
4 1 1, 0 0 6	2.90, 2.89	2.90	35
1 0 6	2.85	2.85	100
5 1 1	2.58	2.58	4
2 1 5	2.52	2.52	4
5 1 4	2.238	2.238	4
3 1 6	2.179	2.179	6
1 0 8	2.153	2.153	10
8 0 1	2.111	2.106	6
5 1 5	2.088	2.087	12
4 1 6	2.063	2.063	6
0 2 0	2.038	2.039	6
6 0 6	2.025	2.023	4
5 0 7	2.005	2.005	4
3 1 7	1.985	1.986	10
6 1 5	1.934	1.933	5
7 1 4	1.881	1.881	8
2 1 8	1.869	1.869	5
5 1 7, 4 2 2	1.799, 1.798	1.799	4
4 2 3	1.752	1.752	4
1 1 9, 9 0 4	1.735, 1.733	1.734	9
6 0 8	1.724	1.723	8
1 2 6	1.658	1.660	8
2 0 11	1.552	1.552	4

Table 2-11. Summary of Crystallographic Data and Structure Analysis for KBi_3S_5

Formula	KBi_3S_5
FW	826.34
a, Å	17.013(5)
b, Å	4.076(2)
c, Å	17.365(4)
α , deg	90.000
β , deg	90.000
γ , deg	90.000
Z; V, Å ³	4; 1204(2)
λ	0.71073 (Mo $K\alpha$)
space group	Pnma (No. 62)
D_{calc} , g/cm ³	4.56
μ , cm ⁻¹	447 (Mo $K\alpha$)
$2\theta_{\text{max}}$, deg	50 (Mo $K\alpha$)
Temp., °C	23
Final R/R _w , %	5.1/6.7
Total Data Measured	1311
Total Unique Data	1311
Data with $F_o^2 > 3\sigma(F_o^2)$	782
No. of variables	59

$$*R = \Sigma(|F_o| - |F_c|) / \Sigma|F_o| \quad R_w = \{\Sigma w(|F_o| - |F_c|)^2 / \Sigma w|F_o|^2\}^{1/2}$$

Table 2-12. Fractional Atomic Coordinates and B_{eq} Values for KBi_3S_5 with Estimated Standard Deviations in Parentheses.

atom	x	y	z	$B_{eq}, \text{\AA}^2$
Bi(1)	0.2380(1)	1/4	0.7111(1)	1.40(8)
Bi(2)	0.0831(1)	-1/4	0.5717(1)	1.25(8)
Bi(3)	0.3433(1)	-1/4	0.8743(1)	1.76(9)
K(1) ^b	0.5019(7)	-3/4	0.7041(8)	1.2(5)
K(2) ^c	0.148(3)	1/4	0.018(3)	1.7(9)
S(1)	0.3535(7)	-1/4	0.7162(7)	1.6(6)
S(2)	-0.0363(8)	-3/4	0.6022(7)	1.9(6)
S(3)	0.1235(6)	-1/4	0.7194(6)	1.1(5)
S(4)	0.2325(6)	1/4	-0.1369(6)	1.3(5)
S(5)	0.1894(7)	1/4	0.5393(7)	1.7(5)

a) $B_{eq} = (4/3)[a^2B(1,1) + b^2B(2,2) + c^2B(3,3) + ab(\cos\gamma)B(1,2) + ac(\cos\beta)B(1,3) + bc(\cos\alpha)B(2,3)]$.

^b78% occupied

^c22% occupied

3. Results and Discussion

3.1 Synthesis and Spectroscopy

The synthesis of KBi_3S_5 was accomplished by dissolving Bi in excess $\text{K}_2\text{S}_{5.6}$ flux at 300 °C followed by isolation in degassed methanol. Dissolving Bi in a slightly more basic flux of $\text{K}_2\text{S}_{5.3}$ affords KBi_3S_5 and a small amount of impurity phase. Increasing the Lewis basicity further with K_2S_x ($x=3.7-4.3$) at 300 °C, results in the formation of $\beta\text{-KBiS}_2$ only.²⁷ The synthesis is also complicated by the narrow temperature window (~290-310 °C) in which the compound forms. Below 290 °C, a poorly crystalline KBi_3S_5 phase results. We note that a phase claimed to have the stoichiometry KBi_3S_5 has been reported in high temperature phase diagram studies in the $\text{Bi}_2\text{S}_3\text{-K}_2\text{S}$ system, but the unindexed powder X-ray diffraction pattern does not resemble the XRD pattern of our compound.²⁸ Under similar conditions, the attempted synthesis of the Rb^+ analog resulted in the formation of the non-isostructural RbBi_3S_5 ⁴ and Bi_2S_3 .

A direct combination reaction between Bi_2S_3 and K_2S (3:1) at 325 °C and 520 °C was performed to determine if KBi_3S_5 could be isolated using this approach. However, the product was identified, by powder X-ray diffraction, to be only a mixture of Bi_2S_3 and $\beta\text{-KBiS}_2$. A third, unidentified phase was also detected in the reaction at 520 °C. This experiment confirms the necessity of the molten salt method as a route to KBi_3S_5 .

Far-IR spectroscopy of KBi_3S_5 shows a very broad absorption starting at 260 cm^{-1} and peaking at 158 cm^{-1} . The Raman spectrum

shows a broad shift at 267 cm^{-1} . These peaks are probably due to the Bi-S stretching vibrations. The similarity of the various BiS_6 octahedra in KBi_3S_5 further complicates the assignments due to extensive overlap of Bi-S absorptions.

KBi_3S_5 was found to be a semiconductor with a very high resistivity at r.t. $10^8\ \Omega\cdot\text{cm}$.

The optical properties of KBi_3S_5 were assessed by studying the UV-Vis-Near/IR reflectance spectra. The spectra confirm the semiconducting nature of the material by revealing the presence of a well defined optical gap as shown in Figure 2-13. The compound exhibits a steep absorption edge from which the band-gap, E_g , can be assessed at 1.21 eV. This transition is determined from a $(\alpha/S)^2$ vs. E plot to be direct in character and it is due to charge transfer from the primarily S-based valence band to the primarily Bi-based conduction band. The E_g of the isomorphous $\beta\text{-RbBi}_3\text{S}_5$ (vide infra) was found to be very similar at 1.18 eV. These band-gap values lie in the optimum range for solar energy absorption and point to possible photoconductivity response with visible light. By comparison, the corresponding band-gap of Bi_2S_3 is 1.3 eV which has been shown to possess photovoltaic properties.²⁹

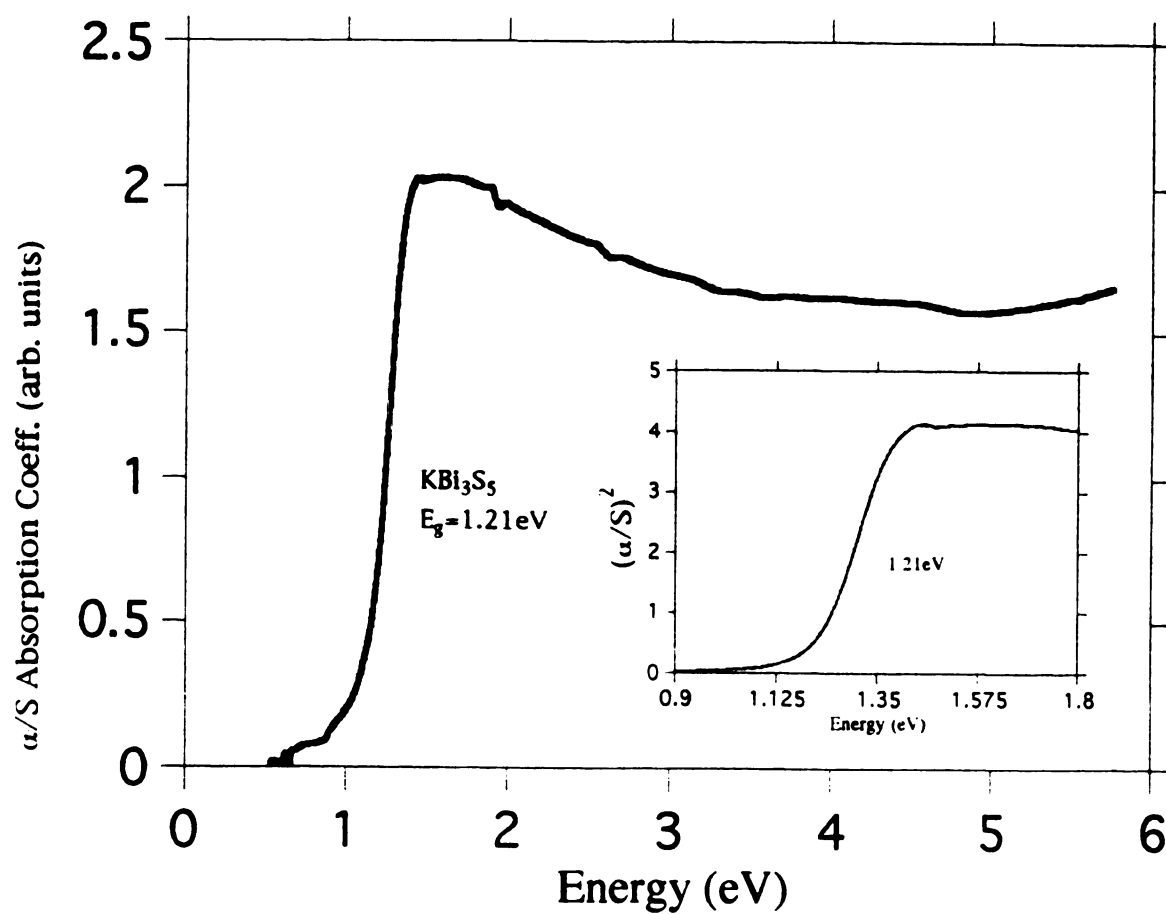


Figure 2-13. Optical absorption spectrum of KBi_3S_5 . Inset shows the $(\alpha/S)^2$ vs. Energy plot.

3.2. Description of Structure.

KBi_3S_5 crystallizes in a different structure type than $\alpha\text{-RbBi}_3\text{S}_5$ ⁴ or CsBi_3S_5 .³ The structure, shown in Figure 2-14, is built up from edge-sharing BiS_6 octahedra forming a three-dimensional $[\text{Bi}_3\text{S}_5]^-$ framework. A remarkable feature of this framework is the presence of large parallel tunnels running along the b-axis. The tunnels are composed of 20-membered rings of alternating Bi and S atoms with S...S distances across the tunnels ranging from 9.45 Å (S(1)-S(1')) to 14.02 Å (S(2)-S(2')). The K^+ ions reside in the tunnels and are disordered over two crystallographic sites with similar coordination environments. The disorder associated with the K^+ ions seems necessary to stabilize the structure. Selected bond distances and bond angles for KBi_3S_5 are given in Table 2-13.

Bi(1) in KBi_3S_5 is found in a distorted octahedral coordination with four equatorial bonds at 2.832(8) and 2.823(7) Å, and a short axial bond of 2.64(1) Å *trans* to a long bond of 3.10(1) Å. The S(4')-Bi(1)-S(5) angle of $162.5(3)^\circ$ suggests that the deviation from a normal 180° angle is caused by the stereochemically active lone pair of Bi. The Bi(2) coordination is also distorted with a short axial distance of 2.66(1) Å, *trans* to a long bond of 3.12(1) Å. This long-short alternation is also seen at the Bi(1,2) sites in CsBi_3S_5 .⁸ A similar environment is found in the naturally occurring bismuth sulfosalts, including Bi(1) in PbBi_2S_4 ¹⁸ and Bi(5) in $\text{PbCu}_4\text{Bi}_5\text{S}_{11}$.¹⁹

Comparison of the unit cell volumes of KBi_3S_5 (1204 Å³) with two other related compounds, CsBi_3S_5 (1036 Å³) and $\alpha\text{-RbBi}_3\text{S}_5$ (991 Å³), show that KBi_3S_5 possesses the largest volume despite the fact

that it contains the smallest alkali ion. This is consistent with the presence of some void space in the crystal. All three compounds have orthorhombic unit cells with the smallest axis being close to 4 Å. Based on the unit cell volumes of the ABi_3S_5 compounds, we expect a dense phase of KBi_3S_5 to have a volume of $\sim 960 \text{ Å}^3$, 20% smaller than that observed. Though we did not encounter such a phase in our studies, we believe it may exist at higher temperatures, thus giving some credibility to the earlier claims.²⁸ The relatively open structure of KBi_3S_5 suggests that the Rb^+ and Cs^+ analogs may be possible under the proper synthetic conditions.

The structure of KBi_3S_5 is reminiscent of hollandite which is composed of MO_6 octahedra ($\text{M} = \text{Ti}^{30}, \text{Ru}^{31}, \text{Mo}^{32}, \text{Mn}^{33}$) linked via edges and corners to form tunnels of various sizes in which alkali and/or alkaline earth metal cations reside. Many of these phases exhibit disorder in the cation sites and have been well-studied because of their ionic conductivity,³⁴ redox intercalation behavior ($\alpha\text{-MnO}_2$),³⁵ and ion-exchange properties.³⁶ Figure 2-15 shows polyhedral representations of the $[\text{Bi}_3\text{S}_5]_n^{n-}$ anion and hollandite anion frameworks for comparison. The unit cell of the hollandite structure is tetragonal with $a=9.8 \text{ Å}$ and $c=2.86 \text{ Å}$.³⁷ The tunnels of KBi_3S_5 ($14.02 \times 9.45 \text{ Å}$) are much larger than those of hollandite ($6.6 \times 4.7 \text{ Å}$). The hollandite framework, shown in Figure 2-15b, is made up of chains of MO_6 octahedra that share opposite edges in the c -direction. The octahedra from one chain share edges with two consecutive octahedra from the other chain to form double chains in the c -direction. The double chains are combined by corner-sharing to form a three-dimensional (2x2) framework. Similarly, the tunnel

structure of KBi_3S_5 (Figure 2-15a) can be viewed as edge-sharing triple chains sharing corners with double chains to form the interior (3x2) structure of the tunnel. KBi_3S_5 is also similar to psilomelane ($\text{Ba}_x\text{Mn}_5\text{O}_{16} \cdot (2-x)\text{H}_2\text{O}$, $0.50 < x < 0.75$) which contains a 3x2 tunnel structure.³⁸

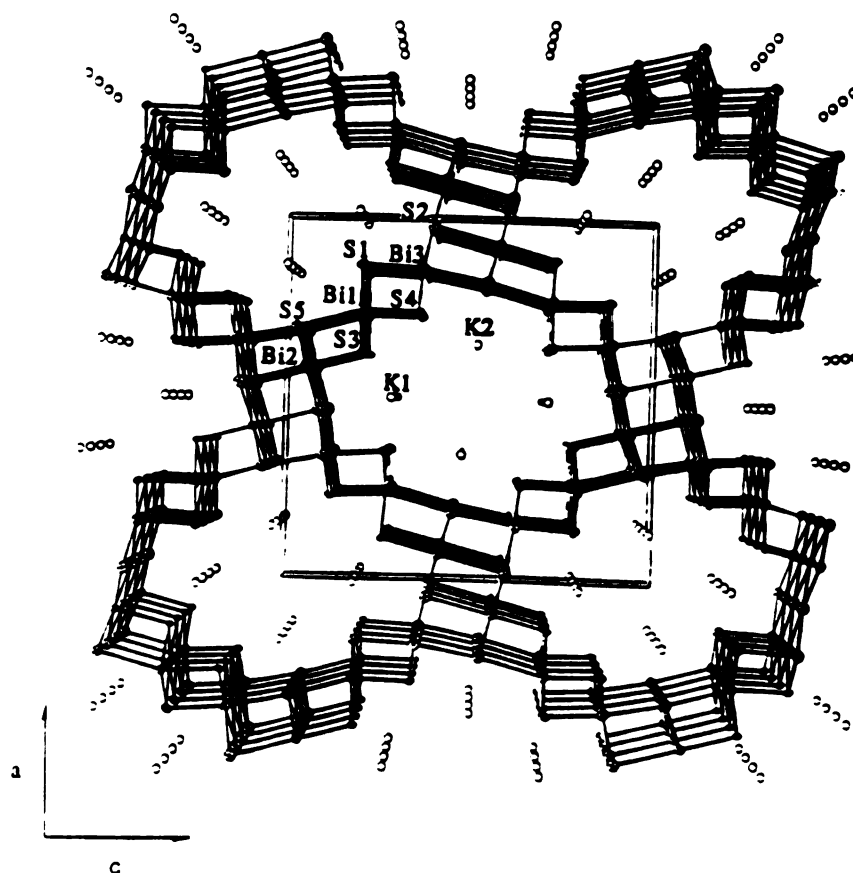


Figure 2-14. The three-dimensional structure of KBi_3S_5 viewed down the b -axis. The shaped ellipsoids are Bi atoms and the open circle represent K atoms.

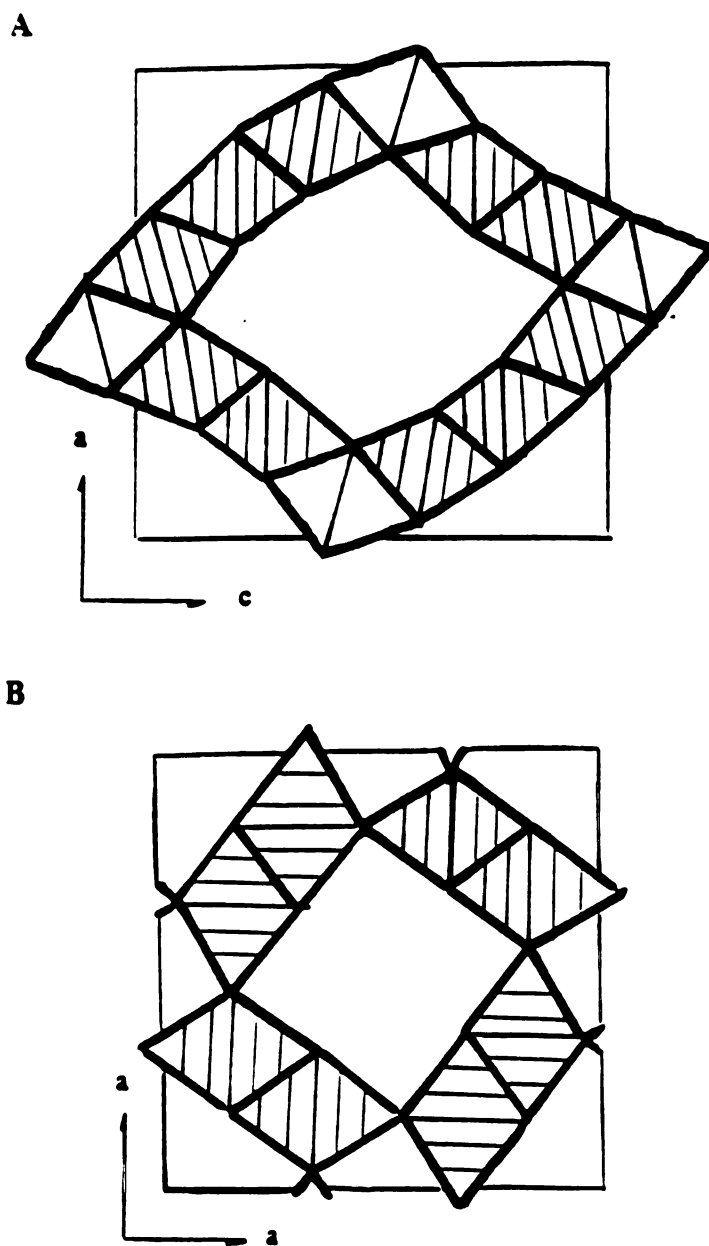


Figure 2-15. (a) Polyhedral representation of the $[\text{Bi}_3\text{S}_5]_n^-$ framework projected in the b -direction. The octahedra that line the tunnel are shaded. (b) Adapted polyhedral representation of the hollandite anion framework projected in the c -direction showing the 2×2 tunnel structure.^{30c}

Table 2-13. Selected Distances (Å) and Angles (deg) in KBi₃S₅ with Standard Deviations in Parentheses.^a

Bi(1)-S(1)	2.833(8) x 2	S(1)-Bi(1)-S(5)	102.5(3)
Bi(1)-S(3)	2.823(7) x 2	S(4')-Bi(1)-S(5)	162.5(3)
Bi(1)-S(4')	2.64(1)	Bi(1)-S(1)-Bi(1')	92.0(3)
Bi(1)-S(5)	3.10(1)	Bi(1)-S(1)-Bi(3)	89.3(3)
Bi(1)-S (mean)	2.8(1)		
Bi(2)-S(2)	2.925(9) x 2	S(2)-Bi(2)-S(3)	179.8(3)
Bi(2)-S(5)	2.782(8) x 2	Bi(2)-S(2)-Bi(2)	88.3(3)
Bi(2)-S(2')	3.12(1)		
Bi(2)-S(3)	2.66(1)	S(1)-Bi(3)-S(5)	172.6(3)
Bi(2)-S (mean)	2.8(2)	Bi(3)-S(4)-Bi(3')	94.2(3)
Bi(3)-S(2)	2.919(9) x 2	K(1)-S(1)	3.25(1)
Bi(3)-S(4)	2.783(7) x 2	K(1)-S(1')	3.25(1)
Bi(3)-S(1)	2.75(1)	K(1)-S(2)	3.43(2)
Bi(3)-S(5)	2.92(1)	K(1)-S(3)	3.19(1)
Bi(3)-S (mean)	2.85(8)	K(1)-S(3')	3.19(1)
		K(1)-S (ave.)	3.3(1)
Bi(1)-Bi(1')	4.076(2)		
Bi(1)-Bi(2)	4.119(2)	K(2)-S(1)	3.44(5)
Bi(1)-Bi(3)	3.923(2)	K(2)-S(4)	3.05(5)
Bi(2)-Bi(3')	4.186(3)	K(2)-S(5)	3.46(4)
Bi(2)-Bi(3'')	4.180(2)	K(2)-S(5')	3.46(4)
Bi-Bi (mean)	4.1(1)	K(2)-S (ave.)	3.3(2)

^aThe estimated standard deviations in the mean bond lengths and the mean bond angles are calculated by the equations $\sigma l = \{\Sigma_n (l_n - l)^2 / n(n-1)\}^{1/2}$, where l_n is the length (or angle) of the n th bond, l the mean length (or angle), and n the number of bonds.

3.3. Thermal Analysis

The thermal behavior of KBi_3S_5 was investigated with differential thermal analysis (DTA). Figure 2-16 shows that upon heating KBi_3S_5 , a broad endotherm occurs at 520 °C. Upon cooling, no corresponding exothermic peak is observed suggesting an irreversible change in the structure even though no change in the physical appearance of the compound was observed. Powder X-ray diffraction (XRD) of the heated sample gave a new XRD pattern, perhaps forming $\beta\text{-KBi}_3\text{S}_5$. The low angle (1 0 1) peak of KBi_3S_5 shifts from 12.13 to 11.33 Å. The XRD peaks from this apparently new phase match those from the minor impurity phase found in the $\text{Bi} + 2.8 \text{ K}_2\text{S}_{5.3}$ reaction mentioned above but do not match those found for the high temperature $\text{K}_2\text{S}/\text{Bi}_2\text{S}_3$ phases.²⁸ Further work is needed to characterize this compound.

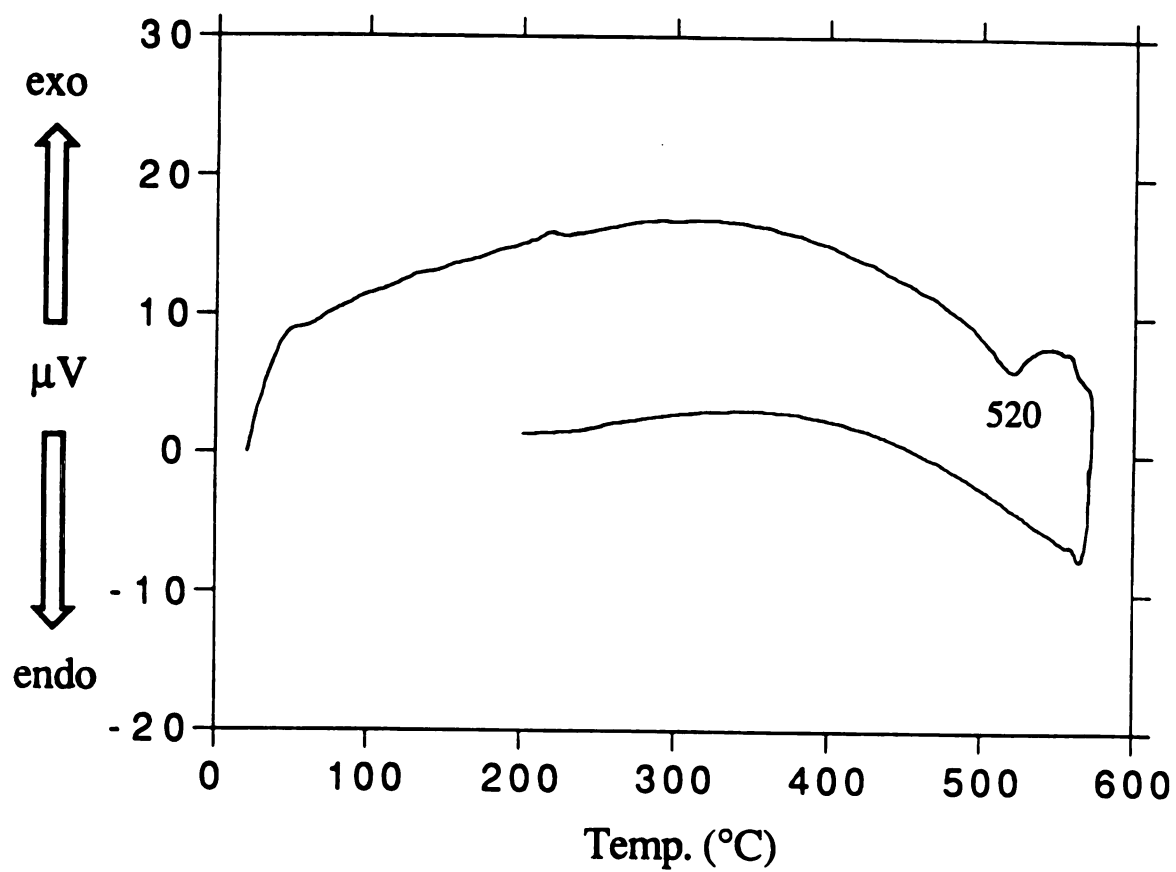


Figure 2-16. DTA thermogram of KBi_3S_5 .

3.4. Ion-Exchange Studies

The relatively open structure of KBi_3S_5 encouraged us to explore possible ion-exchange behavior. For example, ion-exchange studies of KBi_3S_5 were performed in a dilute aqueous HCl solution with the goal of synthesizing a proton-exchanged material. Our first attempt resulted in an air oxidation product $(\text{H}_2\text{O})\text{Bi}_3\text{S}_{4.5}(\text{S}_8)_{0.06}$ instead of a truly topotactic ion-exchanged product.

Figure 2-17 shows the powder X-ray diffraction (XRD) patterns of KBi_3S_5 and $(\text{H}_2\text{O})\text{Bi}_3\text{S}_{4.5}(\text{S}_8)_{0.06}$. The low angle peaks of KBi_3S_5 remain after the reaction, indicating that the framework is more or less intact. However, a number of additional peaks appear which reveal a possible reduction in symmetry, and suggest that the reaction is not really topotactic. Examination of the product with scanning electron microscopy (SEM) shows no change in crystallite size (1-30 μm) and shape suggesting at least a pseudomorphic reaction (see figure 2-18).³⁹

A Thermogravimetric Analysis (TGA) diagram of $(\text{H}_2\text{O})\text{Bi}_3\text{S}_{4.5}(\text{S}_8)_{0.06}$ up to 330 °C is shown in Figure 2-19a. Step I (3.82% weight loss), starting at 140 °C, is due to the loss of one H_2O as confirmed by mass spectrometry. This is immediately followed by Step II (3.84% weight loss), starting at 176 °C, which corresponds to the loss of 1/16 mole of S_8 . The formation of Bi_2S_3 after step II was confirmed by XRD (vide infra). Since the H_2O is not removed until 140 °C, this suggests that H_2O is located inside the tunnels and not on the surface. As a control experiment, KBi_3S_5 was stirred in H_2O for

one hour. The TGA of the product did not show any weight loss up to 400 °C.

The assignment of Step II in figure 2-19a is supported by the mass spectrum which shows m/z peaks corresponding to S_x^+ ($x=1-8$). The dominant peak is found at m/z 64 (S_2^+). The presence of a large intensity S_2^+ peak during this decomposition is corroborated by the large body of evidence that supports this observation. For example, complex sulfur vapor equilibria have been well studied and at temperatures higher than $\sim 320^\circ\text{C}$ and at pressures lower than ~ 1 Torr, the vapor phase of sulfur is dominated by S_2^+ .⁴⁰ The heating of HgS to 308°C under low pressure gave S_2^+ as the major ion peak.⁴¹ To determine if the S_8 fragment was located on the surface of the material or inside the tunnels, the material was washed with CS_2 then ether. TGA of this CS_2 -washed product gave the same result as shown in Figure 2-19a. The mass spectrum of this product up to 300°C also confirmed the loss of H_2O and S_x fragments which confirms that S_8 is not located on the surface of the particles.

Differential Scanning Calorimetry (DSC) of $(\text{H}_2\text{O})\text{Bi}_3\text{S}_{4.5}(\text{S}_8)_{0.06}$ to 400°C gave a large, sharp endothermic peak at 146°C followed by a small, broad exothermic peak at 156°C (see Figure 2-19b). These thermal events correspond to dehydration, loss of S_8 , and subsequent formation of Bi_2S_3 . For comparison, the DSC of KBi_3S_5 performed under identical conditions and featureless.

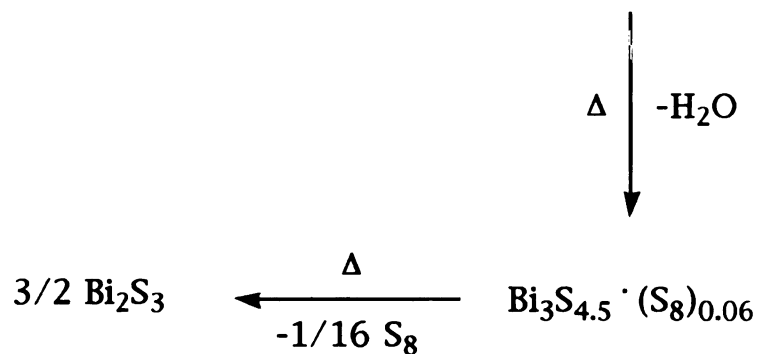
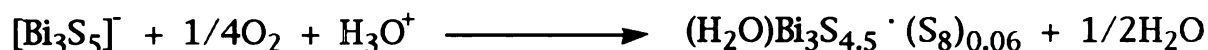
In order to further characterize the properties of $(\text{H}_2\text{O})\text{Bi}_3\text{S}_{4.5}(\text{S}_8)_{0.06}$ the powder XRD pattern (Figure 2-20) was measured as a function of temperature. Peak broadening was observed as the temperature was increased and at 125°C , a mixture

of $(\text{H}_2\text{O})\text{Bi}_3\text{S}_{4.5}(\text{S}_8)_{0.06}$ and Bi_2S_3 was detected. At the final temperature of 145°C , only broad peaks assignable to Bi_2S_3 were observed. The crystallite size was calculated to be $\sim 160 \text{ \AA}$.⁴² Heating $(\text{H}_2\text{O})\text{Bi}_3\text{S}_{4.5}(\text{S}_8)_{0.06}$ to 80°C under vacuum for 11 hours, revealed a mixture of Bi_2S_3 (major product) and $(\text{H}_2\text{O})\text{Bi}_3\text{S}_{4.5}(\text{S}_8)_{0.06}$ by XRD. These data suggest that the framework collapses upon removal of the water and then expels sulfur to form Bi_2S_3 .

The Mid-IR spectrum of $(\text{H}_2\text{O})\text{Bi}_3\text{S}_{4.5}(\text{S}_8)_{0.06}$ did not show any S-S stretching vibrations. Since the proposed concentration of S_8 in the compound is very dilute, it is possible that the intensities of these vibrations are very weak.

Since the ion-exchange chemistry conducted in air gave an oxidation product, the same experiment was carried out under nitrogen atmosphere. XRD of the product gave the same pattern as KBi_3S_5 with broadened peaks and EDS confirmed the presence of K^+ indicating no appreciable ion-exchange.

Based on the data presented, a scheme regarding the reaction of KBi_3S_5 with aqueous HCl is proposed:



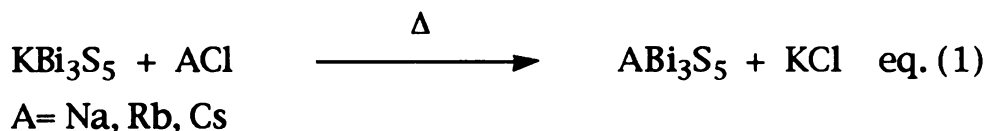
Scheme (A)

In summary, these results suggest that the reaction of KBi_3S_5 with an aqueous HCl solution in air results in the formation of an interesting metastable oxidation product, $(\text{H}_2\text{O})\text{Bi}_3\text{S}_{4.5}(\text{S}_8)_{0.06}$.

We also explored cation-exchange reactions with alkali and ammonium ions. Room temperature reactions with aqueous solutions of various salts (NaCl , Rb_2CO_3 , CsCl , NH_4NO_3) and methanol solutions of cesium acetate did not show ion-exchange. Hydrothermal treatment of KBi_3S_5 at 130°C with alkali metal salt solutions of RbCl and CsCl and gave Bi_2S_3 , while methanothermal treatment of KBi_3S_5 at 85°C with Cs and Na acetate salts did not show ion-exchange.

3.5. Solid State Ion-exchange Reactions with Halide Salts.

The complications arising from the ion-exchange attempts using solvents prompted us to investigate "dry" reactions with solid alkali halide salts according to eq.1.



Solid state ion-exchange is a very useful synthetic method and has been demonstrated in several systems, including $\text{A}_2\text{Mo}_6\text{Q}_6$ ($\text{A} = \text{Na, K, Rb, Cs, Cu, Ag}$; $\text{Q} = \text{S, Se}$),⁴³ $\text{A}_x\text{Nb}_6\text{Q}_8$ ($\text{A} = \text{Na, Rb, K, transition metals}$; $\text{Q} = \text{S, Se, Te}$),⁴⁴ AV_5Q_8 ⁴⁵ and AV_6Q_8 ($\text{A} = \text{Na, K, Rb, Cs}$; $\text{Q} = \text{S, Se, Te}$).⁴⁵ In these systems, the halide salt is heated above its melting point.

Because KBi_3S_5 is metastable, the reaction cannot be heated above the melting point ($>700^\circ\text{C}$) of either NaCl , RbCl or CsCl . It is therefore remarkable that in the RbCl case complete, topotactic ion-exchange occurs below 400°C forming the isostructural $\beta\text{-RbBi}_3\text{S}_5$ (see Table 2-9). At or above 400°C the known denser phase $\alpha\text{-RbBi}_3\text{S}_5$ ⁴ forms, confirming that both KBi_3S_5 and $\beta\text{-RbBi}_3\text{S}_5$ are metastable structures. The fact that this relatively facile ion-exchange reaction is a solid-solid reaction suggests that the exchanging ions possess high ionic mobilities promoted by the large tunnels present in the $[\text{Bi}_3\text{S}_5]^-$ structure.⁴⁶ This suggests that the ABi_3S_5 may be good ionic conductors. The β -phase possesses higher symmetry because the split peaks that are seen at low angles in KBi_3S_5 are single peaks in $\beta\text{-RbBi}_3\text{S}_5$ suggesting a possible transformation to a tetragonal structure. Interestingly, $\beta\text{-RbBi}_3\text{S}_5$ cannot be synthesized by the molten alkali polysulfide approach.

Reactions with NaCl ($200\text{--}400^\circ\text{C}$) resulted in a mixture of NaBiS_2 and Bi_2S_3 . The Na^+ ion may be too small to support the $[\text{Bi}_3\text{S}_5]^-$ framework at this temperature so it converts to the thermodynamically stable layered NaBiS_2 .² Reactions with CsCl gave a mixture of the layered $\gamma\text{-CsBiS}_2$ ¹⁹ and a minor impurity phase. EDS on several $10\mu\text{m}$ needles gave $\text{CsBi}_{3.1}\text{S}_{5.2}$ and analysis on $10\mu\text{m}$ plates resulted in a ratio of $\text{CsBi}_{2.5}\text{S}_{3.4}$. XRD of the mixture did not reveal the presence of CsBi_3S_5 .³ Ion-exchange reactions with solid NH_4Cl and NH_4I ($150\text{--}400^\circ\text{C}$) gave only Bi_2S_3 .

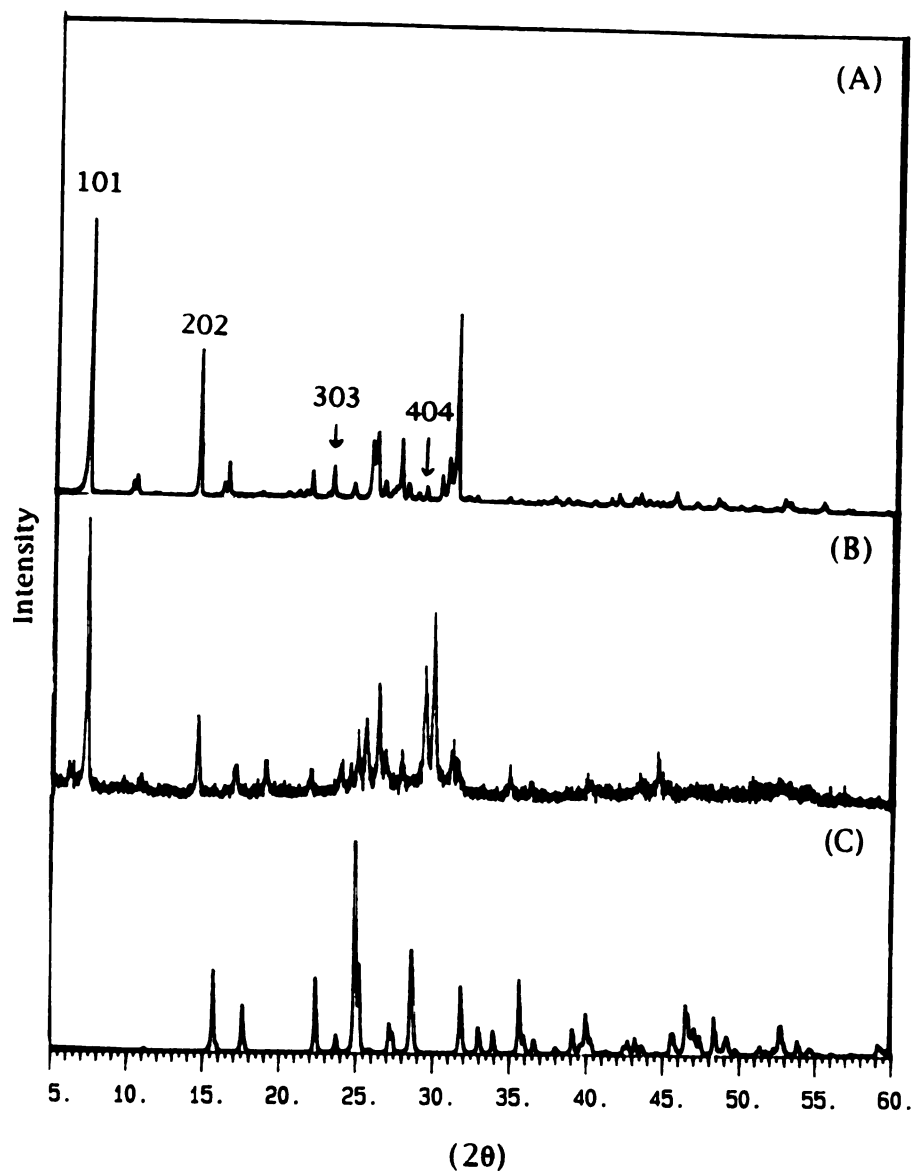


Figure 2-17. Comparison of the X-ray powder diffraction patterns of:
 (a) KBi_3S_5 with selected h0l peaks labeled.
 (b) $(\text{H}_2\text{O})\text{Bi}_3\text{S}_{4.5} \cdot (\text{S}_8)_{0.06}$ and
 (c) Bi_2S_3

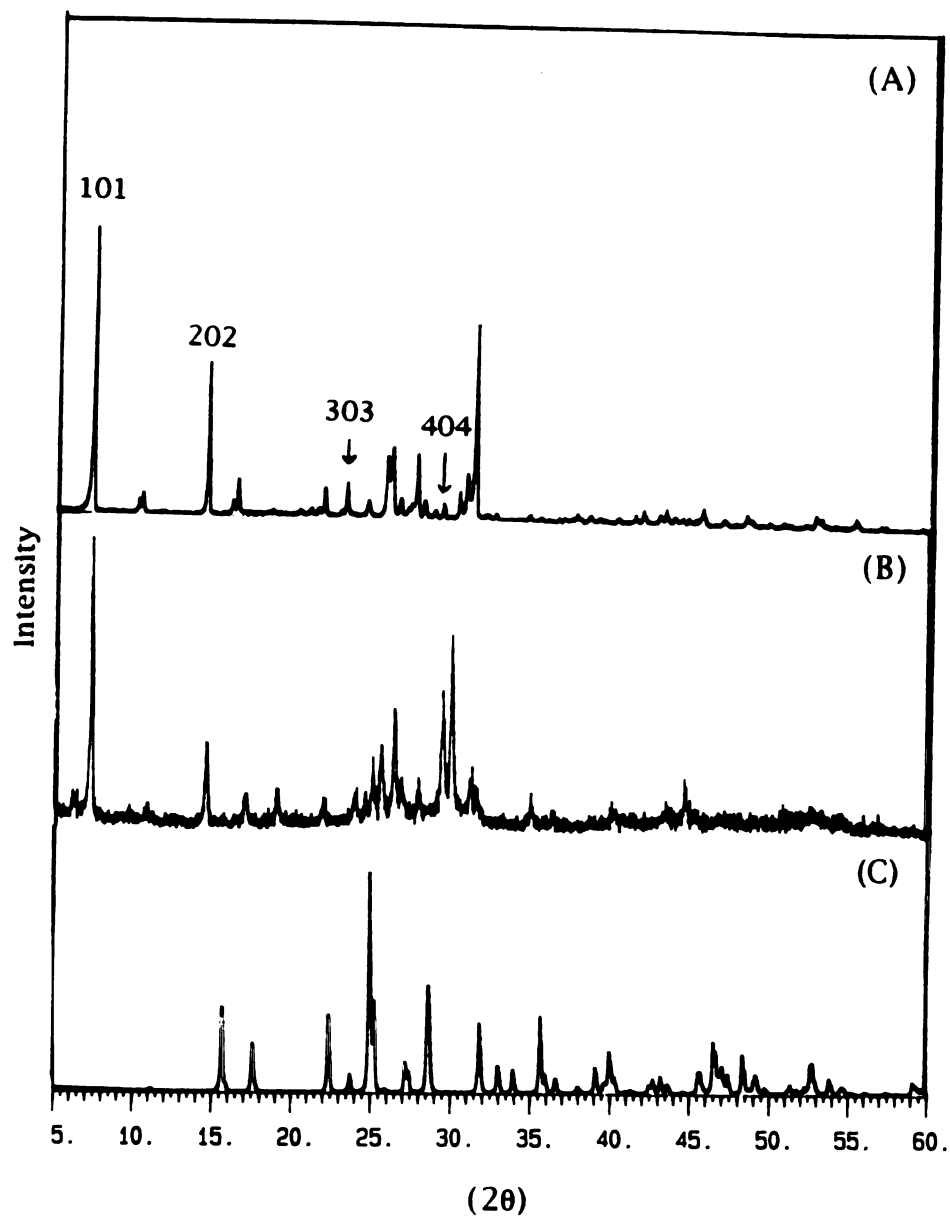
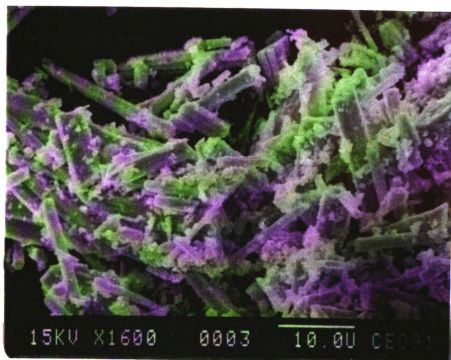


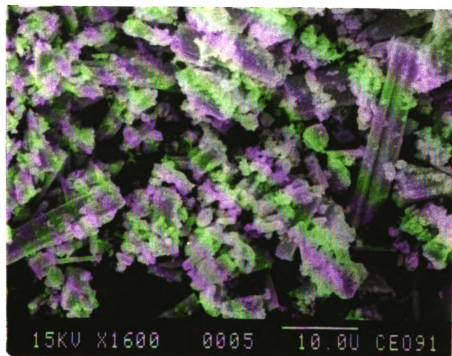
Figure 2-17. Comparison of the X-ray powder diffraction patterns of:
(a) KBi_3S_5 with selected $h0l$ peaks labeled.
(b) $(\text{H}_2\text{O})\text{Bi}_3\text{S}_{4.5}(\text{S}_8)_{0.06}$ and
(c) Bi_2S_3

Figure 2-18: SEM photographs of: (a) KBi_3S_5 before and (b) after reaction with aqueous HCl (66 hours). The white bar at the bottom of the micrographs represents a $10\mu\text{m}$ scale. The magnification is $\times 1600$.

(A)



(B)



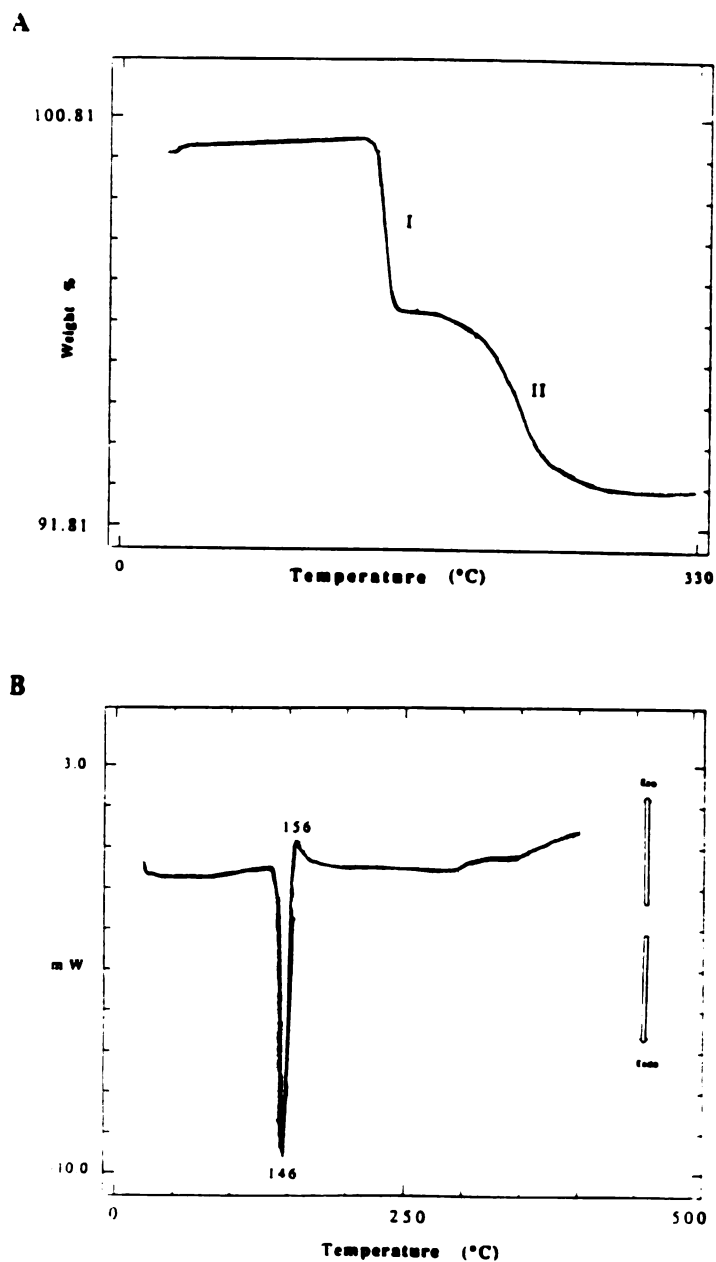


Figure 2-19. (a) Thermogravimetric analysis plot of $(\text{H}_2\text{O})\text{Bi}_3\text{S}_{4.5} \cdot (\text{S}_8)_{0.06}$ with weight % plotted against temperature (°C). Performed under flowing N_2 . Step I (3.82% weight loss starting at 140 °C.) Step II (3.84% weight loss starting at 176 °C). (b) DSC thermogram of $(\text{H}_2\text{O})\text{Bi}_3\text{S}_{4.5} \cdot (\text{S}_8)_{0.06}$.

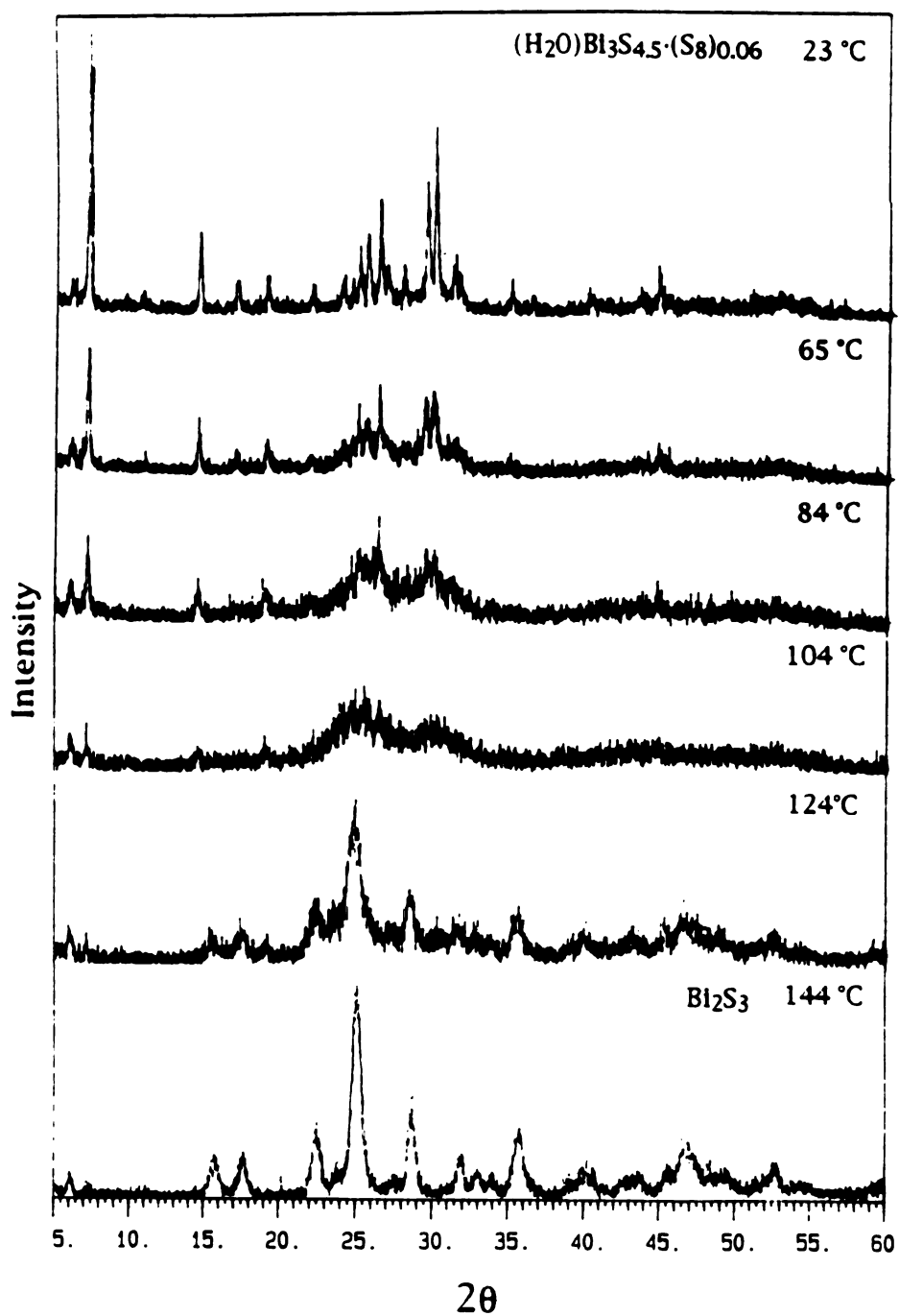


Figure 2-20. Powder XRD pattern of $(\text{H}_2\text{O})\text{Bi}_3\text{S}_{4.5}(\text{S}_8)_{0.06}$ measured as a function of temperature. The transformation to Bi_2S_3 is complete at 124 °C

3.6. Conclusion

The isolation of KBi_3S_5 from a polysulfide flux at a relatively low temperature confirms the usefulness of molten salts in accessing low enough temperatures for the stabilization of reactive solid state materials. Although the void space within this metastable material is not substantial, KBi_3S_5 represents a rare example of a chalcogenide with an open framework and ion-exchange properties. This and other materials provide the basis for further exploratory work to identify not only new open framework, more stable, chalcogenides but also a reliable general synthetic methodology to these materials. Such a methodology could be greatly aided by drawing lessons from the recent preparative success of the more familiar zeolites,⁴⁷ aluminosilicates (MCM-41),⁴⁸ and pillared clays.⁴⁹

List of References

1. (a) Rowe, D. M.; Bhandari, C. M. *Modern Thermoelectrics*, Holt, Rinehart and Winston: London, 1983; p. 103. (b) Borkowski, K.; Przyluski, J. *J. Mat. Res. Bull.* 1987, 22, 381-387.
2. (a) Boon, J. W. *Rec. Trav. Chim. Pays-Bas*, 1944, 63, 32. (b) Glemser, O.; Filcek, M. *Z. Anorg. Allg. Chem.*, 1955, 279, 321-323 (c) Gattow, G.; Zemmann, J. *Z. Anorg. Allg. Chem.*, 1955, 279, 324-327.
3. Kanishcheva, A. S.; Mikhailov, J. N.; Lazarev, V. B.; Trippel, A. F. *Dokl. Akad. Nauk, SSSR (Kryst.)*, 1980, 252, 96-99.
4. Schmitz, D.; Bronger, W. *Z. Naturforsch.*, 1974, 29b, 438-439.
5. Julien-Pouzol, M.; Jaulmes, S.; Laruelle, P. *Acta. Cryst.* 1979, B35 1313-1315.
6. Aurivillius, B. *Acta Chem. Scand.* 1983, A37 399-407.
7. G. Cordier, H. Schäfer, C. Schwidetzky, *Rev. Chim. Miner.*, 1985, 22 676-683.
8. G. Cordier, H. Schäfer, C. Schwidetzky, *Rev. Chim. Miner.*, 1985, 22 631-638.
9. K. Volk, G. Cordier, R. Cook, H. Schäfer, *Z. Naturforsch.*, 1990, 35b 136-140.
10. Liautard, B.; Garcia, J. C.; Brun, G.; Tedenac, J. C.; Maurin, M. *Eur. J. Solid State Inorg. Chem.* 1990, 27, 819-830.
11. Lee, S.; Fischer, E.; Czerniak, J.; Nagasundaram, N. *J. Alloys and Compounds* 1993, 197, 1-5.
12. Iitaka, Y.; Nowacki, W. *Acta Cryst.*, 1962, 15, 691-698.
13. Kupcik, V.; Makovicky, E. *N. Jb. Miner. Mh.*, 1968, 7, 236-237.
14. McCarthy, T. J.; Ngeyi, S.-P.; Liao, J.-H.; DeGroot, D.; Hogan, T.; Kannewurf, C. R.; Kanatzidis, M. G. *Chem. Mater.*, 1993, 5, 331-340.
15. (a) Kanatzidis, M. G. *Chem. Mater.* 1990, 2, 353-363. (b) Kanatzidis, M. G.; Park, Y. *J. Am. Chem. Soc.* 1990, 111, 3767-3769. (c) Kanatzidis, M. G.; Park, Y. *Chem. Mater.* 1990, 2, 99-101. (d) Park, Y.; Kanatzidis, M. G. *Angew. Chem. Int. Ed. Engl.* 1990, 29, 914-915.
16. (a) Sunshine, S. A.; Kang, D.; Ibers, J. A. *J. Am. Chem. Soc.* 1987, 109, 6202-6204. (b) Kang, D.; Ibers, J. A. *Inorg. Chem.* 1989, 27, 549-551.
17. R. L. Bedard, S. T. Wilson, L. D. Vail, E. M. Bennett, E. M. Flanigen, *Zeolites: Facts, Figures, Future* (P. A. Jacobs, R. A. van Sonten, Eds.) (1989) 275.
18. Parise, J. B. *Science*, 1991, 251, 293-294.
19. Dhingra, S.; Kanatzidis, M. G. *Science*, 1992, 258, 1769-1772.
20. Feher, F. *Handbuch der Präparativen Anorganischen Chemie*: Brauer, G., Ed.; Ferdinand Enke: Stuttgart, Germany, 1954; pp. 280-281.
21. Also confirmed by Atomic absorption analysis performed by Oneida Research Services, Inc. on one of our reaction products as a check for our SEM-EDS elemental analysis results.
22. D. K. Smith, M. C. Nichols, M. J. E. Zolensky, POWD10: A Fortran IV program for Calculating X-ray Powder Diffraction Pattern, version 10. Pennsylvania State University, 1983.
23. (a) Wendlandt, W. W.; Hecht, H. G. *"Reflectance Spectroscopy"*, Interscience Publishers, 1966 (b) Kotüm, G. *"Reflectance Spectroscopy"*, Interscience Publishers, 1966

- Spectroscopy*", Springer Verlag, New York, 1969 (c) Tandon, S. P.; Gupta, J. P. *Phys. Stat. Sol.* 1970, 38,363-367.
24. G. M. Sheldrick, In *Crystallographic Computing 3*; G. M. Sheldrick, C. Kruger, R. Doddard, Eds.; Oxford University Press: Oxford, England, 1985; pp 175-189.
 25. TEXSAN: Single Crystal Structure Analysis Software, Version 5.0, (1989). Molecular Structure Corporation, The Woodlands, TX 77381.
 26. Walker, N.; Stuart, D. *Acta Cryst.* 1983, 39A158-166.
 27. This phase is isostructural to RbBiS₂ as evidenced by powder X-ray diffraction.
 28. Berul, S. I.; Lazarev, V. B.; Trippel, A. F.; Buchikhina, O. P. *Russ. J. Inorg. Chem.* 1977, 22(9), 1390-1393.
 29. Bube, R. H. "Photoconductivity of Solids", John Wiley and Sons, Inc., 1960; pp.233-235.
 30. (a) Fanchon, E.; Vicat, J.; Hodeau, J.-L.; Wolfers, P.; Tran Qui, D.; Strobel, P. *Acta Cryst.* 1987, 43B, 440-448. (b) Fanchon, E.; Vicat, J.; Hodeau, J.-L.; Levy, J.-P.; Wolfers, P. *Acta Cryst.* 1987, Sect. A 43(Suppl.) C-129. (c) Bursill; L. A. *Acta Cryst.* 1979, B35, 530-538.
 31. Torardi, C. C. *Mater. Res. Bull.* 1985, 20, 705-713.
 32. Torardi, C. C.; McCarley, R. E. *J. Solid State Chem.* 1981, 37,393-397.
 33. R. G. Burns, M. B. Burns *Manganese Dioxide Symposium*, Tokyo, 1981; Vol. 2, Ch 6.
 34. (a) Khanna, S. K.; Gruner, G.; Orbach, R.; Beyeler, H. U. *Phys. Rev. Lett.* 1981, 47, 255-257. (b) Beyeler, H. U.; Bernasconi, J.; Strässler, S. *Fast Ion Transport in Solids* (P. Vashishta, J. N. Mundy, and G. K. Shenoy, Eds.), North-Holland, New York (1979) p. 503.
 35. Clearfield, A. J. *Chem. Rev.* 1988, 88,125-148.
 36. Shen, X.-M.; Clearfield, A. J. *J. Solid State Chem.* 1986, 64, 270-282.
 37. Byström, A.; Byström, A. M. *Acta Cryst.* 1979, B35,530-538.
 38. Wadsley, A. D. *Acta Cryst.* 1953, 6,433-438.
 39. In a pseudomorphic reaction the product retains the morphology of the starting material but (in contrast to a topotactic reaction) its internal crystal and framework structure has been altered.
 40. Liao, C. L.; Ng, C. Y. *J. Chem. Phys.* 1986, 84(2),778-782.
 41. J. Berkowitz, in *Elemental Sulfur*, edited by B. Meyer (Interscience, New York, 1965).
 42. Debye-Scherrer formula: $D = (0.9 * \lambda * 57.3) / (\beta_{1/2} * \cos\theta)$ (D=ave. crystallite size (Å); λ =rad.wavelength; $\beta_{1/2}$ =peak width at half height; θ =Bragg angle).
 43. Tarascon, J. M.; Hull, G. W.; DiSalvo, F. J. *Mat. Res. Bull.* 1984, 19,915-924.
 44. (a) Huan, G.; Greenblatt, M. *Mat. Res. Bull.* 1987, 22, 505-512. (b) Huan, G.; Greenblatt, M. *Mat. Res. Bull.* 1987, 22,943-949.
 45. Ohtani, T; Sano, Y.; Kodama, K.; Onoue, S.; Nishihara, H. *Mat. Res. Bull.* 1993, 28, 501-508.
 46. Even though this reaction appears to proceed from solid to solid at such a low temperature, one may also imagine the presence of a liquid phase covering the surface of the KBi₃S₅ particles. However no eutectic composition between KCl and RbCl is known below 700 °C.
 47. Ozin, G. *Adv. Mater.*, 1992, 4,612-646.
 48. Kresge, C. T.; Leonowicz, M. E.; Roth, W. J.; Vartuli, J. C.; Beck, J. S. *Nature*, 1993, 359,710-712.
 49. Pinnavaia, T. J. *Science*, 1983, 220,365-371.

CHAPTER 2 (Part 3)

High Temperature Synthesis and Properties of $\text{KBi}_{6.33}\text{S}_{10}$ and $\text{K}_2\text{Bi}_8\text{S}_{13}$

1. Introduction

Group 15 chalcogenide compounds have received considerable attention, due to their potential application as non-linear optical materials,¹ photoelectrics,² and thermoelectrics.³ The most common application that is unique to Group 15 chalcogenides is in the area of thermoelectric cooling materials. The most investigated systems over the past 30 years are various solid solutions of M_2Q_3 ($\text{M}=\text{As}, \text{Sb}, \text{Bi}$; $\text{Q}=\text{S}, \text{Se}, \text{Te}$) compounds.⁴ These materials possess high electrical conductivity and thermoelectric power and low thermal conductivity and are excellent materials for thermoelectric applications near room temperature.⁵ With these properties in mind, it is surprising that very little exploratory synthesis of new ternary bismuth chalcogenide phases has been reported.

Bi is very attractive for study because of its inert $6s^2$ lone pair of electrons which may or may not be manifested structurally in a given compound. Whether the lone pair is stereochemically active or

not affects the lattice structure, the electronic structure and thus the properties of the resulting compounds and thus exploration of the solid state chemistry of Bi is warranted. This issue is related to the larger question of stereochemical activity of a lone pair in compounds with heavy main-group elements in a s^2 configuration.

Outside of the well-known NaCl-type $ABiQ_2$ ($A = \text{Li, Na, K; } Q = \text{S, Se}$)⁶ compounds, the only other phases that have been fully characterized structurally are $RbBiQ_2$ ($Q = \text{S, Se}$),⁷ $CsBi_3S_5$,⁸ $RbBi_3S_5$,⁹ $Tl_4Bi_2S_5$,¹⁰ α -(β -) $BaBi_2S_4$,¹¹ $Cs_3Bi_7Se_{12}$,¹² $Sr_4Bi_6Se_{13}$,¹³ and $BaBiSe_3$.¹⁴ These compounds have been prepared at high ($>450^\circ\text{C}$) temperature by direct combination of the elements or alkali carbonates with Bi and S(Se). In addition, mixed Bi/transition metal/ Q ($Q=\text{S, Se}$) solid solution systems have been investigated including $Cu_{1+3x}Bi_{5-x}Q_8$ ¹⁵ and $Mn_{1-x}Bi_{2+y}Q_4$.¹⁶ Bismuth compounds constitute $\sim 20\%$ of the known naturally occurring sulfosalts, including $PbBi_2S_4$ (galenobismuthite),¹⁷ $PbCu_4Bi_5S_{11}$,¹⁸ $CuBi_5S_8$,¹⁹ and $PbCuBiS_3$.²⁰

Recently, we have synthesized four new ternary bismuth chalcogenides, β -(γ -) $CsBiS_2$,²¹ $K_2Bi_8Se_{13}$,²¹ and KBi_3S_5 ,²² using A_2Q_x ($A=\text{K, Cs; } Q=\text{S, Se}$) fluxes at intermediate temperatures below 400°C that display a wide range of structural diversity. $K_2Bi_8Se_{13}$ possesses interesting thermoelectric properties with an electrical conductivity of 10^{-2} S/cm and a Seebeck coefficient ranging from -210 to $-260\mu\text{V/K}$ at room temperature.²¹ During our investigation, we noticed that there are several high temperature A_2Q/Bi_2Q_3 ($A = \text{Li, Na, K, Rb, Cs; } Q = \text{S, Se, Te}$) phase diagrams reported in the literature.²³ However, the structural information on the possible

phases only consists of unindexed powder X-ray diffraction patterns. It becomes apparent that further work in the high temperature synthesis and structural characterization of new $A_xBi_yQ_z$ compounds is warranted.

This paper describes the high temperature synthesis, structural characterization, optical, and charge transport properties of two new compounds, $KBi_{6.33}S_{10}$ (I) and $K_2Bi_8S_{13}$ (II). Both of these compounds possess new three-dimensional tunnel frameworks based on Bi_2Te_3 - and CdI_2 -type fragments with K^+ ions found in the channels.

2. Experimental Section

2.1. Reagents

Chemicals in this work were used as obtained: (i) bismuth powder, 99.999+% purity, -100 mesh, Aldrich Chemical Co., Inc., Milwaukee, WI. (ii) sulfur powder, sublimed, J. T. Baker Chemical Co., Phillipsburg, NJ. (iii) potassium metal, analytical reagent, Mallinckrodt Inc., Paris, KY (iv) methanol, anhydrous, Mallinckrodt Inc., Paris, KY; DMF, analytical reagent, diethyl ether, ACS anhydrous, EM Science, Inc., Gibbstown, NJ.

2.2. Synthesis

All manipulations were carried out under a dry nitrogen atmosphere in a Vacuum Atmospheres Dri-Lab glovebox. For the preparation of K_2S we used a modified literature procedure.²⁴ The preparation of K_2S is reported in Section 2.2 of Chapter 2 (Part 2).

Bismuth Sulfide, Bi_2S_3 . 2.090 g (10.0 mmol) Bi and 0.496 g (15.5 mmol) S were ground thoroughly with a mortar and pestle. The mixture was transferred to a 6 ml pyrex tube and was subsequently flame-sealed in vacuum ($\sim 10^{-3}$ torr). The reaction was heated to 500 °C over 24 hours in a computer controlled furnace, then isothermed at 500 °C for 4 days, followed by cooling to 100 °C at a rate of 4 °C/hr, then to 50 °C in one hour. The product was ground into a fine powder and stored in the glove box.

$KBi_{6.33}S_{10}$ (I). 0.040 g (0.363 mmol) K_2S and 0.746 g (1.45 mmol) Bi_2S_3 were mixed together with a spatula in a glass vial. Several drops of acetone were placed in a quartz tube (9 mm diameter, 6 ml volume) and it was heated with a flame to create a carbon film on the inside surface of the tube. The mixture was transferred to the carbon-coated quartz tube and was subsequently flame-sealed under diffusion pump vacuum ($\sim 10^{-5}$ torr). The reaction was heated to 750 °C over a 48 hour period in a computer controlled furnace, then isothermed at 750 °C for 6 days, followed by cooling to 550 °C at a rate of 10 °C/hr, then to 50°C in 10 hours. The product was washed with degassed water (50 ml), methanol (20 ml)

and ether (20 ml) to remove any trace amounts of K_2S . 0.733 g (92% yield, based on Bi_2S_3) of shiny silver polycrystalline material was obtained. Quantitative microprobe analysis gave $K_{1.0}Bi_{4.1}S_{5.6}$ (average of four acquisitions).

Dipotassium Tridecasulfido-octabismuthate(III), $K_2Bi_8S_{13}$ (II). The reaction of 0.015 g (0.138 mmol) K_2S and 0.283 g (0.550 mmol) Bi_2S_3 was prepared as above. The mixture was heated to 725 °C over a 48 hour period, then isothermed for 4 days, followed by cooling to 525 °C at 10 °C/hr, then to 50 °C in 10 hours. The product was isolated as above to give 0.294 g (99% yield) of shiny silver crystals and agglomerates. Quantitative microprobe analysis gave $K_{1.0}Bi_{4.6}S_{7.3}$ (average of four acquisitions).

The homogeneity of (I) and (II) was confirmed by comparing the observed and calculated X-ray powder diffraction patterns. The d_{hkl} spacings observed for the bulk materials were compared, and found to be in good agreement with the d_{hkl} spacings calculated from the single crystal data.²⁵ The results are summarized in Tables 2-14 and 2-15.

2.3. Physical Measurements

Mid-IR diffuse reflectance spectra of (I) and (II) were recorded as a solid. The sample was ground into a powder prior to data acquisition. The spectra were recorded in the mid-IR region ($4000-400\text{cm}^{-1}$, 4cm^{-1} resolution) with the use of a Nicolet 740 FT-IR spectrometer equipped with a diffuse reflectance attachment.

The instruments and experimental setups for optical diffuse reflectance measurements, quantitative microprobe analysis on SEM/EDS, and charge-transport measurements are the same as those in Chapter 2 (Part 1) (Section 2.3). The experimental setup for differential thermal analysis (DTA) is the same as that in Chapter 2 (Part 2) (Section 2.3).

2.4. X-ray Crystallography

Both compounds were examined by X-ray powder diffraction for the purpose of phase purity and identification. Accurate d_{hkl} spacings (Å) were obtained from the powder patterns recorded on a Rigaku Rotaflex Powder X-ray Diffractometer with Ni filtered Cu $K\alpha$ radiation operating at 45 kV and 100 mA. The data were collected at a rate of 1.0 deg/min.

Structure solution of $\text{KBi}_{6.33}\text{S}_{10}$. A crystal with dimensions 0.02 x 0.05 x 0.25 mm was mounted on a glass fiber. Intensity data were collected using the ω - 2θ scan mode on a Rigaku AFC6S four-circle automated diffractometer equipped with a graphite-crystal monochromator. The stability of the crystal was monitored by measuring three standard reflections periodically (every 150 reflections) during the course of data collection. No crystal decay was detected. The structure was solved by direct methods using SHELXS86^{26a} and refined by full-matrix least-squares techniques of the TEXSAN package of crystallographic programs.^{26b} An empirical absorption correction based on ψ scans was applied to

the data. Seven bismuth atoms, ten sulfur atoms and a potassium atom were located on mirror planes. After least squares refinement, the isotropic temperature factor for Bi(7) was very high at 12.18 \AA^2 with $R/R_w = 7.4/9.9$. A refinement of its multiplicity indicated a lower occupancy on this site. The occupancy and temperature factor of this atom were refined to give values of 0.263 and 3.945 \AA^2 respectively ($R/R_w = 5.7/6.9$). The coordination environments of the other six bismuth atoms were octahedral while that of Bi(7) was an unusual eight-coordinate site consisting of bond distances ranging from 2.79 to 3.48 Å. At this stage, a model with bismuth atom vacancies seemed to be reasonable. Since the isotropic temperature factor for Bi(6) was also significantly higher (2.707 \AA^2) than those of the other five bismuth atoms (ave. = 1.16 \AA^2), the occupancy and the temperature factor of Bi(6) were also refined to give values of 0.407 and 1.561 \AA^2 respectively ($R/R_w = 5.1/6.0$). The occupancies were fixed at 0.263 (Bi(7)) and 0.407 (Bi(6)). DIFABS correction was applied to the isotropically refined data ($R/R_w = 4.8/5.3$).²⁷ All atoms were refined anisotropically to give a final $R/R_w = 4.3/4.7$. All calculations were performed on a VAXstation 3100/76 computer. As a check for Bi/K disorder, the occupancy of the K site was refined and revealed no change which suggests that the site is fully occupied with K.

Structure Solution of $\text{K}_2\text{Bi}_8\text{S}_{13}$. A crystal with dimensions $0.03 \times 0.05 \times 0.30 \text{ mm}$ was mounted on a glass fiber. Intensity data collection and structure solution methods are the same as above. Friedel pairs were collected due to the possibility of an acentric structure. Eight bismuth atoms, thirteen sulfur atoms and two

potassium atoms were located on mirror planes. After least squares refinement, the isotropic temperature factor for Bi(8) was rather high at 6.50 \AA^2 with $R/R_w = 13.2/14.3$. The occupancy and temperature factor of this atom were refined to give values of 0.331 and 3.31 \AA^2 respectively ($R/R_w = 12.5/13.4$). The coordination environments of the other seven bismuth atoms were octahedral while that of Bi(8) was the same unusual eight-coordinate site as seen in $\text{KBi}_{6.33}\text{S}_{10}$ consisting of bond distances ranging from 2.77 to 3.48 Å. The K(1) and K(2) coordination sites were very similar to that of Bi(8). Refinement of the occupancies of K(1) and K(2) showed large increases to 0.815 for K(1) and 0.814 for K(2). This suggested that more electron density was required at these sites, therefore, a model with Bi and K disordered over all three sites seemed reasonable. Successive refinements taking into account this hypothesis resulted in a formula of $\text{K}_{2.1}\text{Bi}_{7.9}\text{S}_{13}$ where an additional +0.2 charge is needed for electroneutrality ($R/R_w=12.3/13.0$). The occupancies were rounded off and fixed and refinement gave $\text{K}_2\text{Bi}_8\text{S}_{13}$ with no change in the R value. The atomic composition of the Bi-rich site A was found to be 60% Bi and 40% K while sites B and C gave 20% Bi and 80% K. DIFABS correction was applied to the isotropically refined data ($R/R_w=7.5/8.5$).²⁷ All atoms were refined anisotropically except Bi(8), K(1) and K(2) ($R/R_w=7.3/8.2$). Averaging the data did not affect the R value. $\text{K}_2\text{Bi}_8\text{S}_{13}$ is found with positional disorder between Bi and K with a bias toward $\text{K}_{2.1}\text{Bi}_{7.9}\text{S}_{13}$ suggesting a Bi^{3+} or K^+ deficiency. Non-stoichiometry represented by $\text{K}_{2+3x}\text{Bi}_{8-x}\text{S}_{13}$ could be present.

The complete data collection parameters, details of the structure solution and refinement and for both compounds are given in Table 2-16. The coordinates and average temperature factors (B_{eq}) of all atoms and their estimated standard deviations for both compounds are given in Tables 2-17 and 2-18.

Table 2-14. Calculated and Observed X-ray Powder Diffraction Patterns for $\text{KBi}_{6.33}\text{S}_{10}$.

h k l	$d_{\text{calcd.}}, \text{\AA}$	$d_{\text{obs.}}, \text{\AA}$	$I/I_{\text{max}}, (\text{obs})$
2 0 1	10.23	10.20	13
0 0 2	9.72	9.71	8
1 0 2	9.01	9.00	26
1 0 3	6.26	6.24	5
2 0 3	5.71	5.70	64
4 0 2	5.11	5.11	3
0 0 4	4.86	4.85	6
2 0 4	4.51	4.50	14
3 0 4	4.16	4.15	9
6 0 0	4.01	4.00	13
6 0 1	3.93	3.92	7
4 0 4	3.78	3.77	22
1 1 2	3.73	3.74	14
2 0 5	3.70	3.69	16
2 1 2	3.60	3.60	20
3 0 5	3.50	3.49	100
5 0 4	3.42	3.41	52
7 0 1	3.38	3.38	55
2 1 3	3.33	3.33	50
4 0 5	3.28	3.28	5
7 0 2	3.24	2.189	7
4 1 2	3.20	3.20	8
2 0 6	3.13	3.12	10
5 1 1	3.08	3.08	33
2 1 4	3.03	3.03	33
5 0 5	3.02	3.02	16
5 1 2	2.97	2.97	79
4 0 6	2.84	2.84	41
5 1 3	2.81	2.81	33
4 1 4	2.78	2.78	5
6 1 2	2.75	2.75	17
5 1 4	2.63	2.62	5
9 0 2	2.58	2.57	3
4 0 7	2.52	2.52	22
2 1 6	2.487	2.486	4
6 1 4	2.469	2.466	8
7 1 3	2.440	2.437	8
1 0 8	2.418	2.415	3
3 0 8	2.326	2.321	12
0 1 7	2.300	2.297	21
8 1 3	2.271	2.270	5
10 0 3	2.255	2.252	10
3 1 7	2.211	2.208	8
7 1 5	2.181	2.179	9
8 1 4	2.170	2.165	16
10 0 4	2.156	2.149	15

Table 2-14. (cont'd)

h k l	d _{calcd.} , Å	d _{obs.} , Å	I/I _{max} , (obs)
2 0 9	2.126	2.123	5
9 1 3	2.116	2.112	5
1 1 8	2.083	2.081	18
2 1 8	2.060	2.055	33
9 1 4	2.034	2.029	25
3 1 8	2.023	2.021	12
10 1 3, 4 1 8	1.976, 1.975	1.971	10
9 1 5	1.940	1.935	17
5 1 8	1.918	1.916	9
1 1 9	1.905	1.904	5
9 1 6	1.842	1.839	6
8 1 7	1.827	1.824	10
4 2 4	1.802	1.807	6
12 1 0	1.801	1.799	9
12 1 1	1.791	1.791	10
5 1 9	1.776	1.771	15
1 0 11	1.763	1.760	15
7 2 1	1.753	1.754	16
6 0 10	1.749	1.747	12
9 1 7	1.743	1.742	8
2 1 10	1.738	1.736	5
14 0 2	1.692	1.688	10
4 2 6	1.665	1.667	5
14 0 3	1.661	1.662	5
4 2 7	1.591	1.591	5

Table 2-15. Calculated and Observed X-ray Powder Diffraction Patterns for $K_2Bi_8S_{13}$.

h k l	d _{calcd} , Å	d _{obsd} , Å	I/I _{max} (obsd)
0 0 1	17.80	17.45	4
1 0 0	16.82	16.79	7
1 0 -1	12.27	12.23	14
0 0 2	8.90	8.87	28
1 0 2	7.84	7.82	5
2 0 1	7.58	7.57	5
2 0 2	6.09	6.08	29
1 0 -3	5.61	5.60	47
3 0 1	5.33	5.32	5
3 0 -2	4.76	4.76	5
3 0 2	4.73	4.72	5
1 0 -4	4.31	4.30	20
4 0 -1	4.10	4.10	9
3 0 3	4.06	4.06	31
2 0 -4	3.95	3.94	6
4 0 -2	3.81	3.81	25
1 1 -2	3.62	3.61	8
0 0 5	3.56	3.56	14
1 0 -5, 3 0 4	3.49, 3.47	3.48	100
4 0 3	3.42	3.41	43
5 0 0	3.36	3.36	17
1 1 -3	3.30	3.29	24
3 1 1	3.24	3.23	16
5 0 -2	3.15	3.15	17
2 1 3	3.11	3.11	8
3 1 -2	3.10	3.09	11
4 0 4	3.04	3.04	15
4 1 0	2.93	2.92	43
3 1 -3	2.89	2.88	44
2 0 -6	2.80	2.80	16
4 1 2	2.77	2.77	8
4 0 5	2.71	2.70	29
3 1 -4	2.65	2.65	5
1 0 -7	2.52	2.51	20
4 0 6	2.414	2.414	10
1 1 6	2.372	2.368	19
3 0 7	2.308	2.307	8
4 1 -5	2.267	2.260	6
6 0 -5	2.211	2.208	15
3 1 6	2.200	2.198	10
2 0 -8	2.155	2.151	9
1 1 7	2.138	2.134	11
5 1 -5	2.103	2.098	10
8 0 1	2.085	2.082	13
0 2 0	2.038	2.032	15
3 1 7	2.009	2.007	11

Table 2-15. (cont'd)

h k l	d _{calcd} , Å	d _{obsd} , Å	I/I _{max} (obsd)
5 1-6	1.959	1.955	10
7 1 3	1.950	1.948	11
1 1 8	1.938	1.937	8
6 1 5	1.931	1.930	10
2 0 9	1.922	1.919	11
7 1 4	1.871	1.868	6
8 1-2	1.831	1.827	6
3 2 4	1.757	1.754	7
6 0 8	1.736	1.736	17
8 0-6	1.722	1.721	4

Table 2-16. Summary of Crystallographic Data and Structure Analysis for $\text{KBi}_{6.33}\text{S}_{10}$ and $\text{K}_2\text{Bi}_8\text{S}_{13}$.

	I	II
Formula	$\text{KBi}_{6.33}\text{S}_{10}$	$\text{K}_2\text{Bi}_8\text{S}_{13}$
FW	1682.54	2166.82
a, Å	24.05(1)	16.818(2)
b, Å	4.100(2)	4.074(5)
c, Å	19.44(1)	17.801(3)
α , deg	90.000	90.000
β , deg	90.000	90.48(1)
γ , deg	90.000	90.000
Z; V, Å ³	4; 1917	2; 1220(2)
λ	0.71073 (Mo K α)	0.71073 (Mo K α)
space group	Pnma (No. 62)	P2 ₁ /m (No. 11)
D _{calc.} , g/cm ³	5.828	5.900
μ , cm ⁻¹	590 (Mo K α)	588 (Mo K α)
2 θ _{max} , deg	50 (Mo K α)	50 (Mo K α)
Temp., °C	23	23
Final R/R _w , %	4.3/4.7	7.3/8.2
Total Data Measured	2015	3888
Total Unique Data	2015	3792
Data with $F_o^2 > 3\sigma(F_o^2)$	862	1924 (averaged)
No. of Variables	108	131

$$^*R = \Sigma(|F_o| - |F_c|) / \Sigma|F_o| \quad R_w = \{\Sigma w(|F_o| - |F_c|)^2 / \Sigma w|F_o|^2\}^{1/2}$$

Table 2-17. Fractional Atomic Coordinates and B_{eq} Values for $KBi_{6.33}S_{10}$ with Estimated Standard Deviations in Parentheses.

atom	x	y	z	$B_{eq},^a \text{ \AA}^2$
Bi(1)	0.2995(1)	0.25	0.0913(1)	1.2(1)
Bi(2)	0.17185(9)	0.75	0.1898(1)	1.3(1)
Bi(3)	0.4327(1)	0.75	0.0364(1)	1.5(1)
Bi(4)	0.0435(1)	0.25	0.2754(1)	1.6(1)
Bi(5)	0.1502(1)	0.25	-0.0143(1)	2.0(1)
Bi(6) ^b	0.5090(1)	0.75	0.4015(1)	1.6(1)
Bi(7) ^c	0.2219(3)	0.25	0.3830(3)	4.0(3)
K	0.3705	0.25	0.2834(8)	2.6(7)
S(1)	0.0878(6)	0.25	0.1390(9)	2.4(8)
S(2)	0.2227(7)	0.75	0.0332(8)	2.3(8)
S(3)	0.3594(6)	0.75	0.1482(7)	1.9(7)
S(4)	0.5000	0.25	0.0897(8)	1.9(7)
S(5)	0.2375(6)	0.25	0.2294(7)	1.7(7)
S(6)	0.4732(5)	0.75	0.2716(7)	1.5(6)
S(7)	0.4287(8)	0.25	0.4452(8)	3.0(8)
S(8)	0.3621(6)	0.25	-0.0166(7)	1.6(7)
S(9)	0.6227(6)	0.75	0.1930(8)	1.5(7)
S(10)	0.7998(7)	0.75	0.1299(7)	2.0(7)

$$^a B_{eq} = (4/3)[a^2 B(1,1) + b^2 B(2,2) + c^2 B(3,3) + ab(\cos\gamma)B(1,2) + ac(\cos\beta)B(1,3) + bc(\cos\alpha)B(2,3)].$$

^bThis site is 81% occupied.

^cThis site is 53% occupied.

Table 2-18. Fractional Atomic Coordinates and B_{eq} Values for $K_2Bi_8S_{13}$ with Estimated Standard Deviations in Parentheses.

atom	x	y	z	$B_{eq},^a \text{ \AA}^2$
Bi(1)	0.9176(1)	0.25	0.5774(1)	1.27(9)
Bi(2)	1.1729(1)	0.25	0.6245(1)	1.3(1)
Bi(3)	0.6731(1)	0.25	0.5194(1)	1.3(1)
Bi(4)	0.8930(1)	-0.75	0.9783(1)	1.4(1)
Bi(5)	0.6929(1)	-0.25	0.9550(1)	1.3(1)
Bi(6)	1.0134(1)	-0.25	0.7540(1)	1.4(1)
Bi(7)	0.4917(1)	-1.75	0.8849(1)	1.5(1)
Bi(8)(K) ^b	0.2908(3)	-2.25	0.8195(3)	3.5(1)
K(1)(Bi) ^c	0.7268(7)	-2.25	0.7188(8)	5.9(3)
K(2)(Bi) ^c	0.5219(8)	-1.25	0.6542(8)	6.7(3)
S(1)	0.978(1)	-0.25	0.9073(9)	2.0(7)
S(2)	0.8982(8)	0.25	0.7227(8)	1.2(6)
S(3)	0.8082(8)	-0.25	0.559(1)	1.8(7)
S(4)	0.3889(9)	-1.75	0.7739(9)	1.8(7)
S(5)	0.807(1)	-1.25	1.0574(9)	1.8(7)
S(6)	0.7676(8)	-0.75	0.8767(7)	1.5(6)
S(7)	1.0418(8)	-0.75	0.5966(8)	1.5(6)
S(8)	1.131(1)	-0.75	0.7654(9)	1.7(6)
S(9)	0.629(1)	-1.75	0.661(1)	2.3(8)
S(10)	0.5784(7)	-0.25	0.4890(9)	1.5(6)
S(11)	0.573(1)	-1.25	0.820(1)	2.5(8)
S(12)	0.7258(8)	0.25	0.352(1)	1.7(7)
S(13)	0.610(1)	0.25	0.039(1)	2.7(8)

^a $B_{eq} = (4/3)[a^2B(1,1) + b^2B(2,2) + c^2B(3,3) + ab(\cos\gamma)B(1,2) + ac(\cos\beta)B(1,3) + bc(\cos\alpha)B(2,3)]$.

^bThis site contains 60% Bi and 40% K.

^cThis site contains 80% K and 20% Bi.

3. Results and Discussion

3.1. Synthesis, Spectroscopy and Thermal Analysis

The synthesis of pure $\text{KBi}_{6.33}\text{S}_{10}$ (I) can be accomplished by reacting K_2S and Bi_2S_3 (1:4) at 750°C . By lowering the reaction temperature to 725°C , pure $\text{K}_2\text{Bi}_8\text{S}_{13}$ (I I) is obtained. This result suggests that I is more thermodynamically stable than (I I).

The known ternary phase, $\alpha\text{-KBiS}_2$ ⁶ was obtained as a pure phase by reacting K_2S and Bi_2S_3 (1:1) at 725°C . Surprisingly, instead of $\alpha\text{-KBiS}_2$, $\beta\text{-KBiS}_2$ was observed as the major product in the reaction of K_2S and Bi_2S_3 (1:2) at 725°C along with $\text{KBi}_{6.33}\text{S}_{10}$ as a minor product. Increasing the amount of Bi_2S_3 to (1:3) resulted in the formation of $\text{KBi}_{6.33}\text{S}_{10}$ with $\beta\text{-KBiS}_2$ as the minor impurity phase. $\beta\text{-KBiS}_2$ is isostructural to RbBiS_2 ⁷ in which CdCl_2 -type $(\text{BiS}_2)^-$ layers (perpendicular to the c-axis) alternate with Rb^+ ions. Three $(\text{BiS}_2)^-$ layers are found in the unit cell of this compound. The coordination sphere of Bi is perfect octahedral. The results of several direct combination reactions are shown in Table 2-19.

$\text{KBi}_{6.33}\text{S}_{10}$, $\text{K}_2\text{Bi}_8\text{S}_{13}$, and $\beta\text{-KBiS}_2$ belong to the $(\text{A}_2\text{Q})_n(\text{Bi}_2\text{Q}_3)_m$ (A=alkali metal; Q=S, Se) general family of compounds with $n=1$ and $m=6.33, 4, 1$ respectively. The synthesis of new ternary bismuth chalcogenides with various n and m values may be possible e.g. ABi_5Q_8 ($n=1, m=5$).

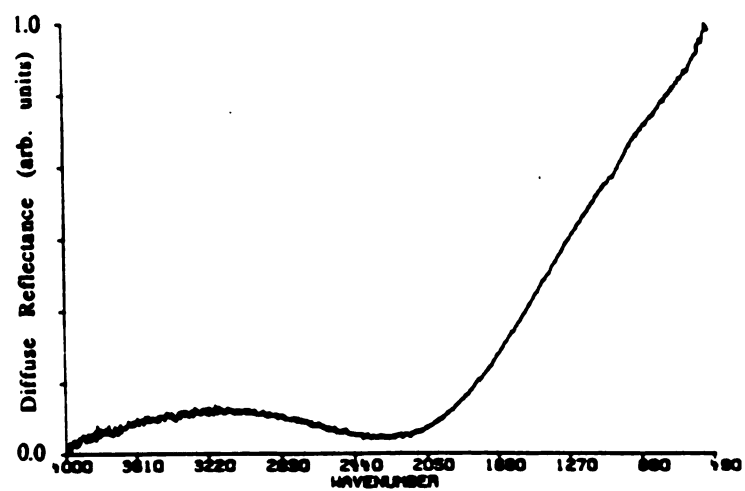
The optical properties of (I) and (I I) were assessed by studying the UV-visible-near IR reflectance spectra of the materials. The compounds absorbed light in the range of 0.5 to 6.2 eV. The spectra confirm that the band gaps, E_g , of these two compounds are less than 0.5 eV (the detection limit of the instrument). Diffuse reflectance Mid-IR spectroscopy was used to probe the small band gap of the compounds. The absorption edges in both compounds were found to be virtually identical in the range of 0.06-0.25 eV (see Figure 2-21). The small band gaps for (I) and (I I) could result from the existence of a narrow dopant level band just below the conduction band which would also give rise to the n-type conduction behavior observed for (I) and (I I) (vide infra).

The thermal behavior of (I) and (I I) was investigated with differential thermal analysis (DTA). $\text{KBi}_{6.33}\text{S}_{10}$ melts congruently at 710 °C while $\text{K}_2\text{Bi}_8\text{S}_{13}$ melts incongruently to give $\text{KBi}_{6.33}\text{S}_{10}$ as evidenced by powder XRD.

Table 2-19. High Temperature $\text{K}_2\text{S}/\text{Bi}_2\text{S}_3$ Reactions.

K_2S	Bi_2S_3	Temp. ($^{\circ}\text{C}$)	Product
1	1	675	$\alpha\text{-KBiS}_2$ + impurity
1	1	725	$\alpha\text{-KBiS}_2$
1	2	725	$\beta\text{-KBiS}_2$ + I (minor)
1	3	725	I + $\beta\text{-KBiS}_2$ (minor)
1	4	675	I
1	4	725	I I
1	4	750	I
1	5	725	II + Bi_2S_3
1	6.33	725	II + Bi_2S_3

(A)



(B)

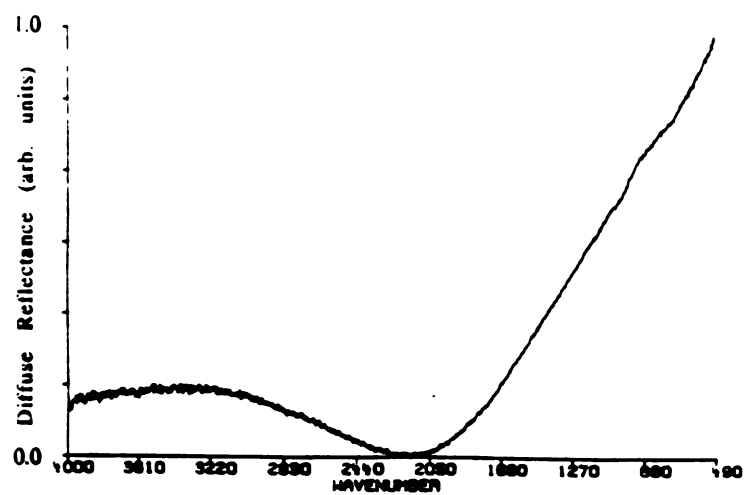


Figure 2-21. Mid-IR diffuse reflectance spectra of (a) KBi_{6.33}S₁₀ and (b) K₂Bi₈S₁₃.

3.2. Description of Structures.

Structure of $\text{KBi}_{6.33}\text{S}_{10}$ (I). This compound has a three-dimensional structure made up of Bi_2Te_3 -type (NaCl-type) blocks and CdI_2 -type fragments that connect to form tunnels filled with eight-coordinate K^+ cations ($\text{K-S}_{\text{ave.}} = 3.3(1) \text{ \AA}$). Selected bond distances and angles for (I) are given in Tables 2-20 and 2-21.

Figure 2-22 shows the packing diagram of the extended structure down the b-axis. The $[\text{Bi}_{6.33}\text{S}_{10}]^-$ framework can be thought of as a hybrid of two different layered structure types interconnected to form a 3-D network. Structural features from the Bi_2Te_3 ²⁸ and CdI_2 ²⁹ lattices are represented in this framework. Figures 2-23a and 2-23b show the structures of the two layered materials. The features of both structure types found in the $[\text{Bi}_{6.33}\text{S}_{10}]^-$ framework are highlighted in Figure 2-23c. The Bi_2Te_3 -type fragments are linked by CdI_2 -type octahedra to form the channel framework. Another interesting feature found in this structure is the presence of small triangular-shaped empty channels that are lined by $\text{Bi}(7)\text{-S}(8)\text{-Bi}(4)\text{-S}(4)\text{-Bi}(3)\text{-S}(9)$. The same type of channels have been observed in $\beta\text{-BaBi}_2\text{S}_4$.¹¹

The existence of Bi_2Te_3 - and CdI_2 -type fragments with Bi in an octahedral coordination site is a common structural motif that runs through much of the known bismuth chalcogenide chemistry. The structure of CsBi_3S_5 ⁸ is comprised of Bi_2Te_3 -type single chains that run along the b-direction and share corners in the a-c plane to form

a three-dimensional tunnel structure filled with Cs^+ ions. In $\text{Cs}_3\text{Bi}_7\text{Se}_{12}$,¹² the $[\text{Bi}_7\text{Se}_{12}]^{3-}$ anion is layered. It contains CdI_2 and Bi_2Te_3 -type fragments that connect in an edge-sharing manner to form a lamellar structure. In $\text{Sr}_4\text{Bi}_6\text{Se}_{13}$,¹³ the highly charged $[\text{Bi}_6\text{Se}_{13}]^{8-}$ anion has a very interesting structure. It contains two-dimensional sheets made up of edge-sharing CdI_2 - and Bi_2Te_3 -type fragments. One-dimensional double chains, comprised of Bi_2Te_3 -type blocks, extend along the b-direction and separate these layers. In BaBiSe_3 ,¹⁴ one-dimensional single chains, comprised of Bi_2Te_3 -type blocks, are linked by unusual $(\text{Se}_x)^{x-}$ chains to form a layered structure. The bonding in this compound is not valence precise so delocalized arguments must be invoked. This compound has a metallic luster.

$\text{Bi}(3)$ and $\text{Bi}(4)$ possess regular octahedral coordination with Bi-S bond distances ranging from 2.80(1) Å to 2.94(1) Å for $\text{Bi}(3)$ and 2.812(9) Å to 2.86(1) Å for $\text{Bi}(4)$. These distances are similar to those reported in CsBi_3S_5 ($\text{Bi}(3)$).⁸ The octahedral coordination environments in $\text{Bi}(1)$, $\text{Bi}(2)$, $\text{Bi}(5)$, and $\text{Bi}(6)$ are distorted with a short bond that is *trans* to a long bond but with normal octahedral angles. This type of coordination environment is very prevalent in bismuth chalcogenide chemistry and results from the influence of the non-bonded, stereochemically active $6s^2$ electron lone pair. For example, the $\text{Bi}(2)$ -S(9) bond distance of 2.57(2) Å is *trans* to a long $\text{Bi}(2)$ -S(1) distance of 3.28(2) Å. This same type of distorted octahedral coordination, bordering on square pyramidal coordination, is found in many compounds including CsBi_3S_5 ($\text{Bi}(1,2)$),⁸ $\text{Ti}_4\text{Bi}_2\text{S}_5$ ¹⁰ and α -(β)- BaBi_2S_4 .¹¹ The sites of $\text{Bi}(6)$ and $\text{Bi}(7)$ are partially

occupied at 81% and 53%, respectively. Bi(7) possesses a distorted trigonal bipyramidal coordination (including the lone pair) with four normal Bi-S bonds ranging from 2.79(1) to 3.21(2) Å. Also, the lone pair is directed at four sulfur atoms with long distances of 3.47(1) and 3.48(1) Å. The axial S(2'')-Bi(7)-S(5) angle is much less than 180° at 148.3(5)° and the equatorial S(10')-Bi(7)-S(10'') angle is 94.5(5)°. These angles are influenced by the stereochemically active lone pair.

Structure of $K_2Bi_8S_{13}$ (II). This compound also possesses a three-dimensional structure made up of Bi_2Te_3 - and CdI_2 -type fragments that connect to form a structure with tunnels. The K^+ cations are disordered with one of the Bi^{3+} ions over three distinct crystallographic sites. This, although not expected, can be rationalized by the similar sizes of K^+ and Bi^{3+} . This structure is quite different from that of its selenium analog $K_2Bi_8Se_{13}$.²¹ Selected bond distances and angles for (I I) are given in Tables 2-22 and 2-23.

Figure 2-24 shows the packing diagram of the extended structure down the b-axis. As in (I), the $[Bi_8S_{13}]^{2-}$ framework is based on structural features from the Bi_2Te_3 and CdI_2 lattices and contains the small triangular-shaped empty channels. The tunnels of (I I) are more open than those of I because more K_2S is present per formula unit. (I I) can be viewed as a derivative of the well-known Bi_2S_3 compound generated by breaking down the Bi_2S_3 framework by incorporation of K_2S in the molar ratio of 1:4 (i.e. $[K_2S][Bi_2S_3]_4$). The corresponding $[K_2S]/[Bi_2S_3]$ ratio in I is 1:6.33 so less K^+ ions are present resulting in smaller channels.

Bi(4) and Bi(6) possess regular octahedral coordination with Bi-S bond distances ranging from 2.77(1) Å to 2.96(2) Å for Bi(4) and 2.80(2) Å to 2.86(1) Å for Bi(6). As in I, the octahedral coordination environments of Bi(1), Bi(2), Bi(3), Bi(5), and Bi(7) are distorted with a short bond that is *trans* to a long bond but with normal octahedral angles. For example, the Bi(2)-S(8) bond distance of 2.61(2) Å is *trans* to a long Bi(2)-S(3") distance of 3.29(2) Å.

Bi(8) is disordered over three sites with K(1) and K(2). The Bi(8) site contains approximately 60% Bi and 40% K while the other two sites contain mainly K (~80%). Bi(8) possesses the same type of distorted trigonal bipyramidal coordination (including the lone pair) as found in Bi(7) (KBi_{6.33}S₁₀), with four normal Bi-S bonds ranging from 2.75(1) to 3.06(2) Å and four longer distances from 3.43(1) to 3.50(1) Å. The two K sites have distances ranging from 2.81(1) to 3.54(2) Å for K(1) and 2.72(2) to 3.66(2) Å for K(2). These distances are similar to those found for the predominantly Bi(8) site. The K-S distances below 3.0 Å are unusual and presumably a result of averaging over the mixed K/Bi sites. There are no known systems that have alkali metal/Bi disorder so we could find no precedence in the literature. The closest example is the Cu_{1+3x}Bi_{5-x}S₈¹⁵ alloy, where Cu⁺ and Bi³⁺ ions are disordered over one site.

Close examination of the known ternary Bi/Q compounds reveals an interesting fact. The e.s.d.'s of the Bi-S and Bi-Se bond lengths are quite high for such structures. For example, values for I and II range from 0.006 to 0.02. Other bismuth chalcogenide crystal structures show high e.s.d.'s for these bonds as follows: CsBi₃S₅

(0.01),⁸ $\text{Tl}_4\text{Bi}_2\text{S}_5$ (0.01-0.02),¹⁰ α -(β -) BaBi_2S_4 (0.01-0.03),¹¹ $\text{Cs}_3\text{Bi}_7\text{Se}_{12}$ (0.011),¹² $\text{Sr}_4\text{Bi}_6\text{Se}_{13}$ (0.011),¹³ BaBiSe_3 (0.014),¹⁴ and β - CsBiS_2 (0.008-0.01).²¹ As the diffracting quality of these crystals seems quite good, no obvious explanation for this has been advanced.

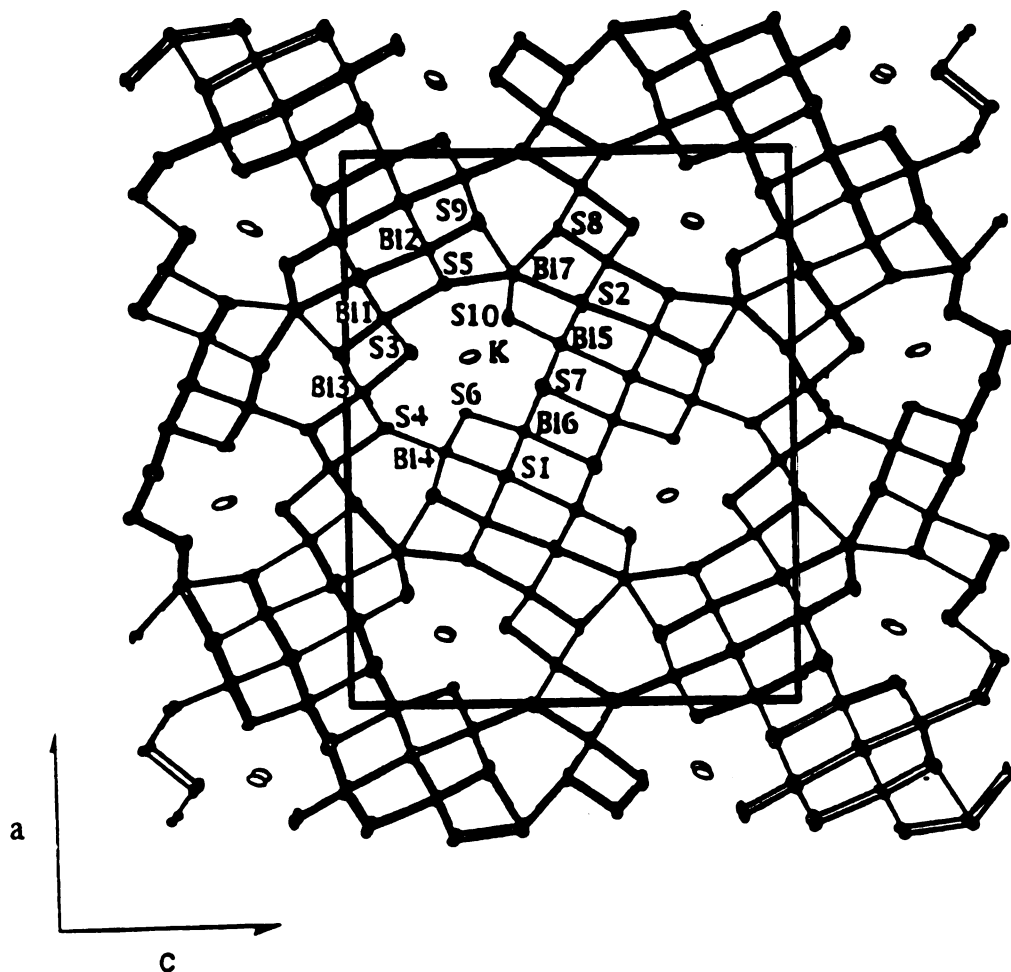


Figure 2-22. ORTEP representation of the packing diagram of $\text{KBi}_{6.33}\text{S}_{10}$ down the b-axis with labeling.

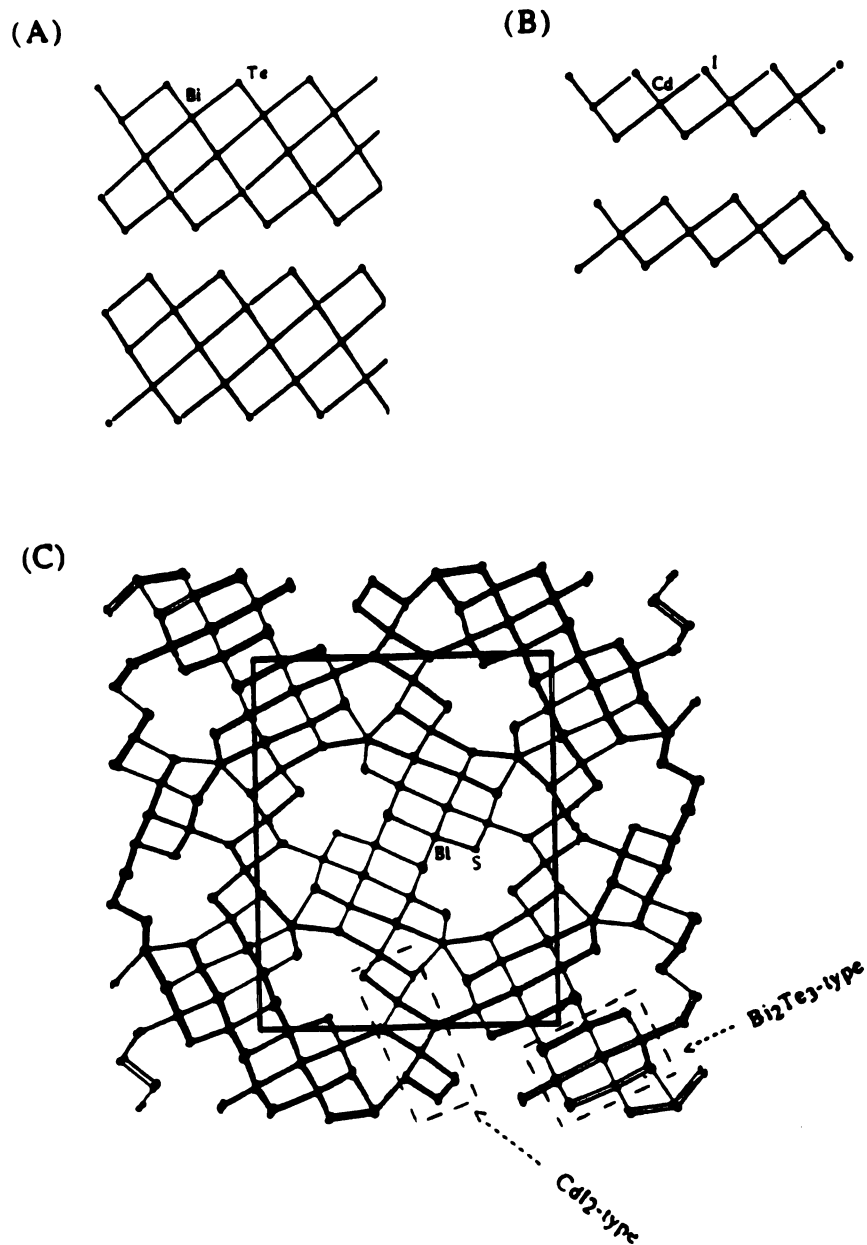


Figure 2-23. Projections of the structures of (A) Bi_2Te_3 (B) CdI_2 and (C) $[\text{Bi}_{6.33}\text{S}_{10}]^-$ framework. Both structure types found in this framework are designated with dashed lines.

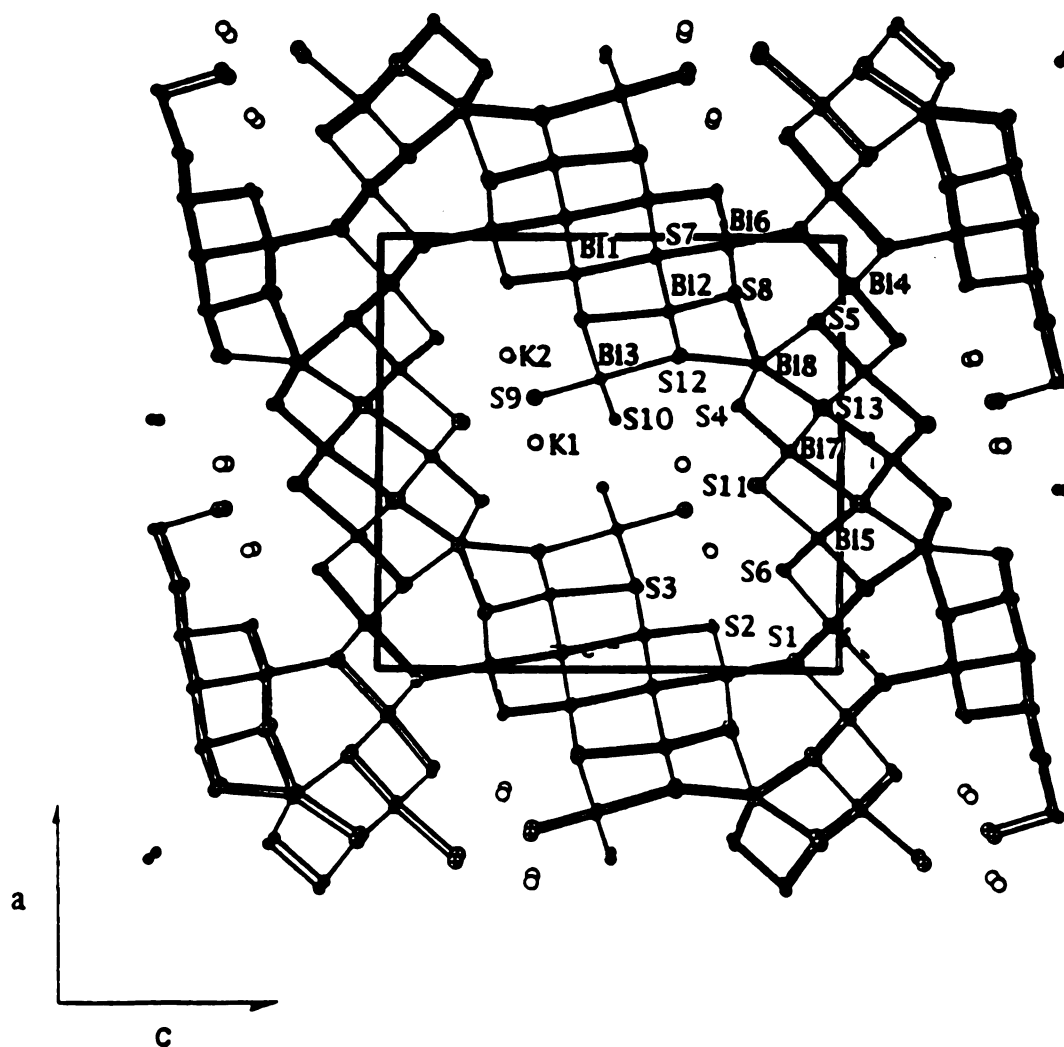


Figure 2-24. ORTEP representation of the packing diagram of $K_2Bi_8S_{13}$ down the b -axis with labeling.

Table 2-20. Selected Distances (Å) in $\text{KBi}_{6.33}\text{S}_{10}$ with Standard Deviations in Parentheses.^a

Bi(1)-S(2)	2.98(1)	Bi(5)-S(1)	3.34(2)
Bi(1)-S(2')	2.98(1)	Bi(5)-S(2)	2.84(1)
Bi(1)-S(3)	2.74(1)	Bi(5)-S(2')	2.84(1)
Bi(1)-S(3')	2.74(1)	Bi(5)-S(7')	2.90(1)
Bi(1)-S(5)	3.07(1)	Bi(5)-S(7'')	2.90(1)
Bi(1)-S(8)	2.58(1)	Bi(5)-S(10)	2.55(1)
Bi(1)-S (mean)	2.8(2)	Bi(5)-S (mean)	2.9(3)
Bi(2)-S(1)	3.04(1)	Bi(6)-S(1)	2.90(1)
Bi(2)-S(1')	3.04(1)	Bi(6)-S(1'')	2.90(1)
Bi(2)-S(2)	3.28(2)	Bi(6)-S(6)	2.67(1)
Bi(2)-S(5)	2.70(1)	Bi(6)-S(7)	2.94(1)
Bi(2)-S(5')	2.70(1)	Bi(6)-S(7''')	2.94(1)
Bi(2)-S(9)	2.57(2)	Bi(6)-S(7''')	3.34(2)
Bi(2)-S (mean)	2.9(3)	Bi(6)-S (mean)	2.9(2)
Bi(3)-S(3)	2.80(1)	Bi(7)-S(2'')	3.21(2)
Bi(3)-S(4)	2.810(6)	Bi(7)-S(5)	3.01(2)
Bi(3)-S(4')	2.810(6)	Bi(7)-S(8)	3.48(1)
Bi(3)-S(4'')	2.94(1)	Bi(7)-S(8')	3.48(1)
Bi(3)-S(8)	2.85(1)	Bi(7)-S(9')	3.47(1)
Bi(3)-S(8')	2.85(1)	Bi(7)-S(9)	3.47(1)
Bi(3)-S (mean)	2.84(5)	Bi(7)-S(10')	2.79(1)
Bi(4)-S(1)	2.86(2)	Bi(7)-S(10'')	2.79(1)
Bi(4)-S(4''')	2.82(1)	Bi(7)-S (mean)	3.2(3)
Bi(4)-S(6')	2.812(9)	K-S(3)	3.34(2)
Bi(4)-S(6'')	2.812(9)	K-S(3')	3.34(2)
Bi(4)-S(9')	2.86(1)	K-S(5)	3.37(2)
Bi(4)-S(9)	2.86(1)	K-S(6)	3.22(1)
Bi(4)-S (mean)	2.84(3)	K-S(6''')	3.22(1)
		K-S(7)	3.44(2)
		K-S(10')	3.15(1)
		K-S(10'')	3.15(1)
		K-S (mean)	3.3(1)

^aThe estimated standard deviations in the mean bond lengths and the mean bond angles are calculated by the equations $\sigma l = \{\sum_n (l_n - l)^2 / n(n-1)\}^{1/2}$, where l_n is the length (or angle) of the n th bond, l the mean length (or angle), and n the number of bonds.

Table 2-21. Selected Angles (deg) in $\text{KBi}_{6.33}\text{S}_{10}$ with Standard Deviations in Parentheses.

S(2)-Bi(1)-S(2')	86.9(4)	S(2)-Bi(5)-S(2')	92.2(5)
S(2)-Bi(1)-S(3)	88.0(4)	S(2)-Bi(5)-S(7'')	88.8(3)
S(3)-Bi(1)-S(3')	96.9(5)	S(2)-Bi(5)-S(10)	89.8(4)
S(3)-Bi(1)-S(8)	91.3(4)	S(7')-Bi(5)-S(7'')	89.9(5)
S(1)-Bi(2)-S(1')	84.7(4)	S(1)-Bi(6)-S(1'')	89.9(5)
S(1)-Bi(2)-S(5)	88.3(3)	S(1)-Bi(6)-S(6)	87.3(4)
S(1)-Bi(2)-S(9)	89.0(4)	S(6)-Bi(6)-S(7)	93.5(4)
S(5)-Bi(2)-S(9)	90.9(4)	S(7)-Bi(6)-S(7''')	88.4(5)
S(3)-Bi(3)-S(4)	94.4(3)	S(5)-Bi(7)-S(10')	80.0(4)
S(3)-Bi(3)-S(8)	84.6(4)	S(5)-Bi(7)-S(10'')	80.0(4)
S(4)-Bi(3)-S(4')	93.7(3)	S(10')-Bi(7)-S(10'')	94.6(5)
S(4)-Bi(3)-S(8)	87.2(2)	S(2'')-Bi(7)-S(5)	148.3(5)
S(1)-Bi(4)-S(6')	85.5(4)		
S(1)-Bi(4)-S(9)	87.2(4)		
S(4)-Bi(4)-S(6')	94.5(3)		
S(4)-Bi(4)-S(9)	92.7(3)		

Table 2-22. Selected Distances (Å) in K₂Bi₈S₁₃ with Standard Deviations in Parentheses.^a

Bi(1)-S(2)	2.611(1)	Bi(6)-S(7)	2.84(2)
Bi(1)-S(3)	2.764(9)	Bi(6)-S(8)	2.84(1)
Bi(1)-S(3')	2.764(9)	Bi(6)-S(8')	2.84(1)
Bi(1)-S(7)	2.93(1)	Bi(6)-S(mean)	2.84(2)
Bi(1)-S(7')	2.93(1)		
Bi(1)-S(7'')	3.18(2)	Bi(7)-S(4)	2.61(1)
Bi(1)-S(mean)	2.9(2)	Bi(7)-S(11)	2.71(1)
		Bi(7)-S(11''')	2.71(1)
Bi(2)-S(3'')	3.29(2)	Bi(7)-S(13'')	3.38(2)
Bi(2)-S(7)	3.04(1)	Bi(7)-S(13''')	2.99(1)
Bi(2)-S(7')	3.04(1)	Bi(7)-S(13''')'	2.99(1)
Bi(2)-S(8)	2.61(2)	Bi(7)-S(mean)	2.9(3)
Bi(2)-S(12')	2.688(9)		
Bi(2)-S(12'')	2.688(9)	Bi(8)-S(4)	2.75(1)
Bi(2)-S(mean)	2.9(3)	Bi(8)-S(4')	2.75(1)
		Bi(8)-S(5'')	3.43(1)
Bi(3)-S(3)	3.13(1)	Bi(8)-S(5''')	3.43(1)
Bi(3)-S(3')	3.13(1)	Bi(8)-S(8'')	3.50(1)
Bi(3)-S(9')	2.63(2)	Bi(8)-S(8''')	3.50(1)
Bi(3)-S(10)	2.639(8)	Bi(8)-S(12''')	3.06(2)
Bi(3)-S(10')	2.639(8)	Bi(8)-S(13''')	3.01(2)
Bi(3)-S(12)	3.12(2)	Bi(8)-S(mean)	3.2(3)
Bi(3)-S(mean)	2.9(3)		
		K(1)-S(2'')	3.53(1)
Bi(4)-S(1)	2.80(1)	K(1)-S(2''')	3.53(1)
Bi(4)-S(1')	2.80(1)	K(1)-S(3'')	3.16(2)
Bi(4)-S(1'')	2.96(2)	K(1)-S(6'')	3.54(2)
Bi(4)-S(5)	2.87(1)	K(1)-S(6''')	3.54(2)
Bi(4)-S(5')	2.87(1)	K(1)-S(9)	2.81(1)
Bi(4)-S(6)	2.77(1)	K(1)-S(9'')	2.81(1)
Bi(4)-S(mean)	2.85(7)	K(1)-S(11''')	3.17(2)
		K(1)-S(mean)	3.3(3)
Bi(5)-S(5')	2.64(2)		
Bi(5)-S(6)	2.78(1)	K(2)-S(4)	3.71(1)
Bi(5)-S(6')	2.78(1)	K(2)-S(4'')	3.71(1)
Bi(5)-S(11'')	3.12(2)	K(2)-S(9)	2.72(1)
Bi(5)-S(13)	2.89(1)	K(2)-S(9''')	2.72(1)
Bi(5)-S(13')	2.89(1)	K(2)-S(10'')	3.10(2)
Bi(5)-S(mean)	2.9(2)	K(2)-S(10''')	3.66(1)
		K(2)-S(10''')'	3.66(1)
Bi(6)-S(1)	2.80(2)	K(2)-S(11)	3.07(2)
Bi(6)-S(2)	2.86(1)	K(2)-S(mean)	3.3(4)
Bi(6)-S(2')	2.86(1)		

^a $\sigma_l = \{\sum_n (l_n - l)^2 / n(n-1)\}^{1/2}$, where l_n is the length (or angle) of the n th bond, l the mean length (or angle), and n the number of bonds.

Table 2-23. Selected Angles (deg) in $K_2Bi_8S_{13}$ with Standard Deviations in Parentheses.

S(2)-Bi(1)-S(3)	91.6(4)	S(5')-Bi(5)-S(6)	91.0(4)
S(2)-Bi(1)-S(7)	88.8(4)	S(5')-Bi(5)-S(13)	89.6(4)
S(3)-Bi(1)-S(3')	95.0(4)	S(6)-Bi(5)-S(6')	94.4(4)
S(3)-Bi(1)-S(7)	88.6(3)	S(13)-Bi(5)-S(13')	89.6(5)
S(3'')-Bi(2)-S(7)	85.1(3)	S(1)-Bi(6)-S(8)	94.7(4)
S(3'')-Bi(2)-S(12)	95.2(4)	S(2)-Bi(6)-S(7)	85.8(3)
S(7)-Bi(2)-S(8)	87.4(4)	S(2)-Bi(6)-S(8')	88.5(3)
S(8)-Bi(2)-S(12')	91.4(4)	S(7)-Bi(6)-S(8)	87.0(4)
S(3)-Bi(3)-S(3')	81.3(3)	S(4)-Bi(7)-S(11)	90.7(4)
S(3)-Bi(3)-S(9)	89.7(4)	S(4)-Bi(7)-S(13''')	88.0(4)
S(9')-Bi(3)-S(10)	91.2(4)	S(11)-Bi(7)-S(13''')	88.4(4)
S(10)-Bi(3)-S(12)	88.8(4)	S(13'')-Bi(7)-S(13''')	88.2(4)
S(1)-Bi(4)-S(1')	93.4(5)	S(4)-Bi(8)-S(4')	95.7(5)
S(1)-Bi(4)-S(6)	95.5(4)	S(4)-Bi(8)-S(5'')	157.4(4)
S(5)-Bi(4)-S(5')	90.4(4)	S(4)-Bi(8)-S(12''')	75.9(4)
S(5)-Bi(4)-S(6)	86.4(4)	S(5''')-Bi(8)-S(12)	126.7(3)

3.3. Electrical Conductivity and Thermoelectric Power Measurements.

Four-probe electrical conductivity measurements on polycrystalline chunks of $\text{KBi}_{6.33}\text{S}_{10}$ showed that the material is a semiconductor with room temperature conductivity $\sigma \sim 10^2$ S/cm which drops to 10^{-4} S/cm at 5 K. Figure 2-25a shows the log conductivity vs. temperature plot for $\text{KBi}_{6.33}\text{S}_{10}$. The data can be fit to the equation shown below suggesting an activation energy of $E_a = 0.045$ eV.

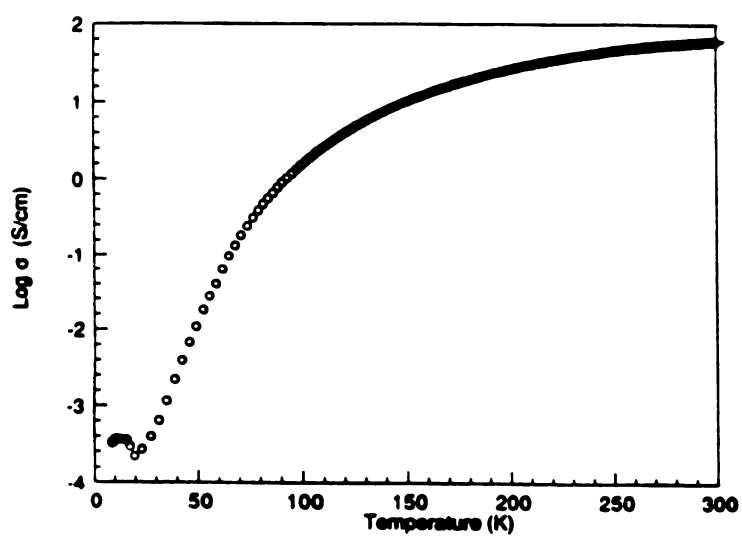
$$\sigma = \sigma_0 e^{-\frac{E_a}{k_B T}} \quad \text{eq. (2)}$$

Where σ =electrical conductivity (S/cm), E_a =activation energy, k_B =Boltzmann constant, and T =temperature (K). Figure 2-25b shows the log conductivity as a function of temperature for $\text{K}_2\text{Bi}_8\text{S}_{13}$. The conductivity of $\sim 10^2$ S/cm (at 300 K) and the weak temperature dependence between 5-300 K coupled with the IR-optical data (vide supra) suggests that this compound is a semi-metal or a narrow band gap semiconductor. The conductivity of $\sim 10^2$ S/cm is compared to the values of other semi-metals such as Bi_2Te_3 (2.2×10^3 S/cm)³⁰ and Bi_2Se_3 ($1.6\text{-}2.0 \times 10^3$ S/cm, Bi_2Te_3 -type)³¹ obtained from single crystals of these materials.

The conductivity measurements alone cannot unequivocally characterize the electrical behavior of (I) and (I I). A complementary probe to address this issue is thermoelectric power (TP)

measurements as a function of temperature. TP measurements are typically far less susceptible to artifacts arising from resistive domain boundaries in the material because they are essentially zero-current measurements. This is because temperature drops across such boundaries are much less significant than voltage drops. Figure 2-26a shows typical TP data of $\text{KBi}_{6.33}\text{S}_{10}$ as a function of temperature. The TP is negative throughout the temperature range studied ($80 < T < 300$ K) with values of $-10 \mu\text{V/K}$ at room temperature. This indicates electron (as opposed to hole) charge transport. The TP becomes more negative as the temperature is decreased from 300 K to 80 K which is characteristic of a semiconductor material. The semiconducting character of this material is also supported by the fact that an optical gap exists in this material in the Mid-IR region (Figure 2-21a). The thermopower vs. temperature plot of $\text{K}_2\text{Bi}_8\text{S}_{13}$ is shown in Figure 2-26b. The TP is negative throughout the temperature range studied ($80 < T < 300$ K) with values of $-2 \mu\text{V/K}$ at room temperature which indicates electron charge transport (n-type material). The weak temperature dependence of the TP is consistent with the semi-metallic behavior of this compound. The optical gap of (I I) (Figure 2-21b) is quite small (< 0.25 eV) and is typical for semi-metals such as Bi_2Te_3 ($E_g = 0.16$ eV).³²

(A)



(B)

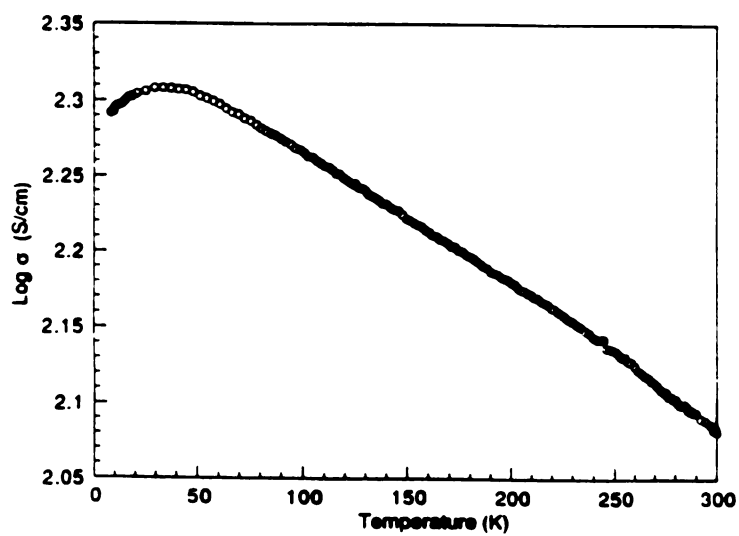
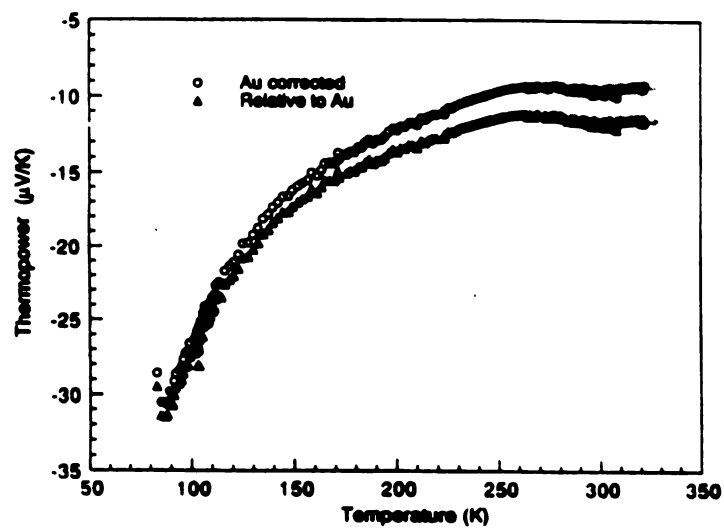


Figure 2-25. Variable temperature electrical conductivity data for polycrystalline chunks of: (a) $\text{KBi}_{6.33}\text{S}_{10}$ and (b) $\text{K}_2\text{Bi}_8\text{S}_{13}$.

(A)



(B)

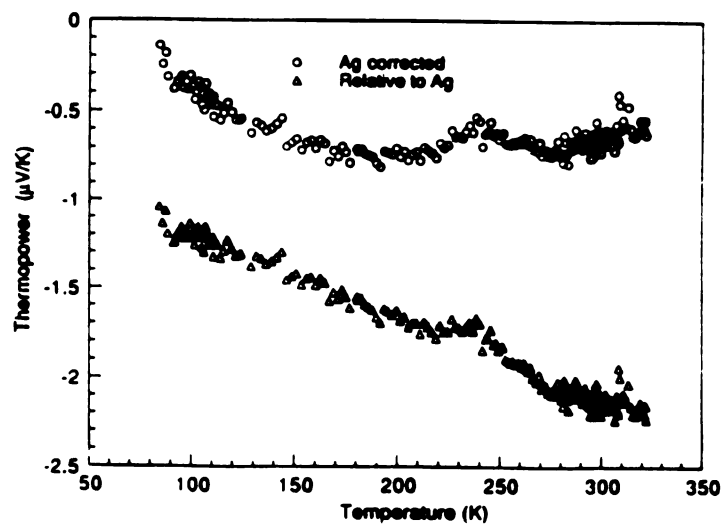


Figure 2-26. Thermoelectric power as a function of temperature for polycrystalline chunks of: (a) $\text{KBl}_{6.33}\text{S}_{10}$ and (b) $\text{K}_2\text{Bl}_8\text{S}_{13}$.

3.4. Conclusions

The high temperature reactions between K_2S and Bi_2S_3 revealed two new phases, $KBi_{6.33}S_{10}$ and $K_2Bi_8S_{13}$, with new structure types. These compounds are n-type conductors with optical band gaps less than 0.25 eV. $KBi_{6.33}S_{10}$ is a semiconductor while $K_2Bi_8S_{13}$ resembles a semi-metal. $KBi_{6.33}S_{10}$ is thermodynamically more stable with respect to $K_2Bi_8S_{13}$ as evidenced by the synthesis temperatures and the thermal analysis data. The need for new generation thermoelectric materials point to more exploratory high temperature synthesis in the A_2Q/Bi_2Q_3 ($A=K, Rb, Cs$; $Q=S, Se, Te$) system hopefully to uncover new compounds with novel structure types and properties that surpass those of the Bi_2Te_3 -based materials.³³

List of References

1. (a) Feichtner, J. D.; Roland, G. W. *Appl. Opt.*, 1972, 11, 993-998 (b) Ballman, A. A.; Byer, R. L.; Eimerl, D.; Feigelson, R. S.; Feldman, B. J.; Goldberg, L. S.; Menyuk, N.; Tang, C. L. *Appl. Opt.*, 1987, 26, 224-227.
2. Ibuki, S; Yoschimatsu, S. *J. Phys. Soc. Japan*, 1955, 10, 549-554.
3. (a) Kaibe, H.; Tanaka, Y.; Sakata, M.; Nishida, I. *J. Phys. Chem. Solids* 1989, 50, 945-950. (b) Jeon, H-W.; Ha, H-P.; Hyun, D-B.; Shim, J-D. *J. Phys. Chem. Solids* 1991, 4, 579-585.
4. (a) Smith, M. J.; Knight, R. J.; Spencer, C. W. *J. Appl. Phys.* 1962, 33(7), 2186-2190. (b) Testardi, L. R.; Bierly, J. N. Jr.; Donahoe, F. J. *J. Phys. Chem. Solids*, 1962, 23, 1209. (c) Champness, C. H.; Chiang, P. T.; Parekh, P. *Can. J. Phys.* 1965, 43, 653-569. (d) Yim, W. M.; Fitzke, E. V. *J. Electrochem. Soc.* 1968, 115, 556-560.
5. (a) Rowe, D. M.; Bhandari, C. M. *Modern Thermoelectrics*, Holt, Rinehart and Winston: London, 1983; p. 103. (b) Borkowski, K.; Przyluski, J. *J. Mat. Res. Bull.* 1987, 22, 381-387.
6. (a) Boon, J. W. *Rec. Trav. Chim. Pays-Bas*, 1944, 63, 32. (b) Glemser, O.; Filcek, M. *Z. Anorg. Allg. Chem.*, 1955, 279, 321-323 (c) Gattow, G.; Zemann, J. *Z. Anorg. Allg. Chem.*, 1955, 279, 324-327.
7. Voroshilov, Y. V.; Peresh, E. Y.; Golovei, M. I. *Inorg. Mater.*, 1972, 8, 777-778.
8. Kanishcheva, A. S.; Mikhailov, J. N.; Lazarev, V. B.; Trippel, A. F. *Dokl. Akad. Nauk, SSSR (Kryst.)*, 1980, 252, 96-99.
9. Schmitz, D.; Bronger, W. *Z. Naturforsch.*, 1974, 29b, 438-439.
10. Julien-Pouzol, M.; Jaulmes, S.; Laruelle, P. *Acta. Cryst.* 1979, B35 1313-1315.
11. B. Aurivillius, *Acta Chem. Scand.* 1983, A37 399-407.
12. G. Cordier, H. Schäfer, C. Schwidetzky, *Rev. Chim. Miner.*, 1985, 22 676-683.
13. G. Cordier, H. Schäfer, C. Schwidetzky, *Rev. Chim. Miner.*, 1985, 22 631-638.
14. K. Volk, G. Cordier, R. Cook, H. Schäfer, *Z. Naturforsch.*, 1990, 35b 136-140.

15. Liautard, B.; Garcia, J. C.; Brun, G.; Tedenac, J. C.; Maurin, M. *Eur. J. Solid State Inorg. Chem.* 1990, 27, 819-830.
16. Lee, S.; Fischer, E.; Czerniak, J.; Nagasundaram, N. *J. Alloys and Compounds* 1993, 197, 1-5.
17. Iitaka, Y.; Nowacki, W. *Acta Cryst.*, 1962, 15, 691-698.
18. Kupcik, V.; Makovicky, E. N. *Jb. Miner. Mh.*, 1968, 7, 236-237.
19. Ohmasa, M.; Nowacki, W. *Z. Kristallogr.* 1973, 137, 422-432.
20. Kohatsu, I.; Wuensch, B. J. *Acta Cryst.* 1971, B27, 1245-1252.
21. McCarthy, T. J.; Ngeyi, S.-P.; Liao, J.-H.; DeGroot, D.; Hogan, T.; Kannewurf, C. R.; Kanatzidis, M. G. *Chem. Mater.*, 1993, 5, 331-340.
22. McCarthy, T. J.; Kanatzidis, M. G. manuscript in preparation.
23. (a) Lazarev, V. B.; Trippel', A. F.; Berul', S. I. *Russ. J. Inorg. Chem.*, 1977, 22 (8), 1218-1220. (b) Trippel', A. F.; Berul', S. I.; Lazarev, V. B. *Russ. J. Inorg. Chem.*, 1980, 25 (10), 1545-1547. (c) Berul', S. I.; Lazarev, V. B.; Trippel', A. F.; Buchikhina, O. P. 1977, 22 (9), 1390-1393. (d) Lazarev, V. B.; Trippel', A. F.; Berul', S. I. *Russ. J. Inorg. Chem.*, 1980, 25 (11), 1694-1697.
24. Feher, F. *Handbuch der Preparativen Anorganischen Chemie*; Brauer, G., Ed.; Ferdinand Enke: Stuttgart, Germany, 1954; pp. 280-281.
25. CERIU: Molecular Simulation Software, Version 3.0, (1992), Cambridge Molecular Design, Waltham, MA 02154
26. (a) G. M. Sheldrick, In *Crystallographic Computing 3*; Sheldrick, G. M., Kruger, C., Doddard, R., Eds.; Oxford University Press: Oxford, England, 1985; pp 175-189. (b) Gilmore, G. J. *Appl. Cryst.*, 1984, 17, 42-46.
27. Walker, N.; Stuart, D. *Acta Cryst.*, 1983, A39, 158-166.
28. Villars, P.; Calvert, L. D. *Pearson's Handbook of Crystallographic Data for Intermetallic Phases*; American Society for Metals: Metals Park, OH, 1985, p. 1494.
29. Mitchell, R. S. *Z. Kristallogr.*, 1956, 108, 296-315.
30. Rosi, F. D.; Abeles, B.; Jengen, R. V. *J. Phys. Chem. Solids*, 1959, 10, 191.
31. Black, J.; Conwell, E. M.; Seigle, L.; Spencer, C. W. *J. Phys. Chem. Solids*, 1957, 2, 240.
32. Li, C. Y.; Ruoff, A. L.; Spencer, C. W. *J. Appl. Phys.* 1961, 32, 1733.
33. Kanatzidis, M. G. work in progress.

[



MICHIGAN STATE UNIV. LIBRARIES



31293010219602



LIBRARY
Michigan State
University

PLACE IN RETURN BOX to remove this checkout from your record.
TO AVOID FINES return on or before date due.

DATE DUE	DATE DUE	DATE DUE
_____	_____	_____
_____	_____	_____
_____	_____	_____
_____	_____	_____
_____	_____	_____
_____	_____	_____
_____	_____	_____

MSU Is An Affirmative Action/Equal Opportunity Institution

c:\circ\datedue.pm3-p.1

CHAPTER 3

Polysulfide Ligands In Solid State Antimony Compounds. Isolation and Structural Characterization of Cs₂Sb₄S₈ and CsSbS₆

1. Introduction

During the past two decades, a variety of synthetic routes have been employed for exploratory synthesis of solid state ternary antimony sulfide compounds. Direct combination of the binary sulfides A₂S/Sb₂S₃ (A= Na, K, Rb, Cs) and (AE)S/Sb₂S₃ (AE=Ca, Sr, Ba) at high temperature has been used to obtain ASbS₂ (A = Na, K, Rb, Cs),¹ Ca₂Sb₂S₅,² Ba₈Sb₆S₁₇,³ and Sr₃Sb₄S₉.⁴ In addition, hydro(solvento)thermal reactions have yielded several additional phases including [N(C₃H₇)₄]Sb₃S₅,⁵ (N₂C₄H₈)Sb₄S₇,⁵ Cs₃Sb₅S₉,⁶ α,β-Rb₂Sb₄S₇,^{7,8} Cs₆Sb₁₀S₁₈·1.2H₂O,⁹ K₂Sb₄S₇·H₂O,¹⁰ K₂Sb₄S₇,¹¹ and TlSb₃S₅.¹² The Sb³⁺ compounds exhibit structural diversity due to the stereochemical effect of the inert lone pair and the tendency of Sb to adopt three,¹³ four,¹⁴ or five⁴ coordination.

To further explore antimony sulfides from a new synthetic angle, the alkali metal polychalcogenide flux method was used. This

method has proven to be an extremely useful low temperature route to access novel compounds.¹⁵ Since there are no known solid state antimony sulfides containing polysulfide ligands, we investigated the utility of this synthetic method in obtaining such compounds. We report here the synthesis, properties, and structural characterization of two new compounds, $\text{Cs}_2\text{Sb}_4\text{S}_8$ (I) and CsSbS_6 (I I), which represent the first two examples of solid state antimony compounds containing polysulfide ligands. (I) is isostructural to $\text{Cs}_2\text{Sb}_4\text{Se}_8$ ¹⁶ while (I I) represents a new structure type.

2. Experimental Section

2.1. Reagents

Chemicals in this work were used as obtained: (i) antimony powder, 99.999+% purity, -200 mesh, Cerac Inc., Milwaukee, WI. (ii) sulfur powder, sublimed, J. T. Baker Chemical Co., Phillipsburg, NJ. (iii) cesium metal, analytical reagent, Johnson Matthey/AESAR Group, Seabrook, NH (iv) methanol, anhydrous, Mallinckrodt Inc., Paris, KY. (v) diethyl ether, ACS anhydrous, EM Science, Inc., Gibbstown, NJ.

2.2. Synthesis

All manipulations were carried out under a dry nitrogen atmosphere in a Vacuum Atmospheres Dri-Lab glovebox. For the preparation of Cs_2S we used a modified literature procedure.¹⁷ The preparation of Cs_2S is reported in Section 2.2 of Chapter 2 (Part 1).

Cesium Tetrasulfidodiantimonate (III), $\text{Cs}_2\text{Sb}_4\text{S}_8$ (I). 0.061 g (0.5 mmol) of Sb, 0.164 g (0.55 mmol) of Cs_2S and 0.128 g (4.00 mmol) of S were thoroughly mixed and transferred to a 6ml pyrex tube which was subsequently flamed sealed in vacuo ($\sim 10^{-3}$ torr). The reaction was heated to 280 °C over 12 hours in a computer-controlled furnace. It was kept at 280 °C for 5 days, followed by cooling to 100 °C at a rate of 2 °C/hr, then to room temperature in one hour. The product, which is stable in water and air, was isolated by dissolving the Cs_2S_x flux with methanol under inert atmosphere to give orange-red crystals and orange powder. Quantitative microprobe analysis on single crystals gave $\text{CsSb}_{1.9}\text{S}_{4.2}$ (average of four data acquisitions) while analysis of the orange powder gave $\text{Cs}_{2.1}\text{SbS}_{3.9}$ (average of three data acquisitions). The orange powder was removed by washing with ethylenediamine, followed by water, MeOH, and ether to give 0.084 g (67% yield based on Sb) of the pure orange-red crystals. Far-IR (CsI matrix) gave six absorbances at 341(w), 328(w), 308(m), 304(m), 236(m) and 233cm^{-1} (m).

Cesium Hexasulfidoantimonate (III), CsSbS_6 (II). The reaction of 0.061 g (0.500 mmol) Sb, 0.149 g (0.500 mmol) of Cs_2S , and 0.144 g (4.5 mmol) of S at 260 °C for 5 days followed by isolation in methanol gave 0.155 g (69% yield based on Sb) of dark orange crystals (air stable). The crystals are insoluble in water but are soluble in ethylenediamine. Quantitative microprobe analysis on the single crystals gave $\text{Cs}_{1.2}\text{Sb}_{1.0}\text{S}_{6.4}$ (average of 3 data acquisitions.). Far-IR (CsI matrix) gave nine absorbances at 484(m),

473(m), 448(w), 365(s), 282(s), 255(s), 248(s), 226(m) and 195cm⁻¹ (s).

2.3. Physical Measurements

The instruments and experimental setups for Infrared measurements, optical diffuse reflectance measurements,¹⁸ and quantitative microprobe analysis on SEM/EDS are the same as those in Chapter 2 (Part 1) (Section 2.3). The experimental setup for differential thermal analysis (DTA) is the same as that in Chapter 2 (Part 2) (Section 2.3).

2.4. X-ray Crystallography

Both compounds were examined by X-ray powder diffraction (XRD) for the purpose of phase purity and identification. Accurate d_{hkl} spacings (Å) were obtained from the powder patterns recorded on a Rigaku rotating anode (Cu K α) X-ray powder diffractometer, Rigaku-Denki/RW400F2 (Rotaflex), at 45 kV and 100 mA with a 1 °/min scan rate. The results are summarized in Tables 3-1 and 3-2.

Single crystal X-ray diffraction data were collected on a Rigaku AFC6 diffractometer and the $\omega/2\theta$ scan technique was used. Neither crystal showed any significant intensity decay as judged by three check reflections measured every 150 reflections throughout the data collection. The space groups were determined from systematic absences and intensity statistics. The structures were solved by direct methods of SHELXS-86¹⁹ and refined by full-matrix least-squares techniques of the TEXSAN package of crystallographic programs.²⁰ An empirical absorption correction based on ψ -scans

were applied to each data set, followed by a DIFABS²¹ correction to the isotropically refined structure. The atomic scattering factors were obtained from reference 20. All atoms were eventually refined anisotropically. All calculations were performed on a VAXstation 3100/76 computer.

During the structural refinement of CsSbS₆, an $R/R_w = 3.0/5.1$ was obtained. After the final least squares cycle, the (1 0 -1) and (0 0 2) reflections were observed to have high $\Delta F/\sigma F$ values at -118.73 and 72.52 respectively. Since we suspected that these two low 2θ reflections might not have been measured properly, we eliminated them from the calculation. Least squares refinement gave $R/R_w = 2.9/4.0$ while the Sb-S bond length standard deviations improved from 0.003 to 0.002.

The complete data collection parameters and details of the structure solution and refinement for both compounds are given in Table 3-3. The coordinates of all atoms, average temperature factors, and their estimated standard deviations for both compounds are given in Tables 3-4 and 3-5.

Table 3-1. Calculated and Observed X-ray Powder Diffraction Patterns for $\text{Cs}_2\text{Sb}_4\text{S}_8$.

h k l	$d_{\text{calcd}}, \text{\AA}$	$d_{\text{obsd}}, \text{\AA}$	I/I _{max} (obsd)
0 1 0	9.44	9.60	6
0 1 1	5.19	5.24	6
-1 1 0	4.96	5.00	3
0 2 0	4.72	4.76	6
1 0 1	3.97	4.00	18
1 1 1	3.81	3.84	8
0 2 1	3.77	3.80	34
-1-2 1	3.70	3.73	17
-1 2 0	3.54	3.56	15
-2 0 1	3.21	3.22	18
0 3 0	3.15	3.16	6
-1 0 2	3.10	3.12	26
1 3 0	3.03	3.04	3
1-2 1	2.89	2.90	100
0-3 1	2.79	2.80	7
-1 3 0	2.66	2.67	4
0 2 2	2.59	2.60	4
0-2 2	2.56	2.57	5
-2 2 1	2.480	2.488	4
2-1 1	2.417	2.424	3
1 4 0	2.341	2.352	6
1 2 2	2.307	2.316	11
-1-4 1	2.248	2.257	7
0 4 1	2.213	2.222	4
-2 2 2	2.156	2.157	5
3 0 0	2.144	2.145	3
-1 4 0	2.107	2.115	4
-1-1 3	2.083	2.076	3
0 0 3	2.051	2.055	3
-3-2 2	1.958	1.963	9
-1 2 3	1.904	1.909	8
1 5 0	1.896	1.894	6
0 4 2	1.885	1.882	8
0-2 3	1.872	1.867	3
-3 2 0	1.843	1.848	4
2-2 2	1.762	1.765	4
-3 0 3	1.717	1.720	3
-4-2 1	1.656	1.659	2
-2 4 2	1.646	1.650	3
-4 0 2	1.603	1.607	3
1 6 0	1.588	1.593	3
-2-4 3	1.581	1.584	3

Table 3-2. Calculated and Observed X-ray Powder Diffraction Patterns for CsSbS₆.

h k l	d _{calcd} , Å	d _{obsd} , Å	I/I _{max} (obsd)
0 1 1	8.67	8.65	6
0 2 0	7.21	7.19	17
0 2 1	6.00	6.00	5
0 0 2	5.43	5.41	8
0 1 2	5.08	5.06	13
1 0 1	4.71	4.70	3
1 1 1	4.48	4.49	4
0 3 1	4.39	4.40	3
0 2 2	4.33	4.33	2
-1 1 2	4.23	4.22	8
1 2 1	3.94	3.93	2
-1 3 1	3.64	3.64	20
0 3 2	3.60	3.60	100
1 1 2	3.49	3.50	2
0 4 1	3.42	3.41	12
1 3 1	3.36	3.36	7
0 2 3	3.23	3.23	37
1 4 0	3.06	3.05	4
-2 1 1	2.88	2.88	7
1 0 3	2.82	2.81	3
0 5 1	2.79	2.78	18
0 0 4	2.71	2.71	10
0 1 4	2.67	2.66	9
1 2 3	2.62	2.62	7
0 2 4	2.54	2.54	5
-1 2 4	2.51	2.50	4
0 6 0	2.402	2.399	30
-2 2 3	2.375	2.374	3
2 4 0	2.250	2.249	2
1 4 3	2.219	2.217	3
0 6 2	2.196	2.194	5
0 4 4	2.167	2.164	12
-1 4 4	2.146	2.142	12
2 3 2	2.114	2.111	2
-2 5 1	2.057	2.056	2
-1 5 4	1.959	1.957	2
0 7 2	1.925	1.923	15
1 6 3	1.828	1.828	2
0 6 4	1.798	1.798	5
1 3 5	1.773	1.771	2
0 2 6	1.754	1.753	2
0 5 5	1.734	1.727	27
-3 1 4	1.730	1.733	21
-1 7 4	1.631	1.630	2
2 4 4	1.611	1.612	5
-2 5 5	1.605	1.606	3

Table 3-3. Summary of Crystallographic Data for Cs₂Sb₄S₈ and CsSbS₆.

	I	II
Formula	Cs ₂ Sb ₄ S ₈	CsSbS ₆
FW	504.65	447.02
a, Å	6.743(1)	5.885(2)
b, Å	9.577(2)	14.413(2)
c, Å	6.367(1)	11.079(2)
α, deg	91.63(1)	90.000
β, deg	104.83(1)	101.69(2)
γ, deg	80.57(1)	90.000
Z; V, Å ³	1; 392	4; 920
λ (Mo Kα)	0.71073	0.71073
space group	P-1 (No. 2)	P2 ₁ /n (No. 14)
D _{calc.} , g/cm ³	4.275	3.226
μ, cm ⁻¹	124.08 (Mo Kα)	81.158 (Mo Kα)
2θmax, deg	60 (Mo Kα)	60 (Mo Kα)
Temp., °C	23	23
Final R/R _w , %	3.2/4.9	2.5/3.9
Total Data Measured	2350	2826
Total Unique Data (Ave.)	2182	2609
Data F _o ² > 3σ(F _o ²)	1889	1926
No. of Variables	65	74
Crystal Dimensions	0.20x0.50x0.70 mm	0.12x0.20x0.30 mm

$$* R = \Sigma(|F_o| - |F_c|) / \Sigma|F_o| \quad R_w = \{\Sigma w(|F_o| - |F_c|)^2 / \Sigma w|F_o|^2\}^{1/2}$$

Table 3-4. Fractional Atomic Coordinates and B_{eq} Values for $Cs_2Sb_4S_8$ with Estimated Standard Deviations in Parentheses.

atom	x	y	z	B(eq)
Cs(1)	0.16496(7)	0.06678(5)	1.32325(8)	1.83(2)
Sb(1)	-0.18018(7)	0.45220(5)	0.66230(8)	1.51(2)
Sb(2)	0.40888(7)	0.32190(5)	0.92176(8)	1.42(2)
S(1)	-0.1566(3)	0.4058(2)	0.2934(3)	1.53(7)
S(2)	0.5781(3)	0.0751(2)	1.0945(3)	1.65(7)
S(3)	0.0745(3)	0.2366(2)	0.8152(3)	1.49(6)
S(4)	0.5233(3)	0.2837(2)	0.5893(3)	1.73(7)

Table 3-5. Fractional Atomic Coordinates and B_{eq} Values for $CsSbS_6$ with Estimated Standard Deviations in Parentheses.

atom	x	y	z	B(eq)
Cs	-0.0826(1)	0.40998(4)	0.18541(5)	2.82(2)
Sb	0.02834(8)	0.09589(4)	0.11379(4)	1.62(2)
S(1)	-0.0049(4)	0.0694(1)	-0.1242(2)	2.05(7)
S(2)	0.1085(4)	0.0673(2)	0.3633(2)	2.37(7)
S(3)	0.0089(3)	0.1923(2)	0.4244(2)	2.28(7)
S(4)	-0.3439(4)	0.1818(2)	0.4124(2)	2.37(8)
S(5)	0.5085(3)	0.2270(1)	0.2373(2)	2.10(7)
S(6)	0.4558(3)	0.1142(1)	0.1209(2)	1.90(7)

$$a) B_{eq} = (4/3)[a^2B(1,1) + b^2B(2,2) + c^2B(3,3) + ab(\cos\gamma)B(1,2) + ac(\cos\beta)B(1,3) + bc(\cos\alpha)B(2,3)].$$

3. Results and Discussion

3.1. Synthesis and Spectroscopy

The syntheses of $\text{Cs}_2\text{Sb}_4\text{S}_8$ and CsSbS_6 were a result of a redox reaction in which the Sb metal is oxidized by polysulfide ions to give Sb^{3+} species. CsSbS_6 was formed from a Sb/ Cs_2S /S ratio of 1/1/9 at 260°C while $\text{Cs}_2\text{Sb}_4\text{S}_8$ can be obtained at 280°C with a ratio of 1/0.9-1.1/8. $\text{Cs}_2\text{Sb}_4\text{S}_8$ appears to be more thermodynamically stable than CsSbS_6 under similar acidic flux conditions. This is supported by thermal analysis data which reveal that CsSbS_6 decomposes to $\text{Cs}_2\text{Sb}_4\text{S}_8$ upon heating (vide infra).

The IR spectroscopic data for CsSbS_6 show absorptions at 484, 473 and 448 cm^{-1} , which we assign to S-S stretching vibrations. Similar absorbances were not observed in $\text{Cs}_2\text{Sb}_4\text{S}_8$ because the S-S bond resides on a center of symmetry. However, the S-S stretching mode is Raman-active and occurs at 474 cm^{-1} . The absorbances found at lower energy for CsSbS_6 (365-195 cm^{-1}) and $\text{Cs}_2\text{Sb}_4\text{S}_8$ (341-233 cm^{-1}) have been tentatively assigned as Sb-S vibrations.

The optical properties of (I) and (II) were assessed by studying the UV/near-IR reflectance spectra of the materials. The spectra confirm the semiconductor nature of the materials by revealing the presence of sharp optical gaps as shown in Figure 3-1. Both compounds exhibit steep absorption edges from which the band-gap, E_g , can be assessed at 2.05 and 2.25 eV respectively. By comparison, the corresponding band-gap of Sb_2S_3 is 1.7 eV.²² A linear relationship is found in both compounds if the square of the

absorption coefficient, $(\alpha/S)^2$ is plotted vs. $(E-E_g)$ suggesting that the band gaps are direct in nature.²³ However, independent confirmation is needed to verify this conclusion. The relatively good air and moisture stability of CsSb₂S₄ and its excellent optical transparency below 2.05 eV make it a good candidate for exploration of its linear and non-linear optical properties. The optical absorption spectrum of (I I) also features absorbances at higher energy which are due to other electronic transitions in the solid, perhaps within the S₅²⁻ fragment.

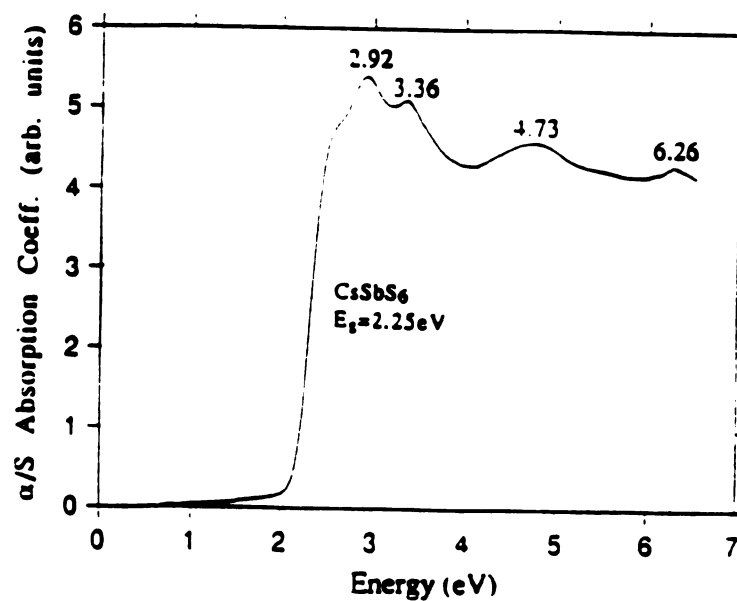
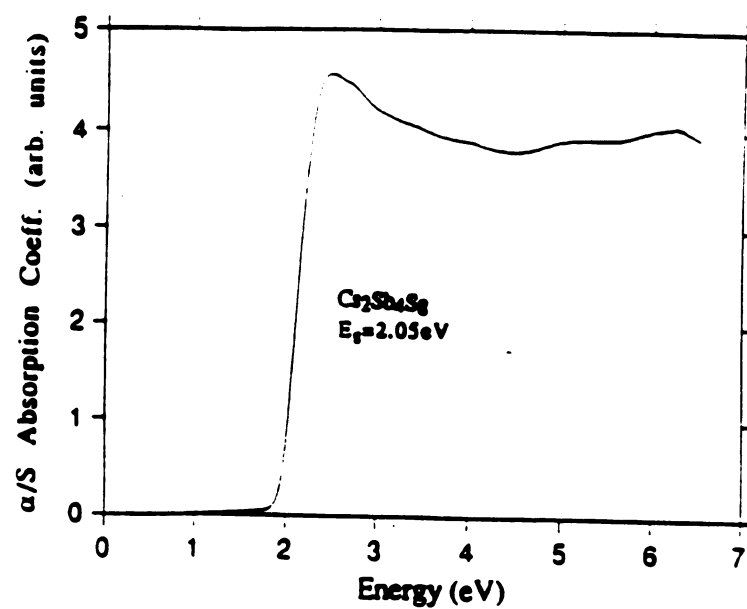


Figure 3-1. (A) Optical absorption spectrum of $\text{Cs}_2\text{Sb}_4\text{S}_8$. (B) Optical absorption spectrum of CsSbS_6 .

3.2 Description of Structures

Structure of $\text{Cs}_2\text{Sb}_4\text{S}_8$ (I). (I) is isostructural to the hydrothermally prepared, $\text{Cs}_2\text{Sb}_4\text{Se}_8$.¹⁶ At the most fundamental level this structure is made up of condensed SbS_3^{3-} pyramids and S_2^{2-} units. Although, overall this structure is three-dimensional, it is assembled by cross-linking one-dimensional $[\text{Sb}_4\text{S}_6]$ parallel chains with disulfide ligands to form sheets that are parallel to the (011) crystallographic plane. Figure 3-2 shows a view of an individual layer of $[\text{Sb}_4\text{S}_8]_n^{n-}$. The layer can alternatively be described as being composed of 14-membered rings of alternating Sb-S atoms and S_2 units. The rings are connected in two dimensions by Sb-S-Sb linkages to form the layer. The layers stack one on top of the other with their 14-membered rings in registry so that they form channels running down the c-axis. The channels are clearly visible in Figure 3-3A. Long Sb-S interactions (3.456(2) Å) between sheets give rise to a second set of channels running down the a-axis that are filled with ten-coordinate Cs^+ ions (Cs-S mean=3.62(4) Å) (Figure 3-3B). Due to these long Sb-S interactions between the sheets, the structure possesses pseudo three-dimensional character. Selected bond distances and bond angles for (I) are given in Table 3-6.

Sb(1) is found in a distorted square pyramidal coordination due to the stereochemically active lone pair at the base of the pyramid (Figure 3-3B). This type of coordination is found in Sb_2S_3 (stibnite).²⁴ The four Sb(1)-S bonds range from 2.418(2) to 2.783(2) Å with a fifth coordination site occupied by a weakly interacting S(4) that has a distance of 3.277(2) Å (Figure 3-3B). This distance is

considerably shorter than the sum of the Sb-S Van der Waals radii (4.05 Å).²⁵ These distances, ranging from the Sb-S bond at 2.418(2) Å to the interaction at 3.277(2) Å, are very comparable to those found in other ternary antimony (III) sulfides, such as Cs₃Sb₅S₉⁵ and β-Rb₂Sb₄S₇.⁸

The coordination environment of Sb(2) could be described as a trigonal pyramid with three bonds ranging from 2.440(2) to 2.592(2) Å (Figure 3-4B). The Sb(2) is also interacting with two sulfur atoms along the top of the trigonal pyramid. A strong interaction is found at 3.022(2) Å with S(1) and a weak interaction is observed with S(1'') at 3.456(2). This type of coordination is observed in Sb₂S₃ (Sb 1)²⁴ and CsSbS₂.^{1d}

Structure of CsSbS₆ (II). CsSbS₆ is the first example of a solid state antimony polysulfide compound. The only other known antimony polysulfide is the molecular dimeric antimony polysulfide complex [Sb₂S₁₅]²⁻ that has been recently prepared by Rauchfuss et al.²⁶ The novel one-dimensional structure of (II) is composed of Sb₂S₂ rhombi that are linked along the a-axis by pentasulfide ligands to form chains (Figure 3-4A). The formula can alternatively be expressed as CsSbS(S₅). These chains are separated by nine-coordinate Cs⁺ ions (mean Cs-S distance = 3.69(3) Å). Figure 3-4B shows the packing diagram of CsSbS₆, along the a-axis (chain axis). Selected bond distances and bond angles for (I) are given in Table 3-7.

The Sb is bonded to four sulfur atoms with bond distances ranging from 2.390(2) to 2.737(2) Å. The coordination around the Sb atom (including the lone pair) is trigonal bipyramidal with the lone

pair at the equatorial position. The repulsion by the lone pair gives rise to a nearly axial S(2)-Sb-S(1) angle of $162.10(6)^\circ$ and an S(1')-Sb-S(6) angle of $99.81(6)^\circ$ in the trigonal plane. The two axial Sb-S bonds ($2.635(2)$ Å, $2.737(2)$ Å) are longer than the two equatorial bonds ($2.390(2)$ Å, $2.515(2)$ Å). This combination of Sb coordination and variation in bond length has been seen in Sb(3) of $\text{Cs}_2\text{Sb}_4\text{S}_7$ ²⁷ where the axial bond lengths of $2.637(4)$ Å and $2.739(5)$ Å and equatorial bond lengths of $2.456(5)$ Å and $2.500(5)$ Å were observed. Several other phases have demonstrated these characteristics including β - $\text{Rb}_2\text{Sb}_4\text{S}_7$ (Sb 1,2)⁸, RbSbS_2 (Sb 1,2)^{1c}, $\text{SrSb}_4\text{S}_7 \cdot 6\text{H}_2\text{O}$ (Sb 4)¹², and $\text{Cs}_2\text{Sb}_8\text{S}_{13}$ (Sb 4).²⁸

The bridging mode of the μ_2 - S_5 ligand has been observed in the one-dimensional solid state compound, KAuS_5 ²⁹ and the basket-like dimer, $[\text{Mo}_2(\text{NO})_2(\text{S}_2)_3(\text{S}_5)(\text{OH})]^{3-}$.³⁰ Normal S-S bond distances are observed in the S_5^{2-} ligand ($2.058(5)$ Å mean).

Solid state compounds containing Q_x^{2-} ligands with $x > 3$ are rare. Some examples include NH_4CuS_4 ³¹, α, β - KCuS_4 ³², CsCuS_6 ³³, $(\text{NH}_4)_2\text{PdS}_{11}$ ³⁴, $\text{K}_2\text{PdSe}_{10}$ ³⁵, $(\text{Ph}_4\text{P})\text{AgSe}_4$ ³⁶, $(\text{Me}_4\text{N})\text{AgSe}_5$ ³⁶, KAuSe_5 ³⁷, $\text{K}_3\text{AuSe}_{13}$ ³⁷ and $\text{K}_2\text{Sn}_2\text{S}_8$.³⁸

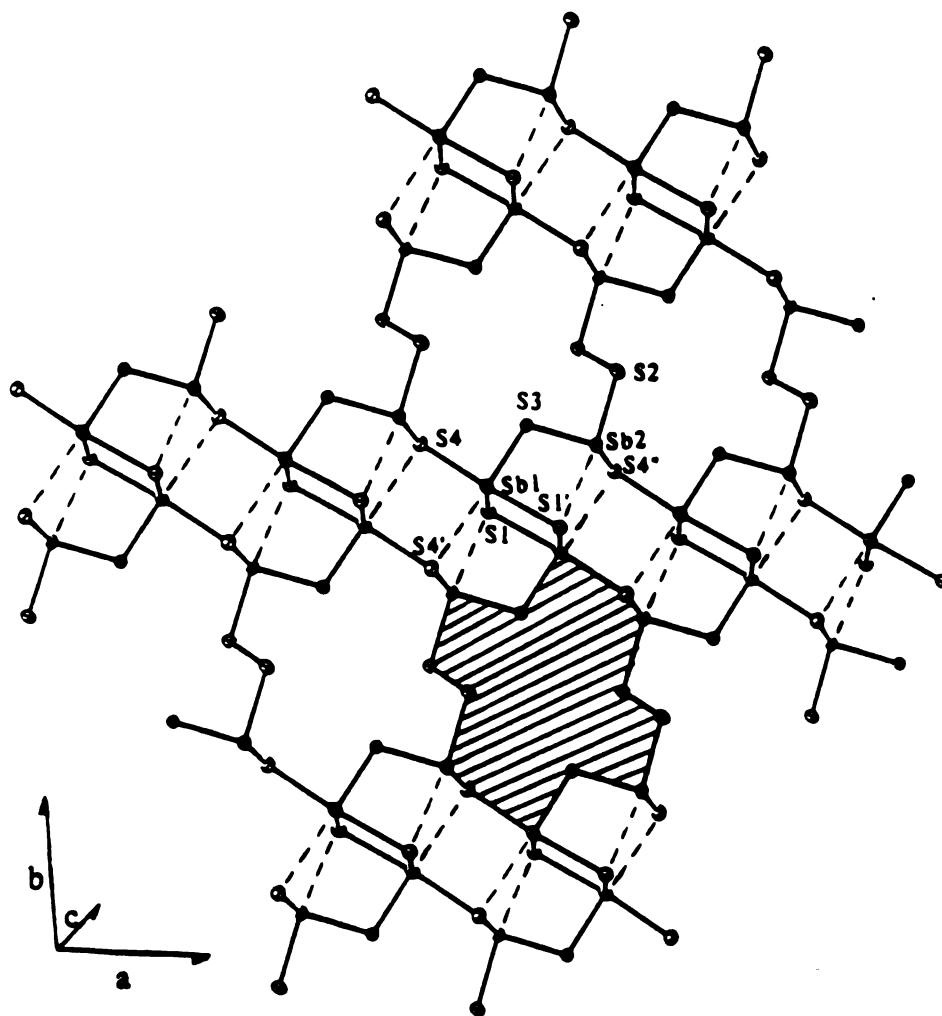


Figure 3-2. Two-dimensional structure of the $[\text{Sb}_4\text{S}_8]_n^-$ anionic framework with labeling as drawn by ORTEP. The dashed lines represent Sb-S long interactions in the range of 3.022(2) to 3.277(2) Å. The shaded area outlines the 14-membered Sb/S rings in the structure.

(A)



(B)

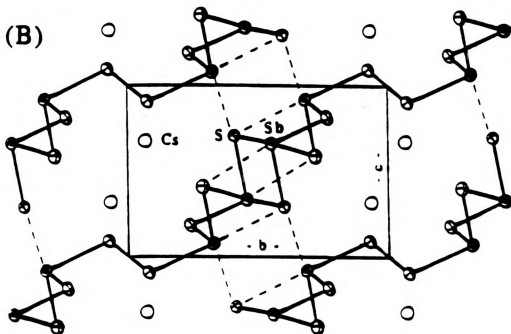
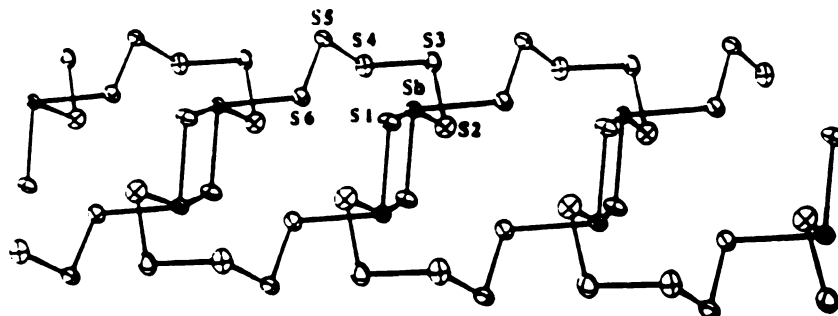


Figure 3-3. (A) Stereoview of $\text{Cs}_2\text{Sb}_4\text{S}_8$ viewed down the $[001]$ direction. (B) Packing diagram of $\text{Cs}_2\text{Sb}_4\text{S}_8$ showing a projection in the $[100]$ direction. The dashed lines represent long Sb-S interactions underscoring the pseudo-3D character of the structure. The shaded ellipsoids are Sb atoms and the open ellipsoids are Cs atoms.

(A)



(B)

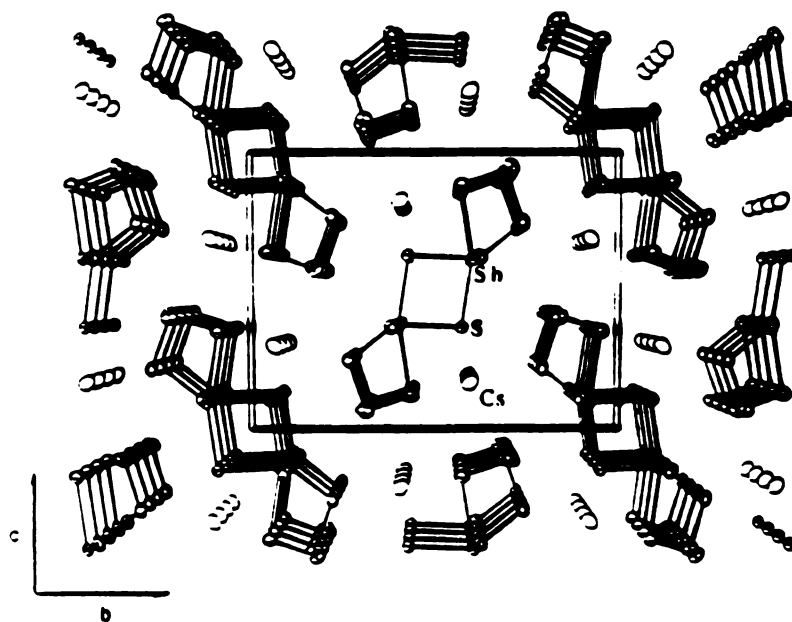


Figure 3-4. (A) Structure of a single $(\text{SbS}_6)_n^{n-}$ chain with labeling. (B) Packing diagram of CsSbS_6 looking down the a-axis (chain axis). The shaded ellipsoids are Sb atoms and the open ellipsoids are Cs atoms.

Table 3-6. Selected Distances (Å) and Angles (°) in Cs₂Sb₄S₈ with Standard Deviations in Parentheses.^a

Sb(1)-S(1)	2.418(2)	S(1')-Sb(1)-S(3)	87.79(6)
Sb(1)-S(1')	2.783(2)	S(1')-Sb(1)-S(4)	171.50(6)
Sb(1)-S(3)	2.501(2)	S(3)-Sb(1)-S(4')	173.65(6)
Sb(1)-S(4)	2.712(2)	S(1)-Sb(1)-S1')	86.47(6)
Sb(1)-S(4')	3.277(2)	S(1)-Sb(1)-S(3)	93.85(7)
Sb(2)-S(1)	3.022(2)	S(1')-Sb(2)-S(1'')	107.81(4)
Sb(2)-S(1'')	3.456(2)	S(1')-Sb(2)-S(2)	172.22(5)
Sb(2)-S(2)	2.592(2)	S(1')-Sb(2)-S(3)	83.55(6)
Sb(2)-S(3)	2.449(2)	S(1')-Sb(2)-S(4')	85.67(6)
Sb(2)-S(4)	2.430(2)	S(2')-Sb(2)-S(2)	79.18(5)
		S(2')-Sb(2)-S(3)	154.03(6)
S(2)-S(2')	2.092(4)		
Sb(1)-Sb(1')	3.798(1)	S(2')-Sb(2)-S(4')	103.23(6)
Sb(1)-Sb(2)	3.898(1)	S(2)-Sb(2)-S(4')	96.18(7)
Sb(2)-Sb(2')	3.833(1)	S(3)-Sb(2)-S(4')	100.83(7)
Cs-Cs'	3.913(1)		
Cs-S(1)	3.576(2)	Cs-S(3)	3.527(2)
Cs-S(2)	3.470(2)	Cs-S(3')	3.632(2)
Cs-S(2')	3.839(2)	Cs-S(3'')	3.534(2)
Cs-S(2'')	3.648(2)	Cs-S(4'')	3.518(2)
Cs-S(2''')	3.850(2)	Cs-S(4''')	3.632(2)
Ave. Cs-S	3.62(4)		

^aThe estimated standard deviations in the mean bond lengths and the mean bond angles are calculated by the equations $\sigma_l = \{\Sigma_n (l_n - l)^2 / n(n-1)\}^{1/2}$, where l_n is the length (or angle) of the n th bond, l the mean length (or angle), and n the number of bonds.

Table 3-7. Selected Distances (Å) and Angles (°) for CsSbS₆ with Standard Deviations in Parentheses.^a

Sb-S(6)	2.515(2)	S(2)-S(3)	2.052(3)
Sb-S(2)	2.737(2)	S(3)-S(4)	2.060(3)
Sb-S(1)	2.635(2)	S(4)-S(5)	2.063(3)
Sb-S(1')	2.390(2)	S(5)-S(6)	2.057(2)
Ave. Sb-S	2.57(8)	Ave. S-S	2.058(2)
		Sb-Sb'	3.711(2)
Cs-S(1)	3.582(2)	Cs-S(5)	3.693(2)
Cs-S(6)	3.629(2)	Cs-S(2)	3.718(2)
Cs-S(1')	3.630(2)	Cs-S(2')	3.786(2)
Cs-S(3)	3.676(2)	Cs-S(4)	3.822(2)
Cs-S(2)	3.679(2)	Ave. Cs-S	3.69(3)
S(6)-Sb-S(2)	90.87(6)	Sb-S(6)-S(5)	97.23(8)
S(6)-Sb-S(1)	85.31(6)	Sb-S(2)-S(3)	101.41(9)
S(6)-Sb-S(1')	99.81(6)	S(2)-S(3)-S(4)	105.4(1)
S(2)-Sb-S(1)	162.10(6)	Sb-S(1)-Sb	95.08(6)
S(2)-Sb-S(1')	78.47(6)	S(6)-S(5)-S(4)	108.7(1)
S(1)-Sb-S(1')	84.91(6)	S(3)-S(4)-S(5)	105.3(1)

^aThe estimated standard deviations in the mean bond lengths and the mean bond angles are calculated by the equations $\sigma_l = \{\Sigma_n (l_n - l)^2 / n(n-1)\}^{1/2}$, where l_n is the length (or angle) of the n th bond, l the mean length (or angle), and n the number of bonds.

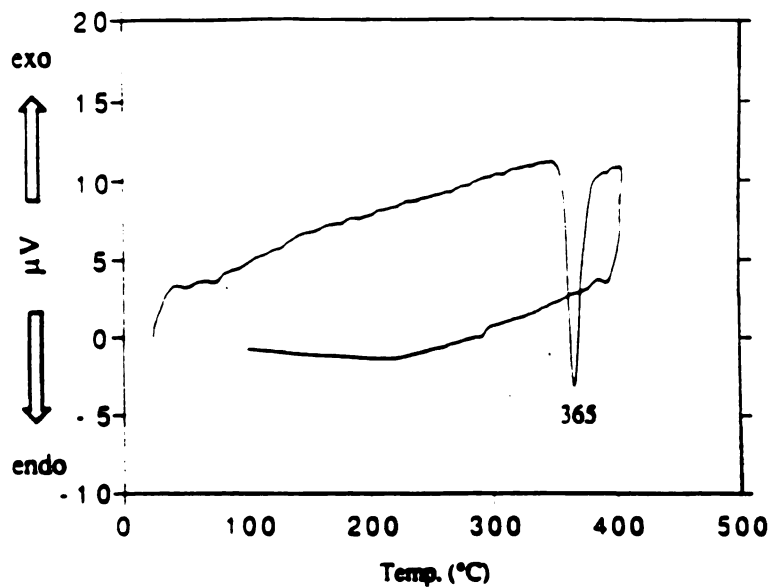
3.3 Thermal Analysis

The thermal behavior of (I) and (I I) was investigated with differential thermal analysis (DTA). Figure 3-5A shows that upon heating compound I, a sharp melting endotherm occurs at 365 °C. Upon cooling, no corresponding exothermic peak is observed, indicating that no crystallization takes place. Red glassy material was observed in the quartz ampule. Powder X-ray diffraction (XRD) of the sample at room temperature gave an amorphous pattern which is characteristic of a glassy material. Upon subsequent reheating a broad exotherm at 291 °C was observed, followed by two endotherms at 364 and 375 °C (see Figure 3-5B). We speculate that occasionally $\text{Cs}_2\text{Sb}_4\text{S}_8$ does not fully convert to glass due to small but significant differences in thermal conditions from run to run. XRD studies show that the exotherm at 291 °C is the result of crystallization of $\text{Cs}_2\text{Sb}_4\text{S}_7$ ^{28,39} from the glassy matrix (see Figure 3-6). Thus, upon heating, $\text{Cs}_2\text{Sb}_4\text{S}_8$ transforms to $\text{Cs}_2\text{Sb}_4\text{S}_7$ via an intermediate glassy state. The small endotherms at 364 and 375 °C are probably due to melting of excess glassy material and perhaps $\text{Cs}_2\text{Sb}_4\text{S}_7$.

Figure 3-7 shows that upon heating compound (I I), a sharp endotherm occurs at 232 °C. Upon cooling, no exothermic peak is observed indicating the absence of crystallization. XRD of the sample at room temperature gave $\text{Cs}_2\text{Sb}_4\text{S}_8$ and Cs_2S . The expelled sulfur was observed to deposit on the opposite end of the ampule from the

sample. The endothermic peak is due to the decomposition of CsSbS_6 to $\text{Cs}_2\text{Sb}_4\text{S}_8$.

(A)



(B)

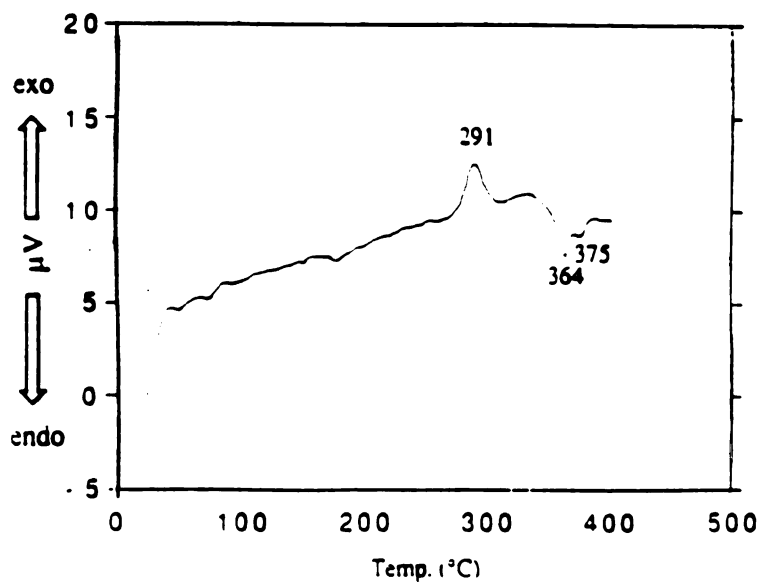
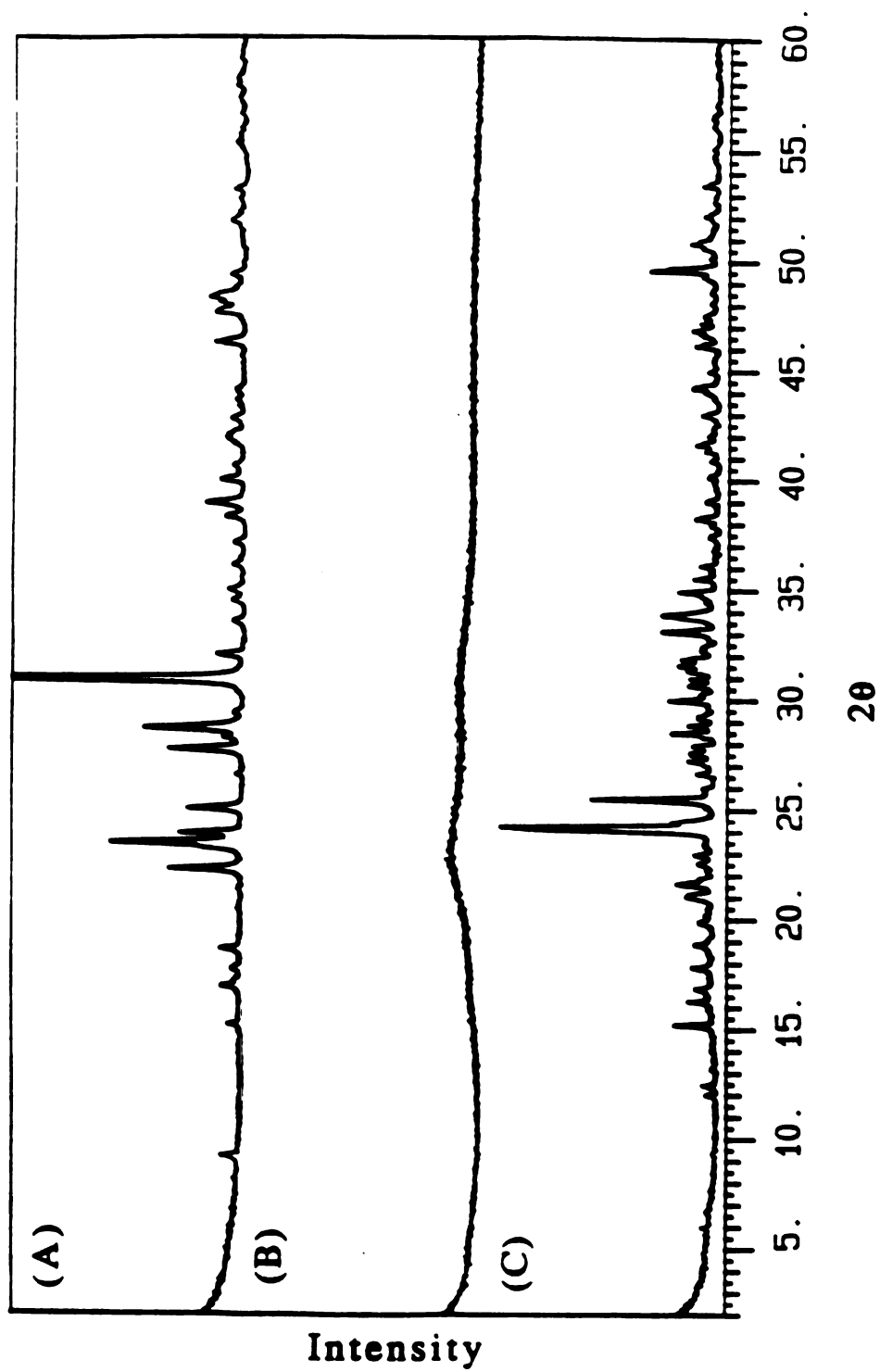


Figure 3-5. (A) Differential thermal analysis (DTA) data for $\text{Cs}_2\text{Sb}_4\text{S}_8$ showing the first heating and cooling cycle. Heat is absorbed at 365 °C as the material melts but is not released upon cooling. (B) Data for reheating showing the crystallization of $\text{Cs}_2\text{Sb}_4\text{S}_7$ at 291 °C, followed by melting of the excess glass at 364 and 375 °C.

Figure 3-6: X-ray diffraction patterns of: (A) $\text{Cs}_2\text{Sb}_4\text{S}_8$ single crystals. (B) material heated to 400 °C then cooled (glassy state). (C) material after reheating to 310 °C (crystallization of $\text{Cs}_2\text{Sb}_4\text{S}_7$).



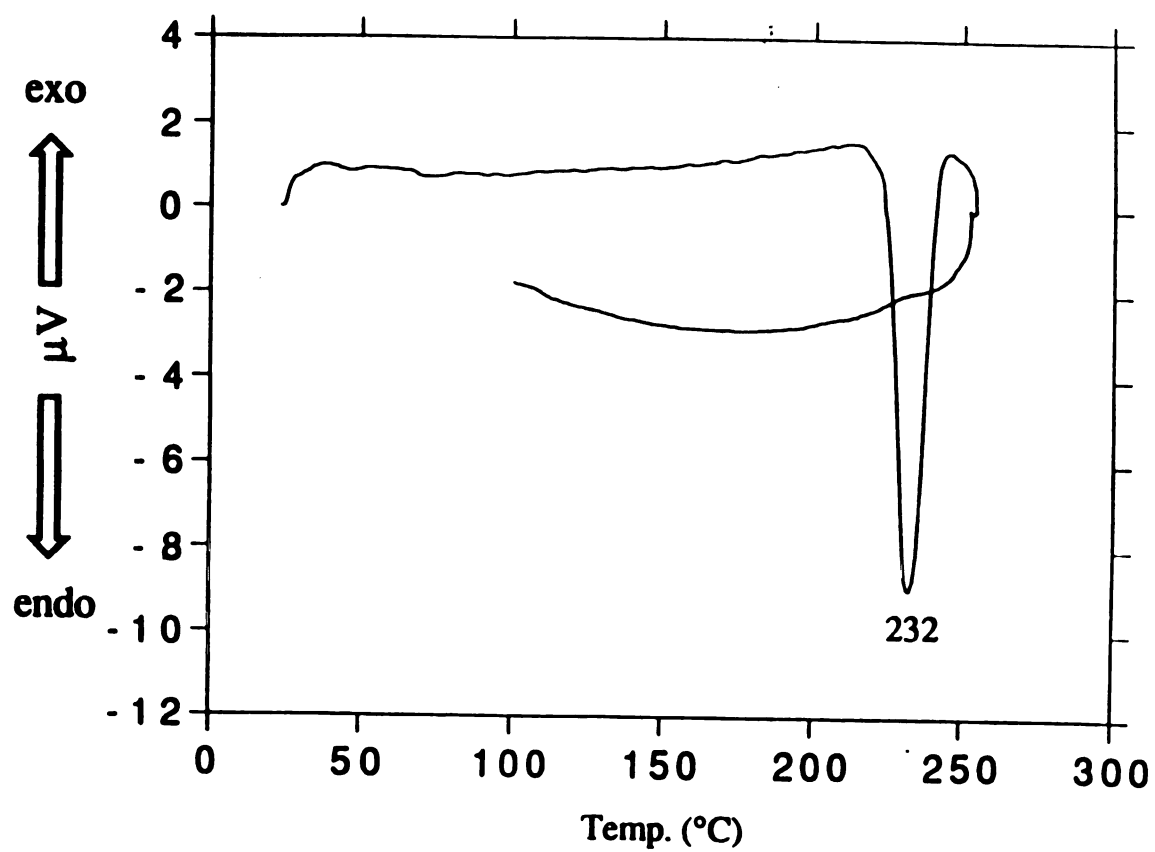


Figure 3-7. DTA of CsSbS_6 shows the endothermic peak at 232 °C corresponding to the decomposition of CsSbS_6 to $\text{Cs}_2\text{Sb}_4\text{S}_8$.

3.4. Conclusion

In summary, we have synthesized the first two examples of polysulfide ligands in solid state antimony compounds using Cs_2S_x fluxes at low temperature ($< 300\text{ }^\circ\text{C}$). (I) and (I I) possess abrupt absorption edges with bandgaps, E_g , of 2.05 and 2.25 eV respectively. (I I) decomposes to (I) at $232\text{ }^\circ\text{C}$ and (I) forms a glass at $365\text{ }^\circ\text{C}$ which transforms to $\text{Cs}_2\text{Sb}_4\text{S}_7$ upon reheating.

It is remarkable that two new phases could be uncovered in a somewhat crowded antimony/sulfide field. Since it appears that ternary antimony (III) sulfides can form many different structure types, we are expanding our effort in the search for new ternary antimony (III) chalcogenides while focusing on relatively low reaction temperatures. The participation of polychalcogenide ligands in solid state frameworks promises to yield new solids with relative open or flexible structures. This work provides concrete evidence that temperatures in combination with alkali polychalcogenide fluxes are excellent reaction media for exploration of new metastable compounds.

List of References

1. (a) Olivier-Fourcade, E.; Phillippot, J.; M. Maurin *Z. Anorg. Allg. Chem.*, 1978, **446**, 159-168. (b) Graf, H. A.; Schafer, H. *Z. Anorg. Allg. Chem.*, 1975, **414**, 211-219. (c) Kanishcheva, A. S.; Kuznetsov, V. G.; Lazarev, V. B.; Tarasova, T. G. *Zh. Strukt. Khim.*, 1977, **18**, 1069. (d) Kanishcheva, A. S.; Mikhailov, Y. N.; Kuznetsov, V. G.; Batog, V. N. *Dokl. Akad. Nauk SSSR*, 1980, **251**, 603-605.
2. Cordier, G.; Schafer, H. *Revue de Chemie Minerale*, 1981, **18**, 218-223.
3. Dorrscheidt, W.; Schafer, H. *Z. Naturforsch.*, 1981, **36b**, 410-414.
4. Cordier, G.; Schwidetzky, C.; Schafer, H. *Revue de Chemie Minerale*, 1982, **19**, 179-186.
5. Parise, J. B.; Ko, Y. *Chem. Mater.* 1992, **4**, 1446-1450.
6. Sheldrick, W. S.; Hausler, H.-J. *Z. Anorg. Allg. Chem.* 1988, **561**, 149-156.
7. Dittmar, V. G.; Schafer, H. *Z. Anorg. Allg. Chem.* 1978, **441**, 93-97.
8. Sheldrick, W. S.; Hausler, H.-J. *Z. Anorg. Allg. Chem.* 1988, **557**, 105-111.
9. Parise, J. B. *J. Chem. Soc., Chem. Commun.*, 1990, **22**, 1553-1554.
10. Eisenmann, B.; Schafer, H. *Z. Naturforsch.*, 1979, **34b**, 383-385.
11. Graf, H. A.; Schafer, H. *Z. Naturforsch.* 1972, **27b**, 735-739.
12. Gostojic, M.; Nowacki, W.; Engle, P. *Z. Kristallogr.* 1982, **159**, 217-224.
13. Dittmar, V. G.; Schafer, H. *Z. Anorg. Allg. Chem.*, 1977, **437**, 183-187.
14. Cordier, G.; Schafer, H.; Schwidetzky, C. *Z. Anorg. Allg. Chem.*, 1984, **39b**, 131-134.
15. (a) Kanatzidis, M. G. *Chem. Mater.* 1990, **2**, 353-363. (b) Kanatzidis, M. G.; Park, Y. *J. Am. Chem. Soc.* 1990, **111**, 3767-3769. (c) Kanatzidis, M. G.; Park, Y. *Chem. Mater.* 1990, **2**, 99-101. (d) Park, Y.; Kanatzidis, M. G. *Angew. Chem. Int. Ed. Engl.* 1990, **29**, 914-915. (e) Sunshine, S. A.; Kang, D.; Ibers, J. A. *J. Am. Chem. Soc.* 1987, **109**, 6202-6204. (f) Kang, D.; Ibers, J. A. *Inorg. Chem.* 1989, **27**, 549-551.
16. Sheldrick, W. S.; Kaub, J. *Z. Anorg. Allg. Chem.* 1986, **536**, 114-118.
17. Feher, F. *Handbuch der Präparativen Anorganischen Chemie*: G. Brauer; Ed.; Ferdinand Enke: Stuttgart, Germany, 1954.
18. (a) Wendlandt, W. W.; Hecht, H. G. "Reflectance Spectroscopy", Interscience Publishers, 1966 (b) Kotüm, G. "Reflectance Spectroscopy", Springer Verlag, New York, 1969 (c) Tandon, S. P.; Gupta, J. P. *Phys. Stat. Sol.* 1970, **38**, 363-367.
19. Sheldrick, G. M. In *Crystallographic Computing 3*; Sheldrick, G. M., Kruger, C., Doddard, R., Eds.; Oxford University Press: Oxford, England, 1985; pp 175-189.
20. TEXSAN: Single Crystal Structure Analysis Software, Version 5.0, (1981). Molecular Structure Corporation, The Woodlands, TX 77381.
21. Walker, N.; Stuart, D. *Acta Crystallogr.*, 1983, **A39**, 158-166.
22. Bube, R. H. "Photoconductivity of Solids", John Wiley and Sons, Inc., 1960; pp. 233-235.
23. Pankove, J. I. in "Optical Processes in Semiconductors" Dover Publications, New York, 1975.
24. Hofmann, W. *Z. Kristallogr.* 1933, **86**, 225.
25. Pauling, L. *The Nature of the Chemical Bond*, 3rd Edition, New York: Cornell University Press, 1966, p. 260.
26. Partha, P. P.; Rauchfuss, T. B.; Wilson, S. R. *J. Am. Chem. Soc.* 1993, **115**, 3316-3317.
27. Dittmar, V. G.; Schafer, H. *Z. Anorg. Allg. Chem.* 1978, **441**, 98-102.
28. Volk, K.; Schafer, H. *Z. Naturforsch.* 1979, **34b**, 1637-1640.

29. Park, Y.; Kanatzidis, M. G. To be submitted for publication.
30. Muller, A.; Eltzner, W.; Bogge, H.; Krickemeyer, E. *Angew. Chem. Int. Ed. Engl.* 1983, 22, 884-885.
31. Burschka, C. *Z. Naturforsch.* 1980, 35B, 1511-1513.
32. Kanatzidis, M. G.; Park Y. *J. Am. Chem. Soc.* 1989, 111, 3767-3769.
33. McCarthy, T. J.; Zhang X.; Kanatzidis, M. G. *Inorg. Chem.*, 1993, 32, 2944-2948.
34. Haradem, P. S.; Cronin, J. L.; Krause, R. A.; Katz, L. *Inorg. Chim. Acta* 1977, 25, 173-179.
35. Kim, K.-W.; Kanatzidis, M. G. *J. Am. Chem. Soc.* 1992, 114, 4878-4883.
36. Huang, S.-P.; Kanatzidis, M. G. *Inorg. Chem.* 1991, 30, 1455-1466.
37. Park, Y.; Kanatzidis, M. G. *Angew. Chem. Int. Ed. Engl.* 1990, 29, 914-915.
38. Liao, J.-H.; Varotsis, C.; Kanatzidis, M. G. *Inorg. Chem.*, 1993, 32, 2453-2462.
39. Indexed Cs₂Sb₄S₇ using "Powder Diffraction File-Inorganic Phases", vol. 32, pg. 214, (1987). Five additional low intensity peaks were also observed which could be due to the presence of a small amount of impurity.

CHAPTER 4

New Quaternary Bismuth and Antimony Thiophosphates $ABiP_2S_7$ (A=K,Rb), $A_3M(PS_4)_2$ (A=K,Rb,Cs; M=Sb,Bi), $Cs_3Bi_2(PS_4)_3$, and $Na_{0.16}Bi_{1.28}P_2S_6$ in Molten Alkali Metal Polythiophosphate Fluxes.

1. Introduction

Recent advances in the development of alkali polychalcogenide fluxes as reaction media at intermediate temperatures ($200 < T < 500^\circ\text{C}$) produced a variety of new ternary and quaternary chalcogenides.¹ This method is particularly useful in stabilizing structural fragments which are not stable at higher temperatures such as long S_x^{2-} ($x=4,5,6$) units.² During our studies with polychalcogenides, we noticed that another set of main group structural units, namely the various thiophosphates $[P_xS_y]^{n-}$, were also rather uncommon in their occurrence in solid state compounds. With the exception of the important MPS_3 class of compounds,³ which contains the ethane-like $[P_2S_6]^{4-}$ ligand, $[P_xS_y]^{n-}$ containing solids are relatively rare. Even

the elementary tetrahedral $[\text{PS}_4]^{3-}$ unit is found only in few compounds.^{4,5,6} A new class of thiophosphates with Group 5 transition metals has been reported and reviewed by Evain et al.⁷ These compounds exhibit structural diversity due to a variety of anionic P/S ligands and a tendency for low dimensionality. Transition metal thiophosphates are of potential importance as low-dimensional cathode materials for secondary lithium batteries.⁸ These compounds are typically synthesized by direct combination of the elements at high temperature (500-800°C).

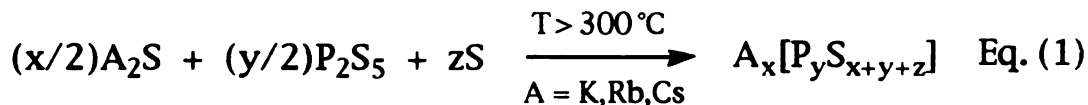
Several main group metal thiophosphates have interesting physical properties as well. InPS_4^{4a} crystallizes in a noncentrosymmetric tetragonal space group (I-4) which gives rise to a high non-linear optical susceptibility and piezo-coefficients⁹ while crystals of GaPS_4^{4b} exhibit a considerable birefringence.¹⁰ $\text{Sn}_2\text{P}_2\text{S}_6$ crystallizes in the acentric space group Pc and undergoes a second order, exothermic phase transition from ferroelectric (Pc) to paraelectric ($\text{P2}_1/\text{c}$) at 60 °C.¹¹ This compound has been shown to be a promising ferroelectric material for use in memory devices.¹²

To date, very little effort has been invested in the synthesis of *quaternary* metal thiophosphate compounds at intermediate temperatures. Thus, we are interested to develop a general methodology by which new thiophosphate (or chalcophosphate) compounds can be consistently obtained in a similar fashion that we have observed in polychalcogenides. Here we report the use of novel low-melting (300-400°C) alkali metal *polythiophosphate* fluxes to synthesize new quaternary metal thiophosphates. This temperature window should allow access to new, metastable compounds that may

not be thermodynamically stable at higher temperatures. Also, we can gain further insight into the complicated Lewis acid-base equilibria that exist among $[P_2S_6]^{4-}$, $[P_2S_6]^{2-}$, $[P_2S_7]^{4-}$, and $[PS_4]^{3-}$ ligands at high temperatures.¹³

We have applied this new molten salt flux to Group 15 (Bi and Sb) metals and application to other p-block elements and transition metals seems very promising.¹⁴ Using these fluxes, we prepared the new compounds $ABiP_2S_7$ ($A=K,Rb$), $A_3M(PS_4)_2$ ($A=K,Rb,Cs$; $M=Sb,Bi$), $Cs_3Bi_2(PS_4)_3$, and $Na_{0.16}Bi_{1.28}P_2S_6$. The structural diversity ranges from the helical one-dimensional noncentrosymmetric chains of $A_3M(PS_4)_2$ and the layered compounds, $ABiP_2S_7$ and $Cs_3Bi_2(PS_4)_2$, to the dense three-dimensional framework of $Na_{0.16}Bi_{1.28}P_2S_6$. Their synthesis, structural characterization, optical and thermal properties are reported.

The formation of molten alkali metal thiophosphate fluxes results from the fusion of alkali metal sulfide, phosphorous pentasulfide, and elemental sulfur (see equation 1).



We view the $A_x[P_yS_z]$ fluxes as a significant variation over the A_2S_x fluxes in that they provide not just P atoms but excess $[P_xS_y]^n-$ anions which act as mineralizers. In other words, the acid/base characteristics of the $A_x[P_yS_z]$ fluxes are very different from those of the A_2S_x fluxes in that they tend to be more basic.¹ The chemical properties of these melts can be controlled by the ratios of their constituent elements. The relatively good solubility properties of

$A_x[P_yS_z]$ salts in water and organic solvents allow for easy isolation of products.

2. Experimental Section

2.1. Reagents

Chemicals in this work were used as obtained: (i) antimony powder, 99.999+% purity, -200 mesh, Cerac Inc., Milwaukee, WI. (ii) bismuth powder, 99.999% purity, -100+200 mesh, Johnson Matthey/AESAR Group, Seabrook, NH; (iii) potassium metal, Aldrich Chemical Co., Inc., Milwaukee, WI; (iv) rubidium metal and cesium metal, analytical reagent, Johnson Matthey/AESAR Group, Seabrook, NH; (v) phosphorous pentasulfide, 99% purity, Aldrich Chemical Co., Inc., Milwaukee, WI; (vi) sulfur powder, sublimed, J. T. Baker Chemical Co., Phillipsburg, NJ. (vii) methanol, anhydrous, Mallinckrodt Inc., Paris, KY. (viii) diethyl ether, ACS anhydrous, EM Science, Inc., Gibbstown, NJ.

2.2. Synthesis

All manipulations were carried out under a dry nitrogen atmosphere in a Vacuum Atmospheres Dri-Lab glovebox. For the preparation of K_2S , Rb_2S , and Cs_2S we used a modified literature procedure.¹⁵ The preparation of K_2S is reported in Section 2.2 of Chapter 2 (Part 2) and that of Cs_2S is reported in Section 2.2 of Chapter 2 (Part 1). The preparation of Rb_2S is the same as that of Cs_2S .

Na₂S. An amount of 2.440 g (0.076 mol) sulfur and 3.50 g (0.152 mol) freshly sliced sodium metal were added to a 250 ml round-bottom flask. A 150 ml volume of liquid ammonia was condensed into the flask at -78 °C (dry ice/acetone) under nitrogen to give a light blue solution. The NH₃ was removed by evaporation under a flow of nitrogen as the bath slowly warmed to room temperature. The pale yellow solid (98% yield) was dried under vacuum overnight, flame-dried, and ground to a fine powder with a mortar and pestle in the glovebox.

KBiP₂S₇ (I). An amount of 0.031 g (0.15 mmol) Bi, 0.100 g (0.450 mmol) P₂S₅, 0.033 g (0.30 mmol) K₂S, and 0.019 g (0.60 mmol) S were thoroughly mixed and transferred to a 6ml pyrex tube which was subsequently flamed sealed in vacuo (~10⁻³ torr). The reaction was heated to 400 °C over 12 hours in a computer-controlled furnace. It was kept at 400 °C for 4 days, followed by cooling to 110 °C at a rate of 4 °C/hr, then to room temperature in one hour. The excess yellow-colored K_xP_yS_z matrix was removed from the red crystals (68% yield) with dimethylformamide (DMF). The crystals are air and water stable. Semi-quantitative microprobe analysis on red crystals gave K_{1.0}Bi_{1.4}P_{2.4}S_{9.3} (average of three data acquisitions). Far-IR (CsI matrix) show absorptions at 600(s), 583(s), 576(ssh), 564(msh), 557(msh), 526(wsh), 464(vs), 412(w), 300(vw), 270(wsh), 250(msh), 247(m), 238(msh), 227(wsh), 208(wsh), 203(wsh), 192(vw), 174(vw), 169(vw), 157(vw), and 149(vw) cm⁻¹.

RbBiP₂S₇ (II). An amount of 0.031 g (0.15 mmol) Bi, 0.100 g (0.450 mmol) P₂S₅, 0.061 g (0.30 mmol) Rb₂S, and 0.029 g (0.90

mmol) S was mixed and heated as above except at 420 °C. Isolation as above gave 0.050 g of red crystals (57% yield, based on Bi). The compound was found to be isostructural to KBiP_2S_7 by powder X-ray diffraction. Semi-quantitative microprobe analysis on red crystals gave $\text{Rb}_{1.0}\text{Bi}_{1.3}\text{P}_{1.9}\text{S}_{7.4}$ (average of three data acquisitions).

$\text{K}_3\text{Sb}(\text{PS}_4)_2$ (III). An amount of 0.018 g (0.15 mmol) Sb, 0.067 g (0.30 mmol) P_2S_5 , 0.033 g (0.30 mmol) K_2S , and 0.029 g (0.90 mmol) S were thoroughly mixed and heated as in (I) above, except at 410 °C. The product was isolated by dissolving the flux with degassed DMF under inert atmosphere and then washing with anhydrous ether to give 0.045 g of yellow needle-like crystals (54% yield, based on Sb). Semi-quantitative microprobe analysis on single crystals gave $\text{K}_{1.8}\text{Sb}_{1.0}\text{P}_{1.7}\text{S}_{7.6}$ (average of three data acquisitions). Far-IR (CsI matrix) show absorptions at 620(m), 612(s), 579(s), 563(s), 546(w), 511(m), 494(m), 409(m), 325(m), 310(m), 287(w), 268(w), 253(w), 238(w), and 167(w) cm^{-1} .

$\text{Rb}_3\text{Sb}(\text{PS}_4)_2$ (IV). An amount of 0.036 g (0.30 mmol) Sb, 0.133 g (0.60 mmol) P_2S_5 , 0.122 g (0.60 mmol) Rb_2S , and 0.038 g (1.20 mmol) S were mixed and heated as in (I) above, except at 450 °C. The product was isolated by dissolving the flux with degassed DMF under inert atmosphere and then washing with anhydrous ether. Final washing with H_2O , MeOH, and ether gave 0.090g of yellow needle-like crystals (43% yield, based on Sb). Semi-quantitative microprobe analysis on single crystals gave $\text{Rb}_{1.7}\text{Sb}_{1.0}\text{P}_{1.5}\text{S}_{6.2}$ (average of three data acquisitions). Far-IR (CsI matrix) show absorptions at 632(s), 624(s), 611(s), 581(s), 564(s),

544(w), 535(w), 510(s), 493(w), 409(w), 341(m), 325(m), 315(m), 298(m), 266(w), 256(w), 240(w), 200(w), 183(w) and 149(w) cm^{-1} .

Cs₃Sb(PS₄)₂ (V). An amount of 0.024 g (0.20 mmol) Sb, 0.067 g (0.30 mmol) P₂S₅, 0.119 g (0.40 mmol) Cs₂S, and 0.077 g (2.40 mmol) S were mixed and heated as in (I) above. The product was isolated as in (I V) to give 0.107 g of yellow needle-like crystals (64% yield, based on Sb). Semi-quantitative microprobe analysis on single crystals gave Cs_{3.0}Sb_{1.0}P_{2.0}S_{8.9} (average of three data acquisitions). Far-IR (CsI matrix) show absorptions at 621(m), 605(s), 577(s), 560(s), 508(m), 493(m), 408(w), 329(w), 316(s), 298(w), 266(w), 262(w), 238(w), 189(w), and 164(w) cm^{-1} .

K₃Bi(PS₄)₂ (VI). An amount of 0.031 g (0.15 mmol) Bi, 0.067 g (0.30 mmol) P₂S₅, 0.066 g (0.60 mmol) Cs₂S, and 0.058 g (1.80 mmol) S were mixed and heated as in (I V). The product was isolated by dissolving the flux with degassed DMF under inert atmosphere and then washing with anhydrous ether to give orange needles and white powder. Final washing with H₂O, MeOH, and ether gave 0.058 g of orange-brown needle-like crystals (60% yield, based on Bi). The crystals appear to be air sensitive. Semi-quantitative microprobe analysis on single crystals gave K_{2.1}Bi_{1.0}P_{1.6}S_{6.9} (average of three data acquisitions). Far-IR (CsI matrix) show absorptions at 616(m), 609(s), 571(s), 550(s), 516(m), 498(m), 412(w), 291(w), 266(w), 226(w), 201(w), 167(w), and 150(w) cm^{-1} .

Rb₃Bi(PS₄)₂ (VII). An amount of 0.031 g (0.15 mmol) Bi, 0.067 g (0.30 mmol) P₂S₅, 0.122 g (0.60 mmol) Rb₂S, and 0.058 g (1.80 mmol) S were heated to 450 °C over 12 hours then isothermed for 6 days, followed by cooling to 150 °C at a rate of 2 °C/hr, then to

room temperature in one hour. The product was isolated as in (I V) to give 0.048 g of orange-brown needle-like crystals (41% yield, based on Bi). The crystals appear to be air sensitive. Semi-quantitative microprobe analysis on single crystals gave $\text{Rb}_{2.1}\text{Bi}_{1.0}\text{P}_{1.2}\text{S}_{6.5}$ (average of three data acquisitions).

$\text{Cs}_3\text{Bi}(\text{PS}_4)_2$ (VIII). An amount of 0.031 g (0.15 mmol) Bi, 0.067 g (0.30 mmol) P_2S_5 , 0.089 g (0.30 mmol) Cs_2S , and 0.019 g (0.6 mmol) S were mixed and heated as in (I I I) above. The product (air and water stable) was isolated as in (V I) to give 0.062 g of orange needle-like crystals (45% yield, based on Bi). Semi-quantitative microprobe analysis on single crystals gave $\text{Cs}_{2.1}\text{Bi}_{1.0}\text{P}_{1.5}\text{S}_{6.3}$ (average of three data acquisitions). Far-IR (CsI matrix) show absorptions at 624(s), 616(s), 610(s), 570(s), 549(s), 513(m), 496(m), 412(w), 304(w), 293(m), 279(w), 264(m), 247(w), 231(m), 186(w), and 160(w) cm^{-1} .

$\text{Cs}_3\text{Bi}_2(\text{PS}_4)_3$ (IX). An amount of 0.031 g (0.15 mmol) Bi, 0.067 g (0.30 mmol) P_2S_5 , 0.179 g (0.60 mmol) Cs_2S , and 0.058 g (1.80 mmol) S were mixed and heated as in (V). The product was isolated as in (V I) to give a mixture of red rectangular block-like crystals ($\text{Cs}_3\text{Bi}(\text{PS}_4)_2$) and orange crystals ($\text{Cs}_3\text{Bi}_2(\text{PS}_4)_3$). Semi-quantitative microprobe analysis on red single crystals gave $\text{Cs}_{1.4}\text{Bi}_{1.0}\text{P}_{1.3}\text{S}_{5.5}$ (average of three data acquisitions). Far-IR (CsI matrix) of manually separated red crystals show absorptions at 585(m), 581(msh), 578(msh), 574(msh), 554(msh), 551(msh), 548(msh), 524(s), 516(s), 500(m), 413(w), 303(msh), 292(m), 261(m), 253(msh), and 239(w) cm^{-1} .

$\text{Na}_{0.16}\text{Bi}_{1.28}\text{P}_2\text{S}_6$ (X). An amount of 0.062 g (0.30 mmol) Bi, 0.200 g (0.90 mmol) P_2S_5 , 0.047 g (0.60 mmol) Na_2S , and 0.038 g (1.20 mmol) S were mixed as above and heated to 400 °C over 12 hours then isothermed for 6 days, followed by cooling to 120 °C at a rate of 4 °C/hr, then to room temperature in one hour. The product was isolated by dissolving the flux with degassed DMF under inert atmosphere and then washing with anhydrous ether to give 0.103 g of dark red chunky crystals (77% yield, based on Bi). Semi-quantitative microprobe analysis on single crystals gave $\text{Bi}_{1.0}\text{P}_{1.9}\text{S}_{5.4}$ (average of three data acquisitions). Elemental analysis at Oneida Research Services gave an Na/Bi ratio of 1.0:9.1. Far-IR (CsI matrix) show absorptions at 535(very broad), 434(s), 375(w), 280(s), 254(w), and 227(m) cm^{-1} .

2.3. Physical Measurements

The instruments and experimental setups for Infrared measurements, optical diffuse reflectance measurements, and quantitative microprobe analysis on SEM/EDS are the same as those in Chapter 2 (Part 1) (Section 2.3). The experimental setup for differential thermal analysis (DTA) is the same as that in Chapter 2 (Part 2) (Section 2.3).

2.4 X-ray Crystallography

The compounds were examined by X-ray powder diffraction (XRD) for the purpose of phase purity and identification. Accurate d_{hkl} spacings (Å) were obtained from the powder patterns recorded on a Rigaku rotating anode (Cu $K\alpha$) X-ray powder diffractometer,

Rigaku-Denki/RW400F2 (Rotaflex), at 45 kV and 100 mA with a 1 °/min scan rate. The results are summarized in Tables 4-1 to 4-3.

Single crystal X-ray diffraction data for $\text{K}_3\text{Bi}(\text{PS}_4)_2$ were collected with a Nicolet P3 four-circle automated diffractometer equipped with a graphite-crystal monochromator at -60 °C. The data were collected with an ω step scan technique because of the long a-axis of 23.894(8) Å. Due to the acentric $\text{P}2_12_12_1$ space group, Friedel pairs were collected so that the correct enantiomer could be refined. Refinement of the right-handed enantiomer gave $R/R_w=5.5/6.0$ while that of the left-handed enantiomer gave 8.0/8.7. In the $\text{A}_3\text{M}(\text{PS}_4)_2$ system, only the $\text{K}_3\text{Bi}(\text{PS}_4)_2$ member could be characterized by single crystal X-ray diffraction studies. Crystals of the other analogs were found to be twinned. The compounds are isostructural as evidenced by the similarity of their respective powder diffraction patterns (Figure 4-1).

Single crystal X-ray diffraction data for $\text{Cs}_3\text{Bi}_2(\text{PS}_4)_3$ and $\text{Na}_{0.16}\text{Bi}_{1.28}\text{P}_2\text{S}_6$ were collected at room temperature on a Rigaku AFC6 diffractometer and the $\omega/2\theta$ scan technique was used. None of the crystals showed any significant intensity decay as judged by three check reflections measured every 150 reflections throughout the data collections. The space groups were determined from systematic absences and intensity statistics. The structures were solved by direct methods of SHELXS-86¹⁶ and refined by full-matrix least-squares techniques of the TEXSAN package of crystallographic programs.¹⁷ An empirical absorption correction based on ψ -scans were applied to each data set, followed by a DIFABS¹⁸ correction to the isotropically refined structure. All atoms were eventually

refined anisotropically. All calculations were performed on a VAXstation 3100/76 computer.

In the case of $\text{Na}_{0.16}\text{Bi}_{1.28}\text{P}_2\text{S}_6$, one bismuth atom, one phosphorous atom, and three sulfur atoms were located on general positions. After least squares refinement, the isotropic temperature factor for Bi was rather high at 4.6 \AA^2 with $R/R_w = 20/25$. The occupancy and temperature factor of this atom were refined to give values of 0.56 and 3.5 \AA^2 respectively ($R/R_w = 15.6/18.2$). In order to maintain electroneutrality ($\text{Bi}_{1.12}\text{P}_2\text{S}_6$), +0.64 of charge must be compensated. At this stage of the refinement, it was apparent that Na must have been incorporated into the compound but no significant Na electron density peaks were observed. It was assumed that Na and Bi were disordered on the same site. Successive refinements taking into account this hypothesis resulted in a formula of $\text{Na}_{0.64}\text{Bi}_{1.12}\square_{0.24}\text{P}_2\text{S}_6$ (\square = vacancy) with an $R/R_w=15.9/18.4$. A final R/R_w of 7.6/8.4 was achieved after DIFABS correction and anisotropic refinement. Elemental analysis suggests that the Na/Bi ratio is 1.0/9.1 which is not consistent with the above refinement. Refinement using this formula gave $\text{Na}_{0.16}\text{Bi}_{1.28}\square_{0.56}\text{P}_2\text{S}_6$ (\square = vacancy) and an increase in the R/R_w (8.3/9.3).

The complete data collection parameters and details of the structure solution and refinement for (I), (V I), (IX), and (X) are given in Table 4-4. The coordinates of all atoms, average temperature factors, and their estimated standard deviations are given in Tables 4-5 to 4-8.

Table 4-1. Calculated and Observed X-ray Powder Diffraction Patterns for KBiP_2S_7 .

h k l	$d_{\text{calcd}}, \text{\AA}$	$d_{\text{obsd}}, \text{\AA}$	$I/I_{\text{max}} (\text{obsd})$
1 0 0	9.50	9.50	75
1 1 0	7.52	7.52	83
0 1 1	7.31	7.30	7
1 1 1	5.77	5.77	12
0 2 1	5.10	5.09	29
2 0 0	4.75	4.75	100
1 2 -1	4.50	4.50	25
2 1 0	4.43	4.43	53
0 1 2	4.27	4.26	11
1 0 -2	4.12	4.10	6
1 1 -2	3.91	3.90	9
1 3 0	3.77	3.76	16
1 3 1, 2 2 1	3.47, 3.46	3.47	51
1 2 2	3.40	3.40	4
2 0 -2	3.30	3.30	3
3 0 0	3.17	3.17	32
0 4 0	3.08	3.07	9
0 1 3	2.94	2.94	16
1 4 0	2.93	2.92	19
1 1 -3	2.82	2.82	11
1 4 1	2.78	2.78	9
0 2 3	2.72	2.72	5
3 2 -1	2.70	2.69	18
1 2 3	2.61	2.61	7
3 1 -2	2.55	2.55	8
3 1 2	2.53	2.53	16
2 1 3	2.491	2.491	5
1 4 -2	2.464	2.458	4
0 3 3	2.438	2.438	4
3 3 -1	2.421	2.420	12
1 5 0	2.382	2.378	60
1 3 3	2.357	2.336	3
0 0 4	2.274	2.273	5
4 1 1	2.253	2.257	10
2 4 2	2.240	2.243	7
1 0 -4	2.217	2.220	11
3 4 0	2.206	2.206	14
2 5 0	2.185	2.186	12
0 5 2	2.164	2.161	22
0 2 4	2.133	2.115	4
3 2 -3	2.073	2.072	5
2 1 4	2.015	2.003	4
3 3 3	1.924	1.902	5
5 1 0	1.878	1.881	9
3 0 -4	1.856	1.856	5
5 1 -1	1.843	1.843	5
1 4 4	1.793	1.788	9
5 0 2	1.747	1.745	3

Table 4-1. (cont'd)

h k l	d _{calcd} , Å	d _{obsd} , Å	I/I _{max} (obsd)
0 7 1	1.726	1.728	10
4 5 0	1.709	1.710	4
0 6 3	1.699	1.700	7
5 3 -1	1.697	1.694	9
1 6 -3	1.674	1.673	3
2 7 -1	1.623	1.623	3
3 4 -4	1.589	1.588	13
4 6 0	1.552	1.554	11
6 1 -1	1.550	1.550	11

Table 4-2. Calculated and Observed X-ray Powder Diffraction Patterns for $K_3Bi(PS_4)_2$.

h k l	$d_{\text{calcd}}, \text{\AA}$	$d_{\text{obsd}}, \text{\AA}$	$I/I_{\text{max}} (\text{obsd})$
2 0 0	11.95	11.75	52
1 0 1	8.46	8.35	47
2 0 1	7.21	7.14	11
3 0 1	5.98	5.93	19
1 1 1	5.30	5.26	29
3 1 0	5.17	5.13	10
2 1 1	4.95	4.95	7
4 1 0	4.49	4.46	11
4 1 1	4.02	4.00	19
3 0 2	3.93	3.96	7
5 1 0	3.91	3.90	4
0 1 2	3.77	3.74	6
6 0 1	3.65	3.63	5
2 1 2	3.59	3.58	15
0 2 0	3.40	3.39	13
5 0 2	3.29	3.27	10
7 0 1	3.19	3.19	7
7 1 0	3.05	3.04	13
8 0 0	2.99	2.98	100
3 2 1	2.96	2.94	5
2 0 3	2.92	2.91	11
4 2 1	2.81	2.80	11
1 1 3	2.74	2.74	11
2 1 3	2.69	2.68	6
5 2 1	2.65	2.64	10
8 1 1	2.62	2.61	6
9 0 1	2.55	2.54	5
6 2 1	2.486	2.474	5
6 0 3	2.405	2.400	10
9 1 1	2.386	2.383	19
5 2 2	2.363	2.357	7
0 0 4	2.262	2.255	6
8 2 0	2.244	2.240	8
7 2 2	2.126	2.121	7
4 2 3	2.111	2.110	9
10 1 2	2.018	2.015	6
9 1 3	1.912	1.909	6
15 1 0	1.551	1.552	5
8 3 3	1.549	1.549	4

Table 4-3. Calculated and Observed X-ray Powder Diffraction Patterns for $\text{Na}_{0.16}\text{Bi}_{1.28}\text{P}_2\text{S}_6$.

h k l	$d_{\text{calcd}}, \text{\AA}$	$d_{\text{obsd}}, \text{\AA}$	$I/I_{\text{max}} (\text{obsd})$
0 1 1	5.76	5.73	38
1 0-1	5.46	5.44	24
1 0 1	5.28	5.26	5
1 1 0	4.87	4.86	19
0 0 2	4.68	4.67	28
1 1-1	4.37	4.36	22
1 1 1	4.28	4.27	64
0 1 2	3.94	3.93	7
0 2 0	3.65	3.64	4
1 1-2	3.42	3.42	13
0 2 1	3.40	3.39	83
1 1 2	3.33	3.33	60
2 0 0	3.27	3.27	14
1 2 0	3.19	3.18	3
1 2-1	3.03	3.03	7
1 2 1	3.00	2.99	8
2 1-1	2.87	2.87	49
2 1 1	2.82	2.81	51
2 0-2	2.73	2.72	25
1 1-3	2.66	2.65	100
2 0 2	2.64	2.63	24
1 2 2	2.61	2.61	7
1 1 3	2.60	2.59	31
2 1-2	2.56	2.55	9
2 1 2	2.482	2.477	16
2 2 0	2.437	2.433	3
0 2 3	2.372	2.367	59
0 0 4	2.341	2.336	24
1 3 0	2.280	2.276	29
1 3-1	2.222	2.217	8
1 3 1	2.209	2.205	9
2 1-3	2.194	2.189	6
1 1-4	2.132	2.132	5
1 1 4	2.089	2.086	4
3 1 1	2.027	2.021	11
2 3 0	1.953	1.951	4
2 2-3	1.946	1.944	6
3 1-2	1.935	1.931	6
2 2 3	1.897	1.895	4
3 1 2	1.886	1.883	10
2 1-4	1.873	1.868	7
3 2-1	1.848	1.848	5
1 3 3	1.831	1.829	4
0 4 0	1.824	1.823	5
3 0-3	1.820	1.817	4
3 2-2	1.758	1.756	10
1 4-1	1.730	1.728	5

h k l	d _{calcd} , Å	d _{obsd} , Å	I/I _{max} (obsd)
3 2 2	1.721	1.719	3
0 2 5	1.666	1.664	4
1 3-4	1.644	1.642	4
2 3 3	1.640	1.638	8
4 0 0	1.638	1.637	4
1 3 4	1.623	1.622	4
2 1-5	1.611	1.609	8
3 3-1	1.608	1.609	5
4 1 0	1.598	1.596	8
2 4 0	1.594	1.591	9
4 1-1	1.584	1.582	4
0 4 3	1.575	1.574	4
0 0 6	1.561	1.560	7

Table 4-4. Crystallographic Data for I, VI, IX, and X.

	I	VI
Formula	KBiP ₂ S ₇	K ₃ Bi(PS ₄) ₂
FW	542.57	644.70
a, Å	9.500(3)	23.894(8)
b, Å	12.303(4)	6.799(3)
c, Å	9.097(3)	9.049(2)
α, deg	90.0	90.0
β, deg	90.59(3)	90.0
γ, deg	90.0	90.0
Z; V, Å ³	4; 1063.1(6)	4; 1470(1)
λ (Mo Kα)	0.71073	0.71073
space group	P2 ₁ /c (No. 14)	P2 ₁ 2 ₁ 2 ₁ (No. 19)
D _{calc.} , g/cm ³	3.339	2.913
μ, cm ⁻¹ (Mo Kα)	184.85	140.81
2θ _{max} , deg	50	50
Temp., °C	23	-60
Final R/R _w , %	2.8/3.1	5.5/6.0
Total Data	2192	3997
Total Unique (Ave.)	2060	1999
Data F _o ² > 3σ(F _o ²)	1672	1745
No. of variables	100	128

Table 4-4. (cont'd)

	IX	X
Formula	Cs ₃ Bi ₂ (PS ₄) ₃	Na _{0.16} Bi _{1.28} P ₂ S ₆
FW	1294.32	525.47
a, Å	18.091(5)	6.554(2)
b, Å	6.791(2)	7.297(2)
c, Å	18.723(3)	9.371(1)
α, deg	90.0	90.0
β, deg	97.95(2)	92.04(2)
γ, deg	90.0	90.0
Z; V, Å ³	4; 2278(1)	2; 447.8(2)
λ (Mo Kα)	0.71073	0.71073
space group	P2 ₁ /c (No. 14)	P2 ₁ /n (No. 14)
D _{calc.} , g/cm ³	3.773	3.731
μ, cm ⁻¹ (Mo Kα)	213.34	236.19
2θ _{max} , deg	50	50
Temp., °C	23	23
Final R/R _w , %	7.0/9.0	7.7/8.5
Total Data	4537	1514
Total Unique (Ave.)	4375	1407
Data F _O ² > 3σ(F _O ²)	2623	892
No. of variables	182	47

$$*R = \Sigma(|F_O| - |F_C|) / \Sigma|F_O| \quad R_w = \{\Sigma w(|F_O| - |F_C|)^2 / \Sigma w|F_O|^2\}^{1/2}$$

Table 4-5. Fractional Atomic Coordinates and B_{eq} Values for KBiP_2S_7 with Estimated Standard Deviations in Parentheses.^a

atom	x	y	z	$B_{eq},^a \text{Å}^2$
Bi(1)	0.34191(3)	0.13823(2)	0.11948(3)	1.26(1)
K(1)	-0.1153(2)	0.1911(2)	-0.1292(2)	2.26(7)
S(1)	0.6536(2)	0.1937(1)	0.1485(2)	1.11(7)
S(2)	0.1161(2)	0.2928(1)	0.1101(2)	1.20(7)
S(3)	0.1655(2)	0.0297(2)	-0.0738(2)	1.27(7)
S(4)	0.4087(2)	0.1716(1)	0.4314(2)	1.16(7)
S(5)	0.5057(2)	-0.0554(1)	0.1860(2)	1.25(7)
S(6)	1.2472(2)	0.5509(1)	0.0802(2)	0.93(6)
S(7)	0.1237(2)	0.0545(2)	0.2942(2)	1.18(7)
P(1)	0.6811(2)	0.0367(1)	0.1997(2)	0.74(6)
P(2)	0.2224(2)	0.1031(1)	0.4811(2)	0.74(6)

Table 4-6. Fractional Atomic Coordinates and B_{eq} Values for $\text{K}_3\text{Bi}(\text{PS}_4)_2$ with Estimated Standard Deviations in Parentheses.^a

atom	x	y	z	$B_{eq},^a \text{Å}^2$
Bi(1)	0.05174(3)	0.0597(1)	0.35126(6)	1.18(2)
K(1)	-0.0755(2)	-0.0045(8)	0.7590(5)	2.9(2)
K(2)	0.2140(2)	-0.4991(8)	0.4096(5)	2.6(2)
K(3)	-0.3127(2)	0.5098(8)	0.9776(5)	2.8(2)
S(1)	0.0683(2)	0.0142(8)	0.6411(5)	1.9(2)
S(2)	0.1845(2)	-0.2484(8)	0.7087(6)	2.1(2)
S(3)	0.1650(2)	-0.031(1)	0.3843(4)	2.3(2)
S(4)	0.1918(2)	0.2370(8)	0.6906(6)	2.2(2)
S(5)	0.0790(2)	0.4370(7)	0.3701(4)	1.5(1)
S(6)	0.1735(2)	0.482(1)	0.0895(6)	2.5(2)
S(7)	-0.0546(2)	0.2199(6)	0.4241(5)	1.6(2)
S(8)	0.0528(3)	0.2317(7)	0.0519(5)	2.0(2)
P(1)	0.1555(2)	-0.0065(7)	0.6119(4)	1.2(2)
P(2)	0.0929(2)	0.4659(7)	0.1418(5)	1.1(1)

$$^a B_{eq} = (4/3)[a^2 B(1,1) + b^2 B(2,2) + c^2 B(3,3) + ab(\cos\gamma)B(1,2) + ac(\cos\beta)B(1,3) + bc(\cos\alpha)B(2,3)].$$

Table 4-7. Fractional Atomic Coordinates and B_{eq} Values for $Cs_3Bi_2(PS_4)_3$ with Estimated Standard Deviations in Parentheses.^a

atom	x	y	z	$B_{eq},^a \text{Å}^2$
Bi(1)	0.07105(7)	0.1923(2)	0.79059(6)	1.24(5)
Bi(2)	0.40215(8)	0.2964(3)	0.50535(7)	3.36(7)
Cs(1)	0.1025(1)	-0.2648(3)	0.9877(1)	2.6(1)
Cs(2)	0.3746(2)	-0.2486(4)	1.3094(1)	3.8(1)
Cs(3)	0.2373(1)	0.2794(3)	0.6310(1)	2.33(9)
S(1)	0.1149(5)	-0.176(1)	0.8046(4)	2.1(3)
S(2)	0.2203(5)	-0.221(1)	0.6669(5)	1.9(3)
S(3)	0.1119(4)	0.235(1)	0.9368(4)	1.6(3)
S(4)	0.0575(5)	0.023(1)	0.6495(4)	1.6(3)
S(5)	0.2739(5)	0.499(1)	0.4517(5)	1.9(3)
S(6)	0.2179(5)	0.192(1)	0.3104(4)	2.4(4)
S(7)	0.4196(6)	-0.491(1)	0.6469(5)	2.8(4)
S(8)	0.4230(5)	0.253(1)	0.3684(4)	2.0(3)
S(9)	0.2775(5)	0.021(1)	0.4737(5)	2.1(4)
S(10)	0.4414(5)	0.736(2)	0.4951(4)	2.8(4)
S(11)	0.4229(6)	0.005(1)	0.6423(5)	2.8(4)
S(12)	0.0634(5)	-0.467(1)	0.6633(4)	1.5(3)
P(1)	0.1193(4)	-0.211(1)	0.6945(4)	1.3(3)
P(2)	0.2222(4)	0.244(1)	0.4178(4)	1.0(3)
P(3)	0.4623(5)	-0.247(1)	0.6072(4)	1.2(3)

Table 4-8. Fractional Atomic Coordinates and B_{eq} Values for $Na_{0.16}Bi_{1.28}P_2S_6$ with Estimated Standard Deviations in Parentheses.^a

atom	x	y	z	$B_{eq},^a \text{Å}^2$
Bi ^b	0.0377(2)	0.6348(2)	0.2470(2)	4.47(7)
S(1)	-0.1147(5)	0.9985(5)	0.2589(4)	1.3(1)
S(2)	0.3455(5)	0.8074(4)	0.4350(4)	1.3(1)
S(3)	-0.3192(5)	1.1981(5)	-0.0417(4)	1.6(1)
P(1)	-0.0644(5)	1.1103(4)	0.0664(3)	0.8(1)
Na ^c	0.0377	0.6348	0.2470	3.5

$$^a B_{eq} = (4/3)[a^2 B(1,1) + b^2 B(2,2) + c^2 B(3,3) + ab(\cos\gamma)B(1,2) + ac(\cos\beta)B(1,3) + bc(\cos\alpha)B(2,3)].$$

^b64% occupied

^c0.08% occupied

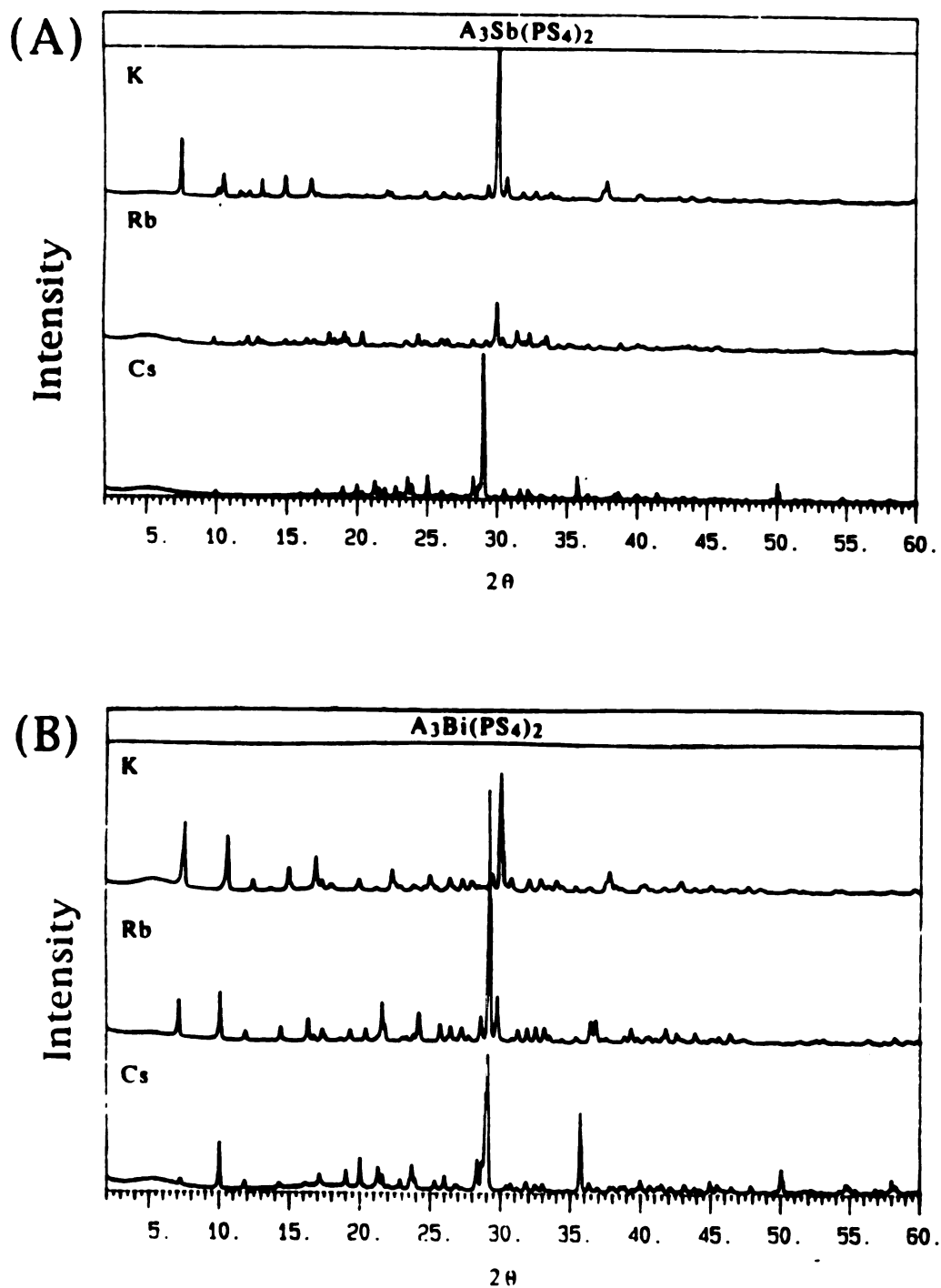


Figure 4-1. Powder X-ray diffracton patterns of: (A) $A_3Sb(PS_4)_2$ and (B) $A_3Bi(PS_4)_2$

3. Results and Discussion

3.1. Synthesis, Spectroscopy and Thermal Analysis

The syntheses were a result of a redox reaction in which the metal is oxidized by polysulfide ions in the $A_x[P_yS_z]$ flux. The resulting metal ions are then coordinated by the highly charged $[PS_4]^{3-}$, $[P_2S_7]^{4-}$, and $[P_2S_6]^{4-}$ ligands. The molten *polythiophosphate* flux method is very effective for crystal growth and isolation of pure products in this system.

Thiophosphate ligand formation appears to be controlled by the metal to P_2S_5 ratio and the Lewis basicity of the alkali metal cation. Stabilization of $[PS_4]^{3-}$ anions is observed in $A_3M(PS_4)_2$ and $Cs_3Bi_2(PS_4)_3$ from a Bi/ P_2S_5 ratio of 1:1.5-2.0. Several attempts to isolate pure $Cs_3Bi_2(PS_4)_3$ resulted in a mixture of $Cs_3Bi_2(PS_4)_3$ and $Cs_3Bi(PS_4)_2$. Increasing the amount of P_2S_5 in the flux (Bi/ P_2S_5 ratio of 1:3) yielded the $[P_2S_7]^{4-}$ ligand in $KBiP_2S_7$. In the Bi/ P_2S_5 / Na_2S /S (1/3/2/4) system, the less basic Na^+ counterion stabilizes a lower 4+ oxidation state for P, which leads to the formation of $[P_2S_6]^{4-}$ anions in $Na_{0.16}Bi_{1.28}P_2S_6$. A second phase was obtained in the Bi/ P_2S_5 / Na_2S /S system using the respective ratio (1/2/2/4-8) at 400 °C. This reaction affords a homogeneous product consisting of dark red twinned crystals of a new compound (evidenced by powder X-ray diffraction).

The far-IR spectrum of $KBiP_2S_7$ (Table 4-9) shows absorbances at 600(s), 583(s), 576(ssh), 564(msh), 557(msh), 526(wsh), 464(vs), 412(w) cm^{-1} . The very strong absorbance at 464 cm^{-1} represents the characteristic P-S-P stretching vibration while the remaining

absorbances are due to -PS_3 stretching vibrations by analogy to $\text{Ag}_4\text{P}_2\text{S}_7$.^{19,20} A second set of absorbances at 300(vw), 270(wsh), 250(msh), 247(m), 238(msh), 227(wsh), 208(wsh), 203(wsh), 192(vw), 174(vw), 169(vw), 157(vw), and 149(vw) cm^{-1} are assigned to Bi-S stretching vibrations and P-S deformation modes.^{19,20,21}

The Far-IR spectra of $\text{A}_3\text{M}(\text{PS}_4)_2$ (III-VIII), $\text{Cs}_3\text{Bi}_2(\text{PS}_4)_3$ (IX), and $\text{Na}_{0.16}\text{Bi}_{1.28}\text{P}_2\text{S}_6$ (X), shown in Table 4-9, are quite complex. Absorptions in the 400-650 cm^{-1} range for (III-IX), are tentatively assigned to P-S vibrational stretching modes by analogy with the vibrational spectra of other $[\text{PS}_4]^{3-}$ containing compounds such as InPS_4 , GaPS_4 , and BiPS_4 .²¹ Absorptions below 400 cm^{-1} are assigned to S-P-S bending modes and M-S vibrations.²² The far-IR spectrum of $\text{Na}_{0.16}\text{Bi}_{1.28}\text{P}_2\text{S}_6$ shows a broad absorption at 535 cm^{-1} which can be assigned to PS_3 stretching vibrations. An assignment of the strong absorption band at ~ 434 cm^{-1} in $\text{Na}_{0.16}\text{Bi}_{1.28}\text{P}_2\text{S}_6$ is not as straightforward. In $\text{Na}_4\text{P}_2\text{S}_6 \cdot 6\text{H}_2\text{O}$, an absorbance at 443 cm^{-1} was ascribed to an out-of-phase PS_3 mode, corresponding to a P-P vibration.²³ The P-P vibration is expected to be IR inactive because it resides on a center of symmetry. Surprisingly, it was not observed in the Raman spectrum. The spectra of $\text{Na}_4\text{P}_2\text{S}_6 \cdot 6\text{H}_2\text{O}$ were described in terms of internal modes of PS_3 groups and combinations of in-phase and out-of-phase translational and rotational motions.²³ Since the P-P bond in $\text{Na}_{0.16}\text{Bi}_{1.28}\text{P}_2\text{S}_6$ also resides on a center of symmetry, a similar situation is assumed to exist in this compound. Thus, by analogy to $\text{Na}_4\text{P}_2\text{S}_6 \cdot 6\text{H}_2\text{O}$, the strong band at 434 cm^{-1} in $\text{Na}_{0.16}\text{Bi}_{1.28}\text{P}_2\text{S}_6$ can tentatively be ascribed to the out-of-phase

translational PS_3 mode. Below 400 cm^{-1} , the bands are assigned to a combination of S-P-S bending modes and M-S vibrations as above.

The optical properties of (I-X) were assessed by studying the UV/near-IR reflectance spectra of the materials. The spectra confirm the semiconductor nature of the materials by revealing the presence of sharp optical gaps as shown in Figures 4-2 to 4-5. The $\text{A}_3\text{M}(\text{PS}_4)_2$ ($\text{A}=\text{K}, \text{Rb}, \text{Cs}$; $\text{M}=\text{Sb}, \text{Bi}$) compounds exhibit steep absorption edges from which the band-gap, E_g , can be assessed at 2.25 (I), 2.25 (I I), 2.75 (I I I), 2.67 (I V), 2.80 (V), 2.26 (V I), 2.21 (V I I) 2.28 eV (V I I I), respectively. Impurity bands are observed in the spectra of $\text{K}_3\text{Bi}(\text{PS}_4)_2$ and $\text{Rb}_3\text{Bi}(\text{PS}_4)_2$ shown in Figures 4-4a and 4-4b. These two compounds are air sensitive which results in some decomposition of the compounds. The band-gap, E_g , of $\text{Na}_{0.16}\text{Bi}_{1.28}\text{P}_2\text{S}_6$ is 1.88 eV (X). The higher energy absorptions found in several of the compounds are readily resolved and are assigned to electronic $\text{S} \rightarrow \text{M}$ charge transfer transitions.

Differential thermal analysis (DTA) shows that KBiP_2S_7 and RbBiP_2S_7 melt at 511 and 488 °C, respectively, and upon cooling form amorphous glasses. $\text{Na}_{0.16}\text{Bi}_{1.28}\text{P}_2\text{S}_6$ melts incongruently at 652 °C to form a mixture of $\text{Na}_{0.16}\text{Bi}_{1.28}\text{P}_2\text{S}_6$ and an impurity phase. The $\text{A}_3\text{M}(\text{PS}_4)_2$ compounds melt congruently, suggesting that large single crystals or microcrystalline thin films can be grown from the melt. Table 4-10 summarizes optical and melting point data for all compounds. Typical thermograms for RbBiP_2S_7 and $\text{Rb}_3\text{Bi}(\text{PS}_4)_2$ are shown in Figure 4-6.

Table 4-9. Far-IR Spectra for (I-X).

KBiP ₂ S ₇	K ₃ Sb(PS ₄) ₂	Rb ₃ Sb(PS ₄) ₂	Cs ₃ Sb(PS ₄) ₂
600(s)	620(s)	632(s)	621(m)
583(s)	612(s)	624(s)	605(s)
576(ssh)	579(s)	611(s)	577(s)
564(msh)	563(s)	581(s)	560(s)
557(msh)	546(w)	564(s)	508(m)
526(wsh)	511(m)	544(w)	493(m)
464(vs)	494(m)	535(w)	408(w)
412(w)	409(m)	510(s)	329(w)
300(vw)	325(m)	493(w)	316(s)
270(wsh)	310(m)	409(w)	298(w)
250(msh)	287(w)	341(m)	266(w)
247(m)	268(w)	325(m)	262(w)
238(msh)	238(w)	315(m)	238(w)
227(wsh)	167(w)	298(m)	189(w)
208(wsh)		266(w)	164(w)
203(wsh)		256(w)	
192(vw)		240(w)	
174(vw)		200(w)	
169(vw)		183(w)	
157(vw)		149(w)	
149(vw)			

K ₃ Bi(PS ₄) ₂	Cs ₃ Bi(PS ₄) ₂	Cs ₃ Bi ₂ (PS ₄) ₃	Na _{0.16} Bi _{1.28} P ₂ S ₆
616(m)	624(s)	585(m)	535(m, broad)
609(s)	616(s)	581(msh)	434(s)
571(s)	610(s)	578(msh)	375(w)
550(s)	570(s)	574(msh)	280(s)
516(m)	549(s)	554(m)	254(w)
498(m)	513(m)	551(msh)	227(m)
412(w)	496(m)	548(msh)	
291(w)	412(w)	524(s)	
266(w)	304(w)	516(s)	
201(w)	293(m)	500(m)	
167(w)	279(w)	413(w)	
150(w)	264(m)	303(msh)	
	247(w)	292(m)	
	231(m)	261(m)	
	186(w)	253(msh)	
	160(w)	239(w)	

Abbreviations: s=strong, m=medium, w=weak, sh=shoulder, v=very

Table 4-10. Optical Band Gaps and Melting Point Data for (I-X).

Formula	E _g (eV)	M. P. (°C)
KBiP ₂ S ₇	2.25	511 (incongruent)
RbBiP ₂ S ₇	2.25	488 (incongruent)
K ₃ Sb(PS ₄) ₂	2.75	549 (congruent)
Rb ₃ Sb(PS ₄) ₂	2.67	471 (congruent)
Cs ₃ Sb(PS ₄) ₂	2.80	521 (congruent)
K ₃ Bi(PS ₄) ₂	2.26	559 (congruent)
Rb ₃ Bi(PS ₄) ₂	2.21	610 (congruent)
Cs ₃ Bi(PS ₄) ₂	2.28	642 (congruent)
NaBiP ₂ S ₆	1.88	652 (incongruent)

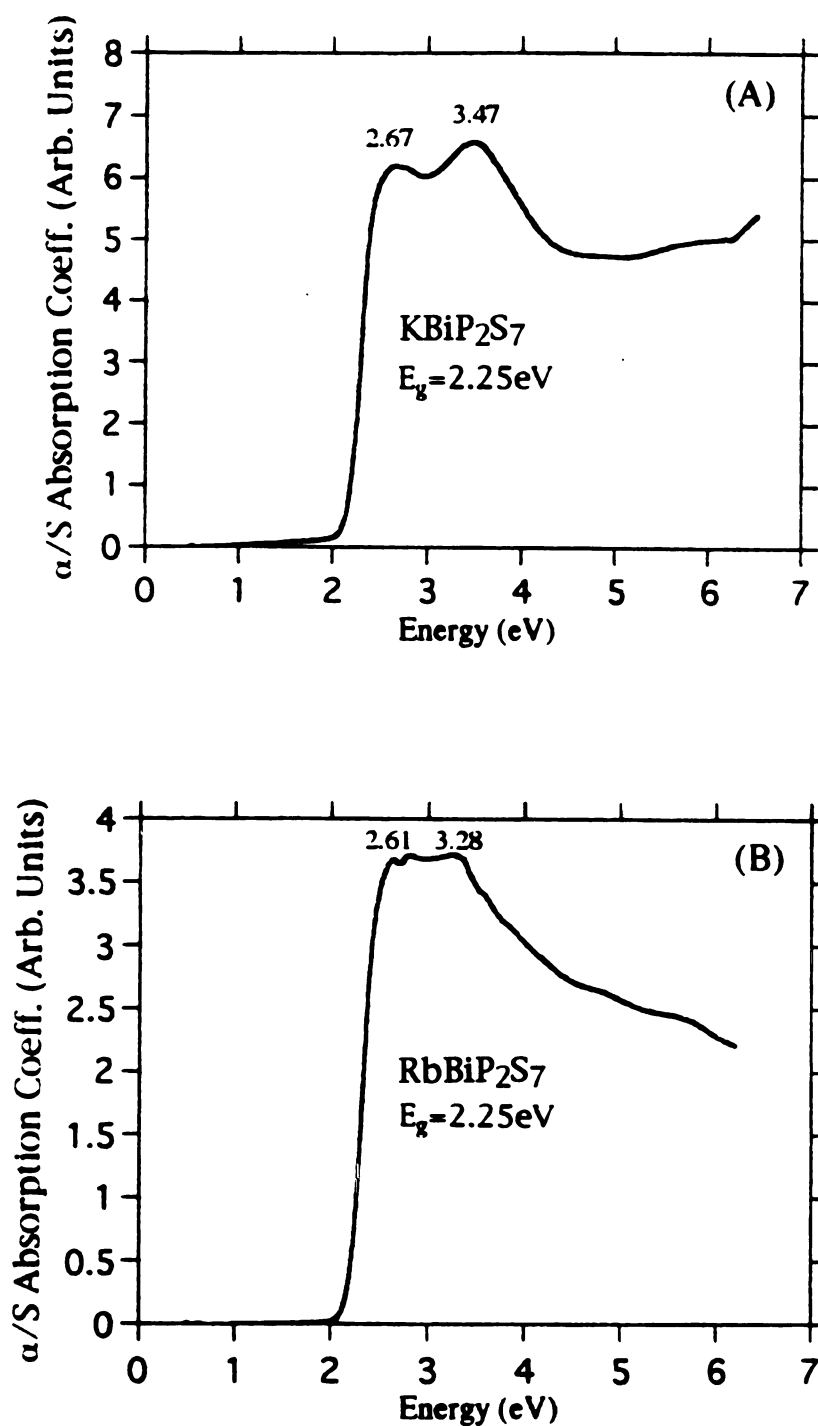


Figure 4-2. Optical absorption spectrum of: (A) KBiP_2S_7 and (B) RbBiP_2S_7

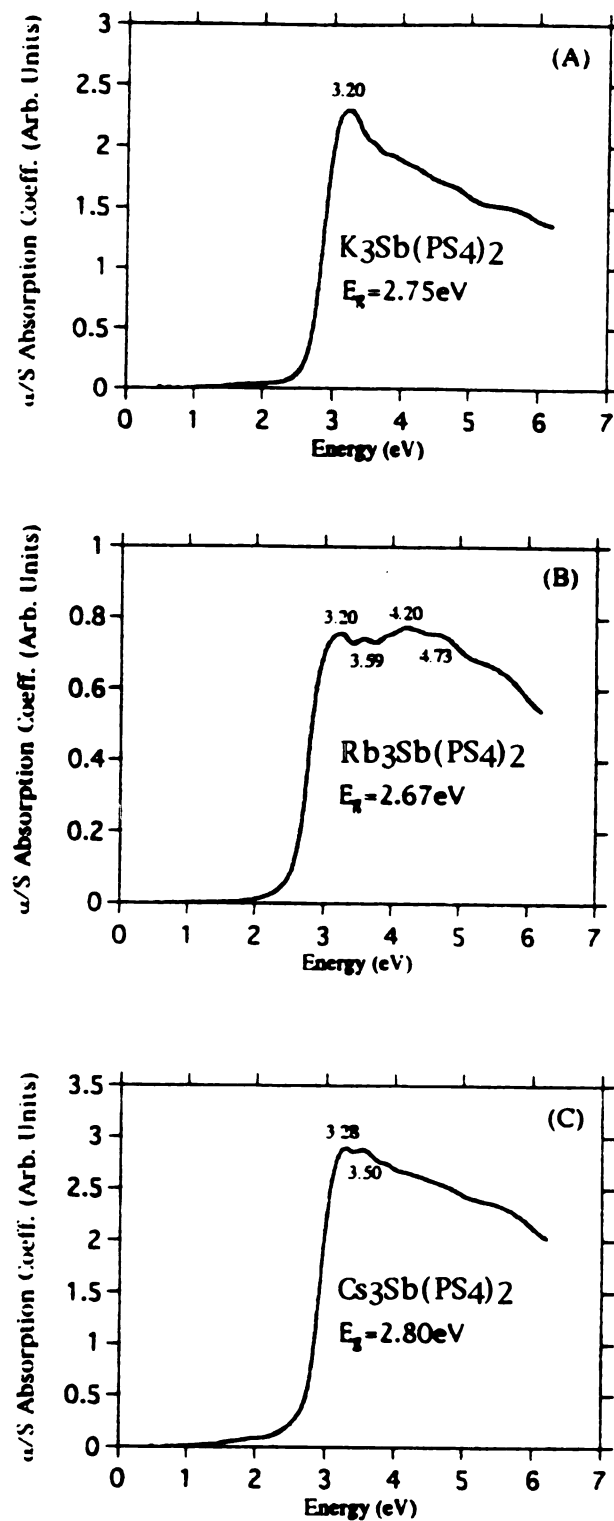


Figure 4-3. Optical absorption spectra of: (A) $\text{K}_3\text{Sb}(\text{PS}_4)_2$ (B) $\text{Rb}_3\text{Sb}(\text{PS}_4)_2$ (C) $\text{Cs}_3\text{Sb}(\text{PS}_4)_2$

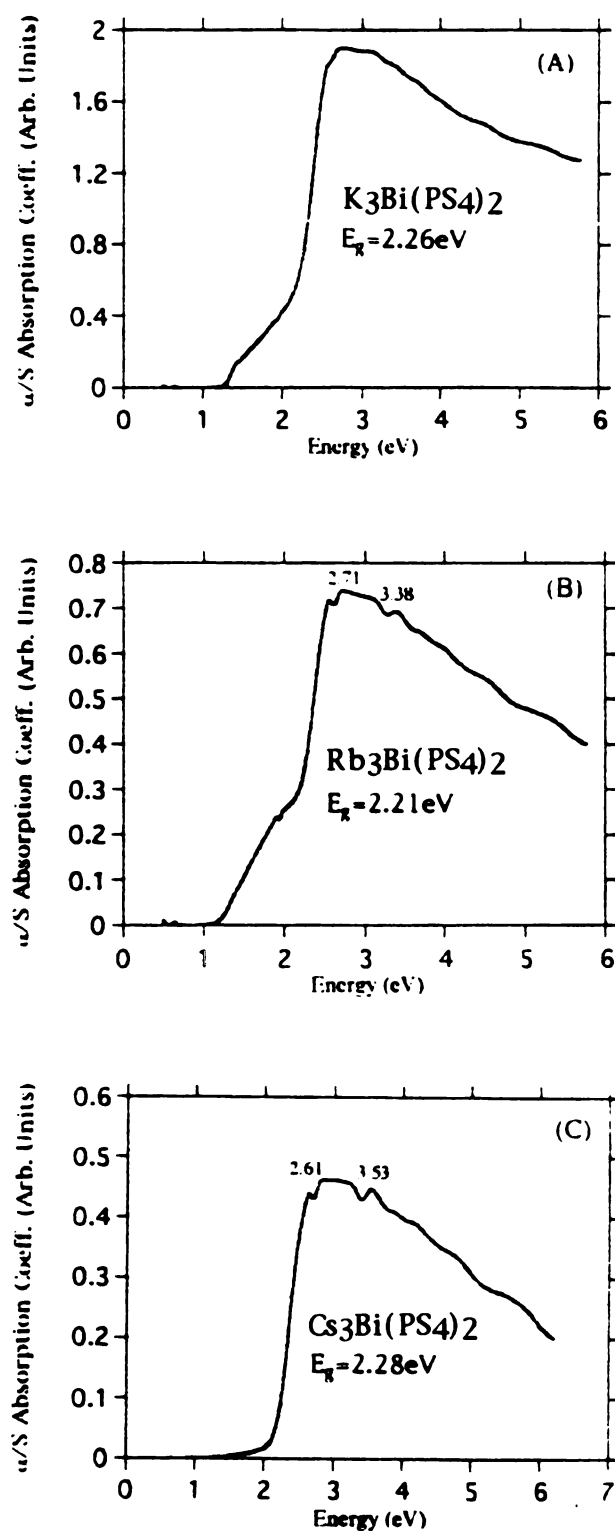


Figure 4-4. Optical absorption spectra of: (A) $\text{K}_3\text{Bi}(\text{PS}_4)_2$ (B) $\text{Rb}_3\text{Bi}(\text{PS}_4)_2$ (C) $\text{Cs}_3\text{Bi}(\text{PS}_4)_2$

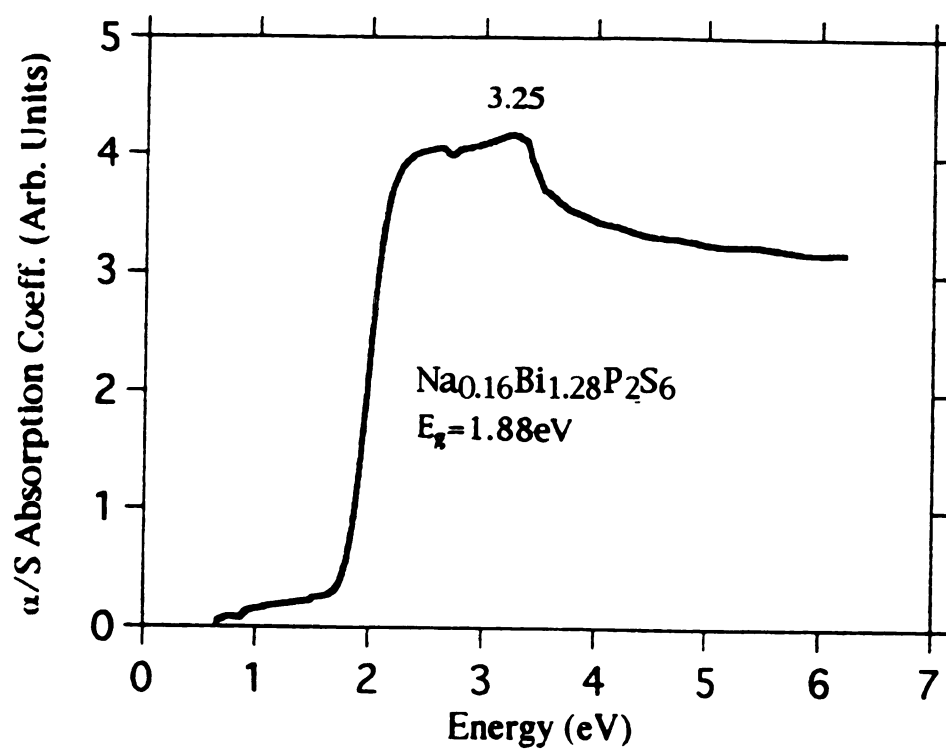


Figure 4-5. Optical absorption spectrum of $\text{Na}_{0.16}\text{BiP}_2\text{S}_6$

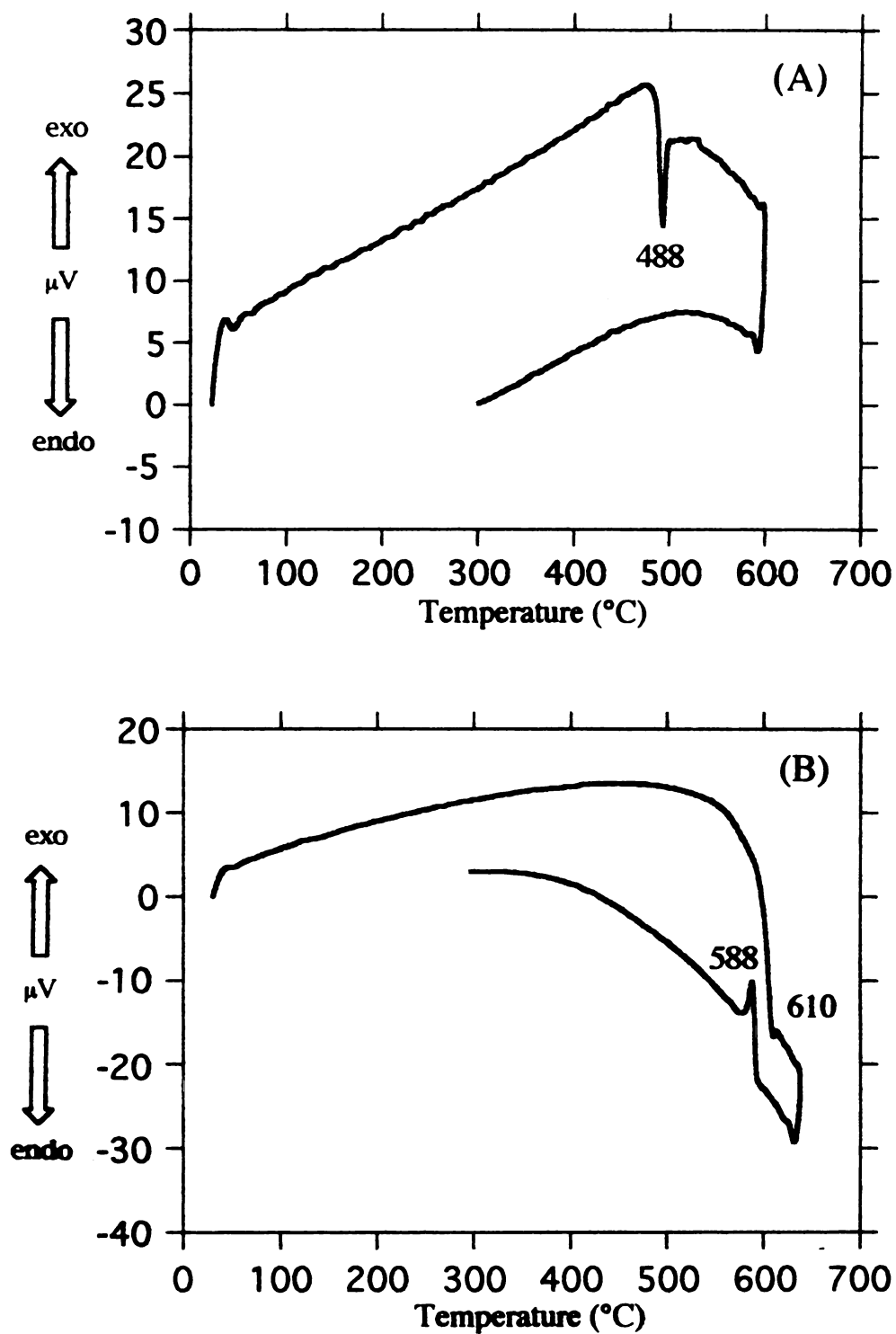
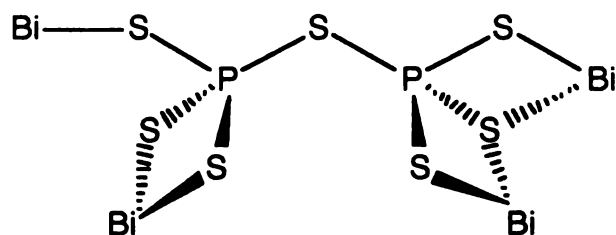


Figure 4-6: Thermograms of: (A) RbBiP_2S_7 and (B) $\text{Rb}_3\text{Bi}(\text{PS}_4)_2$

3.2. Description of Structure.

KBiP₂S₇. KBiP₂S₇ is a layered solid with a complex new structure type (see Figure 4-7). The corrugated layers are separated by eight-coordinate K⁺ ions (K-S mean=3.34(6) Å). Another view of the structure of KBiP₂S₇ is shown in Figure 4-8. The layers are assembled from Bi³⁺ and [P₂S₇]⁴⁻ units forming irregular eight-membered Bi-S-P rings. The P(2)-S₄ tetrahedron of the *pyrothiophosphate* ligand [P₂S₇]⁴⁻ coordinates in a bidentate fashion to Bi and acts as a bridge to a second Bi to form the top side of the eight-membered ring. The Bi atoms are connected at the bottom of the ring by the P(2)-S₄ tetrahedron of a second P₂S₇ group that acts as a tridentate to both Bi atoms. The bridging mode of the [P₂S₇]⁴⁻ fragment is rather complicated and it is illustrated in scheme (A). The rings are connected in two dimensions by P-S-Bi linkages to form the layer. The layers stack with their 8-membered rings in registry so that they form channels running down the a-axis.



Scheme (A)

Selected bond distances and angles are given in Table 4-11. Bi is coordinated by seven S atoms to form a distorted capped trigonal prism (see Figure 4-9). The distances range from 2.761(2) to 3.047(2)Å which compare well with those found in BiPS₄.^{4c} The

coordination geometry is distorted because of the stereochemically active $6s^2$ lone pair of Bi^{3+} . The S(7) atom caps one of the three rectangular faces of the trigonal prism. The lone pair presumably caps one of the other two faces. Inspection of the angles of the face, defined by S(2), S(4), S(1), S(4)' (see Figure 4-10), reveal S(1)-Bi-S(2) and S(4)-Bi-S(4)' angles of $125.46(5)^\circ$ and $113.69(5)^\circ$ respectively. The S(1)-Bi-S(3) and S(4)''-Bi-(5) angles of the second face, defined by S(3), S(4)', S(5), S(1), are larger at $138.29(5)^\circ$ and $130.43(6)^\circ$ respectively, and are probably due to the repulsive effect of the lone pair and the atoms. Each capped trigonal prism shares three edges and one corner with the terminal sulfides of four $[\text{P}_2\text{S}_7]^{4-}$ ligands.

The bridging angle of the $[\text{P}_2\text{S}_7]^{4-}$ ligand in KBiP_2S_7 is $111.2(1)^\circ$ comparable to those found in $\text{Ag}_4\text{P}_2\text{S}_7$ ($113.4(2)^\circ$)²⁴ and $\text{Hg}_2\text{P}_2\text{S}_7$ ($108.63(4)^\circ$).²⁵ The configuration of the PS_4 tetrahedra of the pyrothiophosphate group in KBiP_2S_7 is staggered, with a dihedral angle (S(5)-P(1)-P(2)-S(4)') of $16.6(1)^\circ$. The bridging nature of the S(6) atom results in significantly longer P(1)-S(6) and P(2)-S(6) bond distances (2.115(3) and 2.111(3) Å) compared to the other P-S bond distances (2.003(3)-2.035(3) Å). Similar P-S distances have been observed in $\text{Ag}_4\text{P}_2\text{S}_7$ ²⁴ and $\text{Hg}_2\text{P}_2\text{S}_7$.²⁵

KBiP_2S_7 is structurally related to but significantly different from RbVP_2S_7 ,²⁶ which also possesses a layered structure. The major differences are the coordination number, geometry of the M^{3+} atom, and bonding modes of the $[\text{P}_2\text{S}_7]^{4-}$ ligand. Each VS_6 octahedron of RbVP_2S_7 shares two edges with the PS_4 tetrahedra of two $[\text{P}_2\text{S}_7]^{4-}$ ligands and two corners with the PS_4 tetrahedra of a third $[\text{P}_2\text{S}_7]^{4-}$ ligand to form flat layers. In contrast, the sheets of KBiP_2S_7 are

corrugated. The stereochemically active lone pair of Bi^{3+} also influences the structure of the layers by distorting the BiS_7 polyhedron.

$\text{K}_3\text{Bi}(\text{PS}_4)_2$. The structure of $\text{K}_3\text{Bi}(\text{PS}_4)_2$ is assembled from one-dimensional, helical $[\text{Bi}(\text{PS}_4)_2]_n^{3n-}$ chains running along the crystallographic b-axis. The chain structure is shown in Figure 4-11, and it features two interesting binding modes for a $[\text{PS}_4]^{3-}$ ligand. One $[\text{PS}_4]^{3-}$ ligand bichelates to the Bi metal center while two additional $[\text{PS}_4]^{3-}$ units act as bridges to other Bi atoms to form polymeric chains that are well-separated by K^+ ions (Figure 4-12).

The square pyramidal coordination geometry of BiS_5 features a stereochemically active lone pair of electrons localized at the base of the pyramid. This type of coordination environment is common for Bi^{3+} in a chalcogenide environment. Examples include Bi_2S_3 ,²⁷ $\text{K}_2\text{Bi}_8\text{Se}_{13}$,²⁸ and $\text{Cu}_{1.6}\text{Bi}_{4.8}\text{S}_8$.²⁹ This coordination site consists of four equatorial bonds ranging from 2.673(3) to 2.956(3) Å and a short axial distance of 2.649(4) Å. This short bond is *trans* to two Bi-S(7'),(8') interactions at 3.399(4) and 3.453(5) Å, respectively, which are shorter than the approximate sum of the van der Waals radii (4.2 Å).³⁰

The P-S distances of the $[\text{PS}_4]^{3-}$ ligands vary between the metal bonding and nonbonding positions. In $\text{P}(1)\text{S}_4$, the nonbonding P(1)-S(2),(4) distances are 1.994(5) and 1.997(6) Å while the P(1)-S(1),(3) bond lengths are 2.108(5) and 2.070(4) Å. This difference in bond length is a result of the partial double bond character of the terminal S(2) and S(4) atoms.³¹ The same trend is observed for $\text{P}(2)\text{S}_4$. The nonbonding P(2)-S(6) distance (1.980(5) Å) is shorter than the metal

bonding distances that range from 2.027(5) to 2.091(5) Å. This behavior is not very common in the known M/PS₄ chemistry because the S atoms are usually engaged in metal bonding in these dense three-dimensional structures. A notable exception is Pd₃(PS₄)₂³² where square planar PdS₄ units are connected by PS₄ ligands to form an interesting layered structure. There is one nonbonding terminal S atom on each PS₄ unit that extends into the van der Waals gap and has a P-S(2) bond length of 1.904(1) Å. The other three P-S(1) distances are 2.112(1) Å. The [PS₄]³⁻ ligands in K₃Bi(PS₄)₂ possess normal S-P-S tetrahedral angles that vary between 103.5(2) and 113.8(3)°. Selected bond distances and angles are given in Table 4-12.

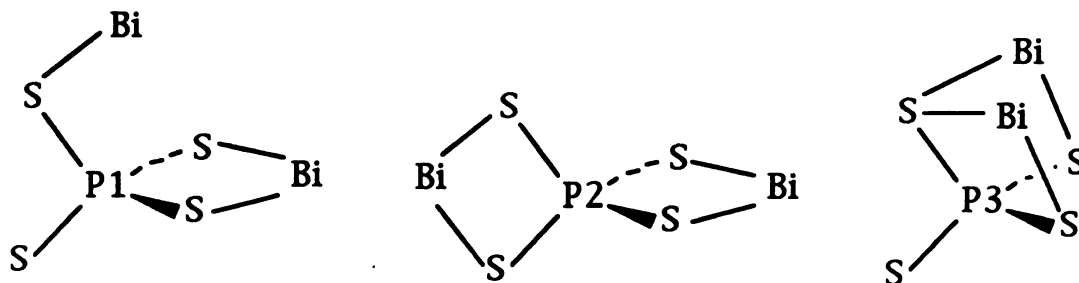
The residual negative charge on the terminal S atoms leads to short K-S bond distances due to the higher electrostatic attraction. The K(1)-S(2) distance is 3.133(6) Å while the other K(1)-S distances range from 3.320(6) to 3.429(5) Å. The eight-coordinate K(2) possesses short distances to S(4), S(6), and S(6') of 3.163(5), 3.154(5), and 3.062(5) Å, respectively, with other K(2)-S distances ranging from 3.283(5) to 3.490(6) Å. The five K(3)-S distances vary between 3.287(5) and 3.536(6) Å.

Cs₃Bi₂(PS₄)₃. The unusual layered structure of Cs₃Bi₂(PS₄)₃ is shown in Figure 4-13. The layers feature the same one-dimensional helical chains that were observed in K₃Bi(PS₄)₂. Instead of a capping PS₄ unit sharing an edge with the equatorial plane of the square pyramidal BiS₅, this ligand acts as a bridge to a Bi₂(PS₄)₂ dimeric unit. This unit is linked to another chain via a second bridging PS₄

ligand to form sheets that are parallel to the [101] crystallographic plane between which Cs^+ ions reside.

The $\text{Bi}_2(\text{PS}_4)_2$ dimer consists of two distorted $\text{Bi}(2)\text{S}_6$ octahedra bridged by two $\text{P}(3)\text{S}_4$ units (see Figure 4-14a). These fragments link the helical chains to form the layered network shown in Figure 4-14b. The influence of the stereochemically active $6s^2$ lone pair of electrons results in a square pyramidal coordination environment for $\text{Bi}(1)$ and a distorted octahedral site for $\text{Bi}(2)$. The $\text{Bi}(1)\text{-S}$ distances are similar to those found in $\text{K}_3\text{Bi}(\text{PS}_4)_3$ with an axial distance of 2.626(8) Å and equatorial distances ranging from 2.692(9) to 2.900(9) Å with two long contacts at 3.312(8) and 3.528(9) Å. The $\text{Bi}(2)\text{-S}$ distances vary between 2.659(8) and 3.08(1) Å. Selected bond distances and angles are given in Tables 4-13 and 4-14.

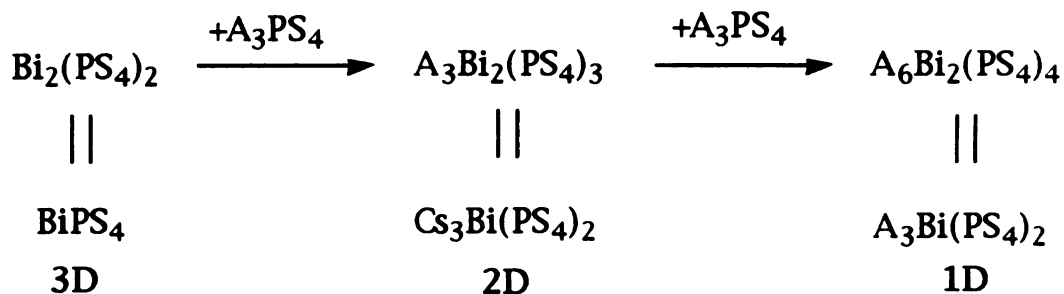
The $[\text{PS}_4]^{3-}$ units ligate to two Bi metal centers via three different bonding modes. $\text{P}(1)\text{S}_4$ coordinates to one Bi atom and bichelates to a second Bi leaving the fourth S atom nonbonding. $\text{P}(2)\text{S}_4$ bichelates to two different Bi atoms. $\text{P}(3)\text{S}_4$ requires three S atoms for bridging between two Bi atoms in the dimeric unit while the fourth S atom is nonbonding. The bonding modes of the $[\text{PS}_4]^{3-}$ ligands are shown in Scheme (B)



Scheme (B)

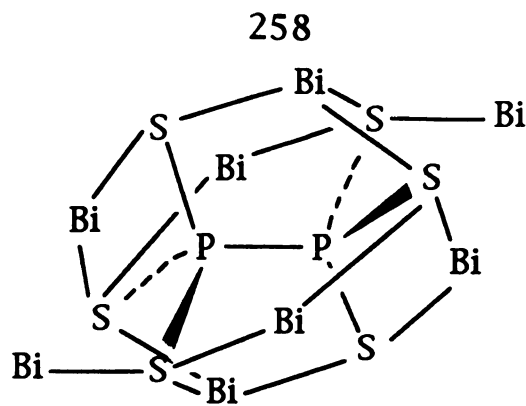
The P-S bond distances range from 1.97(1) to 2.08(1) Å. The shortest distances correspond to terminal P-S bonds as was observed in $\text{K}_3\text{Bi}(\text{PS}_4)_2$.

The structures of the two low dimensional compounds, $\text{K}_3\text{Bi}(\text{PS}_4)_3$ and $\text{Cs}_3\text{Bi}_2(\text{PS}_4)_3$, can be related to that of BiPS_4 .^{4c} The layered $[\text{Bi}_2(\text{PS}_4)_3]^{3-}$ framework can be viewed as a derivative of the known BiPS_4 compound generated by breaking down the dense three-dimensional BiPS_4 framework by incorporation of A_3PS_4 (A=alkali metal). Addition of a second equivalent of A_3PS_4 gives rise to linear $[\text{Bi}(\text{PS}_4)_2]^{3-}$ anionic chains. The increase in the number of counterions produces lower dimensionality. This relationship is outlined in Scheme (C).



Scheme (C)

$\text{Na}_{0.16}\text{Bi}_{1.28}\text{P}_2\text{S}_6$. The structure consists of layers of P_2S_6 groups in the a-b plane separated by a single layer of Bi^{3+} ions (see Figure 4-15). The $[\text{P}_2\text{S}_6]^{4-}$ ligand chelates to eight Bi atoms. Four of the S atoms each trichelate to three Bi atoms while two of the S atoms each bridge two Bi atoms. For clarity, the complicated binding mode of $[\text{P}_2\text{S}_6]^{4-}$ is illustrated separately in Scheme (D).



Scheme (D)

Comparison of the bonding mode of $[\text{P}_2\text{S}_6]^{4-}$ with those observed for $[\text{P}_2\text{Se}_6]^{4-}$ in KMP_2Se_6 ,³³ $\text{Cs}_8\text{M}_4(\text{P}_2\text{Se}_6)_5$,³⁴ $\text{A}_2\text{MP}_2\text{Se}_6$,³⁵ and $\text{A}_2\text{M}_2\text{P}_2\text{Se}_6$ ³⁵ reveals an interesting comparison. Substantial alkali metal cation incorporation into the metal selenophosphate frameworks leads to low dimensional solids. The number of metals bound by the $[\text{P}_2\text{Se}_6]^{4-}$ ligand ranges from one to four. In $\text{Na}_{0.16}\text{Bi}_{1.28}\text{P}_2\text{S}_6$, minimal Na^+ incorporation results in a three-dimensional structure which requires the $[\text{P}_2\text{S}_6]^{4-}$ ligand to bind to eight metals.

Selected bond distances and angles are given in Table 4-15. The BiS_8 coordination site adopts a dodecahedral geometry with distances that range from 2.839(3) to 3.190(4) Å. The Bi-S coordination environment is shown in Figure 4-16. The Bi site is doped with Na^+ and also contains vacancies. Alkali metal/Bi disorder is uncommon and has only been observed in $\text{K}_2\text{Bi}_8\text{S}_{13}$.³⁶ The Bi-S distances are also reasonable for Na-S bonds. For example, Na_6MnS_4 possesses Na-S distances that vary between 2.734(3) and 3.203(3) Å.³⁷ The P-P' bond in $[\text{P}_2\text{S}_6]^{4-}$ is 2.219(6) Å and the P-S distances range from 2.018(4) to 2.032(4) Å. Similar distances have been observed in $\text{Ag}_4\text{P}_2\text{S}_6$.³⁸

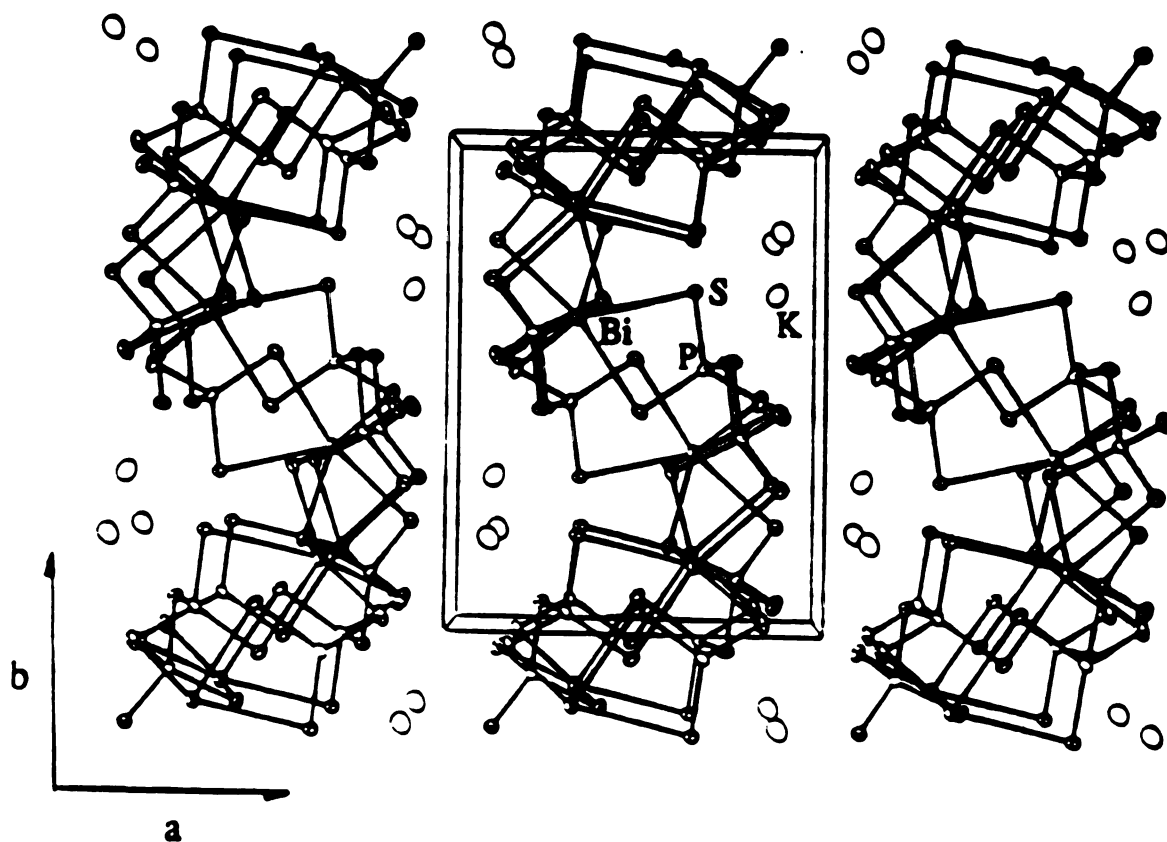


Figure 4-7: ORTEP packing diagram of KBiP_2S_7 looking down the c -axis with labeling.

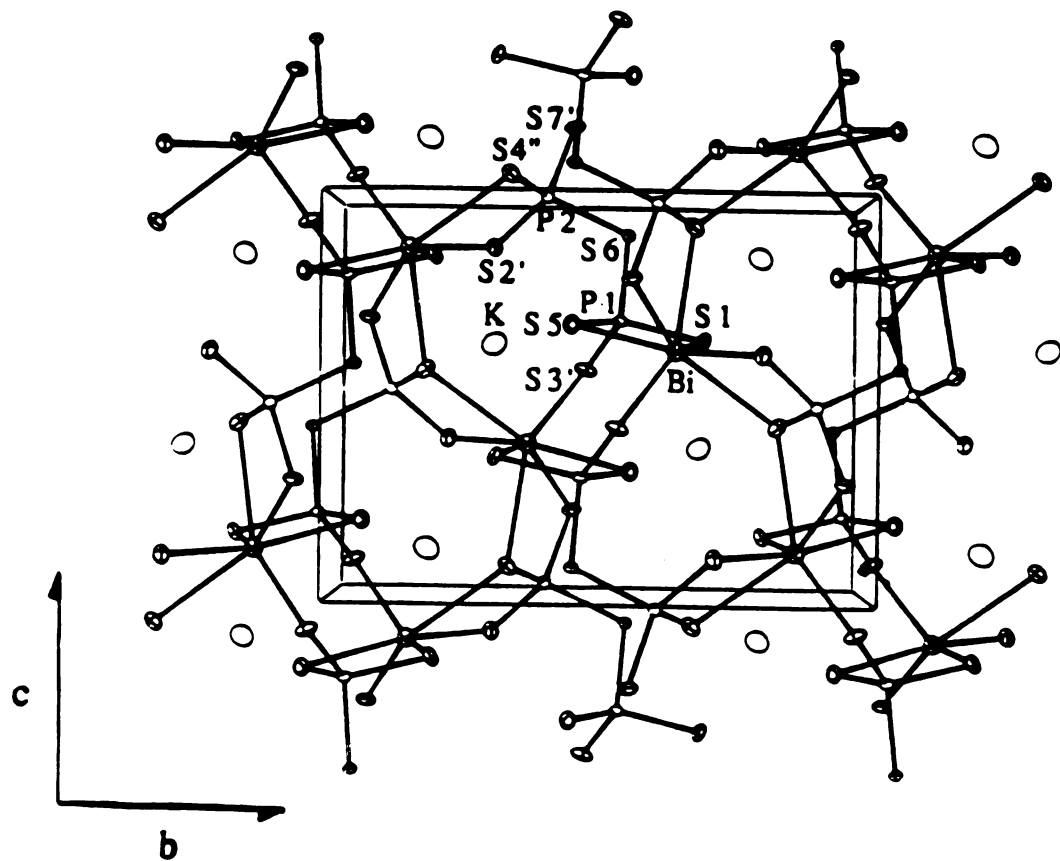


Figure 4-8: ORTEP representation and labeling of the KBiP₂S₇ layer looking down the a-axis.

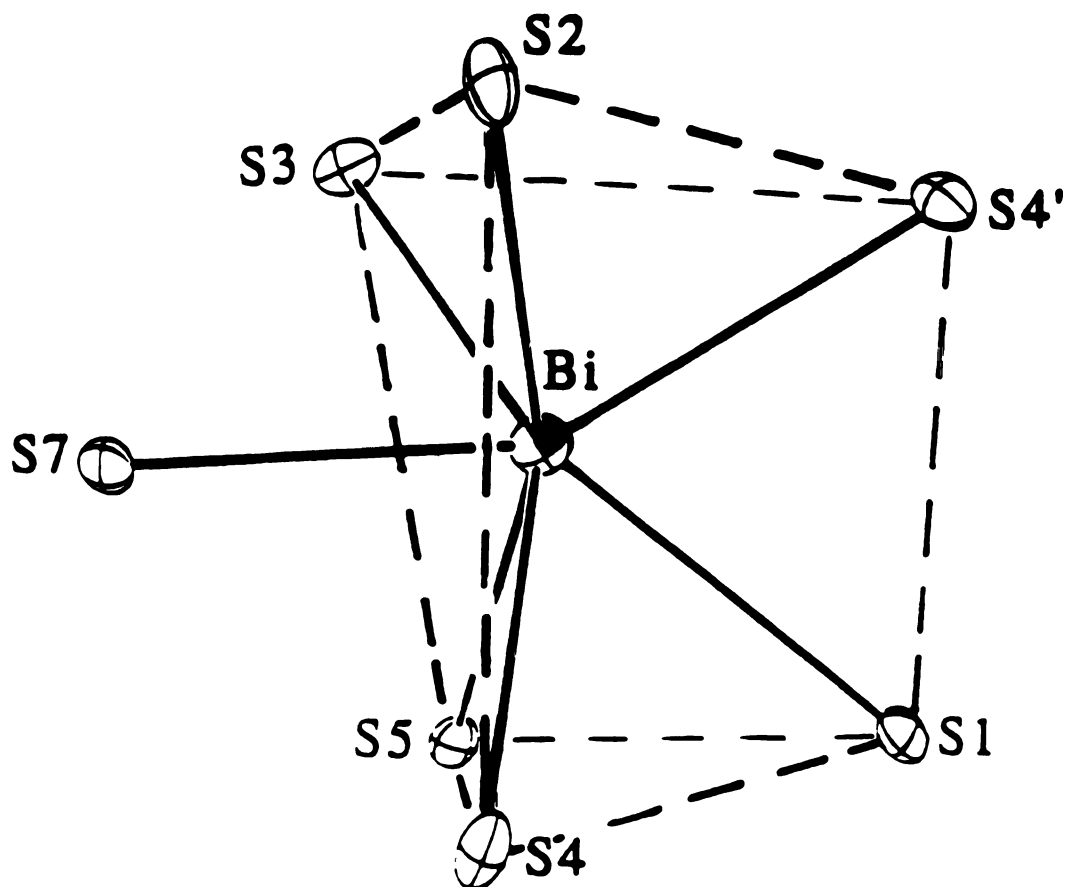


Figure 4-9: ORTEP representation and labeling of the Bi-S coordination site. The polyhedron is outlined with dotted lines for clarity.

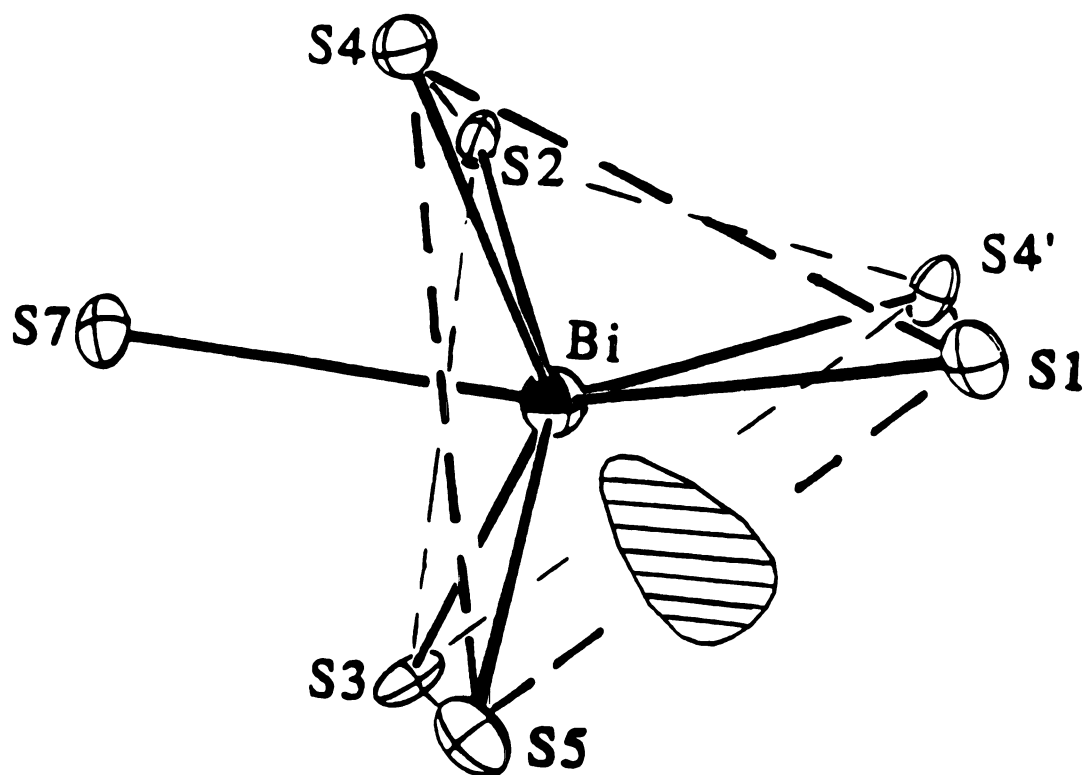


Figure 4-10: ORTEP representation and labeling of the BiS₇ polyhedron viewed from the top of the capped trigonal prism. The probable location of the Bi³⁺ lone pair is shown.

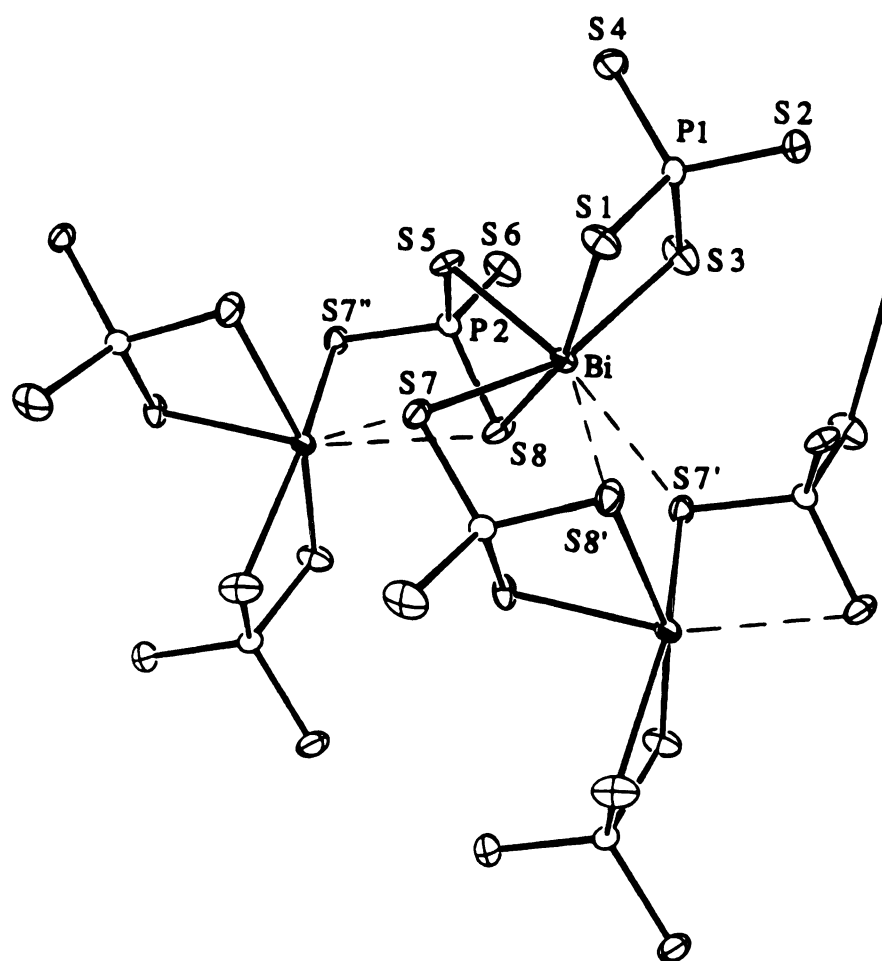


Figure 4-11: A single $[\text{Bi}(\text{PS}_4)_2]^{3-}$ anionic chain.

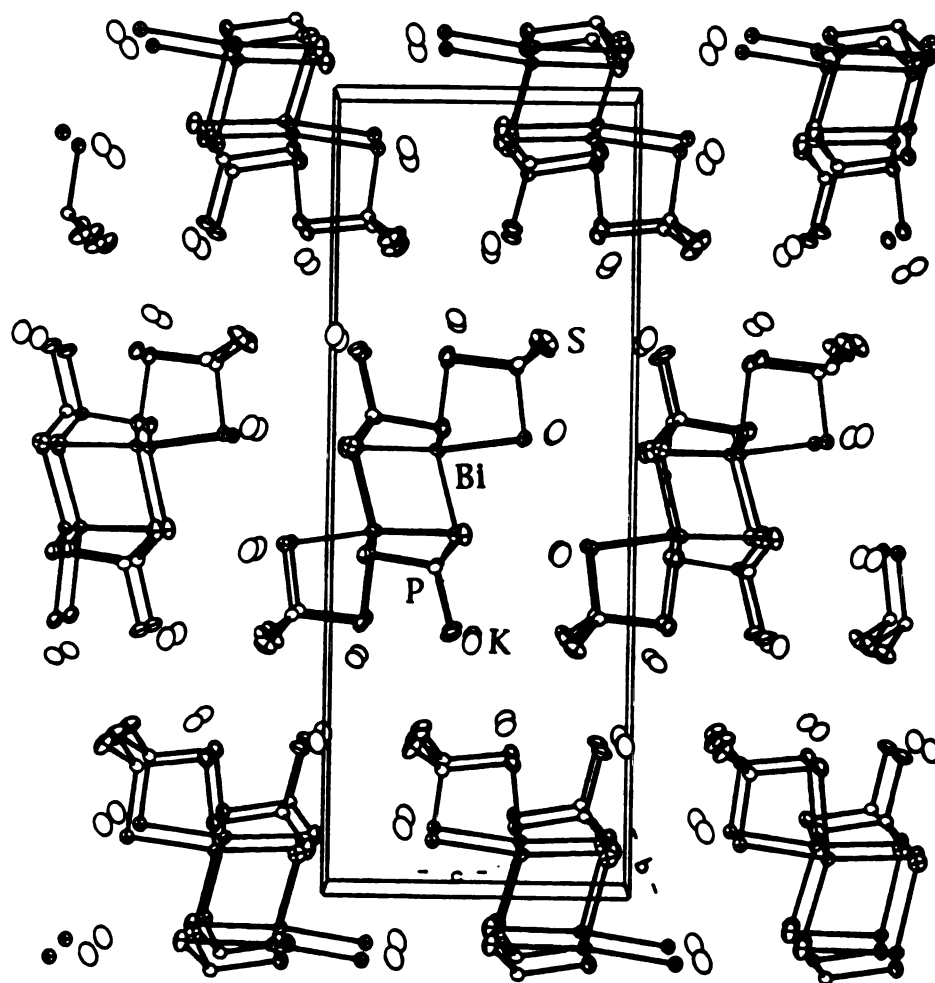


Figure 4-12: ORTEP packing diagram of $K_3Bi(PS_4)_2$ looking down the b-axis with labeling.

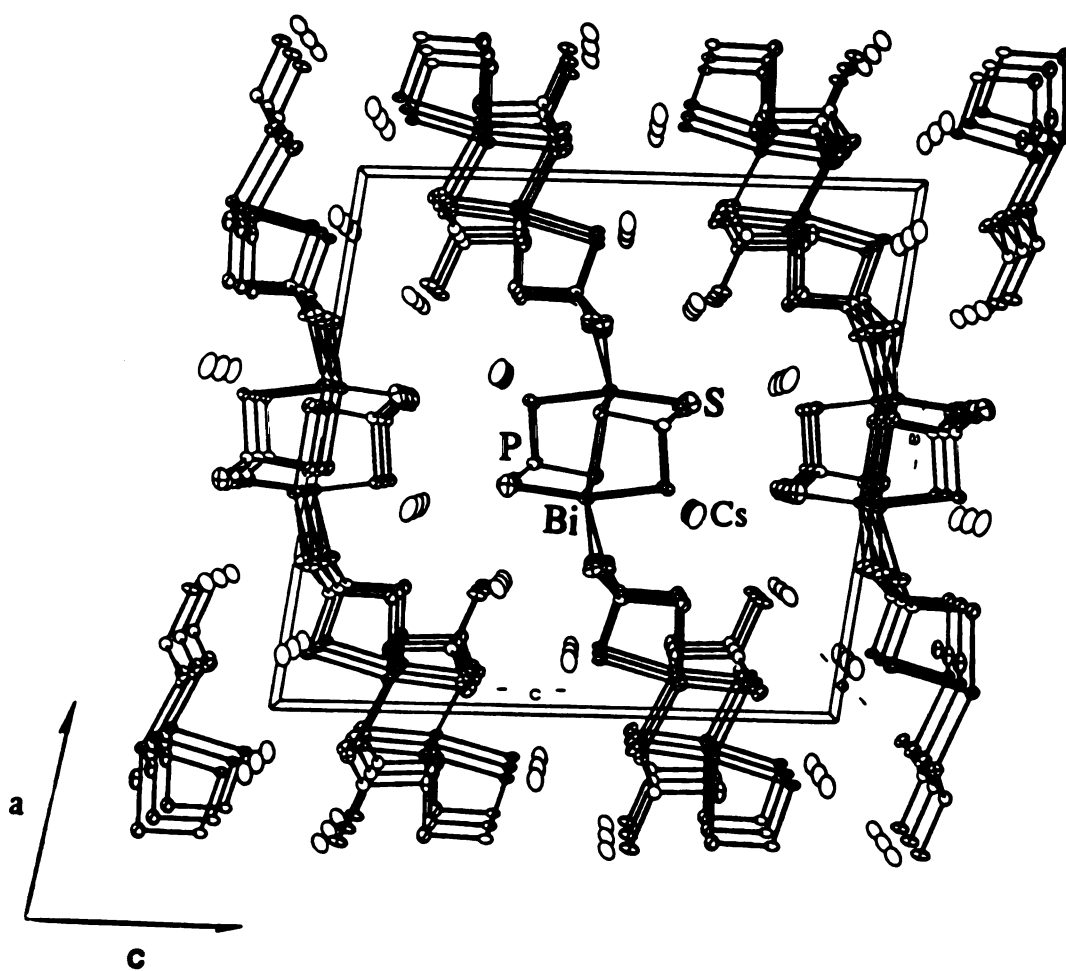


Figure 4-13: ORTEP packing diagram of $\text{Cs}_3\text{Bi}_2(\text{PS}_4)_3$ looking down the b -axis with labeling.

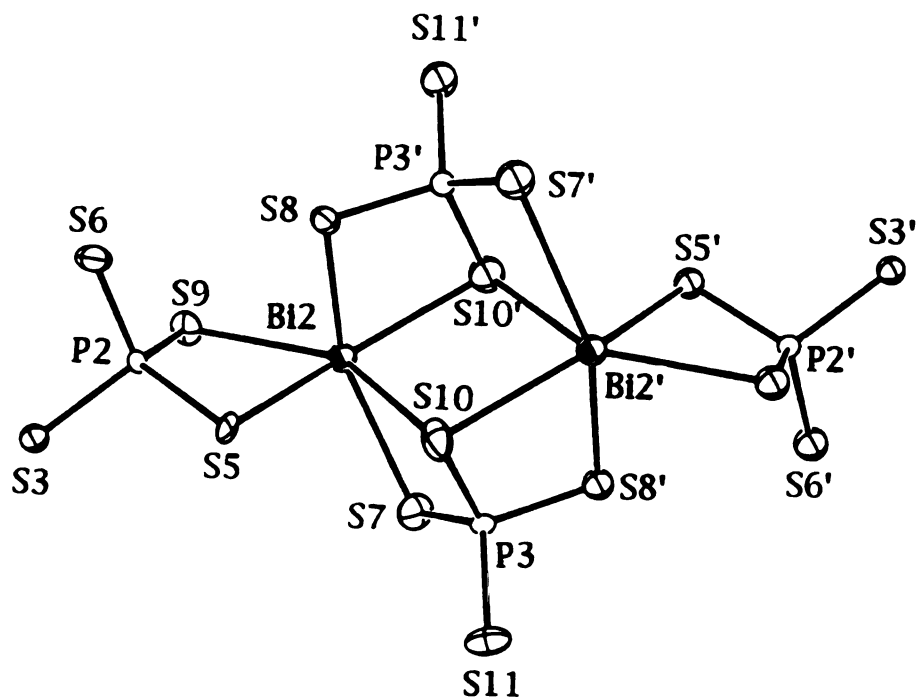
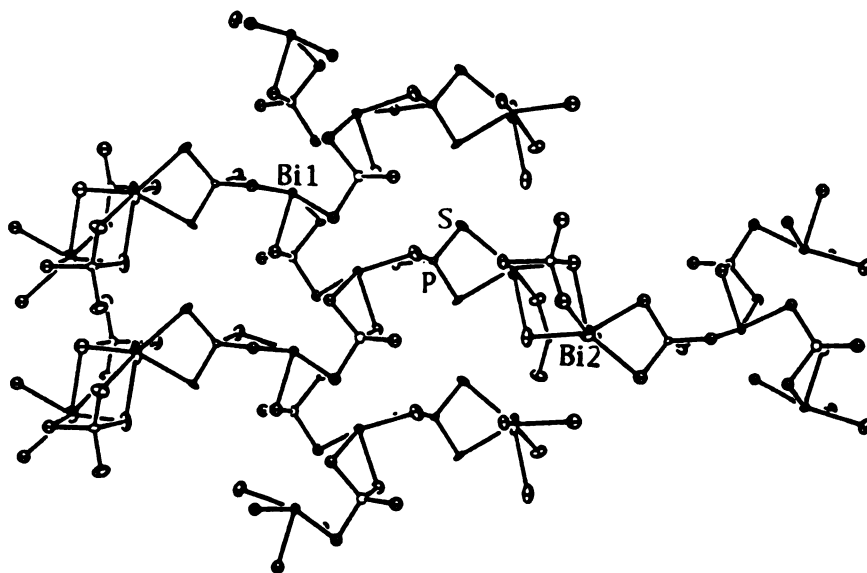
(A)**(B)**

Figure 4-14: (A) The $\text{Bi}_2(\text{PS}_4)_2$ dimeric unit. The $\text{Bi}(2)\text{-Bi}(2')$ distance is $4.519(3)$ Å. (B) A single $[\text{Bi}_2(\text{PS}_4)_3]_n$ $3n$ -layer.

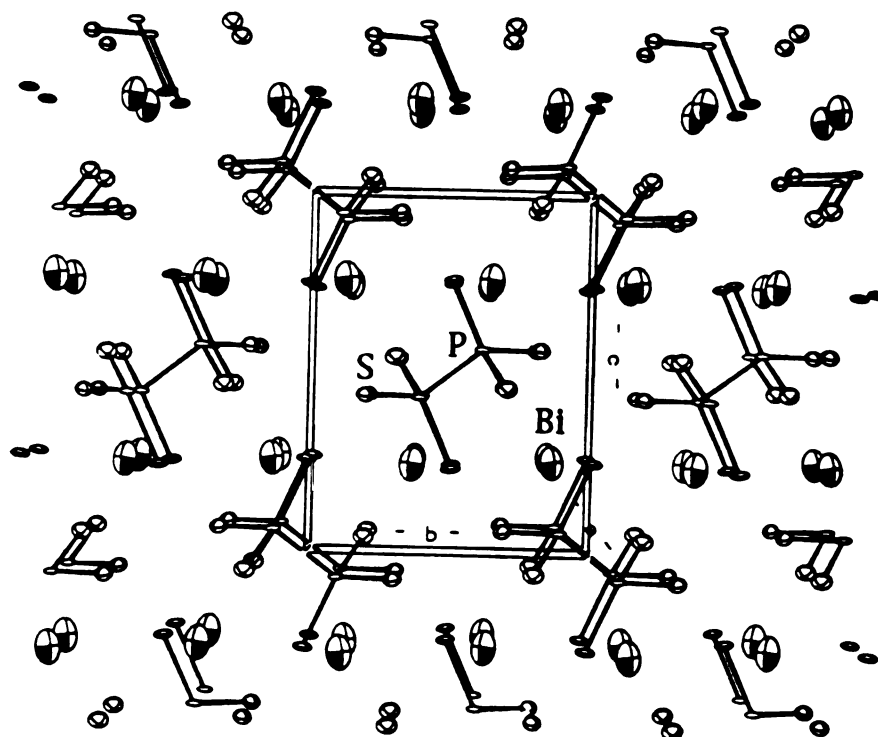


Figure 4-15: ORTEP packing diagram of $\text{Na}_{0.16}\text{BiP}_2\text{S}_6$ looking down the a -axis with labeling. The Bi-S bonds are omitted for clarity.

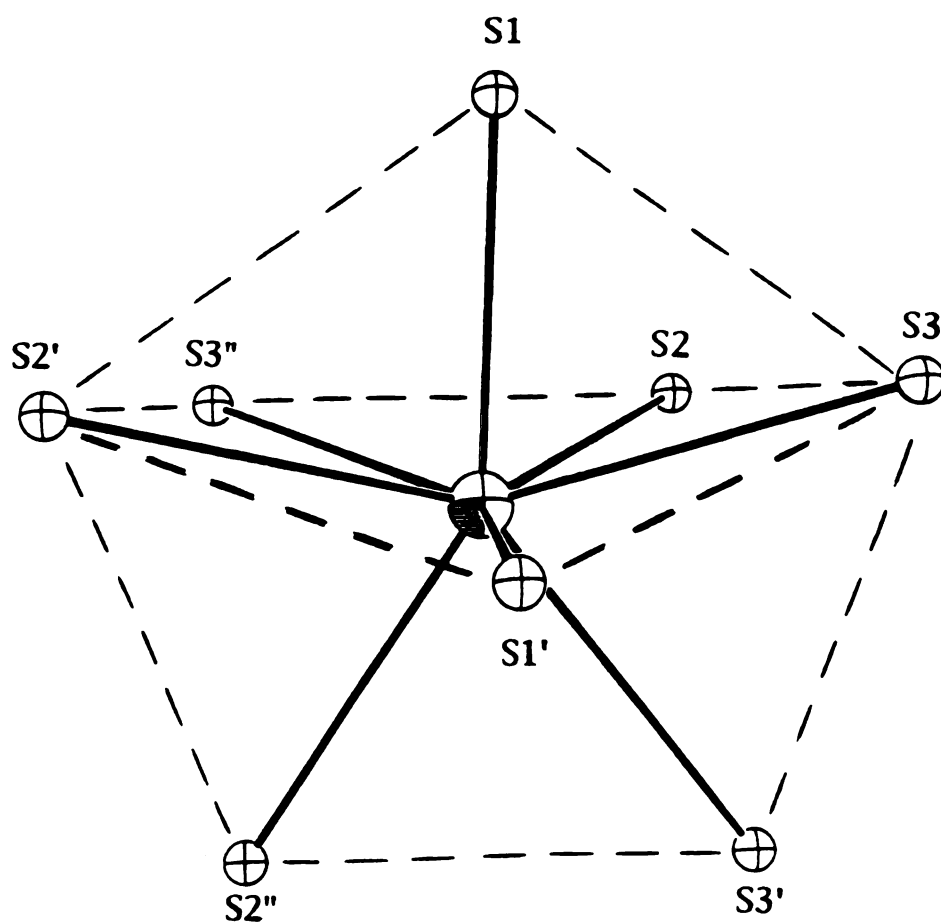


Figure 4-16: ORTEP representation and labeling of the Bi-S coordination site. The polyhedron is outlined with dotted lines for clarity.

Table 4-11. Selected Distances (Å) and Angles (°) for KBiP₂S₇ with Standard Deviations in Parentheses.^a

Bi-S(1)	3.047(2)	S(1)-Bi-S(2)	125.46(5)
Bi-S(2)	2.867(2)	S(1)-Bi-S(3)	138.29(5)
Bi-S(3)	2.761(2)	S(4')-Bi-S(5)	130.43(6)
Bi-S(4)	2.930(2)	S(4)-Bi-S(4')	113.69(5)
Bi-S(4')	2.971(2)	S(1)-Bi-S(4)	71.58(6)
Bi-S(5)	2.906(2)	S(1)-Bi-S(4')	70.16(5)
Bi-S(7)	2.820(2)	S(3)-Bi-S(7)	74.76(6)
Bi-S (ave.)	2.9(1)	S(4)-Bi-S(7)	70.04(6)
		S(3)-Bi-S(5)	93.25(6)
P(1)-S(1)	2.003(3)	S(4)-Bi-S(7)	78.63(5)
P(1)-S(3')	2.035(3)		
P(1)-S(5)	2.018(3)	P(1)-S(6)-P(2)	111.2(1)
P(1)-S(6)	2.115(3)	S(1')-P(1)-S(6)	100.4(1)
P(2)-S(2')	2.015(3)	S(3')-P(1)-S(5)	109.6(1)
P(2)-S(4'')	2.016(3)	S(7')-P(2)-S(6)	98.2(1)
P(2)-S(6)	2.111(3)	S(2')-P(2)-S(4'')	108.1(1)
P(2)-S(7')	2.024(3)		
P-S (ave.)	2.04(4)		
K-S(1)	3.290(3)	K-S(3)	3.359(3)
K-S(1')	3.364(3)	K-S(3')	3.322(3)
K-S(2)	3.323(3)	K-S(6)	3.443(3)
K-S(2')	3.257(3)	K-S(7)	3.374(3)
		K-S (ave.)	3.34(6)

^aThe estimated standard deviations in the mean bond lengths and the mean bond angles are calculated by the equations $\sigma_l = \{\sum_n (l_n - l)^2 / n(n-1)\}^{1/2}$, where l_n is the length (or angle) of the n th bond, l the mean length (or angle), and n the number of bonds.

Table 4-12. Selected Distances (Å) and Angles (°) for $K_3Bi(PS_4)_2$ with Standard Deviations in Parentheses.^a

Bi-S(1)	2.673(3)	S(1)-Bi-S(3)	73.8(1)
Bi-S(3)	2.789(4)	S(1)-Bi-S(5)	91.3(1)
Bi-S(5)	2.649(4)	S(1)-Bi-S(7)	87.4(1)
Bi-S(7)	2.842(5)	S(1)-Bi-S(8)	161.4(1)
Bi-S(8)	2.956(3)	S(3)-Bi-S(5)	88.5(1)
Bi-S (ave.)	2.8(1)	S(3)-Bi-S(7)	157.9(1)
		S(3)-Bi-S(8)	100.4(1)
Bi...S(7')	3.399(4)	S(5)-Bi-S(7)	80.3(1)
Bi...S(8')	3.453(5)	S(5)-Bi-S(6)	70.7(1)
P(1)-S(1)	2.108(5)	S(1)-P(1)-S(2)	109.3(2)
P(1)-S(2)	1.994(5)	S(1)-P(1)-S(3)	103.5(2)
P(1)-S(3)	2.070(4)	S(1)-P(1)-S(4)	109.4(2)
P(1)-S(4)	1.997(6)	S(2)-P(1)-S(3)	109.5(2)
P(2)-S(5)	2.091(5)	S(2)-P(1)-S(4)	112.4(2)
P(2)-S(6)	1.980(5)	S(3)-P(1)-S(4)	112.3(3)
P(2)-S(7)	2.044(5)	S(5)-P(2)-S(6)	113.7(2)
P(2)-S(8)	2.027(5)	S(5)-P(2)-S(7)	107.1(2)
P-S (ave.)	2.04(5)	S(5)-P(2)-S(8)	104.3(2)
		S(6)-P(2)-S(7)	108.4(2)
		S(6)-P(2)-S(8)	113.8(3)
		S(7)-P(2)-S(8)	109.2(2)
		S-P-S (ave.)	109(3)
K(1)-S(1)	3.414(6)	K(3)-S(2)	3.287(5)
K(1)-S(2)	3.133(6)	K(3)-S(3)	3.320(5)
K(1)-S(4)	3.320(6)	K(3)-S(4)	3.438(5)
K(1)-S(5)	3.390(5)	K(3)-S(6)	3.402(6)
K(1)-S(7)	3.429(5)	K(3)-S(6')	3.536(6)
K(1)-S(8)	3.374(5)	K-S (ave.)	3.3(1)
K(2)-S(2)	3.264(5)		
K(2)-S(2')	3.490(6)		
K(2)-S(3)	3.390(6)		
K(2)-S(4)	3.163(5)		
K(2)-S(4')	3.486(6)		
K(2)-S(5)	3.283(5)		
K(2)-S(6)	3.154(5)		
K(2)-S(6')	3.062(5)		

^aThe estimated standard deviations in the mean bond lengths and the mean bond angles are calculated by the equations $\sigma_l = \{\sum_n (l_n - l)^2 / n(n-1)\}^{1/2}$, where l_n is the length (or angle) of the n th bond, l the mean length (or angle), and n the number of bonds.

Table 4-13. Selected Distances (Å) for Cs₃Bi₂(PS₄)₃ with Standard Deviations in Parentheses.^a

Bi(1)-S(1)	2.626(8)	Cs(1)-S(1)	3.520(8)
Bi(1)-S(3)	2.751(7)	Cs(1)-S(2)	3.719(9)
Bi(1)-S(4)	2.859(8)	Cs(1)-S(3)	3.537(9)
Bi(1)-S(6)	2.746(9)	Cs(1)-S(3')	3.538(9)
Bi(1)-S(12)	2.900(9)	Cs(1)-S(4)	3.688(9)
Bi(1)-S (ave.)	2.8(1)	Cs(1)-S(5)	3.729(9)
		Cs(1)-S(9)	3.65(1)
Bi(1)···S(4')	3.528(9)	Cs(1)-S(12)	3.797(9)
Bi(1)···S(12')	3.312(8)	Cs(2)-S(2)	3.590(9)
		Cs(2)-S(7)	3.64(1)
Bi(2)-S(5)	2.764(9)	Cs(2)-S(8)	3.631(9)
Bi(2)-S(7)	3.00(1)	Cs(2)-S(8')	3.649(9)
Bi(2)-S(8)	2.659(8)	Cs(2)-S(10)	3.522(8)
Bi(2)-S(9)	2.925(9)	Cs(2)-S(11)	3.79(1)
Bi(2)-S(10)	3.08(1)	Cs(3)-S(2)	3.485(9)
Bi(2)-S(10')	2.841(9)	Cs(3)-S(2')	3.481(9)
Bi(2)-S (ave.)	2.9(2)	Cs(3)-S(4)	3.746(9)
		Cs(3)-S(6)	3.431(8)
Bi(2)···S(11)	3.219(9)	Cs(3)-S(7)	3.62(1)
		Cs(3)-S(9)	3.59(1)
P(1)-S(1)	2.09(1)	Cs(3)-S(12)	3.710(9)
P(1)-S(2)	1.97(1)	Cs-S (ave.)	3.6(1)
P(1)-S(4)	2.06(1)		
P(1)-S(12)	2.05(1)	Bi(1)-Bi(1')	4.401(2)
P(2)-S(3)	2.08(1)	Bi(2)-Bi(2')	4.519(3)
P(2)-S(5)	2.03(1)		
P(2)-S(6)	2.03(1)		
P(2)-S(9)	2.02(1)		
P(3)-S(7)	2.01(1)		
P(3)-S(8)	2.06(1)		
P(3)-S(10)	2.08(1)		
P(3)-S(11)	2.00(1)		
P-S (ave.)	2.04(4)		

^aThe estimated standard deviations in the mean bond lengths and the mean bond angles are calculated by the equations $\sigma_l = \{\sum_n (l_n - l)^2 / n(n-1)\}^{1/2}$, where l_n is the length (or angle) of the nth bond, l the mean length (or angle), and n the number of bonds.

Table 4-14. Selected Angles (°) for Cs₃Bi₂(PS₄)₃ with Standard Deviations in Parentheses.^a

S(1)-Bi(1)-S(3)	88.0(2)	S(1)-P(1)-S(2)	115.2(5)
S(1)-Bi(1)-S(4)	72.3(2)	S(1)-P(1)-S(4)	102.9(5)
S(1)-Bi(1)-S(6)	89.2(3)	S(1)-P(1)-S(12)	107.0(5)
S(1)-Bi(1)-S(12)	82.5(3)	S(2)-P(1)-S(4)	113.0(5)
S(3)-Bi(1)-S(4)	159.9(2)	S(2)-P(1)-S(12)	109.6(5)
S(3)-Bi(1)-S(6)	73.3(2)	S(4)-P(1)-S(12)	108.6(4)
S(3)-Bi(1)-S(12)	82.2(2)	S(3)-P(2)-S(5)	107.4(5)
S(4)-Bi(1)-S(6)	101.4(3)	S(3)-P(2)-S(6)	106.0(5)
S(4)-Bi(1)-S(12)	99.1(2)	S(3)-P(2)-S(9)	112.3(5)
		S(5)-P(2)-S(6)	114.3(5)
S(5)-Bi(2)-S(7)	93.5(3)	S(5)-P(2)-S(9)	107.6(5)
S(5)-Bi(2)-S(8)	85.9(3)	S(6)-P(2)-S(9)	109.3(5)
S(5)-Bi(2)-S(9)	70.1(2)	S(7)-P(3)-S(8)	109.2(5)
S(5)-Bi(2)-S(10)	71.6(2)	S(7)-P(3)-S(10)	107.4(5)
S(7)-Bi(2)-S(10)	65.8(2)	S(7)-P(3)-S(11)	114.3(5)
S(7)-Bi(2)-S(10')	93.2(3)	S(8)-P(3)-S(10)	105.0(5)
S(8)-Bi(2)-S(9)	86.7(3)	S(8)-P(3)-S(11)	109.7(5)
S(8)-Bi(2)-S(10)	89.0(3)	S(10)-P(3)-S(11)	110.9(5)
S(10)-Bi(2)-S(10')	80.5(3)	S-P-S (ave.)	109(3)

^aThe estimated standard deviations in the mean bond lengths and the mean bond angles are calculated by the equations $\sigma_l = \{\sum_n (l_n - l)^2 / n(n-1)\}^{1/2}$, where l_n is the length (or angle) of the nth bond, l the mean length (or angle), and n the number of bonds.

Table 4-15. Selected Distances (Å) and Angles (°) for Na_{0.16}Bi_{1.28}P₂S₆ with Standard Deviations in Parentheses.^a

Bi-S(1)	2.839(3)	S(1)-Bi-S(1')	89.06(6)
Bi-S(1')	2.944(4)	S(1)-Bi-S(2)	79.03(9)
Bi-S(2)	2.917(3)	S(1)-Bi-S(2')	77.45(9)
Bi-S(2')	3.170(4)	S(1)-Bi-S(3)	70.16(9)
Bi-S(2'')	3.048(3)	S(1)-Bi-S(3'')	82.53(9)
Bi-S(3)	3.190(4)	S(1')-Bi-S(2')	71.62(9)
Bi-S(3')	3.250(4)	S(1')-Bi-S(2'')	88.81(9)
Bi-S(3'')	2.974(4)	S(1')-Bi-S(3)	67.28(9)
Bi-S (ave.)	3.0(1)	S(1')-Bi-S(3')	90.53(9)
		S(2)-Bi-S(3)	74.71(9)
P-S(1)	2.018(4)	S(2)-Bi-S(3')	77.11(9)
P-S(1)	2.032(4)	S(3)-Bi-S(3')	73.1(1)
P-S(1)	2.027(4)		
P-P'	2.219(6)	S(1)-P-S(2)	115.5(2)
		S(1)-P-S(3)	114.6(2)
		S(2)-P-S(3)	110.0(2)
		S(1)-P-P'	106.6(2)
		S(2)-P-P'	103.1(2)
		S(3)-P-P'	105.8(2)

^aThe estimated standard deviations in the mean bond lengths and the mean bond angles are calculated by the equations $\sigma_l = \{\sum_n (l_n - l)^2 / n(n-1)\}^{1/2}$, where l_n is the length (or angle) of the n th bond, l the mean length (or angle), and n the number of bonds.

3.3. Conclusions

The synthesis of new quaternary thiophosphates with $A_x[P_yS_z]$ molten salts provides a useful synthetic approach with broad scope. The $A_x[P_yS_z]$ fluxes provide $[P_xS_y]^{n-}$ units that display remarkable versatility in terms of ligand binding to metals. The high negative charge of these units makes them hard to stabilize in conventional aqueous or organic solvents. The relatively low melting temperatures of the $A_x[PS_y]$ fluxes should allow for the isolation of new or metastable structures and also provide a reliable method for stabilization of $[P_xS_y]^{n-}$ units.

List of References

1. (a) Kanatzidis, M. G. *Chem. Mater.* 1990, 2, 353-363. (b) Kanatzidis, M. G.; Park, Y. *Chem. Mater.* 1990, 2, 99-101. (c) Zhang, X.; Kanatzidis, M. G. *J. Am. Chem. Soc.* 1994, 116, 1890-1898.
2. (a) Kanatzidis, M. G.; Park, Y. *J. Am. Chem. Soc.* 1989, 111, 3767-3769. (b) Park, Y.; Kanatzidis, M. G. *Angew. Chem. Int. Ed. Engl.* 1990, 29, 914-915. (c) Liao, J.-H.; Varotsis, C.; Kanatzidis, M. G. *Inorg. Chem.*, 1993, 32, 2453-2462.
3. (a) Hahn, H.; Klingen, W. *Naturwissenschaften* 1965, 52, 494. (b) Hahn, H.; Ott, R.; Klingen, W. *Z. Anorg. Allg. Chem.* 1973, 396, 271-278.
4. An earlier claim of the existence of the $M_3(PS_4)_2$ (M=first row transition metals) general class of compounds proved incorrect. The reported XRD powder pattern for these materials are identical to those of MPS_3 . (a) Diehl, R.; Carpentier, C.-D. *Acta Cryst.*, 1978, B34, 1097-1105. (b) Buck, P.; Carpentier, C.-D. *Acta Cryst.*, 1973, B29, 1864-1868. (c) Zimmermann, H.; Carpentier, C.-D.; Nitsche, R. *Acta Cryst.* 1975, B31, 2003-2006. (d) Becker, R.; Brockner, W.; Eisenmann, B. *Z. Naturforsch.*, 1987, 42a, 1309-1312. (e) Ferrari, A.; Cavalca, L. *Gazz. Chim. Ital.* 1948, 78, 283-285. (f) Diehl, R.; Carpentier, C.-D. *Acta Cryst.* 1977, B33, 1399-1404. (g) Simon, A.; Peters, K.; Peters, E.-M.; Hahn, H. *Z. Naturforsch.* 1983, 38b, 426-427. (h) Jansen, M.; Henseler, U. *J. Solid State Chem.* 1992, 99, 110-119.
5. (a) Toffoli, P.; Rouland, J. C.; Khodadad, P.; Rodier, N. *Acta Cryst.* 1985, C41, 645-647. (b) Toffoli, P.; Khodadad, P.; Rodier, N. *Acta Cryst.* 1982, B38, 2374-2378. (c) Toffoli, P.; Khodadad, P.; Rodier, N. *Bull. Soc. Chim. Fr.* 1981, 11, 429-432.
6. (a) Mercier, R.; Malugani, J.-P.; Fahys, B.; Robert, G. *Acta Cryst.* 1982, B38, 1887-1890. (b) Fiechter, S.; Kuhs, W. F.; Nitsche, R. *Acta Cryst.* 1980, B36, 2217-2220. (c) Schafer, H.; Schafer, G.; Weiss, A. *Z. Naturforsch.* 1965, 20b, 811. (d) Brec, R.; Evain, M.; Grenouilleau, P.; Rouxel, J. *Rev. Chim. Min.* 1983, 20, 283-294. (e) Brec, R.; Grenouilleau, P.; Evain, M.; Rouxel, J. *Rev. Chim. Min.* 1983, 20, 295-304. (f) Evain, M.; Lee, S.; Queignec, M.; Brec, R. *J. Solid State Chem.* 1987, 71, 139-153. (g) Jandali, M. Z.; Eulenberger, G.; Hahn, H. *Z. Anorg. Allg. Chem.* 1985, 530, 144-154. (h) Weiss, A.; Schafer, H. *Z. Naturforsch.* 1963, 18b, 81-82.
7. Evain, M.; Brec, R.; Whangbo, M.-H. *J. Solid State Chem.* 1987, 71, 244-262.
8. Thompson, A. H.; Whittingham, M. S. *U. S. Patent 4,049,879* 1977. (b) Brec, R.; Le Mehaute', A. *Fr. Patents 7,704,519* 1977.
9. Bridenbaugh, P. M. *Mat. Res. Bull.*, 1973, 8, 1055-1060.
10. Buck, P.; Nitsche, R. A. *Z. Naturforsch.*, 1971, 26b, 731.

11. Scott, B.; Pressprich, M.; Willet, R. D.; Clearly, D. A. *J. Solid State Chem.* 1992, 96, 294-300.
12. Arnautova, E.; Sviridov, E.; Rogach, E. Savchenko, E.; Grekov; A. *Integrated Ferroelectrics*, 1992, 1, 147-150.
13. Menzel, F.; Ohse, L.; Brockner, W. *Heteroatom Chem.* 1990, 1(5), 357-362.
14. McCarthy, T. J.; Kanatzidis, M. G. manuscript in preparation.
15. Feher, F. *Handbuch der Preparativen Anorganischen Chemie*: Brauer, G., Ed.; Ferdinand Enke: Stuttgart, Germany, 1954; pp. 280-281.
16. G. M. Sheldrick, In *Crystallographic Computing 3*; Sheldrick, G. M., Kruger, C., Doddard, R., Eds.; Oxford University Press: Oxford, England, 1985; pp 175-189.
17. TEXSAN: Single Crystal Structure Analysis Software, Version 5.0, (1981). Molecular Structure Corporation, The Woodlands, TX 77381.
18. Walker, N.; Stuart, D. *Acta Cryst.*, 1983, A39, 158-166.
19. Menzel, F.; Ohse, L.; Brockner, W. *Heteroatom Chem.* 1990, 1, 357-362.
20. (a) Queignec, M.; Evain, M.; Brec, R.; Sourisseau, C. *J. Solid State Chem.* 1986, 63, 89-109 (b) Andrae, H.; Blachnik, R. *J. Alloys and Compounds* 1992, 189, 209-215.
21. D'ordyai, V. S.; Galagovets, I. V.; Peresh, E. Yu.; Voroshilov, Yu. V.; Gerasimenko, V. S.; Slivka, V. Yu. *Russ. J. Inorg. Chem.*, 1979, 24, 1603-1606.
22. Pätzmann, U.; Brockner, W.; Cyvin, B. N.; Cyvin, S. J.; *J. Raman Spectr.*, 1986, 17, 257-261.
23. Mathey, Y.; Clement, R.; Sourisseau, C.; Lucazeau, G. *Inorg. Chem.*, 1980, 19, 2773-2779.
24. P. Toffoli, P. Khodadad, N. Rodier, *Acta Cryst.* 1977, B33, 1492-1494.
25. M. Z. Jandali, G. Eulenberger, H. Hahn, *Z. Anorg. Allg. Chem.* 1978, 445, 184-192.
26. Durand, E.; Evain, M.; Brec, R. *J. Solid State Chem.* 1992, 102, 146-155.
27. Kanishcheva, A. S.; Mikhailov, Yu. N.; Trippel, A. F. *Inorg. Mater.* 1981, 17, 1466-1468.
28. McCarthy, T. J.; Ngeyi, S.-P.; Liao, J.-H.; DeGroot, D.; Hogan, T.; Kannewurf, C. R.; Kanatzidis, M. G. *Chem. Mater.*, 1993, 5, 331-340.

29. Liautard, B.; Garcia, J. C.; Brun, G.; Tedenac, J. C.; Maurin, M. *Eur. J. Solid State Inorg. Chem.*, 1990, 27, 819-830.
30. L. Pauling The Nature of the Chemical Bond, 3rd Edition, New York: Cornell University Press, 1966, p. 260.
31. Vos, A.; Wiebenga, E. H. *Acta Cryst.* 1955, 8, 217-223.
32. Simon, A.; Peters, K.; Peters, E.-M.; Hahn, H. *Z. Naturforsch.* 1983, 38b, 426-427.
33. McCarthy, T. J.; Kanatzidis, M. G. *J. Chem. Soc., Chem. Commun.*, 1994, in press.
34. McCarthy, T. J.; Hogan, T.; Kannewurf, C. R.; Kanatzidis, M. G. *Chem. Mater.*, 1994, in press.
35. McCarthy, T. J.; Kanatzidis, M. G. manuscript in preparation.
36. McCarthy, T. J.; Tanzer, T. A.; Chen, L.-H.; Hogan, T.; Kannewurf, C. R.; Kanatzidis, M. G. manuscript in preparation.
37. Bronger, W.; Balk-Hardtdegen, H. *Z. Anorg. Allg. Chem.*, 1989, 574, 89-98.
38. Toffoli, P.; Michelet, A.; Khodadad, P.; Rodier, N. *Acta Cryst.* 1982, B38, 706-710.

CHAPTER 5

Coordination Chemistry of $[P_2Se_6]^{4-}$ in Molten Alkali Metal Polyselenophosphate Fluxes. Isolation of KMP_2Se_6 and $Cs_8M_4(P_2Se_6)_5$ ($M=Sb, Bi$)

1. Introduction

Recently, we reported the synthesis of new quaternary metal thiophosphate compounds ($ABiP_2S_7$; $A=K, Rb$) using molten alkali polythiophosphate fluxes at intermediate temperatures.¹ We have extended this methodology to new quaternary metal selenophosphates, because the chemistry of selenophosphate ligands is not well developed. The rare $[PSe_4]^{3-}$ ligand is found in solid state compounds such as Cu_3PSe_4 ² and Tl_3PSe_4 ,³ and in the unusual tungsten complex, $[W(Se)(PSe_2)(PSe_4)]^{2-}$, which also contains the unprecedented heteroallylic $[PSe_2]^-$ unit.⁴ Most of the known solid state selenophosphates contain the ethane-like $[P_2Se_6]^{4-}$ ligand. These compounds belong to an important $M_2P_2Q_6$ ($Q=S, Se$) family of compounds which are structurally related to CdI_2 .^{5,6} Thus far, transition metals have received the most attention in this system although a few examples with main group elements such as Sn ^{5c,7} and Pb ^{5c,8} are known. Sn and Pb are found in trigonal prismatic sites instead of octahedral sites to form a three-dimensional

structure type. The acentric $\text{Sn}_2\text{P}_2\text{S}_6$ is a promising ferroelectric material for use in memory devices.^{7c} It is noteworthy that $\text{In}_{1.33}\text{P}_2\text{Se}_6$ may be suitable for photovoltaic devices^{9,10} while other members of the $\text{M}_2\text{P}_2\text{Q}_6$ family have been studied for rechargeable battery¹¹ and ion-exchange applications.¹² Recently, several mixed-metal selenophosphates of the $\text{M}_2\text{P}_2\text{Q}_6$ family have been prepared.¹³ These compounds are typically synthesized by direct combination of the elements in the 500-800 °C temperature range. Studies in various laboratories have shown that the $\text{M}_2\text{P}_2\text{Q}_6$ structural type is very thermodynamically stable. In order to explore new metal/selenophosphates at *lower temperatures* and to obtain new structure types we adopted the flux technique using the polyselenophosphate $\text{A}_x[\text{P}_y\text{Se}_z]$ fluxes at <600°C. A key feature of these melts is that they are Se-rich. The $\text{A}_x[\text{P}_y\text{Se}_z]$ fluxes provide excess $[\text{P}_y\text{Se}_z]^{n-}$ anions which bind to metal ions and act as mineralizers. They also provide a strong basic medium which discourages the formation of $\text{M}_2\text{P}_2\text{Se}_6$. We highlight that $\text{A}_x[\text{P}_y\text{Se}_z]$ fluxes *behave significantly different than their sulfur analogs* and stabilize readily $[\text{P}_2\text{Se}_6]^{4-}$ units. This results in solid state compounds with no sulfur analogs.

We report here the synthesis, structural characterization, optical, thermal, and electrical properties of four new quaternary compounds. KBiP_2Se_6 and KSbP_2Se_6 are isostructural and feature a novel layered structure containing the $[\text{P}_2\text{Se}_6]^{4-}$ building block in a remarkably complex bonding mode. $\text{Cs}_8\text{Sb}_4(\text{P}_2\text{Se}_6)_5$ and $\text{Cs}_8\text{Bi}_4(\text{P}_2\text{Se}_6)_5$ also form complex isostructural layered structures and exhibit a rare example of unusually close $\text{Sb}\cdots\text{Sb}$ and $\text{Bi}\cdots\text{Bi}$

interactions, similar in magnitude to those found in the corresponding elements.. The ethane-like $[P_2Se_6]^{4-}$ ligand is found in three unique bonding modes.

2. Experimental Section

2.1. Reagents

Chemicals in this work were used as obtained: (i) antimony powder, 99.999+% purity, -200 mesh, Cerac Inc., Milwaukee, WI; (ii) bismuth powder, 99.999% purity, -100+200 mesh, Johnson Matthey/AESAR Group, Seabrook, NH; (iii) red phosphorus powder, Morton Thiokol, Inc., -100 mesh, Danvers, MA; (iv) selenium powder, 99.5+% purity -100 mesh, Aldrich Chemical Co., Inc., Milwaukee, WI; (v) potassium metal, analytical reagent, Mallinckrodt Inc., Paris, KY; (vi) cesium metal, analytical reagent, Johnson Matthey/AESAR Group, Seabrook, (vii) DMF, analytical reagent, diethyl ether, ACS anhydrous, EM Science, Inc., Gibbstown, NJ.

2.2. Synthesis

Synthesis: All manipulations were carried out under a dry nitrogen atmosphere in a Vacuum Atmospheres Dri-Lab glovebox. For the preparation of K_2Se and Cs_2Se we used a modified literature procedure.¹⁴ The preparation of K_2Se is reported in Section 2.2 of Chapter 1 (Part 1).

Cs_2Se . A 5.00 g (38 mmol) aliquot of slightly heated ($\sim 30^\circ C$) cesium metal was pipetted into a 250-ml round-bottom flask. A

150-ml volume of liquid ammonia was condensed into the flask at $-78\text{ }^{\circ}\text{C}$ (dry ice/acetone bath) under nitrogen to give a dark blue solution. 1.485 g (19 mmol) Se and a Teflon-coated stir bar were added, and the mixture was stirred for 1 h to give a light blue solution. The NH_3 was removed by evaporation under a flow of nitrogen as the bath slowly warmed to room temperature. The pale orange solid (98% yield) was dried under vacuum overnight, flame-dried, and ground to a fine powder in the glove box.

P_2Se_5 . The phosphorous selenide glass " P_2Se_5 " was prepared by heating a stoichiometric ratio of the elements in an evacuated pyrex tube for 24 hours at $460\text{ }^{\circ}\text{C}$ followed by slow cooling to room temperature. This was ground up and stored in a nitrogen glove box.

KBiP_2Se_6 (I). An amount of 0.031 g (0.15 mmol) Bi, 0.206 g (0.450 mmol) P_2Se_5 , 0.047 g (0.3 mmol) K_2Se , and 0.095 g (1.2 mmol) Se was sealed under vacuum in a pyrex tube and heated to $410\text{ }^{\circ}\text{C}$ for 4 days followed by cooling to $110\text{ }^{\circ}\text{C}$ at $4\text{ }^{\circ}\text{C/hr}$. The excess deep red $\text{K}_x\text{P}_y\text{Se}_z$ matrix was removed with DMF to reveal analytically pure dark red rectangular plate-like crystallites of KBiP_2Se_6 (69% yield). Single crystals suitable for data collection were synthesized at $450\text{ }^{\circ}\text{C}$ and were accompanied by a K/P/Se impurity. The crystals are air and water stable. Quantitative microprobe analysis on single crystals gave $\text{K}_{1.0}\text{Bi}_{1.3}\text{P}_{2.1}\text{Se}_{6.3}$ (average of three data acquisitions). Far-IR absorbances are given in Table 5-1.

KSbP_2Se_6 (II). An amount of 0.018 g (0.15 mmol) Sb, 0.206 g (0.450 mmol) P_2Se_5 , 0.047 g (0.3 mmol) K_2Se , and 0.095 g (1.2 mmol) Se were mixed and heated as above, except at $450\text{ }^{\circ}\text{C}$ for 6 days and cooled to $150\text{ }^{\circ}\text{C}$ at $4\text{ }^{\circ}\text{C/hr}$ (75% yield). The compound was found to

be isostructural to KBiP_2Se_6 by powder X-ray diffraction. Quantitative microprobe analysis on red crystals gave $\text{K}_{1.0}\text{Sb}_{1.1}\text{P}_{1.4}\text{Se}_{5.2}$ (average of three data acquisitions).

$\text{Cs}_8\text{Sb}_4(\text{P}_2\text{Se}_6)_5$ (III). An amount of 0.018 g (0.15 mmol) Sb, 0.206 g (0.450 mmol) P_2Se_5 , 0.103 g (0.30 mmol) Cs_2Se , and 0.047 g (0.60 mmol) Se were thoroughly mixed and heated as in (I), except as 460°C for 6 days. The product, which is stable in water and air, was isolated by dissolving the flux with degassed DMF under inert atmosphere and then washing with anhydrous ether to give 0.120 g (75% yield based on Sb) of pure dark red crystals. Quantitative microprobe analysis on single crystals gave $\text{Cs}_{2.3}\text{Sb}_{1.0}\text{P}_{2.3}\text{Se}_{7.2}$ (average of three data acquisitions). Far-IR absorbances are given in Table 5-1.

$\text{Cs}_8\text{Bi}_4(\text{P}_2\text{Se}_6)_5$ (IV). The reaction of 0.031 g (0.15 mmol) Bi, 0.206 g (0.450 mmol) P_2Se_5 , 0.103 g (0.30 mmol) Cs_2Se , and 0.047 g (0.60 mmol) Se under the same conditions as (III) gave 0.155 g (90% yield based on Bi) of black crystals. Quantitative microprobe analysis on the single crystals gave $\text{Cs}_{2.0}\text{Bi}_{1.0}\text{P}_{1.8}\text{Se}_{6.5}$ (average of three data acquisitions.). Far-IR absorbances are given in Table 5-1.

The homogeneity of (I), (III), and (IV) was confirmed by comparing the observed and calculated X-ray powder diffraction patterns. The d_{hkl} spacings observed for the bulk materials were compared, and found to be in good agreement with the d_{hkl} spacings calculated from the single crystal data.¹⁵ The results are summarized in Tables 5-2, 5-3, 5-4.

2.3. Physical Measurements

The instruments and experimental setups for optical diffuse reflectance measurements, far-IR spectroscopy, quantitative microprobe analysis on SEM/EDS, and charge-transport measurements are the same as those in Chapter 2 (Part 1) (Section 2.3). The experimental setup for differential thermal analysis (DTA) is the same as that in Chapter 2 (Part 2) (Section 2.3).

2.4. X-ray Crystallography

All compounds were examined by X-ray powder diffraction for the purpose of phase purity and identification. Accurate d_{hkl} spacings (Å) were obtained from the powder patterns recorded on a Rigaku Rotaflex Powder X-ray Diffractometer with Ni filtered Cu K α radiation operating at 45 kV and 100 mA. The data were collected at a rate of 1.0 deg/min.

Structural solution of Cs₈Sb₄(P₂Se₆)₅. Single crystal X-ray diffraction data for Cs₈Sb₄(P₂Se₆)₅ were collected with a Nicolet P3 four-circle automated diffractometer equipped with a graphite-crystal monochromator. The data were collected with θ -2 θ step scan technique.

Structural solution of KBiP₂Se₆ and Cs₈Bi₄(P₂Se₆)₅. Intensity data for Cs₈Bi₄(P₂Se₆)₅ were collected with a Rigaku AFC6 diffractometer equipped with a graphite-crystal monochromator. The data were collected with the ω /2 θ scan technique.

None of the three crystals showed any significant intensity decay as judged by three check reflections measured every 150

reflections throughout the data collection. The space groups were determined from systematic absences and intensity statistics. The structures were solved by direct methods of SHELXS-86¹⁶ and refined by full-matrix least-squares techniques of the TEXSAN package of crystallographic programs.¹⁷ An empirical absorption correction based on ψ -scans was applied to each data set, followed by a DIFABS¹⁸ correction to the isotropically refined structure. All atoms were eventually refined anisotropically. All calculations were performed on a VAXstation 3100/76 computer.

The complete data collection parameters and details of the structure solution and refinement for (I), (I I I), and (I V) are given in Table 5-5. The coordinates of all atoms, average temperature factors, and their estimated standard deviations are given in Tables 5-6, 5-7, and 5-8.

Table 5-1. Far-IR Data for KMP_2Se_6 and $\text{Cs}_8\text{M}_4(\text{P}_2\text{Se}_6)_5$.^a

I	III	IV
490 (s)	522 (m)	518 (m)
477 (s)	511 (m)	499(s, broad)
453 (w)	500 (m)	460(m, broad)
292 (m)	474 (m)	424 (w)
227 (w)	462 (m)	416 (m)
202 (w)	448 (w)	406 (m)
180 (m)	414 (m)	392 (m)
170 (m)	406 (s)	366 (wsh)
	394 (s)	337 (vw)
	297 (m)	293 (msh)
	287 (s)	289 (m)
	204 (m)	280 (msh)
	188 (w)	253 (wsh)
	177 (m)	249 (wsh)
	149 (s)	226 (w)
		221 (wsh)
		201 (vw)
		192 (m)
		171 (m)
		144 (m)

^aAbbreviations: s=strong, m=medium, w=weak, sh=shoulder, v=very.

Table 5-2. Calculated and Observed X-ray Powder Diffraction Patterns for KBiP_2Se_6 .

h k l	$d_{\text{calcd}}, \text{\AA}$	$d_{\text{obsd}}, \text{\AA}$	$I/I_{\text{max}} (\text{obsd})$
1 0 0	11.53	11.53	100
0 1 1	6.34	6.34	25
1 0 -2	6.14	6.15	46
0 0 2	5.77	5.77	35
2 0 -2	5.13	5.13	8
1 1 -2	4.78	4.78	13
2 1 0	4.59	4.59	44
1 1 2	3.895	3.894	22
3 0 0	3.844	3.841	6
0 2 0	3.798	3.799	7
0 2 1	3.607	3.610	10
1 2 -1	3.561	3.562	21
3 1 -2	3.495	3.493	18
0 1 3	3.432	3.432	6
1 2 1	3.335	3.329	7
1 2 -2	3.230	3.232	8
2 2 0	3.172	3.171	30
3 1 -3	3.119	3.119	4
4 0 -2	3.070	3.062	38
3 1 1	3.028	3.026	66
2 2 1	2.912	2.912	10
4 0 0	2.883	2.881	61
4 1 -2	2.846	2.847	56
1 2 -3	2.797	2.796	30
3 0 2	2.765	2.761	4
2 2 -3	2.734	2.735	15
0 1 4	2.698	2.695	48
1 0 4	2.585	2.586	7
4 0 -4	2.565	2.565	40
3 2 -3	2.542	2.541	19
1 2 3	2.492	2.493	21
5 0 -2	2.479	2.477	25
4 1 -4	2.430	2.430	7
1 3 1	2.380	2.379	25
5 1 -2	2.357	2.355	6
1 1 -5	2.326	2.325	7
0 2 4	2.298	2.297	8
2 2 3	2.235	2.233	5
5 1 0	2.207	2.208	6
4 1 2	2.173	2.172	11
3 3 -1	2.159	2.157	18
4 2 1	2.136	2.134	4
0 3 3	2.115	2.115	4
5 2 -2	2.076	2.076	6
6 0 -2	2.066	2.064	7

Table 5-2. (cont'd)

h k l	d _{calcd} , Å	d _{obsd} , Å	I/I _{max} (obsd)
2 3 2	2.049	2.049	9
5 1 1	2.040	2.036	16
2 1 -6	1.995	1.992	6
5 1 -5	1.981	1.981	5
4 0 -6	1.969	1.971	8
2 2 4	1.947	1.949	6
4 3 -3	1.898	1.899	5
5 1 2	1.855	1.852	13
6 2 -3	1.802	1.799	7
5 3 -1	1.757	1.758	8
4 2 -6	1.748	1.750	12
5 3 -3	1.744	1.745	16
3 1 -7	1.723	1.723	14
2 4 -3	1.710	1.711	11
4 1 4	1.700	1.697	10
4 1 -7	1.689	1.688	5
3 1 5	1.677	1.677	5
3 4 -3	1.660	1.662	6
5 3 1	1.624	1.624	7
1 2 6	1.622	1.620	5
2 4 -4	1.615	1.616	4
7 2 -3	1.603	1.603	8
6 3 -1	1.579	1.579	7

Table 5-3. Calculated and Observed X-ray Powder Diffraction Patterns for $\text{Cs}_8\text{Sb}_4(\text{P}_2\text{Se}_6)_5$.

h k l	$d_{\text{calcd}}, \text{\AA}$	$d_{\text{obsd}}, \text{\AA}$	I/I _{max} (obsd)
1 0 1	11.10	11.13	4
1 1 -1	8.38	8.37	3
2 0 0	7.71	7.74	3
1 1 -2	6.58	6.57	4
1 1 2	6.20	6.22	7
0 1 3	5.25	5.20	4
3 0 1	4.81	4.83	6
1 2 -2	4.67	4.69	2
1 2 -3	4.05	4.05	5
2 1 -4	3.78	3.79	5
3 2 1	3.69	3.70	8
1 3 -1	3.66	3.66	9
0 3 2	3.52	3.52	6
2 3 -1	3.40	3.38	3
3 2 -3	3.33	3.32	4
2 3 -2	3.25	3.25	5
2 2 4	3.10	3.11	100
3 2 -4	3.01	3.01	9
4 1 3	2.99	3.00	11
0 4 0	2.88	2.88	18
2 0 -6	2.85	2.85	21
0 4 1	2.84	2.82	6
1 4 1	2.78	2.77	3
2 2 5	2.73	2.73	3
2 4 -1	2.68	2.68	3
0 3 5	2.60	2.60	3
1 0 -7	2.53	2.54	3
3 3 4	2.458	2.433	6
6 0 2	2.405	2.414	9
4 4 2	2.200	2.203	5
2 4 -5	2.180	2.181	4
5 4 1	2.072	2.075	4
2 4 -6	2.024	2.025	8
6 1 -6	2.006	2.008	5
7 0 -5	1.957	1.958	2
8 1 1	1.871	1.867	4
6 4 2	1.845	1.849	7
6 2 6	1.761	1.764	3
2 6 4	1.701	1.704	8
2 4 -2	1.699	1.695	10
0 2 10	1.691	1.689	9
6 5 -3	1.675	1.677	4
9 2 -1	1.649	1.654	3
4 4 8	1.551	1.554	4
8 4 -4	1.546	1.549	3

Table 5-4. Calculated and Observed X-ray Powder Diffraction Patterns for $\text{Cs}_8\text{Bi}_4(\text{P}_2\text{Se}_6)_5$.

h k l	$d_{\text{calcd}}, \text{\AA}$	$d_{\text{obsd}}, \text{\AA}$	$I/I_{\text{max}} (\text{obsd})$
1 0 1	11.28	11.27	10
1 1 -1	8.43	8.42	7
1 1 1	8.06	8.05	3
2 0 0	7.84	7.84	6
1 1 -2	6.61	6.61	4
2 1 0	6.48	6.47	3
1 1 2	6.27	6.26	8
0 1 3	5.29	5.28	4
3 0 1	4.90	4.89	7
1 2 -2	4.69	4.68	4
1 2 2	4.56	4.55	5
1 2 -3	4.07	4.06	4
2 1 -4	3.81	3.80	7
3 2 1	3.73	3.73	11
1 3 -1	3.67	3.66	6
0 3 2	3.53	3.52	9
2 3 -1	3.41	3.41	6
1 2 4	3.39	3.38	7
3 2 -3	3.35	3.35	7
0 3 3	3.23	3.22	4
2 2 4	3.13	3.12	100
3 2 -4	3.03	3.03	11
4 1 -4	2.98	3.00	7
3 3 -2	2.97	2.97	5
4 2 -3	2.94	2.94	6
2 0 -6	2.87	2.87	18
0 4 1	2.84	2.84	5
1 4 1	2.79	2.78	4
2 2 5	2.76	2.75	6
2 4 0	2.70	2.69	4
1 0 -7	2.55	2.55	4
3 3 4	2.482	2.478	7
6 0 2	2.450	2.446	17
4 1 -6	2.425	2.423	5
0 1 8	2.190	2.185	4
3 5 -1	2.103	2.102	5
5 4 1	2.092	2.089	6
7 2 -2	2.073	2.072	4
2 4 -6	2.033	2.029	11
6 4 2	1.866	1.865	7
8 0 -4	1.858	1.855	5
0 2 10	1.704	1.704	10
6 2 -8	1.699	1.699	10
4 4 8	1.567	1.565	5
8 4 -4	1.562	1.561	5

Table 5-5. Crystallographic Data for KBiP_2Se_6 , $\text{Cs}_8\text{Sb}_4(\text{P}_2\text{Se}_6)_5$ and $\text{Cs}_8\text{Bi}_4(\text{P}_2\text{Se}_6)_5$.

	I	II I	I V
Formula	KBiP_2Se_6	$\text{Cs}_8\text{Sb}_4(\text{P}_2\text{Se}_6)_5$	$\text{Cs}_8\text{Bi}_4(\text{P}_2\text{Se}_6)_5$
FW	783.79	4228.8	4577.7
a, Å	12.403(5)	15.489(3)	15.752(4)
b, Å	7.595(2)	11.505(2)	11.523(2)
c, Å	12.412(3)	17.772(3)	17.916(2)
α , deg	90.000	90.000	90.000
β , deg	111.58(3)	95.59(2)	95.20(2)
γ , deg	90.000	90.000	90.000
Z; V, Å ³	4; 1087(1)	2; 3152	2; 3241
λ	0.71073	0.71073	0.71073
space group	$\text{P}2_1/\text{c}$ (No. 14)	$\text{P}2_1/\text{n}$ (No. 14)	$\text{P}2_1/\text{n}$ (No. 14)
D _{calc.} , g/cm ³	4.788	4.455	4.694
μ , cm ⁻¹	366.75	236.55 (Mo K α)	321.67 (Mo K α)
2 θ max, deg	50 (Mo K α)	50 (Mo K α)	50 (Mo K α)
Temp., °C	23	-80	23
Final R/R _w , %	3.9/4.5	3.2/4.9	5.4/6.7
Total Data Measured	2170	6100	6261
Total Unique Data	2070	5891	6028
Data $F_o^2 > 3\sigma(F_o^2)$	1228	3544	2598
No. of Variables	92	236	236

$$* R = \Sigma(|F_o| - |F_c|) / \Sigma|F_o| \quad R_w = \{\Sigma w(|F_o| - |F_c|)^2 / \Sigma w|F_o|^2\}^{1/2}$$

Table 5-6. Fractional Atomic Coordinates and B_{eq} Values for $KBiP_2Se_6$ with Estimated Standard Deviations in Parentheses.

atom	x	y	z	B_{eq}
Bi	0.11808(7)	0.1546(1)	0.83190(7)	2.05(3)
Se(1)	0.1627(2)	0.5064(3)	0.9237(2)	1.75(8)
Se(2)	0.3109(2)	0.0012(3)	1.0618(2)	2.27(9)
Se(3)	0.3371(2)	0.2001(3)	0.8056(2)	1.91(8)
Se(4)	0.0576(2)	0.3118(3)	0.6116(2)	1.79(8)
Se(5)	0.1159(2)	-0.1839(3)	0.6871(2)	1.73(8)
Se(6)	0.4097(2)	0.7311(3)	0.8841(2)	1.87(8)
K	0.4089(4)	0.5818(7)	1.1387(4)	2.6(2)
P(1)	0.2377(4)	0.6271(8)	0.8037(4)	1.7(2)
P(2)	0.2397(4)	0.4064(7)	0.6850(4)	1.5(2)

$$^aB_{eq} = (4/3)[a^2B(1,1) + b^2B(2,2) + c^2B(3,3) + ab(\cos\gamma)B(1,2) + ac(\cos\beta)B(1,3) + bc(\cos\alpha)B(2,3)].$$

Table 5-7. Fractional Atomic Coordinates and B_{eq} Values for $Cs_8Sb_4(P_2Se_6)_5$ with Estimated Standard Deviations in Parentheses.

atom	x	y	z	B(eq)
Cs(1)	0.4041(1)	0.2492(2)	0.2902(1)	1.54(7)
Cs(2)	0.0910(1)	0.2202(1)	0.2101(1)	1.20(6)
Cs(3)	0.6898(1)	0.2361(1)	0.4081(1)	1.12(6)
Cs(4)	0.9859(1)	0.2475(1)	0.5015(1)	1.23(6)
Sb(1)	0.7848(1)	0.1302(1)	0.15902(8)	0.59(6)
Sb(2)	0.8176(1)	0.3399(1)	0.02670(8)	0.75(6)
Se(1)	0.8796(2)	0.2477(2)	0.2941(1)	0.9(1)
Se(2)	0.7798(2)	0.2365(2)	0.6027(1)	1.0(1)
Se(3)	0.6700(1)	0.0065(2)	0.0655(1)	0.8(1)
Se(4)	0.7796(1)	-0.0265(2)	0.2676(1)	0.8(1)
Se(5)	0.8790(1)	0.5053(2)	-0.0537(1)	0.9(1)
Se(6)	0.6707(1)	0.4752(2)	0.0412(1)	0.76(9)
Se(7)	0.4881(2)	0.2660(2)	0.5043(2)	1.0(1)
Se(8)	0.6179(2)	0.2145(2)	0.1974(1)	0.9(1)
Se(9)	0.5714(1)	-0.0364(2)	0.3475(1)	1.0(1)
Se(10)	0.2645(2)	-0.0173(2)	0.2578(1)	1.2(1)
Se(11)	1.2075(2)	0.2327(2)	0.4060(2)	1.1(1)
Se(12)	1.0322(1)	0.0122(2)	0.3613(1)	1.1(1)
Se(13)	0.5661(1)	0.5026(2)	0.3666(1)	0.8(1)
Se(14)	0.3297(1)	0.4880(2)	0.4408(1)	1.2(1)
Se(15)	1.0502(1)	0.4977(2)	0.3695(1)	1.4(1)
P(1)	1.1547(4)	0.0536(5)	0.4170(3)	0.8(2)
P(2)	0.5823(3)	0.0399(5)	0.1556(3)	0.5(2)
P(3)	0.4423(3)	0.4463(5)	0.5136(3)	0.4(2)
P(4)	0.6380(4)	-0.0775(5)	0.2488(3)	0.5(2)
P(5)	0.2450(3)	0.4385(5)	0.1269(3)	0.6(2)

$$^aB_{eq} = (4/3)[a^2B(1,1) + b^2B(2,2) + c^2B(3,3) + ab(\cos\gamma)B(1,2) + ac(\cos\beta)B(1,3) + bc(\cos\alpha)B(2,3)].$$

Table 5-8. Fractional Atomic Coordinates and B_{eq} Values for $Cs_8Bi_4(P_2Se_6)_5$ with Estimated Standard Deviations in Parentheses.

atom	x	y	z	B(eq)
Cs(1)	0.4040(2)	0.2431(3)	0.2888(2)	3.2(1)
Cs(2)	0.0916(2)	0.2203(3)	0.2102(2)	2.8(1)
Cs(3)	0.6903(2)	0.2363(3)	0.4086(2)	2.7(1)
Cs(4)	0.9861(2)	0.2478(3)	0.5019(2)	2.7(1)
Bi(1)	0.7869(1)	0.1275(1)	0.16063(8)	1.94(6)
Bi(2)	0.8180(1)	0.3368(2)	0.0215(1)	2.49(7)
Se(1)	0.8808(3)	0.2458(4)	0.2945(2)	2.1(2)
Se(2)	0.7796(3)	0.2393(4)	0.6031(2)	2.4(2)
Se(3)	0.6654(3)	0.0033(4)	0.0650(2)	2.1(2)
Se(4)	0.7768(2)	-0.0336(4)	0.2697(2)	2.0(2)
Se(5)	0.8763(3)	0.5093(4)	-0.0605(2)	2.4(2)
Se(6)	0.6694(3)	0.4765(4)	0.0393(2)	2.1(2)
Se(7)	0.4936(3)	0.2662(4)	0.5090(3)	2.4(2)
Se(8)	0.6171(3)	0.2128(4)	0.1974(2)	1.9(2)
Se(9)	0.5726(3)	-0.0395(4)	0.3472(2)	2.6(2)
Se(10)	0.2590(3)	-0.0216(4)	0.2558(2)	2.6(2)
Se(11)	1.2010(3)	0.2304(4)	0.4013(3)	2.5(2)
Se(12)	1.0328(3)	0.0072(4)	0.3610(2)	2.5(2)
Se(13)	0.5595(3)	0.5008(4)	0.3647(2)	2.2(2)
Se(14)	0.3311(3)	0.4777(4)	0.4477(2)	2.9(2)
Se(15)	1.0481(3)	0.4970(4)	0.3649(3)	2.8(2)
P(1)	1.1543(6)	0.0501(9)	0.4161(5)	1.6(4)
P(2)	0.5831(6)	0.038(1)	0.1566(5)	1.7(4)
P(3)	0.4467(6)	0.4451(8)	0.5174(5)	1.4(4)
P(4)	0.6379(6)	-0.0789(8)	0.2491(5)	1.3(4)
P(5)	0.2475(6)	0.4363(9)	0.1292(5)	1.6(4)

$$^aB_{eq} = (4/3)[a^2B(1,1) + b^2B(2,2) + c^2B(3,3) + ab(\cos\gamma)B(1,2) + ac(\cos\beta)B(1,3) + bc(\cos\alpha)B(2,3)].$$

3. Results and Discussion

3.1. Synthesis, Spectroscopy and Thermal Analysis

The syntheses of these compounds were a result of a redox reaction in which the metal is oxidized by polyselenide ions in the $A_x[P_ySe_z]$ ($A=K, Cs$) flux to give M^{3+} species. KMP_2Se_6 crystallizes from a Lewis acidic flux with a $M/P_2Se_5/K_2Se/Se$ ratio of 1/3/2/8. In the case of $Cs_8M_4(P_2Se_6)_5$, a more basic flux consisting of $M/P_2Se_5/Cs_2Se/Se$ (1/3/2/4) was used to obtain pure compounds. For $Cs_8Bi_4(P_2Se_6)_5$, decrease in the amount of P_2Se_5 resulted in Bi_2Se_3 under these conditions.

The far-IR spectra of KMP_2Se_6 and $Cs_8M_4(P_2Se_6)_5$ are characteristically complex and show a large number of absorptions between 522 and 144 cm^{-1} (see Table 5-1). Since systematic IR spectroscopic data for selenophosphate ligands are lacking, and thus we cannot assign P-P and $-PSe_3$ vibrational frequencies. However, it is tempting to assign the first two or three higher frequency vibrations to modes due primarily to P-P stretching.¹⁹

The optical properties of (I)-(IV) suggest that they are wide band-gap semiconductors. The optical absorption spectrum shown in Figure 5-1a indicates that $KBiP_2Se_6$ is optically transparent below the band gap, E_g , of 1.61 eV. The E_g of $KSbP_2Se_6$ is found to be 2.00 eV, see Figure 5-1b. The band-gaps, E_g , of $Cs_8Sb_4(P_2Se_6)_5$ and $Cs_8Bi_4(P_2Se_6)_5$ are 1.58 and 1.44 eV, respectively (see Figure 5-2). The slight decrease in band gap in going from Sb to Bi in $Cs_8M_4(P_2Se_6)_5$ suggests that these metals contribute comparatively

little to the highest energy levels of the valence band, which is most likely dominated by Se-based orbitals. Three absorptions at 2.33, 3.67, 5.37 eV for (III) and two absorptions at 2.11 and 5.26 eV for (IV) are readily resolved and are assigned to electronic Se \rightarrow M charge transfer transitions. Based on the calculated solar conversion efficiency versus band gap plot,²⁰ the band gaps of KBiP₂Se₆ and Cs₈M₄(P₂Se₆)₅ (1.44-1.61 eV) would fall near the peak of conversion efficiency.

Differential thermal analysis (DTA) shows that KBiP₂Se₆, KSbP₂Se₆, Cs₈Sb₄(P₂Se₆)₅, and Cs₈Bi₄(P₂Se₆)₅ melt congruently at 554, 479, 532, and 497 °C respectively, suggesting that large single crystals or microcrystalline thin films can be grown from the melt.

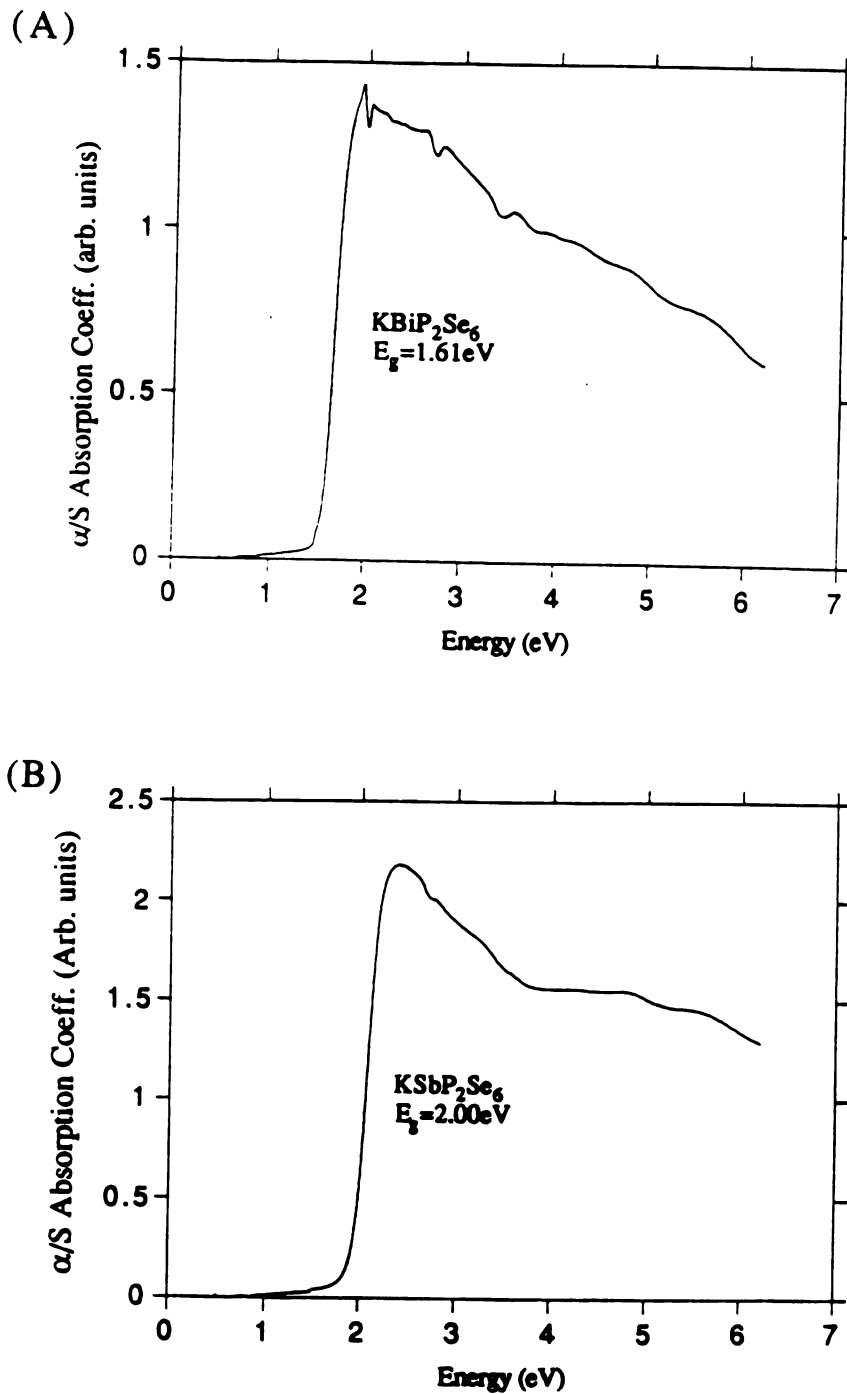
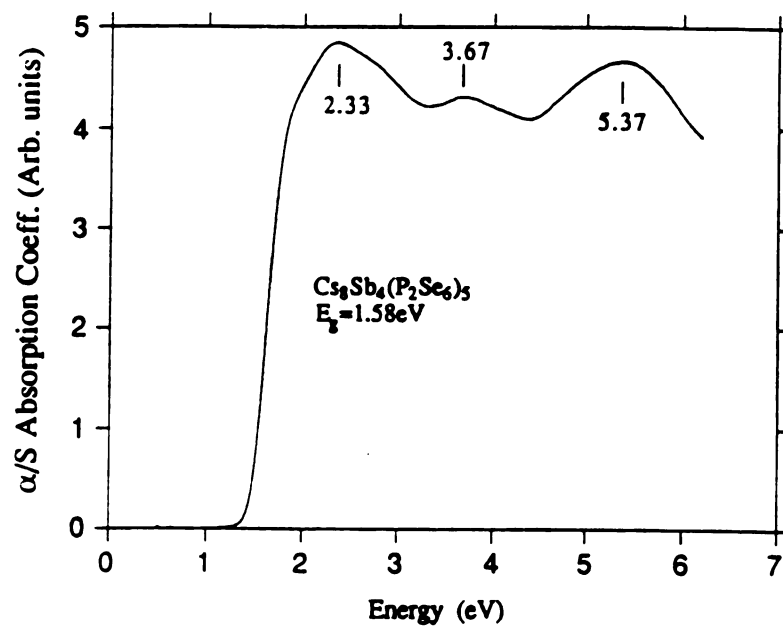


Figure 5-1. Solid state optical absorption spectra of (A) KBiP₂Se₆ and (B) KSbP₂Se₆.

(A)



(B)

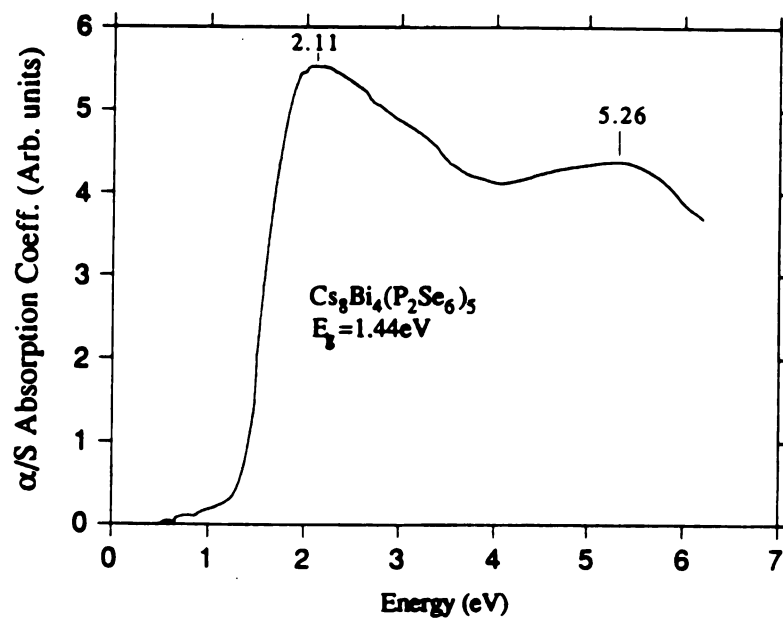
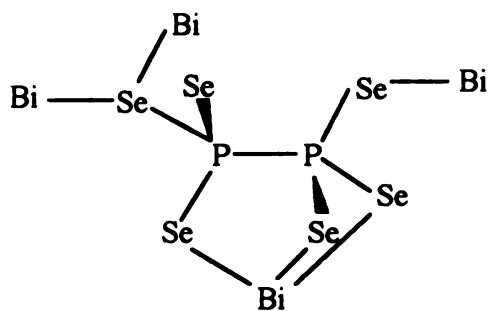


Figure 5-2. (A) Optical absorption spectrum of $\text{Cs}_8\text{Sb}_4(\text{P}_2\text{Se}_6)_5$.
(B) Optical absorption spectrum of $\text{Cs}_8\text{Bi}_4(\text{P}_2\text{Se}_6)_5$.

3.2. Description of Structures

Structure of KMP_2Se_6 . KMP_2Se_6 has the complicated layered structure shown in Figure 5-3. The layers are separated by seven-coordinate K^+ ions ($\text{K-Se mean}=3.36(2)\text{\AA}$). The $[\text{MP}_2\text{Se}_6]^-$ slabs are assembled from chains of distorted corner-sharing BiSe_6 octahedra along the b-axis (see Figure 5-4a). The $[\text{P}_2\text{Se}_6]^{4-}$ ligand trichelates to one Bi while a fourth Se atom acts as a bridge between two other Bi atoms in the chain. The fifth Se is non bonding while the sixth Se connects to a Bi on the neighboring chain to form a layer in the bc-plane (see Figure 5-3). For clarity, the unique connectivity of $[\text{P}_2\text{Se}_6]^{4-}$ is illustrated separately in scheme (A).



Scheme (A)

Selected distances and angles for KMP_2Se_6 are found in Tables 5-9. Bi is coordinated by six Se atoms to form a distorted octahedron. The Bi-Se distances range from $2.821(2)$ to $3.194(3)\text{\AA}$ and compare well with those found in $\text{K}_2\text{Bi}_8\text{Se}_{13}$ ²¹ and $\text{Cs}_3\text{Bi}_7\text{Se}_{12}$.²² The distortion of the octahedron can partly be explained by the stereochemically active $6s^2$ lone pair of Bi^{3+} . The Bi-Se coordination sphere is shown in Figure 5-4b. In accordance with the VSEPR model,²³ lone pair-bond pair repulsions in the bismuth coordination

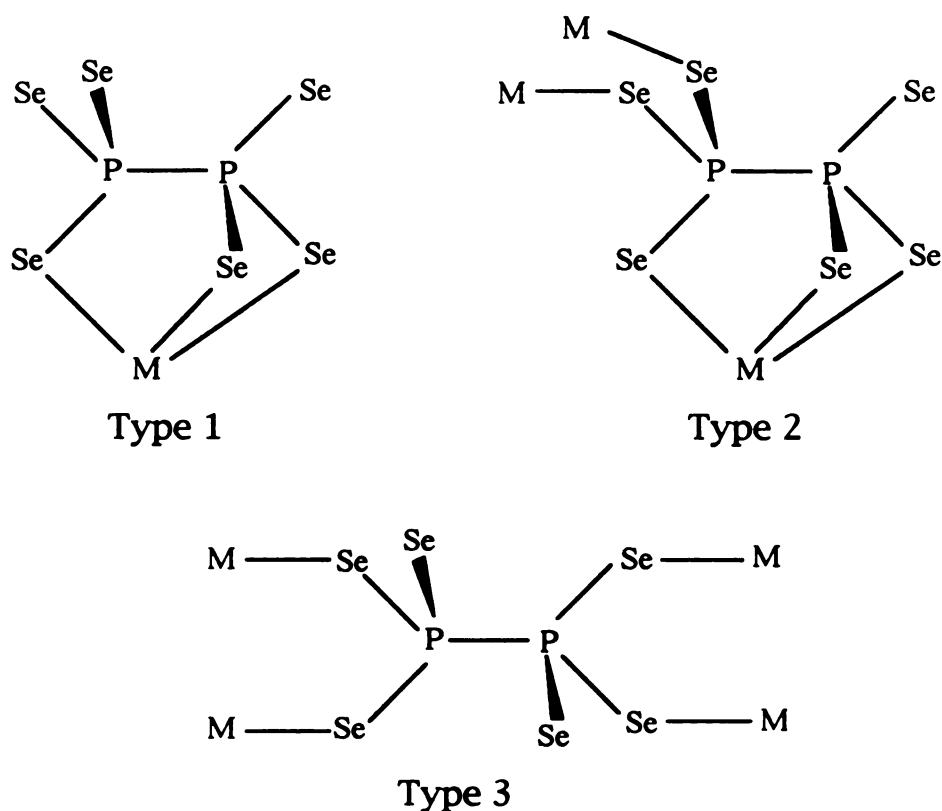
sphere result in longer bond lengths for those bonds adjacent to the lone pair (Bi-Se(2,5,5') 3.079(2)-3.194(3)Å) and shorter lengths for those more remote (Bi-Se(1,3,4) 2.821(2)-2.878(2)Å). In addition, these repulsions give rise to an opening of the bond angles straddling the lone pair (Se(5)-Bi-Se(5)' 118.32(5)°, Se(2)-Bi-Se(5) 126.07(6)°).

The P(1)-P(2) bond in $[\text{P}_2\text{Se}_6]^{4-}$ is 2.238(7)Å and the P-Se distances range from 2.145(5) to 2.223(5)Å. Similar distances have been observed in $\text{Hg}_2\text{P}_2\text{Se}_6$.²⁴

Structure of $\text{Cs}_8\text{M}_4(\text{P}_2\text{Se}_6)_5$. $\text{Cs}_8\text{M}_4(\text{P}_2\text{Se}_6)_5$ possess a remarkably complicated layered structure shown in Figure 5-5. The $[\text{M}_4(\text{P}_2\text{Se}_6)_5]_n^{8n-}$ layers are composed of $[\text{M}_4(\text{P}_2\text{Se}_6)_4]$ zig-zag chains that are linked by additional $[\text{P}_2\text{Se}_6]^{4-}$ ligands to form a staircase layered framework. The layers are interdigitated to form tunnels along the b-direction. There are two kinds of cesium ions, one that fills the tunnels and another located within the layers.

There are three types of $[\text{P}_2\text{Se}_6]^{4-}$ ligands in this structure each possessing unique denticity. Type (1) is a capping ligand that trichelates to the metal while the other three Se atoms are nonbonding (terminal). Type (2) also trichelates to the metal while two of the remaining Se atoms bond to two separate metals and the sixth Se is terminal. Type (3) chelates to four metals leaving two nonbonding Se atoms. The P-P bond resides on a center of symmetry. For clarity, the connectivities of the $[\text{P}_2\text{Se}_6]^{4-}$ ligands are illustrated separately in scheme (B). It is clear that beyond the well known $\text{M}_2\text{P}_2\text{Q}_6$ class of compounds and the few other examples that already exist, the $[\text{P}_2\text{Q}_6]^{4-}$ unit presents excellent new possibilities as

a building block of new frameworks. These possibilities can be readily exploited by the type of molten salt reaction reported here.



Scheme (B)

One of the most distinguishing features found in this structure are the rather short M...M interactions at 3.534(2) Å for Bi and 3.441(2) Å for Sb (see Figure 5-6). For comparison, the sum of the van der Waals radii for Bi and Sb are 4.8 and 4.4 Å. Therefore, the obvious question to ask is are these significant bonding interactions or not? To the best of our knowledge, other examples of such remarkably short distances involving these elements are found only in the corresponding elemental structures. Bi metal has an intralayer bond distance of 3.06 Å and an interlayer distance of 3.52 Å. The

isostructural Sb metal has distances of 2.90 Å and 3.34 Å. The longer distances in these metals are considered weakly bonding in nature.²⁵ We note however that the metals in these forms are in the zero oxidation state while (I I I) and (I V) are formally in the 3⁺ state. If a metal-metal bond exists in these compounds, it must form via the interaction of the lone pairs in Sb³⁺ and Bi³⁺. The M³⁺ (d¹⁰s²) ions with square pyramidal coordination exhibit a stereochemically active lone pair at the base of the pyramid. The bases of the square pyramids in Cs₈M₄(P₂Se₆)₅ face each other in close proximity. A weak interaction of this sort is unusual since lone pair/lone pair interactions should be non-bonding. Perhaps a closer analog to the case described here is the α,β-PbO where weak Pb...Pb bonding interactions (interlayer Pb...Pb distance of 3.87 Å) were proposed to exist by Hoffmann and coworkers.²⁶ Closed-shell bonding interactions have also been observed in other systems such as 2,2',5,5'-tetramethylbistibole ((C₆H₈Sb)₂) in which the lone pairs in each Sb interact with other dimers by Sb...Sb interactions (3.625 Å) to form one-dimensional chains.²⁷ This Sb-Sb bond length alternation is the result of a Peierls distortion as determined from electronic band structure calculations.²⁸ Tetramethyldistibane exhibits similar behavior with an intermolecular Sb-Sb distance of 3.678(1)Å²⁹ while tetrakis(trimethylsilyl)dibismuthane shows a Bi-Bi distance of 3.804(3) Å.³⁰ Although these M...M distances are longer than those observed in (I I I) and (I V) they are similar in origin. It is noteworthy that the case of M...M interaction is unique in (III) and (IV) in the sense that they are the only examples where "inert" ns² lone pairs face directly at each other. Other closed-shell systems

such as the classical d^{10} - d^{10} (Cu^+ , Ag^+ , Au^+) interactions have also been well documented.^{31,32} Extended Hückel calculations by Hoffmann and coworkers have shown that mixing of empty 4s and 4p orbitals with occupied 3d orbitals lowers the energy of the σ and σ^* orbitals for several copper complexes.³³ A similar type of interaction, due to mixing with empty p orbitals, could exist in $\text{Cs}_8\text{M}_4(\text{P}_2\text{Se}_6)_5$. It has also been proposed for several d^{10} - d^{10} complexes that the bridging ligands bring the metals closer in order to maximize M-L interactions.³⁴ Since $\text{Cs}_8\text{M}_4(\text{P}_2\text{Se}_6)_5$ features two $[\text{P}_2\text{Se}_6]^{4-}$ bridging ligands for each dimer, it is possible that the multidentate $[\text{P}_2\text{Se}_6]^{4-}$ coordination is playing an important role. It is not clear whether the interactions contribute significantly in determining the structure or the metals are simply forced to tolerate the short contact due to packing forces.

The rest of the structure is built up as follows. Type 1 ligands cap a metal on each M...M dimeric unit (see figure 5-6) while one Type 2 ligand connects two dimeric units together (see Figure 5-7). These larger units are assembled into $[\text{M}_4(\text{P}_2\text{Se}_6)_4]$ zig-zag chains by additional Type 2 ligands. The zig-zag chains are connected by Type 3 ligands above and below to form the $[\text{M}_4(\text{P}_2\text{Se}_6)_5]_n^{8n-}$ staircase layers as shown in Figure 5-8.

Selected distances and angles for $\text{Cs}_8\text{M}_4(\text{P}_2\text{Se}_6)_5$ are found in Tables 5-10 and 5-11. M(1) and M(2) are found in two similar square pyramidal coordination sites (see Figure 5-6). The M atoms are slightly displaced from their respective square planes. The bond distances of $\text{Cs}_8\text{Sb}_4(\text{P}_2\text{Se}_6)_5$ range from the short axial bond distances of 2.648(3) and 2.613(3) Å to 3.010(3) and 3.039(3) Å for Sb(1) and

Sb(2), respectively. These compare well with the square pyramidal Sb-Se distances found in TlSbSe_2 .³⁵ The bond distances for the Bi analog range from 2.711(4) and 2.682(5) Å to 3.027(5) and 3.037(5) Å which compare well with those found in $\text{K}_2\text{Bi}_8\text{Se}_{13}$.²¹

The P-P bonds of the $[\text{P}_2\text{Se}_6]^{4-}$ ligands are normal at 2.25(1) Å (average). The terminal Se atoms have significantly shorter P-Se distances due to partial double bond character.³⁶ For example, the terminal P(1)-Se(12) distance is 2.108(7) Å while the metal binding Se(6) and Se(11) atoms have P(1)-Se(6) and P(1)-Se(11) distances of 2.222(6) and 2.233(6) Å, respectively.

In $\text{Cs}_8\text{Bi}_4(\text{P}_2\text{Se}_6)_5$, Cs(1,2,4) are located in the tunnels that are created by the interdigitated layers. Cs(1) and Cs(2) are ten-coordinate with average Cs-Se distances of 3.9(1) Å and 3.8(1) Å, respectively. The coordination environment of Cs(1) resembles a tri-capped truncated square prism. Cs(2) possesses a bi-capped square prismatic coordination. The nine-coordinate Cs(3) (ave. 3.8(1) Å) resides within the layers in the center of a mono-capped square prism. Cs(4) is found in a 12-coordinate tetra-capped square prism with an average Cs(4)-Se distance of 3.93(8) Å. The Cs-Se coordination environments are shown in Figure 5-9.

The difference between the sulfur and selenium chemistry in these quaternary systems is partly due to the difference in oxidizing ability of the excess polychalcogenide ligands in these fluxes. In this temperature range polythiophosphate fluxes yield $[\text{P}_2\text{S}_7]^{4-}$ ¹ and $[\text{PS}_4]^{3-}$ ³⁷ ligands with P in the 5+ oxidation state whereas the polyselenophosphate fluxes stabilize the $[\text{P}_2\text{Se}_6]^{4-}$ unit with P in the

4+ oxidation state. This leads to entirely different structural chemistry.

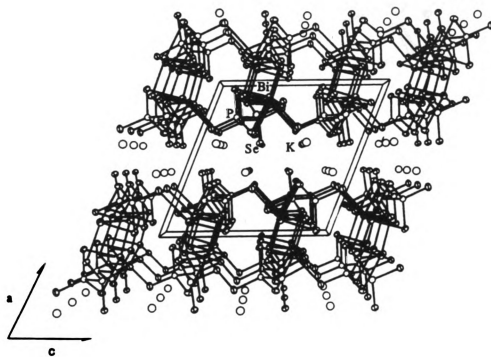


Figure 5-3. The extended structure of KBiP_2Se_6 looking down the b -axis with labeling.

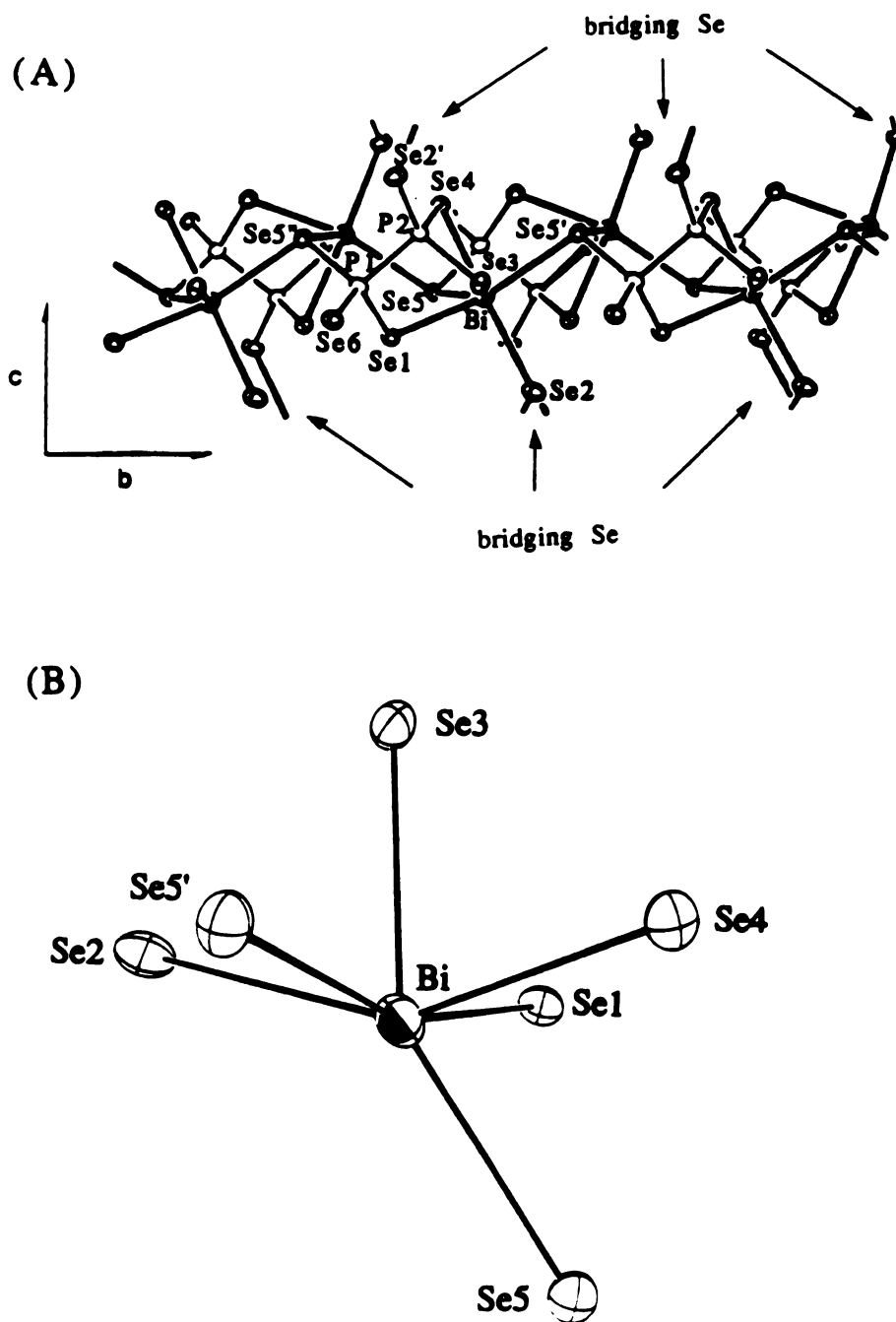


Figure 5-4. (A) Structure and labeling of a $[\text{BiP}_2\text{Se}_6]^-$ chain. The bridging Se atoms connecting the chains into layers are highlighted. (B) The Bi-Se coordination site with labeling.

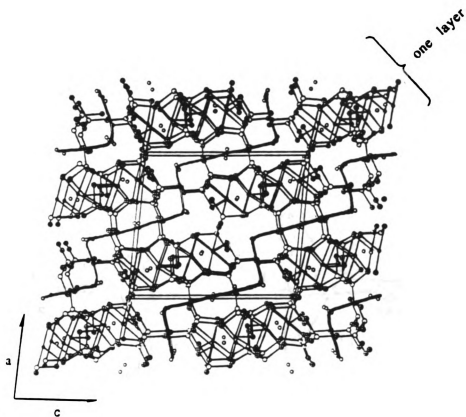


Figure 5-5. Packing diagram of $\text{Cs}_8\text{Bi}_4(\text{P}_2\text{Se}_6)_5$ viewed down the $[010]$ direction. The open circles represent Cs atoms. Dark solid lines highlight the layered nature of the staircase framework.

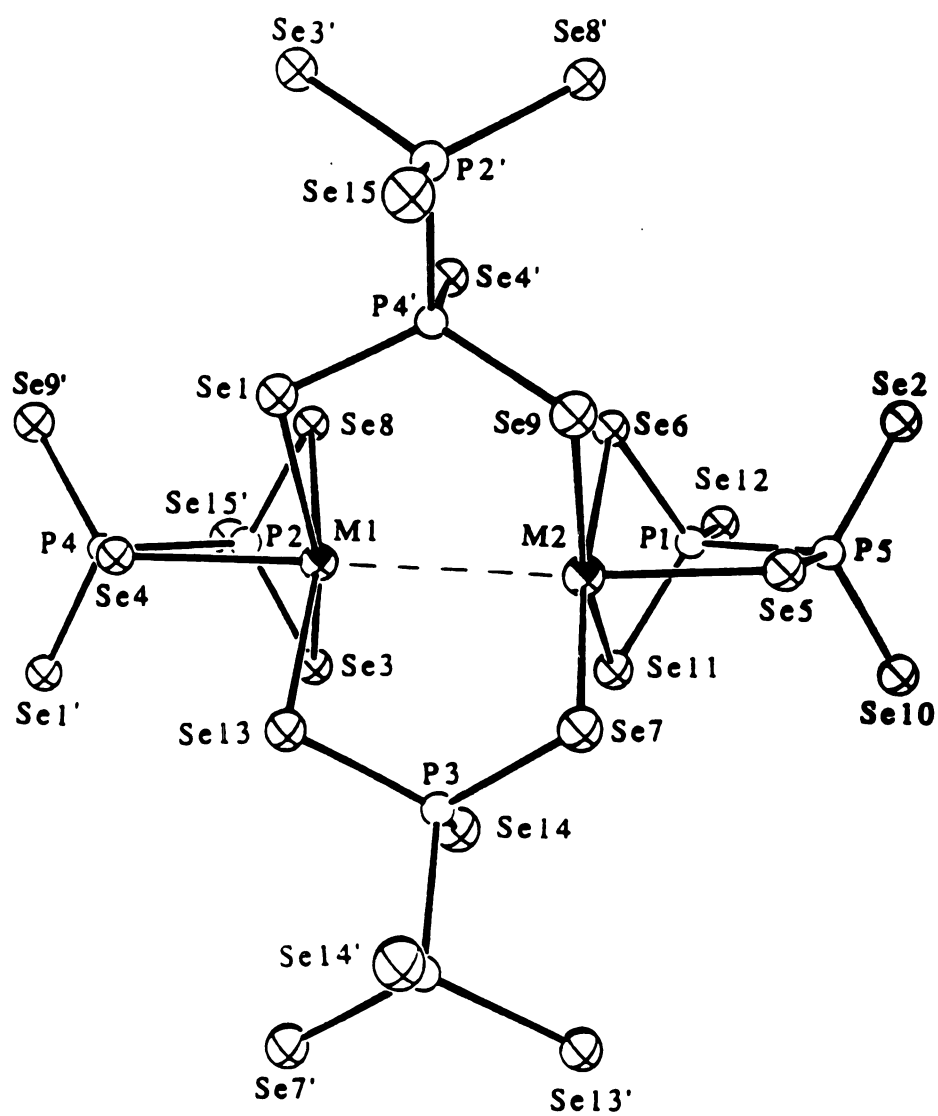
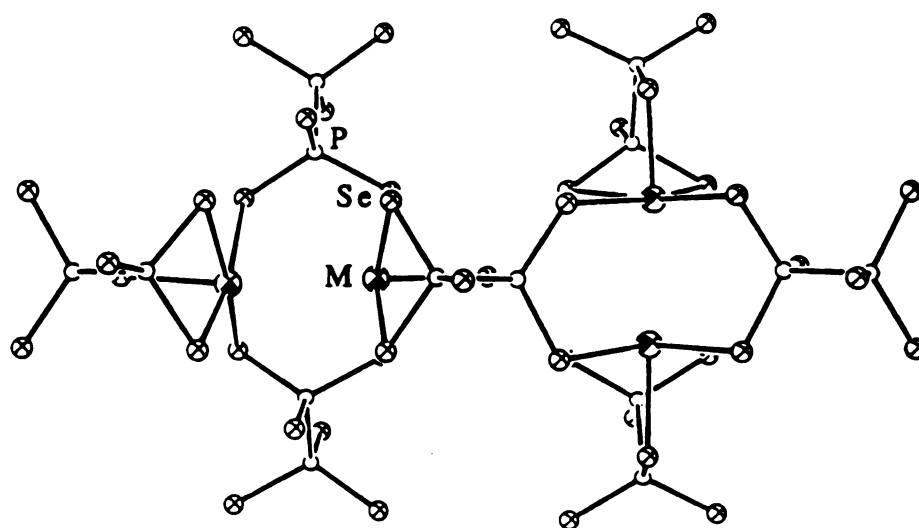


Figure 5-6. Structure of the $[M_2(P_2Se_6)_4]$ dimeric unit showing the $M \cdots M$ interaction.

(A)



(B)

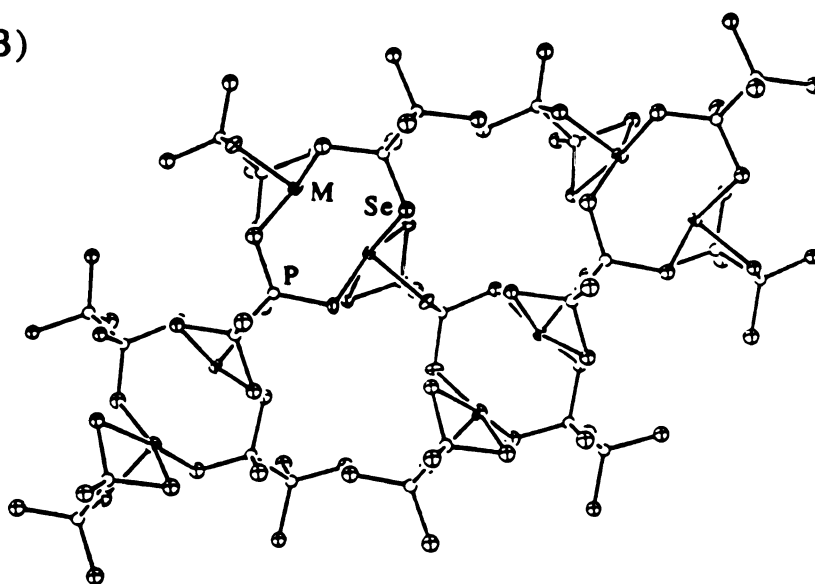


Figure 5-7. (A) Association of two $[M_2(P_2Se_6)_4]$ "dimers" by a $[P_2Se_6]^{4-}$ unit. (B) Further sharing of $[P_2Se_6]^{4-}$ units among "dimers" results in a one-dimensional chain-like structure.

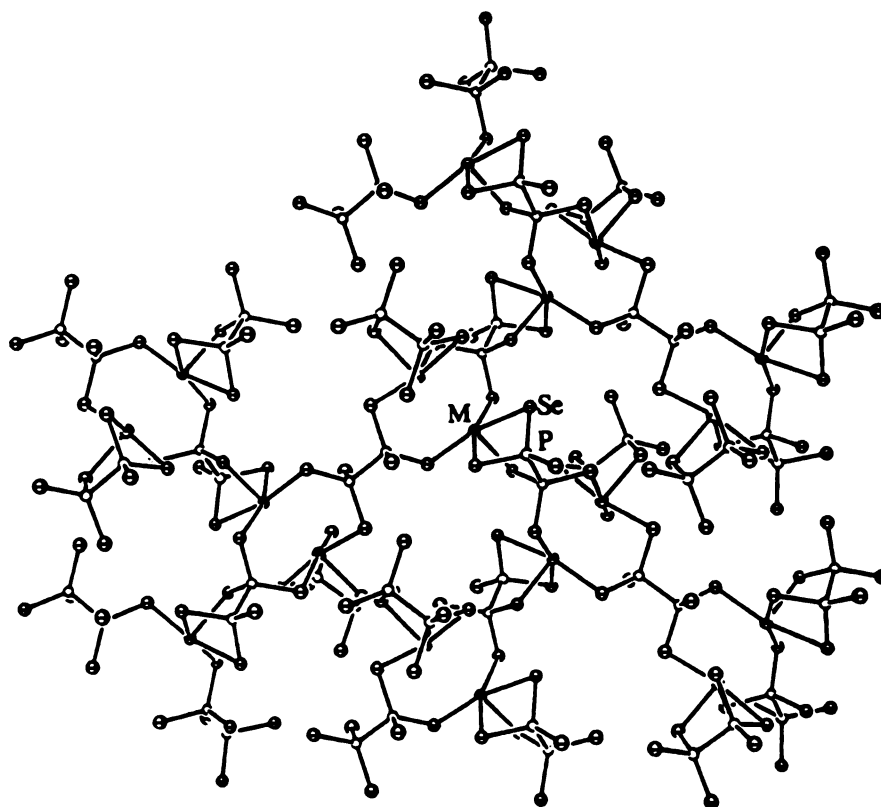


Figure 5-8. Two-dimensional structure of the $[M_4(P_2Se_6)_5]_n^{8-}$ anionic framework with labeling as drawn by ORTEP.

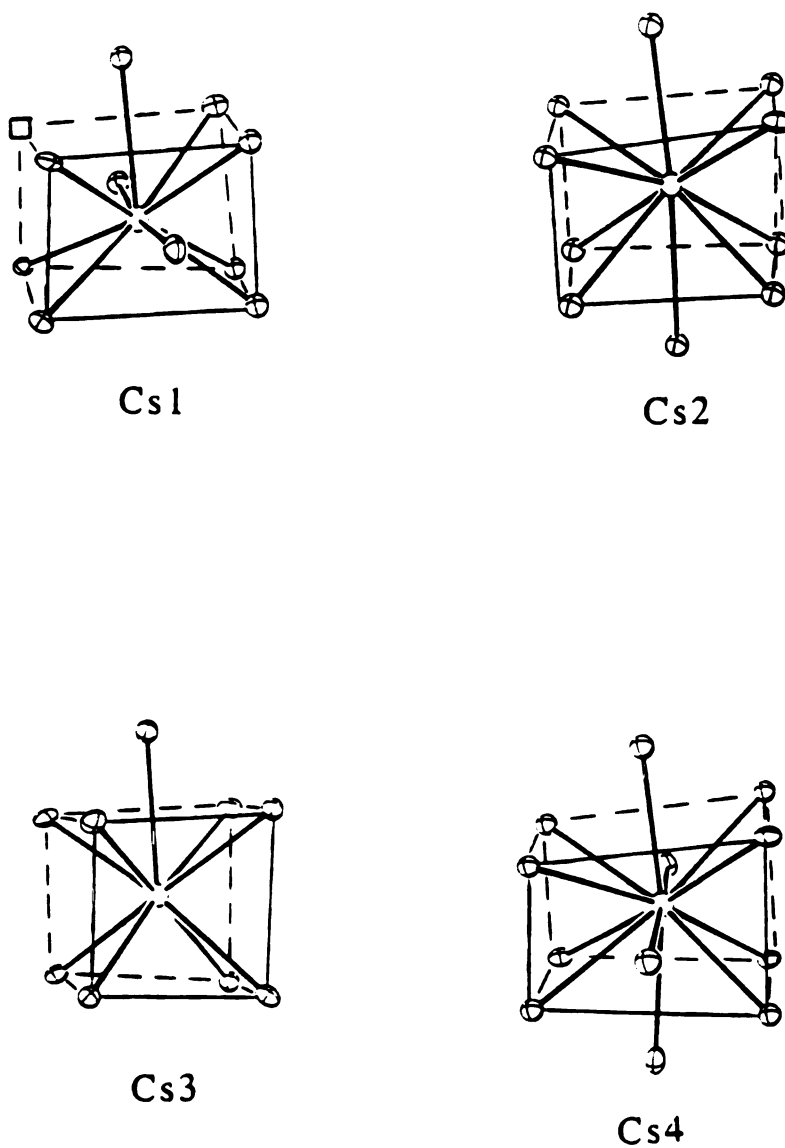


Figure 5-9. The Cs⁺ coordination environments. The open circles represent Cs atoms. The open square in the Cs(1) coordination site represents the vacant corner of the square prism.

Table 5-9. Selected Distances (Å) and Angles (°) in KBiP₂Se₆ with Standard Deviations in Parentheses.^a

Bi-Se(1)	2.878(2)	Se(1)-Bi-Se(2)	90.75(6)
Bi-Se(2)	3.194(3)	Se(1)-Bi-Se(3)	83.17(6)
Bi-Se(3)	2.873(2)	Se(1)-Bi-Se(4)	86.26(6)
Bi-Se(4)	2.821(2)	Se(1)-Bi-Se(5)	72.48(6)
Bi-Se(5)	3.131(2)	Se(2)-Bi-Se(3)	73.54(6)
Bi-Se(5')	3.079(2)	Se(2)-Bi-Se(5)	93.38(6)
Bi-Se (ave.)	3.0(2)	Se(2)-Bi-Se(5')	126.07(6)
		Se(3)-Bi-Se(4)	76.37(6)
P(1)-Se(1)	2.223(5)	Se(3)-Bi-Se(5)	80.93(6)
P(1)-Se(5)	2.198(6)	Se(4)-Bi-Se(5)	81.25(6)
P(1)-Se(6)	2.145(5)	Se(4)-Bi-Se(5')	81.39(6)
P(2)-Se(2)	2.146(5)	Se(5)-Bi-Se(5')	118.32(5)
P(2)-Se(3)	2.197(6)		
P(2)-Se(4)	2.221(6)	Se(1)-P(1)-Se(5)	110.8(2)
P-Se (ave.)	2.19(3)	Se(1)-P(1)-Se(6)	115.5(2)
		Se(5)-P(1)-Se(6)	113.0(3)
P(1)-P(2)	2.238(7)	Se(2)-P(2)-Se(3)	116.9(2)
		Se(2)-P(2)-Se(4)	115.9(2)
K-Se(1)	3.283(5)	Se(3)-P(2)-Se(4)	105.7(2)
K-Se(2)	3.418(6)	Se(1)-P(1)-P(2)	104.0(3)
K-Se(3)	3.320(5)	Se(5)-P(1)-P(2)	103.1(2)
K-Se(3')	3.398(5)	Se(6)-P(1)-P(2)	109.4(3)
K-Se(6)	3.362(5)	Se(2)-P(2)-P(1)	109.4(3)
K-Se(6')	3.357(5)	Se(3)-P(2)-P(1)	102.8(2)
K-Se(6'')	3.356(5)	Se(4)-P(2)-P(1)	104.9(2)
K-Se (ave.)	3.36(5)		

^aThe estimated standard deviations in the mean bond lengths and the mean bond angles are calculated by the equations $\sigma_l = \{\sum_n (l_n - l)^2 / n(n-1)\}^{1/2}$, where l_n is the length (or angle) of the n th bond, l the mean length (or angle), and n the number of bonds.

Table 5-10. Selected Distances (Å) in $\text{Cs}_8\text{M}_4(\text{P}_2\text{Se}_6)_5$ with Standard Deviations in Parentheses.^a

	$\text{Cs}_8\text{Sb}_4(\text{P}_2\text{Se}_6)_5$	$\text{Cs}_8\text{Bi}_4(\text{P}_2\text{Se}_6)_5$
M-M'	3.441(2)	3.534(2)
M(1)-Se(1)	3.010(3)	3.027(5)
M(1)-Se(3)	2.716(3)	2.838(4)
M(1)-Se(4)	2.648(3)	2.711(4)
M(1)-Se(8)	2.905(3)	2.978(5)
M(1)-Se(13)	2.811(3)	2.898(5)
M(1)-Se (ave.)	2.8(1)	2.9(1)
M(2)-Se(5)	2.613(3)	2.682(5)
M(2)-Se(6)	2.789(3)	2.883(5)
M(2)-Se(7')	2.970(3)	3.037(5)
M(2)-Se(9')	3.039(3)	3.132(5)
M(2)-Se(11)	2.739(3)	2.813(5)
M(2)-Se (ave.)	2.8(2)	2.9(2)
P(1)-P(5)	2.240(7)	2.24(1)
P(2)-P(4)	2.244(8)	2.25(1)
P(3)-P(3')	2.26(1)	2.24(2)
P-P (ave.)	2.25(1)	2.24(1)
P(1)-Se(6)	2.222(6)	2.22(1)
P(1)-Se(11)	2.233(6)	2.23(1)
P(1)-Se(12)	2.108(7)	2.13(1)
P(2)-Se(3)	2.230(6)	2.22(1)
P(2)-Se(8)	2.194(6)	2.20(1)
P(2)-Se(15')	2.114(6)	2.12(1)
P(3)-Se(7)	2.204(6)	2.20(1)
P(3)-Se(13)	2.225(6)	2.21(1)
P(3)-Se(14)	2.123(6)	2.15(1)
P(4)-Se(1')	2.158(6)	2.18(1)
P(4)-Se(4)	2.264(6)	2.25(1)
P(4)-Se(9')	2.171(6)	2.16(1)
P(5)-Se(2)	2.139(6)	2.15(1)
P(5)-Se(5)	2.305(6)	2.30(1)
P(5)-Se(10)	2.130(6)	2.13(1)
P-Se (ave.)	2.19(6)	2.19(5)

Table 5-10. (cont'd)

	$\text{Cs}_8\text{Sb}_4(\text{P}_2\text{Se}_6)_5$	$\text{Cs}_8\text{Bi}_4(\text{P}_2\text{Se}_6)_5$
Cs(1)-Se(2)	3.687(3)	3.710(6)
Cs(1)-Se(5)	4.077(3)	4.019(6)
Cs(1)-Se(7)	3.904(4)	4.077(5)
Cs(1)-Se(8)	3.861(3)	3.883(5)
Cs(1)-Se(10)	3.763(3)	3.824(6)
Cs(1)-Se(10')	3.786(3)	3.769(6)
Cs(1)-Se(11)	3.842(3)	3.933(6)
Cs(1)-Se(13)	3.998(3)	4.008(5)
Cs(1)-Se(14)	4.079(3)	4.162(6)
Cs(1)-Se(15)	4.161(3)	4.071(6)
Cs(1)-Se (ave.)	3.9(2)	3.9(1)
Cs(2)-Se(1)	3.743(3)	3.782(6)
Cs(2)-Se(2)	3.679(3)	3.700(6)
Cs(2)-Se(7)	3.849(4)	4.172(5)
Cs(2)-Se(9)	3.836(3)	3.793(6)
Cs(2)-Se(10)	3.868(3)	3.864(6)
Cs(2)-Se(10')	3.769(3)	3.872(6)
Cs(2)-Se(11)	3.765(4)	3.807(6)
Cs(2)-Se(12)	3.775(3)	3.691(6)
Cs(2)-Se(13)	3.661(3)	3.827(5)
Cs(2)-Se(14)	4.059(3)	3.644(5)
Cs(2)-Se (ave.)	3.8(1)	3.8(1)
Cs(3)-Se(1)	3.730(3)	3.783(6)
Cs(3)-Se(2)	3.600(3)	3.638(5)
Cs(3)-Se(3)	3.797(3)	3.829(6)
Cs(3)-Se(5)	3.928(3)	3.983(5)
Cs(3)-Se(6)	3.757(3)	3.788(5)
Cs(3)-Se(7)	3.721(3)	3.737(6)
Cs(3)-Se(8)	3.809(3)	3.863(5)
Cs(3)-Se(9)	3.738(3)	3.792(6)
Cs(3)-Se(13)	3.653(3)	3.723(6)
Cs(3)-Se(14)	4.188(3)	
Cs(3)-Se (ave.)	3.8(2)	3.8(1)
Cs(4)-Se(1)	3.888(3)	3.929(5)
Cs(4)-Se(2)	3.815(3)	3.866(6)
Cs(4)-Se(3)	4.098(3)	4.111(5)
Cs(4)-Se(3')	3.946(3)	3.908(5)
Cs(4)-Se(6)	3.855(3)	3.887(5)
Cs(4)-Se(6')	3.991(3)	3.999(5)

Table 5-10. (cont'd)

	Cs ₈ Sb ₄ (P ₂ Se ₆) ₅	Cs ₈ Bi ₄ (P ₂ Se ₆) ₅
Cs(4)-Se(8)	3.886(3)	3.928(5)
Cs(4)-Se(11)	3.978(3)	3.982(6)
Cs(4)-Se(12)	3.795(3)	3.865(6)
Cs(4)-Se(12')	3.884(3)	3.858(5)
Cs(4)-Se(15)	3.904(3)	3.957(6)
Cs(4)-Se(15')	3.795(3)	3.855(5)
Cs(4)-Se (ave.)	3.90(9)	3.93(8)

^aThe estimated standard deviations in the mean bond lengths and the mean bond angles are calculated by the equations $\sigma_l = \{\sum_n (l_n - l)^2 / n(n-1)\}^{1/2}$, where l_n is the length (or angle) of the n th bond, l the mean length (or angle), and n the number of bonds.

Table 5-11. Selected Angles ($^{\circ}$) in $\text{Cs}_8\text{M}_4(\text{P}_2\text{Se}_6)_5$ with Standard Deviations in Parentheses.

	$\text{Cs}_8\text{Sb}_4(\text{P}_2\text{Se}_6)_5$	$\text{Cs}_8\text{Bi}_4(\text{P}_2\text{Se}_6)_5$
Se(1)-M(1)-Se(4)	76.78(8)	78.1(1)
Se(1)-M(1)-Se(8)	92.21(8)	93.4(1)
Se(1)-M(1)-Se(4)	91.41(8)	90.5(1)
Se(1)-M(1)-Se(4)	97.29(8)	100.3(1)
Se(5)-M(2)-Se(9)	81.48(8)	83.2(1)
Se(5)-M(2)-Se(11)	91.49(9)	91.0(1)
Se(6)-M(2)-Se(9)	94.53(8)	93.4(1)
Se(7)-M(2)-Se(11)	105.29(9)	112.0(1)
M(1)-Se(3)-P(2)	83.1(2)	82.6(3)
M(1)-Se(13)-P(3)	98.2(2)	96.7(3)
M(1)-Se(1)-P(4')	95.8(2)	95.3(3)
M(2)-Se(9)-P(4')	102.3(2)	104.1(3)
M(2)-Se(7)-P(3)	94.5(1)	92.7(3)
M(2)-Se(6)-P(1)	80.7(2)	80.1(3)
Se(6)-P(1)-Se(11)	102.6(3)	103.9(4)
Se(6)-P(1)-Se(12)	116.2(2)	116.1(5)
Se(3)-P(2)-P(4)	102.1(3)	103.2(5)
Se(8)-P(2)-Se(15')	119.2(3)	117.9(5)
Se(13)-P(3)-P(3')	100.4(4)	101.9(6)
Se(7)-P(3)-Se(13)	111.7(3)	111.9(4)
Se(1)-P(4')-Se(9)	115.8(3)	115.3(5)
Se(1)-P(4')-Se(4')	112.4(2)	111.9(5)

3.3. Electrical Conductivity Measurements. Four-probe electrical conductivity measurements on single crystals of $\text{Cs}_8\text{Bi}_4(\text{P}_2\text{Se}_6)_5$ showed that the material is a semiconductor with room temperature conductivity $\sigma \sim 10^{-9}$ S/cm which drops to 10^{-10} S/cm at 253 K. Figure 5-10 shows the conductivity vs. $1000/T$ semilog plot for $\text{Cs}_8\text{Bi}_4(\text{P}_2\text{Se}_6)_5$. The data can be fit to the equation shown below suggesting a gap of $E_g = 1.135$ eV and an activation energy of $E_a = 0.567$ eV.

$$\sigma = \sigma_0 e^{-\frac{E_a}{k_B T}} \quad \text{eq. (1)}$$

The value of 1.135 eV compares to 1.44 eV determined by optical spectroscopy (vide supra). The reason for the discrepancy is not known but may be due to the fact that the electrical conductivity does not represent the intrinsic semiconducting regime but may arise from impurity levels in the gap. It must be noted that the optical measurement is the most reliable E_g indicator. The antimony compound is an insulator.

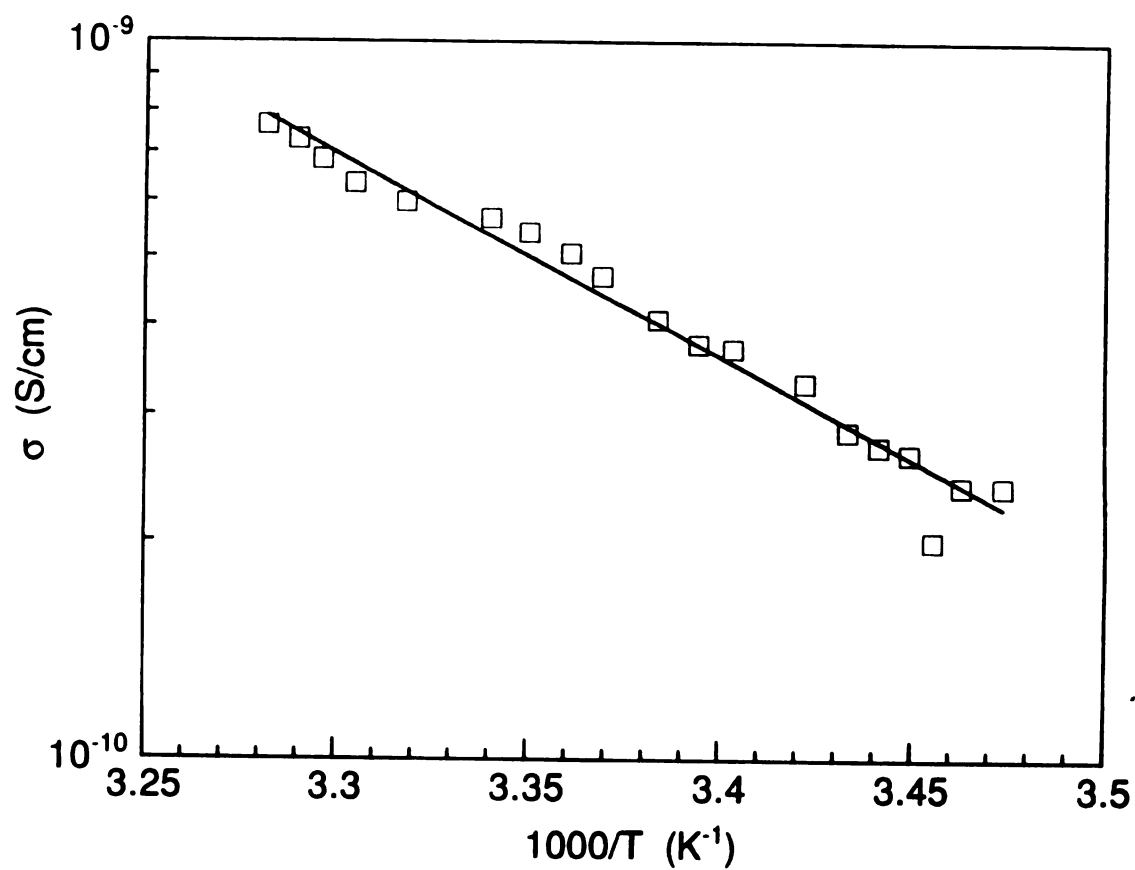


Figure 5-10: Variable temperature electrical conductivity data for single crystals of $\text{Cs}_8\text{Bi}_4(\text{P}_2\text{Se}_6)_5$.

3.4. Conclusions

In conclusion, the synthesis of new quaternary selenophosphates with A/P/Se molten salts provides a useful synthetic approach with broad scope. For example, the new family of $A_2MP_2Se_6$ ($A=K, Rb, Cs$; $M=Mn, Fe$) compounds has been synthesized in this way.³⁸ The advantage of $A_x[P_ySe_z]$ fluxes is that they provide reliably $[P_2Se_6]^{4-}$ units which other conventional aqueous or organic solvents have trouble stabilizing due to the high negative charge. Thus, solid state and coordination chemistry with $[P_2Se_6]^{4-}$ and metal centers becomes tractable based on the method highlighted in this chapter. It would be interesting to see whether changes in the nominal stoichiometry of these fluxes can result in other $[P_xSe_y]^n-$ units as well.

List of References

1. T. J. McCarthy and M. G. Kanatzidis, *Chem. Mater.* 1993, 5, 1061-1063.
2. Garin, J.; Parthe, E. *Acta Crystallogr.*, 1972, B28, 3672-3674.
3. Fritz, I. J.; Isaacs, T. J.; Gottlieb, M.; Morosin, B. *Solid State Commun.*, 1978, 27, 535.
4. O'Neal, S. C.; Pennington, W. T.; Kolis, J. W. *Angew. Chem. Int. Ed. Engl.* 1990, 29, 1486-1488.
5. (a) Klingen, W.; Eulenberger, G.; Hahn, H. *Z. Anorg. Allg. Chem.*, 1973, 401, 97-112. (b) Toffoli, P.; Khodadad, P.; Rodier, N. *Acta Cryst., Sect. B*, 1978, 34, 1779-1781. (c) Klingen, W.; Ott, R.; Hahn, H. *Z. Anorg. Allg. Chem.*, 1973, 396, 271-278. (d) Jandali, M. Z.; Eulenberger, G.; Hahn, H. *Z. Anorg. Allg. Chem.*, 1978, 447, 105-118.
6. (a) Ouvrard, G.; Brec, R.; Rouxel, J. *Mater. Res. Bull.*, 1985, 20, 1181-1189. (b) Lee, S.; Colombet, P.; Ouvrard, G.; Brec, R. *Inorg. Chem.*, 1988, 27, 1291-1294. (c) Lee, S.; Colombet, P.; Ouvrard, G.; Brec, R. *Mater. Res. Bull.*, 1986, 21, 917-928. (d) Durand, E.; Ouvrard, G.; Evain, M.; Brec, R. *Inorg. Chem.*, 1990, 29, 4916-4920.
7. (a) Carpentier, C. D.; Nitsche, R. *Mater. Res. Bull.* 1974, 9, 401-410. (b) Carpentier, C. D.; Nitsche, R. *Mater. Res. Bull.* 1974, 9, 1097-1100. (c) Arnautova, E.; Sviridov, E.; Rogach, E. Savchenko, E.; Grekov; A. *Integrated Ferroelectrics*, 1992, 1, 147-150.
8. (a) Becker, R.; Brockner, W.; Schäfer, H. *Z. Naturforsch.* 1983, 38a, 874-879. (b) Becker, R.; Brockner, W.; Schäfer, H. *Z. Naturforsch.* 1984, 39a, 357-361. (c) Yun, H.; Ibers, J. A. *Acta Cryst.* 1987, C43, 2002-2004.
9. (a) Katty, A.; Soled, S.; Wold, A. *Mater. Res. Bull.*, 1977, 12, 663-666. (b) Diehl, R.; Carpentier, C. D. *Acta Cryst., Sect. B*, 1978, 34, 1097-1105.
10. Etman, M.; Katty, A.; Levy-Clement, C.; Lemasson, P. *Mater. Res. Bull.*, 1982, 17, 579-584.
11. Thompson, A. H.; Whittingham, M. S. *U. S. Patent 4,049,879* 1977. (b) Brec, R.; Le Mehaute', A. *Fr. Patents 7,704,519* 1977.
12. (a) Clement R. *J. Chem. Soc., Chem. Commun.* 1980, 647-648. (b) Michalowicz, A.; Clement R. *Inorg. Chem.* 1982, 21, 3872-3877. (c) Joy, P. A.; Vasudevan, S. *J. Am. Chem. Soc.*, 1981, 114, 7792-7801.
13. Pfeiff, R.; Kniep, R. *J. Alloys and Compounds*, 1992, 186, 111-133.
14. Feher, F. *Handbuch der Präparativen Anorganischen Chemie*; Brauer, G., Ed.; Ferdinand Enke: Stuttgart, Germany, 1954; pp. 280-281.
15. CERIU: Molecular Simulation Software, Version 3.0, (1992), Cambridge Molecular Design, Waltham, MA 02154.
16. G. M. Sheldrick, In *Crystallographic Computing 3*; Sheldrick, G. M., Kruger, C., Doddard, R., Eds.; Oxford University Press: Oxford, England, 1985; pp 175-189.
17. TEXSAN: Single Crystal Structure Analysis Software, Version 5.0, (1981). Molecular Structure Corporation, The Woodlands, TX 77381.
18. Walker, N.; Stuart, D. *Acta Cryst.*, 1983, A39, 158-166.
19. The characteristic stretching frequency range for P-P interactions of similar interatomic distances is about 400-600 cm⁻¹. K. Nakamoto in "Infrared and Raman Spectra of Inorganic and Coordination Compounds", Wiley, New York, 1978.
20. Loferski, J. J. *J. Appl. Phys.*, 1956, 27, 777.

21. McCarthy, T. J.; Ngeyi, S.-P.; Liao, J.-H.; DeGroot, D.; Hogan, T.; Kannewurf, C. R.; Kanatzidis, M. G. *Chem. Mater.*, 1993, 5, 331-340.
22. G. Cordier, H. Schafer and C. Schwidetzky, *Rev. Chem. Miner.*, 1985, 22, 676.
23. (a) R. J. Gillespie, *Can. J. Chem.*, 1960, 38, 818. (b) R. J. Gillespie, *J. Chem. Educ.*, 1963, 40, 295. (c) R. J. Gillespie, *Molecular Geometry*; Van Nostrand Reinhold; London, 1972; p. 6.
24. M. Z. Jandali, G. Eulenberger and H. Hahn, *Z. Anorg. Allg. Chem.*, 1978, 447, 105.
25. (a) Barrett, C. S.; Cucka, P.; Haefner, K. *Acta Cryst.* 1963, 16, 451-453. (b) Cucka, P.; Barrett, C. S. *Acta Cryst.* 1962, 15, 865-872.
26. Trinquier, G.; Hoffmann, R. *J. Phys. Chem.*, 1984, 88, 6696-6711.
27. Ashe III, A. J.; Butler, W.; Diephouse, T. R. *J. Am. Chem. Soc.*, 1981, 103, 207-209.
28. Hughbanks, T.; Hoffmann, R.; Whangbo M.-H.; Stewart, K. R.; Eisenstein O.; Canadell, E. *J. Am. Chem. Soc.* 1982, 104, 3876-3879.
29. Mundt, O.; Riffel, H.; Becker, G.; Simon, A. *Z. Naturforsch.* 1984, 39b, 317-322.
30. Mundt, O.; Becker G.; Rössler, M.; Witthauer, C. *Z. Anorg. Allg. Chem.* 1983, 506, 42-58.
31. (a) Dance, I. G. *Polyhedron* 1983, 2, 1031-1043. (b) Hollander, F. J.; Coucouvanis, D. *J. Am. Chem. Soc.* 1977, 99, 6268-6279. (c) Chadha, R.; Kumar, R.; Tuck, D. G. *J. Chem. Soc., Chem. Commun.* 1986, 188-189. (d) Coucouvanis, D.; Murphy, C. N.; Kanodia, S. K. *Inorg. Chem.* 1980, 19, 2993-2998.
32. (a) Burschka, C.; Bronger, W. *Z. Naturforsch.* 1977, 32B, 11-14. (b) Burschka, C. *Z. Naturforsch.* 1979, 34B, 675-677. (c) Schils, H.; Bronger, W. *Z. Anorg. Allg. Chem.* 1979, 456, 187-193. (d) Savelberg, G.; Schäfer, H. *Z. Naturforsch.* 1978, 33B, 711-713.
33. (a) Merz, K. M.; Hoffmann R. *Inorg. Chem.* 1988, 27, 2120-2127. (b) Mehrotra, P. K.; Hoffmann, R. *Inorg. Chem.* 1978, 17, 2187-2189.
34. (a) Cotton, F. A.; Feng, X.; Matusz, M.; Poli, R. *J. Am. Chem. Soc.* 1988, 110, 7077-7083. (b) Lee, S. W.; Trogler, W. C. *Inorg. Chem.* 1990, 29, 1659-1662.
35. Wacker, K.; Salk, M.; Decker-Schultheiss, G.; Kelley, E. *Z. Anorg. Allg. Chem.*, 1991, 606, 51-58.
36. Vos, A.; Wiegenga, E. H. *Acta Cryst.*, 1955, 8, 217-223.
37. McCarthy, T. J.; Kanatzidis, M. G. work in progress.
38. McCarthy, T. J.; Kanatzidis, M. G. manuscript in preparation.

CHAPTER 6

Synthesis in Molten Alkali Metal Polyselenophosphate Fluxes: A New Family of Transition Metal Selenodiphosphate Compounds, $A_2MP_2Se_6$ ($A=K, Rb, Cs$; $M=Mn, Fe$), $A_2M'_2P_2Se_6$ ($A=K, Cs$; $M'=Cu, Ag$) and $K_4Au_2(P_2Se_6)_2$

1. Introduction

Recently, we have used the chalcophosphate flux method successfully to synthesize several quaternary main group compounds, $ABiP_2S_7$ ($A=K, Rb$),¹ KMP_2Se_6 ($M=Sb, Bi$)² and $Cs_8M_4(P_2Se_6)_5$ ($M=Sb, Bi$).³ The $A_x[P_yQ_z]$ ($Q=S, Se$) fluxes provide excess $A_x[P_yQ_z]^{n-}$ anions which bind the metal ions and perhaps also act as mineralizers. Using polyselenophosphate $A_x[P_ySe_z]$ fluxes below 600°C, we wanted to explore the chemistry of first row transition metals to see if this strongly basic medium would discourage the formation of the well known $M_2P_2Se_6$ compounds. The $M_2P_2Q_6$ ($M=Mn, Fe, Co, Ni, Zn, Cd, V, Mg$; $Q=S, Se$) family of compounds are structurally related to CdI_2 .^{4,5} These compounds possess interesting magnetic⁶ and intercalation properties⁷ and transition metal thiophosphates are of potential importance as low-dimensional cathode materials for secondary lithium batteries.⁸

Substitution of M^{2+} cations by M^+ (Ag, Cu) and M^{3+} (Al, In, Cr, V) has been demonstrated for $M_2P_2Q_6$ compounds to form quaternary chalcophosphates which retain the stable CdI_2 structure-type.⁹ Recently, Clement and coworkers have reported that ion-exchange intercalation of $M_2P_2S_6$ ($M=Cd, Mn$) with a cationic organic dye induces a large second-order optical nonlinearity and permanent magnetization (Mn^{2+}).¹⁰

Although $[P_xSe_y]^{n-}$ units such as $[PSe_4]^{3-}$ and $[P_2Se_6]^{4-}$ can potentially exhibit many different bonding modes giving rise to a wealth of different compounds, relatively little is known about the chemistry of selenophosphate ligands. Presumably, progress in this area has been hindered by the lack of suitable solvents for the dissolution of these highly charged ligands. The rare $[PSe_4]^{3-}$ ligand is found in solid state compounds such as Cu_3PSe_4 ¹¹ and Tl_3PSe_4 .¹² Kolis and coworkers have isolated two transition metal complexes with unusual coordinating $[PSe_2]^-$ and $[PSe_5]^{3-}$ ligands by using "P₄Se₄" glasses in DMF solutions.¹³ We have shown recently that the use of molten alkali selenophosphate fluxes is a convenient method for stabilizing highly charged $[P_xSe_y]^{n-}$ units.

Here we report the synthesis, structural characterization, optical, thermal and magnetic properties of a new class of compounds, $A_2MP_2Se_6$ ($A=K, Rb, Cs; M=Mn, Fe$), $A_2M'P_2Se_6$ ($A=K, Cs; M'=Cu, Ag$), and $K_4Au_2(P_2Se_6)_2$. In the case of Mn and Fe, successful dismantling of the $M_2P_2Se_6$ framework results in the formation of one-dimensional, polymeric anions that are reminiscent of the TiI_3 structure type. Replacement of the octahedral M^{2+} metal centers with $M'^+ \cdots M'^+$ ($M'=Cu, Ag$) pairs gives rise to $Cs_2M'P_2Se_6$. In

$A_2M_2P_2Se_6$, a change in the counterion size (A) (substitution of Cs^+ with K^+) results in dramatic change in structure from a one-dimensional chain to a complex three-dimensional tunnel framework. The structure of $K_4Au_2(P_2Se_6)_2$ features a one-dimensional chain with linear $Au^I Se_2$ and square planar $Au^{III} Se_4$ units bridged by $[P_2Se_6]^{4-}$ ligands. It is a rare example of a mixed valent Au^+/Au^{3+} compound.

2. Experimental Section

2.1. Reagents

Chemicals in this work were used as obtained: (i) iron metal powder, 99.9% purity, -325 mesh, and gold metal powder, 99.95% purity, -325 mesh, Cerac Inc., Milwaukee, WI; (ii) manganese metal powder, 99.9% purity -50 mesh, Aldrich Chemical Co., Inc., Milwaukee, WI; (iii) copper and silver metal powders, Fisher Scientific Co., Fair Lawn, NJ; (iv) red phosphorous powder, Morton Thiokol, Inc., -100 mesh, Danvers, MA; (v) selenium powder, 99.5+% purity -100 mesh, Aldrich Chemical Co., Inc., Milwaukee, WI; (vi) potassium metal, Aldrich Chemical Co., Inc., Milwaukee, WI; (vii) rubidium metal and cesium metal, analytical reagent, Johnson Matthey/AESAR Group, Seabrook, NH; (viii) DMF, analytical reagent, diethyl ether, ACS anhydrous, EM Science, Inc., Gibbstown, NJ; (ix) triethylphosphine, Aldrich Chemical Co., Inc., Milwaukee, WI.

2.2. Synthesis

All manipulations were carried out under a dry nitrogen atmosphere in a Vacuum Atmospheres Dri-Lab glovebox. For the preparation of K_2Se , Rb_2Se , and Cs_2Se we used a modified literature procedure.¹⁴ The preparation of K_2Se is reported in Section 2.2 of Chapter 1 (Part 1).

Cs_2Se . An amount of 5.00 g (0.038 mol) of slightly heated ($\sim 30^\circ\text{C}$) cesium metal was pipetted into a 250-ml round-bottom flask. A 150-ml volume of liquid ammonia was condensed into the flask at 78°C (dry ice/acetone bath) under nitrogen to give a dark blue solution. Selenium (1.485 g, 0.019 mol) and a Teflon-coated stir bar were added, and the mixture was stirred for 1 h to give a light blue solution. The NH_3 was removed by evaporation under a flow of nitrogen as the bath slowly warmed to room temperature. The pale orange solid (98% yield) was dried under vacuum overnight, flame-dried, and ground to a fine powder in the glove box.

Rb_2Se . Same procedure as Cs_2Se .

P_2Se_5 . The amorphous phosphorus selenide glass, " P_2Se_5 ", was prepared by heating a stoichiometric ratio of the elements in an evacuated pyrex tube for 24 h at 460°C . The glass was ground up and stored in a nitrogen glove box.

$\text{K}_2\text{MnP}_2\text{Se}_6$ (I). An amount of 0.014 g (0.25 mmol) Mn, 0.228 g (0.50 mmol) P_2Se_5 , 0.079 g (0.50 mmol) K_2Se , and 0.197 g (2.50 mmol) Se were thoroughly mixed and transferred to a 6ml pyrex tube which was subsequently flame-sealed in vacuo ($\sim 10^{-3}$ torr). The reaction was heated to 450°C over 12 hours in a computer-

controlled furnace. It was kept at 450 °C for 6 days, followed by cooling to 150 °C at a rate of 4 °C/hr, then to room temperature in one hour. The moisture-sensitive product was isolated by dissolving the flux with degassed DMF under inert atmosphere and then washed with anhydrous ether to give orange needle-like crystals and a small amount of gray powder (crystallized flux). Semi-quantitative microprobe analysis on single crystals gave $K_{2.2}Mn_{1.0}P_{2.5}Se_{6.5}$ (average of three data acquisitions). These crystals were used for crystallographic studies. Pure material was obtained by heating Mn/P/K₂Se/Se in a stoichiometric ratio in a pyrex tube at 500°C for 4 days. The product was purified by washing with degassed DMF and ether to give 0.378 g (56% yield, based on Mn) of orange crystallites. Far-IR (CsI matrix) shows absorptions at 478(s), 463(s), 303(m) and 210-143(w) cm⁻¹.

Rb₂MnP₂Se₆ (II). Pure material was obtained by heating a stoichiometric ratio of Mn/P/Rb₂Se/Se as above to give 0.396 g (52% yield, based on Mn) of orange crystallites. The crystallites are moisture sensitive. Semi-quantitative microprobe analysis on single crystals gave $Rb_{1.8}Mn_{1.0}P_{1.5}Se_{4.7}$ (average of three data acquisitions). Far-IR (CsI matrix) shows absorptions at 480(s), 465(s), 304(m) and 201-148(w) cm⁻¹.

Cs₂MnP₂Se₆ (III). An amount of 0.014 g (0.25 mmol) Mn, 0.228 g (0.50 mmol) P₂Se₅, 0.157 g (0.46 mmol) Cs₂Se, and 0.197 g (2.50 mmol) Se were heated as above. The product was isolated by dissolving the flux with degassed DMF under inert atmosphere and then washed with anhydrous ether to give orange needle-like crystals and elemental Se. The crystals appear to be stable in water.

Semi-quantitative microprobe analysis on single crystals gave $\text{Cs}_{2.0}\text{Mn}_{1.0}\text{P}_{2.2}\text{Se}_{6.3}$ (average of three data acquisitions). These crystals were used for crystallographic studies. Pure material was obtained by heating Mn/P/Cs₂Se/Se in a stoichiometric ratio as above to give 0.423 g (49% yield, based on Mn) of orange crystallites. Far-IR (CsI matrix) shows absorptions at 481(s), 464(s), 305(m) and 189-152(w) cm⁻¹.

$\text{K}_2\text{FeP}_2\text{Se}_6$ (IV). An amount of 0.014 g (0.25 mmol) Fe, 0.228 g (0.50 mmol) P_2Se_5 , 0.079 g (0.50 mmol) K_2Se , and 0.197 g (2.50 mmol) Se were heated as in (I) except for 4 days. The moisture sensitive product was isolated by dissolving the flux with degassed DMF under inert atmosphere and then washing with anhydrous ether to give red needle-like crystals, water soluble flux, and elemental Se. This product was allowed to stir in a solution of triethylphosphine (PEt_3) (0.1 ml)/ether (20 ml) for 2 hours. Washing with ether gave red $\text{K}_2\text{FeP}_2\text{Se}_6$ but also black $\text{Fe}_2\text{P}_2\text{Se}_6$ as a minor impurity phase (~5-10%). The presence of $\text{Fe}_2\text{P}_2\text{Se}_6$ was detected by X-ray powder diffraction. Several attempts to obtain pure $\text{K}_2\text{FeP}_2\text{Se}_6$ failed. Semi-quantitative microprobe analysis on the moisture-sensitive red single crystals gave $\text{K}_{1.8}\text{Fe}_{1.0}\text{P}_{1.8}\text{Se}_{4.9}$ (average of three data acquisitions). These crystals were used for crystallographic studies. Pure sample for magnetic susceptibility measurements was obtained by manual separation of $\text{K}_2\text{FeP}_2\text{Se}_6$ crystals. Far-IR (CsI matrix) gave absorbances at 475(s), 466(s), and 303(m) cm⁻¹. Direct combination reactions with Fe/P/ K_2Se /Se at 500 °C gave similar results.

$\text{Cs}_2\text{FeP}_2\text{Se}_6$ (V). An amount of 0.014 g (0.25mmol) Fe, 0.343 g (0.75 mmol) P_2Se_5 , 0.172 g (0.50 mmol) Cs_2Se , and 0.197 g (2.50

mmol) Se were heated as in (I V). The product was isolated as in (IV) above to give 0.112 g of red needle-like crystals (52% yield, based on Fe). Semi-quantitative microprobe analysis on single crystals gave $\text{Cs}_{1.9}\text{Fe}_{1.0}\text{P}_{1.6}\text{Se}_{5.6}$ (average of three data acquisitions). Far-IR (CsI matrix) shows absorptions at 478(s) and 469(m) cm^{-1} .

$\text{Cs}_2\text{Cu}_2\text{P}_2\text{Se}_6$ (VI). An amount of 0.016 g (0.25 mmol) Cu, 0.228 g (0.5 mmol) P_2Se_5 , 0.172 g (0.5 mmol) Cs_2Se , and 0.197 g (2.5 mmol) Se were heated as in (I V). The product was isolated by dissolving the flux with degassed DMF under inert atmosphere and then washed with anhydrous ether to give dark green rectangular block-like crystals and some water soluble flux. The residual flux was removed by washing the product with distilled water, MeOH, and ether to give 0.061 g (53% yield based on Cu) of dark green crystals. Semi-quantitative microprobe analysis on single crystals gave $\text{Cs}_{1.3}\text{Cu}_{1.3}\text{P}_{1.0}\text{Se}_{3.2}$ (average of three data acquisitions). Far-IR (CsI matrix) gave absorptions at 467(m), 454(s), 447(msh), 302(m), 213(vw) cm^{-1} .

$\text{K}_2\text{Ag}_2\text{P}_2\text{Se}_6$ (VII). An amount of 0.027 g (0.25 mmol) Ag, 0.228 g (0.5 mmol) P_2Se_5 , 0.079 g (0.5 mmol) K_2Se , and 0.197 g (2.5 mmol) Se were heated as in (I V). The product was isolated with DMF and washed with ether. Further washing with 0.1 ml PEt_3 in ether (20 ml) gave 0.052g (50% yield, based on Ag) of orange crystals. Semi-quantitative microprobe analysis on single crystals gave $\text{K}_{1.0}\text{Ag}_{1.1}\text{P}_{1.0}\text{Se}_{2.9}$ (average of three data acquisitions). Far-IR (CsI matrix) gave absorbances at 460(m), 443(s), and 302(w) cm^{-1} .

$\text{Cs}_2\text{Ag}_2\text{P}_2\text{Se}_6$ (VIII). An amount of 0.027 g (0.25 mmol) Ag, 0.228 g (0.5 mmol) P_2Se_5 , 0.172 g (0.5 mmol) Cs_2Se , and 0.197 g (2.5

mmol) Se were heated as in (I V). The product was isolated with DMF and washed with ether. Further washing with 0.1 ml $P(Et)_3$ in ether (20 ml) gave 0.084 g (66% yield, based on Ag) of yellow-orange needle-like crystals. Semi-quantitative microprobe analysis on single crystals gave $Cs_{1.0}Ag_{1.3}P_{1.1}Se_{3.2}$ (average of three data acquisitions). Far-IR (CsI matrix) shows absorptions at 452(w, broad) and 302(w) cm^{-1} .

$K_4Au_2(P_2Se_6)_2$ (IX). An amount of 0.049 g (0.25 mmol) Au, 0.343 g (0.75 mmol) P_2Se_5 , 0.079 g (0.5 mmol) K_2Se , and 0.197 g (2.5 mmol) Se were heated as in (I V) above. The product was isolated with DMF and washed with ether to give 0.163 g (80% yield, based on Au) of black rectangular block-like crystals. Semi-quantitative microprobe analysis on single crystals gave $K_{2.8}Au_{1.0}P_{3.0}Se_{8.9}$ (average of three data acquisitions). Far-IR (CsI matrix) shows absorptions 499 (s), 470(m), 429(s), 303(m), 240(w), and 205(w) cm^{-1} .

$K_2Mn_{0.5}Fe_{0.5}P_2Se_6$. An amount of 0.014 g (0.25 mmol) Mn, 0.014 g (0.25 mmol) Fe, 0.457g (1.0 mmol) P_2Se_5 , 0.157 g (1.0 mmol) K_2Se , and 0.395 g (5.0 mmol) Se were heated and isolated as in (IV) to give orange-brown needle-like crystals and elemental selenium. The product was washed with triethylphosphine PEt_3 /ether as above in (I V) to give orange-red crystals of $K_2Mn_{0.5}Fe_{0.5}P_2Se_6$ and black $Fe_2P_2Se_6$ as a minor impurity phase (~5%). The presence of $Fe_2P_2Se_6$ was detected by X-ray powder diffraction. Semi-quantitative microprobe analysis on red-orange single crystals gave $K_{2.1}Mn_{0.5}Fe_{0.5}P_{2.3}Se_{6.1}$ (average of six data acquisitions). Pure

sample for magnetic susceptibility measurements was obtained by manual separation of $\text{K}_2\text{Mn}_{0.5}\text{Fe}_{0.5}\text{P}_2\text{Se}_6$ crystals.

The homogeneity of (I), (III), (VI), (VII), (VIII), and (IX) was confirmed by comparing the observed and calculated X-ray powder diffraction patterns. The d_{hkl} spacings observed for the bulk materials were compared, and found to be in good agreement with the d_{hkl} spacings calculated from the single crystal data.¹⁵ The results are summarized in Tables 6-1 to 6-6.

2.3. Physical Measurements

The instruments and experimental setups for optical diffuse reflectance measurements, far-IR spectroscopy, and quantitative microprobe analysis on SEM/EDS are the same as those in Chapter 2 (Part 1) (Section 2.3). The experimental setup for differential thermal analysis (DTA) is the same as that in Chapter 2 (Part 2) (Section 2.3).

Magnetic susceptibility measurements were carried out using a MPMS Quantum Design SQUID magnetometer over the range of 2-300 K. Single crystals were ground to a fine powder to minimize possible anisotropic effects. In the case of $\text{K}_2\text{FeP}_2\text{Se}_6$, single crystals were carefully hand-picked from the product mixture because of the presence of the minor $\text{Fe}_2\text{P}_2\text{Se}_6$ impurity phase. Corrections for the diamagnetism of the PVC sample containers were applied. Field dependence measurements were performed (at 5 K and 300 K) to determine if the samples experienced saturation of their magnetic signal. For all compounds, magnetization increased linearly with increasing field over the range investigated (0-10,000 Gauss). A suitable magnetic field was chosen from the linear region for temperature dependence measurements (2000-3000 Gauss). The μ_{eff} and θ values were calculated by least-squares fits for the plots of $1/\chi_M$ vs. temperature in the paramagnetic (Curie-Weiss) region from 30-300 K.

2.4. X-ray Crystallography

All compounds were examined by X-ray powder diffraction (XRD) for the purpose of phase purity and identification. Accurate d_{hkl} spacings (Å) were obtained from the powder patterns recorded on a Rigaku rotating anode (Cu $K\alpha$) X-ray powder diffractometer, Rigaku-Denki/RW400F2 (Rotaflex), at 45 kV and 100 mA with a 1 °/min scan rate.

Single crystal X-ray diffraction data were collected on a Rigaku AFC6 diffractometer and the $\omega/2\theta$ scan technique was used. None of the crystals showed any significant intensity decay as judged by three check reflections measured every 150 reflections throughout the data collections. The space groups were determined from systematic absences and intensity statistics. The structures were solved by direct methods of SHELXS-86¹⁶ and refined by full-matrix least-squares techniques of the TEXSAN package of crystallographic programs.¹⁷ An empirical absorption correction based on ψ -scans was applied to each data set, followed by a DIFABS¹⁸ correction to the isotropically refined structure. All atoms were eventually refined anisotropically. All calculations were performed on a VAXstation 3100/76 computer.

In the case of $\text{Cs}_2\text{Cu}_2\text{P}_2\text{Se}_6$, inspection of the residual electron density map revealed two peaks of 2.3 and 2.7 e⁻/Å³ that were ~1.4 Å away from Cu(1) and Cu(2). These sites are located near the centers of symmetry in between the Cu...Cu pairs. Refinement of these pseudo-octahedral sites as Cu positions resulted in no change in the R/R_w and in less than 5% occupancy. The presence of these small

peaks were judged insignificant. No residual electron density peaks were found near the Ag atoms in $\text{Cs}_2\text{Ag}_2\text{P}_2\text{Se}_6$.

In the case of $\text{K}_4\text{Au}_2(\text{P}_2\text{Se}_6)_2$, refinement of the structure gave $\text{K}_2\text{Au}_{0.50}\text{III}\text{Au}_{0.50}\text{IP}_2\text{Se}_6$ with Au(1) in a square planar site and Au(2) found in a linear coordination site. The temperature factor of Au(2) was rather high at 10.0 \AA^2 so the occupancy was refined and found to be 0.25 to give a formula of $\text{K}_2\text{Au}_{0.50}\text{III}\text{Au}_{0.25}\text{IP}_2\text{Se}_6$ which does not balance the charge ($R/R_w=13.4/15.5$). The temperature factors of K(1) and K(2) were also rather high at $\sim 6\text{--}7 \text{ \AA}^2$. A small peak of $4.0 \text{ e}^-/\text{\AA}^3$ was observed in the residual electron density map and can be assigned to a very small amount of Au^+ but does not represent enough electron density for charge balance. The final R/R_w after final DIFABS and anisotropic refinement gave values of 7.6/10.3. The elemental analysis also suggests a Au deficiency but this measurement is complicated by the partial overlap of the Au $M\alpha$ and the P $K\alpha$ X-ray energy lines. More work is needed to obtain a higher quality crystals with improved X-ray diffraction characteristics. Better crystals must be grown with K^+ or perhaps Rb^+ and the data must be recollected.

The complete data collection parameters and details of the structure solution and refinement for (I), (III), (IV), (VI), (VII), (VIII), and (IX) are given in Table 6-7. The coordinates of all atoms, average temperature factors, and their estimated standard deviations are given in Tables 6-8 to 6-14.

Table 6-1. Calculated and Observed X-ray Powder Diffraction Patterns for $\text{K}_2\text{MnP}_2\text{Se}_6$.

$h\ k\ l$	$d_{\text{calcd}}, \text{\AA}$	$d_{\text{obsd}}, \text{\AA}$	$I/I_{\text{max}} (\text{obsd})$
0 1 1, 0 2 0	6.40, 6.35	6.36	100
0 3 1	3.67	3.69	20
0 1 2	3.55	3.55	42
1 1-2	3.43	3.42	9
0 2 2, 2 0 0	3.20, 3.19	3.19	94
1 2-2	3.10	3.10	61
1 4 0	2.84	2.83	48
2 1 1	2.66	2.65	24
1 4 1	2.57	2.56	7
2 2-2	2.51	2.50	11
0 5 1	2.402	2.403	10
2 3-2	2.294	2.295	9
2 4 1	2.065	2.063	5
0 6 1	2.035	2.029	6
0 0 4	1.851	1.848	24
0 6 2	1.837	1.831	12
1 2-4	1.813	1.809	6
2 0-4	1.779	1.774	7
3 3 1	1.759	1.756	7
4 1-1	1.620	1.623	9

Table 6-2. Calculated and Observed X-ray Powder Diffraction Patterns for $\text{Cs}_2\text{MnP}_2\text{Se}_6$.

$h\ k\ l$	$d_{\text{calcd}}, \text{\AA}$	$d_{\text{obsd}}, \text{\AA}$	$I/I_{\text{max}} (\text{obsd})$
0 1 1	6.79	6.78	22
0 2 0	6.51	6.49	14
1 1-1	4.79	4.78	7
1 2 0, 1 1 1	4.59, 4.58	4.58	9
1 2-1	4.04	4.03	24
0 0 2	3.98	3.97	17
0 3 1	3.81	3.80	66
0 2 2	3.40	3.39	100
1 1-2	3.36	3.35	10
0 4 0	3.25	3.25	24
2 0 0	3.23	3.23	38
1 2-2	3.06	3.06	60
0 4 1	3.01	3.01	11
1 2 2	2.95	2.95	56
1 4 0	2.91	2.90	62
2 1 1	2.87	2.86	7
1 3 2	2.63	2.58	5
2 2-2	2.397	2.400	5
2 2 2	2.290	2.286	14
1 2 3	2.260	2.260	6
0 6 0	2.169	2.165	5
0 0 4	1.990	1.985	27
0 1 4	1.967	1.964	8
0 6 2	1.905	1.900	42
3 4 0	1.797	1.799	7
3 2 2	1.783	1.783	6

Table 6-3. Calculated and Observed X-ray Powder Diffraction Patterns for $K_2Ag_2P_2Se_6$.

h k l	$d_{\text{calcd}}, \text{\AA}$	$d_{\text{obsd}}, \text{\AA}$	$I/I_{\text{max}} (\text{obsd})$
0 0 2	10.47	10.47	28
0 1 1	9.90	9.91	44
0 1 2	7.66	7.66	52
1 0-2	6.80	6.78	66
1 1 1	6.37	6.37	70
1 1-2	5.82	5.80	9
0 2 1	5.43	5.42	14
0 0 4	5.23	5.23	14
1 2 1	4.55	4.54	13
0 2 3	4.38	4.37	11
2 0-2	4.02	4.02	16
2 1 0	3.98	3.97	11
2 1-1	3.95	3.94	16
2 0 2	3.87	3.86	10
0 2 4	3.83	3.82	10
2 1-2	3.79	3.78	13
1 1-5	3.64	3.64	15
1 2-4	3.55	3.54	38
1 1 5	3.49	3.48	35
1 3-1	3.40	3.39	71
2 2-1	3.37	3.36	27
2 2-2	3.27	3.26	46
2 0 4	3.21	3.21	10
1 0 6	3.17	3.16	64
2 1 4	3.09	3.09	43
1 1 6	3.05	3.04	23
2 2-4	2.91	2.90	14
3 0 0	2.84	2.83	100
2 1 5	2.81	2.80	52
1 1-7	2.78	2.77	31
2 3-2	2.74	2.74	41
3 0 2	2.70	2.69	49
1 4-1	2.65	2.65	36
2 0 6	2.63	2.62	17
3 1-3	2.61	2.60	11
1 4 2	2.58	2.57	15
2 1 6	2.56	2.55	14
3 2-1	2.53	2.53	38
1 4-3	2.51	2.50	23
2 2-6	2.490	2.483	26
1 0 8	2.462	2.458	15

Table 6-3. (cont'd)

h k l	d _{calcd} , Å	d _{obsd} , Å	I / I _{max} (obsd)
2 2 6	2.379	2.374	11
3 1-5	2.360	2.357	8
0 3 7	2.338	2.335	39
1 2-8	2.317	2.312	17
3 3 0	2.262	2.257	8
1 1-9	2.232	2.231	43
1 3-8	2.104	2.099	16
2 4 5	2.019	2.016	12
4 2 0	1.990	1.987	10
4 2-2	1.975	1.973	24
3 3 6	1.860	1.856	8
3 3-7	1.845	1.848	39
1 6-1	1.825	1.823	10
1 6 1	1.821	1.817	9
4 2 5	1.761	1.760	11
2 1-11	1.754	1.752	10
2 2 10	1.746	1.746	8
4 3-5	1.725	1.723	8
3 1-10	1.712	1.711	11
2 5 6	1.708	1.706	14
2 6-2	1.699	1.696	8
3 5-4	1.688	1.688	10
4 2-8	1.627	1.623	8
4 5 0	1.546	1.545	10

Table 6-4. Calculated and Observed X-ray Powder Diffraction Patterns for $\text{Cs}_2\text{Ag}_2\text{P}_2\text{Se}_6$.

$h\ k\ l$	$d_{\text{calcd}}, \text{\AA}$	$d_{\text{obsd}}, \text{\AA}$	$I/I_{\text{max}} (\text{obsd})$
0 1 1	6.99	6.98	49
0 2 0	6.26	6.26	17
0 3 1	3.74	3.74	32
1 3 0	3.55	3.56	4
0 2 2	3.49	3.49	100
2 0 0	3.39	3.38	9
1 3-1	3.34	3.34	3
1 2-2	3.22	3.21	34
2 1-1	3.15	3.16	18
0 4 0	3.13	3.12	16
1 2 2	3.00	3.00	7
2 2 0	2.98	2.96	10
2 1 1	2.95	2.93	10
1 4 0	2.84	2.84	12
0 1 3	2.74	2.73	17
2 2-2	2.54	2.55	3
1 1 3	2.457	2.447	4
1 4 2	2.310	2.308	4
2 4 1	2.180	2.178	3
0 0 4	2.105	2.102	9
0 4 3	2.089	2.085	4
2 3-3	1.998	1.990	3
0 6 2	1.869	1.865	20
0 4 4	1.747	1.744	7
1 4-4	1.726	1.722	7

Table 6-5. Calculated and Observed X-ray Powder Diffraction Patterns for $\text{Cs}_2\text{Cu}_2\text{P}_2\text{Se}_6$.

h k l	$d_{\text{calcd}}, \text{\AA}$	$d_{\text{obsd}}, \text{\AA}$	$I/I_{\text{max}} (\text{obsd})$
1 1-1	6.85	6.89	18
0 2 0	6.53	6.52	11
2 1 0	4.56	4.55	7
2 0-2	4.02	4.02	10
1 3-1	3.83	2.83	18
2 2 1	3.46	3.46	53
2 2-2	3.43	3.42	100
0 4 0	3.27	3.26	32
2 0 2	3.23	3.22	20
3 1 0	3.15	3.14	29
1 2-3	3.11	3.11	29
1 3 2	3.04	3.01	4
3 2-1	2.95	2.95	23
1 4 1	2.92	2.91	27
3 1 1	2.85	2.85	18
3 2 1	2.67	2.69	4
0 2 4	2.431	2.424	6
4 2 0	2.278	2.247	8
3 5-1	2.050	2.060	6
4 0-4	2.011	2.006	10
4 1-4	1.988	1.985	4
4 4-1	1.980	1.980	3
2 6-2	1.915	1.910	23
0 3 5	1.888	1.898	8
1 2 5	1.880	1.884	15
0 5 4	1.850	1.849	7
4 4-3	1.844	1.845	5
3 4 3	1.799	1.795	4
2 0-6	1.769	1.768	5
4 4-4	1.713	1.710	10
5 0 2	1.707	1.705	9
3 4-5	1.683	1.681	5
0 6 4	1.675	1.673	5
1 1 6	1.644	1.642	5
6 1-2	1.639	1.639	5
5 4-3	1.630	1.631	7
4 6 0	1.622	1.626	7
4 0 4	1.616	1.616	4

Table 6-6. Calculated and Observed X-ray Powder Diffraction Patterns for $\text{K}_4\text{Au}_2(\text{P}_2\text{Se}_6)_2$.

h k l	d_{calcd} , Å	d_{obsd} , Å	I/I_{max} (obsd)
0 1 1	8.89	8.87	100
0 2 0	8.15	8.17	23
1 1 0	6.64	6.62	10
0 2 1	6.46	6.45	7
1 0 1	5.91	5.92	8
1 1-1	5.70	5.68	4
1 1 1	5.56	5.54	3
1 2 0	5.43	5.43	10
0 0 2	5.30	5.37	7
0 1 2	5.04	5.02	4
0 3 1	4.84	4.85	15
0 2 2	4.45	4.44	23
0 4 0	4.08	4.09	21
1 3-1	4.05	4.03	6
1 3 1	4.00	3.99	5
0 3 2	3.80	3.78	19
1 2 2	3.75	3.74	4
2 0 0	3.63	3.63	7
1 4 0	3.56	3.57	3
2 2 0	3.32	3.32	25
0 4 2	3.23	3.23	26
2 2-1	3.19	3.20	12
1 1-3	3.16	3.15	12
0 5 1	3.12	3.13	21
2 3 0	3.02	3.02	8
2 1-2	2.99	2.98	19
2 0 2	2.95	2.95	12
2 3-1	2.93	2.92	12
2 3 1	2.89	2.89	13
2 2 2	2.78	2.77	7
2 4 0	2.71	2.72	21
0 0 4	2.65	2.67	26
0 1 4	2.62	2.63	444
1 5-2	2.61	2.60	15
0 2 4	2.52	2.51	18
0 5 3	2.397	2.395	7
0 7 1	2.275	2.287	11
2 6 0	2.176	2.215	11
2 4 4	1.874	1.870	14
4 2 0	1.774	1.772	11
4 3-1	1.709	1.708	6

Table 6-7. Crystallographic Data for (I), (III), (IV), (VI), (VII), (VIII), and (IX).

	I	III	IV
Formula	K ₂ MnP ₂ Se ₆	Cs ₂ MnP ₂ Se ₆	K ₂ FeP ₂ Se ₆
FW	668.84	856.46	669.75
a, Å	6.5349(9)	6.4761(9)	6.421(2)
b, Å	12.696(3)	13.006(2)	12.720(5)
c, Å	7.589(2)	7.974(1)	7.535(3)
α, deg	90.0	90.0	90.0
β, deg	102.67(2)	93.09(1)	102.58(3)
γ, deg	90.0	90.0	90.0
Z; V, Å ³	2; 614.3(4)	2; 670.6(2)	2; 600.7(7)
λ (Mo Kα)	0.71073	0.71073	0.71073
space group	P2 ₁ /n (No. 14)	P2 ₁ /n (No. 14)	P2 ₁ /n (No. 14)
D _{calc.} , g/cm ³	3.616	4.239	3.703
μ, cm ⁻¹	195.19	225.67	201.59
2θ _{max} , deg	50	50	50
Temp., °C	23	23	23
Final R/R _w , %	2.9/3.4	2.7/3.1	3.9/4.5
Total Data	1236	1361	1213
Total Unique (Ave.)	1134	1245	1113
Data F _o ² > 3σ(F _o ²)	755	676	683
No. of variables	53	53	53

$$*R = \sum(|F_o| - |F_c|) / \sum |F_o| \quad R_w = \{ \sum w(|F_o| - |F_c|)^2 / \sum w|F_o|^2 \}^{1/2}$$

Table 6-7. (cont'd)

	VI	VII	VIII	IX
Formula	Cs ₂ Cu ₂ P ₂ Se ₆	K ₃ Ag ₃ P ₃ Se ₉	Cs ₂ Ag ₂ P ₂ Se ₆	K ₄ Au ₂ (P ₂ Se ₆) ₂
FW	928.61	1244.46	1017.25	1621.74
a, Å	9.958(3)	8.528(6)	6.807(3)	7.272(5)
b, Å	13.067(3)	11.251(6)	12.517(3)	16.30(1)
c, Å	10.730(2)	20.975(4)	8.462(3)	10.615(9)
α, deg	90.0	90.0	90.0	90.0
β, deg	102.46(2)	93.24(3)	95.75(3)	91.83(8)
γ, deg	90.0	90.0	90.0	90.0
Z; V, Å ³	4; 1363(1)	4; 2009(3)	2; 717.3(8)	2; 1257(2)
λ (Mo Kα)	0.71073	0.71073	0.71073	0.71073
space group	P2 ₁ /c (No. 14)	P2 ₁ /c (No. 14)	P2 ₁ /n (No. 14)	P2 ₁ /n (No. 14)
D _{calc.} , g/cm ³	4.524	4.114	4.709	4.281
μ, cm ⁻¹	244.14	198.57	229.30	297.16
2θ _{max} , deg	60	50	50	45
Temp., °C	23	23	23	23
Final R/R _w , %	5.6/6.7	4.5/6.4	3.4/3.9	7.6/10.3
Total Data	4163	4009	1433	1978
Total Unique(Ave.)	3943	3745	1322	1793
Data F _o ² >3σ(F _o ²)	2029	1866	733	989
No. of variables	110	164	56	104

$$*R = \sum(|F_o| - |F_c|) / \sum |F_o| \quad R_w = \{\sum w(|F_o| - |F_c|)^2 / \sum w|F_o|^2\}^{1/2}$$

Table 6-8. Fractional Atomic Coordinates and B_{eq} Values for $K_2MnP_2Se_6$ with Estimated Standard Deviations in Parentheses.

atom	x	y	z	$B_{eq},^a \text{Å}^2$
Se(1)	0.2128(1)	0.32791(7)	0.9293(2)	2.79(4)
Se(2)	0.1797(1)	0.58455(8)	0.7431(1)	2.53(4)
Se(3)	-0.3123(1)	0.44005(8)	0.7311(1)	2.60(4)
Mn(1)	1/2	1/2	1.0000	2.07(7)
P(1)	0.0130(3)	0.4666(2)	0.8665(3)	1.49(8)
K(1)	0.2245(3)	0.8097(2)	1.0394(4)	4.0(1)

Table 6-9. Fractional Atomic Coordinates and B_{eq} Values for $Cs_2MnP_2Se_6$ with Estimated Standard Deviations in Parentheses.

atom	x	y	z	$B_{eq},^a \text{Å}^2$
Cs	0.2453(1)	0.82963(7)	1.02388(8)	2.79(4)
Se(1)	0.2378(2)	0.3319(1)	0.9664(1)	2.05(5)
Se(2)	0.2283(2)	0.5736(1)	0.7540(1)	1.92(5)
Se(3)	-0.2492(2)	0.4195(1)	0.7536(1)	2.01(5)
Mn	1/2	1/2	1.0000	2.0(1)
P	0.0437(4)	0.4609(2)	0.8816(3)	1.4(1)

Table 6-10. Fractional Atomic Coordinates and B_{eq} Values for $K_2FeP_2Se_6$ with Estimated Standard Deviations in Parentheses.

atom	x	y	z	$B_{eq},^a \text{Å}^2$
Se(1)	0.2218(2)	0.3298(1)	0.9321(2)	2.50(6)
Se(2)	0.1876(2)	0.5841(1)	0.7458(2)	2.29(6)
Se(3)	-0.3185(2)	0.4410(1)	0.7334(2)	2.35(6)
Fe	1/2	1/2	1.0000	1.8(1)
P	0.0144(5)	0.4667(2)	0.8667(5)	1.4(1)
K	0.2246(6)	0.8077(3)	1.0432(5)	3.6(2)

$$^aB_{eq} = (4/3)[a^2B(1,1) + b^2B(2,2) + c^2B(3,3) + ab(\cos\gamma)B(1,2) + ac(\cos\beta)B(1,3) + bc(\cos\alpha)B(2,3)].$$

Table 6-11. Fractional Atomic Coordinates and B_{eq} Values for $Cs_2Cu_2P_2Se_6$ with Estimated Standard Deviations in Parentheses.

atom	x	y	z	$B_{eq},^a \text{ \AA}^2$
Cs(1)	0.6126(1)	0.3221(1)	0.1187(1)	2.45(5)
Cs(2)	1.1343(1)	0.1549(1)	0.1595(1)	2.69(5)
Se(1)	0.3607(2)	0.1657(1)	-0.1123(2)	2.23(7)
Se(2)	0.8462(2)	0.1767(1)	0.3762(2)	1.88(7)
Se(3)	1.0054(2)	0.4060(1)	0.2603(2)	2.13(7)
Se(4)	0.7775(2)	0.0768(1)	0.0181(2)	1.64(6)
Se(5)	0.7503(2)	0.5739(2)	-0.0142(2)	2.25(8)
Se(6)	0.4961(2)	0.5810(1)	0.2393(2)	2.03(7)
Cu(1)	0.5486(2)	0.4520(2)	0.4040(2)	2.5(1)
Cu(2)	0.0172(3)	0.4002(2)	0.0378(2)	3.0(1)
P(1)	0.2146(4)	0.0403(3)	-0.1671(4)	1.1(1)
P(2)	0.7197(4)	0.4607(3)	-0.1688(4)	1.2(1)

$$^aB_{eq} = (4/3)[a^2B(1,1) + b^2B(2,2) + c^2B(3,3) + ab(\cos\gamma)B(1,2) + ac(\cos\beta)B(1,3) + bc(\cos\alpha)B(2,3)].$$

Table 6-12. Fractional Atomic Coordinates and B_{eq} Values for $K_2Ag_2P_2Se_6$ with Estimated Standard Deviations in Parentheses.

atom	x	y	z	$B_{eq},^a \text{Å}^2$
Ag(1)	0.5399(3)	0.1570(2)	0.2781(1)	3.3(1)
Ag(2)	0.1814(4)	0.0387(3)	0.3638(1)	4.9(1)
Ag(3)	0.8686(3)	0.2194(2)	0.3972(1)	3.7(1)
Se(1)	0.7647(3)	0.4246(3)	0.4406(1)	2.5(1)
Se(2)	0.8274(3)	0.2472(3)	0.2727(1)	1.9(1)
Se(3)	0.4483(3)	-0.0552(2)	0.3107(1)	1.6(1)
Se(4)	0.5165(3)	0.6416(3)	0.3538(1)	2.3(1)
Se(5)	1.1559(3)	0.1958(3)	0.4522(1)	2.0(1)
Se(6)	1.2695(3)	-0.0106(3)	0.5771(1)	1.9(1)
Se(7)	0.4093(3)	0.3242(3)	0.3541(1)	2.1(1)
Se(8)	0.9135(3)	0.1670(3)	0.5870(1)	2.1(1)
Se(9)	0.9125(3)	0.5601(3)	0.2649(1)	2.1(1)
K(1)	0.1877(7)	0.3442(7)	0.2096(3)	3.0(3)
K(2)	0.5316(7)	0.2078(7)	0.5095(3)	3.4(3)
K(3)	-0.1365(8)	0.0254(7)	0.0999(3)	3.8(3)
P(1)	0.5964(7)	0.4579(6)	0.3600(3)	1.4(3)
P(2)	0.7285(7)	0.4266(6)	0.2700(3)	1.4(3)
P(3)	1.0699(7)	0.0758(7)	0.5256(3)	1.5(3)

$$^aB_{eq} = (4/3)[a^2B(1,1) + b^2B(2,2) + c^2B(3,3) + ab(\cos\gamma)B(1,2) + ac(\cos\beta)B(1,3) + bc(\cos\alpha)B(2,3)].$$

Table 6-13. Fractional Atomic Coordinates and B_{eq} Values for $Cs_2Ag_2P_2Se_6$ with Estimated Standard Deviations in Parentheses.

atom	x	y	z	$B_{eq},^a \text{Å}^2$
Cs	0.2465(2)	0.33282(9)	0.9891(1)	2.94(5)
Ag	0.0405(2)	0.4404(1)	1.3586(2)	3.59(7)
Se(1)	-0.2213(2)	0.1785(1)	1.0414(2)	2.50(7)
Se(2)	0.2367(2)	0.0923(1)	1.2465(2)	2.56(7)
Se(3)	-0.1806(2)	-0.0830(1)	1.2496(2)	2.05(6)
P	-0.0383(6)	0.0403(3)	1.1141(5)	1.6(2)

Table 6-14. Fractional Atomic Coordinates and B_{eq} Values for $K_4Au_2(P_2Se_6)_2$ with Estimated Standard Deviations in Parentheses.

atom	x	y	z	$B_{eq},^a \text{Å}^2$
Au(1)	0	1/2	0	1.4(1)
Au(2)	-1/2	1/2	0	3.3(3)
Se(1)	0.1539(7)	0.6352(3)	0.0257(5)	2.4(3)
Se(2)	-0.0886(8)	0.7352(4)	-0.2368(6)	3.7(3)
Se(3)	0.0168(7)	0.5085(4)	0.2347(4)	2.8(3)
Se(4)	-0.4876(8)	0.4860(5)	0.2163(6)	5.1(4)
Se(5)	0.7142(8)	0.9043(4)	0.0237(5)	3.1(3)
Se(6)	0.3973(8)	0.7644(5)	-0.1868(6)	4.5(4)
K(1)	0.295(2)	0.388(1)	0.471(2)	7(1)
K(2)	0.176(2)	0.821(1)	-0.468(2)	7(1)
P(1)	-0.225(2)	0.433(1)	0.279(1)	1.9(6)
P(2)	0.168(2)	0.6828(9)	-0.173(1)	1.8(6)

$$^aB_{eq} = (4/3)[a^2B(1,1) + b^2B(2,2) + c^2B(3,3) + ab(\cos\gamma)B(1,2) + ac(\cos\beta)B(1,3) + bc(\cos\alpha)B(2,3)].$$

3. Results and Discussion

3.1. Synthesis, Spectroscopy and Thermal Analysis

The syntheses were a result of a redox reaction in which the metal is oxidized by polyselenide ions in the $A_x[P_ySe_z]$ flux. The metal cation centers are then coordinated by the highly charged $[P_2Se_6]^{4-}$ ligands. The molten *polyselenophosphate* flux method is very effective for crystal growth in this system and quite conducive for isolation of pure products. Triethylphosphine has been shown to be very useful for the removal of insoluble byproducts such as $A_x[P_ySe_z]$ species and elemental Se.

Due to the stability of these phases, direct combination reactions $M/P/A_2Se/Se$ at 500 °C were implemented for the preparation of large amounts of pure material. This was particularly useful in the Mn system. The presence of colored DMF solutions during isolation of the products from these reactions suggests that some excess $A_x[P_ySe_z]$ flux was present resulting from incomplete mixing during these reactions. Direct combination reactions in the Fe system resulted in impure material with the known ternary phase, $Fe_2P_2Se_6$, as the impurity.

In the $Cu/P_2Se_5/K_2Se/Se$ and $Ag/P_2Se_5/Rb_2Se/Se$ systems, pure material could not be synthesized. Efforts are continuing in order to obtain single phase products. Powder XRD of the inhomogeneous mixtures suggest that these phases are closely related to $K_2Ag_2P_2Se_6$.

Varying the flux composition resulted in the formation of different compounds. In the Mn/P₂Se₅/K₂Se/Se system, increasing the Lewis basicity of the flux, by doubling the amount of K₂Se, resulted in the formation of red-orange water-soluble crystals that analyzed for K_{4.0}Mn_{1.0}P_{2.0}Se_{8.4}. The solubility and elemental analysis suggest a molecular compound, perhaps K₄Mn(PSe₄)₂. Increased amounts of P₂Se₅ resulted in the formation of the known Mn₂P₂Se₆ compound. In the Fe/P₂Se₅/A₂Se/Se (A=K, Cs) systems, doubling the amount of A₂Se afforded FeSe₂. All reactions with Co and Ni resulted in the formation of the stable binary pyrites (CoSe₂ and NiSe₂).

Similar investigations in the Mn/P₂Se₅/Na₂Se/Se system resulted in the formation of a new phase as evidenced by EDS and XRD. This product crystallizes as air-sensitive, golden-brown, thin plate-like material. Attempts to grow crystals suitable for single crystal X-ray analysis are in progress.¹⁹

The Far-IR spectra of A₂MP₂Se₆ (M=Mn,Fe), shown in Table 6-15, display two strong absorptions at ~480 and ~465 cm⁻¹. These vibrations can be assigned to PSe₃ stretching modes by analogy with MnP₂Se₆ (444 cm⁻¹).²⁰ A description of the medium absorption band at ~305 cm⁻¹ in A₂MP₂Se₆ is not as straightforward. In Mn₂P₂Se₆, a medium absorbance at 316 cm⁻¹ was ascribed to an out-of-phase PSe₃ mode, corresponding to a P-P vibration. The P-P vibration is expected to be IR inactive because it resides on a center of symmetry, however, it was not observed in the Raman spectrum. Similar results were obtained for Na₄P₂S₆·6H₂O. The spectra of Na₄P₂S₆·6H₂O were described in terms of internal modes of PS₃

groups and combinations of in-phase and out-of-phase translational and rotational motions.²⁰ By analogy to these compounds, the medium intensity absorption band at $\sim 305\text{ cm}^{-1}$ for $\text{A}_2\text{MP}_2\text{Se}_6$ can tentatively be ascribed to the out-of-phase translational PSe_3 mode. The weak absorptions below 200 cm^{-1} in $\text{A}_2\text{MnP}_2\text{Se}_6$ have been assigned to translational motions of the metal ions.²⁰ A typical spectrum is shown in Figure 6-1a for $\text{K}_2\text{MnP}_2\text{Se}_6$. The $\text{A}_2\text{M}'_2\text{P}_2\text{Se}_6$ ($\text{M}'=\text{Cu}, \text{Ag}$) compounds possess absorptions in the $440\text{--}470\text{ cm}^{-1}$ range which have been assigned to PSe_3 stretching modes by analogy to the $\text{A}_2\text{MP}_2\text{Se}_6$ compounds. The absorption at 302 cm^{-1} can be assigned to the out-of-phase PSe_3 translational mode (see Table 6-15). The far-IR spectra of $\text{Cs}_2\text{Cu}_2\text{P}_2\text{Se}_6$ and $\text{K}_2\text{Ag}_2\text{P}_2\text{Se}_6$ are shown in Figures 6-1b and 6-1c.

The optical properties of (I-IX) were assessed by studying the UV/near-IR reflectance spectra of the materials. The spectra confirm the semiconducting nature of the materials by revealing the presence of sharp optical gaps. The $\text{A}_2\text{MnP}_2\text{Se}_6$ ($\text{A}=\text{K}, \text{Rb}, \text{Cs}$) compounds exhibit steep absorption edges from which the band-gap, E_g , can be assessed at 2.33 (I), 2.41 (II), and 2.19 (III) eV respectively (see Figure 6-2). The band-gaps of $\text{A}_2\text{FeP}_2\text{Se}_6$ can be assessed at 1.72 (IV), and 2.02 (V) eV respectively (see Figure 6-3). The diffuse reflectance spectrum of $\text{Cs}_2\text{Cu}_2\text{P}_2\text{Se}_6$ suggests the presence of two band-gaps at ~ 0.8 and 2.44 eV (see Figure 6-4a). The band gaps of (VII) and (VIII) are 2.39 and 2.55 eV and are shown in Figures 6-4b and 6-4c. Higher energy absorptions are readily resolved in these spectra and are assigned to electronic $\text{Se} \rightarrow \text{M}$ charge transfer transitions. The difference between the band gaps of $\text{K}_2\text{Ag}_2\text{P}_2\text{Se}_6$

(2.39 eV) and $\text{Cs}_2\text{Ag}_2\text{P}_2\text{Se}_6$ (2.55 eV) can be attributed to the change in the structural architectures of the two compounds. The Ag-Se orbital overlap in the well-separated one-dimensional chains of $\text{Cs}_2\text{Ag}_2\text{P}_2\text{Se}_6$ is expected to be lower than that of the three-dimensional $\text{K}_2\text{Ag}_2\text{P}_2\text{Se}_6$ compound. This is facilitated by the increased coordination number of Ag in the K^+ compound. This effect gives rise to broader bands and thus a smaller band gap for $\text{K}_2\text{Ag}_2\text{P}_2\text{Se}_6$. The band gap of (IX) is 1.55 eV and is shown in Figure 6-5.

Differential thermal analysis (DTA) shows that all compounds melt congruently, suggesting that large single crystals or microcrystalline thin films can be grown from the melt. Table 6-16 shows optical and melting point data for all compounds. A typical thermogram for $\text{Rb}_2\text{MnP}_2\text{Se}_6$ is shown in Figure 6-6.

Table 6-15. Far-IR Data (cm^{-1}) for $\text{A}_2\text{MP}_2\text{Se}_6$, $\text{A}_2\text{M}'_2\text{P}_2\text{Se}_6$, and $\text{K}_4\text{Au}_2(\text{P}_2\text{Se}_6)_2$ Compounds.

$\text{K}_2\text{MnP}_2\text{Se}_6$	$\text{Rb}_2\text{MnP}_2\text{Se}_6$	$\text{Cs}_2\text{MnP}_2\text{Se}_6$	$\text{K}_2\text{FeP}_2\text{Se}_6$	$\text{Cs}_2\text{FeP}_2\text{Se}_6$
478(s)	480(s)	481(s)	475(s)	478(s)
463(s)	465(s)	464(s)	466(s)	469(m)
303(m)	304(m)	305(m)	303(m)	
210-143(w)	201-148(w)	189-152(w)		

$\text{Cs}_2\text{Cu}_2\text{P}_2\text{Se}_6$	$\text{K}_2\text{Ag}_2\text{P}_2\text{Se}_6$	$\text{Cs}_2\text{Ag}_2\text{P}_2\text{Se}_6$	$\text{K}_4\text{Au}_2(\text{P}_2\text{Se}_6)_2$
467(m)	460(m)	452(w,broad)	499 (s)
454(s)			470(m)
447(msh)	443(s)		429(s)
302(m)	302(w)	302(w)	303(m)
213 (vw)			240(w)
			205(w)

Abbreviations: s=strong, m=medium, w=weak, v=very.

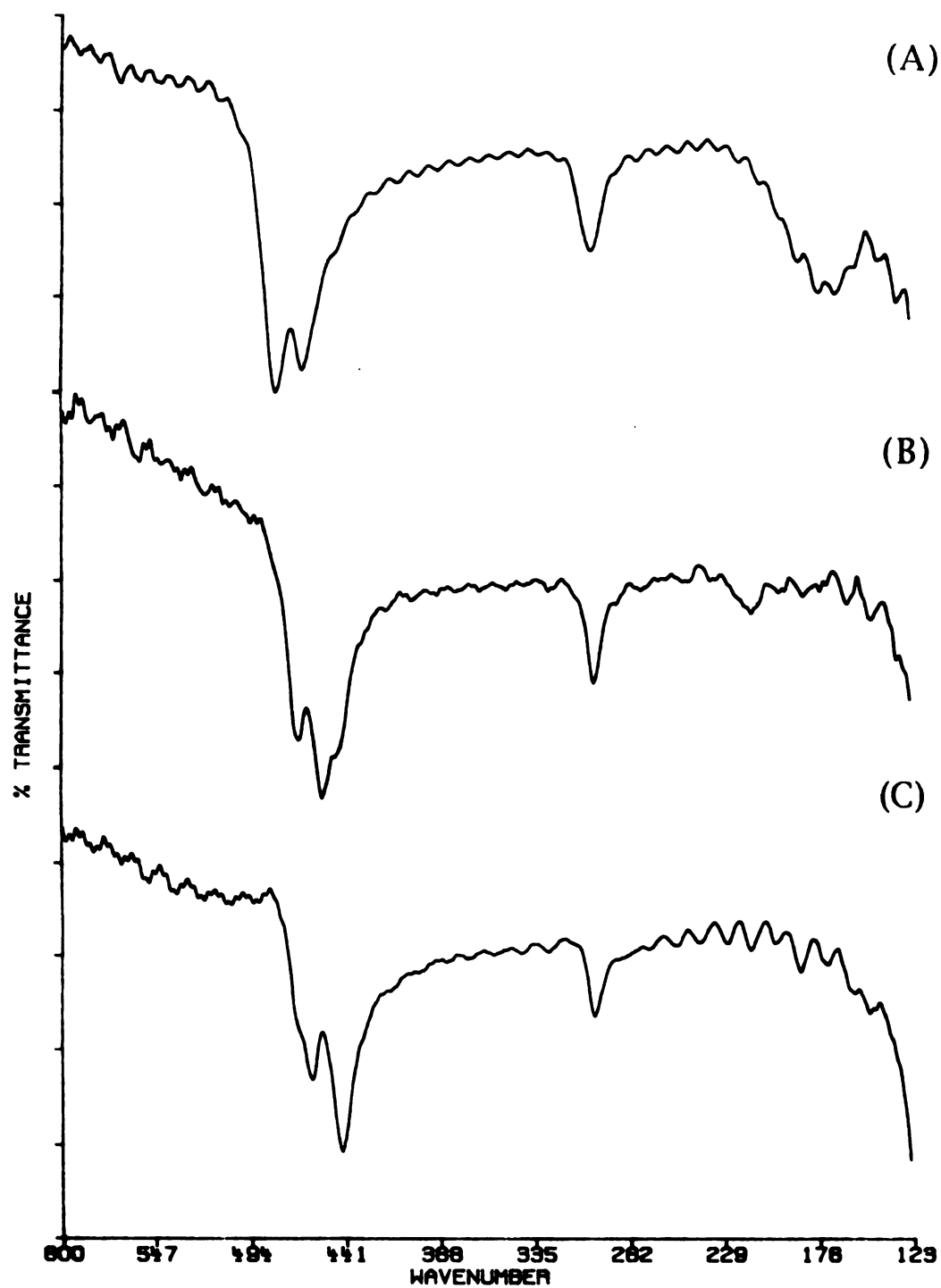


Figure 6-1. Far-IR spectra of: (A) $K_2MnP_2Se_6$ (B) $Cs_2Cu_2P_2Se_6$ and (C) $K_2Ag_2P_2Se_6$

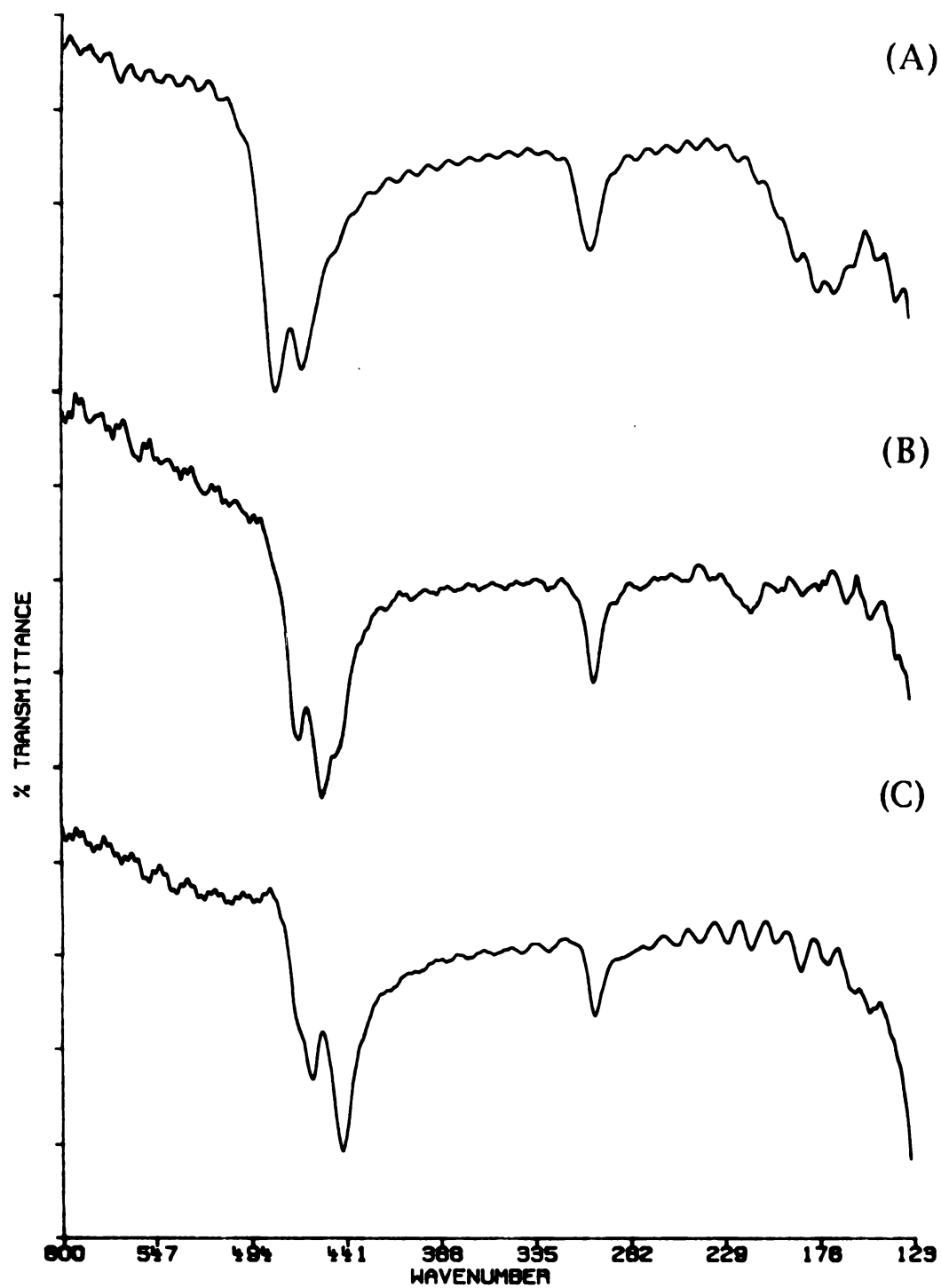


Figure 6-1. Far-IR spectra of: (A) $K_2MnP_2Se_6$ (B) $Cs_2Cu_2P_2Se_6$ and (C) $K_2Ag_2P_2Se_6$

Table 6-16. Optical Band Gaps and Melting Point Data for $A_2MP_2Se_6$, $A_2M'P_2Se_6$, and $K_4Au_2(P_2Se_6)_2$

Formula	E_g (eV)	M. P. ($^{\circ}C$)
$K_2MnP_2Se_6$	2.33	717
$Rb_2MnP_2Se_6$	2.41	781
$Cs_2MnP_2Se_6$	2.19	831
$K_2FeP_2Se_6$	1.72	662
$Cs_2FeP_2Se_6$	2.02	769
$Cs_2Cu_2P_2Se_6$	2.44	670
$K_2Ag_2P_2Se_6$	2.39	542
$Cs_2Ag_2P_2Se_6$	2.55	594
$K_4Au_2(P_2Se_6)_2$	1.55	456

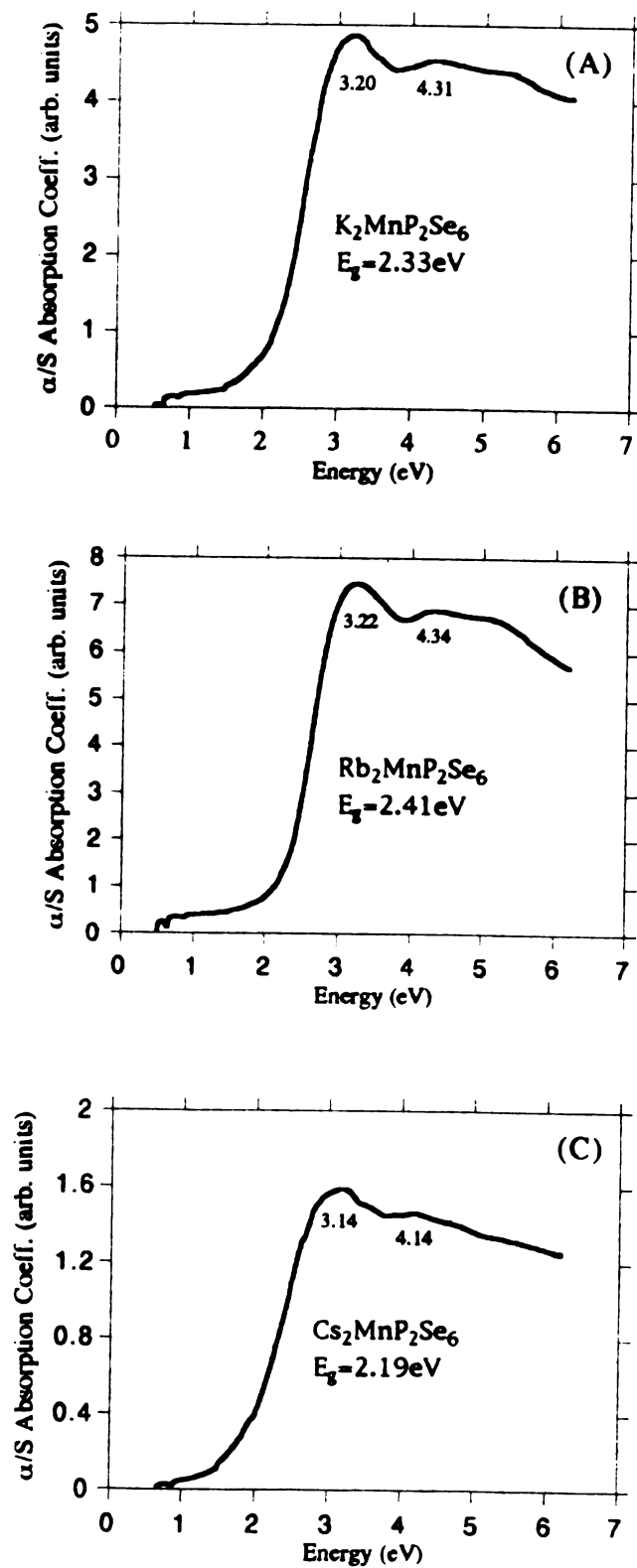


Figure 6-2. Optical absorption spectra of (I), (I I), and (I I I).

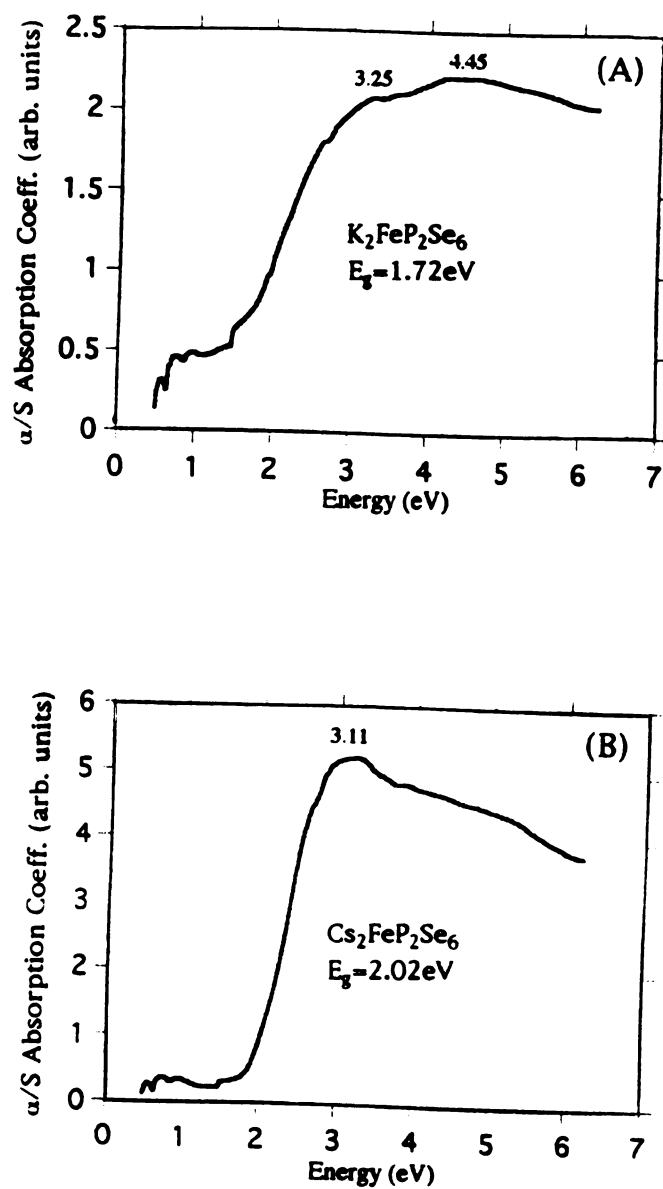


Figure 6-3. Optical absorption spectra of (I V) and (V).

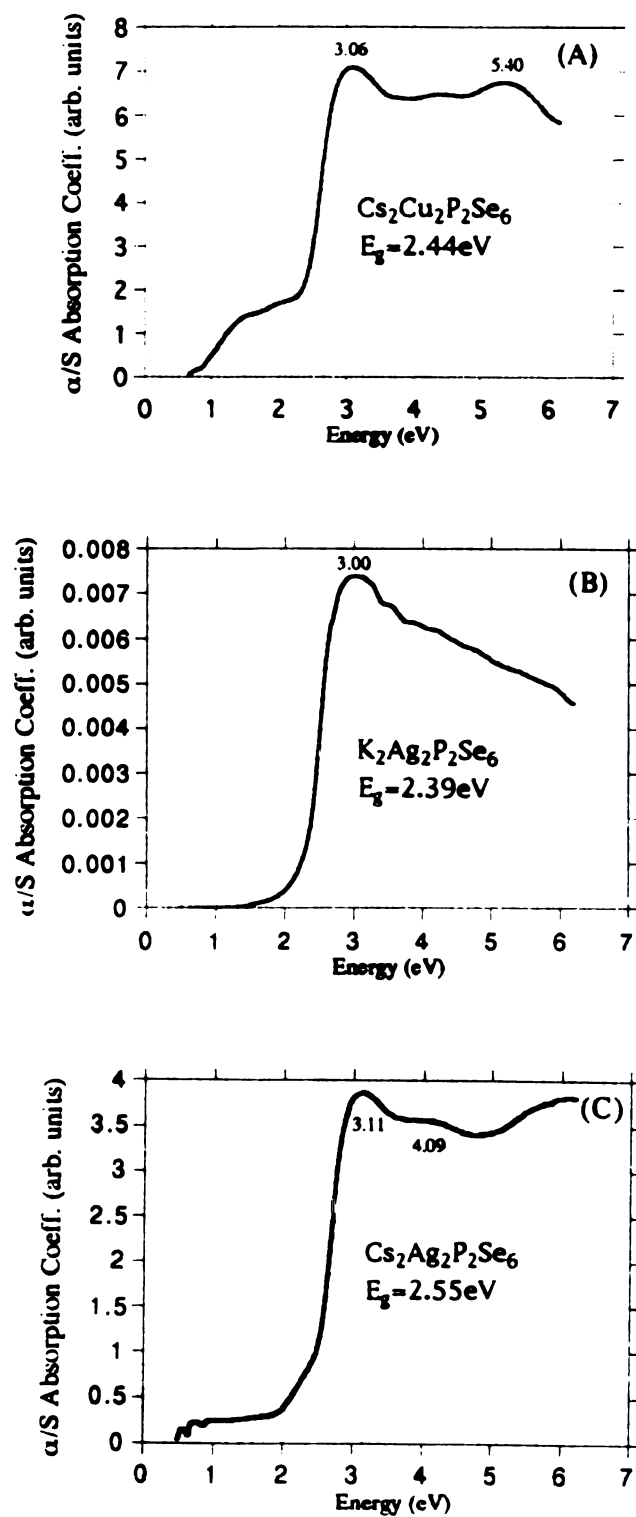


Figure 6-4. Optical absorption spectra of (V I), (V II), and (V III).

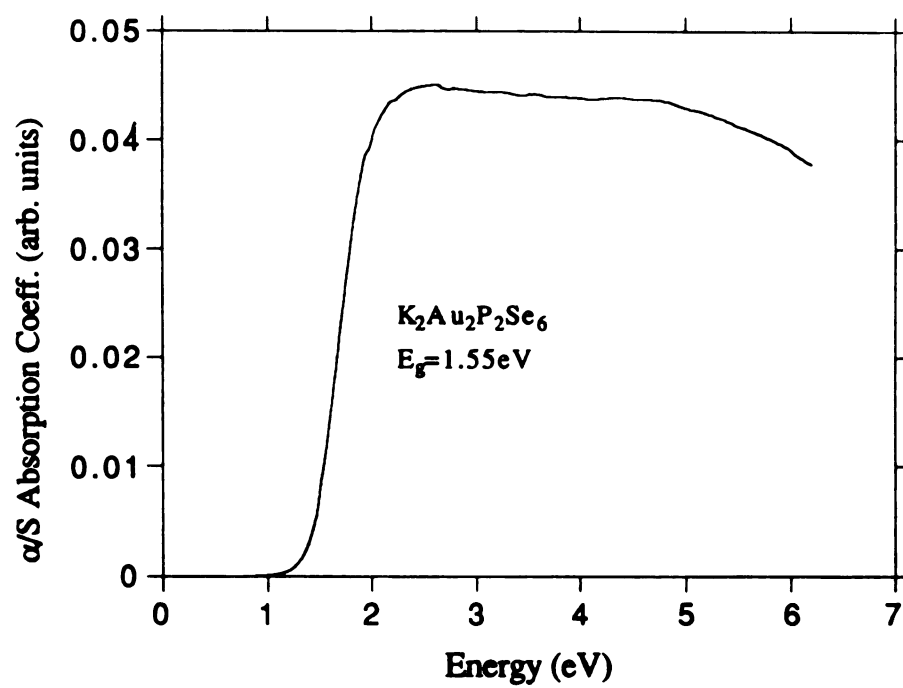


Figure 6-5. Optical absorption spectrum of (I X).

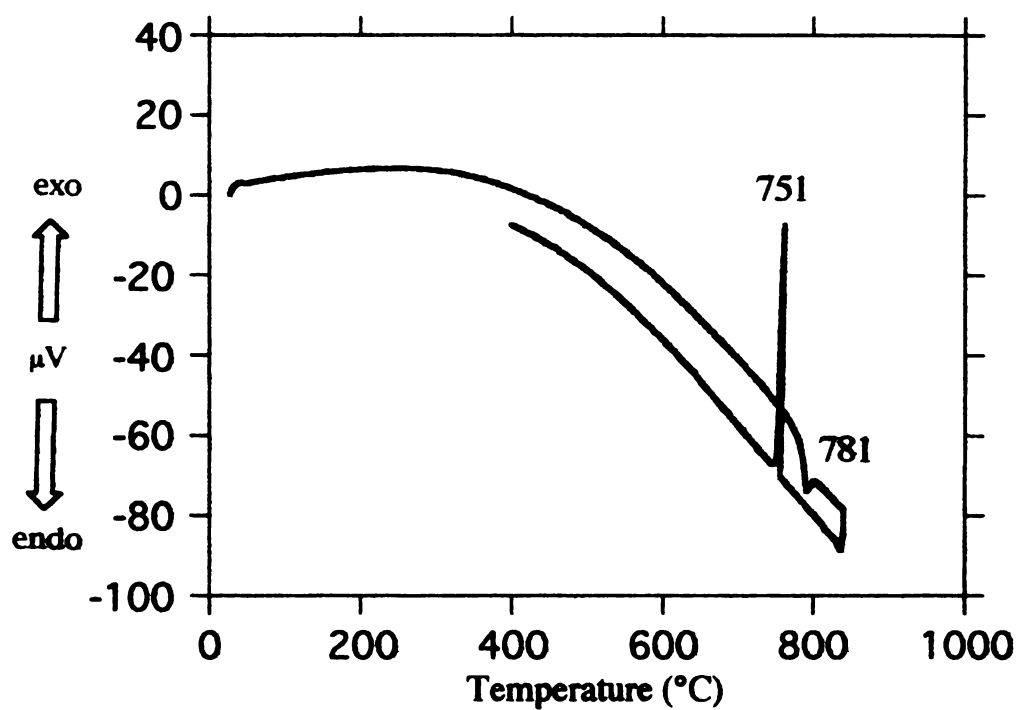


Figure 6-6. Thermogram of $\text{Rb}_2\text{MnP}_2\text{Se}_6$. Melting is observed at 781 °C, followed by recrystallization at 751 °C.

3.2. Description of Structure

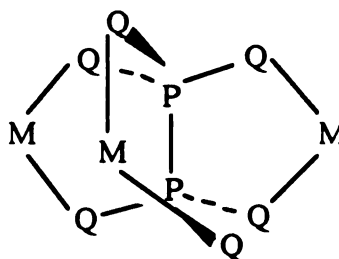
$A_2MP_2Se_6$. The structure of the $[MP_2Se_6]_n^{2n-}$ ($M=Mn, Fe$) anion is closely related to the TiI_3 structure type. Doubling of the TiI_3 formula gives Ti_2I_6 . The $[MP_2Se_6]_n^{2n-}$ anion can be viewed as an ordered substitution of two octahedrally coordinated Ti atoms by M and P_2 respectively and a replacement of six I atoms by Se. The transition metal ion and the P-P pairs of $K_2MnP_2Se_6$ reside in Se octahedra that share triangular faces in the a-direction (Figure 6-7a). These chains are well separated by alkali metal ions (Figure 6-7b).

Mn resides on an inversion center with Mn-Se bond distances ranging from 2.737(2) Å to 2.818(2) Å with a normal P-P' bond of 2.243(5) Å and P-Se distances ranging from 2.173(3) Å to 2.183(3) Å. The Mn-Mn' distance is 6.5249(9) Å. Inspection of the Se(1)-Mn-Se(2) angle of 78.38(3)° for $K_2MnP_2Se_6$ reveals a deviation from an ideal octahedral geometry. This small angle is due to a strained four-membered (Mn-Se(1)-P-Se(2)) ring whereas the less strained five-membered envelope-shaped rings give rise to Se(1)-Mn-Se(3) and Se(2)-Mn-Se(3) angles of 88.23(3)° and 88.60(3)° respectively. Se(1) and Se(2) are above (1.809 Å) and below (-1.730 Å) the calculated Mn-Se(3)-P-P' least squares plane.

There are small differences between the crystal structures of $Cs_2MnP_2Se_6$ and $K_2MnP_2Se_6$ as evidenced by unit cell β angles of 93.09(1)° and 102.67(2)° respectively. In addition, there is a reduction of the a-axis upon moving from K to Cs which corresponds to a shortening of the Mn-Mn distance from 6.5249(9) Å to 6.476(2) Å. A slight reorientation of the $[P_2Se_6]^{4-}$ ligand results in a Mn-

Se(3)-P angle of $99.07(7)^\circ$ in $K_2MnP_2Se_6$ and $95.82(8)^\circ$ in the Cs analog. This conformational change is probably due to differences in packing forces caused by the size difference of the alkali ions. Selected bond distances and angles for (I), (III), and (IV) are given in Table 6-17.

Comparison of $A_2MP_2Q_6$ with the known layered $M_2P_2Q_6$ structure type reveals some interesting structural relationships. It is useful to view that the $M_2P_2Q_6$ lattice is broken up into chains as a consequence of the substitution of one M^{2+} by two K^+ cations. A single layer of $M_2P_2Q_6$ is shown in Figure 6-8a. The M atoms form a hexagonal network and the $[P_2Q_6]^{4-}$ ligand coordinates to three different metal centers as shown in scheme (A).

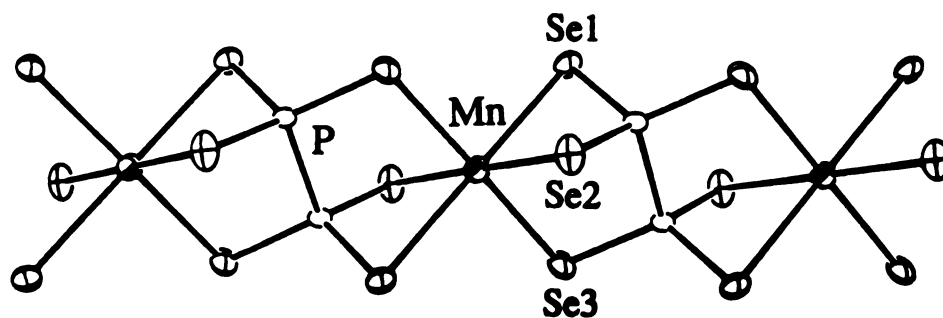


Scheme (A)

Removal of one-half of the M^{2+} cations gives the $[MP_2Q_6]^{2-}$ anion as shown in Figure 6-8b. In order to maintain electroneutrality, two alkali metal ions must be introduced. Although this metal-deficient structure (related to that of $AlCl_3$) may very well be stable with the proper counterion, apparently, the lack of a low energy packing arrangement for the alkali atoms within the layer causes a structural change to a 1-D structure. This generates more space for efficient packing of the alkali ions. It is interesting to speculate that with

alkaline earth cations, such as Ba^{2+} , it may be possible to stabilize the $[\text{MP}_2\text{Q}_6]^{2-}$ layer.

(A)



(B)

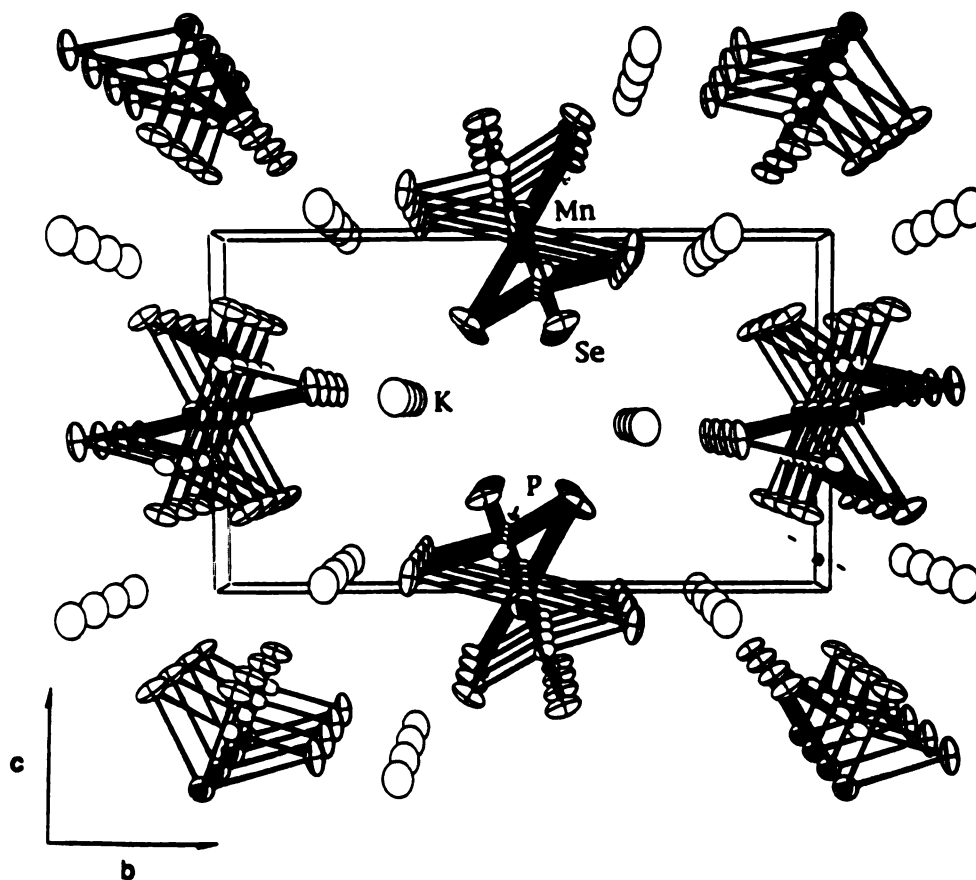


Figure 6-7: (A) ORTEP representation of a single $[\text{MnP}_2\text{Se}_6]_{n^{2n-}}$ chain. (B) Packing diagram of $\text{K}_2\text{MnP}_2\text{Se}_6$ viewed down the $[100]$ direction with labeling.

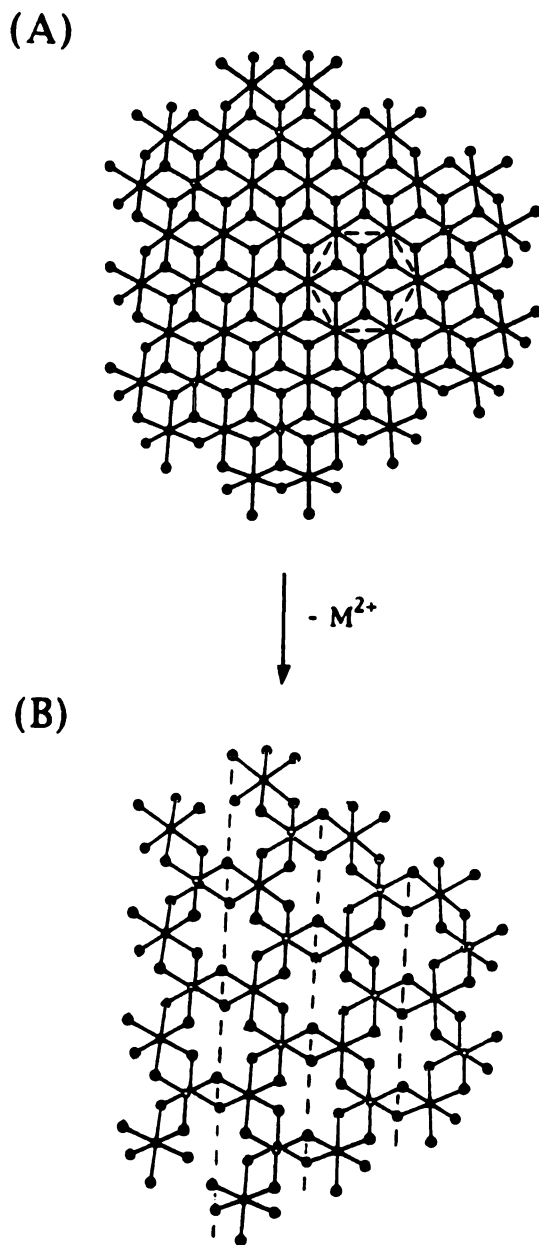


Figure 6-8: (A) A single layer of the $Mn_2P_2Q_6$ framework. The dashed lines indicate the hexagonal arrangement of Mn^{2+} ions. (B) Removal of one-half of the Mn^{2+} ions results in a single layer of the hypothetical $[MnP_2Q_6]^{2n-}$ anion. Dashed lines highlight the possibility of chain formation.

Table 6-17. Selected Distances (Å) and Angles (°) for (I), (I I I), and (I V) with Standard Deviations in Parentheses.^a

Distances	K ₂ MnP ₂ Se ₆	Cs ₂ MnP ₂ Se ₆	K ₂ FeP ₂ Se ₆
M-M'	6.5349(9)	6.476(2)	6.421(2)
M-Se(1)	2.853(1)	2.774(1)	2.782(2)
M-Se(2)	2.746(1)	2.737(2)	2.676(2)
M-Se(3)	2.711(1)	2.818(2)	2.614(2)
M-Se (ave.)	2.77(7)	2.78(4)	2.69(8)
P-P'	2.236(5)	2.243(5)	2.225(7)
P-Se(1)	2.181(2)	2.183(3)	2.182(4)
P-Se(2)	2.181(2)	2.178(3)	2.176(3)
P-Se(3)	2.176(2)	2.173(3)	2.180(4)
P-Se (ave.)	2.179(3)	2.178(5)	2.179(3)
A-Se(1)	3.677(4)	3.916(2)	3.683(5)
A-Se(1')	3.399(3)	3.773(2)	3.398(4)
A-Se(1'')		3.950(2)	
A-Se(2)	3.607(3)	3.965(2)	3.597(4)
A-Se(2')	3.322(3)	3.880(2)	3.330(4)
A-Se(2'')		3.757(2)	
A-Se(3)	3.433(3)	3.978(2)	3.414(4)
A-Se(3')	3.525(3)	3.742(2)	3.538(4)
A-Se(3'')	3.602(3)	3.695(2)	3.573(4)
A-Se (ave.)	3.5(1)	3.9(1)	3.5(1)
Angles			
Se(1)-M-Se(2)	78.38(3)	80.80(4)	80.11(5)
Se(2)-M-Se(3)	88.60(3)	89.83(5)	87.43(5)
Se(1)-M-Se(3)	88.22(3)	89.30(4)	89.36(5)
M-Se(1)-P	76.15(6)	76.25(8)	75.9(1)
M-Se(2)-P	78.55(6)	77.14(7)	78.4(1)
M-Se(3)-P	99.07(7)	95.82(8)	99.1(1)
Se(1)-P-Se(2)	108.45(9)	110.0(1)	107.4(1)
Se(1)-P-Se(3)	117.0(1)	115.3(1)	118.3(2)
Se(2)-P-Se(3)	115.6(1)	115.8(1)	116.7(2)
Se(1)-P-P'	105.6(1)	104.8(2)	105.4(2)

^aThe estimated standard deviations in the mean bond lengths and the mean bond angles are calculated by the equations $\sigma_l = \{\sum_n (l_n - l)^2 / n(n-1)\}^{1/2}$, where l_n is the length (or angle) of the n th bond, l the mean length (or angle), and n the number of bonds.

$\text{Cs}_2\text{Cu}_2\text{P}_2\text{Se}_6$. The structure of the $[\text{Cu}_2\text{P}_2\text{Se}_6]_n^{2n-}$ anion is closely related to the $\text{A}_2\text{MP}_2\text{Se}_6$ structure type and is shown in Figure 6-9a. The M^{2+} ions are replaced by weakly interacting $\text{Cu}^+ \cdots \text{Cu}^+$ dimers that alternate with the P-P pairs along the [101] direction.

The $\text{Cu}(1) \cdots \text{Cu}(1')$ and $\text{Cu}(2) \cdots \text{Cu}(2')$ distances are 2.761(5) Å and 2.731(5) Å respectively. For comparison, the Cu-Cu distance in copper metal is 2.56 Å. This attractive interaction also leads to the displacement of Cu(1) and Cu(2) from their respective trigonal planes by 0.2 Å. These classical $d^{10} \cdots d^{10}$ interactions have been observed in either molecular²¹ or solid state structures such as KCu_3S_2 ,²² $\text{K}_3\text{Cu}_8\text{S}_6$,²³ $\text{Cs}_3\text{Cu}_8\text{Se}_6$,²⁴ and KCuS .²⁵ Normally, the interaction of two filled metal orbitals results in a nonbonding situation due to formation of a bonding and an equally antibonding state. However, extended Hückel calculations by Hoffmann and coworkers have shown that mixing of empty 4s and 4p orbitals with occupied 3d orbitals in these dimers lowers the energy of the σ and σ^* orbitals (see Figure 6-10).²⁶ This hybridization gives rise simultaneously to a more bonding and a less bonding M-M interaction and therefore an overall stabilization. It has also been proposed for several $d^{10} \cdots d^{10}$ complexes that the bridging ligands force the metals closer in order to maximize M-L interactions.²⁷ Since $\text{Cs}_2\text{Cu}_2\text{P}_2\text{Se}_6$ features two $[\text{P}_2\text{Se}_6]^{4-}$ bridging ligands for each dimer, it is possible that the multidentate $[\text{P}_2\text{Se}_6]^{4-}$ coordination is playing an important role in forcing the metals to close proximity. It is not clear whether the interactions contribute significantly in determining the structure or

the metals are simply forced to tolerate the short contact due to packing forces. It is probable that the $A_2MP_2Se_6$ structure type is quite stable and since Cu^+ does not prefer an octahedral coordination, and by itself is not enough to balance the negative charge on that octahedral site, it forms pairs of $CuSe_3$ trigonal planes to conform to the imposed geometry.

The Cu-Se distances range from 2.373(3) Å to 2.417(4) Å which compare well with other Cu-Se trigonal planar species such as $(Ph_4P)_4[Cu_2(Se_4)(Se_5)_2]^{28}$ and $(Ph_4P)_2[Cu_4(Se_4)_{2.4}(Se_5)_{0.6}]^{29}$. The Se(1)-Cu(1)-Se(6), Se(3)-Cu(2)-Se(5) angles are less than 120° at $110.6(1)^\circ$ because of strained (Cu-Se-P'-Se) five-membered rings whereas the remaining Se-Cu-Se angles range from $121.3(1)^\circ$ to $125.7(1)^\circ$. The shortest Cu-Se distances for Cu(1) (2.373(3)Å) and Cu(2) (2.375(3)Å) are trans to the small $110.6(1)^\circ$ angle as more space is allowed for the Se(2) and Se(4) to get closer to the metal center. Selected bond distances and angles for $Cs_2Cu_2P_2Se_6$ are given in Table 6-18.

$Cs_2Ag_2P_2Se_6$. The structure of the $[Ag_2P_2Se_6]_n^{2n-}$ anion is closely related to that of $Cs_2Cu_2P_2Se_6$ and is shown in Figure 6-9b. The major difference is that the volume is roughly half that of $Cs_2Cu_2P_2Se_6$ so there is only one $Ag^+ \cdots Ag^+$ dimer per unit cell. The $Ag \cdots Ag$ distance of 2.919(3) Å falls in the 2.75-3.00 Å range for many solid state Ag compounds with close $Ag^+ \cdots Ag^+$ contacts.³⁰ The Ag^+ ions are not displaced from their distorted trigonal planes as is the case for Cu in (VIII).

The coordination geometry of Ag is distorted trigonal planar with Ag-Se distances ranging from 2.545(2) Å to 2.641(3) Å. These distances compare well with other Ag-Se trigonal planar species.³¹ The Se(1)-Ag-Se(2) angle is less than 120° at 105.55(7)° because of a strained (Ag-Se-P-P'-Se) five-membered envelope-shaped ring whereas the remaining Se-Ag-Se angles are 121.77(8)° and 132.04(9)°. The Se(1)-Ag-Se(3) angle of 132.04(9)° is quite large and compares to the 138.8° angle found in the [(Ph₄P)Ag(Se₄)]_n one-dimensional polymer.^{31a} The shortest Ag-Se distance (Ag-Se(3) = 2.545(2) Å) is trans to the small 105.55(7)° angle as more space is allowed for the Se(3) to get closer to the metal center. Selected bond distances and angles for Cs₂Ag₂P₂Se₆ are given in Table 6-19.

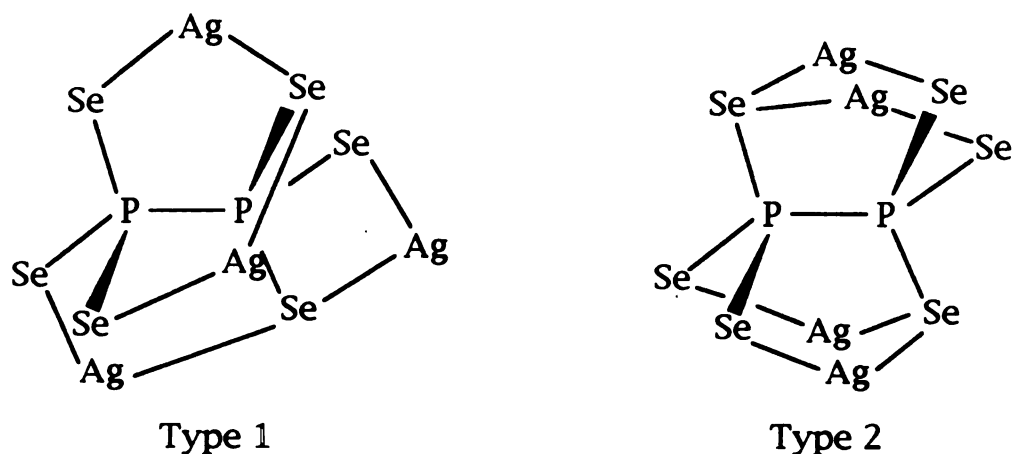
The existence of Cu⁺...Cu⁺ or Ag⁺...Ag⁺ dimers located in octahedral sites in these compounds can hopefully shed some light on the question concerning the nature of Cu(Ag) coordination sites in several cation substitution compounds such as CuCrP₂S₆,³² CuVP₂S₆,^{5d} Cu_{0.52}Mn_{1.74}P₂S₆³³ and Ag₂MnP₂S₆.^{9b} These compounds adopt the stable M₂P₂S₆ structure with cation substitution occurring in the octahedral sites. The crystal structure of CuCrP₂S₆ reveals a Cu electron density cloud which exhibits three extrema.³² One of them is in the middle on a pseudo-octahedral site and the other two are near the trigonal sulfur planes which suggests that CuS₆ octahedral sites, Cu...Cu pairs and vacancies all exist at room temperature and can be fit by a disorder model. Complimentary EXAFS³⁴ studies have confirmed this disorder model but recent low-temperature neutron powder diffraction studies have disputed the existence of bimetallic

entities.³⁵ $\text{Cu}^{+}\cdots\text{Cu}^{+}$ pairs were also assumed to exist in CuVP_2S_6 ,^{5d} which features the same Cu positions as found in CuCrP_2S_6 plus a third tetrahedral site located in the van der Waals gap. The location of copper atoms in $\text{Cu}_{0.52}\text{Mn}_{1.74}\text{P}_2\text{S}_6$ remains uncertain due to some inconsistencies between X-ray diffraction and EXAFS data.³³ It appears that the occurrence of copper pairs in these copper substitution phases is still an open question. In the case of Ag, the structure determination of $\text{Ag}_2\text{MnP}_2\text{S}_6$ ^{9b} confirmed the presence of two silver atoms per octahedron with 81% of the Ag(1) atoms found in trigonal planar coordination (Ag-Ag = 3.38 Å). On each side of Ag(1) are two sites of minor contribution (Ag(2) 13%; Ag(3) 8%). We think that the unequivocal presence of $\text{M}^{+}\cdots\text{M}^{+}$ pairs in our compounds serves to support the presence of $\text{M}^{+}\cdots\text{M}^{+}$ pairs in octahedral sites within the layers of $\text{CuM}^{\text{III}}\text{P}_2\text{S}_6$ compounds.

$\text{K}_2\text{Ag}_2\text{P}_2\text{Se}_6$. The substitution of K for Cs resulted in a dramatic change in the structure of the $[\text{Ag}_2\text{P}_2\text{Se}_6]^{2-}$ anion. $\text{K}_2\text{Ag}_2\text{P}_2\text{Se}_6$ possesses a complicated three-dimensional tunnel framework made up of AgSe_4 tetrahedra linked by P_2Se_6 units (see Figure 6-11). The channels run along the crystallographic a-axis and are filled with K^{+} ions.

There are two types of $[\text{P}_2\text{Se}_6]^{4-}$ ligands in this structure, see scheme (B). Both ligands contain four Se atoms that each bond to a Ag atom and two Se atoms that each bridge two other Ag atoms. The P-P bond in Type (2) lies on a center of symmetry while that of Type (1) does not. In Type (2), the two Se atoms that bridge Ag atoms are

located on opposite sides of the P-P bond. In Type (1), the two Se atoms are situated on the same side of the P-P bond.



Scheme (B)

These are new bonding modes for the $[P_2Se_6]^{4-}$ ligand and differ from those found in KMP_2Se_6 ² and $Cs_8M_4(P_2Se_6)_5$.³ The $[P_2Se_6]^{4-}$ units connect $AgSe_4$ tetrahedra as shown in Figure 6-12.

For comparison, the $[P_2Se_6]^{4-}$ ligand in the known ternary compound, $Ag_4P_2Se_6$, bonds to ten Ag atoms with two Se atoms each bonding to two Ag atoms and the remaining four Se atoms each bonding to three Ag atoms.³⁶ In this structure, P_2Se_6 building blocks are assembled into layers and are linked via $AgSe_4$ tetrahedra to form a dense three-dimensional network. As in the case of the one-dimensional $A_2M_2P_2Se_6$ compounds, $K_2Ag_2P_2Se_6$ can also be viewed as a derivative of $Ag_4P_2Se_6$ generated by breaking down the $Ag_4P_2Se_6$ framework by incorporation of $K_4P_2Se_6$. The addition of K_2Se gives rise to a more open channel structure.

Selected distances and angles for $K_2Ag_2P_2Se_6$ are found in Table 6-20. Ag(1,2) are located in distorted tetrahedral coordination

environments as evidenced by Se-Ag-Se angles that range from 95.1(1) to 130.5(1)° for Ag(1) and 80.9(1) to 130.4(1)° for Ag(2). Ag(3) resides in a fairly regular tetrahedral site with normal angles (103.2(1)-122.1(1)°). The Ag(1,2,3)-Se bond distances fall in the 2.578(4) to 2.797(4) Å range which compare well with those observed in Ag₄P₂Se₆.³⁶ No Ag...Ag contacts are observed as the Ag-Ag distances are long at 3.715(4) and 3.869(4) Å. Normal P-P bonds in the [P₂Se₆]⁴⁻ ligands are observed at 2.278(8) and 2.31(1) Å and the P-Se bonds are typical for Se atoms in bridging positions (2.19(1) Å (mean)).

The higher coordination number of Ag⁺ most likely results from the effect the relatively small K⁺ cation exerts on the [Ag₂P₂Se₆]²⁻ structure. A correlation between the metal coordination number (CN) and the size of the counterion was observed and discussed in the Ag⁺/Se_x²⁻ system earlier.^{31a} The change of the CN for Ag⁺ from three, in Cs₂Ag₂P₂Se₆, to four, in K₂Ag₂P₂Se₆, agrees with the general trend identified in Group 10 polychalcogenides that larger counterions favor a small CN for the Group 10 metal. While a high CN will produce compact structures, a small CN tends to result in expanded or low dimensional structures.

K₄Au₂(P₂Se₆)₂. The preference of Au for a linear or square planar coordination results in a different structure type. The structure of the [Au₂(P₂Se₆)₂]_n⁴ⁿ⁻ anion consists of linear Au⁺ and square planar Au³⁺ units that are linked by bridging [P₂Se₆]⁴⁻ ligands (Figure 6-13). The Au(1)---Au(2) distance is 3.636(3) Å so no metal

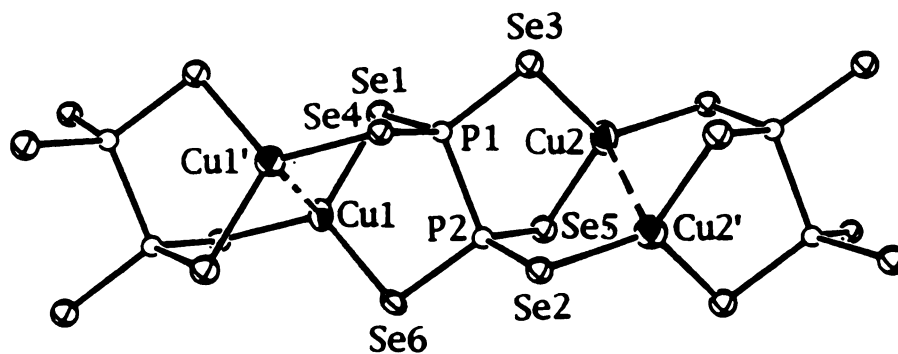
interactions are present. This compound represents one of the few examples of a mixed valent $\text{Au}^+/\text{Au}^{3+}$ compound with the only other examples being α -(β -) AuSe .³⁷

Selected distances and angles for $\text{K}_4\text{Au}_2(\text{P}_2\text{Se}_6)_2$ are found in Table 6-21. $\text{Au}(1)$ resides on a center of symmetry and is surrounded by four Se atoms in a square planar geometry with distances of 2.484(6) and 2.493(5) Å. This compares well with the square planar distances of 2.474(8) and 2.489(8) Å for α - AuSe and 2.496(9) Å for β - AuSe .³⁷ The linear $\text{Au}(2)$ also resides on a center of symmetry and possesses a Au-Se distance of 2.302(7) Å. This distance is shorter than those reported for linear Au^+ in AuSe (2.42(1) to 2.433(9)) Å. This short distance could be a result of the partial occupancy on the $\text{Au}(2)$ site due to averaging.

A close contact between $\text{Au}(2)$ and $\text{K}(2)$ was observed at 3.21(2) Å. It is known that Au^+ has a remarkable affinity for alkali metal cations. Such interactions have been observed in other Au^+ chalcogenide complexes including $[\text{KAu}_9\text{Te}_7]^{4-}$,³⁸ $[\text{K}_2\text{Au}_4\text{Te}_4(\text{en})_4]^{2-}$,³⁹ and the inorganic cryptand, $[\text{NaAu}_{12}\text{Se}_8]^{3-}$.⁴⁰

Due to the inconsistencies in the charge balance and the rather high temperature factors and R/R_w values, a structural redetermination of $\text{K}_4\text{Au}_2(\text{P}_2\text{Se}_6)_2$ must be performed.

(A)



(B)

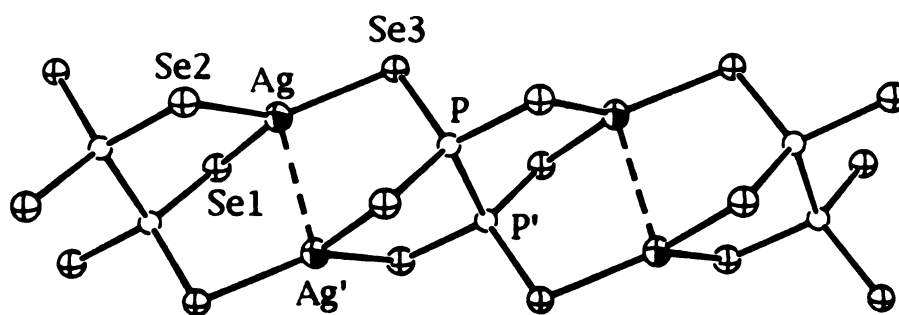


Figure 6-9: (A) A single $[\text{Cu}_2\text{P}_2\text{Se}_6]_n^{2n-}$ chain. (B) A single $[\text{Ag}_2\text{P}_2\text{Se}_6]_n^{2n-}$ chain.

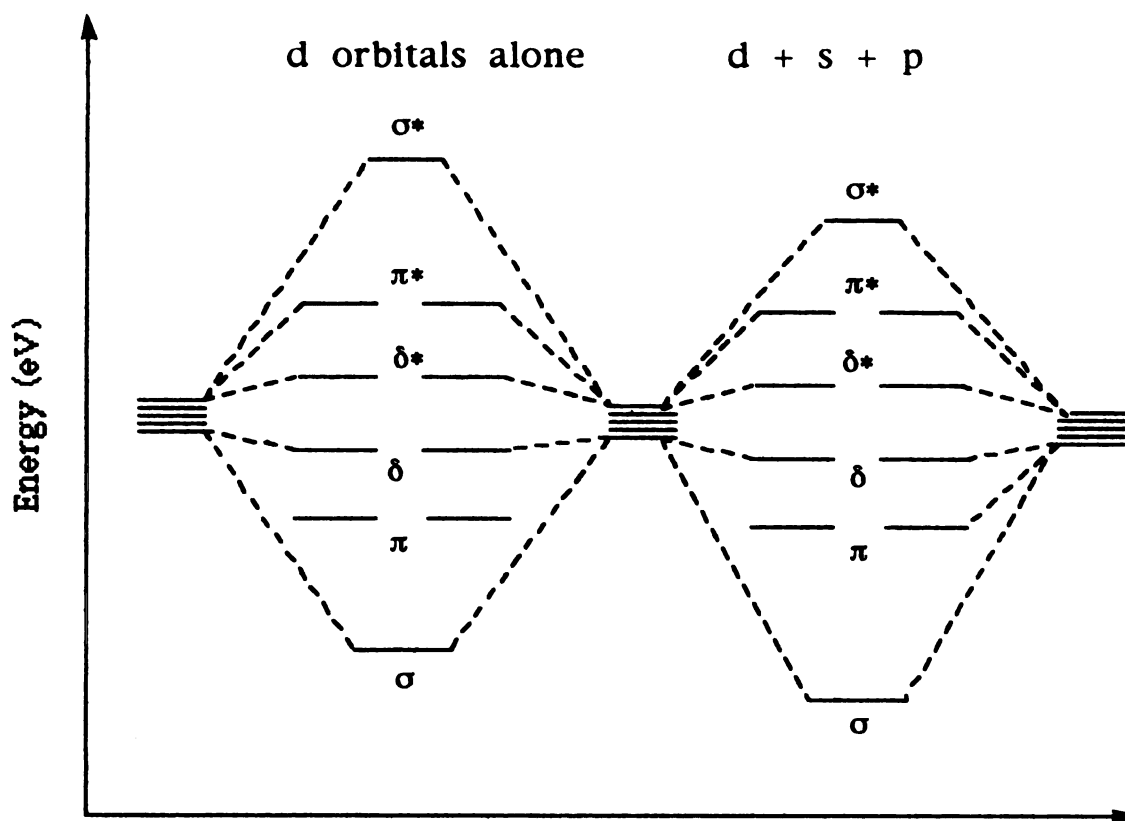


Figure 6-10: Energy levels of the d block of Cu_2^{2+} at a separation of 2.58 Å. Mixing of filled d orbitals with empty s and p orbitals results in a lowering of the antibonding (σ^*) and bonding (σ) energy levels which gives rise to a net bonding interaction. Adapted from reference 26.

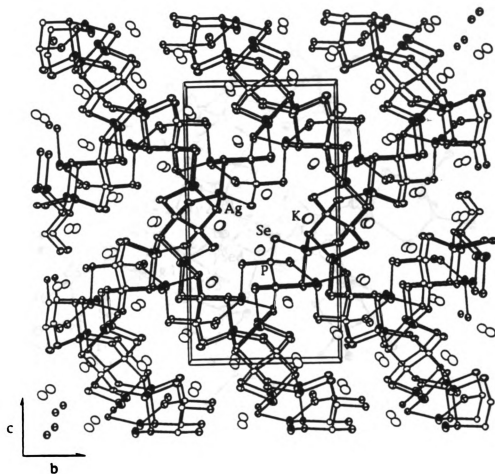


Figure 6-11: Packing diagram of the three-dimensional structure of $K_2Ag_2P_2Se_6$ viewed down the $[100]$ direction with labeling.

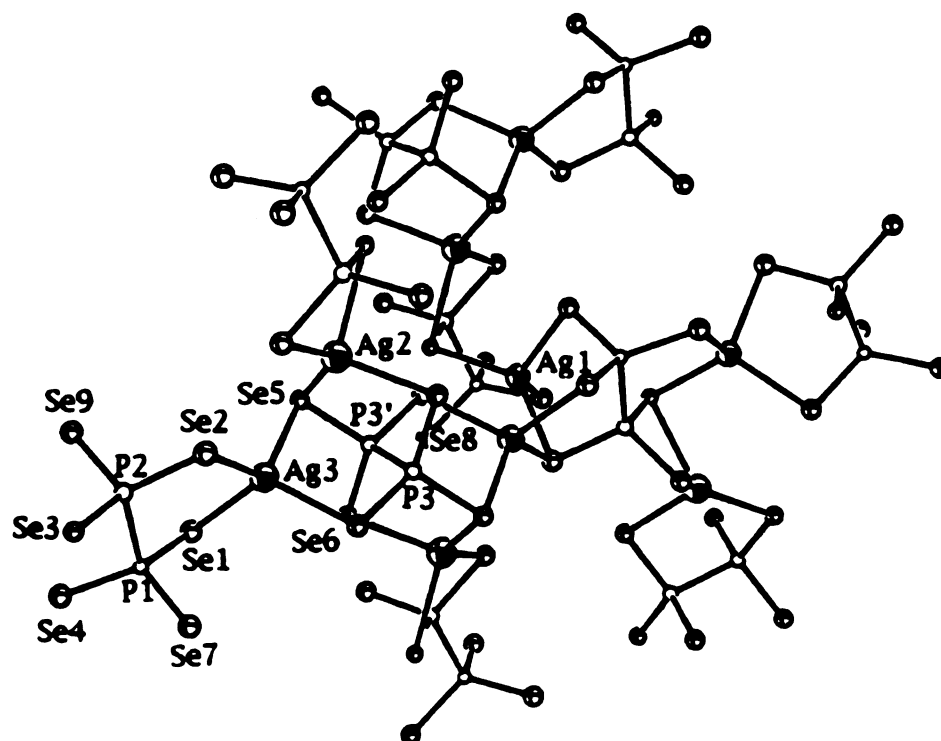


Figure 6-12: ORTEP representation of a fragment of the $[\text{Ag}_2\text{P}_2\text{Se}_6]^{2-}$ anion showing the local AgSe_4 coordination environment with labeling.

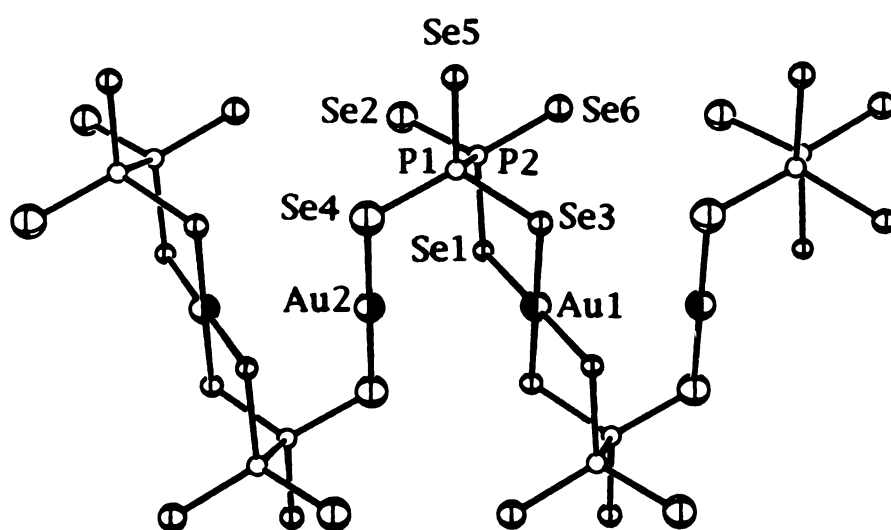


Figure 6-13: A single $[\text{Au}_2(\text{P}_2\text{Se}_6)_2]_n^{2n-}$ chain.

Table 6-18. Selected Distances (Å) and Angles (°) for Cs₂Cu₂P₂Se₆ with Standard Deviations in Parentheses.^a

Cu(1)-Cu(1')	2.761(5)	Se(1)-Cu(1)-Se(4)	125.7(1)
Cu(2)-Cu(2')	2.731(5)	Se(1)-Cu(1)-Se(6)	110.6(1)
		Se(4)-Cu(1)-Se(6)	121.3(1)
Cu(1)-Se(1)	2.400(3)	Se(2)-Cu(2)-Se(3)	123.7(1)
Cu(1)-Se(4)	2.373(3)	Se(2)-Cu(2)-Se(5)	122.5(1)
Cu(1)-Se(6)	2.416(3)	Se(3)-Cu(2)-Se(5)	110.6(1)
Cu(2)-Se(2)	2.375(3)	Se(1)-Cu(1)-Cu(1')	87.3(1)
Cu(2)-Se(3)	2.417(4)	Se(5)-Cu(2)-Cu(2')	84.0(1)
Cu(2)-Se(5)	2.407(4)		
Cu-Se (ave.)	2.40(2)	Se(1)-P(1)-Se(3)	112.6(2)
		Se(1)-P(1)-Se(4)	114.1(2)
P(1)-P(2)	2.260(6)	Se(3)-P(1)-Se(4)	111.4(2)
		Se(2)-P(2)-Se(5)	114.1(2)
P(1)-Se(1)	2.186(4)	Se(2)-P(2)-Se(6)	110.4(2)
P(1)-Se(3)	2.177(4)	Se(5)-P(2)-Se(6)	113.3(3)
P(1)-Se(4)	2.202(5)	Se-P-Se (ave.)	113(2)
P(2)-Se(2)	2.186(4)		
P(2)-Se(5)	2.194(5)		
P(2)-Se(6)	2.187(4)		
P-Se (ave.)	2.189(8)		
Cs(1)-Se(1)	3.733(2)	Cs(2)-Se(1)	3.766(2)
Cs(1)-Se(2)	3.725(2)	Cs(2)-Se(3)	3.766(2)
Cs(1)-Se(2')	3.847(3)	Cs(2)-Se(3')	3.711(3)
Cs(1)-Se(4)	3.861(2)	Cs(2)-Se(4)	3.694(2)
Cs(1)-Se(5)	3.948(2)	Cs(2)-Se(4')	3.780(2)
Cs(1)-Se(5')	3.797(3)	Cs(2)-Se(5)	3.877(2)
Cs(1)-Se(6)	3.887(2)	Cs(2)-Se(6)	3.733(2)
Cs(1)-Se(6')	3.759(2)	Cs-Se (ave.)	3.80(8)
Cs(1)-Se(6'')	3.967(2)		

^aThe estimated standard deviations in the mean bond lengths and the mean bond angles are calculated by the equations $\sigma_l = \{\sum_n (l_n - l)^2 / n(n-1)\}^{1/2}$, where l_n is the length (or angle) of the n th bond, l the mean length (or angle), and n the number of bonds.

Table 6-19. Selected Distances (Å) and Angles (°) for Cs₂Ag₂P₂Se₆ with Standard Deviations in Parentheses.^a

Ag-Ag'	2.919(3)	Se(1)-Ag-Se(2)	105.55(7)
		Se(1)-Ag-Se(3)	132.04(9)
Ag-Se(1)	2.595(2)	Se(2)-Ag-Se(3)	121.77(8)
Ag-Se(2)	2.641(3)	Ag-Ag'-Se(2)	94.05(9)
Ag-Se(3)	2.545(2)	Ag-Ag'-Se(3)	95.72(8)
Ag-Se (ave.)	2.59(5)		
P-Se(1)	2.183(5)	Se(1)-P-Se(2)	110.1(2)
P-Se(2)	2.182(4)	Se(1)-P-Se(3)	115.7(2)
P-Se(3)	2.205(4)	Se(2)-P-Se(3)	109.9(2)
P-Se (ave.)	2.19(1)	Se(1)-P-P'	106.5(3)
P-P'	2.285(8)		
Cs-Se(1)	3.788(2)	Cs-Se(2'')	3.939(2)
Cs-Se(1')	3.819(3)	Cs-Se(3)	3.790(2)
Cs-Se(1'')	4.091(3)	Cs-Se(3')	3.663(3)
Cs-Se(2)	3.720(2)	Cs-Se(3'')	3.725(2)
Cs-Se(2')	3.963(3)	Cs-Se (ave.)	3.8(1)

^aThe estimated standard deviations in the mean bond lengths and the mean bond angles are calculated by the equations $\sigma_l = \{\Sigma_n (l_n - l)^2 / n(n-1)\}^{1/2}$, where l_n is the length (or angle) of the nth bond, l the mean length (or angle), and n the number of bonds.

Table 6-20. Selected Distances (Å) and Angles (°) for K₂Ag₂P₂Se₆ with Standard Deviations in Parentheses.^a

Ag(1)-Ag(2)	3.869(4)	K(1)-Se(4)	3.702(8)
Ag(1)-Ag(3)	3.715(4)	K(1)-Se(6)	3.454(7)
		K(1)-Se(7)	3.487(7)
Ag(1)-Se(2)	2.662(4)	K(1)-Se(8)	3.379(7)
Ag(1)-Se(3)	2.615(4)	K(1)-Se(9)	3.614(8)
Ag(1)-Se(4)	2.786(4)	K(1)-Se(9')	3.360(8)
Ag(1)-Se(7)	2.743(4)	K(2)-Se(4)	3.376(7)
Ag(2)-Se(3)	2.797(4)	K(2)-Se(5)	3.361(7)
Ag(2)-Se(3)	2.578(4)	K(2)-Se(6)	3.661(8)
Ag(2)-Se(3)	2.678(4)	K(2)-Se(6')	3.384(7)
Ag(2)-Se(3)	2.783(4)	K(2)-Se(7)	3.613(8)
Ag(3)-Se(1)	2.653(4)	K(2)-Se(8)	3.586(7)
Ag(3)-Se(1)	2.633(4)	K(3)-Se(4)	3.676(8)
Ag(3)-Se(1)	2.662(4)	K(3)-Se(5)	3.867(9)
Ag(3)-Se(1)	2.695(4)	K(3)-Se(7)	3.423(8)
Ag-Se (ave.)	2.69(7)	K(3)-Se(8)	3.499(9)
		K(3)-Se(9)	3.351(8)
P(1)-P(2)	2.278(8)	K-Se (ave.)	3.5(2)
P(3)-P(3')	2.31(1)		
P(1)-Se(1)	2.188(7)		
P(1)-Se(4)	2.178(8)		
P(1)-Se(7)	2.191(7)		
P(2)-Se(2)	2.186(8)		
P(2)-Se(3)	2.213(7)		
P(2)-Se(9)	2.180(7)		
P(3)-Se(5)	2.205(7)		
P(3)-Se(6)	2.192(7)		
P(3)-Se(8)	2.165(7)	Se(1)-P(1)-Se(4)	113.4(3)
P-Se (ave.)	2.19(1)	Se(1)-P(1)-Se(7)	111.7(3)
		Se(4)-P(1)-Se(7)	115.0(3)
Se(2)-Ag(1)-Se(3)	130.5(1)	Se(2)-P(2)-Se(3)	110.5(3)
Se(2)-Ag(1)-Se(4)	95.1(1)	Se(2)-P(2)-Se(9)	111.1(3)
Se(3)-Ag(2)-Se(5)	130.4(1)	Se(3)-P(2)-Se(9)	111.1(3)
Se(3)-Ag(2)-Se(9)	80.9(1)	Se(5)-P(3)-Se(6)	109.7(3)
Se(1)-Ag(3)-Se(6)	122.1(1)	Se(5)-P(3)-Se(8)	111.5(3)
Se(1)-Ag(3)-Se(2)	102.0(2)	Se(6)-P(3)-Se(8)	113.9(3)

^aThe estimated standard deviations in the mean bond lengths and the mean bond angles are calculated by the equations $\sigma_l = \{\sum_n (l_n - l)^2 / n(n-1)\}^{1/2}$, where l_n is the length (or angle) of the n th bond, l the mean length (or angle), and n the number of bonds.

Table 6-21. Selected Distances (Å) and Angles (°) for $K_4Au_2(P_2Se_6)_2$ with Standard Deviations in Parentheses.^a

Au(1)-Au(2)	3.636(3)	Se(1)-Au(1)-Se(1')	180.00
		Se(1)-Au(1)-Se(3)	80.4(2)
Au(1)-Se(1) x 2	2.484(6)	Se(1)-Au(1)-Se(3')	99.6(2)
Au(1)-Se(3) x 2	2.493(5)	Se(3)-Au(1)-Se(3')	180.00
Au(2)-Se(4) x 2	2.302(7)	Se(4)-Au(2)-Se(4')	180.00
P(1)-Se(3)	2.21(1)	Se(3)-P(1)-Se(4)	114.0(7)
P(1)-Se(4)	2.18(1)	Se(3)-P(1)-Se(5)	109.0(6)
P(1)-Se(5)	2.14(1)	Se(4)-P(1)-Se(5)	112.9(6)
P(2)-Se(1)	2.25(1)	Se(1)-P(2)-Se(2)	111.7(6)
P(2)-Se(2)	2.14(1)	Se(1)-P(2)-Se(6)	109.7(6)
P(2)-Se(6)	2.14(1)	Se(2)-P(2)-Se(6)	113.7(7)
P-Se (ave.)	2.18(5)	Se-P-Se (ave.)	112(2)
P(1)-P(2)	2.25(2)		
K(1)-Se(2)	3.51(2)	K(2)-Se(1)	3.55(2)
K(1)-Se(2')	3.46(2)	K(2)-Se(1')	3.87(2)
K(1)-Se(2'')	3.49(2)	K(2)-Se(2)	3.46(2)
K(1)-Se(4)	3.56(2)	K(2)-Se(2')	3.49(2)
K(1)-Se(5)	3.72(2)	K(2)-Se(5)	3.68(2)
K(1)-Se(5')	3.49(2)	K(2)-Se(6)	3.46(2)
K(1)-Se(5'')	3.57(2)	K(2)-Se(6')	3.35(2)
K(1)-Se(6)	3.38(2)	K(2)-Se (ave.)	3.6(2)
K(1)-Se (ave.)	3.5(1)		
		K(2)-Au(2)	3.21(2) x 2

^aThe estimated standard deviations in the mean bond lengths and the mean bond angles are calculated by the equations $\sigma_l = \{\sum_n (l_n - l)^2 / n(n-1)\}^{1/2}$, where l_n is the length (or angle) of the n th bond, l the mean length (or angle), and n the number of bonds.

3.3 Magnetic Susceptibility. The temperature dependent magnetic susceptibility was collected for $\text{K}_2\text{MnP}_2\text{Se}_6$ (I), $\text{Rb}_2\text{MnP}_2\text{Se}_6$ (I I), $\text{Cs}_2\text{MnP}_2\text{Se}_6$ (I I I), and $\text{K}_2\text{FeP}_2\text{Se}_6$ (I V). All compounds are paramagnetic above ~ 30 K and obey Curie-Weiss law. Typical susceptibility plots at 2000 G are shown in Figure 6-14 for (I I I) and (I V). Table 6-22 lists the magnetic parameters for (I), (I I), (I I I) and (I V). The calculated moments are 5.8, 5.6, 6.0 and 5.4 BM for (I-I V), respectively. These values indicate that the M^{2+} ions in these compounds are in high-spin configurations and agree well with the calculated spin-only moments ($\mu_{\text{eff}} = [4S(S + 1)]^{1/2}$). For comparison, the magnetic moments for $\text{Mn}_2\text{P}_2\text{Se}_6$ and $\text{Fe}_2\text{P}_2\text{Se}_6$ are 6.1 and 5.1 BM, respectively.⁴¹ Below 30 K, the susceptibility show maxima indicating antiferromagnetic coupling below this temperature. Since it is well-known that exchange interactions are very sensitive to small changes in the bond length and angles of the bridging system,⁴² we hoped to observe such effects in the $\text{A}_2\text{MnP}_2\text{Se}_6$ family of compounds. The effect of the small reduction in the M...M distance and slight reorientation of the $[\text{P}_2\text{Se}_6]^{4-}$ ligand upon moving from $\text{K}_2\text{MnP}_2\text{Se}_6$ (Mn-Mn=6.5349(9) Å) to $\text{Cs}_2\text{MnP}_2\text{Se}_6$ (Mn-Mn=6.476(2) Å) is not reflected in the magnetic data. The Néel temperatures (T_N) for $\text{A}_2\text{MnP}_2\text{Se}_6$ vary between 10 and 13 K with Weiss constants (θ) in the -14 to -25 K range. Since the M-M distances are large (> 6.4 Å), it is assumed that the weak antiferromagnetic interactions proceed via a superexchange pathway through the bridging $[\text{P}_2\text{Se}_6]^{4-}$ ligand. A stronger antiferromagnetic interaction is observed in $\text{K}_2\text{FeP}_2\text{Se}_6$ with higher T_N and θ values of 20 K and -43 K. A similar increase in the

interaction upon moving from Mn to Fe is also observed for the strongly antiferromagnetic, two-dimensional $M_2P_2O_6$ ($M=Mn, Fe, Ni$) compounds.⁴¹

The temperature dependent magnetic susceptibility of the solid solution compound, $K_2Mn_{0.5}Fe_{0.5}P_2Se_6$, was performed (at 2000 G) to investigate the possibility of unusual magnetic behavior due to incomplete cancellation of magnetic moments. The magnetic parameters ($T_N=10$ K, $\theta=-32$ K) are comparable to those observed for the $A_2MP_2Se_6$ compounds shown above.

Table 6-22. Magnetic parameters for (I), (I I), (I I I), and (I V).

Formula	μ_{eff} (BM)	θ (K)	T_N (K)
$K_2MnP_2Se_6$	5.8	-25	10
$Rb_2MnP_2Se_6$	5.6	-18	12
$Cs_2MnP_2Se_6$	6.0	-14	13
$K_2FeP_2Se_6$	5.4	-43	20

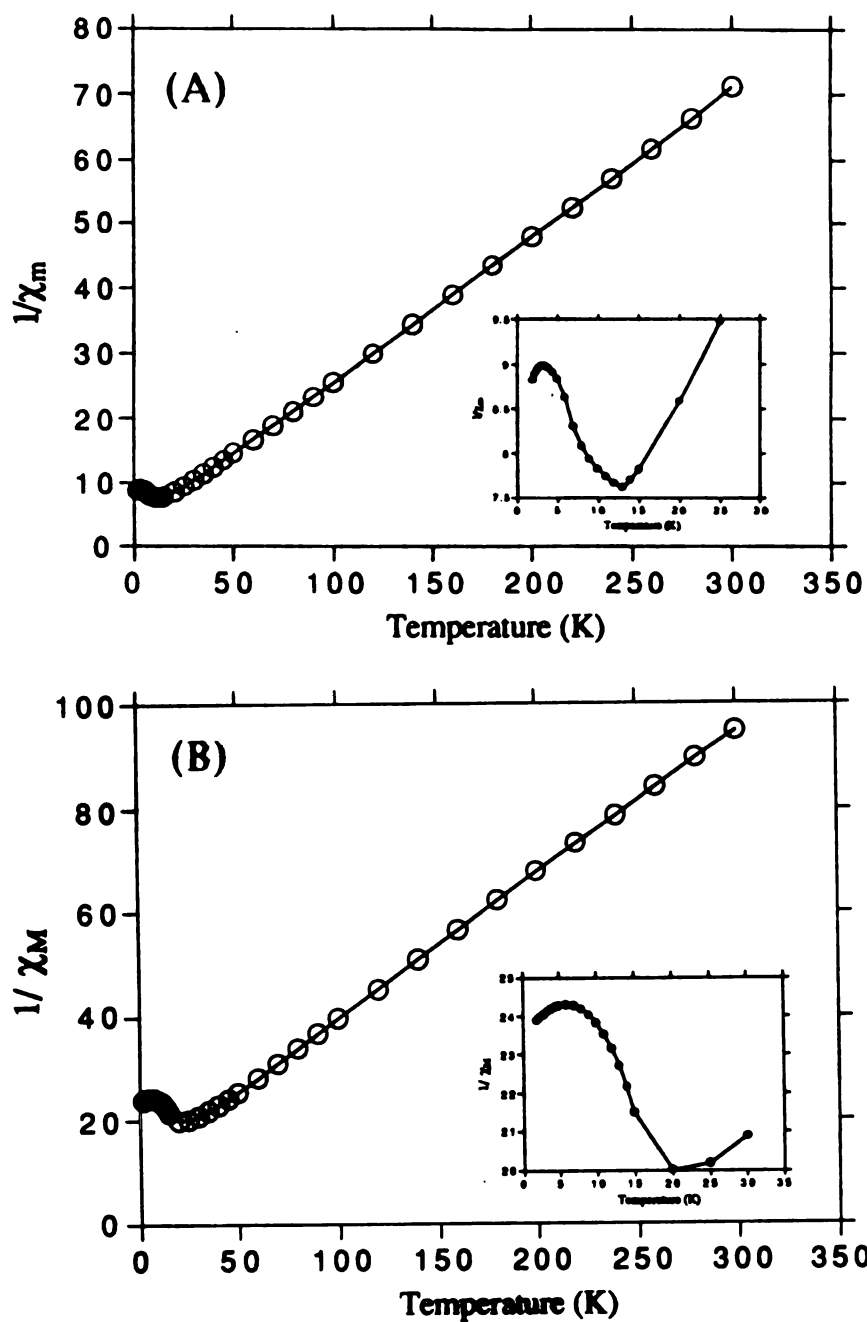


Figure 6-14: Plots of $1/\chi_M$ vs. T taken at 2000 G of applied field over 2-300 K for: (A) $\text{Cs}_2\text{Mn}_2\text{P}_2\text{Se}_6$ and (B) $\text{K}_2\text{FeP}_2\text{Se}_6$. The inset graphs show expanded views of the region 2-30 K.

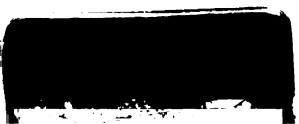
3.4. Conclusions

The general family of one-dimensional $A_2M(P_2Se_6)$ compounds derives from the well known two-dimensional $M_2P_2Se_6$ family by incorporation of $A_4P_2Se_6$. The synthesis of new quaternary selenophosphates in molten $A_x[P_ySe_z]$ salts provides a useful and broad synthetic methodology that can be applied to main group elements as well as transition metals. The $A_x[P_ySe_z]$ fluxes provide reliably $[P_2Se_6]^{4-}$ units that display remarkable versatility in terms of ligand binding to metals. The high negative charge of these units makes them hard to stabilize in conventional aqueous or organic solvents. It would be interesting to see whether changes in the nominal stoichiometry of these fluxes can result in other $[P_xSe_y]^n-$ units as well. For example, by increasing the basicity of the flux, the $[PSe_4]^{3-}$ ligand can be stabilized in $CsPbPSe_4$.¹⁹

List of References

1. McCarthy, T. J.; Kanatzidis, M. G., *Chem. Mater.* 1993, 5, 1061-1063.
2. McCarthy, T. J.; Kanatzidis, M. G. accepted by *J. Chem. Soc., Chem. Commun.*
3. McCarthy, T. J.; Hogan, T.; Kannewurf, C. R.; Kanatzidis, M. G. submitted for publication.
4. (a) Klingen, W.; Eulenberger, G.; Hahn, H. *Z. Anorg. Allg. Chem.*, 1973, 401, 97-112. (b) Toffoli, P.; Khodadad, P.; Rodier, N. *Acta Cryst., Sect. B*, 1978, 34, 1779-1781. (c) Klingen, W.; Ott, R.; Hahn, H. *Z. Anorg. Allg. Chem.*, 1973, 396, 271-278. (d) Jandali, M. Z.; Eulenberger, G.; Hahn, H. *Z. Anorg. Allg. Chem.*, 1978, 447, 105-118.
5. (a) Ouvrard, G.; Brec, R.; Rouxel, J. *Mater. Res. Bull.*, 1985, 20, 1181-1189. (b) Lee, S.; Colombet, P.; Ouvrard, G.; Brec, R. *Inorg. Chem.*, 1988, 27, 1291-1294. (c) Lee, S.; Colombet, P.; Ouvrard, G.; Brec, R. *Mater. Res. Bull.*, 1986, 21, 917-928. (d) Durand, E.; Ouvrard, G.; Evain, M.; Brec, R. *Inorg. Chem.*, 1990, 29, 4916-4920.
6. (a) Odile, J.-P.; Steger, J. J.; Wold, A. *Inorg. Chem.* 1975, 14, 2400-2402. (b) Taylor, B. E.; Steger, J. J.; Wold, A.; Kostiner, E. *Inorg. Chem.* 1974, 13, 2719-2421. (c) Taylor, B. E.; Steger, J. J.; Wold, A. *J. Solid State Chem.* 1973, 7, 461-467.
7. (a) Lagadic, I.; Leautic, A.; Clement, R. *J. Chem. Soc., Chem. Commun.* 1992, 1396-1397. (b) Clement, R.; Audiere, J.-P.; Renard, J.-P. *Rev. Chim. Miner.* 1982, 19, 560-571. (c) Michalowicz, A.; Clement R. *Inorg. Chem.* 1982, 21, 3872-3877. (d) Joy, P. A.; Vasudevan, S. *J. Am. Chem. Soc.*, 1981, 114, 7792-7801.
8. Thompson, A. H.; Whittingham, M. S. *U. S. Patent 4,049,879* 1977. (b) Brec, R.; Le Mehaute, A. *Fr. Patents 7,704,519* 1977.
9. (a) Pfeiff, R.; Kniep, R. *J. Alloys and Compounds*, 1992, 186, 111-133. (b) Evain, M.; Boucher, F.; Brec, R.; Mathey, Y. *J. Solid State Chem.* 1991, 90, 8-16. (c) Lee, S.; Colombet, P.; Ouvrard, G.; Brec, R. *Mat. Res. Bull.*, 1986, 21, 917-928. (d) Leblanc, A.; Ouili, Z.; Colombet, P. *Mat. Res. Bull.*, 1985, 20, 947-954.
10. Lacroix, P. G.; Clement, R.; Nakatani, K.; Zyss, J.; Ledoux, I. *Science*, 1994, 263, 658-660.
11. Garin, J.; Parthe, E. *Acta Crystallogr.*, 1972, B28, 3672-3674.
12. Fritz, I. J.; Isaacs, T. J.; Gottlieb, M.; Morosin, B. *Solid State Commun.*, 1978, 27, 535.
13. (a) O'Neal, S. C.; Pennington, W. T.; Kolis, J. W. *Angew. Chem. Int. Ed. Engl.* 1990, 29, 1486-1488. (b) Zhao, J.; Pennington, W. T.; Kolis, J. W. *J. Chem. Soc., Chem. Commun.* 1992, 265-266.
14. Feher, F. *Handbuch der Präparativen Anorganischen Chemie*: Brauer, G., Ed.; Ferdinand Enke: Stuttgart, Germany, 1954; pp. 280-281.
15. CERius: Molecular Simulation Software, Version 3.0, (1992), Cambridge Molecular Design, Waltham, MA 02154.
16. G. M. Sheldrick, In *Crystallographic Computing 3*; Sheldrick, G. M., Kruger, C., Doddard, R., Eds.; Oxford University Press: Oxford, England, 1985; pp 175-189.
17. TEXSAN: Single Crystal Structure Analysis Software, Version 5.0, (1981). Molecular Structure Corporation, The Woodlands, TX 77381.

18. Walker, N.; Stuart, D. *Acta Cryst.*, 1983, A39, 158-166.
19. McCarthy, T. J.; Chondroudis, K.; Kanatzidis, M. G. work in progress.
20. Mathey, Y.; Clement, R.; Sourisseau, C.; Lucazeau, G. *Inorg. Chem.*, 1980, 19, 2773-2779.
21. (a) Dance, I. G. *Polyhedron* 1983, 2, 1031-1043. (b) Hollander, F. J.; Coucouvanis, D. *J. Am. Chem. Soc.* 1977, 99, 6268-6279. (c) Chadha, R.; Kumar, R.; Tuck, D. G. *J. Chem. Soc., Chem. Commun.* 1986, 188-189. (d) Coucouvanis, D.; Murphy, C. N.; Kanodia, S. K. *Inorg. Chem.* 1980, 19, 2993-2998.
22. Burschka, C.; Bronger, W. *Z. Naturforsch.* 1977, 32B, 11-14.
23. Burschka, C. *Z. Naturforsch.* 1979, 34B, 675-677.
24. Schils, H.; Bronger, W. *Z. Anorg. Allg. Chem.* 1979, 456, 187-193.
25. Savelberg, G.; Schäfer, H. *Z. Naturforsch.* 1978, 33B, 711-713.
26. (a) Merz, K. M.; Hoffmann, R. *Inorg. Chem.* 1988, 27, 2120-2127. (b) Mehrotra, P. K.; Hoffmann, R. *Inorg. Chem.* 1978, 17, 2187-2189.
27. (a) Cotton, F. A.; Feng, X.; Matusz, M.; Poli, R. *J. Am. Chem. Soc.* 1988, 110, 7077-7083. (b) Lee, S. W.; Trogler, W. C. *Inorg. Chem.* 1990, 29, 1659-1662.
28. Müller, U.; Ha-Eierdanz, M.-L.; Kräuter, G.; Dehnicke, K. *Z. Naturforsch.* 1990, 45b, 1128-1132.
29. Cusick, J.; Scudder, M. L.; Craig, D. C.; Dance, I. G. *Polyhedron*, 1989, 8, 1139-1141.
30. Janzen, M. *Angew. Chem. Int. Ed. Engl.* 1987, 26, 1098-1110.
31. (a) Huang, S.-P.; Kanatzidis, M. G. *Inorg. Chem.* 1991, 30, 1455-1466. (b) Kanatzidis, M. G.; Huang, S.-P. *J. Am. Chem. Soc.* 1989, 111, 760-761.
32. Colombet, P.; Leblanc, A.; Danot, M.; Rouxel, J. *J. Solid State Chem.* 1982, 41, 174-184.
33. Maisonneuve, V.; Cajipe, V. B.; Payen, C. *Chem. Mater.* 1993, 5, 758-760.
34. Mathey, Y.; Michalowicz, A.; Toffoli, P.; Vlais, G. *Inorg. Chem.* 1984, 23, 897-902.
35. Mathey, Y.; Mercier, H.; Michalowicz, A.; Leblanc, A. *J. Phys. Chem. Solids*, 1985, 46, 1025-1029.
36. Toffoli, P.; Khodadad, P.; Rodier, N. *Acta Cryst.* 1978, B34, 1779-1781.
37. Rabenau, A.; Schulz, H. *J. Less-Common Metals*, 1976, 48, 89-101.
38. Kanatzidis, M. G.; Huang, S.-P. *Phosphorous and Sulfur*, 1992, 64, 153-160.
39. Haushalter, R. C. *Angew. Chem. Int. Ed. Engl.*, 1985, 24, 432-433.
40. Kanatzidis, M. G.; Huang, S.-P. *Angew. Chem. Int. Ed. Engl.*, 1992, 31, 787-789.
41. (a) Brec, R.; Schleich, D. M.; Ouvrard, G.; Louisy, A.; Rouxel, J. *Inorg. Chem.*, 1979, 18, 1814-1818. (b) Odile, J.-P.; Steger, J. J.; Wold, A. *Inorg. Chem.* 1975, 14, 2400-2402. (c) Taylor, B. E.; Steger, J. J.; Wold, A.; Kostiner, E. *Inorg. Chem.* 1974, 13, 2719-2421. (d) Taylor, B. E.; Steger, J. J.; Wold, A. *J. Solid State Chem.* 1973, 7, 461-467.
42. Crawford, V. H.; Richardson, H. W.; Wasson, J. R.; Hodgson, D. J.; Hatfield, W. E. *Inorg. Chem.*, 1976, 15, 2107-2110.



MICHIGAN STATE UNIVERSITY LIBRARIES



3 1293 03145 3297